Research on Engineering Structures and Materials

www.jresm.org

Volume 10 Issue 2 June 2024

P-ISSN: 2148-9807 E-ISSN: 2149-4088

Research Group

The International Journal of **Research on Engineering Structures and Materials (RESM**) is a peer-reviewed open access journal (p-ISSN: 2148-9807; o-ISSN: 2149-4088) published by MIM Research Group. It is published in February, June, September, and December.

The main objective of RESM is to provide an International academic platform for researchers to share scientific results related to all aspects of mechanical, civil, and material engineering areas.

RESM aims the publication of original research articles, reviews, short communications technical reports, and letters to the editor on the latest developments in the related fields.

All expenditures for the publication of the manuscripts are most kindly reimbursed by *MIM Research Group*. Thus, authors do not need to pay for publishing their studies in the journal.

The scope of the journal covers (but not limited to) behavior of structures, machines and mechanical systems, vibration, impact loadings and structural dynamics, mechanics of materials (elasticity, plasticity, fracture mechanics), material science (structure and properties of concrete, metals, ceramics, composites, plastics, wood, etc.,), nano-materials performances of new and existing buildings and other structural systems, design of buildings and other structural systems, seismic behavior of buildings and other structural systems, repair and strengthening of structural systems, case studies and failure of structural systems, safety and reliability in structural and material engineering, use of new and innovative materials and techniques in energy systems and mechanical aspects of biological systems (biomechanics and biomimetics).

The topics covered in JRESM include:

- Structural Engineering
- Mechanical Engineering
- Material Engineering
- Earthquake Engineering
- Nano-technology
- Energy Systems (Focus on Renewable)
- Biomechanics and Biomimetics
- Environment (Material and Engineering System Related Issues)
- Computer Engineering and Data Science (Material and Engineering System-Related Issues)

Abstracting and Indexing
Please visit http://www.jresm.org for more information.

Graphics and Design

Mehmet Yılmaz myilmaz@jresm.net

RESEARCH on ENGINEERING STRUCTURES & MATERIALS

Research Group

RESEARCH on ENGINEERING STRUCTURES & MATERIALS

Editorial Board

Editorial Office

Publishing Manager		
Mehmet Yılmaz	MIM Research Group	Türkiye
Language Editors		
Gaye Kuru	Uşak University	Türkiye
Mete Çal	MIM Research Group	Türkiye

Advisory Board		
Name and Surname	**Affilation**	**Country**
Waleed A Abbas	University of Technology	Iraq
Muna Khethier Abbass	University of Technology-Iraq	Iraq
Abdul Razak Abdul Karim	University Malaysia Sarawak	Malaysia
Yunika Kirana Abdul Khalik	UNIMAS	India
Mohammad Abdul Mannan	University Malaysia Sarawa	Malaysia
Ahmed Abdullahi	Higher Colleges of Technology	Dubai
Mehmet Ada	Usak University	Türkiye
Mohammad Afrazi	Tarbiat Modares University	Iran
B. Akbari	University of Tehran	Iran
Mustafa Akpolat	Munzur University	Türkiye
Ali Özhan Akyüz	Burdur Mehmet Akif Ersoy University	Türkiye
Waleed Khalid Al-azzawi	Al-Farahidi University	Iraq
Tawalo Ali	Università degli di Napoli Federico II	Italy
Thaer Alrudaini	University of Basrah	Iraq
Raheem Al-Sabur	University of Basrah	Iraq
Denis Anders	Cologne University of Applied Sciences	Germany
Gabriel Arce	Louisiana State University	USA
Nur Farhayu Ariffin	University Malaysia Pahang	Malaysia
E. Arunraj	Karunya Institute of Technology and Sciences	India
Hidayati Asrah	University Malaysia Sabah	Malaysia
Siva Avudaiappan	University of Santiago	Chile
Samuel Awe	Automotive Components Floby AB	Sweden
Chioma Awodiji	University Of Port-Harcourt	Nigeria
Kemal Aydın	Gümüşhane University	Türkiye
Ameer Baiee	University of Babylon	Iraq
Carlos Eduardo Tino Balestra	Western Paraná State University	Brazil

Mohammad Saleh Baradaran	Islamic Azad University of Mashhad	Iran
Peyman Beiranvand	Razi University	Iran
Hadj Bekki	University Ibn Khaldoun of Tiaret	Algeria
Abdelhalim Bensaada	University of Yahia Fares of Medea	Algeria
Mohammed Bentahar	Tahar Moulay University of Saida	Algeria
H. Alperen Bulut	Erzincan University	Türkiye
Esitake Cebolina		Iraq
Halit Cetiner	Isparta University	Türkiye
Kamel Chaoui	Badji Mokhtar University	Algeria
Venkatesh Chava	CVR College of Engineering	India
Maheswaran Chellapandian	Mepco Schlenk Engineering College	India
Xinrong Chengil	Tongji University	China
Sonali Sri Durga Chereddy	CVR College of Engineering	India
Anna Chiaradonna	DICEAA, University of L'Aquila	Italy
Ajay Chourasia	Central Building Research Institute	India
Daniel Cruze	Mohamed Sathak A J College of Engineering	India
Zhaoyan Cui	Nanjing Forestry University	China
Ashish Kumar Dash	Indian Institute of Technology	Indian
Cengiz Görkem Dengiz	Ondokuz Mayıs University	Türkiye
Arindam Dey	Indian Institute of Technology Guwahati	India
Marwan Effendy	Universitas Muhammadiyah Surakarta	Indonesia
Ashraf El-Shamy	National Research Centre	Egypt
Ali Ercetin	Bandırma Onyedi Eylül University	Türkiye
Kemal Ermis	Sakarya University of Applied Science	Türkiye
Uchechi Eziefula	University of Agriculture and Environmental Sciences, Umuagwo	Nigeria
Mingjing Fang	Wuhan University of Technology	China
Christopher Fapohunda	Federal University Oye-Ekiti	Nigeria
Abdelkader Fidjah	University of Djelfa	Algeria
Saeid Foroughi	Konya Technical University	Türkiye

Sharanabasava V. Ganachari	KLE Technological University	India
Zhong Ge	Yunnan University	China
Gökhan Gece	Bursa Teknik University	Türkiye
Mahesh Gopal	College of Engineering and Technology	Ethiopia
Chandrasekhar G L Gotur	Atria Institute of Technology	India
Mert Göksüzoğlu	SAMPA	Türkiye
Layachi Guelmine	B.B.A University	Algeria
Kadir Günaydın	GE Aviation, Marmara Technology Center	Türkiye
Endalkachew Mosisa Gutema	College of Engg and Tech	Ethiopia
Ahmet Güral	Gazi University	Türkiye
Hussein Hamada	University Malaysia Pahang	Malaysia
Taihao Han	Missouri University of Science and Technology	USA
Md. Zia Ul Haq	Panjab University	India
Md. Naimul Haque	East West University	India
Noor Sheena Herayani Harith	University Malaysia Sabah	Malaysia
Shrikant Harle	Ram Meghe College of Engineering and Management	India
Catur Harsito	Universitas Sebelas Maret	Indonesia
Muttaqin Hasan	Syiah Kuala University	Indonesia
Maboud Hekmatifar	Islamic Azad University	Iran
Mohammad Heydari Vini	Islamic Azad University	Iran
Qing Hong	Midwestern University	USA
Oleksii Hrechanyi	Zaporizhzhia National University	Ukraine
Md. Saiful Islam	University Putra Malaysia	Malaysia
Mehmet Zerrakki Işık	Batman University	Türkiye
Ghassan Subhi Jameel	University of Anbar	Iraq
Saifulnizan Jamian	University Tun Hussein Onn Malaysia	Malaysia
Girish M. Joshi	VIT University	India
Bhuria Jyothi		Nepal

Arunkumar K		India
Hossein Kabir	University of Illinois	USA
Pulitha Kavitri		Sri Lanka
Mehmet Kaya	Bozok University	Türkiye
Emre Kemer	Usak University	Türkiye
Pallavi Pradeep Khobragade	Rungta College of Engineering and Technology	India
Cemal Kochan	Dokuz Eylul University	Türkiye
Ali Koçak	Yıldız Technical University	Türkiye
Nitin Kumar	University of California Davis	USA
A. Suresh Kumar	Kalasalingam Academy of Research and Education	India
Sanjeev Kumar	Sanjeev Agrawal Global Educational University	India
Josephine Chang Hui Lai	University Malaysia Sarawak	Malaysia
Ravichandran M	K. Ramakrishnan College of Engineering	India
Uma Mageshwari		India
Lomesh Mahajan	Dr. Babasaheb Ambedkar Technological University	India
Natt Makul	Phranakhon Rajabhat University	Thailand
Anirban Mandal	National Institute of Technology	India
Tahara Ramadzan Md Kassim	International Islamic University Malaysia	Malaysia
Priyansha Mehra	Manipal University	India
Adamah Messan	Laboratoire Eco Matériaux de Construction (LEMC)	France
Suruchi Mishra		Malaysia
Khairul Anwar Mohamad Said	UNIMAS	Malaysia
Fadzli Mohamed Nazri	University Sains Malaysia	Malaysia
Mohsin Talib Mohammed	Kufa University	Iran
Noor Azline Mohd Nasir	University Putra Malaysia	Malaysia

Mohd Syahrul Hisyam Mohd Sani	University Teknologi MARA (UiTM) Cawangan Pahang	Malaysia
Mahmoud Mokhtar	Housing & Building National Research Center	Egypt
Alaa M. Morsy	Arab Academy for Science	Egypt
Rini Mulyani	Senior Lecturer at University Bung Hatta, Padang, Indonesia	Indonesia
Yasmin Murad	University of Jordan Amman	Jordan
Nahida Nazim Musayeva	Azerbaijan National Academy of Sciences	Azerbaijan
Arslan Mushtaq	NUST Institute of Civil Engineering	Pakistan
Maheswaran Muthiah	Kalasalingam Academy of Research and Education	India
Madeva Nagaral	Aircraft Research and Design Centre, Hindustan Aeronautics Limited	India
Salem Nawel	University of Gabes	Tunisia
Amarachi Nkwoada	Federal University of Technology Owerri	Nigeria
Mehrab Nodehi	University of California	USA
Samson Olalekan Odeyemi	Kwara State University	Nigeria
Hayri B. Ozmen	Usak University	Türkiye
İbrahim Öz	Ahi Evran University	Türkiye
Gurusamy P	Chennai Institute of Technology	India
Partheeban Pachaivannan	Chennai Institute of Technology	India
Chitaranjan Pany	Vikram Sarabhi Space Center	India
Rajesh Kumar Paswan	National Institute of Technology Jamshedpur	India
Vikas Patel	National Council for Cement and Building Materials	India
Hiteshkumar Patil	Dr. Babasaheb Ambedkar Technological University	India
Zühtü Onur Pehlivanlı	Kırıkkale University	Türkiye
Amin Moslemi Petrudi	Tehran University	Iran
Hemadri Prasad Raju	Sree Vidyanikethan Engineering College	India

Kalappa Prashantha	Adichunchanagiri University	India
Harris Priya	Kurukshetra University	India
Kavendra Pulkit		India
Helogi Putin		India
Ajibola Ibrahim Quadri	Federal University of Technology	Nigeria
Md. Mijanur Rahman	Military Institute of Science and Technology	Bangladesh
Azida Rashidi	UNIMAS	Malaysia
Badrinarayan Rath	Wollega University	Ethiopia
T.V. Reshma		India
Pier Paolo Rossi	University of Catania	Italy
Md Jalal Uddin Rumi	Military Institute of Science and Technology	Bangladesh
Abbasali Sadeghi	Islamic Azad University	Iran
Mohammed A. Sakr	Tanta University	Egypt
M.Helen Santhi	Vellore Institute of Technology	India
Tamer Saraçyakupoğlu	Istanbul Gelişim University	Türkiye
Divya Sharma	NITTTR Chandigarh	India
Fatheali Shilar	Jain College of Engineering Belgaum	India
Lenganji Simwanda	Stellenbosch University	South Africa
Brijesh Singh	National Council for Cement and Building Materials	India
Navdeep Singh	Dr B R Ambedkar National Inst. of Tech.	India
Rami Sldozian	University of Technology	Iraq
M. Somasundaram	PSG College of Technology	India
Rajkumar Srinivasan	SRM TRP Engineering College Irungalur	India
Rianti Dewi Sulamet-Ariobimo	Universitas Trisakti	Indonesia
Marthin Dody Josias Sumajouw	Sam Ratulangi University	Indonesia
Gülsah Susurluk	Beykent University	Türkiye
Jumrik Taipodia	NIT Arunachal Pradesh	India
Aykut Tamer	Imperial College London	England
Chan Sin Tan	University Malaysia Perlis	Malaysia
Hamide Tekeli	Süleyman Demirel University	Türkiye

Delsye Ching Lee Teo	Melbourne Polytechnic	Australia
Mehmet Topuz	Van Yüzüncü Yıl University	Türkiye
Tuan Norhayati Tuan Chik	University Tun Hussein Onn	Malaysia
Hasan Ulus	Selcuk University	Türkiye
Dilay Uncu	Celal Bayar University	Türkiye
Prem Kumar V	VIT Chennai	India
Harinadh Vemanaboina	Sri Venkateswara College of Engineering and Technology	India
Tadesse Gemeda Wakjira	University of British Columbia	Canada
Gustavo Bosel Wally	Federal University of Rio Grande do Sul	Brazil
Narong Wichapa	Kalasin University	Thailand
I Wiryadi	Mahasaraswati Denpasar University	Indonesia
Omid Aminoroayai Yamani	K. N. Toosi University of Technology	Iran
Guney Guven Yapici	Ozyegin University	Türkiye
Salih Hakan Yetgin	Kütahya Dumlupınar University	Türkiye
Sevim Yolcular Karaoğlu	Ege University	Türkiye
Ana Sakura Zainal Abidin	UNIMAS	Malaysia

In This Issue

Research on Engineering Structures & Materials
MIM Research Group Publications
P-ISSN: 2148-9807
E-ISSN: 2149-4088
http://www.jresm.org

ABSTRACTING / INDEXING

The international journal of Research on Engineering Structures and Materials (RESM) is currently Abstracted/Indexed by Asos Indeks, CiteFactor, Cosmos, CrossRef, Directory of Research Journal Indexing, Engineering Journals (ProQuest), EZB Electronic Journal Library, Global Impact Factor, Google Scholar, International Institute of Organized Research (I2OR), International Scientific Indexing (ISI), Materials Science & Engineering Database (ProQuest), Open Academic Journals Index, Publication Forum, Research BibleScientific Indexing Service, Root Indexing, Scopus, Ulakbim TR Index (Tubitak), Universal Impact Factor and under evaluation by many other respected indexes.

Check web site for current indexing info, www.jresm.org

Research on Engineering Structures & Materials
www.jresm.org
Research Group

Research Article

Dynamic response estimation of an equivalent single degree of freedom system using artificial neural network and nonlinear static procedure

Benbokhari Abdellatif[1, a, *], Chikh Benazouz [1, b], Mébarki Ahmed[2, 3, c]

[1]*Laboratoire des Travaux publics, ingénierie de Transport, environnement, Ecole Nationale Supérieure des Travaux Publics (ENSTP), Kouba, Algiers, Algeria*
[2]*University Gustave Eiffel, UPEC, CNRS, Laboratoire Modélisation et Simulation Multi Echelle (MSME 8208 UMR), Marne-la-Vallée, France*
[3]*Permanent Guest Professor within "High-Level Foreign Talents Programme" Grant, Nanjing Tech University, China*

Article Info

Article history:

Received 18 Aug 2023
Accepted 01 Nov 2023

Keywords:

Nonlinear time history analysis;
Nonlinear static analysis;
Artificial neural networks;
Seismic response prediction;
Machine learning

Abstract

This paper introduces an innovative methodology for predicting the maximum dynamic response of structures using capacity curves and artificial neural networks (ANNs). This novel approach offers a quick and accurate procedure for estimating target displacements, obviating the need for intricate supplementary computations. The method generates a comprehensive dataset encompassing the bilinear representation of a single-degree-of-freedom (SDOF) characteristic, with ground motion parameters as inputs and maximum inelastic displacement as the corresponding output. This dataset is used to train an ANN model, with meticulous calibration of hyperparameters to ensure optimal model performance and predictive precision. The findings of this study demonstrate that the ANN model showed operational efficacy in approximating dynamic displacements. It is notably revealed that the size of the dataset significantly influences the ANN's performance and predictive accuracy. Through comparative analysis with established methodologies such as the displacement coefficient method and the modified coefficient method adopted by the Federal Emergency Management Agency (FEMA), the ANN model emerges as a fast tool for precisely predicting the dynamic response of single-degree-of-freedom systems, particularly those characterized by vibration periods exceeding 0.5 seconds. Consequently, this research culminates in the assertion that the ANN, owing to its inherent simplicity and impressive precision, is an alternative tool for estimating target displacements.

1. Introduction

The seismic response of buildings represents an essential factor in evaluating existing buildings' performance and seismic vulnerability (1–3). This response is known by engineering demand parameters (EDPs) such as roof drift ratio, inter-story drift ratio, base shear, etc. (4,5). Usually, the analyst is interested in capturing the maximum EDPs to evaluate the highest damage level during an earthquake. This valuable information can be used to justify the need to retrofit, strengthen, or demolish the assessed building (6–8).

The Nonlinear time history analysis is the most reliable procedure that can capture the response of the building in terms of displacement, velocity, acceleration, and forces (9–11).

*Corresponding author: a.benbokhari@enstp.edu.dz
[a] orcid.org/0000-0002-0819-0641; [b] orcid.org/0000-0002-7228-9224; [c] orcid.org/0000-0002-3361-2594
DOI: http://dx.doi.org/10.17515/resm2023.40me0818rs

This method is based on solving a complicated equation of motion using numerical methodologies. However, the NL-THA is known for its complexity and the consumed processing time, which sometimes is inconvenient for performing a fast vulnerability and performance assessment. Therefore, the Nonlinear static procedure (NSP) was proposed as an alternative to the NL-THA due to its simplicity and less time-consuming feature (12–14). The NSP is based on finding the relationship between the base shear of the structure and the corresponding roof displacement, and the obtained curve is called the capacity curve. This curve illustrates the buildings' behavior when subjected to a static lateral loading that simulates the dynamic loading generated by the earthquake. It also shows the linear and nonlinear behavior of the building and the rupture point. The NSP is commonly used in performance analysis and performance-based design by calculating the performance point (15). It represents the intersection point between the capacity and the demand curves. The Federal Emergency Management Agency (FEMA) and the Applied Technology Council (ATC) (16) propose many procedures that allow us to estimate the performance point and the target displacement, which is the maximum displacement of a building. The Displacement coefficient method proposed by FEMA 356 (17) uses the four coefficients C0, C1, C2, and C3 to calculate the target displacement of a building. These coefficients are calculated and calibrated using empirical data. In FEMA-440 (18), they proposed to make some modifications to this method. C3, which considers the P-delta effect on displacement, was removed, and the formulas of C1 and C2 were changed. However, these two procedures sometimes provide a good and accurate estimation of the target displacement (19).

Artificial intelligence has recently become an exciting tool used in earthquake engineering, especially in seismic vulnerability assessment of existing buildings and damage prediction (20–28). Due to the simplicity and the high performance of the machine learning (ML) techniques, the analysis became much faster and less complex. Therefore, this work proposes a fast and accurate procedure that uses the NSP and artificial neural networks (ANNs) to estimate the maximum inelastic response of an SDOF system. The process is based on transforming the pushover curve into an idealized curve (transforming a multi-degree-of-freedom system (MDOF) into a single-degree-of-freedom system (SDOF)). Then, a dataset will be generated using the SDOF characteristics to perform NL-THA. The effective vibration period (Ti), the effective mass (M*), and the yielding force limit (fy) are the SDOF's characteristics. On the other hand, 31 artificial ground motions (AGM)parameters were selected to characterize the accelerogram of the earthquake: Peak Ground Acceleration, Peak ground velocity, Peak ground displacement, Arias intensity, Cumulative energy, Acceleration spectrum intensity, displacement spectrum intensity, cumulative absolute velocity, Uniform duration, predominant period, bracket duration, Housner intensity, Spectral acceleration, Spectral velocity, Spectral displacement, significant duration dominant frequency, Bandwidth, and central frequency. The output of the dataset is the maximum absolute inelastic displacement of the SDOF using the NL-THA. Two datasets will be used to train the ANN model (50,096) and (90,000). The investigation will be applied to 10 SDOF systems with various vibration periods (0.1 sec – 3 sec) and four yielding force limit (fy) (fy={100N, 400N, 700N, 1000N}). The comparison will be made between the mean response of each SDOF subjected to 31 artificial ground motions and the NL-THA's results.

2. The Proposed Artificial Neural Networks Model

The supervised ML techniques became a helpful tool in civil and earthquake engineering. Its ability to find the relationship between the input and output features makes it suitable for creating predictable models. The most used ANN technique is based on finding the best

weights and biases corresponding to the lowest error between the predicted and the exact outputs.

The main idea of the proposed method is finding the relationship between the idealization parameters (equivalent SDOF) and the ground motions parameters with the maximum inelastic response, assuming that the dynamic response of the equivalent SDOF system is the same as the MDOF's. The procedure is illustrated in Figure 1 with the following steps.

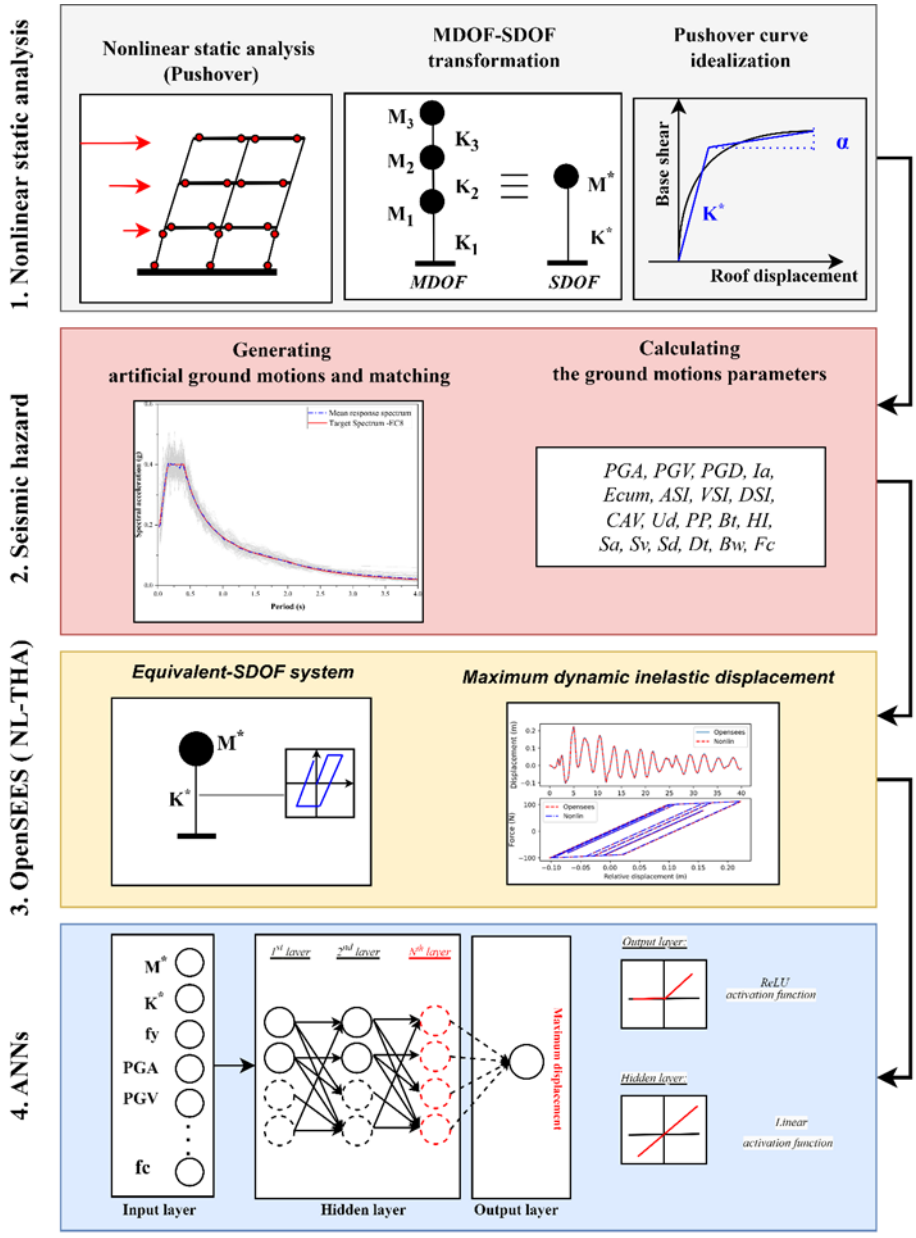

Fig. 1. The followed steps of the proposed ANN-based methodology

The ANN model needs enough datasets to be trained and to achieve high performance. The dataset will be generated by performing NL-THA analysis of equivalent SDOF systems and

artificial ground motions. The output of the dataset will be the maximum inelastic displacement of the equivalent SDOF systems.

2.1. Ground Motion Selection

Earthquakes release energy in the form of waves and vibrations of different intensities. The acceleration records of a ground motion (GM) are the most used characteristics that describe and distinguish an earthquake from another. Each GM has specific characteristics like duration, location, peak ground acceleration, and frequency content that affect the building's response.

Table 1. The generated artificial ground motions and their parameters

	PGA	PGV	PGD	Ecum	Ia	CAV	HI	PP
AGM 1	0.16	0.89	1.27	128.75	20.61	35.75	3.47	0.40
AGM 2	0.19	0.72	0.33	84.47	13.52	28.42	3.06	0.15
AGM 3	0.16	0.81	0.59	123.71	19.81	37.01	3.49	0.40
AGM 4	0.19	0.88	1.08	78.82	12.62	28.95	3.10	0.15
AGM 5	0.19	0.75	0.48	86.92	13.92	28.56	3.00	0.15
AGM 6	0.16	0.87	0.59	120.48	19.29	36.75	3.53	0.30
AGM 7	0.16	0.91	0.34	143.74	23.01	40.08	3.74	0.25
AGM 8	0.18	0.73	0.47	95.91	15.36	31.91	3.26	0.15
AGM 9	0.20	0.76	0.69	93.61	14.99	29.93	3.03	0.15
AGM 10	0.17	0.70	0.48	83.22	13.33	29.78	3.24	0.15
AGM 11	0.17	1.07	0.69	109.57	17.54	34.69	3.46	0.20
AGM 12	0.19	0.74	0.66	68.98	11.05	26.99	2.87	0.25
AGM 13	0.15	1.54	3.65	124.17	19.88	33.46	3.73	0.40
AGM 14	0.15	0.99	0.29	107.16	17.16	30.53	3.76	0.15
AGM 15	0.18	1.41	1.81	92.68	14.81	29.65	3.24	0.30
AGM 16	0.19	0.78	0.74	89.12	14.27	29.09	3.16	0.15
AGM 17	0.24	0.70	0.31	47.51	7.61	20.38	2.36	0.40
AGM 18	0.18	0.66	0.45	80.31	12.86	25.63	3.30	0.15
AGM 19	0.18	1.67	2.38	74.50	11.93	25.20	3.17	0.30
AGM 20	0.20	0.99	1.21	62.50	10.01	23.51	2.87	0.40
AGM 21	0.24	0.62	0.27	55.29	8.85	23.29	2.34	0.40
AGM 22	0.19	0.84	0.53	54.72	8.76	21.38	2.84	0.40
AGM 23	0.16	0.81	0.43	97.59	15.63	35.30	3.33	0.35
AGM 24	0.17	5.98	17.29	130.20	20.85	45.11	3.05	0.30
AGM 25	0.18	0.72	0.51	84.89	13.59	33.06	2.91	0.20
AGM 26	0.17	0.76	0.69	101.06	16.18	36.42	3.15	0.15
AGM 27	0.22	0.83	0.69	64.96	10.40	24.70	2.55	0.25
AGM 28	0.15	2.22	6.03	120.99	19.37	39.59	3.57	0.20
AGM 29	0.21	0.73	1.48	65.88	10.55	25.08	2.58	0.15
AGM 30	0.18	0.78	0.51	104.86	16.79	31.72	3.27	0.20
AGM 31	0.19	0.66	0.81	79.15	12.6	24.63	3.21	0.30

Choosing the right GMs for the seismic vulnerability assessment is crucial for a reliable result. However, in some cases, the number of GMs selected for the study is insufficient due to the unavailability of real GMs. Therefore, using artificial ground motions is adequate to generate ground motions with the same spectral response of a target spectrum.

In this study, 31 artificial ground motions (AGM) have been generated and matched to a target response spectrum of the EuroCode-8, as shown in Figure 2. The AGMs were generated and matched using "SeismoArtif" (29), and the seismic parameters of the generated AGMs are shown in Table 1.

These AGMs are used in the NL-THA after scaling them using a scaling factor that increases and decreases the peak acceleration without changing the frequency content. The dataset will contain the GMs' characteristics that are illustrated as follows:

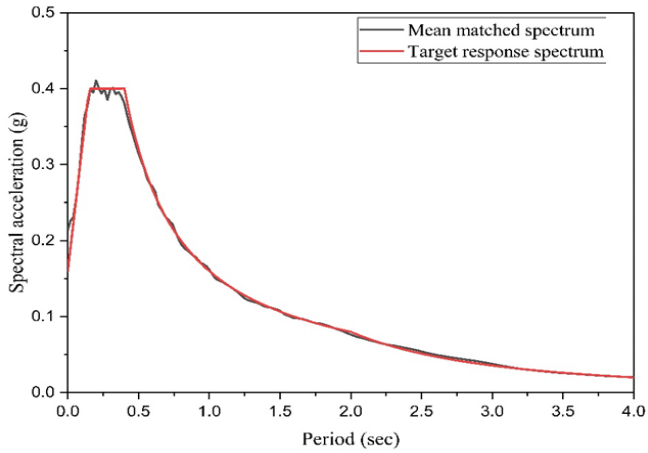

Fig. 2. The target response spectrum and the mean matched spectrum of the generated AGMs

- PGA: Peak Ground Acceleration
- PGV Peak ground velocity
- PGD Peak ground displacement
- Ia: Arias intensity
- Ecum: Cumulative energy
- ASI: Acceleration spectrum intensity
- VSI: velocity spectrum intensity
- DSI: displacement spectrum intensity
- CAV: cumulative absolute velocity
- Ud: Uniform duration
- PP: predominant period
- Bt: bracket duration
- HI: Housner intensity
- Sa: Spectral acceleration
- Sv: Spectral velocity
- Sd; Spectral displacement
- SD: significant duration
- Df: dominant frequency
- Bw: Bandwidth
- Fc: central frequency

2.2. Generating The Dataset

The performance of the ANN model depends on the size and quality of the dataset. It should contain enough information regarding variability and the number of input features. The inputs should describe the effective parameters of the problem and illuminate any unrelated features that may increase the training time and the complexity of the ANN

model. This study aims to use the SDOF characteristics and the GM parameters to estimate the seismic response of an equivalent system. For that reason, 90,000 NL-THA are performed in OpenSees (30) using 31 AGMs that characterize the earthquake. OpenSees model's results are compared to Nonlin's (31) results to validate them, as shown in Figure 3. The maximum inelastic displacement of the SDOF is calculated and stored as an output of the dataset. This dataset contains 24 input parameters and one output. The SDOF characteristics are the fundamental effective vibration period (Ti), the effective mass (M*), and the yielding force (fy). Their variation range is represented in Table 2. The characteristics of the equivalent SDOF systems used to generate the dataset are selected randomly from a selection interval, as shown in Table 2. The random selection has to be uniform, i.e., the choice of each value from the SDOF characteristics (Mass, stiffness, etc.) has the same probability of being selected, and that way, the number of each value will be almost equal, as shown in Figure 4.

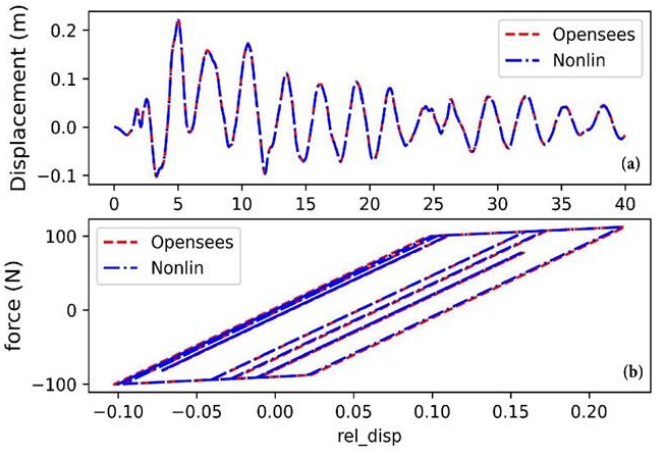

Fig. 3. NL-THA using OpenSees results and Nonlin software case of an SDOF (Mass= 200 Kg, Stiffness= 1000 N , fy= 100 N and El-Centro ground motion): a) Time versus dispalcement response, b) Displacement versus force response

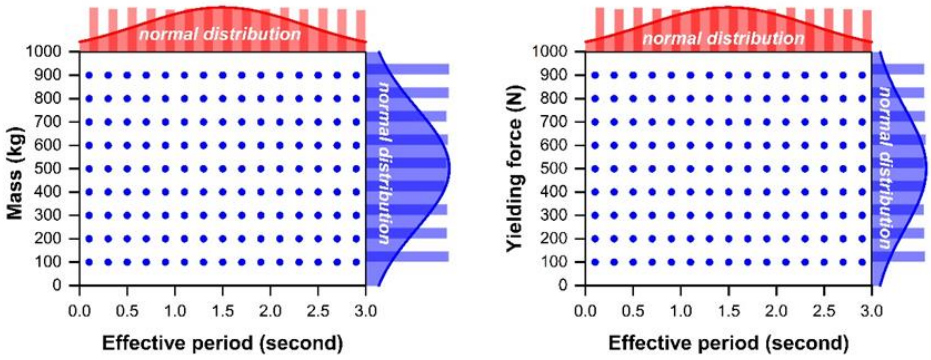

Fig. 4. the SDOF characteristics and their distribution in the generated dataset

The material behavior is considered elastic perfectly plastic (EPP), and no stiffness or strength degradation is considered in this study.

Table 2. Selection interval of the SDOF parameters

SDOF parameter	Minimum	Maximum	Step
Mass (Kg)	100	1000	100
Period (sec)	0.1	3	0.03
Yielding force (N)	100	1000	100

2.3. Training The ANN Model

The ANN is a supervised ML technique that requires inputs and outputs to find the relationship between them. The performance of the ANN model depends on various parameters and steps that will enhance its performance and reduce its complexity. Finding the best hyperparameters is a crucial step that decreases the training time and improves predictability. Activation functions, learning rate, number of epochs, number of hidden layers, and number of neurons are the principal hyperparameters that should be optimized by finding the best combination.

The training is divided into three phases. The first phase is the forward phase, where weights and biases of the hidden layers are initialized with adequate values, and it ends with calculating the outputs in the output layer. After finding the first predicted output, an error should be calculated between the data's and the ANN's output. The best weights and biases are computed using the gradient descent and the chain rule by finding the lowest error. This process should be repeated for all the hidden layers backward until the network is updated. This process is the back-propagation algorithm, which represents the second phase of the training. Lastly, as explained previously, the training dataset should be passed through the network, where weights and bias adjustments should be made. The testing and the validation datasets are used to compare the prediction of the updated network to the exact solution by calculating the correlation coefficient and the mean squared error (MSE) for each iteration. These datasets are an indicator of the performance of the ANN for predicting unseen cases and monitoring the performance of the ANN during the training process.

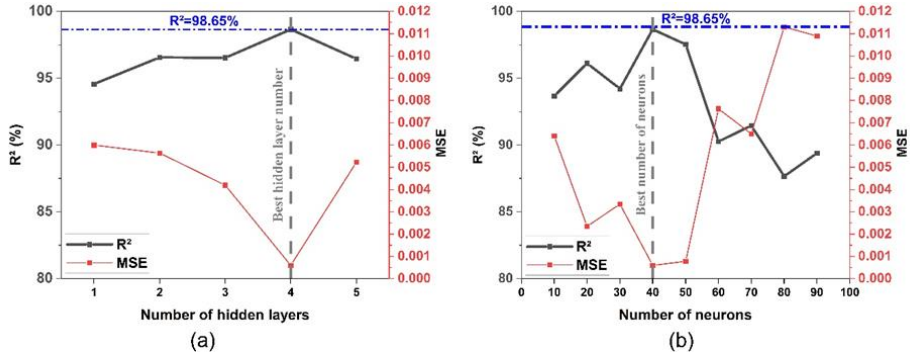

Fig. 5. Selection of best number of a) Hidden layers, b) Neurons

Figure 5 represents the selection of several neurons and hidden layers of the ANN and the corresponding performance criteria. "ReLU" and "Linear" activation functions are used for this ANN model of the hidden and output layers. To select the best number of the hidden layers HL and number of neurons NN, the HL was fixed, and the NN was varied from 10 to 90, calculating the R^2 and MSE each time, as shown in Figure 5 -b. The HL was also changed from 1 to 5; the best performance is illustrated in Figure 5 -a. It was found that four hidden

layers and 40 neurons are the optimum selection that corresponds to the highest correlation coefficient (98.65%) and the lowest mean squared error (0.0007).

3. The Displacement Coefficient Method (FEMA-356) For Target Displacement Estimation

The NL-THA is the most reliable method to estimate the seismic response of structures. Since it is a time-consuming process, a nonlinear static analysis was proposed as an alternative. FEMA-365 proposes two ways to estimate the target displacement of an equivalent SDOF system: the capacity spectrum method (CSM) and the displacement coefficient method (DCM). The CSM is based on transforming the pushover curve (base shear versus top displacement) and the response spectrum (spectral acceleration versus period) into the acceleration displacement response spectrum. Then, a performance point should be determined using proposed algorithms by ATC-40 (19). However, this method represents some instabilities where the performance point cannot be calculated due to the absence of an intersection between demand and capacity curves. This study compares the proposed method to the NL-THA, DCM, and modified coefficient method MCM proposed by FEMA 356 (32) and FEMA 440. (33)

The DCM is expressed in the following equation to estimate the target displacement:

$$\delta_T = C_0 C_1 C_2 C_3 S_a \frac{T^2}{4\pi^2} g \quad (1)$$

Where:

- C_0: is a modification factor to relate the SDOF 's spectral displacement to the MDOF's response.
- C_1: is a modification factor that relates the inelastic expected response to the elastic response.
- C_2: is a modification factor representing the effect of strength and stiffness degradation on the maximum response.
- C_3: is a modification factor that relates the effect of the P-delta effect to the maximum response.
- S_a: is the spectral acceleration of the effective fundamental period of vibration.
- T: is the effective fundamental vibration of the building.

However, FEMA-440 (33) recommended some changes and improvements to the displacement coefficient method DCM. They recommended changing the C1 and C2 formulas and making them based on empirical data.

C1 improved to transform the maximum elastic displacement to an estimate for inelastic systems. C2 was recommended for structures with significant strength and stiffness degradation behaviors. C3 was recommended to be eliminated from equation (1) for strength limit favor.

4. A Comparative Study Between The ANN, DCM, MCM, and the NL-THA

This section aims to calculate the seismic response of various SDOF systems subjected to 31 unseen GMs using the ANN models and the FEMA's procedures, where the NL-THA's results will be used as exact solutions. Two ANN models will be used to study the effect of the dataset's size on the ANN's predictability.

Three statistical criteria will be used to evaluate the performance of each method to the NL-THA's results. 10 SDOF systems with different vibration periods and yielding force

limits but fixed post-yielding ratio α=0% will be studied. These SDOFs' characteristics are illustrated in Table 1. The statistical criteria are shown in Table 2.

Table 2. The used statistical criteria to estimate the performance of each approach to the NL-THA results

Statistical criterion	Equation
Mean Relative Error (MRE)	$=\frac{1}{N}\sum_{i=1} \frac{\delta_{NLTHA,i}-\delta_{estimated,i}}{\delta_{NLTHA,i}} \times 100$
Mean Absolute Error (MAE)	$=\frac{1}{N}\sum_{i=1} \lvert\delta_{NLTHA,i}-\delta_{estimated,i}\rvert$

Where:

- $\delta_{NLTHA,i}$: is the maximum inelastic displacement of the mass under a ground motion 'I'.
- $\delta_{estimated,i}$: is the target displacement estimated using the ANN, DCM or MCM.
- N: is the total number of the used ground motions.

5. Results and Discussion

This paper proposed an ANN model that can predict the maximum inelastic displacement of an equivalent SDOF system using the nonlinear static procedure (pushover analysis). The study generated a dataset to train the model containing the SDOFs' characteristics and the GM parameters. Two datasets were generated containing 50,096 and 90,000 analyses. The aim of generating two datasets is to study the effect of dataset size on the performance of ANN. Then, these models will be compared to existing methods that estimate the target displacement. The NL-THA results have been used to compare the accuracy of prediction and estimation of the methods. The study is applied to 10 SDOF systems (0.1 sec to 3 sec) with different yielding force limits (fy).

Figure 6 represents the predicted, estimated target displacement and the dynamic inelastic response of the SDOF systems using DCM, MCM, ANN, and NL-THA for four yielding limit forces (fy =100 N, 400 N, 700 N, 1000 N) as illustrated in Figure 6-a, Figure 6-b, Figure 6-c and Figure 6-d respectively. The obtained results are the median response of each SDOF system using ANN, DCM, MCM, and NL-THA.

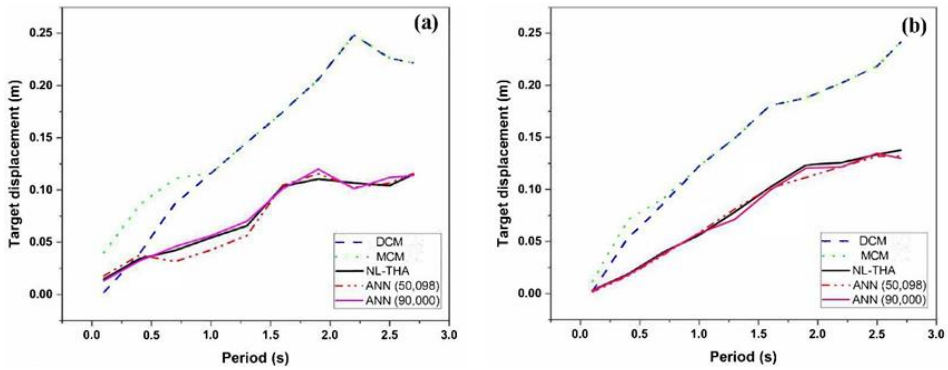

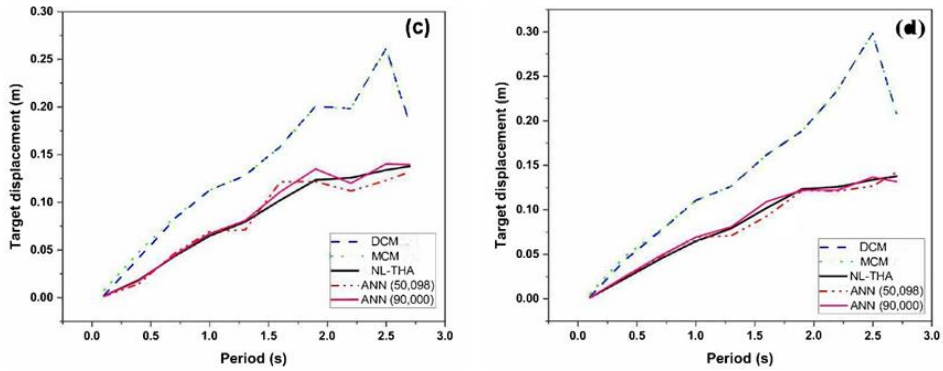

Fig. 6. Target displacement estimation using NL-THA, ANN, DCM and MCM for: a) fy=100 N, b) fy=400 N, c) fy=700N and d) fy= 1000N

Figures 7 and 8 illustrate the MRE and the MAE between the exact solution (NL-THA) and the estimated target displacements.

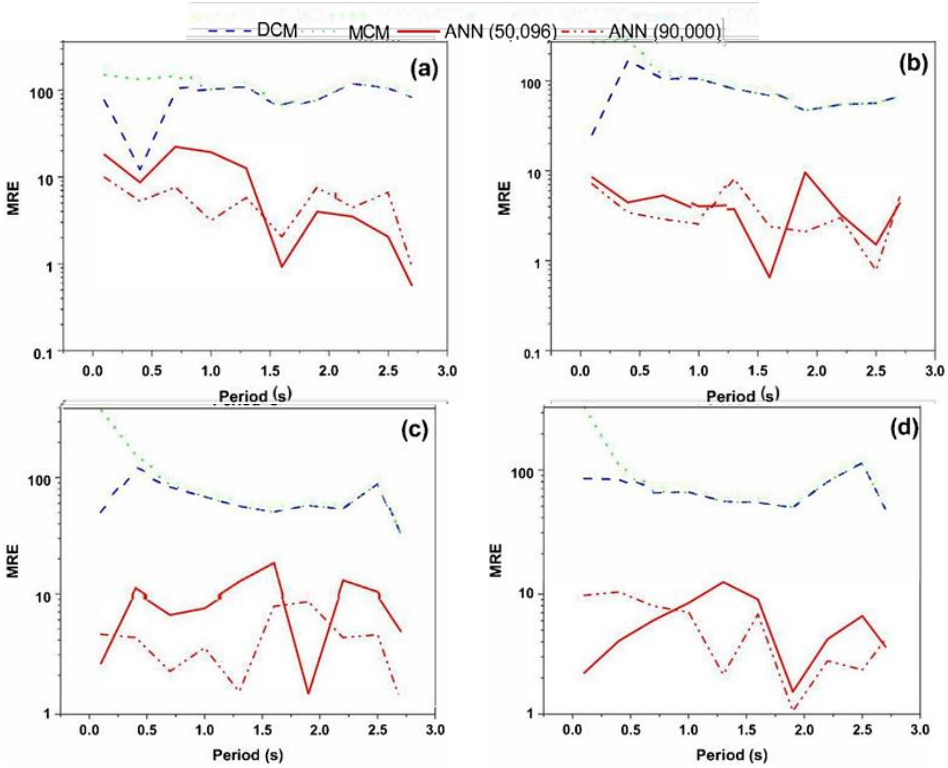

Fig. 7. Mean relative error of the predicted and the NL-THA seismic response of 10 SDOF systems: a) fy=100 N, b) fy=400 N, c) fy=700N and d) fy= 1000N

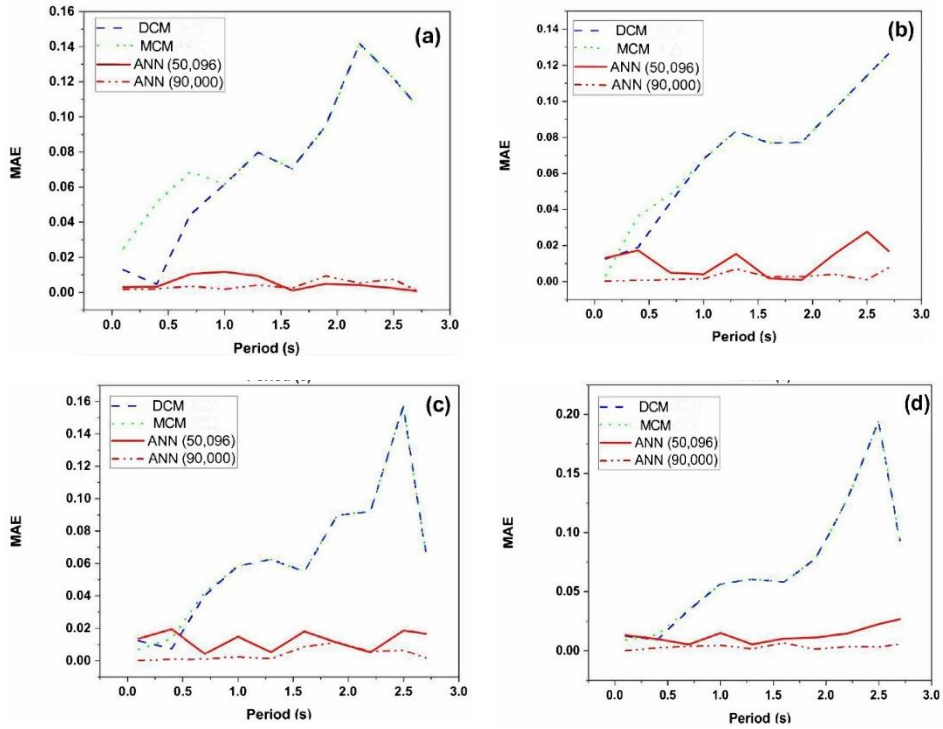

Fig. 8. Mean absolute error between the predicted and the NL-THA seismic response of 10 SDOF systems: a) fy=100 N, b) fy=400 N, c) fy=700N and d) fy= 1000N

The ANN-based method using 50,096 and 90,000 analysis is the nearest to the exact solutions calculated by the NL-THA. DCM and MCM overestimate the maximum inelastic displacement, especially for periods greater than 0.5 sec. Figure 7 shows the relative error between the mean dynamic inelastic response of the SDOFs subjected to 31 AGMs scaled to PGA=0.3 g. The results showed a high overestimation of the dynamic response (>100% in some cases), and the lowest relative error is 16% for the DCM and the MCM for all the cases. On the other hand, the ANN model shows a high predictability of the SDOFs' dynamic response for all the selected yielding limit forces (fy). It was also observed that the size of the used dataset enhanced the performance of the ANN model in terms of MRE. Figure 8 shows that the DCM and the MCM have the highest mean absolute error (>0.1) for all systems with vibration periods higher than 0.5 sec. These methods are promising approaches to estimating the target displacement of rigid and high-frequency buildings. On the other hand, the ANN showed a lower MAE than the DCM and MCM (0.02 was the highest MAE value for both the ANN models and for all the fy).

The ANN model could precisely predict the dynamic response using the SDOF and the ground motion characteristics. In addition, the obtained results were more accurate than the existing methodologies adopted by FEMA-356 and FEMA-440. Using the NSP with the ML showed remarkable predictability of dynamic responses, which makes it less complex and faster than the NL-THA. This hybrid procedure that uses the pushover curve and the ANN can be transformed into software that the analyst can use to estimate the dynamic response of any building without using the NL-THA. However, since the proposed procedure uses the equivalent bilinear curve of the pushover analysis, the higher mode effect can change the seismic response remarkably.

6. Conclusion

The seismic response estimation of structures is essential in assessing their performance and vulnerability. The NL-THA is considered the most reliable method to estimate the seismic demand. Many alternative methods have been developed to reduce the complexity and the computation time of the NL-THA, like Nonlinear static pushover (NSP). FEMA-356 and FEMA-440 proposed two equations to estimate the target displacement. However, their results remain inaccurate sometimes, and they overestimate or underestimate the seismic demand. For that reason, this study introduces a new approach that combines Nonlinear Static Pushover (NSP) analysis and Artificial Neural Networks (ANNs) to rapidly and accurately estimate the maximum inelastic displacement of an equivalent single degree of freedom (ESDOF) system subjected to a ground motion. This ESDOF represents the idealization of the pushover curve by transforming the MDOF system into an SDOF system, making the analysis much more effortless. The procedure is based on generating a dataset that contains various SDOF systems (Their characteristics: effective mass (M), effective stuffiness (K), and limit yielding force (fy)) and the parameters of the artificial ground motions (AGMs). The artificial neural networks were selected as a supervised machine learning algorithm to find the relationship between the ESDOF and the maximum inelastic displacement.

To evaluate the predictability of the ANN-based model, ten SDOF systems with variant vibration periods were selected to calculate the median seismic demand using the displacement coefficient method (DCM) proposed by FEMA-356, the modified coefficient method (MCM) proposed by FEMA-440 and the NL-THA using 31 AGMs. For limit yielding forces were selected fy= [100 N,400 N,700 N,1000 N]. The results were quite promising, showing that the model can predict deformations accurately. It has also been found that the size of the dataset used for training the model affects how well it performs.

This new ANN-based method shows a remarkable accuracy compared to existing alternative methods. The technique provides high accuracy for structures with a vibration period greater than 0.5 seconds, and the first mode is the predominant.

References

[1] Chen J, Xu C, El Naggar HM, Du X. Seismic response analysis of rectangular prefabricated subway station structure. Tunnelling and Underground Space Technology. 2023 Jan 1;131:104795 https://doi.org/10.1016/j.tust.2022.104795

[2] Fu Z, Tian L, Liu J. Seismic response and collapse analysis of a transmission tower-line system considering uncertainty factors. Journal of Constructional Steel Research. 2022 Feb 1;189:107094. https://doi.org/10.1016/j.jcsr.2021.107094

[3] Zhang C, Xu J, Qian Y, Zhang J, Wang R, Wang B. Seismic reliability analysis of random parameter aqueduct structure under random earthquake. Soil Dynamics and Earthquake Engineering. 2022 Feb 1;153:107083. https://doi.org/10.1016/j.soildyn.2021.107083

[4] Kang C, Kwon OS, Song J. Evaluation of correlation between engineering demand parameters of structures for seismic system reliability analysis. Structural Safety. 2021 Nov 1;93:102133. https://doi.org/10.1016/j.strusafe.2021.102133

[5] Xu C, Deng J, Peng S, Li C. Seismic fragility analysis of steel reinforced concrete frame structures based on different engineering demand parameters. Journal of Building Engineering. 2018 Nov 1;20:736-49. https://doi.org/10.1016/j.jobe.2018.09.019

[6] Asteris PG, Chronopoulos MP, Chrysostomou CZ, Varum H, Plevris V, Kyriakides N, et al. Seismic vulnerability assessment of historical masonry structural systems. Engineering Structures. 2014 Mar 15;62-63:118-34. https://doi.org/10.1016/j.engstruct.2014.01.031

[7] Calvi GM, Pinho R, Magenes G, Bommer JJ, Restrepo-Vélez LF, Crowley H. Development Of Seismic Vulnerability Assessment Methodologies Over The Past 30 Years. ISET journal of Earthquake Technology, 2006, 43.3: 75-104.
[8] Kassem MM, Mohamed Nazri F, Noroozinejad Farsangi E. The seismic vulnerability assessment methodologies: A state-of-the-art review. Ain Shams Engineering Journal. 2020 Dec 1;11(4):849-64. https://doi.org/10.1016/j.asej.2020.04.001
[9] Benazouz C, Mehani Y, Leblouba M. Simplified procedure for seismic demands assessment of structures. Structural Engineering & Mechanics. 2016 Aug 10;59:455-73. https://doi.org/10.12989/sem.2016.59.3.455
[10] Kassem MM, Mohamed Nazri F, Noroozinejad Farsangi E. Development of seismic vulnerability index methodology for reinforced concrete buildings based on nonlinear parametric analyses. MethodsX. 2019 Jan 1;6:199-211. https://doi.org/10.1016/j.mex.2019.01.006
[11] Kassem MM, Mohamed Nazri F, Noroozinejad Farsangi E. Using a probabilistic approach to quantify the collapse margin of a retrofitted university building in Beirut. Engineering Science and Technology, an International Journal. 2020 Apr 1;23(2):373-81. https://doi.org/10.1016/j.jestch.2019.05.003
[12] Abu Jame W. Pushover Analysis of Seismic Performance for Steel Trusses Bridges. 2023 May 1 [cited 2023 Aug 14]; Available from: http://scholar.ppu.edu:8080/xmlui/handle/123456789/8910
[13] Kasabe A, Shelar V, Kasabe A, Shelar V. Pushover analysis of building using soft story at different levels. World Journal of Advanced Engineering Technology and Sciences. 2023;9(1):203-10. https://doi.org/10.30574/wjaets.2023.9.1.0160
[14] Zaidir, Wardi S. Pushover Analysis of Rc Frames With Substandard Beam-Column Joints. International Journal of Geomate. 2023 Mar. 29; 24(106):85-92.
[15] Baylon M, Garduque J, Lineses R, Loriaga N. Seismic Vulnerability Assessment of Gilbert Bridge in Laoag, Ilocos Norte Using Capacity -Spectrum Method. 2020.
[16] Seismic Evaluation and Retrofit of Concrete Buildings: A Practical Overview of the ATC 40 Document - Craig D. Comartin, Richard W. Niewiarowski, Sigmund A. Freeman, Fred M. Turner, 2000. https://journals.sagepub.com/doi/abs/10.1193/1.1586093
[17] Yaghmaei-Sabegh S, Neekmanesh S, Ruiz-García J. Evaluation of the Coefficient Method for estimating maximum roof displacement demand of existing buildings subjected to near-fault ground motions. Soil Dynamics and Earthquake Engineering. 2019 Jun 1;121:276-80. https://doi.org/10.1016/j.soildyn.2019.03.015
[18] Improvement of Nonlinear Static Seismic Analysis Procedures. Federal Emergency Management Agency.
[19] Aabbas H, Jarallah H. Comparative Study of the Seismic Assessment According to ATC-40, FEMA-356 and FEMA-440 for Existing Hospital Building Located at Baghdad City. International Journal of Civil Engineering. 2021 May 4;1.
[20] Kalakonas P, Silva V. Seismic vulnerability modelling of building portfolios using artificial neural networks. Earthquake Engineering & Structural Dynamics. 2022;51(2):310-27. https://doi.org/10.1002/eqe.3567
[21] Mangalathu S, Heo G, Jeon JS. Artificial neural network based multi-dimensional fragility development of skewed concrete bridge classes. Engineering Structures. 2018 May 1;162:166-76. https://doi.org/10.1016/j.engstruct.2018.01.053
[22] Menon UA, Nair DS. Seismic Response Prediction of RC Buildings Using Artificial Neural Network. Lecture Notes in Civil Engineering. 2023;284:403-13. https://doi.org/10.1007/978-3-031-12011-4_31
[23] Morfidis K, Kostinakis K. Approaches to the rapid seismic damage prediction of r/c buildings using artificial neural networks. Engineering Structures. 2018 Jun 15;165:120-41. https://doi.org/10.1016/j.engstruct.2018.03.028
[24] Noureldin M, Ali A, Sim S, Kim J. A machine learning procedure for seismic qualitative assessment and design of structures considering safety and serviceability. Journal of

Building Engineering. 2022 Jun 1;50:104190. https://doi.org/10.1016/j.jobe.2022.104190
[25] Oh BK, Glisic B, Park SW, Park HS. Neural network-based seismic response prediction model for building structures using artificial earthquakes. Journal of Sound and Vibration. 2020 Mar 3;468:115109. https://doi.org/10.1016/j.jsv.2019.115109
[26] Rachedi M, Matallah M, Kotronis P. Seismic behavior & risk assessment of an existing bridge considering soil-structure interaction using artificial neural networks. Engineering Structures. 2021 Apr 1;232:111800. https://doi.org/10.1016/j.engstruct.2020.111800
[27] Vafaei M, Adnan A bin, Abd. Rahman AB. Real-time Seismic Damage Detection of Concrete Shear Walls Using Artificial Neural Networks. Journal of Earthquake Engineering. 2013 Jan 1;17(1):137-54. https://doi.org/10.1080/13632469.2012.713559
[28] Won J, Shin J. Machine learning-based approach for seismic damage prediction of building structures considering soil-structure interaction. Sustainability (Switzerland). 2021;13(8). https://doi.org/10.3390/su13084334
[29] SeismoArtif [- Earthquake Engineering Software] - Geotechpedia [Internet]. [cited 2023 Sep 29]. Available from: https://geotechpedia.com/Software/Show/1213/SeismoArtif
[30] Open System for Earthquake Engineering Simulation - Home Page [Internet]. [cited 2023 Sep 29]. Available from: https://opensees.berkeley.edu/
[31] Charney F. NONLIN: Software for structural dynamics and earthquake engineering education. 2007 Jan 1;17:65-76.
[32] FEMA-356. Prestandard and Commentary for the Seismic Rehabilitation of Buildings American Society of Civil Engineers. 2000.
[33] FEMA-440. Improvement of Nonlinear Static Seismic Analysis Procedures.

Research on Engineering Structures & Materials
www.jresm.org
MIM Research Group

Research Article

Evaluation of strength of self-compacting concrete having dolomite powder as partial replacement for cement

R. Vaishnava Kumar [*, a], A. Prabaghar[b]

Civil and Structural Engineering, Annamalai University, Chidambaram, Tamil Nadu, India

Article Info

Article history:

Received 25 July 2023
Accepted 30 Oct 2023

Keywords:

Dolomite powder;
Self-compacting concrete;
Magnesium Oxychloride;
MSH;
Strength properties

Abstract

Now a day, the utilization of self-compacting concrete (SCC) has become popular in creating RC structures. Apart from self-compaction, SCC has got many advantages such as excellent flow ability, filling ability, smooth finish of surface, ease of work etc. The use of waste material in concrete is the area of having scope for researchers for many years. Use of waste material reduces the consumption of cement by construction sector. In this present experimental work, dolomite powder is used as fractional replacement material for cement. The cement in the SCC is replaced by dolomite at fractions of 10%, 20%, 30%, 40%, 50%, 60%, and 70%. Fly ash is also added to the mix at constant fraction of 18% of the cement. The strength of SCC is assessed by performing compression test, splitting tension test and bending test. The test results showed that the use of dolomite powder in SCC is advantageous up to 20% replacement fraction. It is also observed that the strength of DC40 mix (i.e the mix having Dolomite at 40% of cement) is almost equal to the strength of normal SCC. Even at 70% replacement level, the strength of SCC having dolomite achieved is 25 MPa. SEM images are analyzed to identify the spread of hydrated products.

1. Introduction

Cement concrete is widely used in the construction industry as a building material. Cement is the most important component in concrete. It plays a major role on the compressive strength and binder properties of concrete. During the production of cement process, a large amount of CO_2 is released into the global environment due to the burning of argillaceous and calcareous materials at high temperature [1].

Self-compacting concrete (SCC) is one of the innovative concretes which is widely used in present construction sector [2]. The fresh SCC has a capability of flowing, passing and filling into the congested parts of structural elements under its self-weight without any segregation, bleeding and blocking. The SCC consists of high finer materials and lesser volume of coarse aggregate compared to normal concrete to get consistent viscous flow. Some of the industrial wastes are utilized as the secondary ingredients of concrete by many researchers [3]. Fine particles are needed in SCC at higher volume, which is fulfilled by addition industrial wastes like flyash, metakolin, GGBS, dolomite etc as mineral admixtures. Among the industrial wastes, flyash is widely used secondary cementitious material upto certain limit of replacement. Cement is replaced by dolomite powder and obtained optimum compressive strength at 30% is 63.1MPa in the mix also having flyash and slag material [4].

Lime stone is one of the natural minerals and it is used as a raw material in manufacturing of Portland cement up to 20% and dolomite powder is used upto30% as the cementitious

*Corresponding author: apurupvishnu@gmail.com
[a] orcid.org/0000-0003-4051-4842; [b] orcid.org/0009-0004-9691-1569
DOI: http://dx.doi.org/10.17515/resm2023.48ma0725rs

product at low water binder ratio [5, 6]. The previous researchers found that lime stone is affected by dilution, heterogenous nucleation, filling. Now a days it is observed that a particle of lime stone powder below 20 microns is not completely inert and it reacts with cement and participate in C_3S hydration [6]. Due to the use of limestone powder as partial replacement material for cement, carbon footprint can be reduced [5]. Dolomite is one of the minerals obtained from the dolomitic limestone deposits. Dolomite is formed under two processes one is direct precipitation of dolomite from the formation solution and second one is dolomitization process that means dissolution of calcite and reacting with Ca and Mg ions [7]. The presence of magnesium carbonate in the raw material, causes damage of concrete when it is added as raw material in the production of clinker as it forms MgO and later it converts into brucite ($Mg(OH)_2$) during cement hydration process, which creates unsoundness as it is expansive reaction in concrete. It is accepted that the dolomite can be added to the concrete, in the form of powder at the time of making concrete, as it does not produce above stated unsoundness problems in the concrete.

The powder form of dolomite can be obtained from a quarry as a tertiary product [8]. In addition to its low cost, dolomite also offers several enhancements to concrete, such as improved workability, increased compressive strength, and durability [7]. The combination of fly ash and dolomite can replace the cement in concrete at a higher dosage [9]. Incorporating the dolomitic lime stone powder at higher dosage more than 25%, reduces the compressive strength of concrete [10]. The dolomite concrete has a resistance of 1N NAOH solution up to 6 months under immersion. A good rate of compressive strength development can be observed in dolomite concrete having 2% nano silica [11].

The objective of this study is to assess the impact of replacing cement with dolomite powder on properties of SCC such as compressive strength, splitting tensile strength and bending strength.

2. Materials

Cement, fly ash, dolomite powder, fine aggregate, coarse aggregate, super plasticizer and water are used to prepare SCC. The cement used is, of choice for general concreting purposes, Ordinary Portland Cement (OPC 53 grade) that conforms to IS: 12269 standards. The Specific gravity of cement is 3.15 and fineness of cement is 4.48% which is less than 10% as per IS 4031 part-1. Dolomite is a mineral composed of calcium magnesium bicarbonate, formulated as $CaMg(CO_3)_2$. The Dolomite Powder used in this study is collected at a place called Piduguralla which is famous as lime city of Andhra Pradesh. Specific Gravity of dolomite powder is 2.86 which should be appeared as very white smooth nature.

Fly ash is a waste product produced by burning coal in thermal power projects. Fly ash is procured from the Vijayawada Thermal Power Station located nearby Vijayawada city of Andhra Pradesh. The specific gravity of fly ash is 2.30. The sand used in this study conforms to grading zone-II as per IS: 383-1970 and has a specific gravity of 2.60. The fineness modulus of the sand is 2.68. Polycarboxylate ether-based superplasticizer (PCE) confirming to IS 9102 is a new generation of high-performance concrete admixture and specific gravity of superplasticizer is 1.08 is used in this study.

3. Experimental Program

M40 grade SCC mix is used in this study having weight ratio of 1:0.219:1.899:2.083:0.01:0.43 (Cement, fly ash, Fine aggregate, coarse aggregate, super plasticizer and water respectively). All materials for making SCC were mixed properly to obtain a fresh SCC mix. The fresh SCC mix flow properties were assessed and are within the limits specified by EFNARC [12]. For easy de-moulding, oil was applied to the inner faces of mould. The SCC was poured into the moulds to prepare test specimens. The casted

specimens were de-moulded after 24 hours and cured in water for 7days and for 28 days. Then the specimens were tested till failure using the universal testing machine (Figure 1, 2 & 3).

Fig. 1. Failure of cube specimen under compressive load

Fig. 2. Split tensile test on SCC specimen

Fig. 3. Flexural test on SCC specimen

4. Test Results and Discussion

4.1 Fresh Properties of Concrete

After obtaining satisfactory SCC mix from various trial mixes, cement was replaced by dolomite powder at different percentages. Mixes are designated as DC0, DC10, DC20, DC30, DC40, DC50, DC60 and DC70 respectively. Mix without dolomite powder is designated as DC0 which is control mix.

Table 1 Values of slump flow test

Mix designation	Average Diameter D in mm	T500 in sec
DC0	731	3.37
DC10	705	3.51
DC20	706	3.40
DC30	713	3.20
DC40	723	2.79
DC50	729	2.48
DC60	690	2.12
DC70	689	2.05

Fig. 4. Slump flow of DC0 mix proportion

4.2 Hardened Properties of Concrete

After completion of curing of specimens, the following specimens are tested under compressive testing machine and universal testing machine. The compressive strength test results are presented in Figure 5. The values obtained as ratio between compressive strength of concrete having dolomite (f_{cd}) and compressive strength of normal concrete i.e without dolomite (f_{co}) are shown in Table 2. The variations in f_{cd}/f_{co} are shown in Figure 11(a,b). The splitting tension strength test results are presented in Figure 8. The values obtained as ratio between splitting tension strength of concrete having dolomite (f_{td}) and splitting tension strength of normal concrete i.e without dolomite (f_{to}) are shown in Table 2. The variations in f_{td}/f_{to} are shown in Figure 12(a,b). The flexural strength test results are presented in Figure 9. The values obtained as ratio between Flexural strength of concrete having dolomite (f_{rd}) and Flexural strength of normal concrete i.e without dolomite (f_{ro}) are shown in Table 2. The variation in f_{rd}/f_{ro} are shown in Figure 13.

4.2.1 Cube Compressive Strength

The cube compressive strength of SCC having dolomite increases as percentage of dolomite increases in the mix upto 20% dolomite replacement. replaced of higher percentages of dolomite i.e more than 20% decreases the compressive strength of SCC having dolomite. By replacement of cement by dolomite to the normal SCC, the maximum percentage of increase in compressive strength is 45% which is observed at 20% cement replaced with dolomite. At 40% replacement level, the compressive strength of dolomite concrete is more or less equal to the compressive strength of normal concrete. It can be understood that 40% of cement can be replaced with dolomite powder without adversely affecting the compressive strength of the mix. The cost of dolomite powder is 2.6 times cheaper than that of cement. Hence it is economical to use the dolomite powder in the mix as a partial replacement material to cement. Also, by saving the consumption of cement, release of CO_2 into the environment during the manufacturing of cement can be minimized. Even at 70% cement replacement level with dolomite, 25MPa compressive strength is achieved. At 70% replacement level, the compressive strength of dolomite concrete is dropped to 54% compared to the compressive strength of normal concrete.

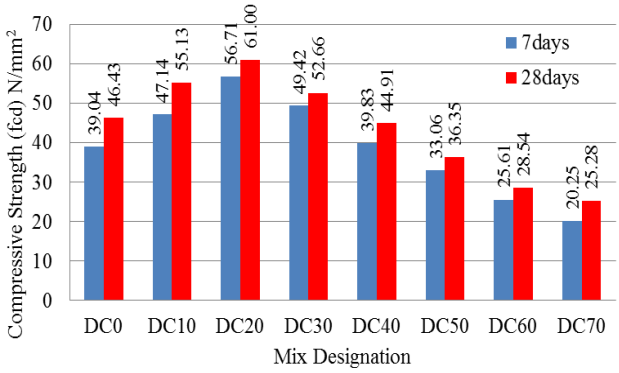

Fig. 5. Cube compressive strength of SCC at 7 days and 28 days

4.2.2 Cylinder Compressive Strength

The variation in cylinder compressive strength of SCC having dolomite powder follows the trend of cube compressive strength.

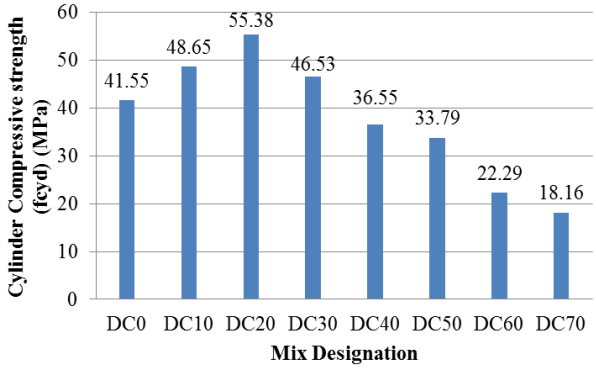

Fig. 6. Cylinder compressive strength of SCC at 28 days

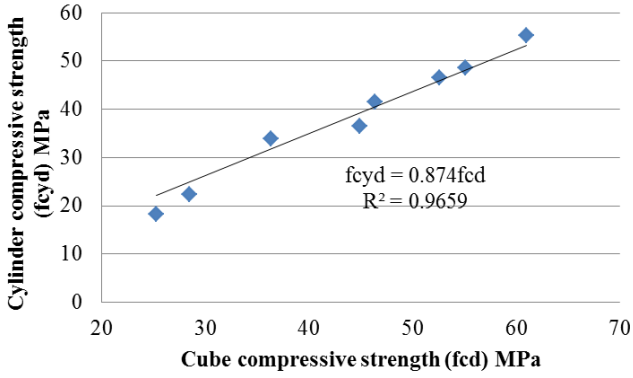

Fig. 7. Relation between f_{cyd} and f_{cd} at 28days

The cylinder compressive strength of SCC having dolomite increases as percentage of dolomite increases in the mix up to 20% dolomite replacement. replacement of higher

percentages of dolomite i.e more than 20%, decreases the cylinder compressive strength of SCC having dolomite.

Table 2. The ratio of strength of SCC having dolomite and strength of SCC not having dolomite

Mix ID	Percentage of Dolomite powder (D)	f_{cd}/f_{co}		f_{td}/f_{to}		f_{rd}/f_{ro}
		7 days	28 days	7 days	28 days	28 days
DC0	0	1.00	1.00	1.00	1.00	1.00
DC10	10	1.21	1.19	1.19	1.11	1.16
DC20	20	1.45	1.31	1.25	1.19	1.27
DC30	30	1.27	1.13	1.03	1.01	1.09
DC40	40	1.02	0.97	0.94	0.87	0.94
DC50	50	0.85	0.78	0.77	0.77	0.77
DC60	60	0.66	0.61	0.64	0.64	0.64
DC70	70	0.52	0.54	0.34	0.52	0.43

By replacement of dolomite to the normal SCC, the maximum percentage of increase in cylinder compressive strength is 33.28% which is observed at 20% cement replaced with dolomite. A plot between cube compressive strength values and cylinder compressive strength values at 28 days curing age is drawn which is shown in figure. A linear regression line passing through the origin is observed. From which it can be seen that the cylinder compressive strength is 0.874 times the cube compressive strength. The regression line is precisely close to the experimental values.

4.2.3 Splitting Tension Strength

The splitting tension strength of concrete having dolomite increases as percentage of dolomite increases in the mix up to 20% dolomite replacement. At 30% level of replacement, the splitting tension strength of dolomite concrete is equal to splitting tension strength of normal concrete. At 70% replacement level, the splitting tension strength of dolomite concrete is dropped to 48.34% compared to the splitting tension strength of normal concrete.

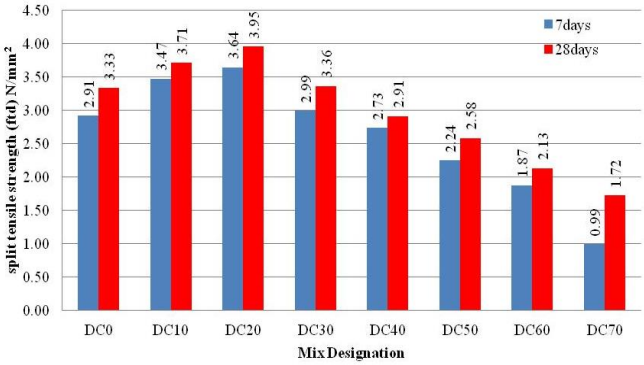

Fig. 8. Splitting tension strength of SCC at 7 and 28 days

4.2.4 Flexural Strength

As percentage of dolomite increases, the flexural strength also increases up to 20% replacement level. The flexural strength of dolomite concrete at 40% replacement level is equal to the flexural strength of normal concrete. At 70% replacement level, the flexural strength of dolomite concrete is dropped to 57% compared to the flexural strength of normal concrete.

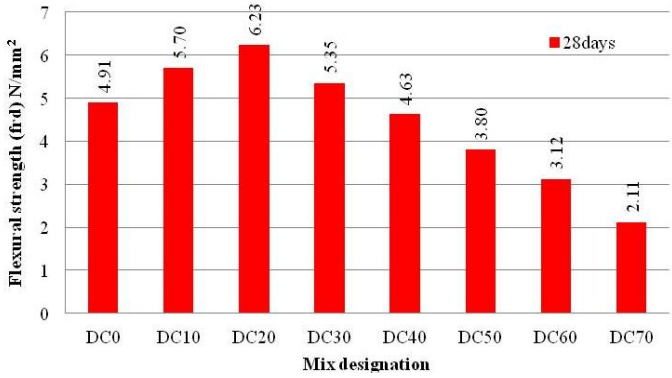

Fig. 9. Flexural strength of SCC at 28 days

Cube compressive strength values and flexural strength values at 28 days curing age are plotted as shown in figure 9. The trend line is passing through the origin. From which it can be perceived that the flexural strength is 0.102 times the cube compressive strength. The regression line fits well with in the experimental values.

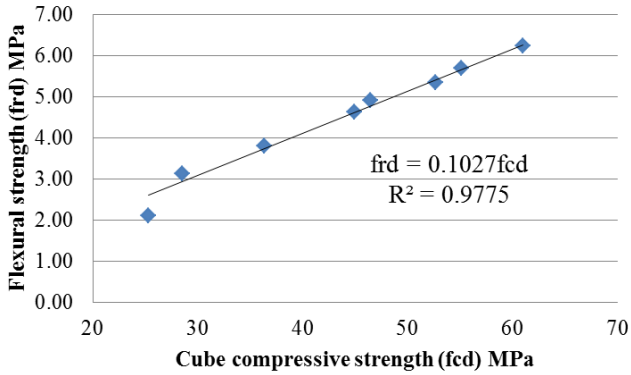

Fig. 10. Relation between f_{rd} and f_{cd} at 28days

4.2.5 Prediction of Strength

Curves are developed by taking ratio of strength of dolomite concrete to strength of normal concrete on Y-axis and percentage of dolomite in the mix on X-axis. Figure 11 shows the plot between f_{cd}/f_{co} and percentage of dolomite. A trend line is also drawn to develop the best fit equation between f_{cd}/f_{co} and percentage of dolomite in the mix. By knowing the percentage of dolomite in the mix, compressive strength of concrete can be predicted by the developed equation.

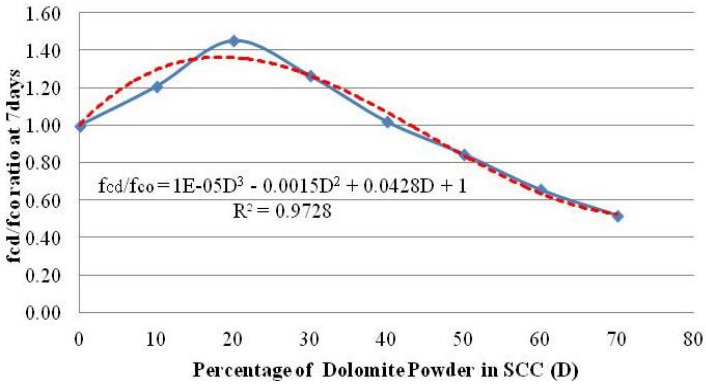

a) At 7days

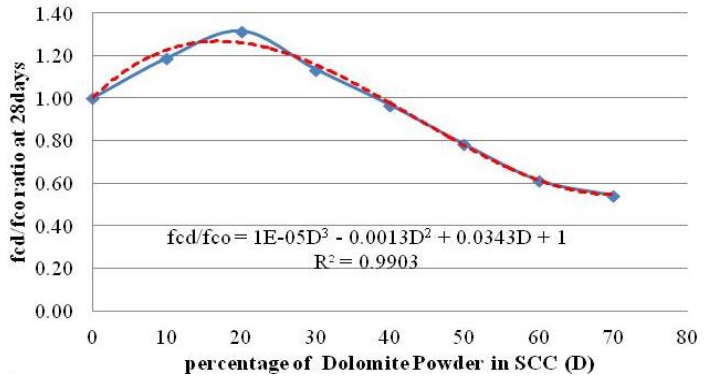

b) At 28days

Fig. 11. (a-b) Variation of f_{cd}/f_{co} with percentage of dolomite powder

Likewise, curves are developed to predict splitting tension strength and flexural strength. The developed equations, predicted values of the strength and percentage error in predicting strength are given table. Out of twenty-four predicted strength values, the percentage error of nineteen values is falling below/nearer to 10%, which shows that the predicted strength values are matching well with the experimental values.

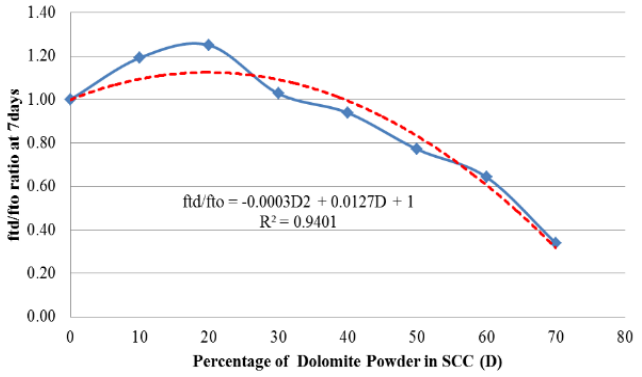

a) At 7days

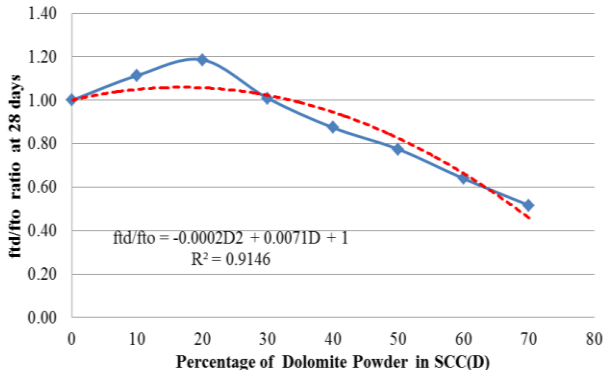

b) At 28days

Fig. 12. (a-b) Variation of f_{td}/f_{to} with percentage of dolomite powder

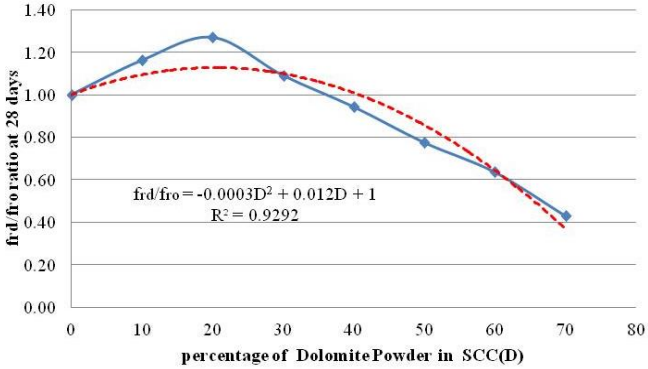

Fig. 13. Variation of f_{rd}/f_{ro} with percentage of dolomite powder

Table 3. Predicted strength of SCC using the developed equations and percentage error

Designation	Compressive strength (N/mm²) f_{cd}/f_{co}=1E-05D³ - 0.0013D² + 0.0343D + 1 R^2 = 0.9903		Splitting tension strength (N/mm²) f_{td}/f_{to}=-0.0002D² + 0.0071D + 1 R^2 = 0.9146		Flexural strength (N/mm²) f_{rd}/f_{ro}=-0.0003D² + 0.012D + 1 R^2 = 0.9292	
	Predicted	% Error	Predicted	% Error	Predicted	% Error
DC0	46.43	0.00	3.33	0.00	4.91	0.00
DC10	56.78	3.00	3.50	-5.66	5.30	-7.06
DC20	57.85	-5.16	3.54	-10.47	5.49	-11.89
DC30	52.42	-0.46	3.44	2.38	5.48	2.51
DC40	43.27	-3.65	3.21	10.31	5.28	14.18
DC50	33.20	-8.66	2.85	10.35	4.89	28.46
DC60	24.98	-12.47	2.35	10.37	4.29	37.54
DC70	21.40	-15.31	1.72	0.09	3.50	16.31

5. SEM Analysis

Using scanning electron microscope (SEM) images, hardened concrete quality can be analyzed by studying the microstructure of concrete [12]. The hydration phase and the mineral additives used can be identified in the SEM image [13]. The topography and pattern of a material can be identified in the SEM micrographs. In this experiment, photos were taken after mounting the crushed concrete fragments on the SEM stub [14]. The curing age of all SCC mixes is of 28 days. SEM pictures of DC0, DC10, DC20, DC30, DC40, DC50, DC60, and DC70 mixes are presented in Figure 14 (DC0-DC70). The presented images demonstrate the distinct spreading of CSH (Calcium Silicate Hydrate gel), MSH (Magnesium Silicate Hydrate gel), $Ca(OH)_2$, unreacted dolomite, voids etc.[15-21].

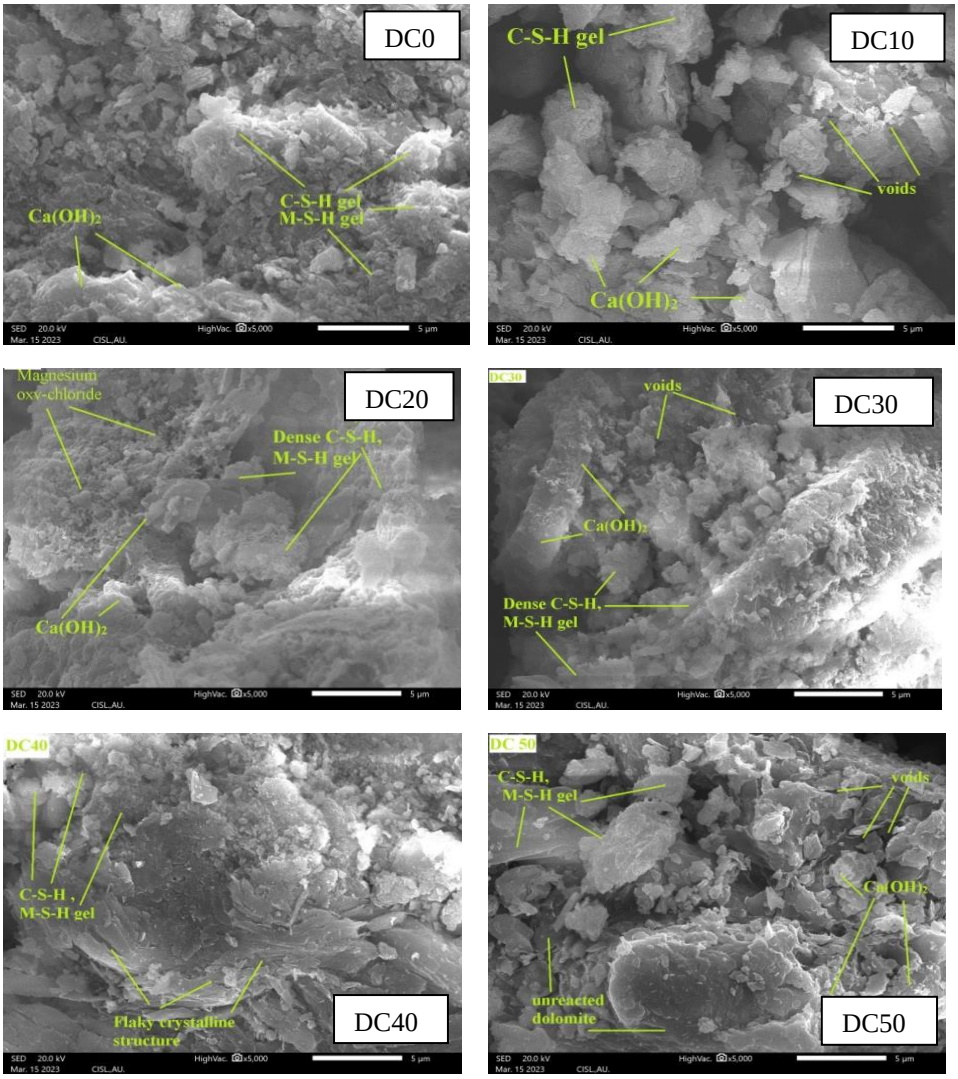

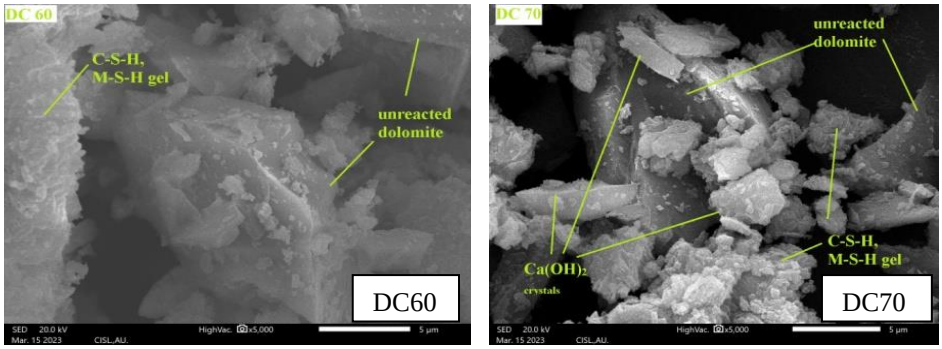

Fig. 14. (DC0-DC70) SEM Images of SCC mixes

CSH reflection is brighter than that of MSH. Like CSH, MSH also processes cementitious property. Mg ions are smaller than Ca ions in size. The flaky crystals are of 3-phase Magnesium oxy-chloride. Small needles are of 5-phase Magnesium oxy-chloride [22-24]. Both 3-phase and 5-phase oxy-chlorides are stable at normal temperature and at 8 to10 pH. When cement is replaced with dolomite powder, the pH of all mixes ranges from 9.8 to 10.9. Ca $(OH)_2$ appears as bright crystal in SEM images. The beneficial effect of Dolomite particles can be understood by observing the spread of dense, non-porous hydrated products like CSH, MSH and Magnesium oxy chlorides [25-28].

The image of DC0 shows porous structure of hydrated products. Ca $(OH)_2$ can be observed along with porous CSH gel. The images of DC10, DC20 and DC30 reflect the dense hydrated products. The hydrated products, CSH and MSH together can be observed as a dense non crystalline matrix. In the image of DC40, more flaky nature of hydrated product of dolomite can be observed [29-34]. The unreacted dolomite powder crystals can be seen in the images of DC50, DC60 and DC70.

6 Conclusions

The following conclusions are drawn from the study.

- For all the mixes, the fresh self-compacting concrete properties i.e slump flow, T500 results were achieved satisfactorily as per EFNARC guidelines.
- At higher dosages of dolomite powder i.e more than 40%, It is observed that time taken to spread 500mm is lesser than that of lower dosage mixes but within the limits as per guidelines.
- The flow diameter of all SCC mixes having dolomite powder is less than that of control SCC mix i.e DC0.
- The compressive strength of SCC can be increased due to the use of dolomite by replacing partially the cement in the mix i.e up to 30%. The maximum percentage of increase in the compressive strength is 31% at the replacement level of 20% at the age of 28 days.
- The maximum increase in compressive strength is 45% at the replacement level of 20% at the age of 7 days.
- The maximum increase in splitting tension strength is 19% at the replacement level of 20% at the age of 28 days.
- The maximum increase in splitting tension strength is 25% at the replacement level of 20% at the age of 7 days.
- The maximum increase in flexural strength is 27% at the replacement level of 20% at the age of 28 days.

- At 40% replacement of cement with dolomite, the compressive strength, splitting tension strength and flexural strength values of SCC having dolomite are almost equal to the corresponding strength values of normal SCC i.e DC0.
- Equations are developed to predict compressive strength, splitting tension strength and flexural strength of SCC having dolomite by knowing the corresponding strength of normal SCC (DC0) i.e. SCC which is not having dolomite.
- At lower dosages of Dolomite powder (i.e. up to 30%), the hydration products are seen as well spread dense amorphous matter in the SEM micrographs. At higher dosages, unreacted dolomite particles are observed in the SEM micrographs.

Nomenclature

SCC – Self Compacting Concrete
DC0 – Self Compacting Concrete without Dolomite Powder (Control Mix)
DC10 – Self Compacting Concrete with Dolomite Powder as 10% replacement.
DC20 – Self Compacting Concrete with Dolomite Powder as 20% replacement.
DC30 – Self Compacting Concrete with Dolomite Powder as 30% replacement.
DC40 – Self Compacting Concrete with Dolomite Powder as 40% replacement.
DC50 – Self Compacting Concrete with Dolomite Powder as 50% replacement.
DC60 – Self Compacting Concrete with Dolomite Powder as 60% replacement.
DC70 – Self Compacting Concrete with Dolomite Powder as 70% replacement.
$Ca(OH)_2$ – Calcium Hydroxide
f_{cd} – compressive stress of concrete cube with dolomite powder
f_{co} – compressive stress of concrete cube without dolomite powder
f_{rd} – Flexural stress of concrete cube with dolomite powder
f_{ro} – Flexural stress of concrete cube without dolomite powder
f_{td} – Indirect tension stress of concrete cube with dolomite powder
f_{to} – Indirect tension of concrete cube without dolomite powder
f_{cyd} – cylindrical compressive stress of concrete cube with dolomite powder
CSH – Calcium Silicate Hydrate gel
MSH – Magnesium Silicate Hydrate gel
EFNARC – The European Federation of Specialist Construction Chemicals and Concrete Systems.
$CaMg(CO_3)_2$ – Calcium Magnesium Bicarbonate

References

[1] Khan MI, Challa B, Varma SH, Abdy Sayyed MA. Sorptivity and Durability Assessment of Dolomite Impregnated Ternary Concrete. IJRTE. 2019 Jul 30;8(2):5676-81. https://doi.org/10.35940/ijrte.B2896.078219

[2] Nguyen H. Enhancement of engineering properties of slag-cement based self-compacting mortar with dolomite powder. Journal of Building Engineering. 2019 Jul;24:100738. https://doi.org/10.1016/j.jobe.2019.100738

[3] Nguyen H, Chang T, Shih J, Suryadi Djayaprabha H. Enhancement of low-cement self-compacting concrete with dolomite powder. Construction and Building Materials. 2018 Feb;161:539-546. https://doi.org/10.1016/j.conbuildmat.2017.11.148

[4] Jiangtao Xu, Duyou Lu, Hooton RD. Effect of dolomite powder on the hydration and properties of calciumsulfoaluminate cements made with different gypsum contents. Construction and Building Materials. 2019 Jul 23; 225:302-310. https://doi.org/10.1016/j.conbuildmat.2019.07.050

[5] Huamei Y, Zhen H, Yixin S. Early Carbonation Behavior of High-volume Dolomite Powder-cement Based Materials. Journal of Wuhan University of Technology-Mater. Sci. Ed. 2015 Jun;30(3):541-549. https://doi.org/10.1007/s11595-015-1186-6

[6] Marija J R, Ivan G, Dubravka B. Modfications of Dolomite-Based Self-Compacting Concrete Properties Using Mineral Additives. Technical Journal. 2015; 22(1):233-240. https://doi.org/10.17559/TV-20140327212200

[7] Krishnan S, Bishnoi S. Understanding the hydration of dolomite in cementitious systems with reactive aluminosilicates such as calcined clay. Cement and Concrete Research. 2018 Mar 20;108: 116-128. https://doi.org/10.1016/j.cemconres.2018.03.010

[8] Bakhtina T, Lyubomirskiy N, Bakhtin A. Dolomite binding materials with low CO2 emission. Materials Today:Proceedings, International Conference on Modern Trends in Manufacturing Technologies and Equipment, 1998-2004, 2019. https://doi.org/10.1016/j.matpr.2019.07.060

[9] Balakrishnan SD, Paulose KC. Workability and strength characteristics of self-compacting concrete containing fly ash and dolomite powder. AJER. 2013; 2: 43-47.

[10] Olesia M, Grigory Y, Irina M, Sergey S. Effect of Dolomite Limestone Powder on The Compressive Strength of Concrete. Procedia Engineering, 11th International Conference on MBMST, 775 - 780, 2013. https://doi.org/10.1016/j.proeng.2013.04.098

[11] Salah AEG-AEE, Essam AE-AK, Sayieda R R Z, Reham A-E M. Effect of nano-SiO2 (NS) on dolomite concrete towards alkali silica reaction. HBRC Journal. 2018; 14:165-170. https://doi.org/10.1016/j.hbrcj.2016.08.004

[12] Khan M, Cao M, Ali M. Effect of basalt fibers on mechanical properties of calcium carbonate whisker-steel fiber reinforced concrete. Construction and Building Materials. 2018;192: 742-753. https://doi.org/10.1016/j.conbuildmat.2018.10.159

[13] Singh G, Siddique R. Strength properties and micro-structural analysis of self-compacting concrete made with iron slag as partial replacement of fine aggregates. Construction and Building Materials. 2016; 127:144-152. https://doi.org/10.1016/j.conbuildmat.2016.09.154

[14] Choudhary R, Gupta R, Nagar R. Impact on fresh, mechanical, and microstructural properties of high strength self-compacting concrete by marble cutting slurry waste, flyash, and silica fume. Construction and Building Materials. 2020;239: 117888. https://doi.org/10.1016/j.conbuildmat.2019.117888

[15] Wang F, Kong X, Jiang Li, Wang D. The acceleration mechanism of nano-C-S-H particles on OPC hydration. Construction and Building Materials. 2020;249: 118734. https://doi.org/10.1016/j.conbuildmat.2020.118734

[16] Mostafa J, Mojtaba F, Mohammad F. Effects of fly ash and TiO2 nanoparticles on rheological, mechanical, microstructural and thermal properties of high strength self-compacting concrete. Mechanics of Materials. 2013; 61:11-27. https://doi.org/10.1016/j.mechmat.2013.01.010

[17] Esfandiari J, Loghmani P. Effect of perlite powder and silica fume on the compressive strength and microstructural characterization of self-compacting concrete with lime-cement binder. Measurement. 2019; 147:106846. https://doi.org/10.1016/j.measurement.2019.07.074

[18] Muhammed Y D, Atahan H N. Strength, elastic and microstructural properties of SCC with colloidal nano silica addition. Construction and Building Materials. 2018; 158:295-307. https://doi.org/10.1016/j.conbuildmat.2017.10.041

[19] Wu T, Yang X, Wei H, Liu X. Mechanical properties and microstructure of lightweight aggregate concrete with and without fibers. Construction and Building Materials. 2019; 199:526-539. https://doi.org/10.1016/j.conbuildmat.2018.12.037

[20] Vardhan K, Siddique R, Goyal S. Strength, permeation and micro-structural characteristics of concrete incorporating waste marble. Construction and Building Materials. 2019; 203:45-55. https://doi.org/10.1016/j.conbuildmat.2019.01.079

[21] Ríos JD, Mínguez J, De La Concha AM, Vicente MA, Cifuentes H. Microstructural analyses of the addition of PP fibres on the fracture properties of high-strength self-compacting concrete by X-ray computed tomography. Construction and Building Materials. 2020; 261:120499. https://doi.org/10.1016/j.conbuildmat.2020.120499

[22] Bernard E, Lothenbach B, Goff FL, Pochard I, Dauzères A. Effect of magnesium on calcium silicate hydrate (C-S-H). 2017;97:61-72. https://doi.org/10.1016/j.cemconres.2017.03.012

[23] Gomes CM, Adla DS. Oliveira De. Chemical phases and microstructural analysis of pastes based on magnesia cement. Construction and Building Materials. 2018;188: 615-620. https://doi.org/10.1016/j.conbuildmat.2018.08.083

[24] Karthikeyan N, Sathishkumar A, Dennis J R W. Effects on setting, strength and water resistance of sorel cement on mixing fly ash as an additive. International journal of mechanical engineering and robotics research. 2014; 3(2):251-256.

[25] Vandeperre LJ, Liska M, Al-Tabbaa M. Microstructures of reactive magnesia cement blends. Cement & Concrete Composites. 2008;30: 706-714. https://doi.org/10.1016/j.cemconcomp.2008.05.002

[26] Jagadisha A, Balakrishna Rao K, Nayak G, Kamath M. Influence of nano-silica on the microstructural and mechanical properties of high-performance concrete of containing EAF aggregate and processed quarry dust. Construction and Building Materials. 2021; 304:124392. https://doi.org/10.1016/j.conbuildmat.2021.124392

[27] Ruan Y, Jamil T, Chuanlin H, Gautam BP, Jing Y. Microstructure and mechanical properties of sustainable cementitious materials with ultra-high substitution level of calcined clay and limestone powder. Construction and Building Materials. 2022; 312:125416. https://doi.org/10.1016/j.conbuildmat.2021.125416

[28] Nuruzzaman M, Kuri JC, Sarker PK. Strength, permeability and microstructure of self-compacting concrete with the dual use of ferronickel slag as fine aggregate and supplementary binder. Construction and Building Materials. 2021; 318: 125927. https://doi.org/10.1016/j.conbuildmat.2021.125927

[29] Khitab A, Kırgız M S, Nehdi M L, Mirza J, Galdino A G D S, Pour AK. Mechanical, thermal, durability and microstructural behavior of hybrid waste-modified green reactive powder concrete. Construction and Building Materials. 2022;344 :128184. https://doi.org/10.1016/j.conbuildmat.2022.128184

[30] Moghaddam F, Sirivivatnanon V, Vessalas K. The effect of fly ash fineness on heat of hydration, microstructure, flow and compressive strength of blended cement pastes. Case studies in Construction Materials. 2019;10: e00218. https://doi.org/10.1016/j.cscm.2019.e00218

[31] Yu H, Meng T, Zhao Y, Liao J, Ying K. Effects of basalt fiber powder on mechanical properties and microstructure of concrete. Case Studies in Construction Materials. 2022;17: e01286. https://doi.org/10.1016/j.cscm.2022.e01286

[32] Guo L, Wang W, Zhong L, Guo L, Zhang F, Guo Y. Texture analysis of the microstructure of internal curing concrete based on image recognition technology. Case Studies in Construction Materials. 2022;17: 00492. https://doi.org/10.1016/j.cscm.2022.e01360

[33] Liu Y, Yan Z, Duan W, Huang G, Yao Y. Modification of microstructure and physical properties of cement-based mortar made with limestone and alum sludge. Journal of Building Engineering. 2022;58:105200. https://doi.org/10.1016/j.jobe.2022.105000

[34] Li Z, Bian Y, Zhao Ji, Wang Y, Yuan Z. Recycled concrete fine powder (RFP) as cement partial replacement: Influences on the physical properties, hydration characteristics, and microstructure of blended cement. Journal of Building Engineering. 2022;62: 105326. https://doi.org/10.1016/j.jobe.2022.105326

Research on Engineering Structures & Materials
www.jresm.org
Research Group

Research Article

Experimental and factorial design of the mechanical and physical properties of concrete containing waste rubber powder

Ameur Belmouhoub*[1, a], Assia Abdelouahed[1, b], Ammar Noui[2, c]

[1]*Dept. of Civil Eng., 20 Août 1955 University of Skikda, Algeria*
[2]*Dept. of Civil Eng., Mohamed El Bachir El Ibrahimi University of Bordj Bou Arreridj, Algeria*

Article Info

Article history:

Received 10 Aug 2023
Accepted 20 Oct 2023

Keywords:

Rubber;
Mechanical and physical properties;
Performance;
Substitution;
Full factorial design;
Waste

Abstract

The application of waste rubber in the Civil Engineering is considered one of the most effective solutions for managing this waste. Therefore, the aim of this study is to analyze the effect of rubber substituted in cement on the physical and mechanical properties of concrete using the general full factorial design method, and compare the laboratory results with the results of the JMP pilot test program, and find out if there is a match between the results. The rubber powder is used as a mass substitute in cement at rates of 0%, 2%, 4%, 6% and 8%. The fresh properties were evaluated through workability, air content, and fresh density tests, whereas the hardened properties were assessed using tests of compressive strength, flexural strength, and ultrasonic pulse velocity. These concretes have the workability from 8 to 14.5 cm, fresh density from 2.20 to 2.38 (g/cm^3). The air content ranged from 1.2 to 1.9%. Furthermore, the compressive strength ranged from 22.85 to 43.97 MPa, while the flexural strength ranged from 4.86 to 7.03 MPa. In addition, ultrasonic velocity from 3831.42 to 4098.36 (m/s). Accordingly, it was concluded that the concrete with 2% of rubber represented significantly better compressive strength compared to the ordinary concrete. The numerical modeling is assessed to have an appropriate determined coefficient R^2 close to 1 for the workability, fresh density, air content, compressive strength, flexural strength, and ultrasonic pulse velocity.

1. Introduction

The exponential rise in population and transportation growth is increasing the tire manufacturing for automobiles [1]. Waste tires that are no longer in use produce a significant amount of rubber waste. In 2017, the production of tires in the world exceeded 2.9 billion tires per year [2]. By 2030, 1200 million more motor vehicle tires are predicted to be produced with 5000 million of those destined for landfills [3]. The accumulation of waste rubber tires has negative effects on the environment and human health [4]. Rubber is not biodegradable, and its combustion produces toxic gases that are harmful to humans [5]. Additionally, the aggregation of waste rubber provides an ideal environment for the breeding of dangerous insects that could cause significant illnesses among people [6]. Researchers attempted to provide an appropriate guideline for recycling waste materials in a way that protects the environment and contributes to economic growth. 46% of this rubber waste was used as fuel for generating energy, while 36% of it was buried, and 21% was used in the field of civil engineering. Researchers investigated the impact of recycled rubber on the properties of concrete and discovered that it offers one of the most effective means to eliminate this waste, recycled rubber was utilized as modifiers or additives in

*Corresponding author: a.belmouhoub@univ-skikda.dz
[a] orcid.org/0009-0002-9468-8717; [b] orcid.org/0000-0001-5671-7033; [c] orcid.org/0009-0005-6325-7131
DOI: http://dx.doi.org/10.17515/resm2023.54me0810rs

Portland Cement Concrete (PCC) combinations and asphalt paving mixtures [7]. Accordingly, Maher Al-Tayeb et al. [8] employed rubber powder with a content of 2.5%, 5%, and 10% substituted in cement. They found that the workability increased with increasing the percentage of rubber. As well, the compressive strength decreased by 19%, 32%, and 53% for concrete containing 2.5%, 5%, and 10% rubber, respectively. Wang et al. [9] demonstrated an increase in workability with an increase in the percentage of rubber. In addition, Steyn et al. [10] used three types of waste (low-density polyethylene plastic, rubber, and glass) in proportions of 15% and 30% as a substitution in fine aggregates. The results obtained show that rubber and glass increase air content. Pelisser et al. [11] report that rubberized concrete has a reported 13% lower density than ordinary concrete. Gupta et al. [12] register that replacing the natural fine aggregate by 20% with rubber ash results in a decrease in compressive strength and flexural strength of 28.77% and 32.87%, respectively. Singh et al. [13] used crumb rubber as a fine aggregate in concrete. They found the compressive strength decreased with increasing the amount of crumb rubber. The 15% replacement of crumb rubber as fine aggregates led to a 35% reduction in compressive strength as well as a decrease in ultrasonic pulse velocity compared to the reference concrete. Bisht and Ramana [14] used rubber powder in concrete at a ratio of 0%, 4%, 4.5%, 5%, and 5.5%. They observed that the flexural strength decreased by 2.9% and 16.5% for concrete containing 4% and 5.5% rubber powder, respectively. Pavankalyan et al. [15] used crumb rubber as a substitution for fine aggregates by 5% to 20%. The results obtained show that the compressive strength and ultrasonic pulse velocity decreased with increasing the percentage of rubber; the compressive strength decreased from 48 to 21.39 MPa for the mix CR0 and the mix CR20, respectively, compared to the reference concrete. In a study conducted by Najim and Hall [16], they replaced the fine and coarse aggregate, as well as a combination of both, with crumb rubber by 5% to 15%. The results indicated that the ultrasonic pulse velocity decreased as the amount of rubber replacement increased.

Table 1. Results of concrete with rubber obtained by the authors

Authors	Substitution	Results
Maher Al-Tayeb et al. [8] and Wang et al. [9]	Rubber powder substitution in cement	Workability increased with an increase the rubber powder
Pelisser et al. [11]	Rubber used in concrete	Fresh density decreased by 13% compared to ordinary concrete
Chylík et al. [22]	Crumb rubber used in concrete	Air content increased with an increase the crumb rubber
Gupta et al. [12]	Replaced the fine aggregates by 20% with rubber ash	Compressive strength and flexural decreased by 28.77% and 32.87%, respectively
Singh et al. [13]	Used crumb rubber as fine aggregates in concrete	Compressive strength and ultrasonic pulse velocity decreased with an increase rubber

Experiment design JMP is a statistical program that is used to plan and evaluate experiments that test scientific hypotheses, as well as to help users comprehend the findings and make well-informed decisions [17, 18]. The aim of this study is to analyze the effect of rubber substituted in cement on the physical and mechanical properties of concrete using the general full factorial design method, compare the laboratory results

with the results of the JMP pilot test program, and find out if there is a match between the results.

2. Materials and Methods

2.1 Materials

In this work, six different types of materials are used to make the concrete: cement, rubber, sand (0/3), gravel (3/8), gravel (8/15), and water.

2.1.1 Cement

The cement used is of type CRS-CEMI-42.5 and was brought from the Ain Kebira Company, which is located in Setif, in the east of Algeria. The chemical properties, physical properties, and granulometric analyzer of this cement are stated in Table 2, Table 3, and Figure 3, respectively.

2.1.2 Rubber

The rubber waste used in this research is in the form of powder. It was brought from the El Hachimia plant, which is located in Bouira in the east of Algeria. The chemical properties, physical properties, and granulometric analyzer of this rubber are stated in Table 4, Table 5, and Figure 3, respectively.

The surface of the rubber is so smooth that it was treated with 10% NaOH and laid in this solution for 20 minutes. After extracting it from this solution, it is cleaned with water and then dried in the air. The aim of this treatment is to increase the adhesion of rubber to form a strong bond between rubber and cement, the figure 1 a) and b) present the rubber used in this research before and after treatment.

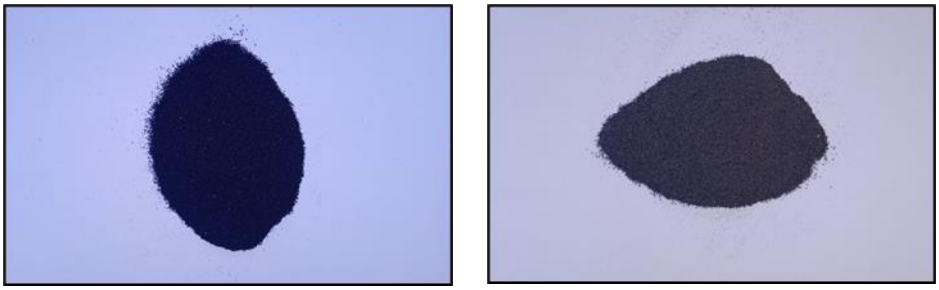

(a) (b)

Fig. 1. (a) Rubber before treatment, (b) rubber after treatment

2.1.3 Sand

The sand used in this research, sand of class 0/3, was brought from Oued Souf, situated in south Algeria. The physical properties, chemical properties, and granulometric analyzer of this sand are stated in Tables 5 and 6, respectively.

2.1.4 Gravel

The gravel used in this research gravel 3/8 and 8/15, was brought from the quarry Laala Aci-Mazara-Ain Lahdjar-Setif in the east of Algeria. The physical properties, chemical properties, and granulometric analyzer of this gravel are stated in Tables 5, 7, and 8, respectively.

2.1.5 Water

In this research, potable water was used in all the mixes.

Table 2. Chemical composition of the cement

Designation	Content (%)
CaO %	62.04
Al_2O_3%	4.59
Fe_2O_3%	5.08
SiO_2%	23.41
MgO%	1.74
Na_2O%	0.17
K_2O%	0.34
Cl%	0.05
SO_3%	1.46
C_3S%	36.50
C_2S%	39.90
C_3A%	3.50
C_4AF%	15.40

Table 3. Physical composition of the cement

Designation	Value
Apparent density (g/cm^3)	3.10
Absolute density (g/cm^3)	1.05
BSS (cm^2/g)	2800.20
Initial setting time (min)	90
Final setting time (min)	260

Table 4. Chemical properties of the rubber

Chemical components	Value (%)
Rubber hydrocarbon	46.05
Acetone extract	15.20
Inorganic sulfur	0.60
Ash content	4.55
Carbon black	29.70
SiO_2	0.55
TiO_2	0.15
ZnO	1.70
CaO	0.55
$Fe_2O_3 + Al_2O_3$	0.3
Fiber content	0.42
Water content	0.80

Table 5. Characteristics of sand (0/3), gravel (3/8), gravel (8/15), and rubber

Characteristics	sand (0/3)	gravel (3/8)	gravel (8/15)	rubber
Absolute density (g /cm^3)	2.55	2.66	2.66	0.94
Apparent density (g/cm^3)	1.62	1.36	1.42	0.34
Fineness modulus (%)	1.97	/	/	/
Sand equivalent (%)	81.61	/	/	/
Absorption (%)	2.5	0.99	0.99	

Table 6. Granulometric analyzer of sand (0/3

Sand 0/3	Cumulative refusal (g)	Cumulative refusal (%)	Passing (%)
4	8	0.8	99.2
2	33	3.3	96.7
1	138	13.8	86.2
0.5	580	58	42
0.25	927	92.7	7.3
0.125	989	98.9	1.1
0.063	993	99.3	0.7
Bottom	993	99.3	0.7

Table 7. Granulometric analyzer of gravel (3/8)

Gravel 3/8	Cumulative refusal (g)	Cumulative refusal (%)	Passing (%)
10	0	0	100
8	22	1.37	98.63
6.3	505	31.56	68.44
4	1488	93	7
2	1598	99.87	0.13
Bottom	1598	99.87	0.13

Table 8. Granulometric analyzer of gravel (8/15)

Gravel 8/15	Cumulative refusal (g)	Cumulative refusal (%)	Passing (%)
16	15	0.5	99.5
12.5	589	19.63	80.37
10	1281	42.7	57.3
8	2410	80.33	19.67
6.3	2998	99.93	0.07
Bottom	2998	99.93	0.07

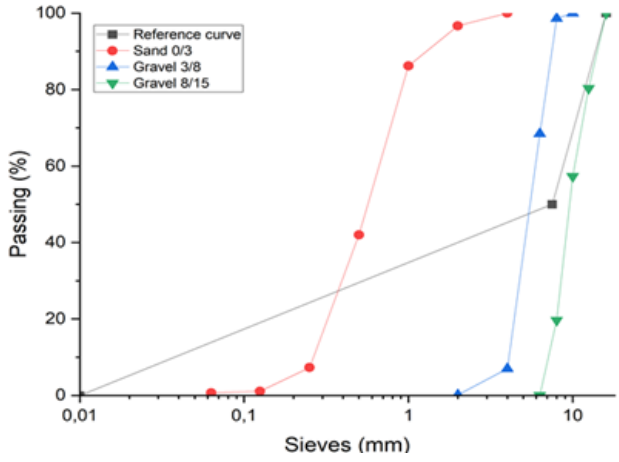

Fig. 2. Granulometric curve of the sand 0/3, gravel 3/8 and gravel 8/15

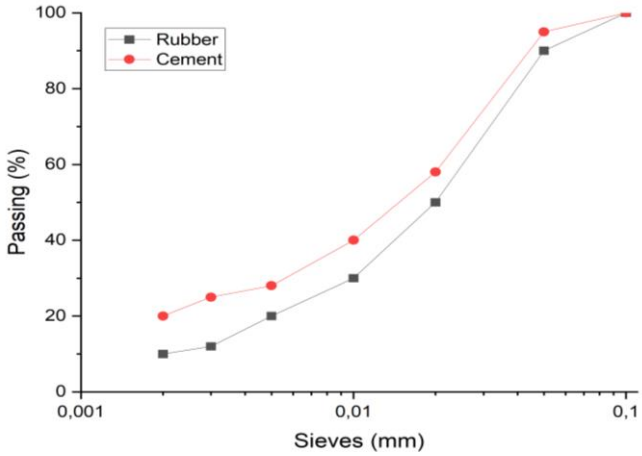

Fig. 3. Granulometric curve of the cement, and rubber

From Figure 2 and Figure 3, the particle size of sand, gravel 3/8, and gravel 8/15 was determined by a granulometric analyzer according to the NF EN 933-1 standard, and the particle size of cement and rubber was determined using a laser diffraction particle size analyzer according to the NF P 94-05792 standard.

2.2. Experimental Methods

In this work, the Dreux-Gorisse method is used. The Dreux-Gorisse method is an empirical method used to estimate the absolute density of concrete. It is based on the relationship between the absolute density of concrete and the absolute mass of its components (sand, gravel, cement, and water).

Table 9. The quantities of gravel, sand, cement, water, and rubber in one cubic meter

Mixes	Gravel 8/15 (Kg/m³)	Gravel 3/8 (Kg/m³)	Sand 0/3 (Kg/m³)	Cement (Kg/m³)	Water (L/m³)	Rubber (Kg/m³)
0	689	219	741	400	209	0
2	689	219	741	392	209	8
4	689	219	741	384	209	16
6	689	219	741	376	209	24
8	689	219	741	368	209	32

Table 10. The tests used with standards

Tests	Standards
Workability	NF EN 12350-2
Fresh density	NF EN 12350-6
Air content	NF EN 12350-7
Compressive strength	NF EN 12390-3
Flexural strength	NF EN 12390-5
Ultrasonic pulse velocity	NF EN 12504-4

Rubber powders were used to partially replace cement in the concrete at replacement weight ratios of 0, 2, 4, 6, and 8%. 0% of rubber powder was used as a reference, at every age, three pieces are used. The test specimens produced from the fresh concrete were stored for 24 hours in ambient laboratory conditions (20 °C). After 24 hours, the samples

were removed from the molds. Subsequently, the test pieces were immersed in water until the time of the test. The molds used in these tests were 7 x 7 x 28 cm^3 and 10 x 10 x 10 cm^3.

4. Results

4.1. Fresh properties

This section displays three different types of tests: workability, fresh density, and air content.

4.1.1. Workability

The workability values of rubber concrete measured in the laboratory are presented in Figure 4. From figure 4, it can be seen that the workability increases when the amount of rubber increases. It was seen that the minimum value of the workability was 8 cm for control concrete (0% of rubber), and the highest value of the workability was 14.5 cm for concrete containing 8% rubber. The increase in workability was slight until the percentage of 6% of waste, where the increase was in rush.

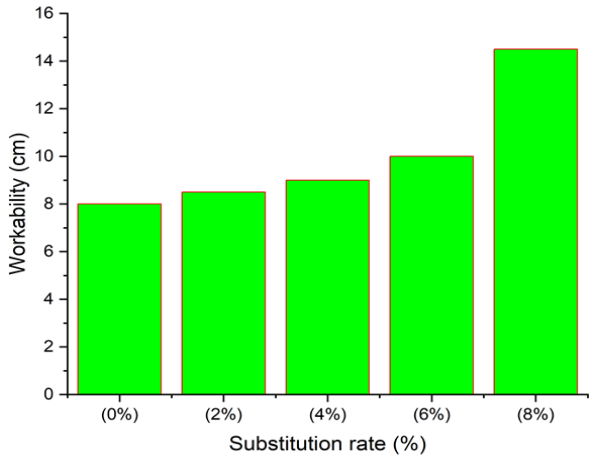

Fig. 4. Workability values with different rubber rations added to concrete

This increase in workability is due to the smooth surface of the rubber and its nature that does not absorb water, which makes the concrete more plastic, on the other hand, the presence of bulk water in the mixture. A similar result was given by [8, 9].

4.1.2. Fresh Density

The fresh density tests at rates of 0%, 2%, 4%, 6%, and 8% from the added rubber are presented in figure 5. The fresh density decreases as the ratio of rubber increases. The lowest density recorded is 2.20 g/cm^3 for concrete containing 8% of rubber, and the highest density is 2.38 g/cm^3 for concrete containing 0% of rubber. The incorporation of 2%, 4%, 6%, and 8% of rubber in concrete results in a decrease in fresh density of 2.10%, 2.94%, 5.46%, and 7.56%, respectively, as compared to ordinary concrete.

This drop is due to the fact that the density of rubber powder is much lighter compared to the density of natural aggregates (0.94 for rubber powder and 2.66 for natural aggregates). As well, the presence of rubber in cement and water can affect the hardening and cohesion processes of concrete, leading to the formation of voids in the concrete. This causes a decrease in density. These results are consistent with those obtained by some authors [19, 20].

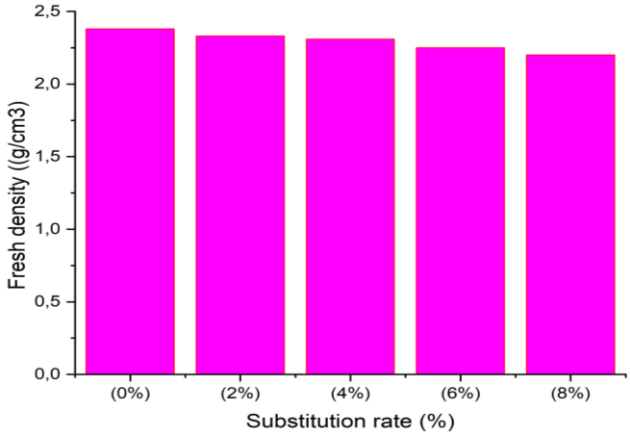

Fig. 5. Fresh density values with different rubber rations added to concrete

4.1.3. Air Content

The results of the air content test are presented in Figure 6. It has been observed from figure 6, that the air content increases with an increase in the percentage of rubber, and it was also found that the higher percentage of air content is 1.9% for concrete containing 8% rubber, which corresponds to an increase of 58% compared to normal concrete, and the low percentage of air content is 1.2% for concrete containing 0% rubber.

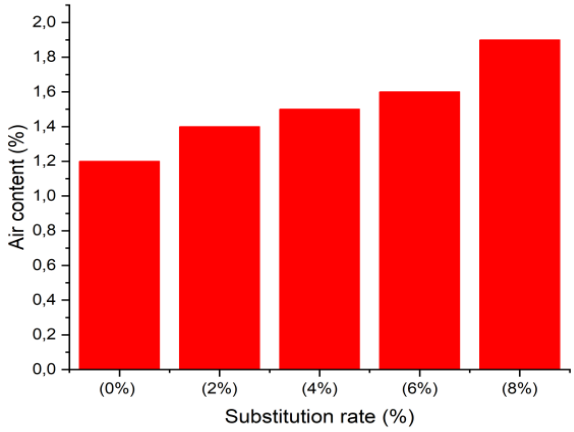

Fig. 6. Air content values with different rubber rations added to concrete

This increase is due to the low adhesion between the rubber powder and the cementitious matrix, which creates voids between the particles, so each time we increase the percentage of rubber, the air content increases, and on the other hand, the presence of rubber powder can create bubbles when mixed with concrete. These bubbles can trap air inside the concrete mass, increasing the amount of occluded air. These results are consistent with those obtained by some authors [21, 22].

4.2. Hardened Properties

In this section, three different sorts of tests are used: compressive strength, flexural strength, and ultrasonic pulse velocity.

4.2.1. Compressive Strength

The compressive strength of the samples was determined at the age of 28 days; the results are shown in Figure 7. It was seen that the maximum value of compressive strength is 43.97 MPa for concrete containing 2% rubber compared to ordinary concrete. After this value, the compressive strength continued to drop when increasing the percentage of rubber; the lowest recorded value is 22.85 MPa for concrete containing 8% rubber, which corresponds to a decrease of 47% compared to normal concrete. These results are consistent with those obtained by Abdullah et al. [23] found that the compressive strength for foamed concrete containing 6% and 9% of rubber continued to develop comparable to the reference concrete, except for the mixture, which contains 12% of rubber, whose resistance has decreased.

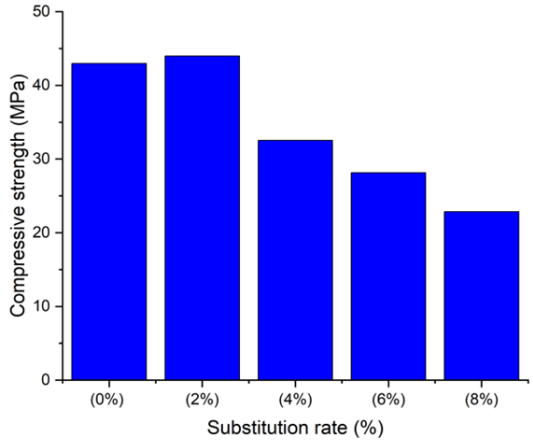

Fig. 7. Variation of compressive strength with different rubber rations added to concrete

This drop in compressive strength may be attributed to the low cohesion between the rubber granules and the cement, which creates voids in the mixture and leads to a decrease in compressive strength, and the poor hardness of rubber compared to natural aggregates. As well, rubber waste has a lower density than traditional aggregates, which means it can take up more space in the mixture. This can lead to a decrease in the amount of cement and aggregates in the mixture, which affects the compressive strength. These results are consistent with those obtained by [19, 22, 24].

4.2.2. Flexural Strength

The flexural strength of the samples was determined at the age of 28 days; the results are shown in Figure 8.

It was observed that the flexural strength at 28 days decreases when the percentage of rubber increases, the minimum value of flexural strength is 5 MPa for concrete containing 8% rubber, and the maximum value of flexural strength is 7.03 MPa for concrete containing 0% of rubber. Flexural strength decreases by up to 31% for concrete containing 8% rubber and decrease of 10% for concrete containing 2% rubber when compared to ordinary concrete. This decrease in flexural strength may be due to the same factors that caused a

reduction in compressive strength. On the other hand, rubber has a strength that is lower than the strength of natural aggregate. These results are consistent with those obtained by [24, 25, 26].

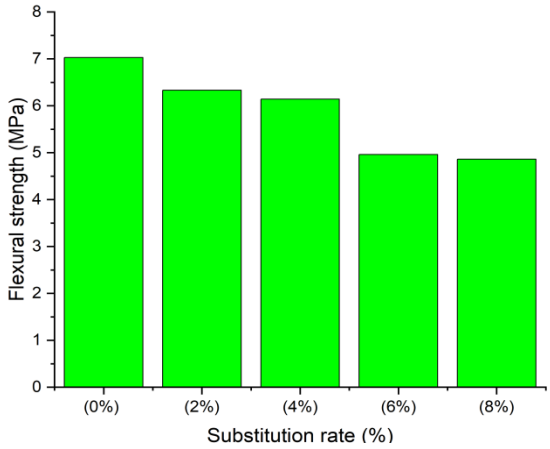

Fig. 8. Flexural strength of different concretes

4.2.3. Ultrasonic pulse velocity

Figure 9 shows the evolution of the ultrasonic pulse velocity of the concretes studied as a function of rubber substitution rates. Each time the percentage of rubber was increased, there was a drop in ultrasonic speed; the lowest value shown is 3831.42 m/s for concrete containing 8% of rubber.

The ultrasonic pulse velocity decreases by 2.24%, 3.55%, 4.31%, and 6.51% for concrete containing 2%, 4%, 6%, and 8% of rubber, respectively compared to the ordinary concrete. This drop in the speed of propagation of ultrasonic waves is explained by composites' higher levels of water and air content, which causes an increase in the time of ultrasonic propagation. Rubber waste present in concrete can create discontinuous interfaces or areas of low density, which can lead to a decrease in ultrasonic speed. This increase reduces the speed of propagation. These results are in agreement with those obtained by some authors [15, 27, 28].

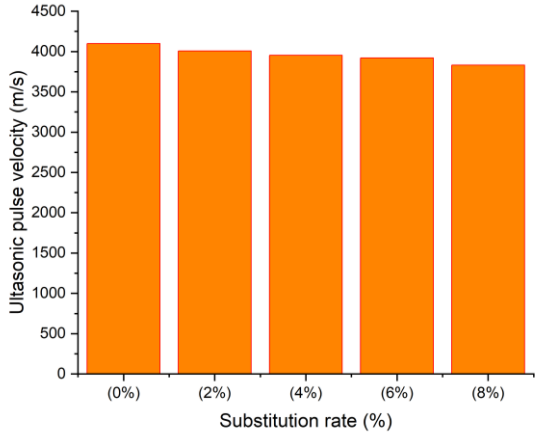

Fig. 9. Ultrasonic pulse velocity values with different rubber rations added to concrete

5. Modeling of The Physique and Mechanical Response

5.1 Statistical Study with Factorial Design Approach

An efficient statistical method for planning experimental research and assessing the primary and secondary effects between variables and independent effect variables is the factorial design [29, 30]. The anticipated result is taken from the mathematical equation shown below:

$$Y = X_0 + X_1 R \quad (1)$$

Where: (Y) is the expected response and (X_0, X_1,) are the model coefficients, and R is the rubber (%).

5.2 Correlation

(Workability, Density, Air content, compressive strength, Flexural strength and ultrasonic pulse velocity). The results of the experimental tests presented in Table 11. We have five experiments proposed by full factorial design.

Table 11. Experimental results

Test	Rubber (%)	Workability (cm)	Density (kg/m³)	Air content (%)	Compressive strength (MPa)	Flexural strength (MPa)	Ultrasonic (m/s)
1	0	8	2.38	1.2	42.96	7.03	4098.36
2	2	8.5	2.33	1.4	43.97	6.33	4006.41
3	4	9	2.31	1.5	32.54	6.14	3952.57
4	6	10	2.25	1.6	28.15	4.96	3921.57
5	8	14.5	2.20	1.9	22.85	4.96	3831.42

5.3 Verification of the Proposed Models' Validity

The correlation between the observed and predicted values is presented in Figure 10, and the experimental results of characterization tests are presented in Table 12. From figure 10, it can be seen that there is a high relationship between the results observed and the results predicted.

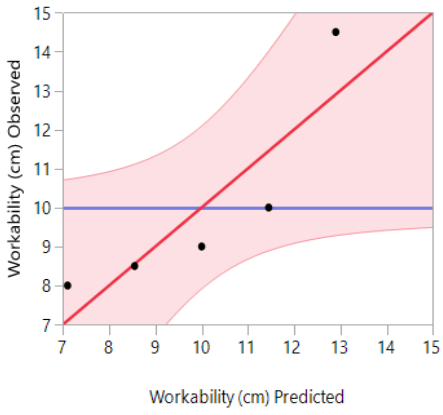

(a) Workability

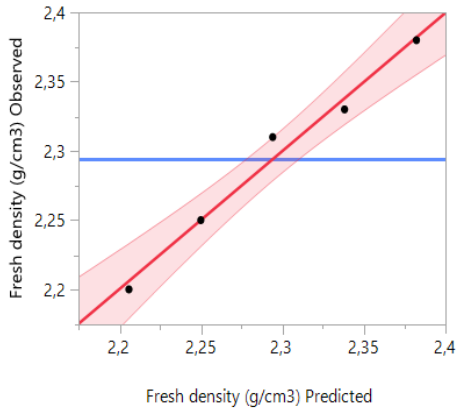

(b) Fresh density

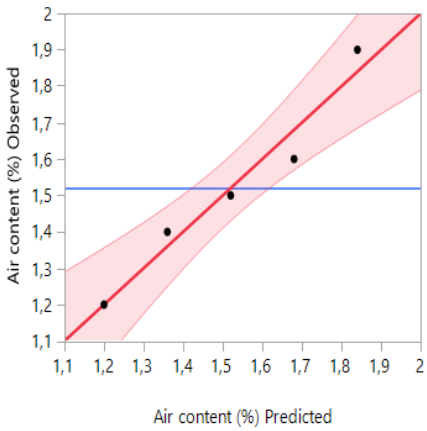

(c) Air content

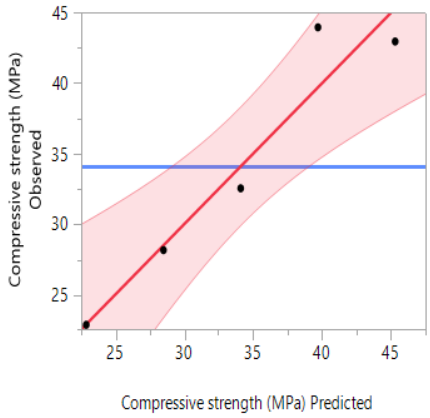

(d) Compressive strength

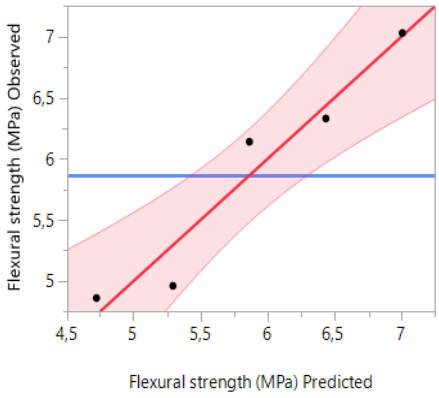

(e) Flexural strength

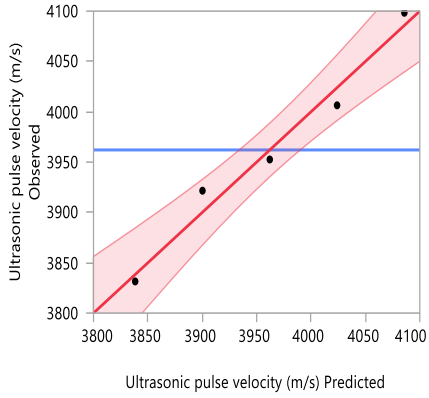

(f) Ultrasonic pulse velocity

Fig. 10. Correlation between the observed and predicted responses a workability, fresh density, air content, compressive strength, flexural strength, and ultrasonic pulse velocity

It can be said that the applied models are very accurate in predicting the behavior of rubber in the physical and mechanical properties of concrete, and from Table 12. It can be observed that the correlation coefficients are between 0.76 and 0.97 and are close to 1, which indicates a good correlation between the predicted and experimental models.

Table 12. Experimental results of characterization tests

	Workability	Fresh density	Air content	Compressive strength	Flexural strength	Ultrasonic velocity
R^2	0.76	0.98	0.95	0.92	0.93	0.97
Adjusted R^2	0.68	0.97	0.94	0.89	0.91	0.96
R MSE	1.46	0.01	0.06	2.95	0.26	18.79
Mean of Response	10	2.29	1.52	34.09	5.86	3962.06

5.4 Workability

Figure 11a shows the main effects plots for the workability response of the concrete, taking into account the factors of the content of the rubber (%). It can be seen that the workability increases from 7.1 to 12.9 cm due to the change in the percentage of rubber from 0 to 8%. It was also seen that the rubber powder content has a positive effect on this response. These results agree with the mathematical equation, eq. 2.

$$Workability\ (cm) = 10 + 2.9\left(\frac{Rubber - 4}{4}\right) \quad (2)$$

From the residue diagram as a function of the predicted values (graph 11b), it can be seen that normalized residuals are greater than +1.5 and less than -1.5. This suggests that there is a little discrepancy between the expected and experimental results in the chart.

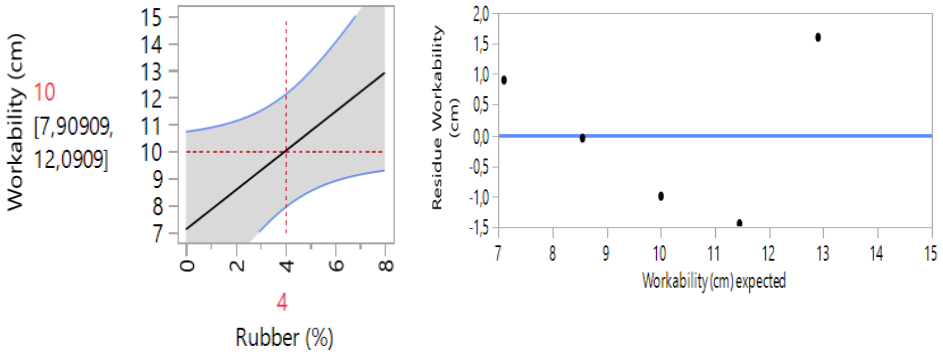

(a) (b)

Fig. 11. (a)Main effects plot, (b) graph perform the residues as a function of the predicted values

5.5 Fresh Density

Figure 12a shows the main effects plots for the fresh density response of the concrete. It can be noted that with an increase in the percentage of rubber from 0 to 8%, the fresh density decreases from 2.38 to 2.20 g/cm³.

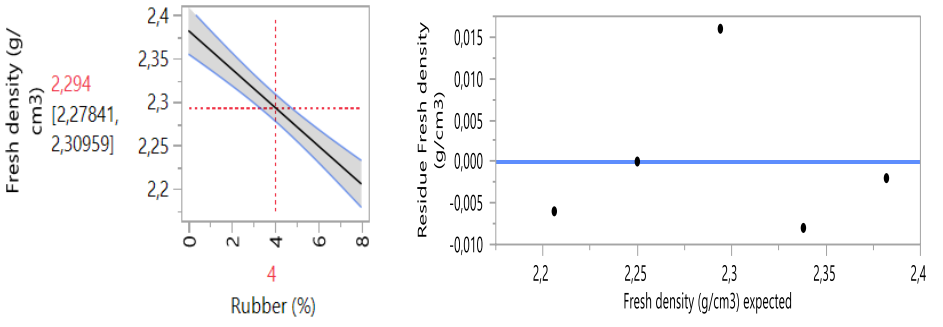

(a) (b)

Fig. 12. (a) Main effects plot (b) graph perform the residues as a function of the predicted values

It has also been observed that the content of rubber powder has an influence on the response, which shows that when increasing the amount of rubber, the density decreases. These results agree with the mathematical equation Eq. 3;

$$Fresh\ density\ (g/cm3) = 2.294 - 0.088\left(\frac{Rubber-4}{4}\right) \quad (3)$$

From the graph 12b of the residues as a function of the predicted values, it is quite clear that normalized residuals are greater than +0.015 and less than -0.010. The model indicates a negligible difference between the experimental value and the adjusted value.

5.6 Air Content

From figure 13a, it can be noted that the air content increases from 1.2 to 1.8% with an increase in the percentage of rubber from 0 to 8%. While the increase in the content of rubber powder has a slight influence on the air content. These results agree with the mathematical equation Eq. 4;

$$Air\ content\ (\%) = 1.52 + 0.32\left(\frac{Rubber-4}{4}\right) \quad (4)$$

It is pretty obvious from the graph 13b showing the residues as a function of the expected values that the normalized residuals are greater than +0.05 and smaller than -0.1. It indicates that the points are distributed consistently along the diagonal. This indicates the convergence of the experimental and numerical results.

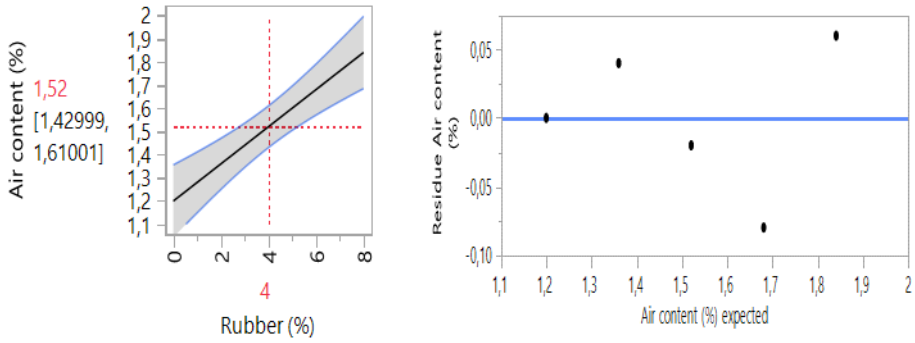

(a) (b)

Fig. 13. (a) Main effects plot (b) graph perform the residues as a function of the predicted values

5.7 Compressive Strength

Figure 14a shows the main effect plots for the compressive strength response of the concrete. Show clearly that the increase in rubber powder decreases the compressive strength; remarkably, indeed, the content of rubber powder presents a high negative effect on the response. As can be seen, there was a significant decrease in the compressive strength from 45.30 to 22.88 MPa due to the change in the percentage of rubber from 0 to 8%. These results agree with the mathematical equation Eq. 5;

$$Compressive\ strength\ (MPa) = 34.094 - 11.208\left(\frac{Rubber-4}{4}\right) \quad (5)$$

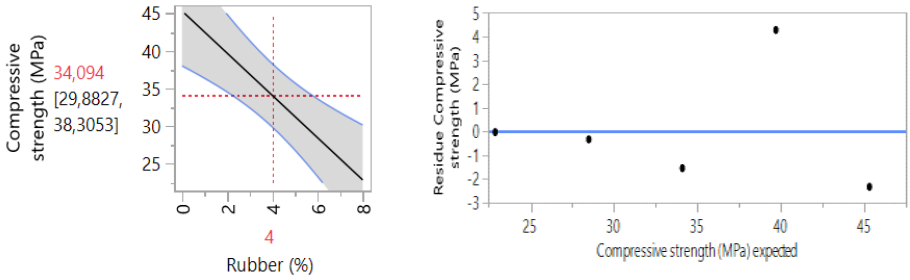

(a) (b)

Fig. 14. (a) Main effects plot (b) graph perform the residues as a function of the predicted values

From the graph 14b, which shows the residues as a function of the predicted values, it is quite clear that normalized residuals are greater than +4 and less than -3. There are no points dispersed, and the points are distributed consistently along the diagonal.

5.8 Flexural Strength

Figure 15a shows the main effect plots for the flexural strength response. It can be noted that the flexural strength decreases from 7 to 4.72 MPa with increasing the percentage of rubber from 0 to 8%. It may be noted that the rubber powder has a small negative effect on this response. These results agree with the mathematical equation Eq. 6;

$$Flexural\ strength\ (MPa) = 5.864 - 1.142\left(\frac{Rubber-4}{4}\right) \quad (6)$$

From the residue diagram as a function of the predicted values (graph 15b), it was seen that normalized residues were greater than +0.3 and less than -0.4. The model indicates a negligible difference between the experimental value and the adjusted value.

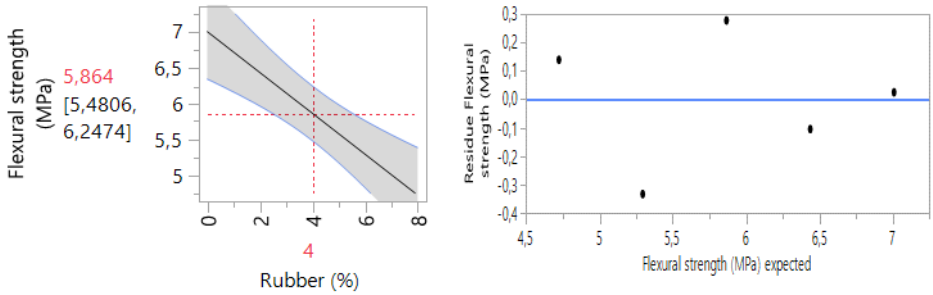

(a) (b)

Fig. 15. (a) Main effects plot (b) graph perform the residues as a function of the predicted values

5.9 Ultrasonic Pulse Velocity

Figure 16a shows the main effect plots for the ultrasonic pulse velocity response of the concrete, taking into account the factors of the content of the rubber (%). It can be seen

that the ultrasonic pulse velocity decreases from 4085.81 to 3838.32 m/s with increasing the percentage of rubber from 0 to 8%.
The increase in the content of rubber powder has a small influence on the response. These results agree with the mathematical equation
Eq. 7;

$$Ultrasonic\ pulse\ velocity\ (m/s) = 3962.066 - 123.744\left(\frac{Rubber-4}{4}\right) \quad (7)$$

From the residue diagram as a function of the predicted values (graph 16b), it was seen that normalized residues were greater than +20 and less than -20. Thus, the planned model specifies an insignificant discrepancy between the adjusted value and the experimental value.

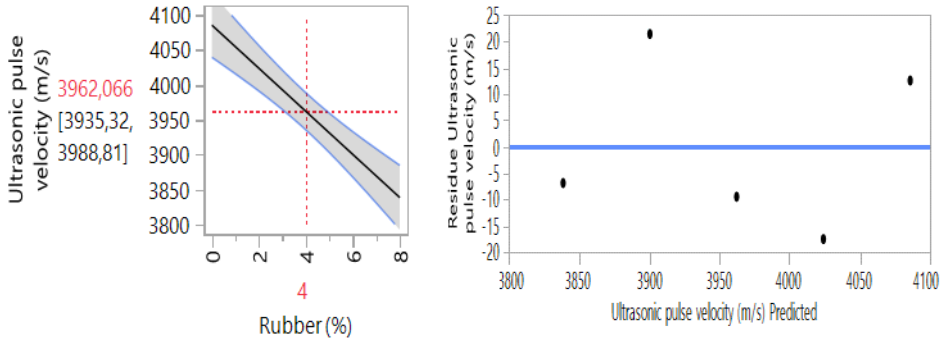

(a) (b)

Fig. 16. (a) Main effects plot (b) graph perform the residues as a function of the predicted values

5.10 Comparison of Predicted Values with Experimental Values Using the JMP Model

After presenting the results, it is noted that the deviation of the prediction values compared to the experimental values is acceptable.

Table 13. Workability

N	Rubber (%)	workability (cm)	Predicted Workability (cm)	Residue Workability (cm)
1	0	8	7.1	0.9
2	2	8.5	8.55	-0.05
3	4	9	10	-1
4	6	10	11.45	-1.45
5	8	14.5	12.9	1.6

Table 14. Fresh density

N	Rubber (%)	Predicted density(g/cm^3)	Residue Density (g/cm^3)	Residue Fresh density (g/cm^3)
1	0	2.38	2.382	-0.002
2	2	2.33	2.338	-0.008
3	4	2.31	2.294	0.016
4	6	2.25	2.25	0
5	8	2.20	2.206	-0.006

Table 15. Air content

N	Rubber (%)	Air content (%)	Predicted Air content (%)	Residue Air content (%)
1	0	1.2	1.20	0
2	2	1.4	1.36	0.04
3	4	1.5	1.52	-0.02
4	6	1.6	1.68	1.68
5	8	1.9	1.84	0.06

Table 16. Compressive strength

N	Rubber (%)	Compressive Strength (MPa]	Predicted compressive strength (MPa)	Residue Compressive Strength (MPa)
1	0	42.96	45.302	-2.342
2	2	43.97	39.698	4.272
3	4	32.54	34.094	-1.554
4	6	28.15	28.48	-0.34
5	8	22.85	22.886	-0.036

Table 17. Flexural strength

N	Rubber (%)	Flexural Strength (MPa)	Predicted Flexural Strength (MPa)	Residue Flexural Strength (MPa)
1	0	7.03	7.006	0.024
2	2	6.33	6.435	-0.105
3	4	6.14	5.864	0.276
4	6	4.96	5.293	-0.333
5	8	4.86	4.722	0.138

Table 18. Ultrasonic pulse velocity

N	Rubber (%)	Ultrasonic (m/s)	Predicted Ultrasonic (m/s)	Residue Ultrasonic (m/s)
1	0	4098.36	4085.810	12.55
2	2	4006.41	4023.938	-17.528
3	4	3952.57	3962.066	-9.496
4	6	3921.57	3900.066	21.376
5	8	3831.42	3838.322	-6.902

6. Conclusion

Based on the experimental results obtained and numerical modeling in the current study of concrete containing waste rubber in the proportions of 0%, 2%, 4%, 6%, and 8%, the following conclusions were drawn:

The workability and air content of concrete increase with the increase in the levels of rubber powder. Partial cement replacement with rubber powder by 2%, 4%, 6%, and 8% led to a decrease in the fresh density of 2.10%, 2.94%, 5.46%, and 7.56%, respectively, compared to the reference concrete. Using rubber powder in concrete decreases the compressive strength with an increase in the amount of rubber, the decrease in compressive strength is 47% for concrete containing 8% of rubber when compared to the reference concrete.

The flexural strength decreases by 10%, 13%, 29.44%, and 30.86% for replacement levels of rubber powder of 2%, 4%, 6%, and 8%, respectively, compared to the reference concrete. As the replacement ratio of rubber powder in concrete increases, the ultrasonic pulse velocity decreases by 2.24%, 3.55%, 4.31%, and 6.51% for replacement levels of rubber powder of 2%, 4%, 6%, and 8%, respectively, compared to the reference concrete.

Adding 2% rubber waste to the concrete gave it good strength, greater than normal concrete strength. Statistical parameters show good correlation coefficients (R^2= 0.76; 0.98; 0.95; 0.92; 0.93; and 0.97) for workability, fresh density, air content, compressive strength, flexural strength, and ultrasonic pulse velocity, respectively. The values of (R^2) are close to 1, which shows a good correlation between the predicted and experimental models. This leads us to the conclusion that the model in use is reliable and effective at predicting the effect of waste rubber on concrete that has been examined for its mechanical and physical properties.

This study provides valuable information about the use of this numerical model in the field of civil engineering in order to obtain reliable and accurate results.

Acknowledgements

The authors are extremely appreciative of the University of SKIKDA and the University of Bordj Bou Arreridj, Algeria.

References

[1] Siddika A,Al Mamun Md, Alyousef R ,Mugahed Amran Y,Aslani F, Alabduljabbar H. Properties and utilizations of waste tire rubber in concrete: A review.Construction and Building Materials, 2019; 224: 711- 731. https://doi.org/10.1016/j.conbuildmat.2019.07.108

[2] Raffoul S, Garcia R, Escolano-Margarit D, Guadagnini M, Hajirasouliha I, Pilakoutas K. Behaviour of unconfined and FRP-confined rubberised concrete in axial compression. Construction and Building Materials, 2017; 147: 388- 397. https://doi.org/10.1016/j.conbuildmat.2017.04.175

[3] Ferronato N, Torretta V. Waste Mismanagement in Developing Countries: A Review of Global Issues. International Journal of Environmental Research and Public Health, 2019; 16(6), 1060. https://doi.org/10.3390/ijerph16061060

[4] Mohajerani A, Burnett L, Smith J. V, Markovski S, Rodwell G, Rahman M. T, Kurmus H, Mirzababaei M, Arulrajah A, Horpibulsuk S, Maghool F. Recycling waste rubber tyres in construction materials and associated environmental considerations: A review. Resources, Conservation and Recycling, 2020; 155, 104679. https://doi.org/10.1016/j.resconrec.2020.104679

[5] Bisht K, Ramana P.V. Evaluation of mechanical and durability properties of crumb rubber concrete.Construction and Building Materials. 2017:155:811-817. https://doi.org/10.1016/j.conbuildmat.2017.08.131
[6] Guelmine L, Hadjab H, Benazzouk A. Effect of elevated temperatures on physical and mechanical properties of recycled rubber mortar. Construction and Building Materials. 2016; 126: 77-85. https://doi.org/10.1016/j.conbuildmat.2016.09.018
[7] Dong Q,Huang B, Shu X. Rubber modified concrete improved by chemically active coating and silane coupling agent. Construction and Building Materials.2013:48:116-123. https://doi.org/10.1016/j.conbuildmat.2013.06.072
[8] Al-Tayeb M. M, Abu Bakar B. H, Akil H. M, Ismail H. Effect of Partial Replacements of Sand and Cement by Waste Rubber on the Fracture Characteristics of Concrete. Polymer-Plastics Technology and Engineering, 2012. 51(6), 583-589. https://doi.org/10.1080/03602559.2012.659307
[9] Wang HY. Chen BT. Wu YW. A study of the fresh properties of controlled lowstrength rubber lightweight aggregate concrete (CLSRLC). Constr Build Mater 2013;41:526-31. https://doi.org/10.1016/j.conbuildmat.2012.11.113
[10] Steyn Z.C, Babafemi A.J,Fataar H, Combrinck R. Concrete containing waste recycled glass, plastic and rubber as sand replacement. Construction and Building Materials, 2020, Volume, 269, 121242. https://doi.org/10.1016/j.conbuildmat.2020.121242
[11] Pelisser F, Zavarise N,Longo TA,Bernarin AM. Concrete made with recycled tire rubber: effect of alkaline activation and silica fume addition. Journal of Cleaner Production, 2011; 19: 757-763. https://doi.org/10.1016/j.jclepro.2010.11.014
[12] Gupta T, Siddique S,Sharma R, Chaudhary S. Investigating mechanical properties and durability of concrete containing recycled rubber ash and fibers. Journal of Material Cycles and Waste Management, 2021; 23: 1048-1057. https://doi.org/10.1007/s10163-021-01192-w
[13] Singh G, Tiwary A. K, Singh S, Kumar R, Chohan J. S, Sharma S, Li C, Sharma P, Deifalla A. F. Incorporation of Silica Fumes and Waste Glass Powder on Concrete Properties Containing Crumb Rubber as a Partial Replacement of Fine Aggregates. Sustainability, 2022; 14(21), 14453. https://doi.org/10.3390/su142114453
[14] Bisht K, Ramana P. Waste to resource conversion of crumb rubber for production of sulphuric acid resistant concrete. Construction and Building Materials, 2019; 194, 276-286. https://doi.org/10.1016/j.conbuildmat.2018.11.040
[15] Pavankalyan K, Durga Prasad R, Pradeep Kumar S. Mechanical and Durability Studies on Concretes Containing Crumb Rubber Fine Aggregate. IOP Conference Series: Earth and Environmental Science, 2022; 1086(1), 012013. https://doi.org/10.1088/1755-1315/1086/1/012013
[16] Najim KH,Hall M. Mechanical and dynamic properties of self-compacting crumb rubber modified concrete. Construction and Building Materials, 2012; 27:521-530. https://doi.org/10.1016/j.conbuildmat.2011.07.013
[17] Azimi-Pour M, Eskandari-Naddaf H. Synergistic effect of colloidal nano and micro-silica on the microstructure and mechanical properties of mortar using full factorial design. Constr. Build. Mater, 2020; 261,120497. https://doi.org/10.1016/j.conbuildmat.2020.120497
[18] Mutuk T, Mesci B. Analysis of mechanical properties of cement containing boron waste and rice husk ash using full factorial design. J. Clean. Prod. 2014; 69, 128-132. https://doi.org/10.1016/j.jclepro.2014.01.051
[19] Liu M. L, Zhang G. D, Ding Y. F, Wei L, Wang Y, Zhang X. Z. Research on Properties of the Concrete with Waste Rubber Powder. Materials Science Forum, 2016; 852, 1443-1449. https://doi.org/10.4028/www.scientific.net/MSF.852.1443

[20] Djebien R, Bouabaz A, AbbasY. Effect of Recycled Tire Rubber and Marble Waste on Fresh and Hardened Properties of Concrete. Civil and Environmental Engineering Reports, 2022; 32(1), 218-239. https://doi.org/10.2478/ceer-2022-0013
[21] Dong Q, Huang B, Shu X. Rubber modified concrete improved by chemically active coating and silane coupling agent. Construction and Building Materials, 2013; 48:116-123. https://doi.org/10.1016/j.conbuildmat.2013.06.072
[22] Chylík R, Trtík T, Fládr J, Bílý P. Mechanical properties and durability of crumb rubber concrete, IOP Conf. Series: Materials Science and Engineering, 2017; 236:012093. https://doi.org/10.1088/1757-899X/236/1/012093
[23] Abdullah S. R.EFFECT OF RUBBER POWDER PARTICLE ON THE STRENGTH OF FOAMED CONCRETE. International Journal of GEOMATE, 2017; 13(38). https://doi.org/10.21660/2017.38.80292
[24] Li W, Wang X. C, Zhang J. P. An Overview of the Study and Application of Rubberized Portland Cement Concrete. Advanced Materials Research, 2012; 598, 374-378. https://doi.org/10.4028/www.scientific.net/AMR.598.374
[25] Sof A. Effect of waste tyre rubber on mechanical and durability properties of concrete - A review. Ain Shams Engineering Journal, 2018; 9:2691-2700. https://doi.org/10.1016/j.asej.2017.08.007
[26] Gupta T, Chaudhary S, Sharma R. Assessment of mechanical and durability properties of concrete containing waste rubber tire as fine aggregate. Construction and Building Materials, 2014; 73:562-574. https://doi.org/10.1016/j.conbuildmat.2014.09.102
[27] Si R,Wang J,Guo Sh,Dai Q,Han S. Evaluation of Laboratory Performance of Self-Consolidating Concrete with Recycled Tire Rubber. Journal of Cleaner Production,2018.P.823-831. https://doi.org/10.1016/j.jclepro.2018.01.180
[28] Najim K.B, Hall M.R. Mechanical and dynamic properties of self-compacting crumb rubber modified concrete. Constr. Build. Mater, 2012; 27:521-530. https://doi.org/10.1016/j.conbuildmat.2011.07.013
[29] Nordstokke D, Colp S.M. Factorial Design Encyclopedia of Quality of Life and Well-Being Research, 2014; 2144-2145. Springer, Dordrecht. https://doi.org/10.1007/978-94-007-0753-5_982
[30] Gelis K, Ozbek K, Celik, A.N, Ozyurt O. A novel cooler block design for photovoltaic thermal systems and performance evaluation using factorial design. J. Build. Eng, 2021; 48, 10. https://doi.org/10.1016/j.jobe.2021.103928

Research on Engineering Structures & Materials
www.jresm.org
MIM Research Group

Research Article

Domestic wastewater reduction using constructed wetlands

Cut Suciatina Silvia*[1,a], Muhammad Ikhsan[1,b], M. Faisi Ikhwali[2,c]

[1]*Dept. of Civil Eng., Faculty of Engineering, University of Teuku Umar, Indonesia*
[2]*Dept. of Environmental Eng., Faculty of Science and Technology, UIN Ar-Raniry Banda Aceh, Indonesia*

Article Info

Article history:

Received 24 Sep 2023
Accepted 08 Nov 2023

Keywords:

Eichhornia crassipes
pandanus;
Amaryllifolius;
Scirpus grossus;
Domestic wastewater;
Constructed wetlands

Abstract

Domestic wastewater is household liquid waste that comes from sinks, bathrooms, and wastewater from washing machines. In Johan Pahlawan Sub-district, West Aceh District, the community and government's concern is still low towards achieving environmental health where the coverage of wastewater management has not been optimized. This is shown by people who do not manage wastewater properly. One of the alternative domestic wastewater management technologies is the concept of constructed wetlands with phytoremediation techniques. This study aims to determine the efficiency of reducing wastewater concentrations using phytoremediation with Eichhornia Crassipes plants, Pandanus amaryllifolius plants and Scirpus grossus plants. After the phytoremediation process with the concept of CWs-SF and CWs-SSF, it shows that the use of pandanus has not been effective in reducing contaminant levels in domestic wastewater. While Eichhornia Crassipes and Scirpus grossus plants are much better at reducing wastewater concentrations. The efficiency of reducing BOD values with a contact time of 3 to 9 days can reduce BOD levels by 80%-91%, COD and TSS can reduce the wastewater to 89%-90%, the temperature of the wastewater has been qualified with Eichhornia Crassipes and wlingen plants with 29^{0}C, and the pH of the wastewater has increased to 7.5-8.

1. Introduction

Wastewater is water that has undergone physical, chemical, or biological changes owing to the addition of specific substances. Most daily activities depend on water, so waste is discharged into the channel. Body wastes (feces and urine), hair shampoo, hair, food scraps, fat, laundry detergent, fabric softeners, toilet paper, chemicals, detergent, household cleaners, dirt, and microorganisms (germs) that can harm the environment [1-3]. Domestic wastewater is the liquid or waste produced by households and includes groundwater. Greywater originating from sinks, kitchen sinks, dishwashers, and washing machines can contain soluble contaminants, such as soap, detergents, and dirt. The type of contaminants of greywater detergents, organic and microbial, require distinct treatment processes [4-8].

Approximately 30%–50% of the wastewater dumped into sewers is greywater. It will be easier for sewage treatment plants to use less water if this greywater is recycled and managed separately. Conventional wastewater treatment techniques, such as activated sludge and biological nutrient removal technology or chemical methods, have been used to treat wastewater from other hazardous chemicals. Wastewater disposal creates an uncomfortable environment, and the germs can multiply. Wastewater can cause several problems for humans, the environment, and water. The waste liquid gradually turned

*Corresponding author: coetsilvia@utu.ac.id
[a] orcid.org/0000-0002-8198-1677; [b] orcid.org/0000-0001-5895-4366; [c] orcid.org/0000-0001-9120-6052
DOI: http://dx.doi.org/10.17515/resm2023.20ma0924rs

black and smelled. This condition disrupts the surrounding environment and spreads disease. There have been many studies on greywater characteristics [9,10]

Greywater management issues harm the ecosystem, particularly in residential areas. Environmental issues that frequently arise can affect health and cause the drainage canal to smell badly. Phytoremediation techniques are alternative options for treating wastewater. The use of plants to clean waste is known as phytoremediation. Despite the potential of this method for wastewater reclamation, phytoremediation is only successful in shallow and deep locations, where plant roots may develop and employ plant remediation systems that prevent toxins from seeping into groundwater [11,12]. Phytoremediation is an eco-friendly technology based on plants (aquatic and semiaquatic) and microorganisms in water degraded from the soil, sediment, and aquatic plants [13-15]. One currently used technique that is becoming increasingly important in phytoremediation is the creation of wetlands for wastewater treatment [16,17]. The most advantageous and environmentally friendly method is using aquatic plants to reduce toxins that their roots can absorb, stems and leaves because they are readily available and more effectiveness.

The phytoremediation concept of constructed wetlands is a low-cost and efficient technique for wastewater treatment. In comparison, traditional wastewater treatment and constructed wetlands are simple, require minimal operation and maintenance, and are highly effective in removing pollutants [19-25]. Constructed wetlands are artificial systems built using the natural processes of wetland plants, soils, and microbial assemblages that live there to help treat wastewater. In a more regulated setting, there is more benefit from many activities in natural wetlands, where the CWs concept offers ecological wastewater treatment systems. Chemical, physical, and biological principles determine the cost of constructed wetland treatment processes. These include absorption, microbial biodegradation, desorption, fragmentation, and oxidation [26-27]. The effectiveness of constructed wetlands is affected by the plant species chosen, the substance of the wastewater to get treated, the pace of seedling growth, the amount of biomass produced, and the total quantity of plants in the sewage system [28-31].

The reduction of wastewater content using plant roots through the CWs concept has been performing by several researchers. CWS is highly effective when applied to manage wastewater in small-area housing. This study examined the removal of microorganisms from domestic wastewater of a single household in Kentucky using Typha Latifolia L. cattails or fescue was cultivated in the wetlands with polyculture methods (Festuca Arundinacea Schreb). The vegetated systems demonstrated removal efficiency for BOD (75%) and TSS (88%). Cattail performance can be improved when plants are cut after growth and can reduce BOD and TSS inputs. For all wastewater characteristics, polyculture systems appeared to offer the best and most reliable treatment while being least sensitive to seasonal fluctuations (12).

Several studies on greywater management using phytoremediation techniques with constructed wetlands have been performed, such as using Phragmites Karka as a horizontal subsurface flow for wastewater (sewage) treatment. Before the treatment, the wastewater was dark black and a bad smell. After managing a constructed wetland with Phragmites Karka plants, CWs became clean and odorless. After 96 hours of hydraulic residence times, the concentration of TDS, TSS, nitrate, phosphate, BOD, and COD at 60.37%, 63.19%, 94.69%, 92.95%, 61.47%, and 64.74%. The results show that root zone technology is suitable for managing wastewater and reducing the contamination load on groundwater (19).

Experiments conducted by several researchers to test the effectiveness of pandanus wetlands showed that the value of COD decreased from 70 mg/L to 39.25 mg/L, and

phosphate decreased to 1.10 mg/L and 19.42 mg/L. That proves that constructed wetlands with phytoremediation using pandanus plants can reduce the level of wastewater to a safe level when released into the community environment (20).

An experiment to investigate the improvement of removal efficiency using Lotus (Nelumbo nucifera) and Hydrilla Verticillata co-planted with one control unit. The results showed that the system with Lotus plants showed the best removal efficiency for Hydrilla wastewater management. However, this study emphasizes that Lotus and Hydrilla can provide alternative aquatic plant systems for wastewater treatment (21).

In Kuta Padang Village, West Aceh District, the community and government continue to show little care for environmental health, which harms the availability of wastewater management services. Based on EHRA (Environmental Health Risk Assessment) in 2015, 50.46% of the pollution was caused by improper sewerage, where home wastewater was released directly into canals without any treatment. The environment and community health will be affected if this situation persists (Sanitation Working Group, 2015). The current condition identified many households in the Johan Pahlawan Sub-district directly discharging wastewater into the drainage channel, which will increase pollution of water quality and the environment. Based on these conditions, this study aims to determine the efficiency of reducing wastewater content in the form of BOD, COD, TSS, pH, and temperature, using the phytoremediation of *Eichhornia Crassipes, Scirpus Grossus plants*, and *Pandanus Amaryllifolius*. The concept used is the Constructed Wetlands with Surface Flow and sub-surface flow systems. An environmentally sustainable waste management effort of using phytoremediators as green plants can transform pollutants into harmless substances.

2. Materials and Methods

2.1. Research Area and Wastewater Sampling

This research area was in the Kuta Padang Village in Johan Pahlawan District, West Aceh Regency, Aceh Province, Indonesia. Kuta Padang area have around 1.02 km^2. This area is downtown, where field conditions indicate that domestic wastewater is discharged directly into the city's drainage canals. This condition will have an impact on environmental health. This research uses quantitative and experimental description research methods. BOD, COD, TSS, pH, and temperature parameters testing at the Laboratory of the Industrial Research and Standardization Center of Banda Aceh City. The research time starts from February to March 2023. Wastewater collection was carried out for 3 (three) days, namely in the morning at 09.00 WIB and in the afternoon at 17.00 when the activities of using water were at their peak.

Fig. 1. Research area

2.2. Eichhornia Crassipes, Scirpus Grossus Plants, and Pandanus Amaryllifolius

Eichhornia Crassipes is a plant that floats in water and has roots with a height of about 0.4-0.8 meters, no stems, leaves are oval, and the tip is pointing at the base, the base of the stalk is swollen and has fibrous roots. This plant conveniently spreads through water bodies, so it is often referred to as a weed because it has a fast-growing speed. Eichhornia crassipes plants hold great promise for pollutant removal due to their fast growth rate and extensive root system. In addition, this plant can be cultivated and planted for wastewater treatment and water purification (22).

Scirpus Grossus has fibrous roots with white to brown color, triangular stems, and leaves 2 m or more long with a thickness of 10 mm. This plant is an aquatic plant with the common name Wlingen (Indonesia) and can be used to treat domestic wastewater with phytoremediation and wetland systems. Scirpus Grossus can absorb metals with the highest concentrations in the root, stem, and leaf zones (23).

Pandanus (Indonesian) or Pandanus Amaryllifolius i s a plant with fragrant leaves with a height of 1.2 m - 1.5 m, a leaf length of 80 cm, and a width of 60 cm - 90 cm. The leaves are palm frond-shaped, sharp, unserrated. The roots are large and can support the plants when they are tall. Pandanus is one of the plants that can manage domestic wastewater. Some of the research results proved effective in assimilating pollutants contained in domestic greywater. These plants are beginning their use as a medium in natural wastewater management processes (20).

Fig. 2. Eichhornia Crassipes, Scirpus Grossus Plants, and Pandanus Amaryllifolius

2.3. The Variables of This Study

Figure 3 shows the variables in this study, namely the independent variable and the dependent variable. Independent variables consist of Eichhornia crassipes, Scirpus grossus, Pandanus amaryllifolius, and domestic wastewater. The dependent variable consists of BOD, COD, TSS values, Temperature, and pH before and after phytoremediation with the CWs concept.

2.4. Materials and Instruments

Materials and instrument in this study are used:

- Eichhornia Crassipes, Scirpus Grossus plants and Pandanus Amaryllifolius (Fig. 2)
- Acclimatization and the number of plant clumps (Fig. 4)
- Gravel, sand and soil media (Fig. 4)
- tap water, bucket, PVC pipe and etc. (Fig. 4)

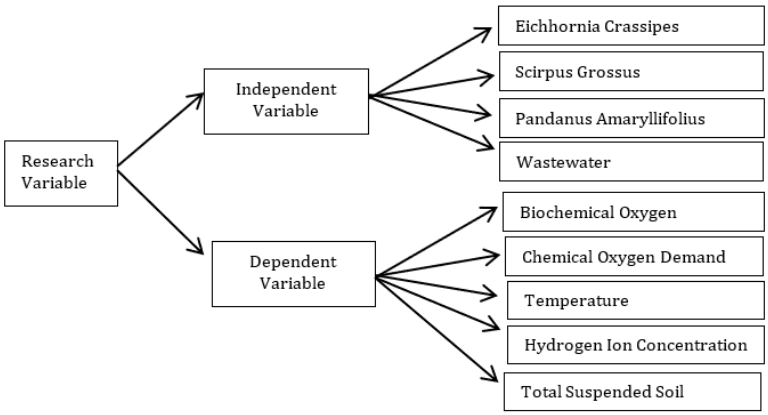

Fig. 3. Research variable of this study

2.5. Reductions Efficiency Pollutant

Reduction efficiency (E, in %) pollutant concentration according to the International Water Association (IWA) proposes an equation to calculate the percentage of pollutant removal using the formula: (24)

$$E = \frac{C_0 - C_1}{C_0} x100\% \quad (1)$$

where: C_o and C_1 are the average concentrations of influent and effluent.

2.6. Research Procedure

The following is the implementation of the research that consists of several stages:

Step 1: Sampling of wastewater at the research location at Kuta Padang Village. Furthermore, examination of wastewater samples before testing the Constructed Wetlands (CWs) with phytoremediation. The wastewater sample examination includes BOD, COD, TSS, pH, and temperature parameters.

Step 2: Preparation of Constructed Wetlands (CWs) media. Setting up CWs-SF and CWs-SSF, then Prepare filter media using gravel, coral sand, soil, and activated carbon. Gravel and sand sizes have a diameter of 15 mm and 0.25 mm. CWs media each for 3 (three) plants used (Fig. 4).

Step 3: Preparation of aquatic plants and acclimation with 5 clumps/stem each. These plants are allowed to adapt to the media for 7 days.

Step 4: Observation of wastewater samples with a contact time of 1 day and 3 days.

Step 5: Testing wastewater after the phytoremediation process by examining the BOD, COD, temperature, and water pH parameters.

Step 6: Analysis of the efficiency and effectiveness of reducing wastewater content before and after the phytoremediation process.

Fig. 4. Materials, procedures and observations

3. Results

Plant roots have an optimal role in reducing contaminants from domestic wastewater. The physical condition of three plants from the first day to the ninth day of observation was still in good condition.

3.1. Before Phytoremediation with CWs

Wastewater testing at the Baristand laboratory (Industrial Research and Standardization Center) resulted in the parameters tested being BOD, COD, pH, TSS, and Temperature. The Biological Oxygen Demand (BOD) is the amount of oxygen in organisms required to stabilize organic matter into CO_2 and H_2O in the waste. Chemical Oxygen Demand (COD) is the amount of oxygen in mg required to oxidize organic and inorganic materials/substances in one liter of wastewater. COD values are usually higher when compared to BOD values as stable materials in the BOD test can oxidize in the COD test.

Table 1. Wastewater content results before phytoremediation

Parameter	Waste water quality standard requirements	results before phytoremediation			description
		Sample 1	Sample 2	Sample 3	
BOD	30 mg/L	116,36	142,4	151,76	Unqualified
COD	100 mg/L	489,37	500,15	502,96	Unqualified
TSS	30 mg/L	242	246	248	Unqualified
Temperature	27 - 29	30	31	31	Unqualified
pH	6 - 9	7,4	5,8	5,55	Unqualified

Total Suspended Solid (TSS) is the number of suspended solids (mg) in one liter of water. Suspended solids consist of particles that are smaller in weight and size than sediment, insoluble in water, and cannot settle immediately. Suspended solids cause water turbidity, such as fine clay, various types of organic matter, and cells of microorganisms. pH is a measurement of acidity as a parameter of water quality because it can control the chemical

reactions that occur and determine the activity of microorganisms in the decomposition of domestic household wastewater. Wastewater Content Results Before Phytoremediation were given in Table 1. Table 1. shows that the wastewater levels of the 3 (three) samples tested for the parameters BOD, COD, TSS, pH, and temperature before phytoremediation have exceeded the wastewater quality standard threshold set by the Minister of Environment Regulation No. 68 of 2016.

3.2. Wastewater Quality Test Results After Phytoremediation with CWs

Based on Table 1, which shows that wastewater at the research site does not meet the requirements of wastewater quality standards, the next step is to test wastewater with the concept of Constructed Wetlands (CWS) with phytoremediation. Constructed wetlands with the surface flow (CWS-SF) are used for Eichhornia Crassipes and with the subsurface flow (CWs-SSF) for Pandanus Amaryllifolius and Scirpus Grossus plants. Before observation, a plant is acclimatization processed for at least 7 (seven) days. The plants used were 5 (five) clumps/stems of uniform size. During the acclimatization process, the three plants were able to live well. The results of wastewater content after the phytoremediation with the concept of CWs will be compared between the initial domestic wastewater concentration and after phytoremediation in each parameter. Table 2, Table 3, and Table 4 below show the test results of wastewater content after phytoremediation with observation times using Eichhornia Crassipes plants, Pandanus, and Wlingen plants.

Table 2. Wastewater content results after phytoremediation with 1-day observation

Parameter	standard	Results after phytoremediation with 1- day observation					
		Eichhornia Crassipes	Reduction (%)	Pandanus Amaryllifolius	Reduction (%)	Scirpus Grossus	Reduction (%)
BOD	30	58.04	57.59	112.3	17.93	42.8	68.7
COD	100	77.21	84.48	252.11	49.32	75.11	84.9
TSS	30	40.97	83.30	102.26	58.32	38.32	84.4
Temperature	27 - 29	29		31		30	
pH	6 - 9	7.33		7.5		7.43	

Table 2. with a contact time of 1 day, shows that Eichhornia Crassipes and Wlingen were better at reducing pollutants from wastewater than the pandanus plant. Phytoremediation using pandanus plants can reduce wastewater content for values BOD, COD, and TSS. Although it can reduce pollutants, the results have not yet complied with wastewater quality requirements. Eichhornia Crassipes and Scirpus Grossus plants can reduce BOD values by 50% - 70%, although the decrease in BOD values with a contact time of 1 day has not been able to meet the requirements of wastewater quality standards. The COD and TSS reduction using Eichhornia Crassipes and Scirpus Grossus plants can reduce contaminants by 80%-85%, and the pH of wastewater has increased above 7. Based on the test, the more effective wastewater management of the CWs concept with phytoremediation techniques is using Wlingen plants.

Figure 3 shows the trend of decreasing wastewater parameters, that the contact time of wastewater with plant roots for one day, showing the parameters have reduced from the results of wastewater testing before phytoremediation. Eichhornia Crassipes and Scirpuss Grossus plants can reduce COD parameters below the maximum limit of 100 mg/L and have complied with the requirements of wastewater quality standards by the Minister of Environment Regulation No. 68 of 2016.

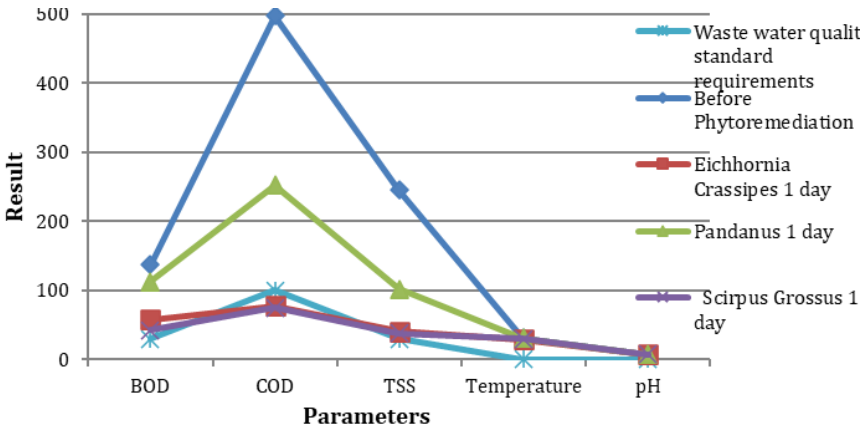

Fig. 5. The trend of wastewater parameter reduction with 1-day contact time

Table 3. Wastewater content results after phytoremediation with 3-day observation

Parameter	standard	Results after phytoremediation with 3- day observation					
		Eichhornia Crassipes	Reduction (%)	Pandanus Amaryllifolius	Reduction (%)	Scirpus Grossus	Reduction (%)
BOD	30	22.25	83.74	106	22.54	26.01	81.0
COD	100	52	89.55	218.05	56.17	53	89.3
TSS	30	28.66	88.32	94.34	61.55	25.09	89.8
Tempera-ture	27 - 29	29		31		29	
pH	6 - 9	8		7.72		7.59	

Table 3. with a contact time of 3 days, shows that Eichhornia Crassipes and Scirpus Grossus (Wlingen) plants are much better at reducing pollutants from wastewater than Pandanus plants. Phytoremediation using pandanus plants can reduce wastewater content for BOD, COD, and TSS values. Although it can reduce pollutants, the results have not yet complied with wastewater quality requirements. With a contact time of 3 days, Eichhornia Crassipes and Wlingen plants can reduce BOD levels by 81%-84%, and the reduced BOD levels have qualified the wastewater quality requirements. The reduction in COD and TSS levels can reduce contaminants to 89%. The temperature is qualified, and the pH of wastewater has increased to 7.5-8. Based on the test, the more effective wastewater management of the CWs concept with phytoremediation techniques is using Eichhornia Crassipes and Wlingen plants.

Figure 4 shows the trend of decreasing wastewater parameters, that the contact time of 3 days with plant roots, showing the parameters can reduce wastewater testing before phytoremediation. Eichhornia Crassipes and Scirpuss Grossus plants can reduce BOD, COD, TSS, pH, and temperature parameters according to wastewater quality standard requirements by the Minister of Environment Regulation No. 68 of 2016.

Table 4 with a contact time of 9 days, shows that Eichhornia Crassipes and Wlingen plants can reduce pollutants from wastewater much better than pandanus plants. Phytoremediation using pandanus plants can reduce wastewater content for BOD, COD, and TSS. Although it can reduce pollutants, the results have not yet complied with

wastewater quality requirements. With a contact time of 9 days, Eichhornia Crassipes and Wlingen plants can reduce BOD levels by 80%-91% and have qualified the wastewater quality requirements. The reduction of COD and TSS levels by 89%-90%, the temperature is qualified, and the pH of the wastewater has increased to 7.5-8.

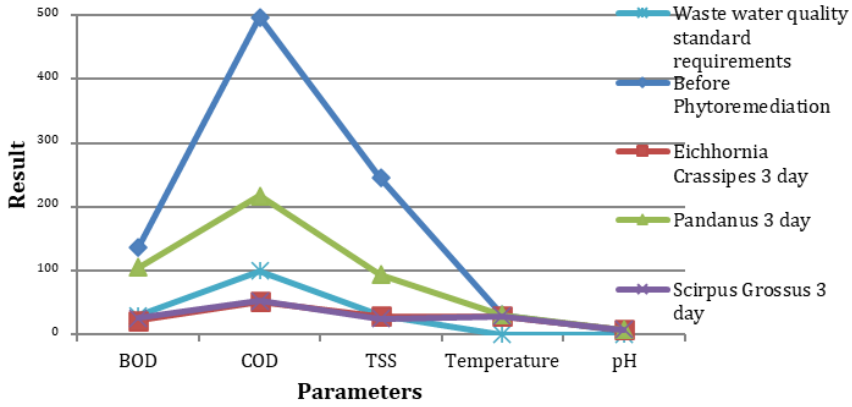

Fig. 6. The trend of wastewater parameter reduction with 3-day contact time

Table 4. Wastewater content results after phytoremediation with 9-day observation

Parameter	standard	Results after phytoremediation with 9- day observation					
		Eichhornia Crassipes	Reduction (%)	Pandanus Amaryllifolius	Reduction (%)	Scirpus Grossus	Reduction (%)
BOD	30	11.65	91.49	101.89	25.54	3.39	97.5
COD	100	49.28	90.09	203.9	59.01	35.68	92.8
TSS	30	26.5	89.20	87	64.54	17.8	92.7
Tempera-ture	27 - 29	29		30		29	
pH	6 - 9	8.08		7.94		7.64	

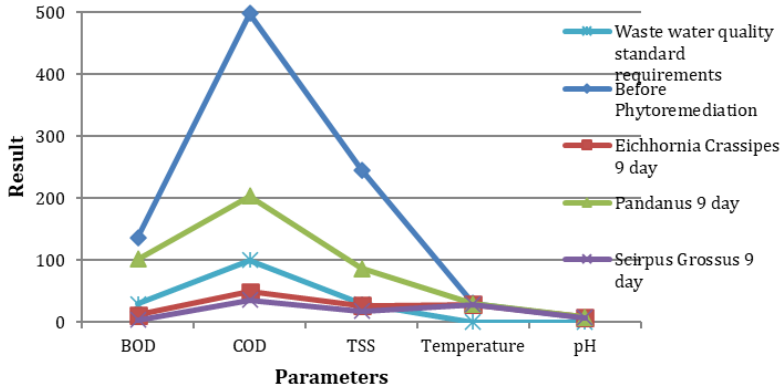

Fig. 7. The trend of wastewater parameter reduction with 9-day contact time

Figure 7 shows the trend of decreasing wastewater parameters with plant roots of 9 days. All parameters can reduce wastewater testing before phytoremediation. Values of BOD, COD, TSS, pH, and temperature parameters are below the maximum limit of 30 mg/L. Wastewater management with the CWs concept using Eichhornia Crassipes and Wlingen plants can reduce wastewater levels, increasing the pH and temperature parameters according to wastewater quality standard requirements by the Minister of Environment Regulation No. 68 of 2016

4. Discussion

The results show that Eichhornia Crassipes and Scirpuss Grossus plants can reduce contaminants in graywater. The decrease in BOD value is due to the nature of the two plants being able to do several things, such as adsorb various organic materials in the form of ions from microorganism decomposition and remove oxygen required by microorganisms for the oxidation process of degrading microorganisms. The more contact time with wastewater, the greater the organic matter in the form of ions can absorbed and affect the decrease in BOD. The more contact time with wastewater, the greater the organic matter in the form of ions can absorbed and affect the decrease in BOD. The results of previous research by (25) using Scirpuss Grossus plants with a contact time of 10 days using 300 grams of Scirpuss Grossus plants TSS before treatment amounted to 57 mg/L to 9.67 mg/L with a percentage decrease of 83.04%, pH before treatment 8.08 to 7.02 with a percentage decrease of 13.12%, BOD before treatment 73.83 mg/L to 30.84 mg/L with a percentage decrease of 58.23%, nitrite before treatment 0.2982 to 0.1541 with a percentage decrease of 48.32%. The results of this study are much more effective and efficient than the research (25), where the results of this study using 300 grams of clumps or 5 Scirpuss Grossus stems with a contact time of 9 days reduced BOD levels to 97.5%, reduced COD parameters 92.8%, TSS dropped by 92.7, lowered pH to 29^{0}C and increased pH 7.64.

Eichhornia Crassipes plants can reduce contaminants in greywater. The decrease in plants with a contact time of 1 day using 250 grams of water hyacinth plants decreased BOD by 166.40 mg/L to 86.4 mg/L, COD by 264.4 mg/L to 98.13 mg/L, pH by 8.7 to 7.48, and TSS by 346.4 mg/L to 112.4 mg/L (26). The results of this study are much more effective and efficient than the research (26), where the results of this study using 250 grams of clumps or 5 (five) clumps and contact time of 9 days effectiveness reduced BOD levels by 91.49%, COD by 90.02%, TSS by 89.20%, reduced pH to 290C and increased pH by 8.08.

The decrease in COD value is due to microorganisms found in the roots of Eichhornia Crassipes, where this phytoremediation process has an optimal role in the absorbent of organic pollutants. The plant can absorb contaminants through its roots. Microorganisms that grow at the roots of Eichhornia Crassipes plants can effectively reduce COD values because the total microorganisms increase, and microorganisms can adapt to the environment (27). The increase in the pH value of wastewater is due to the photosynthesis process that can utilize the CO_2 concentration in wastewater. Changes in pH value are due to photosynthesis and respiration activities of aquatic plants. Photosynthesis requires carbon dioxide (CO_2), which the autotroph component transforms into monosaccharides. A decrease in CO_2 can increase the pH of the wastewater (28).

Eichhornia Crassipes plants will capture suspended solids in wastewater through the roots system. In the phytoremediation test with a contact time of 9 days, the colors of the leaf edge turned yellow, and the roots of the Eichhornia Crassipes plant seemed to be slimy due to contaminants that have not been absorbed and adhered in the Eichhornia Crassipes roots. This research is in line with another study that the part of the plant that first dies is the leaves. Due to the metabolism of leaf dying, the color of the leaf edges becomes

yellowing and withering, and then the leaves dry out. Eichhornia Crassipes then began to grow on the stem of the leaves, and the roots of the plants died off. Roots look slimy on the 10th day due to contaminants or nutrients that have not been absorbed and have not attached to the roots of Eichhornia crassipes. All plants rotted and died on the 14th day. (25)

5. Conclusions

The CWS concept using phytoremediation of Eichhornia Crassipes and Wlingen plants with an observation time of 3-9 days can reduce wastewater quality. There was a decrease in BOD, COD, TSS, and temperature parameters, as well as an increase in pH value and met the requirements of wastewater requirements according to Article 1 Paragraph 2 of the Regulation of the Minister of Environment and Forestry of the Republic of Indonesia Number 68 of 2016 concerning Domestic Wastewater Quality Standards. With a contact time of 9 days, shows that Eichhornia Crassipes and Scirpuss Grossuss plants can reduce pollutants from wastewater much better than pandanus plants. Phytoremediation using pandanus plants can reduce wastewater content for BOD, COD, and TSS. Although it can reduce pollutants, the results have not yet complied with wastewater quality requirements. Eichhornia Crassipes can reduce BOD levels 91.49%, COD levels 90.09%, TSS levels 89.20%, the temperature is qualified, and the pH of the wastewater has increased to 8.08. Scirpuss Grossuss plants can reduce pollutants for BOD levels 97.5%, COD and TSS levels by 92.8%, the temperature is qualified, and the pH of the wastewater has increased to 7.64. The wastewater content value of the research results using domestic wastewater before and after phytoremediation is much more effective in decreasing compared to previous studies. The efficiency of this pollutant value reduction depends on the difference or number of clumps and the contact time of wastewater with plant roots. With a contact time of 9 days, Eichhornia Crassipes and Scirpuss Grossuss plants can reduce BOD levels by 80%-91% and have qualified the wastewater quality requirements. The reduction of COD and TSS levels by 89%-90%, the temperature is qualified, and the pH of the wastewater has increased to 7.5-8.

Acknowledgement

The author would like to thank the Dean of the Faculty of Engineering at the University of Teuku Umar, Aceh Dr. Ir. Irwansyah, S.T., M.Eng, IPM, all lecturers and educational staff of the Faculty of Civil Engineering, University of Teuku Umar. I hope this study can provide input regarding the benefits of the research result on domestic wastewater management using aquatic plants with constructed wetland media and can be a reference for the community to apply to households. This research is an internal grant from Teuku Umar University with several SK 37/UN59.7/SPK-PPK/2023.

References

[1] Amoatey P, Bani R. Wastewater Management. In: Waste Water - Evaluation and Management [Internet]. InTech; 2011. p. 379-98. https://doi.org/10.5772/16158
[2] Tchobanoglous G, Burton FL, Stensel HD. Wastewater Engineering: An Overview. In: McGraw-Hill, editor. Wastewater Engineering: Treatment and Reuse (Fourth Edition). New York: Metcalf and Eddy, Inc; 2003.
[3] Andreadakis A, Noutsopoulos C, Mantziaras I., Kouris N. Greywater Characterization and Treatment. In: Hellenic Water Association. 2015. p. 328-34.
[4] Rinitha P. Grey Water Treatment by Phytoremediation Technique-A Comparative Study using Vetiver Grass and Lemon Grass. Int J Eng Res Technol. 2022;10(06):101-5.

[5] Jefferson B, Palmer A, Jeffrey P, Stuetz R, Judd S. Grey water characterisation and its impact on the selection and operation of technologies for urban reuse. Water Sci Technol. 2004;50(2):157-64. https://doi.org/10.2166/wst.2004.0113
[6] Patankar S, Chavan J, Dharane A, Patade S, Kate S. Greywater Treatment Using Wetland : A Review. Int J Innov Res Sci Eng Technol. 2020;9(4):1334-7.
[7] Mustafa H., Hayder G, Solihin M., Saeed R. Applications of Constructed Wetlands and Hydroponic Systems in Phytoremediation of Wastewater. In: Proceedings IOP Conference Series: Earth and Environmental Science. 2021. p. 1-8. https://doi.org/10.1088/1755-1315/708/1/012087
[8] Kuslu Y. An Example of Constructed Wetland Planning for a Rural Settlement in Turkey. J Environ Waste Manag. 2019;6(2):315-20.
[9] Calheiros CSC, Castro PML, Gavina A, Pereira R. Toxicity Abatement of Wastewaters from Tourism Units by Constructed Wetlands. Water. 2019;11(2623):1-13. https://doi.org/10.3390/w11122623
[10] Farraji H. Wastewater Treatment by Phytoremediation Methods. In: Wastewater Engineering: Types, Characteristics and Treatment Technologies Chapter 7. Malaysia; 2014. p. 206-2018.
[11] Herath I, Vithanage M. Phytoremediation in Constructed Wetlands. Phytoremediation Manag Environ Contam. 2015;2(January):243-63. https://doi.org/10.1007/978-3-319-10969-5_21
[12] Karathanasis AD, Potter CL, Coyne MS. Vegetation effects on fecal bacteria, BOD , and suspended solid remo v al in constructed wetlands treating domestic wastewater. Ecol Eng. 2003;20(March):157-69. https://doi.org/10.1016/S0925-8574(03)00011-9
[13] Andreo-martínez P, García-martínez N, Almela L. Domestic Wastewater Depuration Using a Horizontal Subsurface Flow Constructed Wetland and Theoretical Surface Optimization : A Case Study under Dry Mediterranean Climate. Water. 2016;8(434):1-18. https://doi.org/10.3390/w8100434
[14] Weis JS, Weis P. Metal Uptake , Transport and Release by Wetland Plants : Implications for Phytoremediation and Restoration. Environ Int. 2004;30:685-700. https://doi.org/10.1016/j.envint.2003.11.002
[15] Barya MP, Gupta D, Thakur TK, Shukla R, Singh G, Mishra VK. Phytoremediation performance of acorus calamus and canna indica for the treatment of primary treated domestic sewage through vertical subsurface flow constructed wetlands: A field-scale study. Water Pract Technol. 2020;15(2):528-39. https://doi.org/10.2166/wpt.2020.042
[16] Vymazal J. Removal of nutrients in various types of constructed wetlands. Sci Total Environ. 2007;380(1-3):48-65. https://doi.org/10.1016/j.scitotenv.2006.09.014
[17] Angassa K, Leta S, Mulat W, Kloos H, Meers E. Evaluation of Pilot-Scale Constructed Wetlands with Phragmites karka for Phytoremediation of Municipal Wastewater and Biomass Production in Ethiopia. Environ Process. 2019;6(1):65-84. https://doi.org/10.1007/s40710-019-00358-x
[18] Rahman M-A, Rahaman M-H, Yasmeen S, Rahman MM, Rabbi FM, Shuvo OR, et al. Phytoremediation Potential of Schumannianthus dichotomus in Vertical Subsurface Flow Constructed Wetland. Environ Challenges. 2022;9(October):1-9. https://doi.org/10.1016/j.envc.2022.100631
[19] Chavan B, Dhulap V. Designing and Testing of Wastewater in Constructed Wetland Using Phragmites Karka. Int J Phys Soc Sci. 2012;2(12):205-11.
[20] Yusof Y, Hamid KHK, Rodhi MNM. A study of Sewage Treatment System by Pandanus Amaryllifolius in Man-Made Wetland. Indian J Res. 2014;3(10):101-4.
[21] Kanabkaew T, Puetpaiboon U. Aquatic plants for domestic wastewater treatment : Lotus (Nelumbo nucifera) and Hydrilla (Hydrilla verticillata) systems. Songklanakarin, J Sci Technol. 2004;26(5):749-56.

[22] Latip SNHM, Damanhuri SNA, Ibrahim ND, Chin KB, Nasruddin MF. Utilization of water hyacinth in constructed wetlands for wastewater treatment. IOP Conf Ser Earth Environ Sci. 2022;1105(1). https://doi.org/10.1088/1755-1315/1105/1/012032
[23] Prakoso D, Tangahu BV. Desain Ipal Komunal Limbah Domestik Perumahan Sukolilo Dian Regency dengan Teknologi Constructed Wetland. IPTEK J Proc Ser. 2017;3(5):239-46. https://doi.org/10.12962/j23546026.y2017i5.3140
[24] Dewi YS. Efektivitas Jumlah Rumpun Tanaman Eceng Gondok (Eichhornia Crassipes (Mart) Solm) Dalam Pengendalian Limbah Cair Domestik. J Teknol Lingkung. 2016;13(2):151. https://doi.org/10.29122/jtl.v13i2.1414
[25] Sari FDN. Fitoremediasi Limbah Rumah Tangga Oleh Tanaman Wlingen (Scirpus Grossus) , Kiapu (Pistia Stratiotes), Dan Teratai (Nymphea Firecrest). Universitas Sumatera Utara Medan; 2013.
[26] Ryanita PKY, Arsana IN, Juliasih NKA. Fitoremediasi Dengan Tanaman Air untuk Mengolah Air Limbah Domestik. J Widya Biol. 2020;11(2):76-89.
[27] Herman YW., Suastuti DA, Suprihatin IE, Dwijani W, Sulihingtyas. Fitoremediasi Menggunakan Tanaman Eceng Gondok (Eichhornia Crassipes) Untuk Menurunkan Cod Dan Kandungan Cu Dan Cr Limbah Cair Laboratorium Analitik Universitas Udayana. Cakra Kim (Indonesian E-Journal Appl Chem. 2017;5(2):137-44.
[28] Ningrum YD, Ghofar A, Haeruddin. Efektivitas Eceng Gondok (Eichhornia crassipes (Mart .) Solm) sebagai Fitoremediator pada Limbah Cair Produksi Tahu. J Maquares. 2020;9(2):97-106. https://doi.org/10.14710/marj.v9i2.27765

Research on Engineering Structures & Materials
www.jresm.org
MIM Research Group

Research Article

Vehicle anti-lock brake system - dynamic modeling and simulation based on MATLAB Simulink and CarSim

Adugna Fikadu Geleta[a], Mahesh Gopal[*, b], Muleta Tiki Lemi[c]

Dept. of Mechanical Engg, College of Eng. and Technology, Wollega University, Nekemte, Ethiopia

Article Info

Article history:

Received 01 June 2023
Accepted 30 Oct 2023

Keywords:

Anti-Lock brake system;
MATLAB/Simulink;
Fuzzy logic controller;
CarSim

Abstract

The anti-lock brake system (ABS) is a safety feature for automobiles that regulates brake pressure and delivers predictable braking in the majority of circumstances by monitoring wheel lock-up. It necessitates the creation of a robust control system due to the unknown uncertainties on the braking system induced by altering the vehicle model dynamics and road conditions. To progressively decrease the automobile accidents caused by abrupt braking and will achieve the best brake performance. The mathematical model was developed considering vehicle speed, and slip ratio between the tire and the road conditions and simulation was done for Super Urban Vehicle of the ABS using Fuzzy logic controller and CarSim software in MATLAB/Simulink are the main objectives of this study. With the assistance of the fuzzy logic control approach and the MATLAB/Simulink software, a quarter-vehicle dynamic model was developed to simulate under a variety of road circumstances, such as wet and dry conditions, and at different speeds. Finally, it was determined that the braking distance was decreased and the vehicle stability was maintained during the simulation process by comparing the results of the simulation performed using the CarSim software connected to MATLAB/Simulink and the performance of the built controller.

1. Introduction

A road vehicle must constantly alter its velocity and distance following shifting traffic circumstances to be used safely and reliably. This is accomplished by designing a system that utilizes the limited amount of traction between the tire and the road as effectively as possible under all of the expected operating situations that the vehicle would experience during regular operation. The most crucial accident-avoidance systems on a car that must consistently function in a variety of situations are without a doubt the brakes, steering, and tires. Any braking system's effectiveness is thus constrained by the degree of traction present at the tire-road contact.

The authors [1], [2] discussed the ABS and its components. The simulation model was developed using ADAMS; this model was used to determine the performance of the brakes in different situations, such as when the vehicle is turning and when the brakes are applied. The researchers [3]developed a predictive control algorithm (PCA) for an ABS. The algorithm is designed to minimize the braking distance under any given road conditions and to stabilize automobile behavior. The suggested algorithm is verified, tested and compared with conventional ABS and the results show that it can significantly reduce the wheel slip and improve vehicle stability. For modeling the dynamic behavior of pneumatic heavy vehicle brakes with incorporated ABS, [4] suggested a novel model. The model is used to assess the effectiveness of incorporated ABS and examine the impact of different

*Corresponding author: adugnaf@wollegauniversity.edu.et
[a] orcid.org/0009-0004-4322-7683; [b] orcid.org/0000-0001-7672-5399; [c] orcid.org/0000-0002-2179-2882
DOI: http://dx.doi.org/10.17515/resm2023.22me0601rs

settings on braking performance. The outcomes demonstrate that the model is capable of faithfully simulating the dynamic behavior of the integrated anti-lock braking system. The authors [5] discussed and developed a Hardware-in-the-Loop Simulations (HILS) system for active brake control systems. The author includes the verification method and outcomes of the HILS system in addition to describing the development and execution of the system, which comprises a controller approach, a brake system of control model, and a vehicle model. An ABS-focused sliding mode control strategy was introduced by [6] and the simulations and trials on a real-time ABS system show the efficacy of the suggested approach. Results reveal that in terms of system stability, robustness, and speed response, the suggested technique performs better than the state-of-the-art conventional control methods. The authors [7] present a controller algorithm for an automobile ABS using MATLAB/Simulink environment and also provide valuable insight into the performance of the controller system and its components. Mathematical modeling was developed by [8] based on the dynamic behavior of the ABS and simulation was done using Simulink under different operational conditions and also discusses the possibilities of further improvements in the system such as active control, improved component design, and sensor technology. The most effective architecture for an ABS employing a linear time-varying (LTV) model and a stability requirement was suggested. The outcomes demonstrate that the suggested non-linear controller performs better than the conventional one [9]. To create an accurate tire model that is appropriate for ABS simulations, [10] developed a discrete tire modeling approach for ABS simulations. This algorithm provides a complete examination of tire-road interaction. To obtain the required braking reaction, [11] introduced a linear control approach for an ABS that utilizes fuzzy logic and employs a proportional-derivative (PD) controller. The findings demonstrate that the suggested controller may deliver a smooth and precise braking response with minimal overshoot.

The authors [12] conducted a simulation model using Simulink, to and discuss the implications of ABS performance. The researcher [13] proposed an electric car with an axle motor that offered a linear parameter variable system to improve the observer and enhance robustness against parameter uncertainty and external disturbances using simulation. The MATLAB / Simulink software was used for modeling and simulation. The fuzzy control door limit control strategy was used to get results very accurate. The researcher suggested that the fuzzy logic controller is an effective means of modeling and simulating an ABS [14]. To increase the vehicle's stability and safety, the author [15] built an ABS control system employing CarSim, MATLAB/Simulink, and LabVIEW as the communication tool for an integrated electro-hydraulic braking system. The researcher [16] explained the operation of ABS and the MATLAB ABS mathematical models used to simulate the system. The Carsim simulation software is used and the results of both the simulation software are compared. The design of a regenerative anti-lock braking system (RABS) controller for an electric vehicle has been demonstrated by [17]. The authors additionally navigate through how to use the results of simulations to verify the system's performance using the fuzzy logic controller technique. The authors suggested that the controller can deliver a safe and dependable regenerative braking system for an electric vehicle.To study the dynamic characteristics of ABS system, the MATLAB was used to simulate the model of the ABS system. The simulation findings demonstrate that the wheel slip ratio may be decreased by adjusting the wheel braking pressure through the ABS control system, preventing the wheel from locking and enhancing vehicle stability [18]. A simulation model was designed by [19] to visualize the system behavior and optimum brake performance of ABS. To increase the safety of electric vehicles, an integrated electronic hydraulic brake system (IEHBS) was developed in two representative scenarios of the regenerative and ABS processes using simulation software such as MATLAB/Simulink, AMESim, and CarSim [20]. MATLAB Simulink was used to run

the simulation, to obtain the desired level of wheel slip, [21] developed a mathematical model using the Lugre Friction and Burckhardt Friction models of the ABS. To enhance braking performance and prevent wheel locking, [22] suggested a sliding-mode control (SMC) method based on MATLAB and CARCISM. The outcomes demonstrate that the suggested method outperforms the traditional ABS in terms of stability and braking distance. A fixed-time slip control method for ABS in electric vehicles was described by [23] based on an extended-state observer (ESO). The outcomes demonstrate that the suggested technique outperforms the other controllers in terms of wheel slip, braking torque, and vehicle speed deviation. Using MATLAB/Simulink, [24] carried out the modelling and simulation of the ABS. The simulation results demonstrate the suggested ABS's capacity to produce stable and good dynamic performance. The researcher [25] suggested a control strategy based on a model predictive control (MPC) approach, which uses a linear state-space model of the system and also discussed the design of an output feedback adaptive controller and the execution of a processor-in-the-loop (PIL) validation test. The co-simulation platform that combines CarSim and Simulink to mimic an automobile ABS was created by [26]. The platform was used to evaluate the anti-lock braking system's performance at various vehicle speeds and road surface conditions. The outcomes demonstrated that the co-simulation platform could successfully analyze the behavior of the anti-lock braking system and recreate it with accuracy.

Researchers have conducted numerous experiments in ABS technology, developed a wide range of models, algorithms, and methods to improve braking performance, including linear and nonlinear parameter varying methods, generalised predictive control method, PID controller HILS method, longitudinal wheel model, Car tyre model, Lugre Friction Model, Burckhardt Friction Model, Bang-Bang control algorithm, adaptive fuzzy fractional order sliding mode control, fuzzy sliding mode control, CAE methods and also used different advanced software such as ADAMS, Fuzzy, MATLAB, Simlink. Despite the extensive assessment of the literature, there is minimal research available considering vehicle speed, tyre slip ratio, and road conditions. This study aims to address the gap by providing an in-depth investigation of the SUV of ABS technology using a Fuzzy logic controller and the CarSim software and contributes to the field by addressing gaps in the literature. This work describes a dynamic mathematical model developed using a fuzzy logic control approach and the MATLAB/Simulink software to simulate under a wide range of road conditions and to solve critical issues for industry specialists to manage brake pressure to provide predictable braking.

2. Modeling of the Vehicle Dynamics System

2.1. Longitudinal Vehicle Dynamics Model

A quarter-vehicle model with three degrees of freedom is modeled to mimic a vehicle's longitudinal dynamics, taking into consideration straight-line emergency braking up until stopping. A single sprung mass (the automobile body) is coupled to an unsprung mass (the wheel) for the vehicle's longitudinal dynamics modeling, and Fig. 1 depicts the vertical dynamics influence of the vehicle on traction. As indicated that the tire is modeled as a linear spring and damping element, whereas the suspensions within the sprung mass and unsprung mass are modeled as linear viscous damper and spring elements.

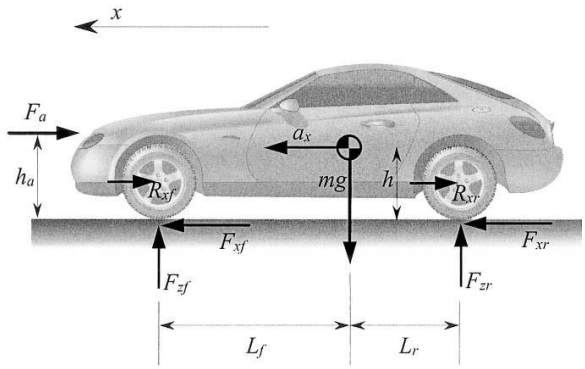

Fig. 1. Vehicle longitudinal dynamics

The resultant force of a moving vehicle is provided by Newton's second law:

$$\sum F = m_v * a \implies F_x - F_a - F_r = m_v * a \tag{1}$$

Since the vehicle's acceleration is the derivative of speed, this expression may be rewritten as

$$m_v * \dot{v} = F_x - F_a - F_r \implies \dot{v} = \frac{F_x - F_a + F_r}{m_v} \tag{2}$$

Where, m_v is the summation of the quarter sprung mass, m_s and unsprung (wheel) mass i.e.,

$$m_v = m_w + \frac{1}{4} m_s \tag{3}$$

Drag force is created by aerodynamic resistance force (F_a) and rolling resistance force (F_r), two force components that act parallel to and in opposition to the vehicle's motion.

Where - the aerodynamic force (F_a) is expressed as:

$$F_a = \frac{1}{2}(\rho * C_d * A_f * V^2) \tag{4}$$

For passenger automobiles with mass in the range of 800-2000 kg, [27] claim that the frontal area A_f the following connection between vehicle mass and the frontal area may be used: $A_f = 1.6 + 0.00056(m - 765)$

The energy that a vehicle must transfer to its tires to drive across a surface at a constant speed is known as the rolling resistance force (F_r), and it may be calculated as follows:

$$F_r = C_r * m_v * g \tag{5}$$

Therefore, the following formula may be used to get the net force or overall Vehicle longitudinal force (F_x) :

$$F_x = m_v * a - F_a - F_r \tag{6}$$
$$= m_v * a - \frac{1}{2}(\rho * C_d * A_f * V^2) - \frac{1}{4} * C_r * m_v * g$$

2.2. Tire Dynamics Model

Braking forces are produced at the intersection of the tire and the road surface when braking torque is applied to a wheel, according to [28]. As illustrated in Fig. 2, the longitudinal force generated at each tire is known to be influenced by the longitudinal slip ratio, the tire-road friction coefficient, and the applied normal force.

The traction force of the tire (F_x) is given by:

$$F_x = \mu(\lambda) * F_z \tag{7}$$

Where, the normal force on the wheel (the reaction force from the ground to the tire) is the load due to the quarter vehicle weight and longitudinal weight transfer and which is given by:

$$F_z = m * \frac{g}{4} + F_l \tag{8}$$

As a result of braking, the longitudinal weight transfer load, F_l, is represented as follows:

$$F_l = \frac{1}{2L}(m_v * h_{cg} * \dot{v}) \tag{9}$$

Where, h_{cg} is center of gravity height and,

L is wheelbase (the distance between the front and rare wheel)

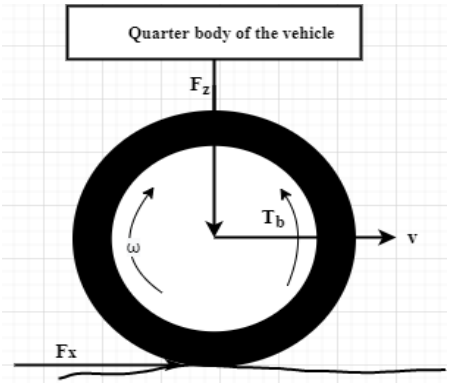

Fig. 2. Free body diagram of single wheel

The direct reduction in the wheel angular velocity (ω) is caused by the rotational acceleration of a body, decelerating the vehicle at the quantity owing to braking torque (T_b) applied to the wheel radius(R), and moment of inertia(I). This equation may be used to model the rotational dynamics of a wheel:

$$\sum T_y = I * a = I * \dot{\omega} \tag{10}$$
$$I * \dot{\omega} = F_{net} * R - T_b \qquad \Rightarrow \dot{\omega} = \frac{1}{I}(F_{net}) * R - T_b$$

Where, $F_{net} = F_x - F_a - F_r$

From the dynamic angular motion equation of the wheel, the angular acceleration of the wheel α is the ratio of net torque (i.e., $T_t - T_b$) and wheel moment of inertia, I_w.

$$I * \dot{\omega} = F_{net} * R - T_b \Rightarrow \dot{\omega} = \frac{1}{I}(F_{net}) * R - T_b \tag{11}$$

$$T_t = I_w * \alpha$$

Where, is the wheel moment of inertia I_w, is calculated from the mass of the wheel m_w, and the radius of the wheel r_w, as follows:

$$I = \frac{1}{2} m_w * r_w^2 \quad (12)$$

The braking torque T_b and the brake force F_b, which act at the point where a single wheel meets the ground, are connected as follows:

$$T_b = F_b * r \quad (13)$$

Where, r is the wheel cylinder radius. The area of the wheel cylinder and the hydraulic pressure in the braking system both influence the force that the pads apply to the rotor. The following equation may be used to determine the maximum braking torque:

$$T_{b,max} = P * A * r_e \quad (14)$$

r_e is the effective radius (torque radius) of a brake disc from the center of the brake pads, which is the mean of the outside diameter and inside diameter of the disc. The radius of the wheel cylinder is taken as 0.034 m and the torque due to pressure on the wheel cylinder is about 1.

2.3. Tire-Road Friction Coefficient Characteristics and Estimation

The complicated friction dynamics between the tire and the varied road conditions are discussed in this section using an empirical model. The real-time estimate of the tire-road friction coefficient has been proposed using a variety of various methodologies in the literature. As stated by [29], the tractive forces generated by a tire during braking or acceleration are proportional to the normal forces of the road acting on the tire.

The road coefficient of adhesion (also known as the friction coefficient), which is symbolized by the symbol(μ), varies based on the road surface.

Since the goal of an ABS is to control the torque given to the driven wheels to reduce tire slide, it can only function within the stable zone of the $\mu - \lambda$ characteristic, shown in Fig. 8.

The slip ratio is the point obtained during emergency braking scenarios, at which the tangential velocity of the tire surface (wheel speed) and the longitudinal speed of the vehicle are not the same. So, the wheel longitudinal slip ratio λ (from Fig. 8) is defined by the normalized difference between the vehicle speed v and the speed of the wheel perimeter(R. ω).

$$\lambda = \frac{v - \omega * R}{v} \equiv 1 - \frac{\omega * R}{v} \quad (15)$$

Differentiating the equation mentioned equation by time (t):

$$\dot{\lambda} = \frac{\dot{v}(1-\lambda) - R * \dot{\omega}}{v} \quad (16)$$

Substituting equations (2) and (8) into the previous equation gives the following result in equation (14):

$$\dot{\lambda} = -\frac{1}{v}\left(\frac{\mu * F_z}{M}(1-\lambda) - \left[\frac{\mu * R * F_z - T_b}{I}\right] R\right) = -\frac{\mu.*}{v}\left[\frac{(1-\lambda)}{M} + \frac{R^2}{I}\right] + \frac{R}{I*v} * T_b \quad (17)$$

Understanding the relationship between the slipping ratio and the coefficient of friction between tire and road is too important to understand the main control requirement, and

the friction coefficient as a function of slip ratio is known as the magic formula which has derived from experimental data and is given by the following function.

$$\mu(\lambda) = \left[C_1\left(1 - e^{C_2 * \lambda}\right) - C_3 * \lambda\right] \tag{18}$$

The Formula cannot be directly applied for the detection of tire-road friction coefficient efficiently due to the enormous amount of factors involved. For purposes of identifying the tire-road friction coefficient, MATLAB/Simulink uses a look-up table in place of the Formula.

Table 1. Surface friction parameters of different road conditions [30]

Surface conditions	C_1	C_2	C_3
Dry asphalt	1.2801	23.9900	0.5200
Wet asphalt	0.8570	33.800	0.3470
Ice	0.1946	94.1290	0.0646

As shown in Fig. 3, the road coefficient of friction is a nonlinear function of wheel slip (λ) and the coefficient of friction reduces from the dry to ice road conditions. This shows how the friction coefficient μ(λ) increases with slip λ up to a valueλ_0, where it attains its maximum value μ_0. For higher slip values, the friction coefficient will decrease until the wheel is locked. As the plots indicate, increasing slip can increase the tractive force between the tire and road surface by an increase in μ.

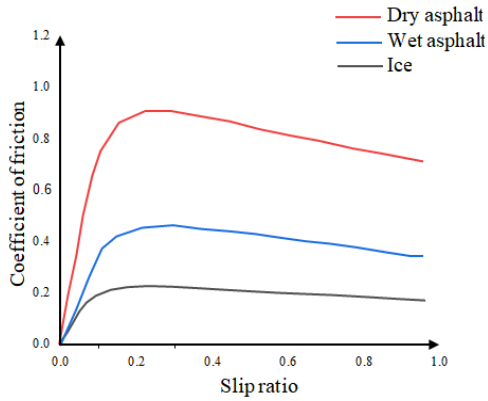

Fig. 3. Slip ratio vs. friction coefficient for various road conditions

On wet surfaces or roads contaminated by dirt, the brake force coefficient typically spans the range of 0.2 to 0.65 which is summarized in Table 2 [29]. Consider the tire force characteristics in Fig. 4 to comprehend that the longitudinal slip ratio affects braking forces. It demonstrates that, until it reaches a maximum (peak) value, the tire longitudinal force normally grows linearly with the slip ratio. Beyond this point, the tire force's strength diminishes and stabilizes at a fixed amount. As a result, the road surface adhesion coefficient curve divides the whole wheel slip range into two regions: the stable zone and the unstable region [29].

The wheel speed falls, the slip ratio rises, and the ground brake force progressively reduces until the vehicle wheel is locked if the wheel slip is caused by brake torque that is greater than ground brake torque. As a result, the goal of the suggested control strategy based on a look-up table is to keep the wheel slip ratio within the stable range during the braking process of the vehicle.

Table 2. Maximum values of the coefficient of friction for different road conditions

Road conditions	Maximum friction coefficient	Optimum slip (λ_0)
Dry asphalt	0.85	
Wet asphalt	0.45	0.2
Icy road	0.2	

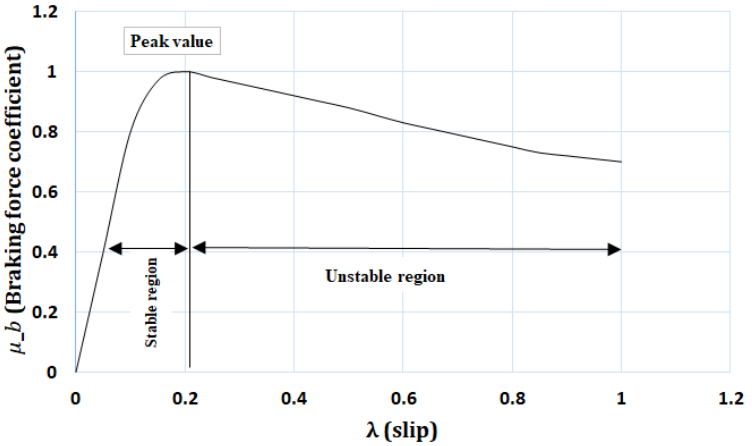

Fig. 4. Characteristics function of tire-road friction

2.4. Fuzzy Logic Rules

Fuzzy approaches are used in intricate and imprecise processes when there is no mathematical model or the mathematical model is significantly nonlinear. Fuzzy logic controllers are capable of representing knowledge in the form of linguistic rules and encompassing a high level of complexity with a small number of rules.

The fuzzy logic controller (FLC) consists of 4 main processes;

- Fuzzification is the process of converting a crisp (actual integer) input into a fuzzy set and determining an input's percentage membership in overlapping sets.
- The inference mechanism converts the fuzzy input into a fuzzy output,
- Rules: Mamdani's technique uses rules to determine outputs depending on inputs and rules.
- Defuzzification is needed to transform the fuzzy output into a numerical number. It integrates all fuzzy actions into a single fuzzy action and converts that single fuzzy action into a clear, executable system output.

In complex and imprecise systems for which either no mathematical model exists or the model is significantly nonlinear, fuzzy approaches are used [31]. According to [32] fuzzy logic controllers may express information comparatively simply in the form of language rules and can handle a considerable deal of complexity with a small number of rules. Both the inputs and output are crucial in the Fuzzy logic control approach. For the inputs and outputs, Gaussian membership functions (MFs) are used. Gaussian MFs are chosen as the best choice for obtaining adequate parameter values for a more robust control system. The MF range for the input and output is [-1, 1]. The controller's output is brake pressure, which regulates vehicle slippage and maintains safety.

Table 3. The fuzzy logic base rule

No.	Error	Error rate	ΔP
1	Zero (ZE)	Negative Big (NB)	Big Pressure Increase (BPI)
2	Negative Big (NB)	Zero (ZE)	Big Pressure Increase (BPI)
3	Negative Big (NB)	Positive Small (PS)	Medium Pressure Increase (MPI)
4	Positive Small (PS)	Negative Big (NB)	Medium Pressure Increase (MPI)
5	Zero (ZE)	Negative medium (NM)	Medium Pressure Increase (MPI)
6	Negative medium (NM)	Zero (ZE)	Medium Pressure Increase (MPI)
7	Zero (ZE)	Negative Small (NS)	Small Pressure Increase (SPI)
8	Negative Small (NS)	Zero (ZE)	Small Pressure Increase (SPI)
9	Positive Small (PS)	Negative Small (NS)	Pressure Hold (PH)
10	Negative Small (NS)	Positive Small (PS)	Pressure Hold (PH)
11	Positive Big (PB)	Negative Small (NS)	Medium Pressure Decrease (MPD)
12	Negative small (NS)	Positive Big (PB)	Medium Pressure Decrease (MPD)
13	Zero (ZE)	Zero (ZE)	Pressure Hold (PH)
14	Positive Small (PS)	Zero (ZE)	Small Pressure Decrease (SPD)
15	Zero (ZE)	Positive Small (PS)	Small Pressure Decrease (SPD)
16	Positive medium (PM)	Zero (ZE)	Medium Pressure Decrease (MPD)
17	Zero (ZE)	Positive medium (PM)	Medium Pressure Decrease (MPD)
18	Positive Big (PB)	Zero (ZE)	High Pressure Decrease (HPD)
19	Zero (ZE)	Positive Big (PB)	High Pressure Decrease (HPD)

The output of the Fuzzy logic controller (FLC) is the brake torque or change in pressure and the fuzzy member-ship languages used are: big pressure decrease (BPD), medium pressure decrease (MPD), small pressure decrease (SPD), pressure hold (PH), small pressure increase (SPI), medium pressure increase (MPI), and big pressure increase (BPI) as shown in Table 3.

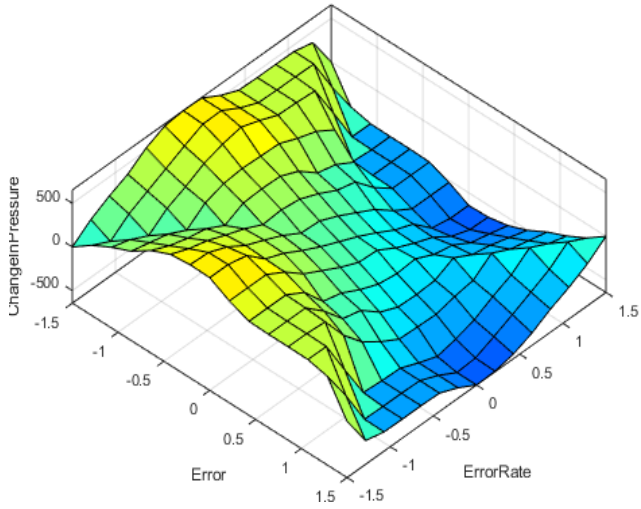

Fig. 5. Fuzzy logic controller surface characteristics

This surface viewer shows the output surface for any system output versus any one (or two) inputs. The control surface of a two-input and single-output system is shown in Fig. 5, where error and error rate represent inputs and change in pressure represents the controller output.

2.5. ABS Simulation in CarSim

The simulation parameters for CarSim are set here as shown in Fig. 6 The full vehicle simulation of ABS model is used in the CarSim software, which is interlinked with MATLAB. Some additional parameter's behavior like pressure can be used as compared to MATLAB ABS model. The simulation time is set to 10 seconds in all.

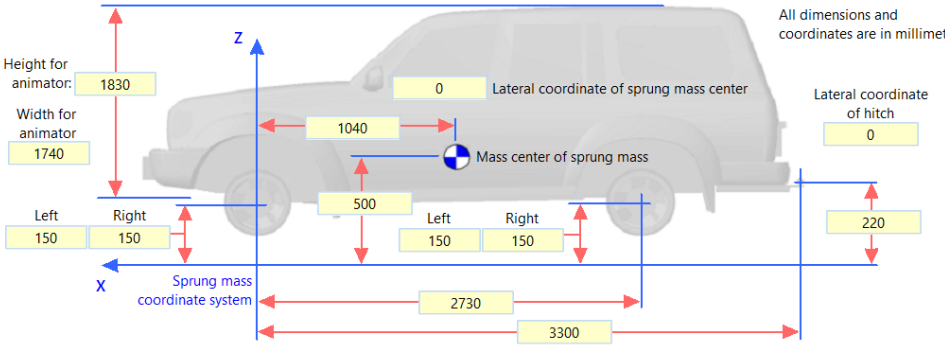

Fig. 6. Vehicle parameters in CarSim

3. Results and Discussion

3.1. MATLAB Simulation Result Using The Fuzzy Logic Controller

The simulation results were given for both dry and wet road conditions. As the result shows, braking time increases as the friction coefficient reduces due to the road condition and the same is true for speed.

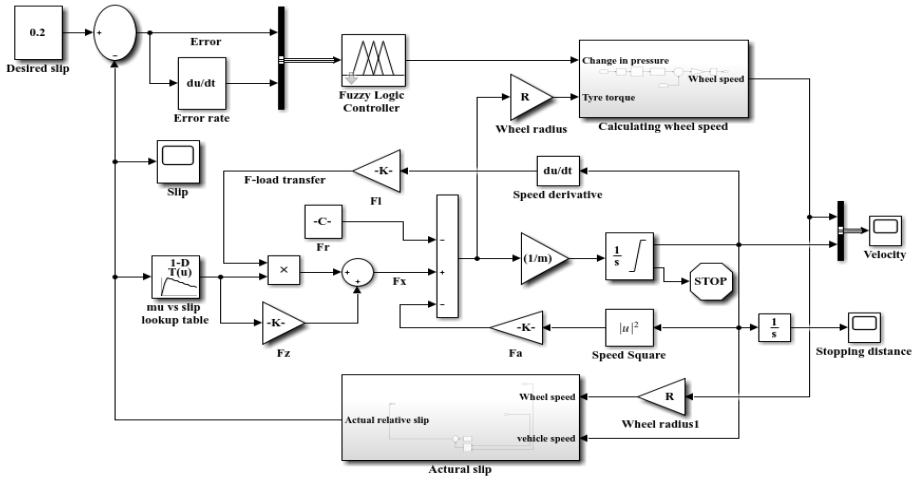

Fig. 7. Quarter vehicle model on MATLAB/Simulink with fuzzy logic controller

As the initial speed of the vehicle increases, the braking time and braking distance increase. Fig. 7 shows the MATLAB/Simulink model of the system with the fuzzy logic controller.

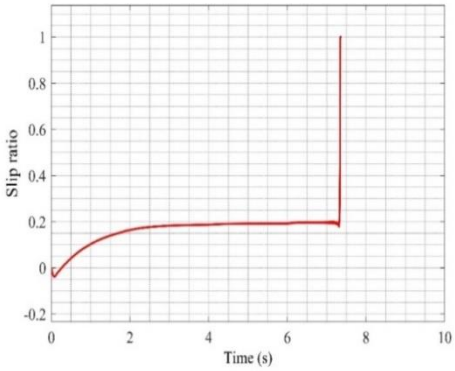

a) Slip ratio

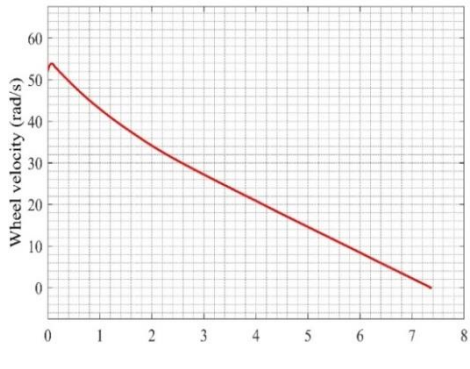

b) Wheel Velocity

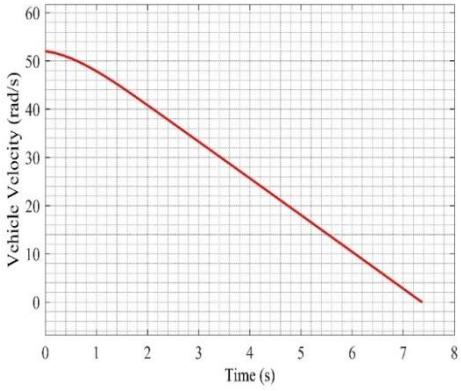

c) Angular vehicle speed

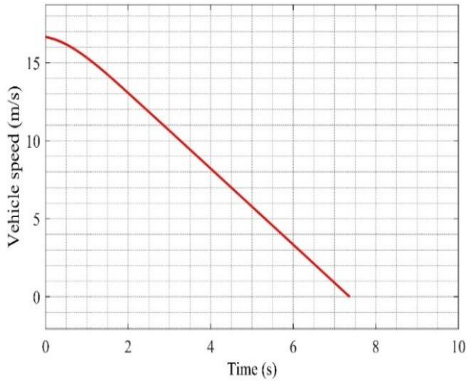

d) Vehicle linear velocity

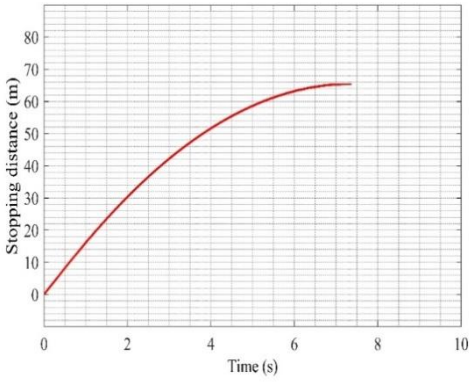

e) Stopping distance

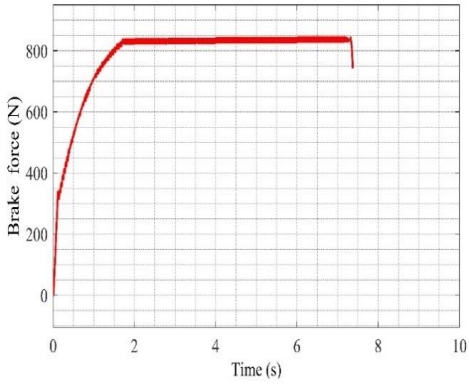

f) Brake force

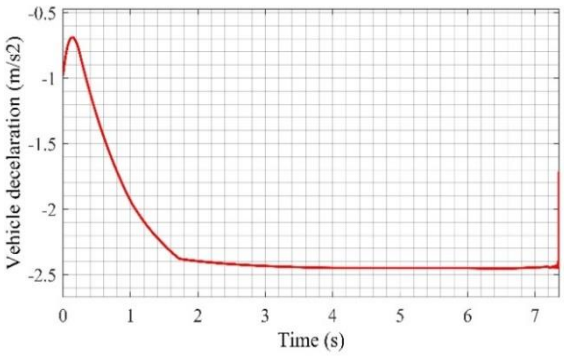

g) vehicle deceleration

Fig. 8. Simulation results of ABS with FLC at 60 km/hr

The purpose of the controller is to maintain the vehicle slip as close as possible to the value of 0.2 which was achieved in this work as shown in Fig. 8 (a). Consequently, vehicle stability is maintained with the help of a developed fuzzy logic controller, by which the actual slip is maintained as close as possible to the desired value of the slip.

From the simulation study, it has been seen that the stability of the vehicle is more stable as compared to the other models in which wheel speed suddenly comes to zero at a time of 7 seconds after braking. Braking force as shown in Fig. 8 (f), is the most important parameter of the brake system which is directly related to braking torque and braking distance since it is the amount of force needed to achieve assumed braking parameters for the mechanical vehicle.

To obtain the maximum braking torque to stop the vehicle within a minimum distance, the location of the peak as the controller has been exhibited. In the case of conventional braking systems or other controlling mechanisms, after the brake is applied to the wheel, it takes 10 to 14 seconds to let it slow down and regain traction, which takes only about 7 seconds in this study.

A velocity graph for both wheels and vehicle has been obtained, and it shows that both the velocity curves converge at a point when the vehicle is stopped, which ensures the vehicle stops without skidding.

3.2. CarSim Simulation

The second simulation is realized by CarSim simulation to confirm the performance of the proposed fuzzy logic controller. Since, the ABS model of the CarSim software represents the full vehicle simulation, and can be taken as a vehicle test under given circumstances, it was interlinked with MATLAB/Simulink for further simulation and comparison.

The wheel cylinder pressure variation is one of the additional parameters used in the CarSim ABS model for hatchback SUV vehicles. The braking pressure applied to the brake pedal is about 3 MPa, which was kept constant. Then, MATLAB/Simulink was integrated with CarSim & the parameters used are the same, in which the achieved result is almost similar to that illustrated in Fig. 9.

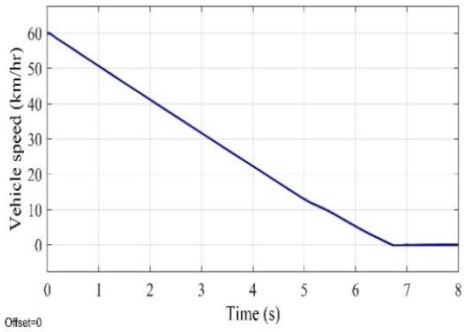

a) Vehicle velocity

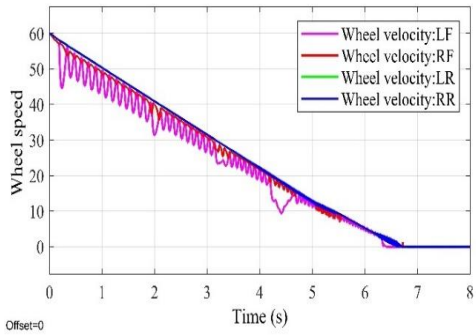

b) Wheel velocity

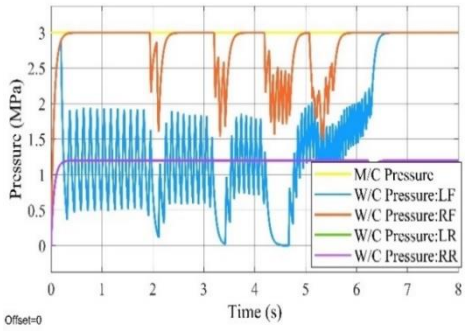

c) Wheel and master cylinder pressure

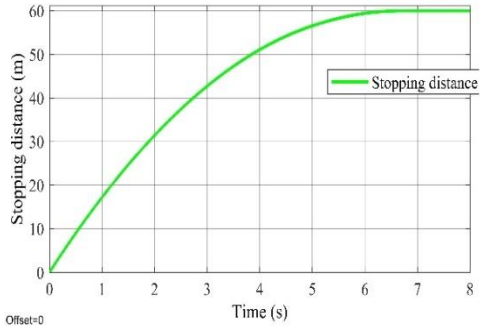

d) Stopping distance

Fig. 9. Simulation results of ABS in CarSim at 60 km/hr

At the end of the simulation, it gives the required wheel cylinder pressure that is to be applied to each wheel of the vehicle and the wheel control pressure increases quickly back to system or master cylinder pressure as the vehicle velocity drops below the velocity threshold and comes to rest, as shown in Fig. 9 (c). From the simulation results, the wheel cylinder pressure variation has been obtained for each wheel.

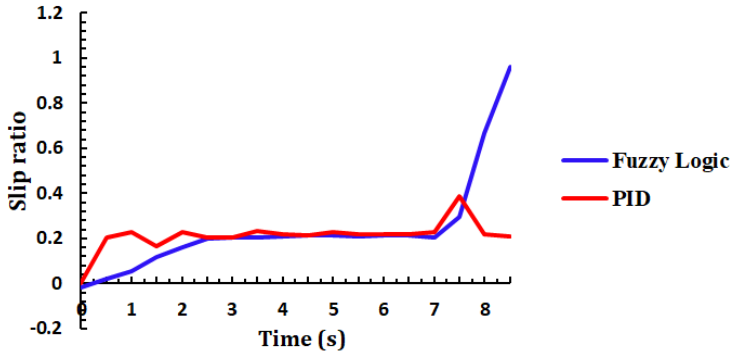

Fig. 10. Comparsion of Fuzzy and PID slip ratio

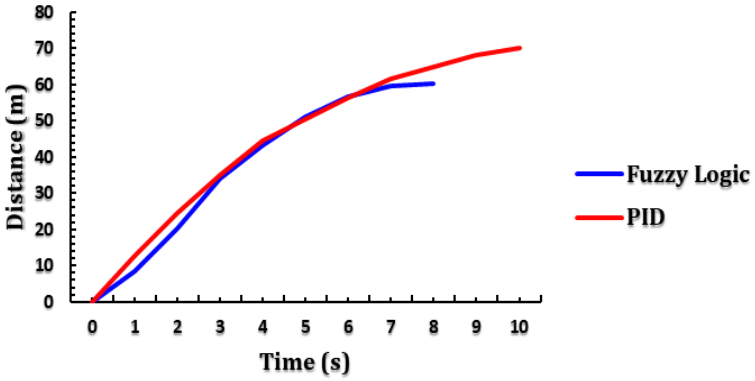

Fig. 11. Comparsion of Fuzzy and PID Braking distance

The front and rear brake system pressure has their proportion and the front brake pressure is more compared to the rear. The authors compared fuzzy logic to a MATLAB/Simulink PID controller. The slip control by the fuzzy logic controller system has an excellent convergent rate, but the PID has a relatively sluggish convergence rate, as shown in Fig. 10. The ABS response employing a fuzzy logic controller performs better by regulating longitudinal slip about 0.2 during braking till the vehicle stops. This enables the vehicle to stop without skidding after the 7th second.

The fuzzy logic with PID controllers' braking distances are also compared, and the findings demonstrate that the fuzzy logic controller achieves a lower brake distance, as shown in Fig. 11. After 7 seconds, the fuzzy logic brake distance is 63 meters, whereas the PID distance is 670 meters in 14 seconds. Based on these results, the fuzzy logic controller is to be more effective for the ABS than the PID controller.

The results demonstrate that the suggested fuzzy logic controller is successful in regulating the vehicle longitudinal model and achieves better performance than PID controllers.

From the results of the two model, it was observed that the model created in the CarSim program produces results that are more exact, detailed, and accurate than the model created in the MATLAB software. This occurs when a full-vehicle system model is utilized in CarSim whereas the MATLAB/Simulink model is developed using the quarter model of a car. In light of this, it can be said that the created controller for a quarter-car model performs well and converges quickly.

Conclusion

Two simulations illustrating the effect of ABS on vehicle braking system handling were presented in this study; in MATLAB/Simulink and CarSim. The quarter vehicle is modeled and its brake performance is studied in MATLAB/Simulink using a fuzzy logic controller and interlinked with CarSim software. A comparison has also been made with a developed ABS model to investigate the performance of the controller. The Fuzzy logic control strategy has been simulated for SUVs and makes the vehicle act as smart equipment under complex driving conditions. The simulation results show that the developed fuzzy logic controller ensures avoidance of wheel locking, even in different road conditions, even if the braking time and distance increase as the friction coefficient reduces. For both wheels and the vehicle, the velocity curves converge at a point when the vehicle became stop. Thus, the controller ensures the vehicle stops without skidding. It ensures that the anti-lock braking system guarantees higher speeds with minimum risks by reducing the stopping distance and maintaining the stability of the vehicle.

- The vehicle stability and braking performance have been improved by contributing additional braking with the help of a fuzzy logic controller strategy to the standard EBD and conventional braking systems. The proposed controller shows better performance to minimize the slip error as compared to the conventional controller, and hence, it maintains the stability of the vehicle and reduces the stopping distance of the vehicle.
- For validation purposes and to address a few limitations of the ABS model, the simulation was also conducted in CarSim software linked with MATLAB/Simulink. The outcome demonstrates that the wheel cylinder pressure is properly controlled and the braking stability is enhanced during the simulation process.
- The results of slip ratio and braking performance are compared utilizing fuzzy logic to a MATLAB/Simulink PID controller. The fuzzy logic controller successfully regulates the vehicle longitudinal model and achieves enhanced performance than PID controllers

Reference

[1] Ozdalyan B, Blundell M V. Anti-lock braking system simulation and modelling in ADAMS. IEEE Conf Publ. 1998;(457):140-4. https://doi.org/10.1049/cp:19980628

[2] Eriksson T. Co-Simulation of Full Vehicle Model in Adams and Anti-Lock Brake System Model in Simulink-master. Master's thesis in Applied Mechanics. 2014; Available from: https://publications.lib.chalmers.se/records/fulltext/199941/199941.pdf

[3] Anwar S, Ashrafi B. A predictive control algorithm for an anti-lock braking system. SAE Tech Pap. 2002;(724). https://doi.org/10.4271/2002-01-0302

[4] Dunn AL, Heydinger GJ, Rizzoni G, Guenther DA. New model for simulating the dynamics of pneumatic heavy truck brakes with integrated anti-lock control. SAE Tech Pap. 2003;2003(724). https://doi.org/10.4271/2003-01-1322

[5] Hwang, T, Roh J, Park K, Hwan, J, Lee K H, Lee K, Kim YJ. Development of HILS systems for active brake control systems. In: SICE-ICASE International Joint Conference. 2006. p. 4404-8. https://doi.org/10.1109/SICE.2006.314663

[6] Baek S, Song J, Yun D, Kim H, Boo K. Application of a sliding mode control to anti-lock brake system. 2008 Int Conf Control Autom Syst ICCAS 2008. 2008;307-11. https://doi.org/10.1109/ICCAS.2008.4694661

[7] Zhang X, Lou Y, Yang X. Study of control logic for automobile anti-lock braking system. Proc - Int Conf Intell Comput Technol Autom ICICTA 2008. 2008;1:493-7. https://doi.org/10.1109/ICICTA.2008.476

[8] Wang X, Wang Q. Modeling and simulation of automobile anti-lock braking system based on simulink. J Adv Manuf Syst. 2012;11(2):99-106. https://doi.org/10.1142/S0219686712500084

[9] Mirzaei M, Mirzaeinejad H. Optimal design of a non-linear controller for anti-lock braking system. Transp Res Part C Emerg Technol [Internet]. 2012;24:19-35. https://doi.org/10.1016/j.trc.2012.01.008

[10] Sivaramakrishnan SV. Discrete Tire Modeling for Anti-lock Braking System Simulations Discrete Tire Modeling for Anti-lock Braking System Simulations. Methods. MS Thesis. Blacksburg, Virginia. 2013. Available from: https://vtechworks.lib.vt.edu/bitstream/handle/10919/51424/Veppathur_Sivaramakrishnan_S_T_2013.pdf;sequence=1 .

[11] Jain C, Abhishek R, Dixit A. Linear Control Technique for Anti-Lock Braking System. J Eng Res Appl www.ijera.com [Internet]. 2014;4(8):104-8. Available from: https://www.ijera.com/papers/Vol4_issue8/Version%201/O04801104108.pdf

[12] Gong T, Yan H, Liu PF. Modeling and Simulation for Anti-Lock Braking System (ABS) of Automobiles Based on Simulink. Appl Mech Mater. 2014;716-717:1504-7. https://doi.org/10.4028/www.scientific.net/AMM.716-717.1504
[13] Li Y, Zhang J, Lv C. Robust control of anti-lock brake system for an electric vehicle equipped with an axle motor. SAE Tech Pap. 2014;1. https://doi.org/10.4271/2014-01-0140
[14] Xiao L, Hongqin L, Jianzhen W. Modeling and Simulation of Anti-lock Braking System based on Fuzzy Control. Iarjset. 2016;3(10):110-3. https://doi.org/10.17148/IARJSET.2016.31021
[15] Liu T, Yu Z, Xiong L, Han W. Anti-Lock Braking System Control Design on An Integrated-Electro-Hydraulic Braking System. SAE Int J Veh Dyn Stability, NVH. 2017;1(2):298-306. https://doi.org/10.4271/2017-01-1578
[16] Sundaram G, Sathyam S. Modelling and Simulation of a Vehicle Powertrain and Anti-Lock Braking System. 2017;0869(1):18-24. Available from: https://www.researchgate.net/publication/321085372_Modelling_and_Simulation_of_a_Vehicle_Powertrain_and_Anti-Lock_Braking_System
[17] Aksjonov A, Vodovozov V, Augsburg K, Petlenkov E. Design of regenerative anti-lock braking system controller for 4 in-wheel-motor drive electric vehicle with road surface estimation. Int J Automot Technol. 2018;19(4):727-42. https://doi.org/10.1007/s12239-018-0070-8
[18] Cao F, Chen C, Zhou L. Research on Simulation of Anti-lock Braking System Based on MATLAB. 2018;166(Amcce):839-44. https://doi.org/10.2991/amcce-18.2018.147
[19] Alaboodi* AS, Algadah KM. Anti-Lock Braking System Components Modelling. Int J Innov Technol Explor Eng. 2019;9(2):3969-75. https://doi.org/10.35940/ijitee.B7248.129219
[20] Li C, He C, Yuan Y, Zhang J. Braking evaluation of integrated electronic hydraulic brake system equipped in electric vehicle. Proc 2019 IEEE 3rd Inf Technol Networking, Electron Autom Control Conf ITNEC 2019. 2019;(Itnec):2361-5. https://doi.org/10.1109/ITNEC.2019.8729155
[21] Dankan Gowda V, Ramachandra AC, Thippeswamy MN, Pandurangappa C, Ramesh Naidu P. Modelling and performance evaluation of anti-lock braking system. J Eng Sci Technol. 2019;14(5):3028-45. Available from: https://jestec.taylors.edu.my/Vol%2014%20issue%205%20October%202019/14_5_39.pdf
[22] Yu D, Wang W, Zhang H, Xu D. Research on anti-lock braking control strategy of distributed-driven electric vehicle. IEEE Access. 2020;8:162467-78. https://doi.org/10.1109/ACCESS.2020.3021193
[23] You, S., Gil, J., & Kim W. Fixed-Time Slip Control With Extended-State Observer Using Only Wheel Speed for Anti-Lock Braking Systems of Electric Vehicles. IEEE Trans Intell Transp Syst. 2021;1-11. https://doi.org/10.1109/TITS.2021.3055980
[24] Cao W. Modeling and simulation of the anti-lock braking system based on MATLAB/Simulink. J Phys Conf Ser. 2021;1941(1):012075. 5. https://doi.org/10.1088/1742-6596/1941/1/012075
[25] El-bakkouri J, Ouadi H, Giri F, Saad A. Optimal control for anti-lock braking system: Output feedback adaptive controller design and processor in the loop validation test. Proc Inst Mech Eng Part D J Automob Eng. 2022. https://doi.org/10.1177/09544070221140938
[26] He X, Cheng H, Liu Z, Yang J, Ma D. Research on Co-simulation of Anti-lock Brake System Based on Carsim and Simulink. IEEE Inf Technol Networking, Electron Autom Control Conf ITNEC 2021. 2021;808-12. https://doi.org/10.1109/ITNEC52019.2021.9586820

[27] Tang,Y, Wang Y, Han M, Lian Q. Adaptive fuzzy fractional-order sliding mode controller design for antilock braking systems. J Dyn Syst Meas Control. 2016;138(4):041008. https://doi.org/10.1115/1.4032555
[28] Bhasin K. A Review Paper on Anti-Lock Braking System (ABS) and its Future Scope. Int J Res Appl Sci Eng Technol. 2019;7(8):372-5. https://doi.org/10.22214/ijraset.2019.8053
[29] Harifi A, Aghagolzadeh A, Alizadeh G, Sadeghi M. Designing a sliding mode controller for antilock brake system. EUROCON 2005 - Int Conf Comput as a Tool. 2005;I:258-61. https://doi.org/10.1109/EURCON.2005.1629910
[30] He Y, Lu C, Shen J, Yuan C. Design and analysis of output feedback constraint control for antilock braking system with time-varying slip ratio. Math Probl Eng. 2019;8193134. https://doi.org/10.1155/2019/8193134
[31] Gowda DV, Ra C. Slip Ratio Control of Anti-Lock Braking System with Bang-Bang Controller. Int J Comput Tech [Internet]. 2017;4(1):97-104. Available from: http://www.ijctjournal.org/Volume4/Issue1/IJCT-V4I1P15.pdf
[32] Modi D, Padia Z, Patel K. Fuzzy Logic Anti Lock Brake System. ... J Sci Eng Res [Internet]. 2012;3(7):1-8. Available from: http://www.ijser.org/researchpaper/FUZZY-LOGIC-ANTI-LOCK-BRAKE-SYSTEM.pdf

Research on Engineering Structures & Materials
www.jresm.org
Research Group

Research Article

Manufacturing of testing specimens from tough HDPE-100 pipe: Turning parameters optimization

Sabrina Mammeri[1,2,a], Kamel Chaoui[*1,b], Khaider Bouacha[1,c]

[1]*Mechanics of Materials and Plant Maintenance Research Laboratory (LR3MI), Mechanical Eng. Dept., Faculty of Technology, Badji Mokhtar University, P.O. Box 12, 23005, Annaba, Algeria*
[2]*Mechanical Eng. Dept., Faculty of Sciences and Technology, Mohamed-Chérif Messaadia University, P.O. Box 1553, Souk-Ahras 41043, Algeria*

Article Info

Article history:

Received 14 July 2023
Accepted 01 Nov 2023

Keywords:

HDPE pipe;
Tool geometry;
Machining;
Taguchi method;
Filament curvature;
Optimization

Abstract

Numerous machining operations are required in order to manufacture standard and non-standard specimens for mechanical testing of polymers. The present work focuses on the machinability of HDPE-100 pipe to prepare the utmost regular filaments with specified thickness and width. The study is set to establish mathematical correlations between surface quality (total roughness; Rt), cutting temperature (T°), filament uniformity (L) and corresponding cutting conditions. The latter include Vc (cutting speed), f (feed rate) and ap (depth of cut), combined with tool geometry (i.e., rake angle: γ and cutting-edge angle: κr). A mixed Taguchi L_{18} plan is adopted to organize and process the experimental runs. ANOVA and RSM (Response Surface Methodology) are employed to construct prediction models and optimize subsequent machining results. It is found that T (cutting temperature) and surface roughness criteria (Ra, Rt) are strongly affected by f and Vc. In addition, ANOVA results related to the height of filament bends (L) are likewise studied as a function of tool angles γ and κr. It is noted that cutting process is influenced by κr as it explains ~19% contributions of the total variation of parameter L, while γ, Vc and f show a little influence. It is deduced that optimum input parameters, represented by Vc, f, ap, γ and κr, are respectively 160 m/min, 0.5 mm/rev, 4 mm, (-6°) and 90° when turning tough HDPE material.

1. Introduction

Nowadays, countless polymer products are used for various daily life applications as substitutes for metallic materials because of technical advantages and economic considerations [1]. However, when adapting manufacturing techniques of metals to plastic materials, the reworked situations require rigorous and particular approaches for quality and strength control since polymer properties are usually lower than those of metallic components [2,3]. It is noted that polymer properties are essentially linked to their chemical structures, which determine a completely chaotic state (amorphous structure) or a partially ordered state (semi-crystalline structure). Such states allow specific properties in terms of flexibility and/or stiffness as well as resistance to common operating environments. Current standards requirements are actively contributing to ameliorate plastics processing methods and their integration especially into the piping industry [4]. This industry is dominated by high-density polyethylene (HDPE) pipes, which constitute an important underground substructure for water and natural gas distribution and transmission networks.

*Corresponding author: kamel.chaoui@univ-annaba.dz
[a] orcid.org/0009-0002-1961-8305; [b] orcid.org/0000-0001-6532-9462; [c] orcid.org/0000-0002-9349-5967
DOI: http://dx.doi.org/10.17515/resm2023.38ma0714rs

Although, plastics machining is not frequent compared to metals, it is becoming unavoidable as HDPE pipes are proposed for extreme applications such as contacts with hot, corrosive or radioactive fluids requiring new testing standards with substantial modifications. In most encountered machining cases, as described by Alauddin et al. [5], specific recommendations are discussed for orthogonal cutting, drilling, milling and grinding of thermoplastics. Usually, machining regime optimization for thermoplastics involves cutting regime parameters (i.e., speed, feed rate and depth of cut); however, additional controlling factors such as temperature, tool geometry and chip geometry may be taken into account in order to avoid structure alteration by thermal degradation [6] or large-scale deformations [7-10]. Salles and Gonçalves [8] studied the machining of UHMWPE (ultra-high molecular weight polyethylene) and surface quality parameters. They concluded that the observations made when turning such material are somewhat similar to the turning of aluminum and wood. Although many authors relate machinability of polymers to cutting speed, its influence on the surface finish in this case, is found to be insignificant. On the other hand, the cutting temperature does have great influence on final surface quality of this polymer [8].

Tamrin et al. [9] employed grey relational analysis for three different thermoplastics in order to determine an optimized set of machining parameters based on precision laser cutting. This process improves product quality and minimizes both service costs and operating errors. The ANOVA results show that such radiation power process has prevailing influence on the zone affected by heat generation for all studied thermoplastics. Silva et al. [10] investigated the precision turning of polyamide reinforced with 30% glass fiber as a function of feed rates and tool materials. They found that radial forces are the greatest, tailed respectively by cutting and feed ones. The polycrystalline diamond tool showed the lowest forces in relation to the best surface finish, followed by ISO uncoated carbide tool having a chip breaker. Irrespectively of the cutting regime parameters and tool material, continuous coiled microchips are produced in all checked cases. Chabbi et al. [11] examined machining parameters (*Vc*; *ap*; *f*) effects on force components, machine-tool power, roughness criteria and production as a function of time while turning POM-C (polyoxymethylene) polymer with a cemented carbide tool. Also, the analysis of output parameters includes a full factorial design (L27) followed by RSM and ANN techniques combined with desirability function optimization. From ANOVA analysis, it is concluded that *f* is the utmost significant factor influencing *Ra* with more than 66% contribution. However, tangential cutting force is mostly affected by *ap* and *f* parameters while the cutting power is evenly marked by the three main input cutting parameters. For minimal finish surface roughness issued from a turning process, the study gives 628 m/min, 0.08 mm/rev, and 1 mm as the optimized cutting parameters respectively for *Vc*, *f* and *ap*. For the turning process of PTFE (Polytetrafluoroethylene) polymer, Azzi et al. [12] analyzed the effects of input cutting regime parameters (i.e., *ap*; *f*; *Vc*) on roughness criteria (*Ra*, *Rz*) and material removal rate (MRR) using an L27 Taguchi design. Through ANOVA, it is concluded that *Ra*, *Rz* and MRR are effectively influenced by *f* (feed rate). The final optimization minimizing *Ra*, *Rz* and MRR, realized in the same way as in the previous study [11], gave a cutting regime with 270 m/min, 0.126 mm/rev and 2mm respectively for *Vc*, *f* and *ap.*

Kaddeche et al. [13] investigated surface finish, cutting forces and specifically cutting temperature changes while turning grade 80 and grade 100 polyethylene pipes materials. It is noticed that *f* (feed rate) is a dominant factor on roughness criteria and HDPE-80 roughness is much lower than that of HDPE-100. In addition, as anticipated from other studies, higher *Vc* values ameliorate surface quality nevertheless they increase cutting temperature leading to surface deterioration and material fusion. The other parameters are well discussed as a function of both pipe grades. Hamlaoui et al. [14] studied the

machining of HDPE-100 pipe for preparation of ISO specimens. They used RSM and desirability in order to assess the appropriate machining regime. They concluded that RSM and ANOVA approaches are suitable to describe the process of turning of HDPE-100 when considering both surface roughness and temperature measurements data as a function cutting regime conditions. Again, *f* remains as the most influencing parameter in order to minimize surface roughness for all the criteria, while *T* (temperature) is determined by *Vc* and *ap*. When considering temperature, the most secure case is given for 32°C which is a well-accepted upper bound by plastic pipe standards.

Fig. 1 shows a set of machined specimen geometries from HDPE pipe and which are considered for mechanical properties characterization. Fig. 1a exhibits typical gas pipe sections with yellow markings in the form of straight lines. It is possible to identify standard and non-standard specimens (Figs. 1b–1h) as machined from the pipe and respectively used for many testing conditions:

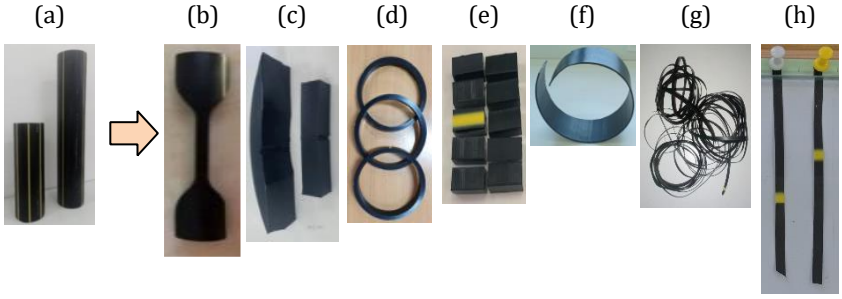

Fig. 1. Diverse testing specimen geometries machined from HDPE pipe

(b) tensile strength and creep; (c) impact fracture (Charpy); (d) residual stresses, (e) liquid sorption and (f) internal stresses relaxation. The last two cases are curled (g) and straight (h) filaments, continuously machined in a given direction, and are used to study mechanical and structural heterogeneities across pipe wall imparted by manufacturing processes [4,15-17]. Non-standard geometries are usually studied for specific applications and once technically approved by major pipe users; preliminary standards are prepared and put into standardized investigations to promote them as new standards. These specimen configurations serve different purposes and they include well-known ISO standards [4,16].

The objective of this study is to design appropriate machining conditions to obtain a uniform and continuous filament from an HDPE pipe. Later on, the filament will serve as specimens for mechanical testing and for investigating structure heterogeneity across the pipe wall. Aside from usual output machining parameters for plastics (i.e., roughness and temperature), minimizing filament curvature is considered as a criterion for filament geometrical uniformity. The study is based on RSM to construct correlations between input parameters (*Vc*, *f*, *ap*, *κr* and *γ*) and output ones which are cutting temperature (*T*), two roughness criteria (*Ra*, *Rt*) and filament curvature (*L*). Temperature and roughness values are predicted via the development of a second-order model through desirability. The analysis of variance method served to check the order of factor contributions to the cutting temperature.

2. Basic Approaches

The main goal of RSM is to optimize a process response when it is influenced by a number of variables. It has been successfully employed for many engineering production processes

[18-19]. According to literature [20-25], the RSM procedure is generally summarized in six different steps and is successfully applied in many experimental investigations available in literature [20-25].

Common relationships between input and output parameters are constructed via linear (1st order) and quadratic (2nd order) models as shown elsewhere [18-25]:

- First order model:

$$Y_k = a_0 + \sum_{i=1}^{n} a_i \cdot X_i + \varepsilon \quad (1)$$

where n is the number of variables and ε is item error.

- Second order model:

$$Y_k = a_0 + \sum_{i=1}^{n} a_i \cdot X_i + \sum_{i=1}^{n} a_{ii} \cdot X_i^2 + \sum\sum_{i<j}^{n} a_{ij} \cdot X_i \cdot X_j + \varepsilon \quad (2)$$

where Y_k is the desired output response, a_0 is constant, a_i, a_{ii} and a_{ij} are respectively, the coefficients of linear, quadratic and cross product terms. X_i are the coded variables.

Desirability (D) is a successful criterion for response optimization used to analyze polymer machining data or related others materials [14,18-25]. As a geometric mean of transformed responses, a nil D (i.e., D=0) reveals that selected response arrangement is just unacceptable. However, the proposed arrangement becomes an ideal case as D approaches unity (D≈1). D is defined as [20-25]:

$$D = \left(\prod_{i=1}^{n} d_i^{w_i} \right)^{\frac{1}{\sum_{j-1}^{n} w_i}} \quad (3)$$

where d_i and w_i are respectively the desirability and the weighting for the i^{th} targeted response. The number of responses for a given measuring position is termed n. Upper and lower limits should be given to each goal for a synchronized optimization.

The present study considers two surface roughness criteria (Ra and Rt), a cutting temperature (T) and a height of the filament bend (L) as output variables. The filament bend response is introduced after observing side filament curvature that is detrimental for mechanical properties measurements and should be lowered to a minimum. When searching for a minimum, the desirability limits are expressed as follows [18-23]:

$$\begin{cases} d_i = 1; & (if\ response\ < low\ value) \\ 1 \geq d_i \geq 0; & (if\ reponse\ varies\ from\ low\ to\ high) \\ d_i = 0, & (if\ response\ > high\ value) \end{cases} \quad (4)$$

In this optimization case, the combined advantages consist to have a good surface quality, the lowest cutting temperature and the less curved filament. Minimizing temperature is another essential requirement to avoid HDPE excessive heating and possible thermal degradation.

3. Experimental Procedure

The gas pipe material (HDPE-100), employed in this investigation, is pigmented with carbon black. Its external diameter (OD) is 200 mm and its thickness (t) is 11.4 mm (i.e.; SDR=17.6). Each work piece is 300 mm pipe portion (Figs. 1 and 2). This pipe is intended for the transportation and distribution of natural gas in urban areas. It is purchased from

the CHIALI Co. (Wilaya of Sidi Bel-Abbès, Algeria). It is designed according to European and Algerian standards (namely, EN 1555-2 and NA 7591-2) for medium pressure networks (4 bars) and can withstand tests from 6 to 10 bars gauge.

A succession of orthogonal turning operations is programmed on a tube work-piece (Fig. 2). A wooden mandrel is manufactured in order to reinforce holding the HDPE work-piece (Fig. 2a). Two mild-steel end caps are designed to secure both sides of the wooden tube-mandrel assembly to ensure eliminating any unwanted radial movement during operation (Fig. 2b). The dimensions of the basic system geometry and its machined parts are regular and verifiable throughout the experimental progression. Machining experiments are carried out in dry conditions using a parallel lathe (Type: SN-40; Spindle power: 6.6 kW). A commercially K20 carbide cutting tool is employed in this investigation as HDPE is a soft material and does not require special turning tool. Tool angles are selected within published polymer machining recommended intervals (γ: -6° and 15°; α: 6°; λ: 6° and κr: 30°, 60° and 90°) [7-14].

Roughness criteria (*Ra* and *Rt*) are measured via a roughness meter (Type: Surftest 301 Mitutoyo) as depicted in Fig. 2c. A calibrated special set-up is made in the lab to follow temperature changes using a developed application on a smart phone cell (Fig. 2d). In principle, for a given machined filament, the measurements are repeated 3 times and then averaged whenever needed. Usually, polymer chips or machining filaments are considerably distorted and sloped because of stresses and deformations imposed by cutting tool forward movements and work-piece rotation. From preliminary tests, Fig. 3 shows three (3) bent filament portions and two (2) relatively straight ones; both lots are obtained in different conditions (see also respectively, Fig. 1g and Fig. 1h).

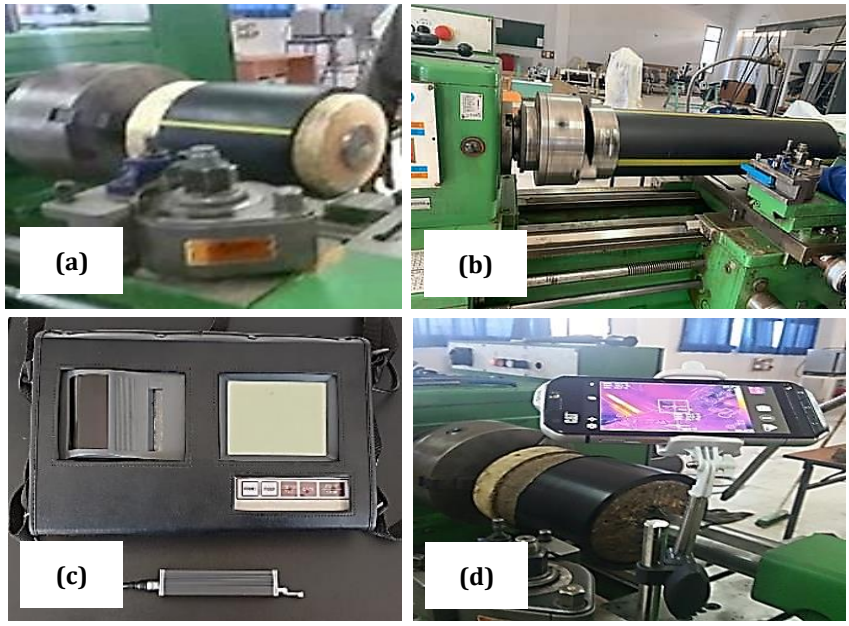

Fig. 2. Machining experimental setup

In order to allow performing acceptable tensile tests on such filaments, it is advised to minimize curliness upon machining. Therefore, a geometric criterion (L) is also combined with output parameters in order to lessen filament lateral curvature. For instance, a similar approach is employed in the case of milling of polymers to control burr height that may

limit the field of technical applications. Usually, this extra chip (or burr) of material is the result of plastic deformation due to the cutting process and is highly influenced by feed rate and other parameters for micro-milling of thermoplastic PMMA (polymethylmethacrylate) [26-28]. Parameter L is measured, in the same specific conditions, using the normal deviation from a 70 mm length of tangent to the filament (Fig. 3a).

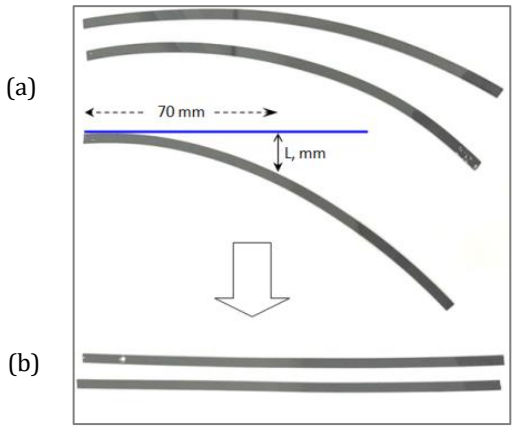

Fig. 3. Description of L parameter from low contrast photos of machined HDPE filaments; (a) large and (b) very low curvature

In order to initiate the study, an experimental design is chosen. It consists of 18 runs as explained in section 4.1 and it is based on three levels and five factors (i.e.; machining parameters) as reported in Table 1.

In this specific work, the polymer chips are intended to serve as mechanical test specimens for a subsequent study of properties heterogeneity imparted by the extrusion process of the HDPE pipe. Thus, the main imposed conditions on the process of obtaining the filament comprise continuity and regularity of the chip, a cutting temperature below 40°C and the least possible deformations. Finally, the manufacturing process of the desired final specimen configuration should take advantage from optimal machining parameters.

Table 1. Levels of the cutting regime input parameters

Level	Vc	f	ap	γ	κr
	(m/min)	(mm/rev)	(mm)	(°)	(°)
1	100	0.37	2	−6	30
2	140	0.53	3	-	60
3	560	0.67	4	15	90

It is established that opposite effects govern the influence of speed (Vc) on both temperature and surface quality. In this scenario, it is advantageous to keep a relatively high cutting speed, but this does not help lowering cutting temperature as stated in polymer machining guidelines [29,30]. Carr and Feger [7] showed that the roughness of a thermoplastic polyimide as a function of the speed Vc or the rake angle γ passes through a minimum established by laboratory tests.

Consequently, the process variables and the 3 levels are selected inside the working limits proposed and published by tool manufacturers research studies dedicated to

thermoplastics [7,9,10-12,29,30]. In this study, this critical phase is corroborated with some preliminary laboratory trials and available experimental literature dedicated to HDPE machining [6,8,13,14]. It is understood that selected process variables have pronounced effects on the quality of output characteristics, forming the three levels adopted herein.

4. Results and Discussion

4.1 Experimental Planning (Taguchi L_{18})

The performance characteristics (cutting temperature, total and arithmetic mean surface roughness criteria, and height of the filament bend) are measured after turning operations using Taguchi L_{18} mixed level. The results are exhibited in Table 2 and output data suggest that the highest cutting temperature (39.6°C) is recorded at the highest levels of *Vc* and *f*. Viscous friction during polymer material removal is strongly active in heat generation. In fact, the cutting temperature corresponding to these machining conditions (Run No.3, Table 2) is very close to the upper limit temperature allowed by standards for HDPE materials (i.e.; 40°C). Inversely, lower cutting speeds of 100 m/min and lower values f and *ap* are associated with much lower temperatures (28.5°C) but not always with required roughness criteria [13,14,29,30]. On the other side, the highest filament height bend (7.5mm) seems to be favored by higher *Vc*, *f* and *ap*. This state illustrates severe and intense machining conditions for semicrystalline polymers and is in direct relationship with cutting temperature changes [31]. At this stage, it is concluded that the upper limit parameters of level 3, especially *Vc* and *f* (Table 1) cannot be optimized values.

4.2 Analysis of Variance (ANOVA)

Based on experimental data, ANOVA results are used to identify input factors which significantly affect performance parameters. Table 3 presents this analysis for the cutting temperature (Table 3a), the surface roughness criteria (Tables 3b-3c) and the logarithmic height of the filament bend, *Ln(L)*, (Table 3d).

Table 2. Input and output data based on (L_{18})

Run N°	Cutting Parameters					Performance Characteristics			
	Vc (m/min)	*f* (mm/rev)	*ap* (mm)	*γ* (°)	*κr* (°)	*T* (°C)	*Ra* (µm)	*Rt* (µm)	*L* (mm)
1	100	0.37	2	-6	30	28.5	0.97	0.61	4.3
2	140	0.53	3	-6	30	32.9	1.18	0.74	3.8
3	560	0.67	4	-6	30	39.6	0.98	0.52	7.5
4	100	0.67	3	-6	60	32.3	1.44	0.78	1.5
5	140	0.37	4	-6	60	31.7	0.81	0.39	1.3
6	560	0.53	2	-6	60	35.8	0.86	0.42	1.4
7	100	0.53	2	-6	90	31.1	1.05	0.60	1.1
8	140	0.67	3	-6	90	33.4	1.29	0.69	1.3
9	560	0.37	4	-6	90	32.8	0.41	0.14	0.5
10	100	0.53	4	15	30	30.7	1.39	0.75	2.9
11	140	0.67	2	15	30	32.6	1.55	0.97	1.2
12	560	0.37	3	15	30	33.5	0.69	0.32	2.4
13	100	0.67	4	15	60	32.4	1.42	0.89	5.2
14	140	0.37	2	15	60	29.6	0.96	0.48	1.8
15	560	0.53	3	15	60	34.8	0.92	0.51	1.6
16	100	0.37	3	15	90	28.5	0.64	0.41	2.7
17	140	0.53	4	15	90	30.8	0.95	0.53	4.3
18	560	0.67	2	15	90	36.2	1.41	0.63	1.9

It is found that subsequent models are satisfactory. Principal significant factors are rake angle (γ), cutting-edge angle (κr), and regime parameters (Vc, f and ap).

Table 3a. ANOVA of cutting temperature

Label	DF	Seq SS	CP%	Adj SS	Adj MS	F-tests	P-value
Model	8	128.777	98.10	128.777	16.0971	58.07	0.000
Linear	5	122.478	93.30	121.873	24.3746	87.94	0.000
γ	1	4.500	3.43	4.500	4.5000	16.24	0.003
κr	1	2.083	1.59	3.120	3.1197	11.26	0.008
Vc	1	74.427	56.70	70.380	70.3804	253.92	0.000
f	1	39.998	30.47	41.995	41.9947	151.51	0.000
ap	1	1.470	1.12	1.653	1.6530	5.96	0.037
Square	1	2.228	1.70	2.228	2.2277	8.04	0.020
$Vc*Vc$	1	2.228	1.70	2.228	2.2277	8.04	0.020
2-way interaction	2	4.071	3.10	4.071	2.0356	7.34	0.013
$\kappa r *Vc$	1	1.861	1.42	1.726	1.7260	6.23	0.034
$Vc*f$	1	2.211	1.68	2.211	2.2106	7.98	0.020
Error	9	2.495	1.90	2.495	0.2772		
Total	17	131.271	100.00				

From Tables 3a–3c, T, Ra and Rt are intensely affected by f and Vc. The most significant factor on the parameters Ra and Rt remains f explaining respectively 51.92% and 63.67% contributions of the overall discrepancy. Next major contribution on Ra and Rt is dictated by Vc with respectively, 29.45% and 15.89% the contributions.

Table 3b. ANOVA of Ra

Label	DF	Seq SS	CP%	Adj SS	Adj MS	F-tests	P-value
Model	6	0.71800	98.19	0.71800	0.119666	99.70	0.000
Linear	5	0.70398	96.28	0.67429	0.134859	112.36	0.000
γ	1	0.02000	2.74	0.02000	0.020000	16.66	0.002
κr	1	0.06901	9.44	0.04674	0.046744	38.94	0.000
Vc	1	0.21531	29.45	0.21531	0.215313	179.39	0.000
f	1	0.37965	51.92	0.37965	0.379646	316.30	0.000
ap	1	0.02001	2.74	0.01483	0.014831	12.36	0.005
2-way interaction	1	0.01402	1.92	0.01402	0.014021	11.68	0.006
$\kappa r*Vc$	1	0.01402	1.92	0.01402	0.014021	11.68	0.006
Error	11	0.01320	1.81	0.01320	0.001200		
Total	17	0.73120	100.00				

Table 3c. ANOVA of Rt

Label	DF	Seq SS	CP%	Adj SS	Adj MS	F-tests	P-value
Model	8	1.68662	98.87	1.68662	0.210827	98.02	0.000
Linear	5	1.55005	90.86	1.32176	0.264352	122.90	0.000
γ	1	0.04909	2.88	0.04909	0.049089	22.82	0.001
κr	1	0.08501	4.98	0.03699	0.036987	17.20	0.002
Vc	1	0.27101	15.89	0.28786	0.287864	133.83	0.000
f	1	1.08614	63.67	0.88167	0.881667	409.89	0.000
ap	1	0.05880	3.45	0.01507	0.015065	7.00	0.027
2-way interaction	3	0.13657	8.01	0.13657	0.045525	21.16	0.000
$\kappa r*Vc$	1	0.07199	4.22	0.09001	0.090008	41.85	0.000
$\kappa r*f$	1	0.04514	2.65	0.03722	0.037218	17.30	0.002
$\kappa r*ap$	1	0.01944	1.14	0.01944	0.019441	9.04	0.015
Error	9	0.01936	1.13	0.01936	0.002151		
Total	17	1.70598	100.00				

For the cutting temperature, cutting speed (Vc) is in first position with a contribution of 56.70% followed by f explaining 30.47% of overall discrepancy. Table 3d presents the ANOVA results corresponding to the height of the filament bends (L) as a function of process parameters (γ, κr, Vc, f and ap). It is shown that the main effects of these process parameters are all significant with respect to the height of the filament bends. While, the most significant process parameter is the cutting-edge angle (κr), which explains 18.99% contributions of the total variation, followed by the depth of cut (ap) (6.56 %).

Moreover, it can be realized that γ, Vc and f show a relatively small influence on the height of the filament bends. However, for rake angle (γ), cutting-edge angle (κr) and depth of cut (ap) interactions, influence degrees are very important in comparison to the remaining terms, especially, for rake angle (γ) and cutting-edge angle (κr), which explains 40.78%.

In Fig. 4, main effects deduced from this study are sketched out. It should be noted that overlooked variables are supposed to be kept constant around an averaged value bounded by two assumed levels. They indicate that T is significantly affected by two regime parameters namely Vc and f as per Fig. 4a. In addition, the graphs reveal that, whenever Vc and f increase, corresponding cutting temperature increases as expected.

Nevertheless, for polymeric materials, cutting speed remains an important input parameter. Indeed, any increase in Vc, inevitably will lead to a rise in T because friction dominates in the so-called “second shear zone”. Conversely, at lower cutting speed, lower heat is generated and results in lessened temperatures values [14]. Similarly, when f increases, the filament section and the deformed material volume increase and hence the temperature increases, particularly, in the first shear zone by deformation [23].

Obviously, it is noted that Ra and Rt criteria are highly affected by f as shown in Figs. 4b and 4c. Usually technical literature accepts that parameter f or its squared form (f^2) have a cumulative effect on the geometric surface roughness criteria.

Table 3d. ANOVA of Ln(L)

Label	DF	Seq SS	CP%	Adj SS	Adj MS	F-tests	P-value
Model	11	7.61434	99.63	7.61434	0.69221	146.38	0.000
Linear	5	2.72088	35.60	2.85707	0.57141	120.83	0.000
γ	1	0.33220	4.35	0.65938	0.65938	139.43	0.000
κr	1	1.45100	18.99	1.08021	1.08021	228.42	0.000
Vc	1	0.19806	2.59	0.23008	0.23008	48.65	0.000
f	1	0.23788	3.11	0.08199	0.08199	17.34	0.006
ap	1	0.50174	6.56	0.85242	0.85242	180.25	0.000
Square	2	0.19429	2.54	0.75633	0.37816	79.97	0.000
*Vc*Vc*	1	0.17789	2.33	0.52553	0.52553	111.13	0.000
*f*f*	1	0.01640	0.21	0.65735	0.65735	139.00	0.000
2-way interaction	4	4.69917	61.49	4.69917	1.17479	248.42	0.000
*γ*κr*	1	3.11632	40.78	3.50141	3.50141	740.42	0.000
*γ*ap*	1	0.61899	8.10	1.45922	1.45922	308.57	0.000
*κr*ap*	1	0.46017	6.02%	0.77480	0.77480	163.84	0.000
*Vc*ap*	1	0.50369	6.59	0.50369	0.50369	106.51	0.000
Error	6	0.02837	0.37	0.02837	0.00473		
Total	17	7.64271	100.00				

(a)

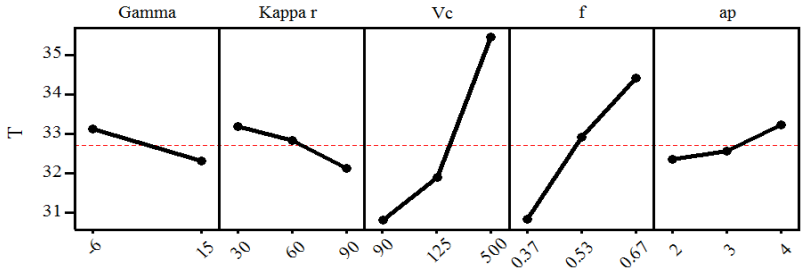

(b)

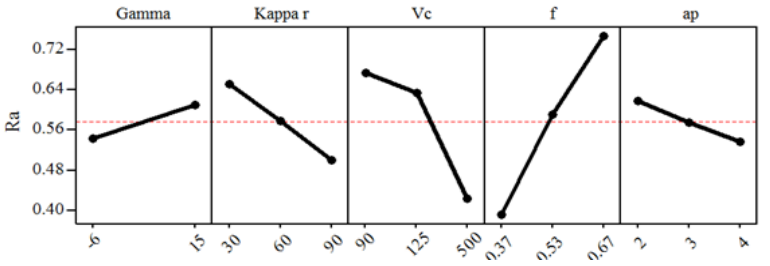

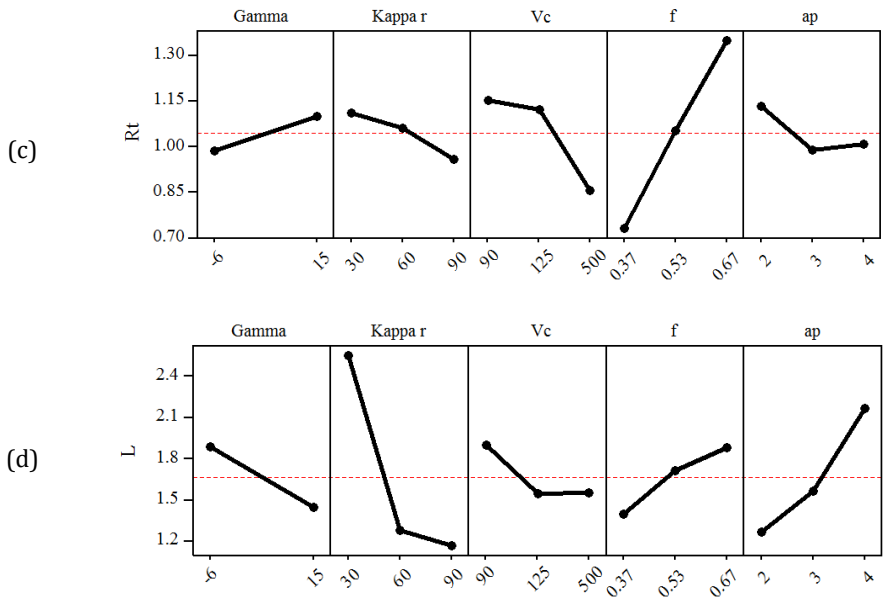

Fig. 4 Principal effect-plots for outputs : (a) *T*, (b) *Ra*, (c) *Rt* and (d) *L*

Parameter *Vc* is associated with important trend variations. For instance, surface roughness is progressively perfected by increasing *Vc*. In cutting processes, it is also well known that higher cutting speed leads to a better surface finish while the deformation velocity influences, to some extent, the residual properties of the workpiece material. It is also accepted that the higher the speed, the less substantial the plastic comportment is. The flow of plastically deformed lateral material of the workpiece along cutting-edge direction can enhance peaks heights and valleys depths of surface irregularities [13,14,23,32]. As shown in Fig. 4d, height of the filament bends (*L*) decreases considerably with the decrease of the cutting-edge angle (*κr*). Additionally, it should be emphasized that uncut chip thickness is explained by means of the combined effects of parameters *f*, *ap* and *κr*. In other words, as the angle *κr* is reduced, the chip width is enlarged. The latter is a direct consequence of cutting-edge active span increase. This results in an intensification of the heat amount taken away from the cutting zone by chip formation and hence, the chip deformation and height of the filament bends increase. However, as the cutting-edge angle (*κr*) increases, the amount of heat evacuated by the chip is lessened and the spiral-shape chip tends to form. This results in a decrease in the height of the filament bends. No significant changes are observed on the performance characteristics because of variations in the rake angle (*γ*), since it mainly influenced the tool nose resistance.

4.3 RSM Models

The relationship between process parameters (*Vc, f, ap, γ* and *κ)* and performance characteristics (*T*, *Ra*, *Rt* and *L*) are correlated using RMS. Each prediction model is developed at 95% confidence level with Minitab 19 experimental design software and it is based on regression analysis using least square method.

The initial regression equations of the performance characteristics are based on input parameters and corresponding interactions. It should be noted that the RSM can be also used to obtain an exponential model through the natural logarithmic transformation of a

process parameter and its performance characteristics. The following equations for performance characteristics are obtained (Eqs. 5-8):

$$T = 21.28 - 0.048\,\gamma + 0.003\,\kappa r + 0.04\,Vc + 8.41 f - 0.384\,ap - 0.005 * 10^{-2}\,Vc^2 - 0.006 * 10^{-2}\,\kappa r * Vc + 0.014\,Vc * f\,; \quad [R^2 = 98.10\%] \tag{5}$$

$$Ra = 0.429 + 0.318 * 10^{-2}\,\gamma - 0.004\,\kappa r - 0.0009\,Vc + 1.145 f - 0.356\,ap + 0.006 * 10^{-3}\,\kappa r * Vc; \quad [R^2 = 98.19\%] \tag{6}$$

$$Rt = 0.883 + 0.005\,\gamma - 0.009\,\kappa r - 0.149 * 10^{-2}\,Vc + 0.946\,f + 0.075\,ap + 0.014 * 10^{-2}\,\kappa r * Vc + 0.017\,\kappa r * f - 0.002\,\kappa r * ap; \quad [R^2 = 98.87\%] \tag{7}$$

$$L = e^{\left(4.977 - 0.2967\,\gamma + 0.02381\,\kappa r + 0.02256\,Vc - 29.13\,f + 0.3747 ap - 0.000039 Vc^2 + 28.58\,f^2 + 0.001750\,\gamma * \kappa r + 0.07055\,\gamma * ap - 0.01396\,\kappa r * ap + 0.001313\,Vc * ap\right)}; \quad [R^2 = 99.63\%] \tag{8}$$

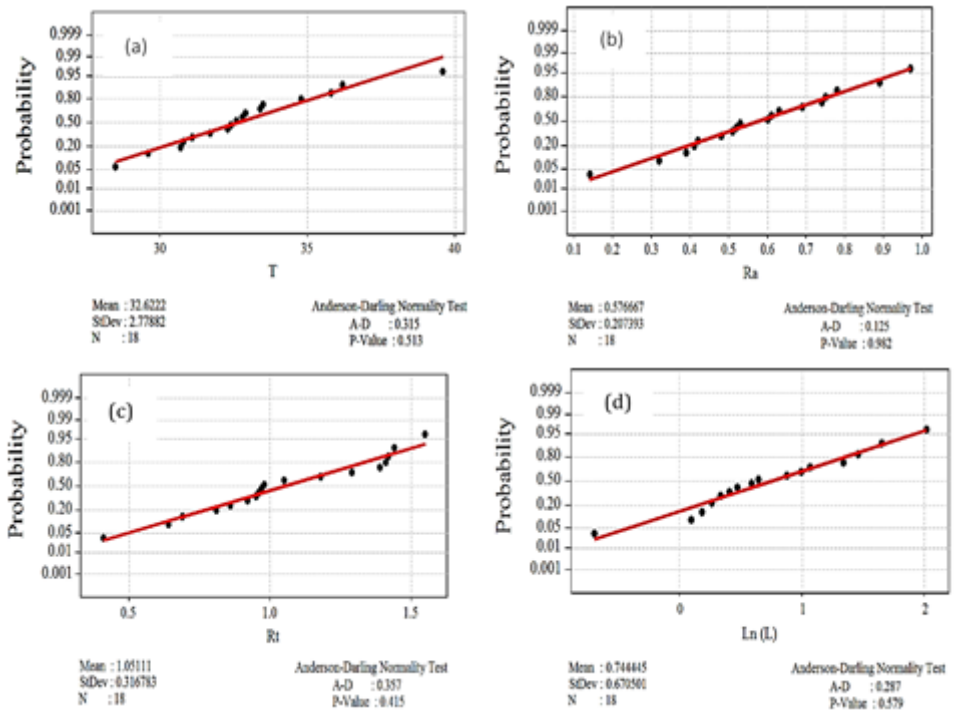

Fig. 5. Normal probability plots for: (a) *T*°, (b) *Ra*, (c) *Rt* and (d) *Ln(L)*

These RSM models are applicable only within stated range levels according to Table 1. High percent of R^2-values (98.10% ÷ 99.63%) for equations (5) to (8) indicate consistent appraises for each described output parameter. Based on the Anderson-Darling normality test, it is shown that calculated probabilities of residual variations as a function of predicted responses follow closely a straight line as plotted in Fig. 5.

Concerning *Ra*, *Rt* and *T*, as shown in Figs. 5a-c, the corresponding *P*-values (0.513; 0.982; 0.415) are above the 5% significance level, implying a normal distribution. For the height of chip/filament bend case, data linearization required a normalization using the

logarithmic transformation and A-D test *P*-value for *L* and *Ln(L)* increased respectively from 0.013 to 0.579 as shown in Fig. 5d [33]. The corresponding determination coefficients (R^2) indicate very satisfactory correlations.

4.4 RSM 3-D Plots

Significant combined effects of the process factors are selected and illustrated in Figs. 6-9 in the form of 3-D responses surface plots respectively for *T*°, *Ra*, *Rt* and *Ln(L)*. Figs. 6a-b show the effects of *Vc*, *f* and cutting-edge angle (*κr*) on measured machining temperature. It is observed that the cutting speed effect is the highest compared to that of *f* and *κr*. The cutting temperature increase is explained by the frictional activities at the chip-tool cutting interface. The maximum value of temperature is reached within the 350 to 550 m/min cutting speed range.

Most significant interactions are found between *Vc* and *f*, where the lowest cutting temperature is accomplished with the lowest *Vc* and the lowest *f* combinations (Fig. 6b). At lower cutting speeds, it is also observed that no important changes affected the cutting

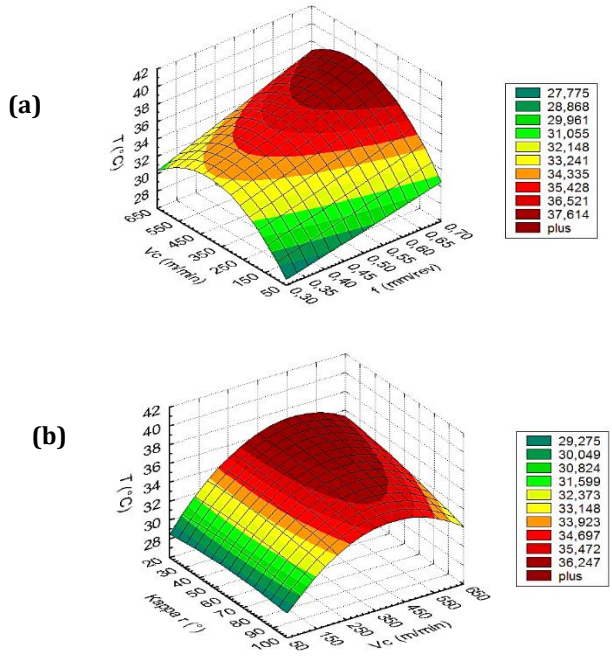

Fig. 6. Response surface for cutting T° as a function of: (a) *Vc* and *f*; (b) *κr* and *Vc*

temperature because of cutting-edge angle variations (Fig. 6b). When turning HDPE pipe material with a high-speed steel tool, Hamlaoui et al. [14] found that the cutting temperature is principally affected by *Vc* and *ap* as compared to *f*. The introduction of cutting-edge angle gave a better insight on *T* variations.

Estimated response surface plots for *Ra* and *Rt* as a function of parameters (*Vc*, *f*, *ap* and the angle *κr*) are illustrated in Figs. 7-8. In Fig. 7, it can be seen that *Vc* has the greatest influence on *Ra* and its discrepancy is high when compared to that caused by cutting-edge angle. Also, Fig. 7 shows that *Ra* is improved by increasing cutting speed as expected. No substantial changes are observed for *Ra* due to cutting-edge angle variations at higher *Vc*. Conversely, for lower cutting speed values, *κr* effect becomes important. The best surface roughness quality in terms of *Ra* is achieved at the highest cutting-edge angle and the

highest cutting speed combination. This is a new finding compared to results of previous studies [13,14].

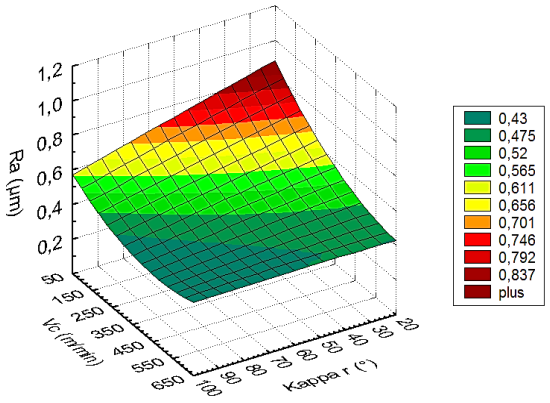

Fig. 7. Response surface for Ra as a function of *Vc* and *κr*

Fig. 8 presents the variations of roughness criterion *Rt* as function cutting regime parameters (*Vc, f, ap*) and cutting-edge angle. In Fig. 8a, it is observed that higher depth of cut and higher cutting-edge angle significantly improved *Rt* by almost two folds (from 1.3 down to ~0.63µm). This corroborates the previous results discussed in the *Ra* case.

The Figs. 8a-b show the maximum opposite effects on *Rt* caused by increasing *ap* and *f*. At the highest cutting-edge angle, the variation *Rt* is 75% at the lower limits of *ap* and *f* (i.e., 1.8 mm and 0.30 mm/rev) and only 55% at the upper limits (i.e., 4.2 mm and 0.70 mm/rev). The best *Rt* value (0.3 µm) is obtained for a feed rate of 0.3 mm and a maximum cutting-edge angle. As expected, higher feed rates contribute to extensive deformations of the machined polymer surface and on the evacuated chip. In addition, Fig. 8b suggests that *Rt* is around 1.4 µm and almost independently of *κr* for the highest feed rate.

A similar behavior is observed for the variation of *Rt* as function of cutting speed and cutting-edge angle (Fig. 8c). It is observed that highest roughness values (~1.4 µm) are obtained for lowest cutting-edge angles and the lowest cutting speed. It is understood that cutting time is long enough to cause extensive deformation at the machined surface under the tool action. On the other side, when *κr* is increased for low speeds *Rt* is slightly ameliorated (~0.92µm).

Globally, at the highest *κr*, *Rt* becomes almost constant as a function of *Vc*. It is concluded that the best combination is obtained when *κr* is the lowest and *Vc* is the highest (*Rt*~ 0.5µm) which is three folds lower than that of 50 m/min. The best surface quality, expressed in terms of *Rt*, is achievable combining the highest *κr* with either the lowest *f* or the lowest *ap*. Moreover, the most significant interactions are found between *f* and *κr*.

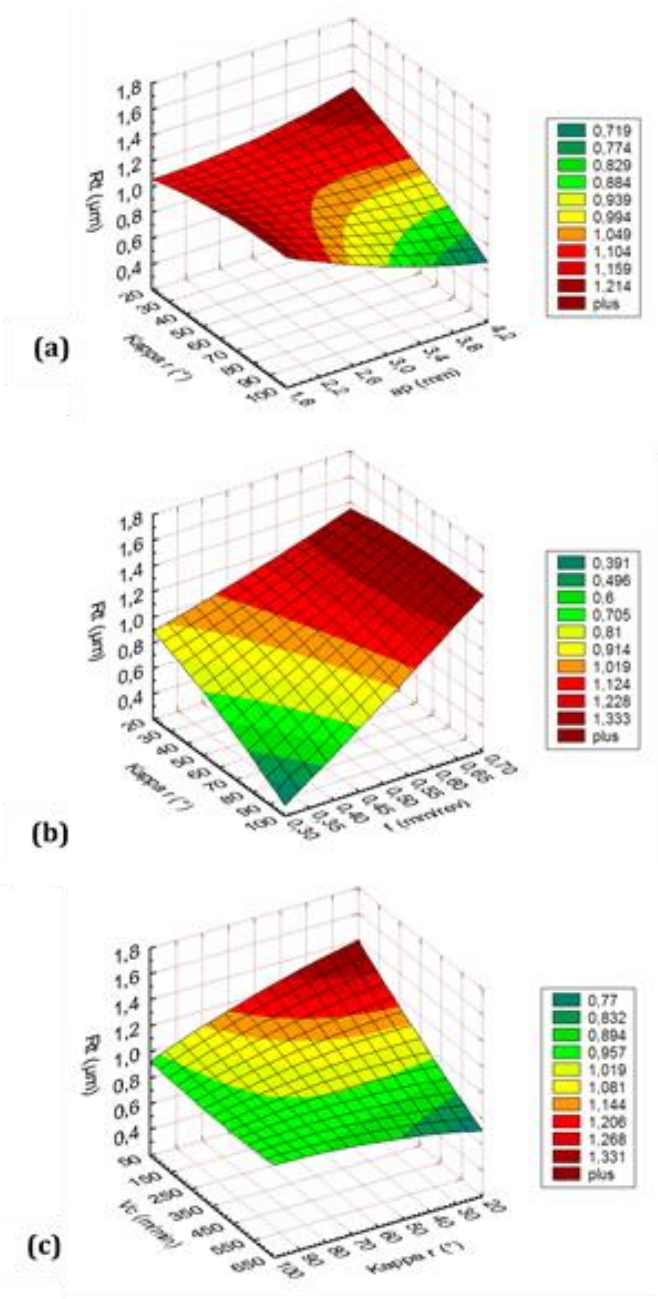

Fig. 8 Response surface for Rt as a function of: (a) *κr*, *ap;* (b) *κr*, *f*; (c) *Vc*, *κr*

Fig. 9 presents chip/filament curvature parameter, which has been defined earlier in Section 3, as a function of *ap*, *Vc* and *κr*. From Fig. 9a, it can be seen that cutting-edge angle has the highest decreasing effect on filament height bend. No really significant changes are observed on the filament height bend values as a function of *ap* variation especially at higher cutting-edge angles and higher cutting speeds (Fig. 9a-b). The possible explanation is in relation to the generated heat at the interface chip-cutting tool which softens cut

material as discussed earlier. A rise in *Vc* between 100 and 350 m/min, increased the interface tool-chip temperature regardless of *f* and *κr* values (Fig. 6).

As a result, there is a decrease of maximum shearing forces within the shear area and at the tool-chip interface. Furthermore, the shearing angle is increased and, at the same time, the chip thickness is lessened. It follows, the filament will tend to be ribbon-shaped as the contact area tool-chip becomes smaller. Beyond this limit (350 m/min), as cutting speed increases, the filament height bend increases and subsequently, it becomes more curved. The best uniform filament can be achieved with the highest cutting-edge angle and *Vc* in the interval 350–450 m/min. There is agreement between RSM 3-D plots and experimental results.

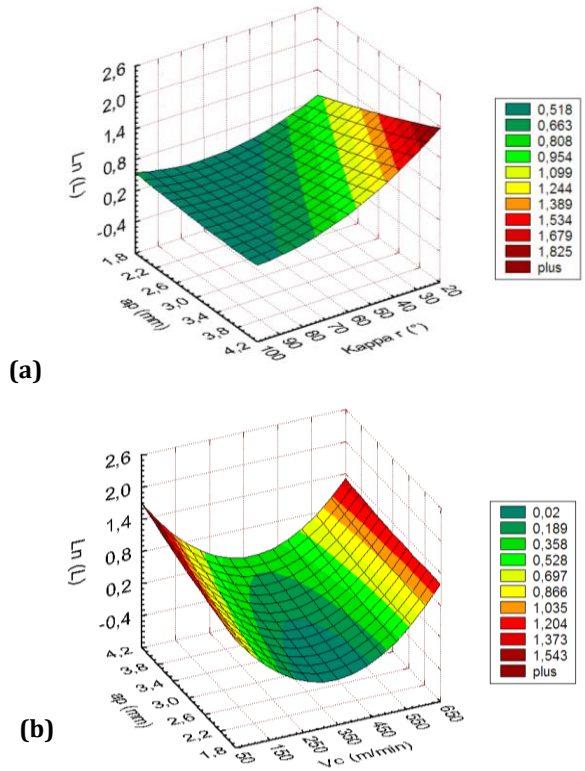

Fig. 9. Response surface for *Ln(L)* as a function of: (a) *ap*, *κr* and (b) *ap*, *Vc*

4.5 Optimization Using Composite Desirability

A principal goal for an experimental approach is to help investigate optimal values for the cutting parameters. In this case, regime parameters become the desired values for the sought output parameters during HDPE pipes turning process. In other words, the use of RSM helps identifying the arrangement of input (geometric and regime) parameters (i.e., *γ*, *κr*, *Vc*, *f* and *ap*) that conjointly optimize cutting temperature, surface roughness criteria and the lowermost filament bend height. As defined in [24], the composite desirability (D) is the resultant of weighted geometric individual desirabilities. In order to reduce machined filament dimensional deviations, cutting parameters are restricted within bottom and top permissible limits as applied in various studies [11,12,14,20,23,]. There

are several factors restraining the cutting process parameters for HDPE pipe material and some of them have been quoted in published literature [5,13,14,17].

The limitations taken into account, in the case of HDPE, cover 4 categories in relation to: *(i)* cutting regime, *(ii)* tool geometry, *(iii)* surface quality and *(iv)* upper limit temperature. They are given by the inequalities (9-16):

$$(i)\begin{cases} 100 \le Vc \le 560 & (9) \\ 0.48 \le f \le 0.52 & (10) \\ 3.9 \le ap \le 4.0 & (11) \end{cases}$$

$$(ii)\begin{cases} -6° \le \gamma \le +15 & (12) \\ +30° \le \kappa r \le +90° & (13) \end{cases}$$

$$(iii)\begin{cases} Ra \le 0.24\ \mu m & (14) \\ Rt \le 0.59\ \mu m & (15) \end{cases}$$

$$(iv)\ \begin{cases} T \le 34°C & (16) \end{cases}$$

The optimized solution without any constraints for *T*, *Ra*, *Rt* and *Ln(L)* is given Tables 4a and 4b. All responses are rated with the same weight and importance since there is no indication to opt for different schemes. Table 4a shows the results of RSM optimization without constraints for targeted values of cutting temperature *(T)*, surface roughness criteria *(Ra, Rt)* and logarithmic height of the filament bend *(Ln(L))*. Later on, the lowest value of *L* is extracted and examined. For the optimal desirability, the proposed technical solution is given in Table 4b. It clearly displays tool angles as stated in literature, i.e., a negative γ and a maximum κr. However, *Vc* remains high and such condition can affect drastically the obtained filaments since they are not massive and bulky like machined parts capable of evacuating most generated heat.

Table 4a. Parameters for optimized solution without constraints

Response	Goal	Lower	Target	Upper	Weight	Importance
Ln (L)	Minimum	-	-0.693	2.015	1	1
Ra	Target	0.140	0.240	0.970	1	1
Rt	Target	0.410	0.590	1.550	1	1
T	Target	28.5	34.0	39.6	1	1

Table 4b. Optimized solution with constraints for *T*, *Ra*, *Rt* and *Ln(L)*

γ	κr	*Vc*	*f*	*ap*	*Ln(L)*	*Ra*	*Rt*	*T*	Composite Desirability
-4.497	90	550.014	0.438	3.831	-0.693	0.240	0.590	34.0	1.000

It should be noted that the corresponding value for parameter *L* is 0.5 mm. Alternatively, the corresponding calculated responses optimization for output parameters are summarized in Fig. 10.

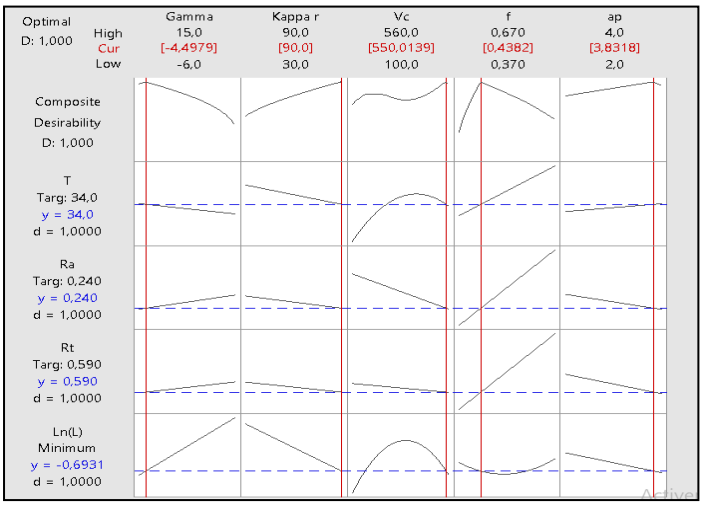

Fig. 10. Recapitulation of response optimization without constraints

Likewise, Tables 5a and 5b illustrate the results of RSM optimization with constraints and Fig. 11 gives the corresponding response optimization for the output parameters. From preliminary tests, temperature variations can be under control using optimized feed rate and cutting speed. The remaining difficulties concern especially *L* and to some extend *Ra*. For these reasons, importance and weight indices are maximized for both *Ln(L)* and *Ra* as shown in Table 5a. *Ln(L)* and *Ra* are set respectively at 6 and 5 times the weights (and importance) of *T* or *Rt* in order to reduced filament curvature and approach a more or less a rectilinear shape.

Table 5a. Parameters for optimized solution with constraints

Response	Goal	Lower	Target	Upper	Weight	Importance
Ln (L)	Minimum	-	-0.693	2.015	6	6
Ra	Target	0.140	0.460	0.970	5	5
Rt	Target	0.410	0.820	1.550	1	1
T	Target	28.5	33.0	39.6	1	1

Table 5b. Optimized solution with constraints for *T*, *Ra*, *Rt* and *Ln(L)*.

γ	*κr*	*Vc*	*f*	*ap*	*Ln(L)*	*Ra*	*Rt*	*T*	Composite Desirability
-6	90	160.225	0.515	4	-1.227	0.460	0.821	32.98	0.9995

In the machining guidelines of polymers, it is usually recommended that cutting edges should have generous relief angles (i.e., important cutting-edge angles) associated to negative back rake angle in order to keep at a minimum any eventual rubbing and/or abrasion action. These recommendations contribute to ameliorate surface roughness during machining. In the present case, both *κr* (≤90°) and *γ* (-6°) are in adequate intervals

for the machining of HDPE. Another important conclusion deals with the relatively reduced cutting speed (160 m/min) which is acceptable as an equilibrated level between *T* and *Ra* requirements. The corresponding obtained actual value of *L* is 0.293 mm which largely sufficient when testing in traction soft and bendable filaments.

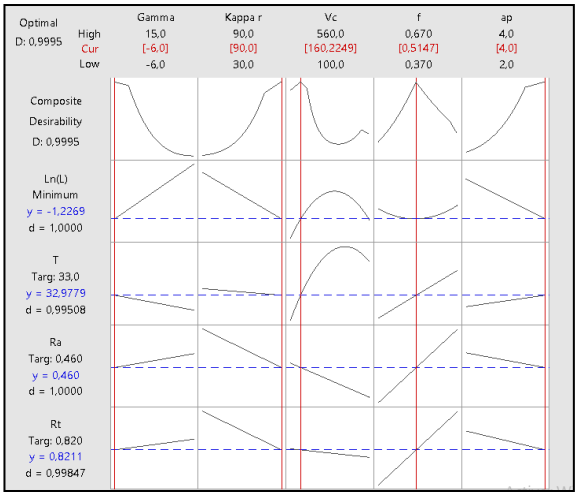

Fig. 11. Recapitulation of response optimization with constraints

The other important parameter is temperature which is well below the 40°C upper limit. The value of *ap* is intentionally kept high enough as it will serve as a built-in geometric dimension of the filament during testing. It should be noted that the corresponding value for parameter *L* is 0.293 mm.

4.6. Analysis of Predicted Results

The analysis of predicted results is a necessary step in order to decide on the optimization validity. Figs. 12 (a-d) summarize the variances between experimental and modeled responses for *T*, *Ra*, *Rt* and *Ln(L)* respectively. It is found that quadratic models can basically characterize the machining system under these experimental conditions.

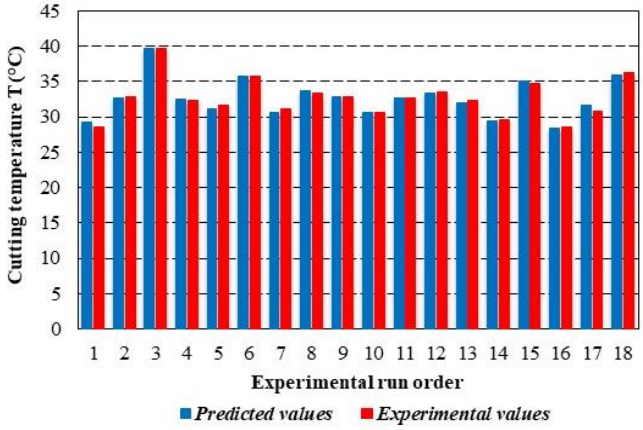

(a)

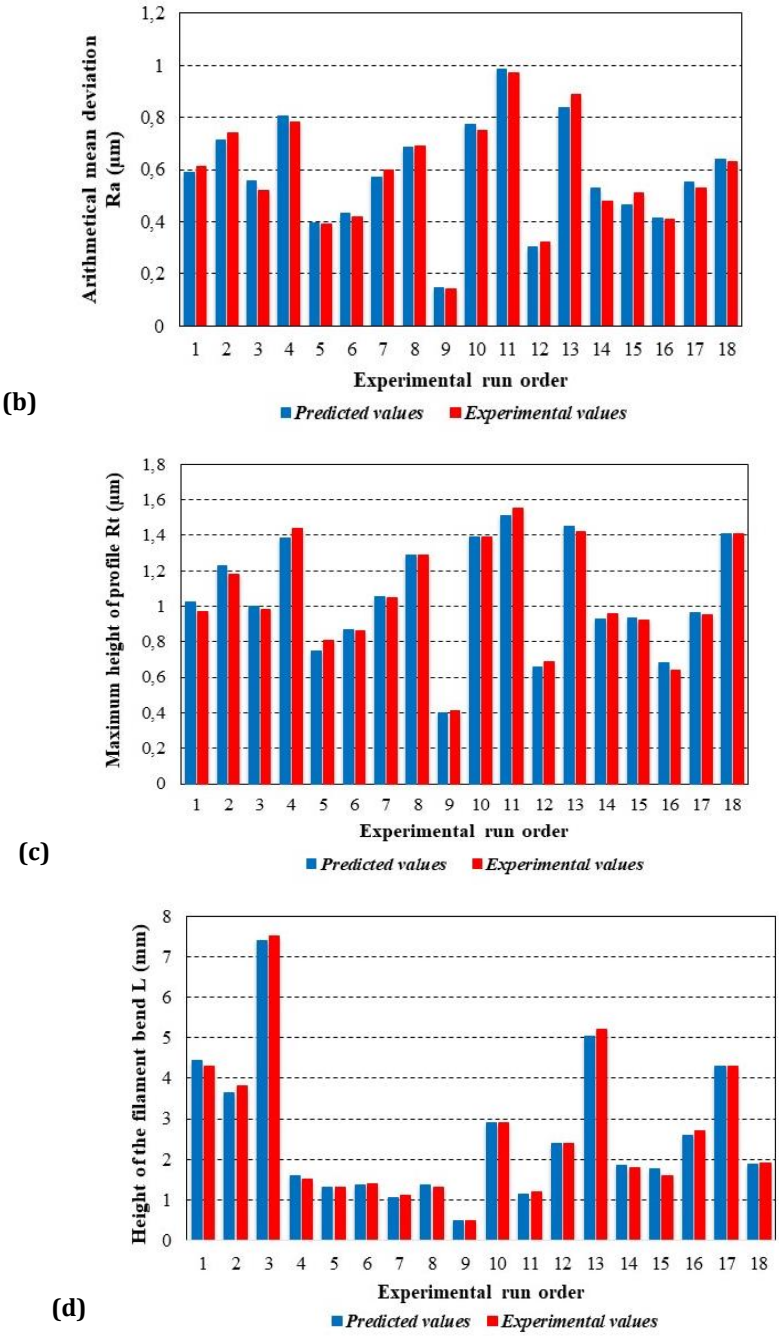

Fig. 12. Experimental and predicted data for: (a) *T*, (b) *Ra*, (c) *Rt* and (d) *L*

For semi-crystalline materials that exhibit both viscous and elastic characteristics when undergoing machining operations, both composite desirability and quadratic models can be employed for multi-objective optimizations. It is noted that HDPE is a thermoplastic with very low glass transition and melting temperatures. Literature indicates that viscous properties of HDPE play a considerable effect on the machined surface quality as viscous

deformation is critically relying on both strain rate and cutting temperature [6,31]. In other words, disproportionate viscous–plastic scaling or tearing, at a high *Vc*, can be drastically limited by evacuating the heat generated by friction. The effects of rake angle (γ), feed rate (f) and some molecular properties are also discussed for others polymers [25-28,31,32].

5. Conclusion

This work is intended to ameliorate previous studies dedicated to the optimization of machining conditions of HDPE pipes to manufacture mechanical testing specimens [13,14]. Both studies [13] and [14] were undertaken respectively in 2012 and 2017, using a conventional Tagushi approach, together with ANOVA and desirability analyses for HDPE-80 and HDPE-100. However; in this study, the number of input and output parameters is extended to cover respectively cutting tool geometry and ultimate shape of the machined filament (chip). The main conclusions are:

- Besides usual cutting parameters regime (*Vc*, *f* and *ap*), the effects of both rake (γ) and cutting-edge (κr) angles are considered as supplementary input parameters. Conversely, for output parameters, a new information representing the height of bends (L) is recorded to appraise the machined filament curvature along with cutting temperature and roughness criteria.
- It is found that *f* and *Vc* are strongly affecting temperature (T) and surface roughness criteria (*Ra*, *Rt*). When considering the total variation of *Ra* and *Rt*, the effects of *f* explained respectively 51.92% and 63.67% of the contributions. The limited effects of *Vc* revealed only 29.45% and 15.89% respectively for *Ra* and *Rt*.
- Alternatively, for cutting temperature, *Vc* effects come is in the first position followed by those of feed rate with respectively 56.70% and 30.47% contributions of the total variation. Graphically, it is deduced that as *Vc* and *f* increase, T increases as expected. For polymeric semicrystalline materials, it is accepted that *Vc* remains the most important input parameter and the temperature rise is caused particularly in the second shear zone where friction dominates. Similarly, when *f* increases, the filament section and the deformed material volume increase and hence the temperature increases, particularly in the first shear zone by deformation. The maximum value of the cutting temperature is reached within the 350 to 550 m/min cutting speed range.
- Concerning the newly introduced parameter, i.e.; height of the filament bends (L), it is shown that the main effects of process factors are all significant but at different degrees. The most significant one remains the cutting-edge angle (κr), which explains 18.99% contributions of the total variation, followed by the depth of cut (ap) with 6.56 %. Also, it is found the height of the filament bends (L) decreases considerably with the increase of the cutting-edge angle (κr). It is explained that as the cutting-edge angle (κr) increases, the amount of heat evacuated by the out-going chip is lessened and the spiral-shape filament is likely to form.
- The RSM models allowed to predict the performance characteristics for any combination of factor levels for the adopted ranges. The Anderson-Darling test for normality indicates that predicted responses for *T*, *Ra*, *Rt* and *Ln(L)* follow normal laws.
- The validation experiments demonstrate that the obtained mathematical models allowed to correctly predict cutting temperature, surface roughness criteria and filament height bend values within a 95% confidence interval. Very satisfactory determination coefficients (>98%) are noted.
- The best optimized solution is obtained with imposing high constraints on output parameters (L and *Ra*). It is revealed that *Vc*=160 m/min (as a main input) and a

filament bend height L=0.293mm (as a main output) are reasonable and most practical conditions for a regular and uniform filament. In addition, the proposed solution is favored with a generous cutting-edge angle (κr) combined with a negative back rake angle (γ) which helps keeping at a minimum both rubbing and abrasion actions.

- Finally, the multi-objective optimization approach based on the composite desirability technique and quadratic RSM models is shown to be an adequate method to control performance characteristics when machining tough HDPE pipe materials.

Acknowledgements

This study is a part of the work program defined for the PRFU Research Project "*Mechanical behavior and remaining life of HDPE pipes subjected to operating and environmental conditions*"; Code A11N01UN230120190008; LR3MI, UBM Annaba, Algeria. This project is supported by DGRSDT-MESRS (Algerian Ministry of Higher Education and Scientific Research).

Nomenclature

AD:	Anderson-Darling normality test.
ap:	Depth of cut (mm)
D:	Desirability
DL:	Degrees of freedom
f:	Feed rate (mm/rev)
F:	Fisher test
L:	Filament height bend (or curvature) (mm).
P:	Error value compared at 5.
P-value:	Probability value
R^2:	Determination Coefficient
Ra:	Arithmetic mean roughness (µm)
Rt:	Total roughness (µm)
RSM:	Response Surface Methodology
SDR:	Pipe diameter to thickness ratio
T:	Temperature (°C)
Vc:	Cutting speed (mm/min)

Greek Letters:

α :	Clearance angle (°);
γ:	Rake angle (°)
κr:	Cutting-edge (or steering) angle (°)
λ:	Cutting edge inclination angle (°).

References

[1] Nguyen QK, Mwiseneza C, Mohamed K, Cousin P, Robert M, Benmokrane B. Long-term testing methods for HDPE pipe - advantages and disadvantages: A review. Eng. Fract. Mech., 2021; 246: 107629. https://doi.org/10.1016/j.engfracmech.2021.107629

[2] Jagtap UT, Mandave AH. Machining of Plastics: A Review. Int. J. Eng. Res. & Gen. Sci., 2015; 3(2): 577-581. www.ijergs.org

[3] Berneck J. Plastics instead of metals. Kunststoffe International, 2012; 9: 57-59. www.kunststoffe-international.com

[4] Handbook of *Polymer Testing: Short-Term Mechanical Tests. The Rubber and Plastics Specialists*, Editor: Brown R., Rapra Technology Limited, UK, 2002. http://www.rapra.net

[5] Alludin M, Choudhury IA, El Badarie MA, Hashmi MSJ. Plastics and their machining: A review, J. Mater. Proc. Technol, 1995; 54(1-4): 40-46. https://doi.org/10.1016/0924-0136(95)01917-0
[6] Kaiser MS, Fazlullah F, Ahmed SR. A comparative study of characterization of machined surfaces of some commercial polymeric materials under varying machining parameters. J. Mech. Eng., Automation & Control Syst, 2020; 1(2): 75-88. https://doi.org/10.21595/jmeacs.2020.21643
[7] Carr WJ, Feger C. Ultraprecision machining of polymers. 1993; 15, 4: 221-237. https://doi.org/10.1016/0141-6359(93)90105-J
[8] Salles JLC, Gonçalves MTT. Effects of machining parameters on surface quality of the ultra-high molecular weight polyethylene (UHMWPE). Materia, 2002; 8 (1): 1-10. http://www.materia.coppe.ufrj.br/sarra/artigos/artigo10119/10119.pdf
[9] Tamrin KF, Nukman Y, Choudhury IA, Shirley S. Multiple-objective optimization in precision laser cutting of different thermoplastics. Optics and Lasers in Engineering, 2015; (67): 57-65. https://doi.org/10.1016/j.optlaseng.2014.11.001
[10] Davim JP, Silva LR, Festas A, Abrão AM. Machinability study on precision turning of PA66 polyamide with and without glass fiber reinforcing. Materials and Design, 2009; 30(2): 228-234. https://doi.org/10.1016/j.matdes.2008.05.003
[11] Chabbi A, Yallese MA, Nouioua M, Meddour I, Mabrouki T, Girardin F. Modeling and optimization of turning process parameters during the cutting of polymer (POM C) based on RSM, ANN, and DF methods, Int. J. Adv. Manuf. Technol, 2017; 91: 2267–2290. https://doi.org/10.1007/s00170-016-9858-8
[12] Azzi A, Boulanouar L, Laouisi A. Modeling and optimization of machining parameters to minimize surface roughness and maximize productivity when turning polytetrafluoroethylene (PTFE). Int. J. Adv. Manuf. Technol. 2022; 123: 407–430. https://doi.org/10.1007/s00170-022-10160-z
[13] Kaddeche M, Chaoui K, Yallese MA. Cutting parameters effects on the machining of two high density polyethylene pipes resins, Mechanics & Industry, 2012; 13(5): 307-316. https://doi.org/10.1051/meca/2012029
[14] Hamlaoui N, Azzouz S, Chaoui K, Azari, Yallese MA. Machining of tough polyethylene pipe material: surface roughness and cutting temperature optimization. Int. J. Adv. Manuf. Technol. 2017; 92, 5(8): 2231-2245. https://doi.org/10.1007/s00170-017-0275-4
[15] Niglia J, Cisilino A, Seltzer R, Frontini P. Determination of impact fracture toughness of polyethylene using arc-shaped specimens. 2002; 69 (12):1391-1399 https://doi.org/10.1016/S0013-7944(02)00008-5
[16] Broughton WR, Maxwell AS. Ageing of polymeric materials, A National Measurement Good Practice Guide. 2007:103. https://eprintspublications.npl.uk/3866/1/mgpg103.pdf
[17] Kiass N, Khelif R, Bounamous B, Amirat A, Chaoui K. Experimental study of mechanical and morphologic al properties in HDPE-80 gas pipe. Mechanics & Industry, 2006; 7: 423-432. https://doi.org/10.1051/meca:2006056
[18] Bouacha K, Yallese MA, Mabrouki T, Rigal JF. Statistical analysis of surface roughness and cutting forces using response surface methodology in hard turning of AISI 52100 bearing steel with CBN tool. Int. J. Refract. Met. & Hard Mater. 2010; 28(3): 349–361. https://doi.org/10.1016/j.ijrmhm.2009.11.011
[19] Davoodi B, Eskandari B. Tool wear mechanisms and multi-response optimization of tool life and volume of material removed in turning of N-155 iron-nickel-base superalloy using RSM. Measurement. 2015; 68: 286-294. https://doi.org/10.1016/j.measurement.2015.03.006
[20] Gutema EM, Gopal M, Lemu HG. Temperature Optimization by Using Response Surface Methodology and Desirability Analysis of Aluminum 6061. Materials. 2022; 15(17): 5892. https://doi.org/10.3390/ma15175892

[21] Parida AK, Routara BC, Bhuyan RK. Surface roughness model and parametric optimization in machining of GFRP composite: Taguchi and Response surface methodology approach. Materials Today: Proceedings. 2015; 2(4-5): 3065–3074. https://doi.org/10.1016/j.matpr.2015.07.247
[22] Subramanian AVM, Nachimuthu MDG, Cinnasamy V. Assessment of cutting force and surface roughness in LM6/SiC_p using response surface methodology. J. Appl. Res. & Technol. 2017; 15(3): 283–296. https://doi.org/10.1016/j.jart.2017.01.013
[23] Chabbi A, Yallese MA, Meddour I, Nouioua M, Mabrouki T, Girardin F. Predictive modeling and multi-response optimization of technological parameters in turning of Polyoxymethylene polymer (POM C) using RSM and desirability function. Measurement, 2017; 95: 99-115. https://doi.org/10.1016/j.measurement.2016.09.043
[24] Derringer G, Suich R. Simultaneous optimization of several response variables. J. Qual. Technol. 1980; 12(4): 214-219. https://doi.org/10.1080/00224065.1980.11980968
[25] Khuri AI. Mukhopadhyay S. Response surface methodology. WIREs Computational Statistics, 2010; 2(2): 128-149. https://doi.org/10.1002/wics.73
[26] Yan Y, Mao Y, Li B, Zhou P. Machinability of thermoplastic polymers: PEEK, PI, and PMMA. Polymers (Basel), 2020; 13 (1): 69-83. https://doi.org/10.3390/polym13010069
[27] Reichenbach IG, Bohley M, Sousa Fabio FJP, Aurich Jan C. Micromachining of PMMA—manufacturing of burr-free structures with single-edge ultra-small micro end mills Int. J. Adv. Manuf. Technol., 2018; 96:3665–3677. https://doi.org/10.1007/s00170-018-1821-4
[28] Giasin K, Ayvar-Soberanis S. An Investigation of Burrs, Chip formation, Hole Size, Circularity and Delamination during Drilling Operation of GLARE using ANOVA, Composite Structures, 2016; 159:745-760. http://dx.doi.org/10.1016/j.compstruct.2016.10.015
[29] Mitsubishi Chemical Group. Guide To Machining Plastic Parts, Metric System. Machinist's Toolkit. (Consulted on 6 Sept. 2023) https://www.mcam.com/mam/41701/MCG-Machinist-Toolkit-A4-EU-metric.pdf
[30] Curbell Plastics, Inc. Plastic Turning Machining Guidelines. (Consulted on 6 Sept. 2023) https://www.curbellplastics.com/services-capabilities/fabrication-machined-parts/plastic-machining-guidelines/plastic-turning-machining-guidelines/
[31] Xiao KQ, Zhang LC. The role of viscous deformation in the machining of polymers. Int. J. Mech. Sci, 2002; 44 (11): 2317-2336. https://doi.org/10.1016/S0020-7403(02)00178-9
[32] Alateyah AI, El-Taybany Y, El-Sanabary S, El-Garaihy WH, Kouta H. Experimental Investigation and Optimization of Turning Polymers Using RSM, GA, Hybrid FFD–GA, and MOGA Methods. Polymers, 2022; 14 (17): 3585-3610. https://doi.org/10.3390/ polym14173585
[33] Yap BW, Sim CH. Comparisons of various types of normality tests. J. Statistical Computation and Simulation, 2011; 81(12): 2141-2155 http://dx.doi.org/10.1080/00949655.2010.520163

Research on Engineering Structures & Materials
www.jresm.org

Research Article

Corrosion behavior of fiber laser welded Ti-6Al-4V alloy rods with different pH and temperature in 0.9 wt% NaCl medium

Arife Kübra Yontar [*1,3,a], Sinem Çevik [1,2,b]

[1]*Department Mechanical and Metal Technologies, Ondokuz Mayis University, Samsun, Turkey*
[2]*Department of Metallurgical and Materials Engineering, Ondokuz Mayıs University, Samsun, Turkey*
[3]*Department of Nanoscience and Nanotechnology, Ondokuz Mayis University, Samsun, Turkey*

Article Info

Article history:

Received 21 Aug 2023
Accepted 30 Oct 2023

Keywords:

Ti-6Al-4V alloys;
Fiber laser welding;
Corrosion resistance;
NaCl solution;
Weight changes

Abstract

The corrosion resistance of laser welded samples was carried out in a shaken incubator in body-simulated liquid environments and kept at pH3-5 and 25-50°C conditions for 24 hours. It was determined that acicular α' martensite structures were formed in the fusion regions and these structures increased the hardness of the alloy by 20% compared to the base metal. The welded samples had the highest tensile strength of 144 MPa. Weight changes after the corrosion test were calculated and the highest weight loss was found to be 0.0025 g for the sample with an initial weight of 4.1394 g. TiO_2 oxides and {1 0 0} and {1 1 1} chamber-shaped salt crystals were formed larger and more intensely in the fusion zones than the base metal. Dental metallic implant welding with fiber laser will have higher corrosion resistance in oral use with different temperature and pH environments compared to screw joints.

1. Introduction

Titanium and its alloys have become very popular in biomaterial production with their superior properties. Ti-6Al-4V alloy has been a very common titanium alloy as an implant material [1–6]. The high preference for Ti-6Al-4V alloy as a biomaterial is due to high corrosion and abrasion resistance, low density, biocompatibility, high tensile strength and hardness properties. Its high corrosion resistance and biocompatibility are thanks to the thin oxide (TiO_2) layer formed on the outer surface of the metal due to titanium contact with oxygen [7–13]. These TiO_2, and TiO_3 layers formed on the surface may lose their properties by being affected by some environmental factors. The most important of these factors are temperature, pH and concentrations of fluoride, sodium and chlorine in the environment. Cl- or Na- ions can penetrate the surface and form an unstable layer, making re-passivation more difficult [14]. In addition, the difference that occurs between the titanium phases also makes a difference in the homogeneity of the oxide layer growth. Titanium and its alloys can corrode due to physical (stress, abrasion, forces, etc.) and chemical (acidic food and beverages, toothpaste, etc.) variable effects during their use in the body environment. Apart from these, heat treatments and applications also affect the corrosion properties of the metal because of the microstructure changes [15–20]. For this reason, it is critical for engineering and health applications to examine the effects of temperature and pH external factors on the welded parts of the Ti-6Al-4V alloys. It is desired that the metallic biomaterials to be used in the body or mouth be biocompatible and should not be corroded. As a result, titanium alloys with good corrosion resistance and

*Corresponding author: kubra.demirbas@omu.edu.tr
[a] orcid.org/0000-0003-1486-9332; [b] orcid.org/0000-0002-3506-7892
DOI: http://dx.doi.org/10.17515/resm2023.39ma0821rs

biocompatibility are used to make implants. Titanium and its alloys are generally used in acidic environments, especially in the mouth, drinking water and pool pipes, industrial coating boilers, etc. They can corrode in environments containing chloride ions. In such environments with high chloride ion concentrations, corrosion attacks occur more and cause alloy corrosion. Although the Ti-6Al-4V alloy is normally corrosion resistant, it can erode fast in hostile situations that dissolve the protective oxide layer. Titanium, on the other hand, can only be protected against corrosion assaults if a stable and continuous surface layer is formed on the Ti-6Al-4V alloy [21, 22]. Various surface treatments are carried out to increase the osseointegration properties and corrosion resistance of the implants. These methods include coating, laser surface roughening, electrochemical treatment, and thermal spraying.

Titanium alloys have a highly reactive chemical structure and their high melting points make it difficult to weld them. When the temperature exceeds 400 °C during welding, various gases such as oxygen, hydrogen and nitrogen can be easily absorbed on the surface, causing metallurgical defects to appear in the welding region. The ductility of titanium alloys decreases as they absorb intermediate elements such as oxygen, nitrogen and hydrogen onto their surfaces. Moreover, oxygen and nitrogen are powerful stabilizers in Ti-6Al-4V alloys and promote martensitic' development, resulting in brittle damage in the weld zone or surface. The creation of an oxygen-enriched outer layer known as the -case as a result of oxygen diffusion is difficult to manage. In order to weld titanium alloys, several fusion welding processes such as gas tungsten arc welding, gas metal arc welding, plasma arc welding, electron beam welding, and laser beam welding are employed [23–26]. However, the most effective joining method known is the fiber laser welding method. Fiber laser welding is a joining method that increases the production of metal materials. Although the fiber laser welding method increases the mechanical strength of metals, it can reduce their corrosion resistance. The fiber laser welding method creates a narrow welding seam due to its low energy density and adjustable heat input properties. For this reason, errors such as thermal stresses and micro-cracks in the welding zone and the heat-affected zone occur at very low rates [27–30]. Since the welding speed is faster than other welding methods in laser welding applications, the heat input occurring in the metal during the welding process is lower. Low heat input increases the cooling rate in the fusion zone, which causes the microstructure formed in the fusion zone to differ from the microstructure of the base metal. Changes in the microstructure of the metal after welding cause the behavior of the metal to change against corrosive effects [31–35]. Although Ti-6Al-4V can be successfully welded by the fiber laser method, a decrease in corrosion resistance may occur due to the following reasons; large dislocations, Fe element migration near grain boundaries and grains becoming coarser, β phase separation, increase in the number of anion vacancies, alpha exponent(α/) in the fusion region [36]. Ti-6Al-4V alloy corrosion resistance and high-temperature application are primarily determined by its microstructure, phase distribution, and finishing heat treatment parameters. There are three types of phase-dependent microstructures: (1) natural grainy layered structure (where α + β → β transformation occurs) that occurs after a gradual cooling or heat treatment above the β-trans temperature, i.e. Tβ; (2) fine coaxial (spherical) structure formed following deformation in the binary phase of the α + β field (below Tβ) where the α-phase is propagates in the β-matrix, and (3) bimodal microstructure comprised of primary α- in β grains phase and thin-layered α + β colonies [37].

Various corrosion tests have already been carried out on implant materials and titanium alloys in the literature, using methods such as open circuit potential (OCP), potentiodynamic and potentiostatic tests, and electrochemical impedance spectroscopy (EIS) [38–40]. Again, in these studies, corrosion behavior was investigated by using 0.9 wt wt% NaCl, Kroll or Hank solutions [41–44]. However, there are currently no studies carried

out by creating a naturally corrosive environment after fiber laser welding of Ti-6Al-4V (Gr5) alloys in rod form. The corrosion properties of implants that are used in the mouth and that have been treated with fiber laser welding are very important. The changes in the surface of the source area of the acidic environments they are exposed to during eating and drinking are a situation that needs to be examined. For this reason, the joint ability of this Gr 5 alloy by fiber laser welding method and the corrosion properties of the fusion zones was investigated. In addition to the heat treatment that the metal alloy is exposed to due to the welding process, the pH values and temperature of the solution environment to which the alloy is exposed also affect the corrosion behavior. [45–49]. It is known that metals exposed to acidic environments and high temperatures have an increased tendency to corrode [50–54]. The fiber laser welded Ti-6Al-4V alloy rods corrosion characteristics have been interpreted by examining 0.9 wt% NaCl solution at pH3 and 5 values and at 25 and 50 ˚C temperatures. Base metal, heat-affected zone and fusion zone microstructures and weight changes after the corrosion test of welded alloys were studied. This study sheds light on the development of fiber laser welding applications of Ti-6Al-4V alloy and reveals the corrosion behavior after welding.

2. Experimental Procedures

Ti-6AI-4V (grade 5) rods with a diameter of 5 mm were used in fiber laser welding applications. The chemical compound of Ti-6Al-4V samples specified in the technical data sheets (TDS) is given in Table 1. Fiber laser welding of the samples was carried out using 300 W LWI V Mobile Flexx II machine using the parameters shown in Table 2 and carried out by a welder in an industrial company. Before the corrosion test, tensile test and Vickers hardness tests were carried out to observe the effect of fiber laser welding on the mechanical properties of the titanium alloy. All samples were used according to ASTM E8M-89b standards to determine the tensile properties. A parallel gauge tensile specimen having a 5 mm diameter and a 25 mm gauge length was prepared with the weld joint at the center of the gauge length. The tensile test performed using universal testing equipment (Model 5982, Instron (100 kN), a screw-driven machine operating at room temperature at a crosshead speed of 2 mm min^{-1}, with a starting strain rate of 0.55×10^{-3} s^{-1}.

Table 1. Chemical composition of Ti-6Al-4V

Element	Weight (%)
Ti	Remaining main part
AI	5.5-6.5
V	3.5-4.5
Fe	0.25
C	0.08
N	0.05
H	0.012
O	0.13

Vickers hardness test was carried out in a TMTECK Micro-hardness tester HV- 1000B using 0.49 kg load (HV0.5) and a dwell time of 15 s. Hardness values were obtained with a total of 9 indentations that recessed at 0.5 mm intervals along the entire specimen surface from the outer surface of the rod specimens as the fusion zone (FZ), towards the center of the specimen the heat affected zone (HAZ), and the base metal zone (BM). After the tensile test, the corrosion test was performed on the cracked surfaces in the welded area. The microstructural and chemical characterization of fractured surfaces after the test was examined with an 80mm^2 X-MAX detector on a JEOL 7001F Field Emission (FE) Scanning Electron Microscope with an EDS attachment. Energy dispersive spectroscopy (EDS) was

used to do a semi-quantitative chemical examination on materials. The process flow chart and schematic representation of laser welding application and corrosion testing are shown in Fig. 1 and 2. In total, 3 groups of samples were prepared and these are the unwelded reference sample and the welded A and B samples, respectively.

Table 2. Fiber laser welding parameters

Parameters	A sample	B sample
Laser Power	73 V	67.5 V
Impact Energy	25.4 J	11.9J
Beam Diameter	900µ	900µ
Pulse Frequency	10 Hz	20Hz
Laser Pulse Width	8.5ms	4.8m

After the fiber laser welding application, the samples were prepared using the metallography method for the microstructural investigations of the welded zones. The preparation process first started by cutting the welded bar samples into small pieces by cutting them in half vertically from the welding areas. The cut sample parts were first molded with the cold bakelite molding method. The molded samples were sanded with abrasives of 180, 320, 600, 800 and 1200, respectively, and then polished with a 1-micron diamond suspension to remove scratches from cutting and sanding and to create a surface that is flawless. After the polishing process, the surfaces were etched and made ready for microscopic examinations. The samples were etched with Kroll's reagent (85 mL H_2O + 10 mL HNO_3 + 5 mL HF) in ASTM E407 solution by keeping them in a magnetic stirrer at 65˚C for 3 minutes. Since Gr 5 Titanium alloys are used as implants in dentistry, the corrosion test environment was prepared based on the changing pH and temperature parameters in the oral environment caused by eating and drinking. It is a well-known phenomenon that acidic and hot beverages corrode tooth enamel and metallic implants than cold ones [55–58]. In addition to temperature and pH changes, it is necessary to examine the effects of internal body environments on these alloys, which are exposed to high heat input due to the welding process.

Previous studies have reported that osteoblasts can be severely damaged by a thermal impulse of 42 ˚C. It has been determined that intraoral temperatures reach 67-77 ˚C during use and hot water/liquid consumption. However, the maximum temperature that living tissue can withstand has been determined as 50 ˚C. In line with similar studies and information, the temperatures chosen to simulate both hot and cool oral environments were 25 and 50 ˚C [59, 60]. To simulate acidic beverage environments, 0.9 wt% NaCl solutions at pH 3 and 5 were prepared using lemon juice.

Table 3. Corrosion test parameters and sample names

Parameters	Samples
pH3 and 25°C	R1, A1 and B1
pH5 and 25°C	R2, A2 and B2
pH3 and 50°	R3, A3 and B3
pH5 and 50°C	R4, A4 and B4

In this way, both more natural ingredients and the most realistic eating and drinking exposure environment were created. The corrosion test was carried out by keeping each sample placed in 50 mL 0.9 wt% NaCl serum at pH3 and 5 and temperatures and 25 and 50 °C in a shaking incubator for 24 hours with stirring. Names and groups of reference and welded samples prepared for corrosion tests are given in Table 3. R samples are control

samples without fiber laser weld jointing. A1, B1, A2, B2, A3, B4, A4 and B4 samples were obtained after the tensile tests of A and B samples welded with the parameters in Table 2. 4 samples were prepared for corrosion testing for both samples A and B.

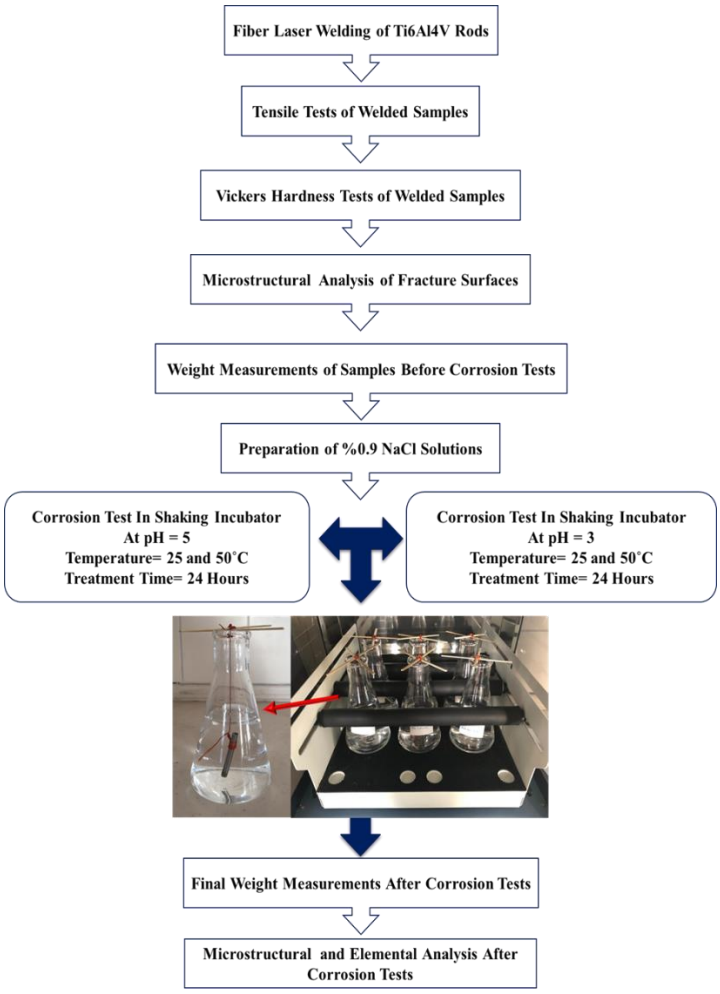

Fig. 1. Process flow chart of the study (İmage shows the samples in NaCl solution and shaking incubator assembly)

The first weights were measured before the samples were placed in the solution. The 0.9 wt% NaCl solution was prepared at pH 3 and 5 and all samples were placed by suspending in the erlenmeyer and shaking incubator as shown in Fig.1. All samples placed in the solution were kept in the shaking incubator according to pH groups for 24 hours at 25° C and 50° C, respectively. After the samples were kept in a shaking incubator for 24 hours, they were removed from erlenmeyer and dried at 27° C in the oven. Finally, after the corrosion test, the final weights of the samples were measured and the test was terminated.

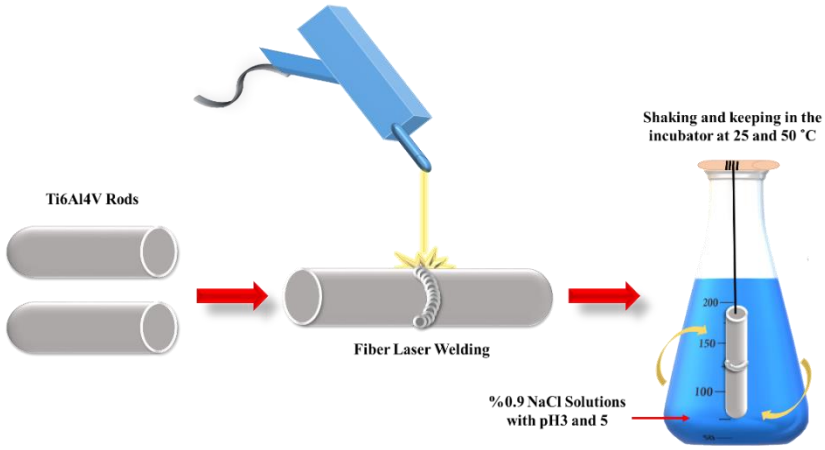

Fig. 2. Schematic representation of laser welding application and corrosion testing

3. Results and Discussion

3.1. Tensile Tests and Vickers Hardness

The images of the samples subjected to the tensile test before and after the test are given in Fig. 3. Since titanium is a highly ductile and durable metal, the non-welded R sample showed a ductile fracture behavior as expected. The fracture surface of the R sample used as a control has a conical structure as shown in Fig. 3. It was observed that the tensile strength of the R sample (957 MPa) matched the values given in the literature [61, 62]. After the tensile test, the A and B specimens were brittlely fractured from their welded parts to be parallel and straight to the rod specimen sections. The heat input used in the welding process of the A sample, which is two times more than that of the B sample, caused the weld depth of the A sample to be greater and the weld seems to be wider. Since the metal has a faster melting and cooling time with high heat input, the weld seam narrows as the heat input increases. While the weld seam thickness of sample A was 9 mm, sample B was 6mm. Insufficient weld depths of the A and B samples caused the joint strength and tensile strength to decrease 9 times compared to the R sample. In addition, the brittle structure resulting from martensitic transformations in the weld area also reduced the tensile strength of the joint areas. This decrease in the tensile strength of the welded parts is an expected situation. Studies [63–65] have shown that this decrease and rupture occurs with a brittle fracture behavior.

As shown in Fig.3, the edges of the outer surfaces of the rods are fusion zones (completely melted) and as it moves inwards from the surface area of the metal, first the HAZ is reached and then the base metal. Fig. 4(b) shows the microhardness distributions in the cross-section of the fusion zone, HAZ and BM zones of the samples. Fig.4(c-d) SEM images show that martensitic α' (dendritic) formations occur in the fusion region. This phase, which is caused by high heat input and rapid cooling in the FZ, increased the hardness of the FZs for A and B samples by 4-23% and 16-31%, respectively, compared to the BM. Higher welding speeds, or less heating input, cause the coarser α′ martensite microstructure to develop within the finer β grains, which increases the hardness values of the B sample in the welding alloy [66]. While the highest hardness value of the fusion zone for sample A was 438 HV0.5, it was calculated as 501 HV0.5 for sample B. The hardness values of the BM were measured as 338 and 341 HV0.5. These values can be considered as standard for Ti-6Al-4V alloy. Omoniyi et al. [62] joined Ti-6Al-4V sheets with 2.6-2.8 kW power values

using laser welding. Vickers hardness measurements showed that the BM was 343 ± 12 HV0.5 and the weld zones were 426 ± 17 HV0.5. Chen et al. [61] showed the BM hardness values of the titanium sheets joined by laser welding using a power of 2.2 kW in the range of 280-300 HV0.5, and the values of the FZ as 372 HV0.5.

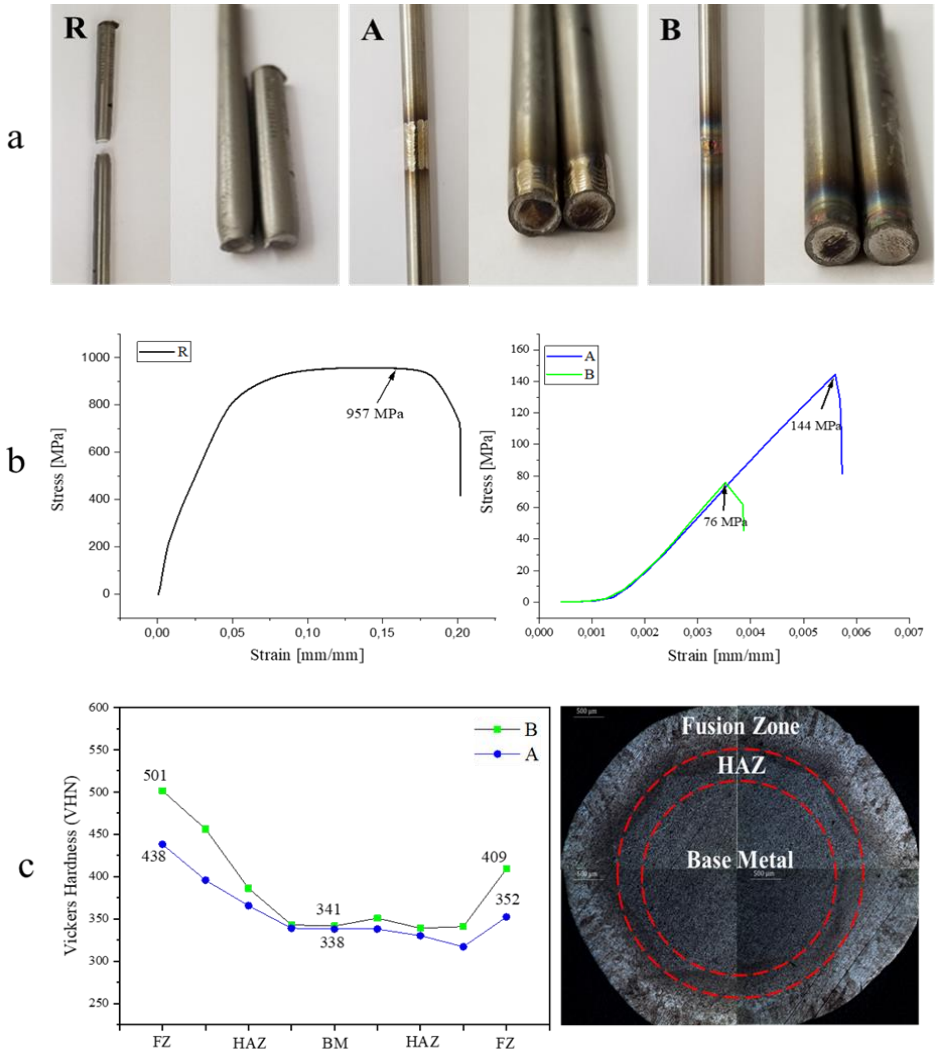

Fig. 3. (a) Non-welded R and fiber laser welded A and B sample images before and after tensile tests, (b) Tensile test result graphs and (c) Vickers Hardness test result graph of reference and fiber laser welded A and B specimens

When the test results are considered, the tensile strengths are decreased and Vickers hardness are increased due to the increase of the laser beam impact energy. This is because, it can be shown that the microstructure of the weld zones of samples as can be seen from Fig.5(c-d), together with the high temperature and rapid cooling used during the welding process, makes the metal structure brittle and hard due to the presence of α'-martensite [67, 68, 68].

3.2. Weight Changes with Temperature and pH

Acicular α′ martensites in the columnar β grains formed in the fusion regions of samples A and B, which were exposed to high heat input during welding, changed the microstructure. As a result of this change, the changes in the fracture fusion surfaces that occurred after the tensile test were observed in the saltwater environment. In this way, the effect of the welding process on the corrosion behavior of the titanium alloy was investigated. Fig.4 shows the weight changes of the reference sample and the welded samples after the corrosion test comparatively. Weight changes at each pH and temperature values are shown in separate graphs. The results show that the weight changes of the fiber laser welded samples differ from each other in varying temperature and pH environments.

As can be clearly seen from Fig.5, the fusion zones of the Ti-6Al-4V alloy had a two-phase α/ and α microstructure. The alloy's tendency to corrosion changed due to this microstructural alteration during laser welding. In the post-weld cooling process, the previous β phase shifts into a stable α phase. The α phase nucleates homogeneously in the previous β phase columnar grains and expands spontaneously up to the grain boundaries. The rates of α-phase nucleation are heavily dependent on the initial laser power temperature and the post-process cooling rates. It is established that the α plate's thickness diminishes with increasing cooling rate. The α phase degradation is an important factor in changing the corrosion properties of Ti-6Al-4V alloys. In addition, the homogeneous allocation of both α and β phases obtained from alloying elements in the structure also plays an important role in corrosion behavior [37]. As presented in Eq. (1), (2), (3), (4), the detailed mechanism of removing the passive layer occurs after immersion in NaCl solution with the formation of novel passive film as a result of the protons' decrease produced during the oxidation of titanium. This mechanism indicates the possible formation of a TiO_2 layer that may have formed on the surface of the samples. The mechanism introduces further metal disintegration and oxide production, with a completely decreased hydrogen state promoting the formation of hydrides in the solution interface layer [69].

$$Ti \rightarrow Ti3+ + 3e- \quad (1)$$

$$Ti + 2H2O \rightarrow TiO2 + 4H+ + 4e- \quad (2)$$

$$H+ + e- \rightarrow H \quad (3)$$

$$Ti3+ + H2O \rightarrow TiO2+ + 2H+ + e- \quad (4)$$

The dissolution of the passive oxide layer after processing the fiber laser welded fractured surfaces in aqueous NaCl solution has been characterized by use of EDS and weight loss analyses. Based on the elemental combination of the EDS results in Table 4, a high variation is seen in the samples' nominal substance after NaCl treatment. Some surface passive layers, such as oxides or carbides, may be the cause of the discrepancy. After 24h of treatment with an aqueous 0.9 wt. % NaCl solution, the highest weight loss observed was 0.0025 g for B4 sample. In the NaCl environment with high temperature and lower hydrogen density, the amount of dissolution on the metal surface increased. The low pH(3) environment caused metal dissolution on the surface of the R1 sample. Some of the dissolved Ti elements accumulated as TiO_2 as seen in Fig.6. It is observed that weight increase occurred in reference samples at 50˚C and pH 5 environments.

This increase is due to the thickening of the oxide layer on the surface with the decrease in the amount of hydrogen, and in addition, the dissolution of more metal and the formation of various oxides and carbides on the surface. Since titanium is a metal with low thermal conductivity, the cooling rate after laser welding is also significantly lower. As the cooling

rate decreases, the transformation rate from the β phase to the α martensite phase decreases and the grain size becomes thicker. It is known that as the phase and grain sizes increase, the corrosion resistance decreases [37]. For this reason, the weight losses on the laser-welded surfaces were discovered to be greater than the reference samples. Similarly, it has been determined that an increase in temperature to 50°C causes an increase in weight loss. The fact that the weight loss is less than that of the B4 sample may be the large size NaCl crystallization seen on the surface of the A3 sample in Fig. 6.

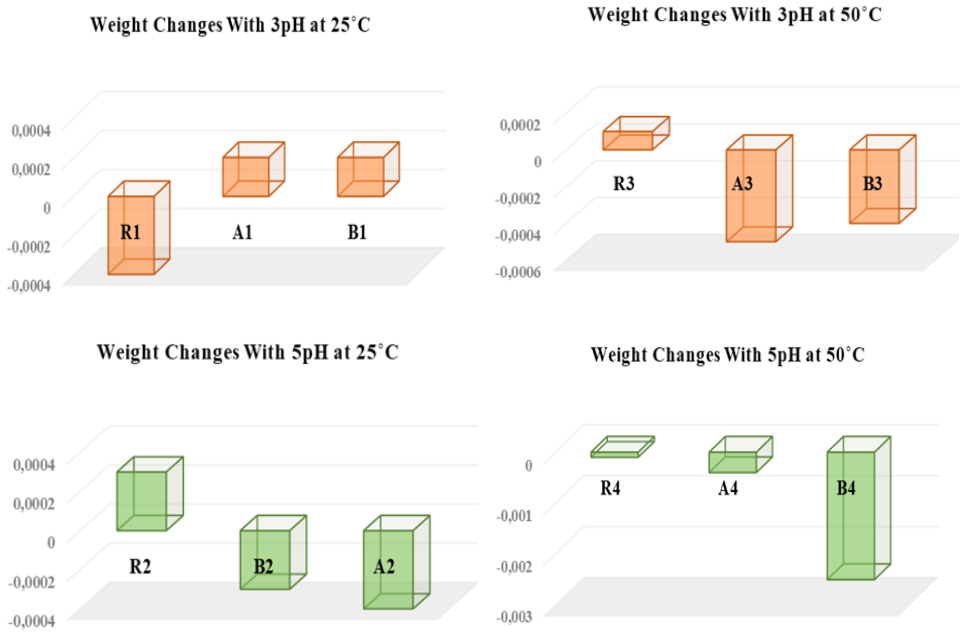

Fig. 4. Weight changes after corrosion tests at different pH and temperature conditions

Table 4. The highest weight differentiated samples EDS element compositions before and after NaCl treatment

Sample	Element	Atomic% Ti-6Al-4V		Weight Change
		Before NaCl Treatment	After NaCl Treatment	
R1	Ti	89,7	77,9	-0,0004
	Al	6	5,6	
	V	4	3,1	
	O	0	6,2	
B4	Ti	82,8	51,5	-0,0025
	Al	5,5	3	
	V	3,4	2,2	
	O	0	4,1	
A3	Ti	81,3	66	-0,0005
	Al	4,9	4,4	
	V	3	2,8	
	O	0	5,7	

It was also seen that the oxygen (O) ratios in Table 4 were in the order of R1>A3>B4 and the weight losses had the reverse order. The increase in the amount of oxygen on the surfaces indicates the amount of the oxide layer formed. Since the oxide layers act as a protector, the weight loss that occurs on the surfaces where the presence of oxide is higher is lower. It has been revealed that the durability to corrosion of the samples exposed to the fiber laser welding process after NaCl interaction decreases and this resistance decreases with the increase in temperature and the pH value of the environment.

3.3. Microstructural Analysis

Before the corrosion test, microstructural characterization of the FZ, HAZ and BM was performed from the metallographic prepared. The microstructure of the BM Ti-6Al-4V consists mainly of white coaxial intergranular β-phase and gray coaxial spherical α-phase, as shown in Fig.5(a) at low and high magnification of SEM image. The intergranular β-phase in the BM is scattered throughout the matrix of the spherical α-phase with various grain sizes. Kroll's reagent's strong oxidizing capability can etch the α phase, so It looks like darker in comparison to the β phase. Therefore, the β phase appears brighter in SEM images [70]. The fiber laser welding process is divided into two stages: heating and cooling, and the microstructure of the Ti-6Al-4V alloy is affected by the cooling rate. During the heating phase, the volume fraction of the β-phase increases and completely converts into the β-phase at 975 °C, and the β-phase remains stable up to 1605 °C. Depending on the cooling rate, the phase transformation ensures that the welded joint takes place from α to β in the heating phase and from β to α/α'' in the cooling phase in the ITAB and fusion zone. When the heat input is low, the cooling rate is faster; when the heat input is large, the cooling rate is slower. When a large amount of heat is applied, the temperature of the fusion zone and the BM rises, and the thermal gradient difference between the fusion zone and the one next to BM reduces, triggering the formation of the transition zone HAZ [21, 63]. The HAZ microstructure seen in Fig.5(b) consisted predominantly of α contains a little quantity of primary α near the weld metal.

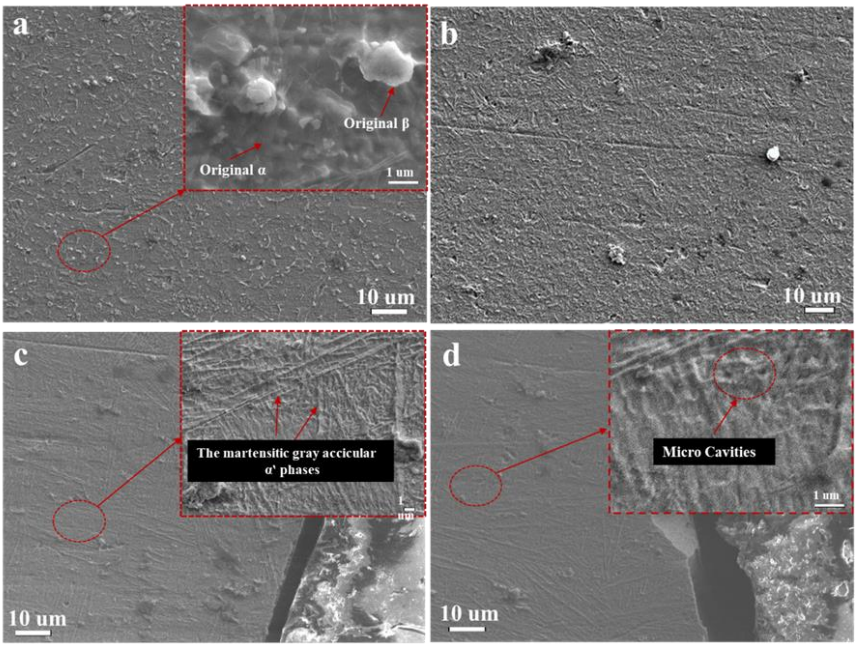

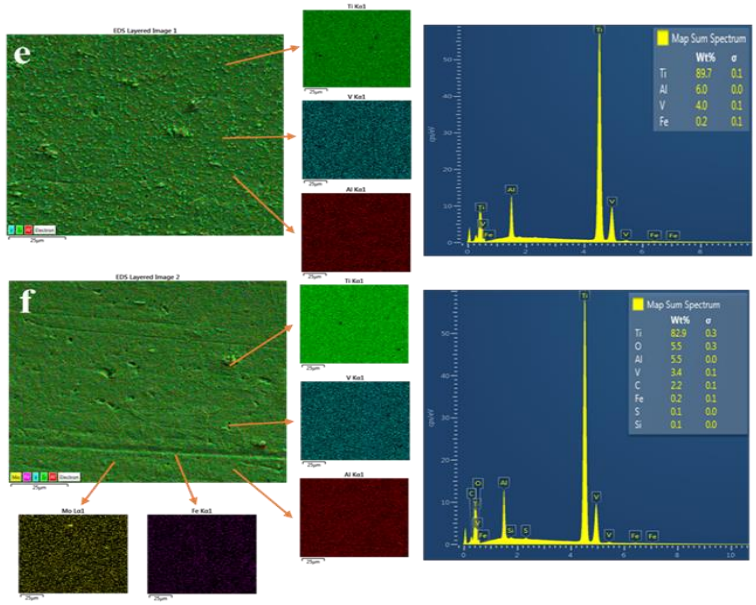

Fig. 5. SEM images of (a) base metals, (b) heat affected zones, (c) A3 sample fusion zone, (d) B4 sample fusion zone and EDS results of (e) base metals, (f) fusion zones before NaCl treatment

As shown in Fig.5(c-d), the microstructure features of the FZ are mostly composed of gray acicular α' martensite, a supersaturated, unstable α phase generated by diffusionless transition of the β phase. The acicular α' martensite microstructure of the fusion region of sample A3 is larger and more homogeneous than the colonies in the microstructure of sample B4. Microstructure investigations showed that the phases in FZ have a coarse martensite microstructure when energy input is increased, as shown in Fig.5(c-d). In addition, it was determined that microcavities due to insufficient melting occurred in the fusion region of the B4 sample, which was welded with lower energy. Fig.5(e-f) EDS mapping results show that the elemental distribution in the fusion region, unlike the BM region, contains 82.9% Ti, 5.5% Al, 5.5% O, 3.4% V and other different elements.

While the ratios of titanium, aluminum and vanadium decreased, the amount of oxygen on the surface increased significantly. This is due to the oxygen absorbed to the surface with temperature and melting during the titanium welding process, which is sensitive to oxygen. The presence of oxygen may also have caused the creation of a passive protective TiOx layer on the titanium alloy surface. Apart from this, it was observed that different elements from the environment and solder metal penetrated the surface at very low rates.

The SEM images given in Fig.6 show that the fractured surface occurs as a typical ductile fracture after the tensile test. The fracture surface is similar to the fracture surface images shown in the literature [71–73] and shows a typical ductile material behavior, consisting of coaxial pits alongside fluctuations and micro-voids, implying that there has been localized plastic deformation that occurred before fracture. After the corrosion test, SEM and EDS analyses were performed on the fractured surfaces of the samples with the highest weight change. Factors such as microstructural and elemental changes and NaCl crystallization that may have caused weight changes were investigated. The elements detected by SEM and EDS spectrum analyses of the R1 fractured surface after NaCl

treatment shown in Fig.5 mainly contain 31% Ti, 28.1% O, 3.8% Al, 1.4% V, 1.7% Na and 0.5% Cl by weight. This high oxygen content implies that corrosion products or an oxide layer are present on the surface. This was verified by the lower than initial % Ti and Al % in the alloy. It can be said that oxides such as Al_2O_3 and TiO_2 are therefore formed on the surface of the R1 sample [74]. Cui et.al. [75] and Qin et.al. [76] proved that TiO_2, Ti_2O_3 and TiO are the main components of passive films formed by titanium and its alloys. When the oxide coating is forming on the surface of the Ti alloy, TiO and Ti_2O_3 are formed first, and this reaction continues and partially turns up to the greatest valence oxide levels (TiO_2). Because the highly concentrated NaCl environment causes an increase in the halide ion (Cl^-) and this ion has an advantageous impact on the corrosion process. This way, it advances the reactions between the metal and the electrolyte. The change in oxide film thickness with NaCl medium can be attributed to the high Cl- concentration accelerating the conversion from Ti_2O_3 and TiO to TiO_2. Therefore, a thicker and less corrosion-resistant oxide film is formed in NaCl solutions. These reactions can be further accelerated by an increase in temperature or a low-pH environment. It can be said that the TiO_2 oxides formed on the surface of the R1 sample occur with the low pH environment and the presence of Cl^- ions. Similarly, Saha et.al. [77] showed that the anti-corrosion ability of the titanium surface due to Cl- ion attack increased after the production of the nano porous oxide layer. In addition, they stated that the annealed Ti6Al4V sample showed a slightly higher Icorr value than the anodized Ti6Al4V sample, and the corrosion inhibition ability decreased slightly after annealing. It is known that the microstructure obtained by melting at high temperature and then cooling to room temperature reduces the resistance against corrosion and the fiber laser welding process also created this effect. As shown in Fig.6, the decrease in the main alloy element ratios on the surfaces of the laser welded A3 and B4 samples is higher than that of the R1 sample, and the formation of corrosion products such as oxides and salt crystals on the surfaces is due to the reasons mentioned above.

Fig.7 EDS mapping and spectral analyses showed that after NaCl treatment, high levels of C and O elements appeared in the BM and FZ, and similarly Na and Cl elements were present on the surfaces. It is thought that C, O, Fe, Ca, Mg and Si elements, which exist on the surfaces apart from the main alloying elements, adhere to the surface from the external environment during the welding process. The presence of especially high levels of oxygen and carbon indicates that various oxides and carbides may have formed on the surface. C and O are more present at the boundaries connecting the HAZ region to the fusion region, as seen in Fig. 7 EDS-line results.

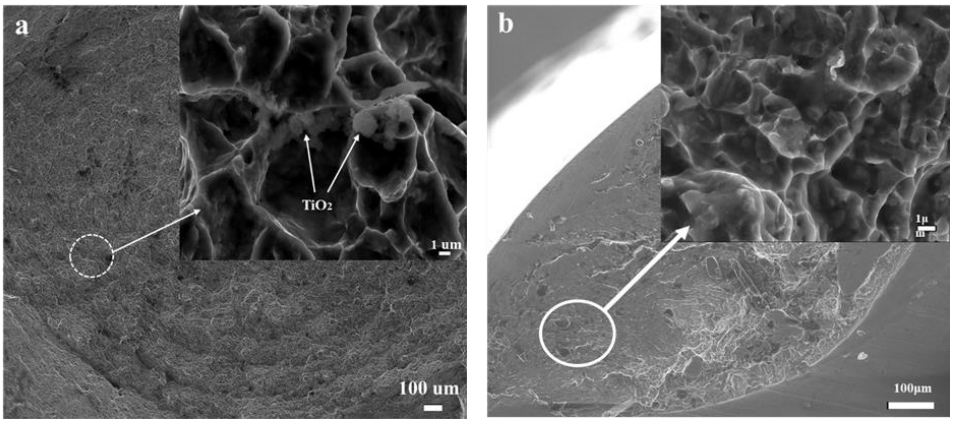

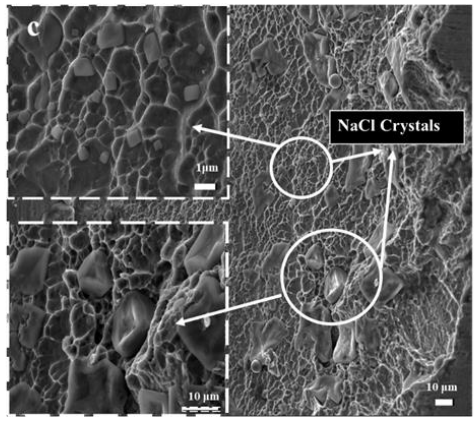

Fig. 6SEM images of (a) R1, (b) B4 and (c) A3 fracture surfaces after corrosion test

Since these regions are more protruding and porous, it was expected that oxygen and corrosion products adhere to the surface more. It is assumed that while some of the Na and Cl elements accumulated on the surface dissolve as salt crystals, the other part forms various nanostructures on the surface. Various studies have proven that Na^+ and Cl^- ions serve a significant influence in the formation of nanostructures and oxides. Yang et.al. [78] were produced hematite (α-Fe_2O_3) nanoplates with using NaCl, which is an N-type semiconductor. Due to the positive charge of the (α-Fe_2O_3) nanoplates, Due to hydrogen bonding between the positive and negative charge, they were coated with a layer of Cl^- ions when redistributed in a NaCl solution. The accumulation of Na^+ ions resulted in the formation of NaCl crystals and thus the self-assembly of the nanoplates. Because of its outstanding resistance to corrosion and diverse commercial and industrial uses in domains such as catalysts, magnetic devices, pigments, gas sensors, and rechargeable, it is a stable and valuable material. They are used in lithium-ion batteries in addition to other biological and medicinal disciplines. Shi et al. [79] synthesize monolayer WS2 crystals on SiO_2/Si substrate which is one typical example of the semiconducting transition-metal dichalcogenides (TMDCs) materials in one semi-sealed quartz tube, by utilizing NaCl as a growth stimulant. They also stated that the WS2 crystals' quantity and size have increased astoundingly throughout the time NaCl is introduced. Liu et al. (2014) [80] investigated in the selective photocatalytic destruction of CIP, a novel surface molecular imprinted NaCl/TiO_2 photocatalyst was developed. Chlorine was utilized in the solid-state approach to dope TiO_2. Among the chlorides, NaCl/TiO_2 nanomaterials had the highest photocatalytic activity of K^+, Na^+, Mg_2^+, $NH4^+$, Zn_2^+ and Ba_2^+. Shu et.al. (2020) [81] used a NaCl-based solid-solution technique to create porous metal oxides containing finely distributed noble metal NPs in a one-pot process. The well-dispersion of metal chlorides on NaCl, i.e. the mechanochemical production of MClx-NaCl solid solution, was discovered to be a critical step in controlling the porosity of metal oxides and the dispersion of noble metal species. In this approach, a number of porous metal oxides and related catalysts (FexOy, Cr_2O_3, Co_3O_4, Pd-FexOy, Pt-Cr_2O_3, and Rh-Co_3O_4) have been developed and successfully be prepared. In summary, Na^+ and Cl^- ions positively affect the synthesis and production of metallic nanoparticles, oxides and catalysts. Studies have also shown that Cl ions attack metal ions and create new structures. The 0.9 wt% NaCl solution was the cause of the reduction of the main metal alloy elements seen on the surfaces after the corrosion test and the formation of oxides of oxygen, carbon and other elements on the surface. These formations were triggered more by increasing temperature and decreasing pH. The increase in NaCl crystals and oxide layer formation also increases the resistance of the

metal against corrosion. It was determined that the weight change results given in Fig.4 were directly proportional to the SEM and EDS results. Because the weight losses in the A3 and R1 samples, where the salt crystals and TiO_2 oxides are more, were much lower than in the B4 sample. This proves that corrosion-induced wear on the metal surface or ion distribution is less. SEM and EDS mapping and spectrum results of the BM and FZ of sample A3 presented in Fig.6 show that high rates of salt crystals are formed on the surfaces. Na and Cl elements, present at the rates of 1.1% and 0.5% in the BM, increased to 16.5% and 11.5% in the fusion region. The reason for this can be shown that the martensite structure in the fusion region has a lower resistance to corrosion and that Cl- ions and oxygen are more absorbed into the surface. The EDS-line results given in Fig.6(c) also clearly showed that the presence of Na and Cl elements increased sharply from the BM to the fusion zone. In the B4 sample, on the other hand, it was determined from the EDS-line analysis that the NaCl ratios in the BM and FZ were very low and at the same ratios. NaCl salts crystallized in the A3 fusion region are {1 0 0} and {1 1 1} hopper-shaped forms. In Ref. [50, 82, 83] studies, they claimed that hopper cubes and tiny vicinal faces of the octahedron are created. The top (1 1 1) face of a NaCl crystal nucleated with a triad axis nearly parallel to the glass substrate will also develop approximately hopper-shaped.

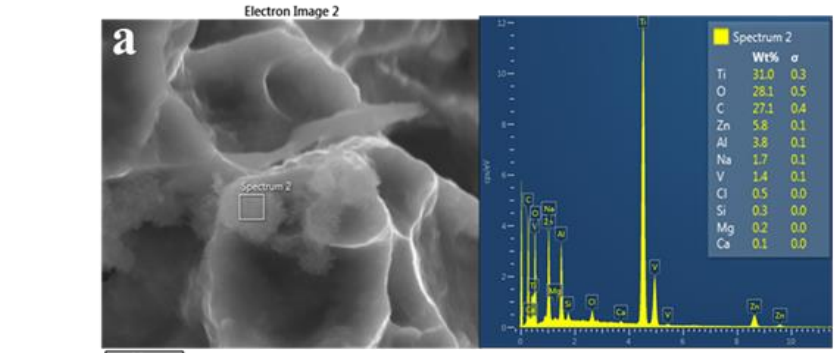

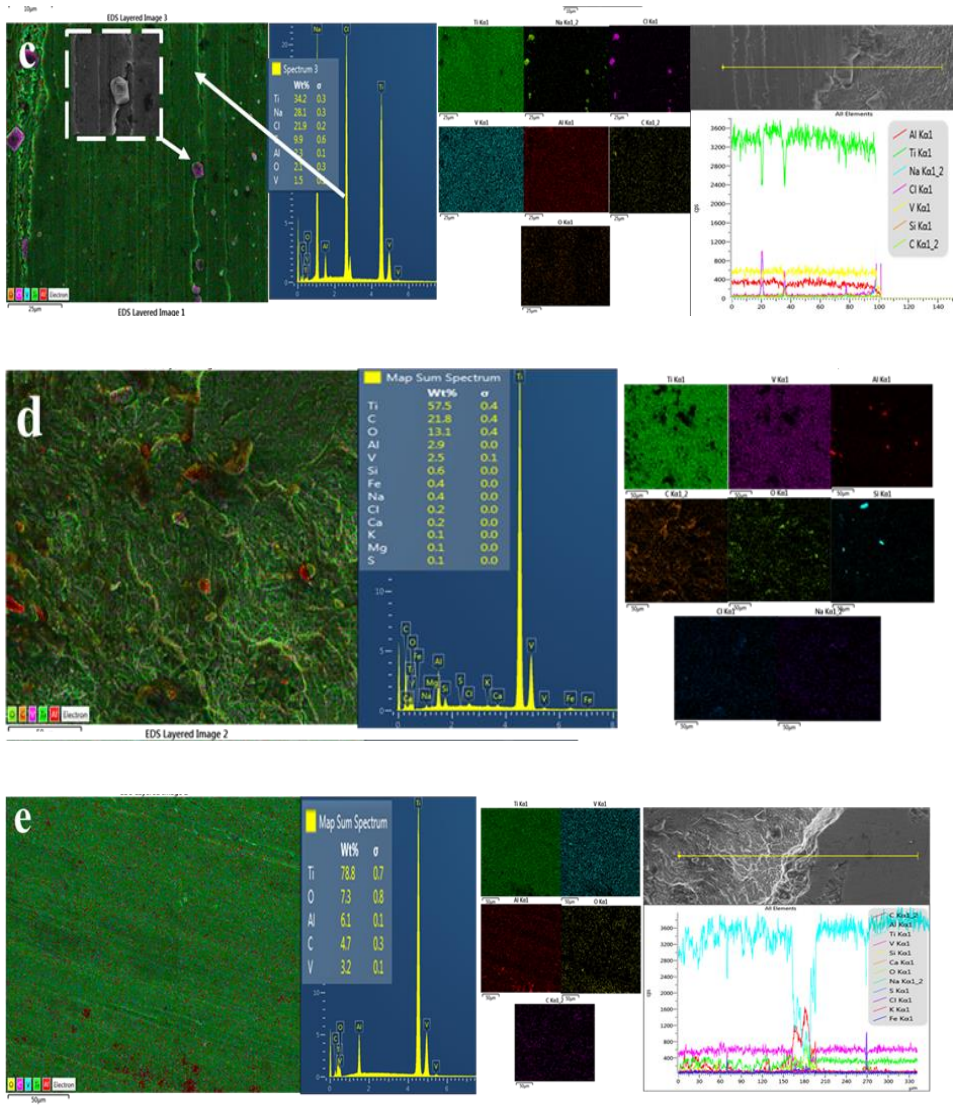

Fig. 7. EDS distribution of the elements on (a) R sample, (b) fusion zone of A3, (c) base metal of A3, and (d) fusion zone of B4, (e) base metal of B4

It was determined that the salt crystals and TiO2 on the surface of the fiber laser welded A3 sample, together with the combination of low pH and NaCl environment, allowed it to grow critically more than the B4 sample. Apart from this, according to the Vickers hardness values in Fig.3(b), the martensitic transformations of the FZ region of the A3 sample combined with higher welding energy, causing higher hardness than BM, are more sensitive to corrosion products than the other welded samples. created. The sizes of these formed crystals were calculated using the Image J program on SEM images. The crystal sizes range from 2-10 μm and they average 8 μm in size.

5. Conclusions

Ti-6Al-4V alloy rods, which are of great importance in biomedical and industrial applications, were joined by fiber laser welding technology. Tensile and microhardness mechanical tests were carried out after the welding process. Among the welded samples, the highest strength was obtained in sample A with 134 MPa. The hardness tests performed on the surfaces after the welding process showed that the a' martensitic phase transformation in the fusion zone increased the hardness values on average 1.5 times. For the purpose of determining the corrosion behavior of the fiber laser welded Ti-6Al-4V (Gr5) rod alloys fractured surfaces after the tensile test by creating a naturally corrosive and hot environment. The samples were exposed to pH3-5, 25-50°C temperatures and 0.9 wt% NaCl environment for 24 hours in a shaking incubator. According to the weight change measurements made before and after the corrosion test, the highest weight loss occurred in the B4 sample with 0.0025 g. The microstructure changes and formations on the fractured surfaces before and after NaCl treatment were compared with SEM and EDS analyses. The formation of gray acicular a' martensitic phases was observed in the fusion and heat-affected zones. It has been shown that the fusion zones tend to react with more oxygen than the BM, leading to TiO_2 oxide formations and NaCl crystallizations. It was determined that the FZ regions, whose hardness values increased after welding, had a higher tendency to undergo corrosion. NaCl crystals and oxide layer, which formed on the A3 sample have significant and larger sizes compared to the B4 sample. These layers increased the corrosion resistance of this sample and provided a very low weight loss of 0.0005. The damaged area in Ti-Al-4V implants was simulated with the fractured surface created by the tensile test after joining with fiber laser welding. It was understood that due to the martensitic microstructure changes and the rough structure that occurred after the tensile test, the fusion regions were more prone to corrosion in high-temperature and low-pH environments. Apart from these, it has been proven that NaCl crystallization conditions are met and that small-size (8um) crystals can be obtained. In this way, a method was introduced to obtain hopper-shaped NaCl that can be used to synthesize various catalysts, oxides and nanostructures.

Acknowledgment

All studies were conducted at Ondokuzmayıs University, Faculty of Engineering, Metallurgical and Materials Engineering Laboratory.

References

[1] Anuwar M, Jayaganthan R, Tewari VK, Arivazhagan N. A study on the hot corrosion behavior of Ti-6Al-4V alloy. Materials Letters 2007; 61(7): 1483-8 https://doi.org/10.1016/j.matlet.2006.07.058

[2] Ciszak C, Popa I, Brossard J-M, Monceau D, Chevalier S. NaCl induced corrosion of Ti-6Al-4V alloy at high temperature. Corrosion Science 2016; 110: 91-104 https://doi.org/10.1016/j.corsci.2016.04.016

[3] Krząkała A, Służalska K, Dercz G, et al. Characterization of bioactive films on Ti-6Al-4V alloy. Electrochimica Acta 2013; 104: 425-38 https://doi.org/10.1016/j.electacta.2012.12.081

[4] López MF, Gutiérrez A, Jiménez JA. In vitro corrosion behaviour of titanium alloys without vanadium. Electrochimica Acta 2002; 47(9): 1359-64. https://doi.org/10.1016/S0013-4686(01)00860-X

[5] Rodrigues DC, Valderrama P, Wilson TG, et al. Titanium Corrosion Mechanisms in the Oral Environment: A Retrieval Study. Materials (Basel) 2013; 6(11): 5258-74. https://doi.org/10.3390/ma6115258

[6] Yao Z, Marck M. NaCl-induced hot corrosion of a titanium aluminide alloy. Materials Science and Engineering: A 1995; 192-193(10): 994-1000. https://doi.org/10.1016/0921-5093(95)03345-9
[7] BALOYI NM, Popoola API, Pityana SL. Microstructure, hardness and corrosion properties of laser processed Ti6Al4V-based composites. Transactions of Nonferrous Metals Society of China 2015; 25(9): 2912-23. https://doi.org/10.1016/S1003-6326(15)63917-6
[8] Gil FJ, Delgado L, Espinar E, Llamas JM. Corrosion and corrosion-fatigue behavior of cp-Ti and Ti-6Al-4V laser-marked biomaterials. J Mater Sci Mater Med 2012; 23(4): 885-90. https://doi.org/10.1007/s10856-012-4572-z
[9] Khan MA, Williams RL, Williams DF. The corrosion behaviour of Ti-6Al-4V, Ti-6Al-7Nb and Ti-13Nb-13Zr in protein solutions. Biomaterials 1999; 20(7): 631-7. https://doi.org/10.1016/S0142-9612(98)00217-8
[10] Lin X-z, Zhu M-h, Cai Z-b, Dou B-j, Cui X-j. Torsional fretting corrosion behaviours of Ti6Al4V alloys in Hank's simulated body fluid. Corrosion Engineering, Science and Technology 2019; 54(4): 298-309. https://doi.org/10.1080/1478422X.2019.1589675
[11] Singh R, Martin M, Dahotre NB. Influence of laser surface modification on corrosion behavior of stainless steel 316L and Ti-6Al-4V in simulated biofluid. Surface Engineering 2013; 21(4): 297-306. https://doi.org/10.1179/174329405X55320
[12] Xu Y, Lu Y, Sundberg KL, Liang J, Sisson RD. Effect of Annealing Treatments on the Microstructure, Mechanical Properties and Corrosion Behavior of Direct Metal Laser Sintered Ti-6Al-4V. J. of Materi Eng and Perform 2017; 26(6): 2572-82. https://doi.org/10.1007/s11665-017-2710-y
[13] Zaveri N, McEwen GD, Karpagavalli R, Zhou A. Biocorrosion studies of TiO2 nanoparticle-coated Ti-6Al-4V implant in simulated biofluids. J Nanopart Res 2010; 12(5): 1609-23. https://doi.org/10.1007/s11051-009-9699-6
[14] Jáquez-Muñoz JM, Gaona-Tiburcio C, Cabral-Miramontes J, et al. Electrochemical Noise Analysis of the Corrosion of Titanium Alloys in NaCl and H2SO4 Solutions. Metals 2021; 11(1): 105. https://doi.org/10.3390/met11010105
[15] Ertek Emre H. The corrosion behaviour of as-welded and post-weld heat treated Ti6Al4V alloy in simulated body fluid. Materials Letters 2019; 254(3): 162-6. https://doi.org/10.1016/j.matlet.2019.07.056
[16] Garcia-Ramirez MJ, Lopez-Sesenes R, Rosales-Cadena I, Gonzalez-Rodriguez JG. Corrosion behaviour of Ti-Ni-Al alloys in a simulated human body solution. Journal of Materials Research and Technology 2018; 7(3): 223-30. https://doi.org/10.1016/j.jmrt.2017.07.003
[17] Karimzadeh F, Heidarbeigy M, Saatchi A. Effect of heat treatment on corrosion behavior of Ti-6Al-4V alloy weldments. Journal of Materials Processing Technology 2008; 206(1-3): 388-94. https://doi.org/10.1016/j.jmatprotec.2007.12.065
[18] Manam NS, Harun WSW, Shri DNA, et al. Study of corrosion in biocompatible metals for implants: A review. Journal of Alloys and Compounds 2017; 701(3): 698-715. https://doi.org/10.1016/j.jallcom.2017.01.196
[19] Yang X, Dong X, Li W, Feng W, Xu Y. Effect of solution and aging treatments on corrosion performance of laser solid formed Ti-6Al-4V alloy in a 3.5 wt. % NaCl solution. Journal of Materials Research and Technology 2020; 9(2): 1559-68. https://doi.org/10.1016/j.jmrt.2019.11.082
[20] Zavanelli RA, Guilherme AS, Pessanha-Henriques GE, Arruda Nóbilo MA de, Mesquita MF. Corrosion-fatigue of laser-repaired commercially pure titanium and Ti-6Al-4V alloy under different test environments. J Oral Rehabil 2004; 31(10): 1029-34. https://doi.org/10.1111/j.1365-2842.2004.01336.x
[21] Nabhani M, Shoja Razavi R, Barekat M. Corrosion study of laser cladded Ti-6Al-4V alloy in different corrosive environments. Engineering Failure Analysis 2019; 97: 234-41. https://doi.org/10.1016/j.engfailanal.2019.01.023

[22] 2022 Medical Technologies Congress (TIPTEKNO). IEEE; 2022.
[23] Zhou S, Zhang J, Wang J, Yang G, Wu K, Qin L. Effect of Oxygen Levels in Tent Shielding Atmosphere on Microstructural and Mechanical Properties of Ti-6Al-4V Fabricated by Wire Arc Additive Manufacturing. J. of Materi Eng and Perform 2022; 31(7): 5269-78. https://doi.org/10.1007/s11665-022-06684-w
[24] Yang Z, Li J, Zhang B, Li J. Microstructures and mechanical properties of a titanium alloy thick plate joint after electron beam welding plus solution-aging. Journal of Materials Research and Technology 2022; 19(5-8): 913-22. https://doi.org/10.1016/j.jmrt.2022.05.091
[25] Raut N, Yakkundi V, Sunnapwar V, Medhi T, Jain VKS. A specific analytical study of friction stir welded Ti-6Al-4V grade 5 alloy: Stir zone microstructure and mechanical properties. Journal of Manufacturing Processes 2022; 76(1): 611-23. https://doi.org/10.1016/j.jmapro.2022.02.036
[26] Irmak E, Ugurlu B, Incesu A. Investigation of Tribocorrosion Properties of Titanium Implant used in Orthopedics. In: Investigation of Tribocorrosion Properties of Titanium Implant used in Orthopedics; 2022. IEEE; 1-4. https://doi.org/10.1109/TIPTEKNO56568.2022.9960164
[27] Li C, Muneharua K, Takao S, Kouji H. Fiber laser-GMA hybrid welding of commercially pure titanium. Materials & Design 2009; 30(1): 109-14. https://doi.org/10.1016/j.matdes.2008.04.043
[28] Kuryntsev SV, Morushkin AE, Gilmutdinov AK. Fiber laser welding of austenitic steel and commercially pure copper butt joint. Optics and Lasers in Engineering 2017; 90(9): 101-9. https://doi.org/10.1016/j.optlaseng.2016.10.008
[29] Miranda RM, Assunção E, Silva RJC, Oliveira JP, Quintino L. Fiber laser welding of NiTi to Ti-6Al-4V. Int J Adv Manuf Technol 2015; 81(9-12): 1533-8. https://doi.org/10.1007/s00170-015-7307-8
[30] Quintino L, Costa A, Miranda R, Yapp D, Kumar V, Kong CJ. Welding with high power fiber lasers - A preliminary study. Materials & Design 2007; 28(4): 1231-7. https://doi.org/10.1016/j.matdes.2006.01.009
[31] Hafez KM, Katayama S. Fiber laser weldin g of AISI 304 stainless steel plates. Quarterly Journal of The Japan Welding Society 2009; 27(2): 69s-73s. https://doi.org/10.2207/qjjws.27.69s
[32] Lai R, Cai Y, Wu Y, Li F, Hua X. Influence of absorbed nitrogen on microstructure and corrosion resistance of 2205 duplex stainless steel joint processed by fiber laser welding. Journal of Materials Processing Technology 2016; 231: 397-405. https://doi.org/10.1016/j.jmatprotec.2016.01.016
[33] Miranda R, Costa A, Quintino L, Yapp D, Iordachescu D. Characterization of fiber laser welds in X100 pipeline steel. Materials & Design 2009; 30(7): 2701-7. https://doi.org/10.1016/j.matdes.2008.09.042
[34] Pekkarinen J, Kujanpää V. The effects of laser welding parameters on the microstructure of ferritic and duplex stainless steels welds. Physics Procedia 2010; 5: 517-23. https://doi.org/10.1016/j.phpro.2010.08.175
[35] Zhang L, Lu JZ, Luo KY, et al. Residual stress, micro-hardness and tensile properties of ANSI 304 stainless steel thick sheet by fiber laser welding. Materials Science and Engineering: A 2013; 561: 136-44. https://doi.org/10.1016/j.msea.2012.11.001
[36] Vikas KSR, Rahul, Ramana VSNV, Reddy GM, Rao KS. Influence of heat treatments on corrosion behavior of Ti64 friction welds. Chemical Data Collections 2022; 42(24): 100940. https://doi.org/10.1016/j.cdc.2022.100940
[37] Pazhanivel B, Sathiya P, Sozhan G. Ultra-fine bimodal (α + β) microstructure induced mechanical strength and corrosion resistance of Ti-6Al-4V alloy produced via laser powder bed fusion process. Optics & Laser Technology 2020; 125(6): 106017. https://doi.org/10.1016/j.optlastec.2019.106017

[38] Mahlobo MGR, Chikosha L, Olubambi PA. Study of the corrosion properties of powder rolled Ti-6Al-4V alloy applied in the biomedical implants. Journal of Materials Research and Technology 2022; 18(4): 3631-9. https://doi.org/10.1016/j.jmrt.2022.04.004
[39] Cui Y-W, Chen L-Y, Qin P, et al. Metastable pitting corrosion behavior of laser powder bed fusion produced Ti-6Al-4V in Hank's solution. Corrosion Science 2022; 203: 110333. https://doi.org/10.1016/j.corsci.2022.110333
[40] Lim B-S, Cho H-R, Choe H-C. Corrosion behaviors of macro/micro/nano-scale surface modification on Ti-6Al-4V alloy for bio-implant. Thin Solid Films 2022; 754: 139314. https://doi.org/10.1016/j.tsf.2022.139314
[41] Lebea L, Ngwangwa HM, Desai DA, Nemavhola F. Corrosion Resistance of 3D-Printed Titanium Alloy Ti64-ELI Parts for Dental Application. Appl Bionics Biomech 2022; 2022: 1804417. https://doi.org/10.1155/2022/1804417
[42] Metalnikov P, Ben-Hamu G, Eliezer D. Corrosion behavior of AM-Ti-6Al-4V: A comparison between EBM and SLM. Prog Addit Manuf 2022; 7(3): 509-20. https://doi.org/10.1007/s40964-022-00293-8
[43] Qiao Q, Tam LM, Cristino VAM, Kwok CT. Surface hardness and corrosion behavior of laser surface-alloyed Ti6Al4V with copper. Surface and Coatings Technology 2022; 444(22): 128663. https://doi.org/10.1016/j.surfcoat.2022.128663
[44] Rahmouni K, Besnard A, Oulmi K, et al. In vitro corrosion response of CoCrMo and Ti-6Al-4V orthopedic implants with Zr columnar thin films. Surface and Coatings Technology 2022; 436: 128310. https://doi.org/10.1016/j.surfcoat.2022.128310
[45] Assis Ferreira N de, Senna PM, do Lago DCB, Senna LF de, Sampaio-Filho HR. Influence of stress corrosion on the mechanical properties of laser-welded titanium. J Prosthet Dent 2016; 115(3): 356-62. https://doi.org/10.1016/j.prosdent.2015.09.002
[46] Le Guéhennec L, Soueidan A, Layrolle P, Amouriq Y. Surface treatments of titanium dental implants for rapid osseointegration. Dent Mater 2007; 23(7): 844-54. https://doi.org/10.1016/j.dental.2006.06.025
[47] Mohammed MT, Khan ZA, Siddiquee AN. Surface Modifications of Titanium Materials for developing Corrosion Behavior in Human Body Environment: A Review. Procedia Materials Science 2014; 6: 1610-8. https://doi.org/10.1016/j.mspro.2014.07.144
[48] Pazos L, Corengia P, Svoboda H. Effect of surface treatments on the fatigue life of titanium for biomedical applications. J Mech Behav Biomed Mater 2010; 3(6): 416-24. https://doi.org/10.1016/j.jmbbm.2010.03.006
[49] Vasilescu E, Drob P, Raducanu D, et al. Effect of thermo-mechanical processing on the corrosion resistance of Ti6Al4V alloys in biofluids. Corrosion Science 2009; 51(12): 2885-96. https://doi.org/10.1016/j.corsci.2009.08.014
[50] Aquilano D, Pastero L, Bruno M, Rubbo M. {100} and {111} forms of the NaCl crystals coexisting in growth from pure aqueous solution. Journal of Crystal Growth 2009; 311(2): 399-403. https://doi.org/10.1016/j.jcrysgro.2008.11.006
[51] Elagli K, Traisnel M, Hildebrand HF. Electrochemical behaviour of titanium and dental alloys in artificial saliva. Electrochimica Acta 1993; 38(13): 1769-74. https://doi.org/10.1016/0013-4686(93)85075-A
[52] Fojt J, Joska L, Málek J. Corrosion behaviour of porous Ti-39Nb alloy for biomedical applications. Corrosion Science 2013; 71: 78-83. https://doi.org/10.1016/j.corsci.2013.03.007
[53] Souza JCM, Barbosa SL, Ariza E, Celis J-P, Rocha LA. Simultaneous degradation by corrosion and wear of titanium in artificial saliva containing fluorides. Wear 2012; 292-293(9): 82-8. https://doi.org/10.1016/j.wear.2012.05.030
[54] Vieira AC, Ribeiro AR, Rocha LA, Celis JP. Influence of pH a nd corrosion inhibitors on the tribocorrosion of titanium in artificial saliva. Wear 2006; 261(9): 994-1001. https://doi.org/10.1016/j.wear.2006.03.031

[55] Arakelyan M, Spagnuolo G, Iaculli F, et al. Minimization of Adverse Effects Associated with Dental Alloys. Materials (Basel) 2022; 15(21. https://doi.org/10.3390/ma15217476
[56] Mohammed NB, Daily ZA, Alsharbaty MH, et al. Effect of PMMA sealing treatment on the corrosion behavior of plasma electrolytic oxidized titanium dental implants in fluoride-containing saliva solution. Mater. Res. Express 2022; 9(12): 125401. https://doi.org/10.1088/2053-1591/aca7b5
[57] Nagay BE, Cordeiro JM, Barao VAR. Insight Into Corrosion of Dental Implants: From Biochemical Mechanisms to Designing Corrosion-Resistant Materials. Curr Oral Health Rep 2022; 9(2): 7-21. https://doi.org/10.1007/s40496-022-00306-z
[58] Paolone G, Mandurino M, Pavan F, Mazzitelli C, Cantatore G. Novel Dental Restorative Solutions for Natural Teeth and Implants. Bioengineering (Basel) 2022; 9(12). https://doi.org/10.3390/bioengineering9120772
[59] Arakji H, Osman E, Aboelsaad N, Shokry M. Evaluation of implant site preparation with piezosurgery versus conventional drills in terms of operation time, implant stability and bone density (randomized controlled clinical trial- split mouth design). BMC Oral Health 2022; 22(1): 567. https://doi.org/10.1186/s12903-022-02613-4
[60] Thadathil Varghese J, Babaei B, Farrar P, Prentice L, Prusty BG. Influence of thermal and thermomechanical stimuli on a molar tooth treated with resin-based restorative dental composites. Dent Mater 2022; 38(5): 811-23. https://doi.org/10.1016/j.dental.2022.04.010
[61] Chen Z, Wang B, Duan B. Mechanical Properties and Microstructure of a High-Power Laser-Welded Ti6Al4V Titanium Alloy. J. of Materi Eng and Perform 2020; 29(4): 2296-304. https://doi.org/10.1007/s11665-020-04737-6
[62] Omoniyi P, Mahamood R, Arthur N, et al. Laser Butt Welding of Thin Ti6Al4V Sheets: Effects of Welding Parameters. J. Compos. Sci. 2021; 5(9): 246. https://doi.org/10.3390/jcs5090246
[63] Ertek Emre H, Arslan Ş. Effect of laser welding on microstructure and mechanical properties of biomedical Ti6Al4V. Appl. Phys. A 2019; 125(11): 1071. https://doi.org/10.1007/s00339-019-3045-3
[64] Kumar P, Sinha AN. Effect of heat input in pulsed Nd: YAG laser welding of titanium alloy (Ti6Al4V) on microstructure and mechanical properties. Weld World 2019; 63(3): 673-89. https://doi.org/10.1007/s40194-018-00694-w
[65] Sepe R, Franchitti S, Borrelli R, Di Caprio F, Armentani E, Caputo F. Correlation between real geometry and tensile mechanical behaviour for Ti6Al4V electron beam melted thin specimens. Theoretical and Applied Fracture Mechanics 2020; 107(3): 102519. https://doi.org/10.1016/j.tafmec.2020.102519
[66] Rominiyi AL, Mashinini PM. Continuous wave laser welding of Ti6Al4V alloy joints: Microstructure and mechanical properties. Materials Letters 2023; 336: 133934. https://doi.org/10.1016/j.matlet.2023.133934
[67] Ohkubo C, Watanabe I, Ford JP, Nakajima H, Hosoi T, Okabe T. The machinability of cast titanium and Ti-6Al-4V. Biomaterials 2000; 21(4): 421-8. https://doi.org/10.1016/S0142-9612(99)00206-9
[68] Meyer U, Bühner M, Büchter A, Kruse-Lösler B, Stamm T, Wiesmann HP. Fast element mapping of titanium wear around implants of different surface structures. Clin Oral Implants Res 2006; 17(2): 206-11. https://doi.org/10.1111/j.1600-0501.2005.01184.x
[69] Pazhanivel B, Sathiya P, Muthuraman K, Sozhan G. Influence of NaCl environment on stress corrosion cracking of additive manufactured Ti-6Al-4V alloy. Engineering Failure Analysis 2021; 127: 105515. https://doi.org/10.1016/j.engfailanal.2021.105515
[70] Shahsavari M, Imani A, Schaller RF, Asselin E. Corrosion evaluation of Ti-6Al-4V manufactured by electron beam melting in Ringer's physiological solution: An in vitro

study of the passive film. J Appl Electrochem 2022; 52(6): 1003-19. https://doi.org/10.1007/s10800-022-01683-0
[71] Fernandes MF, Oliveira Velloso VMd, Cornelis Voorwald HJ. Investigation of the damage and fracture of Ti-6Al-4V titanium alloy under dwell-fatigue loadings. Procedia Structural Integrity 2022; 35: 141-9. https://doi.org/10.1016/j.prostr.2021.12.058
[72] Gao F, Sun Z, Yang S, Jiang P, Liao Z. Stress corrosion characteristics of electron beam welded titanium alloys joints in NaCl solution. Materials Characterization 2022; 192(1): 112126. https://doi.org/10.1016/j.matchar.2022.112126
[73] Wang Y, Zhao H, Ma H, Zhang Y. The effect of thickness on fracture characteristics of TC4 titanium alloy sheets. Archiv.Civ.Mech.Eng 2022; 22(4): 129. https://doi.org/10.1007/s43452-022-00473-x
[74] Abdo HS, Sherif E-SM, El-Serehy HA. Manufacturing of Ti-6%Al and Ti-6%Al-4%V Alloys and Their Corrosion in Sodium Chloride Solutions. Crystals 2020; 10(3): 181. https://doi.org/10.3390/cryst10030181
[75] Cui Y-W, Chen L-Y, Chu Y-H, et al. Metastable pitting corrosion behavior and characteristics of passive film of laser powder bed fusion produced Ti-6Al-4V in NaCl solutions with different concentrations. Corrosion Science 2023; 215: 111017. https://doi.org/10.1016/j.corsci.2023.111017
[76] Qin P, Chen LY, Liu YJ, et al. Corrosion and passivation behavior of laser powder bed fusion produced Ti-6Al-4V in static/dynamic NaCl solutions with different concentrations. Corrosion Science 2021; 191: 109728. https://doi.org/10.1016/j.corsci.2021.109728
[77] Saha SK, Park YJ, Cho SO. Fabrication of highly ordered nanoporous oxide layer on Ti6Al4V surfaces for improved corrosion resistance property. Journal of Molecular Structure 2021; 1223: 129244. https://doi.org/10.1016/j.molstruc.2020.129244
[78] Yang P, Wang D, Zhao J, Shi R. Facile synthesis of hematite nanoplates and their self-assembly generated by domain growth of NaCl. Materials Research Bulletin 2015; 65(13): 36-41. https://doi.org/10.1016/j.materresbull.2015.01.002
[79] Shi B, Zhou D, Qiu R, et al. High-efficiency synthesis of large-area monolayer WS2 crystals on SiO2/Si substrate via NaCl-assisted atmospheric pressure chemical vapor deposition. Applied Surface Science 2020; 533: 147479. https://doi.org/10.1016/j.apsusc.2020.147479
[80] Liu X, Lv P, Yao G, et al. Selective degradation of ciprofloxacin with modified NaCl/TiO2 photocatalyst by surface molecular imprinted technology. Colloids and Surfaces A: Physicochemical and Engineering Aspects 2014; 441(208): 420-6. https://doi.org/10.1016/j.colsurfa.2013.10.005
[81] Shu Y, Chen H, Chen N, et al. A Principle for Highly Active Metal Oxide Catalysts via NaCl-Based Solid Solution. Chem 2020; 6(7): 1723-41. https://doi.org/10.1016/j.chempr.2020.04.003
[82] Madsen RSK, Motuzas J, Vaughan J, Julbe A, Diniz da Costa JC. Fine control of NaCl crystal size and particle size in percrystallisation by tuning the morphology of carbonised sucrose membranes. Journal of Membrane Science 2018; 567: 157-65. https://doi.org/10.1016/j.memsci.2018.09.003
[83] Quilaqueo M, Aguilera JM. Crystallization of NaCl by fast evaporation of water in droplets of NaCl solutions. Food Research International 2016; 84(2): 143-9. https://doi.org/10.1016/j.foodres.2016.03.030

Research on Engineering Structures & Materials
www.jresm.org
MIM Research Group

Review Article

Carbon nanotubes: revolutionizing construction materials for a sustainable future: A review

Khristina Maksudovna Vafaeva [1,a], Rachid Zegait*[2,b]

[1]*Peter the Great St. Petersburg Polytechnic University, St. Petersburg, Russia*
[2]*Faculty of Science and Technology, Ziane Achour University of Djelfa, Djelfa, Algeria*

Article Info

Article history:

Received 18 Aug 2023
Accepted 13 Nov 2023

Keywords:

Carbon nanotubes;
Material enhancers;
Construction;
Ongoing research;
Building materials;
Mechanical properties

Abstract

This review article explores the use of carbon nanotubes (CNTs) as material enhancers in construction and their advantages. It emphasizes ongoing research to gather accurate data on CNT-enhanced material properties and their role in creating more efficient and stronger building materials. The various methods of obtaining and incorporating CNTs into building materials, including chemical vapor deposition and electric arc synthesis, are discussed. A comparative analysis of building materials with and without CNTs is presented to examine their characteristics. The article also discusses future prospects for CNTs in various industries. The study aims to investigate experimental methods for obtaining CNTs, their properties, and their introduction into building materials. The research methodology involves studying literature sources, analyzing experimental results, and examining the structural, mechanical, and electronic properties of CNTs. Analytical methods based on scientific articles and publications related to CNTs in construction were used to ensure the article's reliability, validity, completeness, and objectivity. The research highlights CNTs' potential as material enhancers in construction, owing to their unique mechanical properties, such as high strength, stiffness, and corrosion resistance. Specific studies demonstrating the use of CNTs to increase the strength of concrete and other construction materials are provided, indicating the promising application of CNTs in future construction projects. However, technical challenges must be addressed, and appropriate standards and regulations should be developed before practical implementation.

1. Introduction

The global construction industry is undergoing a paradigm shift as sustainability takes center stage in the pursuit of a greener and more environmentally conscious future [1]. Traditional construction materials like concrete and steel have long been essential for infrastructure development but contribute to environmental issues due to their carbon emissions and resource depletion [2,3]. To address sustainability concerns, carbon nanotubes (CNTs) have emerged as a groundbreaking alternative [4]. CNTs are microscopic cylindrical structures composed of carbon atoms, offering extraordinary mechanical, electrical, and thermal properties [5]. They are exceptionally strong yet lightweight, allowing for efficient load distribution and enhanced durability [6]. Integrating CNTs in construction materials provides several advantages. Their use significantly reduces the carbon footprint, as they enhance structural integrity and require less material, lowering energy consumption and greenhouse gas emissions during production and transportation [7,8]. CNTs also enable the development of self-sensing and self-healing materials, allowing real-time monitoring of structural health and microcrack repair, extending material lifespan, and reducing maintenance needs [9].

*Corresponding author: zegait.rachid@gmail.com , r.zegait@univ-djelfa.dz,
[a] orcid.org/0000-0002-7422-5494; [b] orcid.org/0000-0001-7976-0595
DOI: http://dx.doi.org/10.17515/resm2023.42ma0818rv

Furthermore, CNTs offer opportunities for energy-efficient infrastructure through enhanced electrical conductivity for energy storage systems and smart grid technologies, and thermal conductivity for insulation materials, optimizing energy consumption in buildings [10,11].

While CNTs show immense promise, challenges like large-scale production, cost-effectiveness, and environmental risks must be addressed [12]. Continued research and collaboration between academia, industry, and policymakers are essential to unlock their full potential and pave the way for a sustainable future.

The unique properties of CNTs extend beyond construction, finding applications in various industries to improve material strength, deformability, and durability [13,14]. Their integration into construction materials creates new composites with enhanced characteristics, such as increased strength and reduced shrinkage in concrete. Functional coatings with properties like waterproofing, fire resistance, and corrosion protection can improve the quality and lifespan of construction materials [15,16]. The literature highlights the extensive research into CNTs in construction, showcasing their potential to revolutionize the field and create materials and structures with improved properties and efficiency. Nanotechnology, including CNTs, has opened exciting possibilities for the construction industry, enabling the development of innovative materials and structures [17,18]. Numerous review articles delve deeply into specific directions. For instance, Norizan et al. [19] provides a comprehensive review of existing research and introduces novel findings on the functionalization of carbon nanotubes to enhance their sensitivity and selectivity in detecting various chemical compounds. This advancement holds potential applications in diverse fields, including medicine, environment, and industry. The article highlights the significant role of carbon nanotubes as chemical sensors, emphasizing that functionalization can significantly enhance their performance and detection efficiency.

Garg et al. [20] explores the utilization of carbon nanotubes as strengthening agents in composite materials. The authors examine various methods for obtaining and evaluating carbon nanotubes, as well as their application in composite materials to enhance mechanical properties. The article discusses the potential advantages and limitations of integrating carbon nanotubes into composite materials.

Similarly, Anzar et al. [21] offers an overview of the diverse applications of carbon nanotubes in biomedicine. This encompasses their use as nanovectors for drug delivery, materials for tissue engineering, biomarkers, and various other applications. Fiyadh et al. [22] review different adsorption methods, investigate the mechanisms of interaction between carbon nanotubes and heavy metals, and provide an overview of parameters influencing adsorption efficiency, such as nanotube size, shape, pH of the medium and metal concentration. They further explore the application of carbon nanotubes in removing heavy metals from water solutions, soil, and wastewater.

Sajid et al. [23] present an overview of various applications of carbon nanotube-based adsorbents in water purification, including the removal of organic and inorganic pollutants, heavy metals, pharmaceuticals, and other harmful substances. The article discusses the interaction mechanisms between carbon nanotubes and water pollutants, encompassing adsorption and ion exchange processes.

The impact of carbon nanotubes on concrete properties is also examined in [24]. The review summarizes existing research on the use of carbon nanotubes in concrete and their influence on its mechanical and physicochemical properties. Various methods of incorporating carbon nanotubes into the concrete matrix, such as mixing, spraying, and modified nanotube application, are discussed, along with the effects on strength, elasticity, fracture resistance, and other mechanical properties of concrete.

Franklin et al. [25] primarily focuses on the assembly and modification techniques of carbon nanotube transistors, as well as the underlying principles of their electronic performance. The authors also address issues related to enhancing the efficiency and stability of carbon nanotube transistors. Additionally, the article presents examples of their applications in diverse fields, including electronics.

Alsubaie et al. [26] explores the vibration response of functionally graded carbon nanotube-reinforced composite (CNTRC) beams using a higher-order shear deformation beam theory. The beams are reinforced with single-walled carbon nanotubes in a polymer matrix and supported by a viscoelastic foundation. Various reinforcement distribution patterns and porosity distributions are considered. The study incorporates damping coefficient, Winkler's, and Pasternak's parameters to analyze viscosity effects on the foundation. Results indicate that adding a damping coefficient enhances vibration performance, especially with increased spring constant factors. The fundamental frequency rises with higher porosity coefficients, suggesting a significant impact of porosity on beam vibrational characteristics [26].

Madenci et al. [27] investigates the application of carbon nanotubes (CNTs) in strengthening polymer matrix composites through experimental tensile testing and fabrication of carbon nanotube reinforced composite (CNTRC) beams. The study explores various micromechanical models to optimize the mechanical properties of CNTRC materials. The research concludes that the optimal CNT amount for reinforcing composite beams is 0.3%, as higher concentrations lead to reduced tensile capacity. A comparison between experimental results and Finite Element Models using ABAQUS demonstrates good conformance. The study also evaluates Young's Moduli using the prediction models Halpin-Tsai and Mixture-Rule, revealing accurate predictions by Halpin-Tsai and significantly lower accuracy with Mixture-Rule [27].

Zhang et al. [28] investigates the wave propagation behavior of carbon nanotube reinforced composite (CNTRC) beams on an elastic foundation, employing various higher order shear deformation beam theories such as Euler and Timoshenko theories. Wave equations for CNTRC beams are derived using the Euler-Lagrange principle, and the relationship between wave number and circular frequency is established through the eigenvalue method. Phase and group velocities are determined as functions of wave number, and material properties of CNTRC beams are estimated using the mixture rule. Comparative analysis with Euler and Timoshenko beam theories is conducted to validate findings. The mathematical model is numerically verified against existing results, and the study explores the impact of CNT enhancement modes, volume fraction, spring factor, and other factors on CNTRC beam wave propagation behaviors [28].

Mangalasseri et al. [29] delves into the energy harvesting properties of a magneto-electro-elastic cantilever beam enhanced with carbon nanotubes (CNT) during transverse vibration. Employing a lumped parameter model to mathematically represent the coupled multiphysics problem, the study explores the impact of factors like CNT distribution, substrate material, and length-to-thickness ratio on energy harvesting behavior. The research aims to enhance comprehension of smart material-based energy harvesting systems, specifically those reinforced with CNT, offering potential implications for the design and analysis of CNT-based smart structures [29].

Arshid et al. [30] explores the vibration analysis of functionally graded microplates with polymeric nanocomposite patches, incorporating porosity and hygrothermal effects. The microplates feature three layers, including an FG porous core and piezoelectric nanocomposite face sheets with stiffness-enhancing CNTs. Using a quasi-3D shear deformation theory and modified couple stress theory, the equations of motion are derived. Figure-presented results allow assessment of material properties, geometry, foundation moduli, and hygrothermal effects on vibrational behavior. Findings indicate that increasing

CNT volume fraction improves mechanical properties, subsequently raising natural frequency. Notably, the study emphasizes the substantial impact of accounting for the hygrothermal environment in analyzing these structures [30].

Huang et al. [31] introduces a size-dependent model for analyzing the static stability of doubly curved micro-panels made of advanced composites reinforced with carbon-based materials. The research combines a seven-unknown shear deformation theory in curvilinear coordinates with a non-classical approach to assess the mechanical performance of micro-size shells accurately. Utilizing a virtual work of Hamilton statement and an analytical technique based on double-Fourier series, the study analyzes micro shells with fully simply supported conditions at edges. Results show that CNTs reinforced composite curved shells exhibit a hardening response under buckling, with the critical buckling load highest for spherical panels, followed by elliptical, cylindrical, and hyperbolic panels. Moreover, changes in CNTs weight fraction significantly impact the static stability characteristics of CNTs reinforced composite curved size-dependent shells [31].

Heidari et al. [32] addresses the need to enhance the realism of engineering models for nanocomposites, critiquing past studies that assumed idealized properties of carbon nanotubes (CNTs). The study focuses on incorporating real-world complexities like nanotube waviness, defects, and aggregation observed in experiments. It introduces size effects into nanocomposite models, validating their accuracy through comparisons with experimental data and theoretical models. The article presents numerical examples illustrating buckling behaviors of nanocomposites, emphasizing the application of nonlocal theory to account for size effects. Overall, it is the first comprehensive exploration of these aspects, providing a crucial reference for future research in nanocomposite materials [32].

Undertaking a comprehensive review in the field of carbon nanotube applications within building materials is justified by several compelling reasons. First, it offers a methodical framework for gathering and comparing data from a myriad of sources. This systematic approach enhances comprehension by researchers and engineers as they navigate the wealth of available information. Second, the review serves as a spotlight on the pivotal challenges confronted by those working with carbon nanotubes in building materials. Through this scrutiny, critical obstacles come to the fore, pinpointing areas ripe for further exploration and unveiling the realm's untapped potential.

Furthermore, this review becomes a tapestry that weaves together diverse data from research articles, patents, and technical reports. This comprehensive mosaic fosters a panoramic understanding while circumventing potential distortions from cherry-picked examples.

Despite the extensive research into carbon nanotubes, there are a number of gaps in this area. The first shortcoming is the lack of wider comparative research comparing the properties of many building materials with and without CNTs. This limits the ability to make an objective comparison and identify clear benefits of using CNTs in construction. Therefore, more detailed studies based on comparative analysis can be a valuable contribution to the field. In addition, a more detailed discussion of the technical issues and challenges associated with the industrial scaling up of CNT production and its economic feasibility is essential for the practical introduction of CNTs in the construction industry and requires further research and development. In light of the above, this study also aims to fill knowledge gaps and present new results related to the use of CNTs in construction. This review can also provide recommendations on how to overcome current technical and environmental challenges to ensure a more sustainable and efficient use of CNTs in the construction industry.

This review also covers all aspects of CNT properties and their impact on construction materials, allowing us to assess the full potential of CNTs and their applicability in various construction industries. Additionally, previous studies may be limited in their methodology

and scope. Some may be based on a small sample of data or use outdated data analysis methods and tools. This paper improves the methodological approach using modern data analysis tools and a wide range of literature sources to obtain more comprehensive and reliable results.

The practical significance of this review article lies in its ability to systematically inform interested industries and to move towards a more sustainable future by exploring the potential use of CNTs as material amplifiers. The article highlights the problems that need to be solved before practical implementation and gives an idea of current research in this area.

2. Methodology

This section provides a comprehensive outline of the study's methodology. It begins with the careful formulation of research goals and objectives. A thorough search of scientific literature is conducted using Scopus and Google Scholar databases to gather a wide range of relevant works. The collected data undergo meticulous analysis using Python and VOSviewer software. Python is employed for data processing, statistical analyses, and result visualization, while VOSviewer aids in creating a visual representation of the literature landscape, highlighting key themes and authors. The study then delves into diverse methods for carbon nanotube production, including CVD, electrochemical deposition, and mechanical stretching, alongside insights from illustrative studies. Catalysts for CVD are scrutinized for their impact on nanotube formation. Strategies for integrating carbon nanotubes into building materials are explored, covering blending, coating, and functionalized nanotube incorporation, with a focus on enhanced properties. The research tasks encompass defining goals, selecting methods, investigating nanotube properties, and processing results. This culminates in drawing meaningful conclusions from the accumulated data and comparative analyses. The following steps outline the methodological process (Fig 1) :

2.1. Literature Search

A thorough literature search was conducted using two primary databases : the Scopus bibliographic and abstract database and the Google Scholar search engine. The search was performed by employing a combination of relevant keywords and phrases related to the research topic. The selected keywords were carefully chosen to ensure a comprehensive coverage of the relevant literature.

2.2. Data Extraction

After obtaining the search results, data from the Scopus database was downloaded in the RIS format (Research Information Systems) to facilitate further analysis. The RIS format is widely used for bibliographic data exchange and is compatible with various data analysis tools.

2.3. Data Analysis in Python

Data analysis was performed using the Python programming language, leveraging its powerful libraries for data manipulation and analysis. The bibliographic data downloaded in the RIS format was processed and cleaned to ensure the accuracy and consistency of the dataset. Python's data analysis libraries, such as Pandas and NumPy, were utilized for data cleaning, transformation, and preparation.

2.4. VOSviewer Analysis

In addition to the Python-based data analysis, the data was also imported into VOSviewer, a powerful bibliometric analysis software. VOSviewer allowed us to create visual representations of the co-occurrence of keywords, authors, and publications within the dataset. This analysis provided valuable insights into the most prominent research themes, patterns, and interconnections among different concepts.

2.5. Integration of Results

The findings from both the Python-based data analysis and the VOSviewer analysis were integrated to create a comprehensive picture of the literature landscape related to the research topic. The combined results enabled us to identify key research trends, influential authors, and significant clusters of related publications.

2.6. Interpretation and Discussion

The interpreted results from the data analysis were discussed in the context of the research objectives and existing literature. The implications of the findings were critically analyzed to draw meaningful conclusions and identify potential areas for future research.

By adopting this methodological approach, the study aimed to ensure a robust and systematic exploration of the existing literature and provide a solid foundation for the subsequent stages of analysis and discussion.

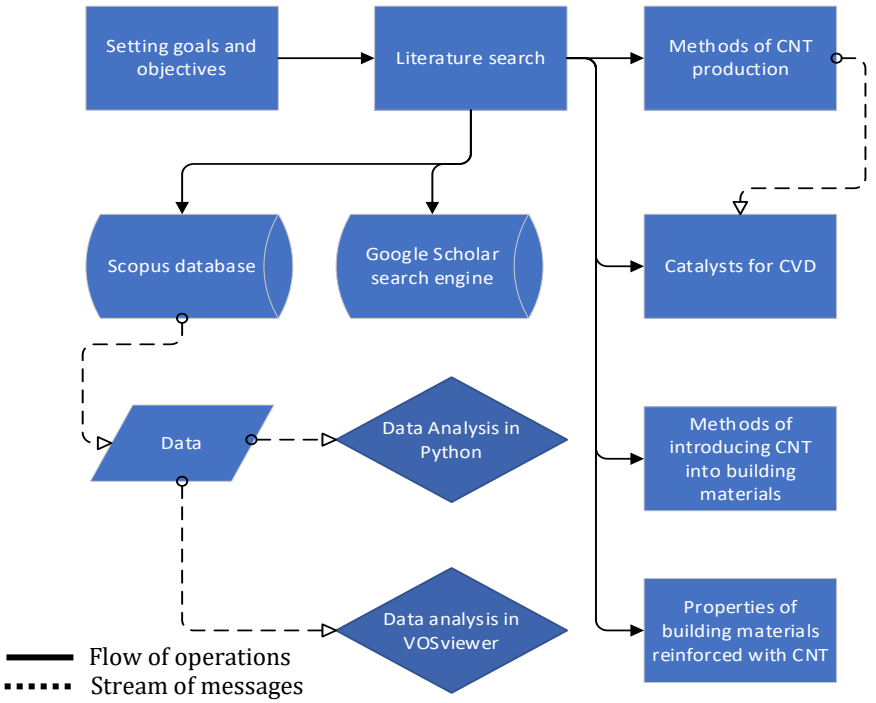

Fig. 1. Methodology flowcharte

3. Results and Discussion

3.1 CNTs Analysis in Research Literature: 2019-2023

To gather relevant information, a literature search was conducted using the Scopus bibliographic and abstract database, as well as the Google Scholar search engine. The search results were visualized using the VOSviewer software, which facilitated the analysis of keywords found in the publications. The data covered a significant number of articles for 2019-2023: a total of 57,633 articles were found. Of these, 11,816 articles for 2019 were used in visualization and analytics, 20,000 articles (due to the fact that Scopus database allows you to upload no more than 20,000 results to one file at a time) for 2020 (a total of 23,520 articles were found in 2020), 20,000 articles for 2021 year (23,580 articles were found), 20,000

articles for 2022 (24,490 articles were found) and 20,000 articles for 2023 (22,237 articles were found). This comprehensive study of research articles highlights the growing interest and importance of carbon nanotubes in various fields, including construction.

Figure 2 illustrates the distribution of frequently encountered keywords in publications over time. These keywords include nanocomposites, single-walled CNTs, polymers, supercapacitors, heat resistance, tensile strength, and other relevant terms. On the other hand, Figure 3 presents the clustering results of the same search query.

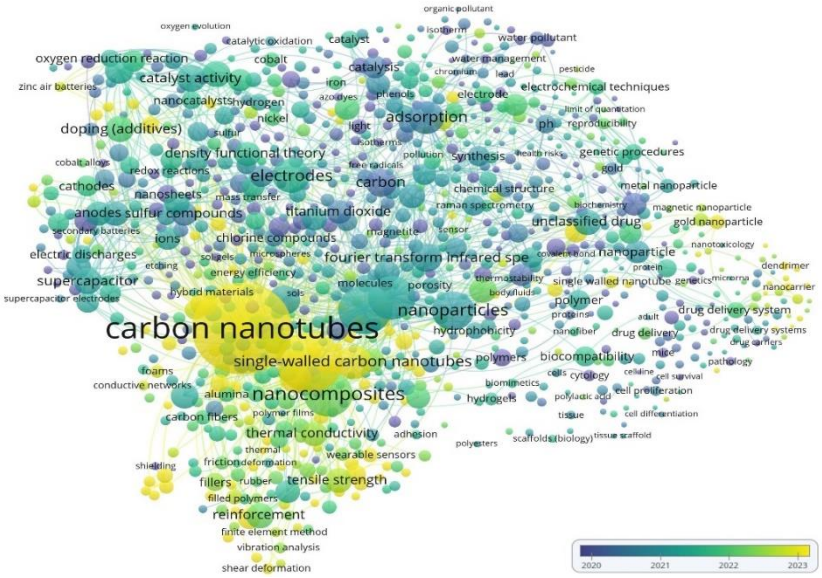

Fig. 2. Search results for "carbon nanotubes" in Scopus

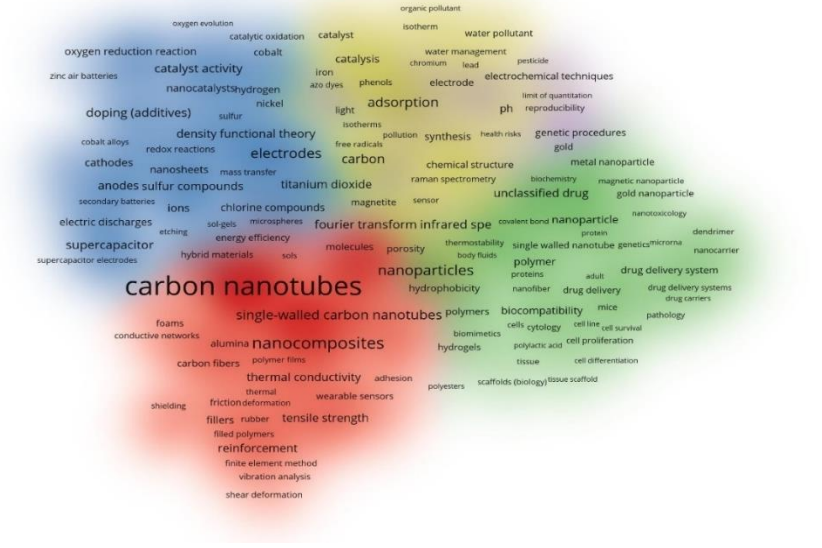

Fig. 3. Results of the "carbon nanotubes" search query in Scopus by cluster

A set of articles published between 2019 and 2023 related to the query "carbon nanotubes" was extracted. Subsequently, an analysis was conducted using Python scripts, and the Pandas and Matplotlib libraries were employed to process and visualize the data.

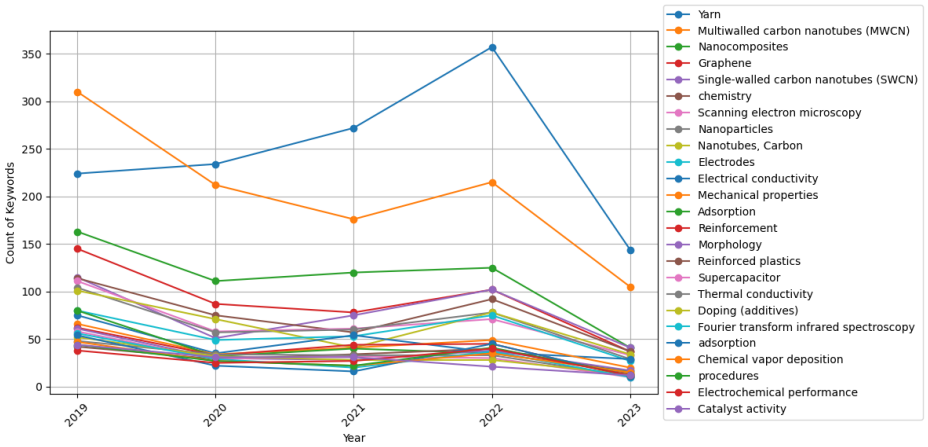

Fig. 4. Results of keyword analysis by articles

Figure 4 depicts the distribution of the 25 most frequent keywords in the articles, categorized by year (Fig 4). The results presented in Figure 4 were generated by excluding certain words from the search, namely "Review", "Article", "Priority journal", "Controlled study", "Graphene", "Carbon nanotubes", "Nanotechnology", and "Nanoparticle". These words were excluded due to their high frequency and tendency to appear in nearly all articles. Conversely, Figure 6 showcases a histogram containing all keywords, including the highly frequent ones, presenting the grouping of the 15 most frequent keywords by publication year.

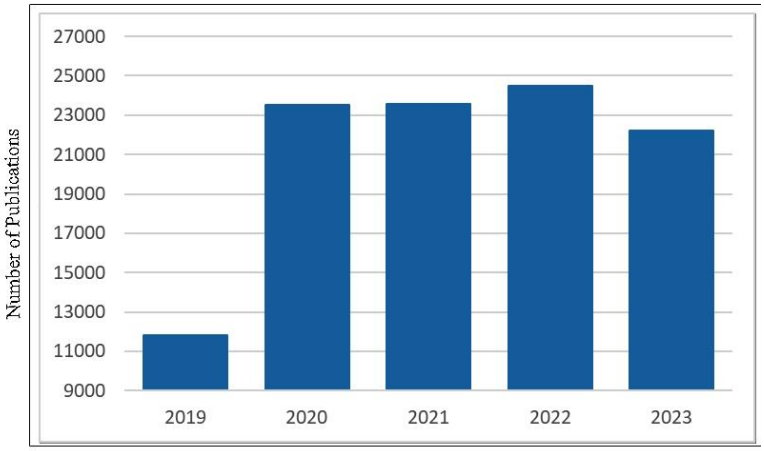

Fig. 5. Number of articles by year

Figure 5 shows a histogram of the total number of publications for the query "carbon nanotubes" in the Scopus database. As can be seen in Figure 5, the number of articles for this query peaks in 2022. The number of articles shows a decrease in 2023. This decrease in 2023 can be explained by the fact that the data only cover the period up to September 2023, which is not the full year of data collection.

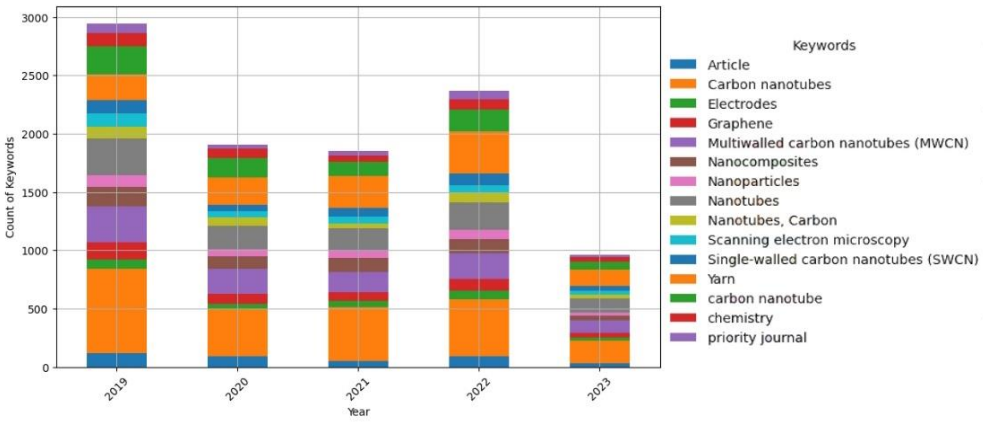

Fig. 6. The most high-frequency keywords

Using the Jupyter Notebook web development tool and the Word Cloud library, word clouds were generated to visualize the search results. The word cloud of frequently encountered words in the abstracts of review articles is displayed in Figure 7a, while Figure 7b presents the word cloud of high-frequency keywords. A cloud of words frequently found in the abstracts of all reviewed articles is shown in Figure 8a, and a cloud of high-frequency keywords is shown in Figure 8b. These visual representations offer an intuitive means to observe the prominence and relevance of various words within the search results.

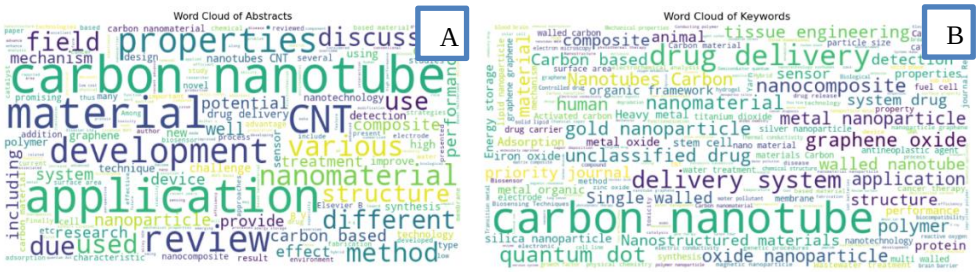

Fig. 7. Word cloud (a) abstracts of review articles, (b) keywords

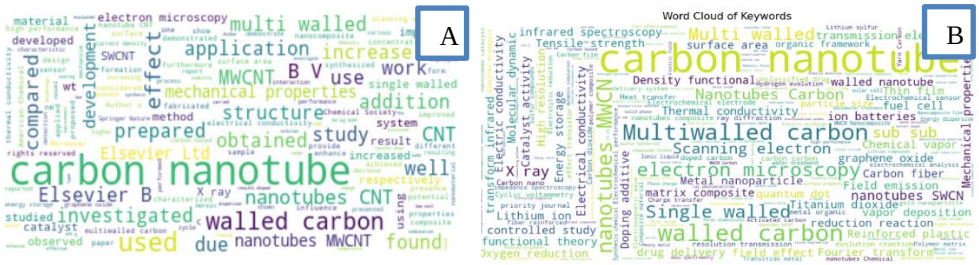

Fig. 7. Word cloud (a) abstracts of all articles, (b) keywords

3.2 Methods of CNT production

CNT production methods encompass various techniques used to create carbon-based nanotubes. Among them, the most common methods include hydrocarbon pyrolysis, laser ablation of graphite, electric arc synthesis, and chemical vapor deposition (CVD).

Hydrocarbon pyrolysis involves decomposing hydrocarbons into carbon and other byproducts to produce CNTs [33, 34]. This method is extensively utilized for large-scale CNT production. Pyrolysis of hydrocarbons, also known as pyrogenic synthesis, entails the decomposition of organic compounds into carbon, hydrogen, and oxygen at high temperatures. It is a widely employed approach for producing carbon nanomaterials like carbon nanotubes, fullerenes, and graphene.

Special equipment called a pyrolysis unit (Fig.8) is employed for the pyrolytic synthesis of hydrocarbons. The unit consists of a reaction chamber where the synthesis occurs and a gas supply system. To prevent contamination of nanomaterials, the reaction chamber is typically made of stainless steel or ceramics. The pyrolytic synthesis process initiates by heating the hydrocarbons to temperatures exceeding 700°C. At this temperature, the hydrocarbons decompose into carbon, hydrogen, and various gases. The carbon remains in the form of nanoparticles that subsequently aggregate.

One notable advantage of pyrolytic synthesis is its capability to produce carbon nanomaterials with high purity and uniformity. Furthermore, this method allows for control over the size and shape of the resulting nanomaterials. However, pyrolytic synthesis does have some drawbacks, such as high equipment costs and energy consumption. Additionally, the hydrocarbon pyrolysis method may not be suitable for producing all types of CNTs and may be limited in cases where specific properties are desired (e.g. high electrical conductivity or resistance to oxidation).

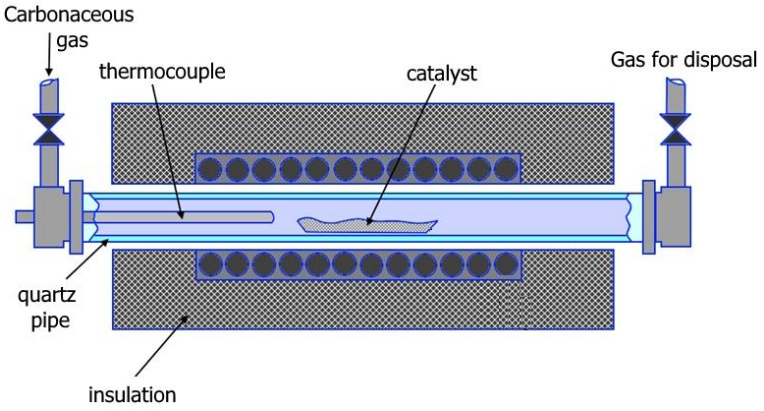

Fig. 8. Schematic diagram of a horizontal batch rector for pyrolysis of carbon-bearing gases [35]

Laser ablation of graphite involves the use of powerful laser radiation to evaporate and subsequently condense graphite in a vacuum (Figure 9). This process breaks down graphite crystals into individual carbon atoms, which then assemble into nanoparticles [36, 37].

Laser ablation of graphite is capable of producing ultra-dispersed carbon nanostructures, including carbon nanotubes, carbon nanofibers, carbon nanoribbons, and more. These nanomaterials possess unique properties such as high electrical conductivity and mechanical strength, making them highly promising for diverse applications. Additionally, laser ablation of graphite is an environmentally friendly method as it does not require the use of chemicals or high temperatures, thus making it attractive for industries like automotive, aviation, and space.

However, one of the main challenges associated with laser ablation is the difficulty in controlling the process of obtaining carbon nanostructures. The high temperature and pressure generated during ablation make it challenging to precisely control the size and shape

of the resulting nanoparticles. This variability can impact the properties and application of the nanotubes. Another drawback is the high cost of laser ablation equipment and materials. This method necessitates expensive laser equipment and specialized materials like graphite. Moreover, the ablation process itself is time-consuming and energy-intensive. Low productivity can also be considered a disadvantage of laser ablation. While this method produces carbon nanostructures with a high degree of purity and uniformity, it may be less efficient compared to other nanoparticle production methods.

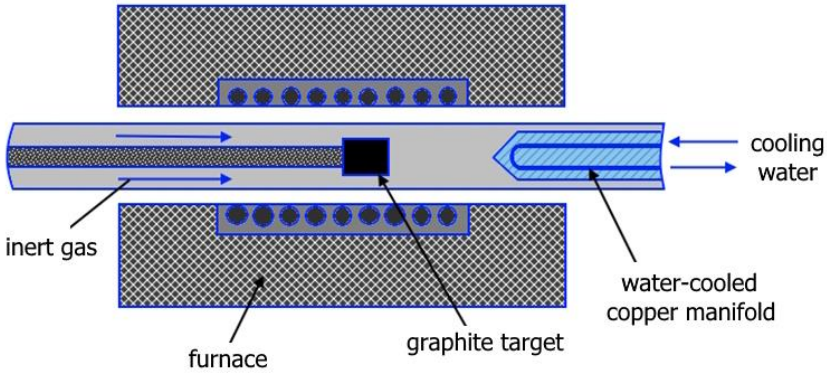

Fig. 9. Schematic diagram of a machine for CNT production by laser ablation [35]

In a study conducted by the authors [38], they successfully synthesized graphene sheets in two stages at room temperature and normal pressure. The process involved laser ablation of graphite, followed by repeated irradiation of suspensions after removing the graphite target. X-ray analysis confirmed the production of different carbon materials.

Several factors influence the synthesis of carbon nanotubes through laser ablation, including temperature, catalyst selection, choice of inert gas, laser power, wavelength, pressure, and fluid dynamics near the carbon target [39]. These parameters must be carefully controlled during the synthesis of CNTs.

Electric arc synthesis is another method utilized for producing CNTs. This technique involves the use of an electric arc to heat and melt a metal catalyst such as graphite or nickel (Fig.10). The molten metal is then cooled and crystallized, resulting in the formation of nanotubes. During the synthesis process, the nanotubes emerge from the catalyst and are collected in bundles, which can be subsequently cleaned and shaped to the desired size and form. The main advantages of electric arc synthesis for CNTs are its simplicity, speed, and controllability. Additionally, this method does not require the use of expensive catalysts, thereby reducing production costs.

Electric arc synthesis offers a versatile approach for producing various carbon nanomaterials, including carbon nanotubes and carbon nanoparticles, with diverse sizes and shapes. Despite its drawbacks such as high energy consumption and low yield, it remains a widely employed method in scientific and industrial fields involved in the synthesis and application of carbon nanomaterials [40, 41].

Chemical vapor deposition (CVD) is one of the most prevalent methods for producing carbon nanotubes [43, 43]. It enables the synthesis of large-diameter and high-purity CNTs. CVD involves the decomposition and condensation of organic compounds in the gas phase onto a catalyst surface at high temperatures.

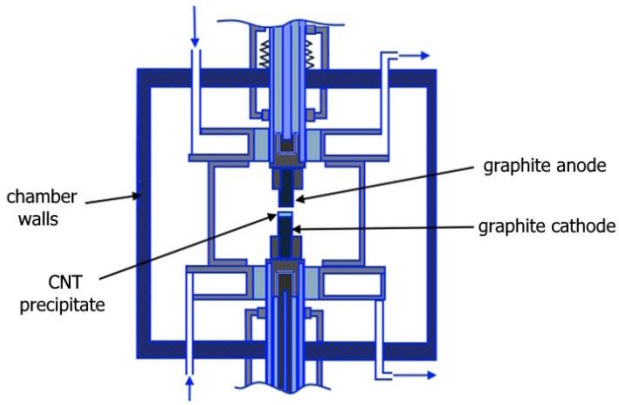

Fig. 10Schematic diagram of a plant for producing CNT by electric arc synthesis [35]

In CVD, specialized reactors are employed where high temperatures (typically ranging from 700 to 1,000 degrees Celsius) and pressures are maintained (Figure 11). The reactor is filled with a gas mixture comprising a reagent (e.g., benzene or acetylene) and a catalyst (commonly graphite or nickel). At elevated temperatures, the reagent decomposes into gaseous products, which subsequently condense on the catalyst's surface. This process leads to the formation of nanotubes that accumulate on the surface and continue to grow until they reach a specific diameter.

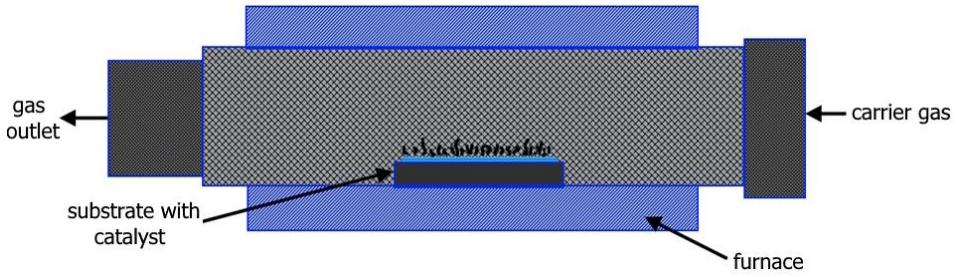

Fig. 11 Chemical vapor deposition (CVD) method [44]

Chemical vapor deposition (CVD) is not only utilized for producing carbon nanotubes but also for other types of carbon nanomaterials, including amorphous carbon and carbon nanoparticles. The method offers the advantage of controlling the size and shape of the resulting structures by adjusting process parameters such as temperature, pressure, and gas mixture composition. CVD is capable of generating nanotubes with varying diameters and shapes, making it a versatile technique for numerous applications.

CVD finds applications in various fields, including microelectronics. In microelectronics, CVD is employed for producing integrated circuits and other electronic devices. The method of CVD offers several advantages:

Precise control: CVD allows for meticulous control over the size and shape of nanomaterials through precise adjustment of process parameters.

High purity: CVD produces nanomaterials with high purity and low impurity concentrations due to its robust process control.

Convenience and efficiency: The CVD process are easily automated, enabling precise adjustment of process parameters. Moreover, the method is highly efficient, yielding significant volumes of nanomaterials.

Unique properties: CVD-derived nanomaterials often exhibit distinctive physical and chemical properties that are not typically observed in materials produced through other methods.

Thus, chemical vapor deposition is a powerful and effective approach for producing carbon nanomaterials with exceptional properties, making it a popular choice in scientific research [45, 46]. For instance, a study [47] compared single-walled carbon nanotubes produced via CVD with those obtained using an improved electric arc synthesis method. The results revealed that CVD-produced nanotubes exhibited superior dispersion into thin fibers, even at the monolayer level.

In another work [48], mechanical properties and corrosion resistance of composites reinforced with CVD-produced carbon nanotubes at varying mass fractions (0.1%, 0.2%, and 0.5%) were investigated. The study determined that the most corrosion-resistant structure was achieved in composites reinforced with 0.2% CNTs.

Chemical Mechanical Exfoliation (CME) is a method for producing high-purity carbon nanotubes (CNTs) through a combination of chemical and mechanical processes. The process involves the preparation of graphite as a starting material, followed by chemical functionalization to facilitate subsequent processing. Mechanical exfoliation, which can be achieved through various methods, separates graphite layers and forms CNTs. Purification and characterization complete the process, providing high-quality CNTs with controlled properties [49–52].

The Floating Catalyst Method utilizes catalyst nanoparticles suspended in a gaseous carbon source to produce high-quality CNTs. The process involves catalyst preparation, reactor installation, catalyst suspension in a carrier gas, introducing the carbon source, catalytic growth, nanotube recovery, and post-treatment. This method offers controlled CNT production with various properties but requires careful control of catalyst parameters and addressing potential impurities [53–55].

The Template-Assisted Growth method directs CNT growth using templates with defined nanopores. Steps include template preparation, catalyst deposition, introducing a carbon source, nanotube growth within the template's nanopores, template removal, and post-treatment [56–59]. This method provides precise control over CNT diameter, length, and alignment and is compatible with various substrates [60].

Plasma Enhanced Chemical Vapour Deposition (PECVD) is a technique for creating Uniform Nanotube Arrays (UNAs) via plasma-assisted chemical reactions [61–65]. It involves substrate preparation, precursor gas introduction, plasma discharge, thin film deposition, and post-processing. PECVD offers controlled UNA production, uniform characteristics, and versatility across different substrates for applications in various industries [66–68].

Electrochemical Deposition (ECD) is another method for producing UNAs on a conductive substrate through an electrochemical cell [69–71]. It involves substrate preparation, immersion in an electrolyte solution, application of an electric potential, nanotube growth, and post-processing [72–74]. ECD allows precise control over nanotube dimensions and produces uniform arrays for applications in energy storage, catalysis, sensors, and electronics [75–79].

Solvothermal Method: This method involves a hydrothermal reaction in a solvent at high temperatures and pressures to synthesize CNTs with controlled properties and structures [80–84]. The process includes precursor preparation, reactor setup, sealing, reaction and

growth, cooling, product recovery, and post-treatment [85–88]. It shows promise for CNT synthesis but has limitations such as cost, complexity, and environmental impact [89–96].

Mechano-thermal Synthesis: This approach combines mechanical activation and thermal treatment to produce highly ordered and crystalline CNTs [97–99]. Mechanical forces are used to break down precursor carbon materials, creating amorphous carbonaceous precursors [100–102]. Subsequent thermal treatment at high temperatures transforms these precursors into well-aligned CNTs [103,104]. Challenges include the need for precise control of mechanical activation and high-temperature processing [105,106].

Flame Synthesis: This technique uses a controlled combustion process to generate CNTs by decomposing precursor solutions in a high-temperature flame [97,106,107]. It offers continuous and scalable production, allowing adjustments in CNT size, diameter, and structure. Challenges include controlling CNT growth and dealing with unwanted byproducts [106,108,109].

Chemical Vapor Infiltration (CVI): CVI involves the deposition of carbon atoms onto a substrate through the controlled decomposition of gaseous precursors [110–112]. It allows for versatile, large-scale production, and the ability to tailor CNT properties. Deposition conditions impact growth rate, structural characteristics, and alignment [113–116].

Electrolysis: The Electrolysis method applies an electric current to a carbonaceous electrode immersed in an electrolyte solution [117,118]. This process leads to the direct synthesis of CNTs, providing control over their growth conditions and properties[119,120]. Challenges include low yield, slow growth rates, and the need to control CNT morphology and purity [121–123].

Understanding the advantages and disadvantages of various CNT production methods is crucial for selecting the most suitable approach for specific tasks. Table 1 provides an overview of CNT production methods, offering brief descriptions of their principles of action along with their advantages and disadvantages. The benefits and disadvantages mentioned in this table are not exhaustive and may vary depending on specific process parameters and conditions.

Table 1. Methods of CNT production

The method	Principle of operation	Benefits	Disadvantages
Pyrolysis of hydrocarbons [124–132]	Decomposition of organic compounds at high temperature	Low cost, high performance, scalability, good controllability of process parameters	CNTs may contain impurities, which can reduce their quality and properties; small diameter of CNTs; CNTs may be less resistant to oxidation than nanotubes produced by other methods
Laser ablation of graphite [106,133–138]	Effects of laser radiation on carbon materials	Possibility to produce single- and multi-layer CNTs of different shapes, high purity	High equipment costs, limited product volume, difficulty in controlling process parameters
Electric arc fusion [139–145]	Heating of carbon materials in an electric arc	Production of various sizes of CNTs, high synthesis rate	Limited size, need for inert gases, high cost, risk of CNT damage
Chemical vapor deposition (CVD) [146–154]	Reaction between a carbon source and other reagents in the gas phase	Ability to produce CNTs on different substrates, control of size and shape of nanostructures, high productivity, scalability	Risk of reaction byproducts that can adversely affect the quality of the resulting tubes, difficulty in setting up the process

The method	Principle of operation	Benefits	Disadvantages
Chemical Mechanical Exfoliation (CME) [155–160]	Mechanical exfoliation of layered carbon materials	Simple and low-cost method, production of high-quality CNTs with good crystallinity	Limited scalability, difficulty in achieving uniformity in CNT properties
Floating Catalyst Method [55,161–168]	Suspension of catalyst nanoparticles in a gaseous carbon source	Production of single- and multi-walled CNTs, high purity, control over diameter and alignment	High equipment costs, limited product volume, difficulty in controlling process parameters
Template-Assisted Growth [58,59,169–175]	Utilization of templates or nanopores to direct CNT growth	Precise control over diameter, length, and alignment of CNTs, scalability	Template removal can be challenging, limited choice of template materials
Plasma Enhanced Chemical Vapor Deposition (PECVD) [63,65,176–179]	Chemical reaction in a plasma environment	High deposition rate, good control over CNT properties, compatibility with various substrates	Plasma-induced damage to CNTs, requirement for specialized equipment
Electrochemical Deposition [180–185]	Electrochemical reaction for CNT growth on a conductive substrate	Controlled growth of CNTs, precise control over dimensions and alignment	Limited scalability, potential for electrode contamination
Solvothermal Method [84,186–192]	Hydrothermal reaction in a solvent at high temperatures and pressures	Synthesis of CNTs with regulated properties and structures	Limited scalability, high temperature and pressure requirements
Mechano-thermal Synthesis [97,193–198]	Combination of mechanical activation and thermal treatment	Production of highly ordered and crystalline CNTs, scalability	Potential for impurities, careful control of mechanical activation parameters required
Flame Synthesis [199–205]	Controlled combustion of hydrocarbon or carbon-containing precursors	Continuous production, control over CNT size and structure, in situ functionalization	Challenges in controlling CNT growth and uniformity, potential formation of unwanted byproducts

The characteristics of nanotubes obtained can vary based on the method used and process conditions. In conclusion, each of these methods possesses its own advantages and disadvantages, and the selection of a specific method depends on the particular requirements and production conditions.

For instance, pyrolysis of hydrocarbons is the most commonly employed method; however, it may result in the formation of impurities and structural defects in the nanotubes. Laser ablation of graphite yields nanotubes with high purity but necessitates costly equipment. Electric arc synthesis produces nanotubes with larger diameters but incurs high energy costs. Chemical vapor deposition allows for precise control over the structure and properties of nanotubes.

Therefore, the choice of CNT production method should be justified and based on a compromise between quality requirements and economic efficiency.

3.3. Catalysts for CVD

Chemical vapor deposition (CVD) is a widely employed and cost-effective technique for manufacturing carbon nanotubes (CNTs). During CVD, CNTs are synthesized by depositing the dissociation products of hydrocarbons onto a metal catalyst that serves as a "seed," followed by the growth of nanotubes on the catalyst surface.

The selection of a suitable catalyst plays a crucial role in achieving efficient CNT generation through the CVD method. An ideal catalyst should possess a high surface area, acting as the active center for chemical reactions, and offer a sufficiently high temperature for carbide decomposition. These catalysts can also be employed in the synthesis of other carbon nanostructures like graphene or fullerenes. The choice of catalyst depends on the desired structure and properties of the nanoparticles.

Chemical vapor deposition catalysts are primarily composed of metals or their oxides and are instrumental in expediting the formation of carbon nanostructures. Nickel is one of the most commonly used catalysts for CVD, enabling the synthesis of CNTs with high purity and uniform structure. Other metals such as copper, chromium, and molybdenum are also utilized as catalysts. Additionally, carbon precursors like graphite or CNTs can function as catalysts for CNT synthesis.

For instance, a copper-based catalyst can be employed in CNT synthesis. When a carbon-containing gas such as acetylene is heated, nanotubes form on the copper surface, which can then be separated from the catalyst for various applications.

Numerous catalysts are employed for CNT production via CVD under diverse conditions. These catalysts include metals like iron (Fe), nickel (Ni), cobalt (Co), their alloys, as well as surface-modified metals and their oxides.

While iron and nickel were initially the most prevalent catalysts for CNT production through CVD, researchers have been exploring more effective catalysts in recent years to achieve high-quality CNTs [206–208]. Studies indicate that iron alloys with other metals such as copper (CuFe) or cobalt (FeCo) can enhance productivity and purity during the CVD process. In CVD, carbon nanomaterials are formed by the interaction between carbon and various gases, typically hydrogen, carbon monoxide, or acetylene. Catalysts can comprise metals, oxides, hydroxides, or other substances, accelerating the decomposition of carbon-containing gases into carbon atoms and molecules, which subsequently combine into nanostructures.

The choice of catalyst depends on the desired properties of the resulting nanomaterials and the specific synthesis conditions. Ongoing advancements in catalyst research for CNT production via chemical vapor deposition allow for continual updates and improvements to this method [209–218]. It is important to select the most appropriate catalyst for specific process conditions and the desired properties of the nanotubes.

Table 2 below presents catalysts and their properties for CVD. However, it is worth noting that the size and quality of CNTs may slightly vary depending on process conditions such as temperature, pressure, and gas mixture composition. The first column of Table 2 denotes the catalyst (or elemental basis for combined catalysts) with corresponding references to studies utilizing them for CNT production. The subsequent columns in Table 2 provides general information and characteristics of each catalyst, independent of the referenced studies in the first column. This is because catalyst properties can differ based on the process conditions of vapor deposition, including temperature and pressure. Therefore, selecting the most suitable catalyst for specific process conditions and desired nanotube properties is crucial.

Table 2. CVD catalysts

Catalyst	Diameter of nanotubes	Quality of nanotubes	Features
Ferrocene [219-221]	~ 10-20 nm	Low	Ferrocene-based nanotubes are not only of low quality, but also heterogeneous in width. | It is quite unstable and can form a heterogeneous film.
Ni [222-224]	~ 10-100 nm	High	Ni-based nanotubes are of high quality and have a single-wall structure. Quite cheap and widespread catalyst. Provides high quality nanotubes and very few defects in the structure.
Co [225,226]	~ 5-50 nm	Very high	Co-derived nanotubes are of very high quality and have a single-wall structure, which makes them possible for use in electronics. It is also a cheap catalyst.
Fe [227-230]	~ 10-100 nm	Average	Fe-based nanotubes are of average quality and may contain additional defects in the structure. It is chemically stable but forms a lower quality film than Ni, Co.
Al [231,232]	~ 10-60 nm	Average	Al-based nanotubes are of average quality and may contain additional defects in the structure. It is not the best catalyst, but can be used to produce nanotubes of a certain type.
Pt [233,234]	~5-50 nm	Very high	One of the best sparse catalysts: provides very high quality and purity of nanotubes.
Pd [235,236]	~5-50 nm	Very high	Similar to Pt in its characteristics, but cheaper.
Ti [237]	~5-100 nm	Average	Provides good quality nanotubes and a structure different from that obtained with other catalysts.
Mo [238]	~5-50 nm	Average	It can be used to produce multiwalled nanotubes.
Cu [239-242]	~5-50 nm	High	It has high catalytic activity for CVD reaction. It can be used to produce nanotubes of different materials.
Au [243,244]	~5-50 nm	Low	It is not the best catalyst for the CVD reaction and is not normally used for producing nanotubes.
Co Ni Au [235]	Various sizes	Miscellaneous	Combinations of catalysts can combine the advantages of different materials. For example, the combination of Co and Ni gives very good nanotube quality, and the combination of Ni and Au gives good charge transfer properties.

Table 2 clearly illustrates the substantial variation in cost, nanotube quality, and defectiveness among catalysts. The selection of a specific catalyst depends on numerous factors, including availability and cost. For instance, Fe serves as an inexpensive catalyst, enabling the production of nanotubes at low temperatures and pressures. However, the resulting nanotubes exhibit lower quality and often contain numerous defects. On the other hand, Pt is highly expensive but yields high-quality nanotubes with a low defect rate. Moreover, catalysts can be combined to enhance results [246-249]. For example, the combination of Ni and Co yields nanotubes of the highest quality and low defect levels, whereas the combination of Cu and Ni enables the production of nanotubes with diverse materials.

This section provides a concise overview of catalysts utilized in the CVD method, underscoring their significant influence on the properties of carbon nanotubes. Consequently, selecting an appropriate catalyst becomes crucial in achieving desired carbon nanotube properties, such as size and structure, and should align with specific requirements.

3.4. Methods of Introducing CNT Into Building Materials

The incorporation of carbon nanotubes (CNTs) into building materials has emerged as a novel and increasingly popular strategy for enhancing their mechanical and physical properties. Recent years have witnessed numerous studies exploring the utilization of CNTs in diverse building materials, including concrete and reinforced polymers [250,251].

Mechanical introduction stands out as one of the primary approaches for integrating CNTs into building materials. This method involves simply adding nanotubes to the material during its preparation in the form of dust, powder, or liquid. To ensure a more uniform dispersion of CNTs within the material, techniques such as ultrasonic or magnetic treatment can be employed [252–254]. Ultrasonic processing facilitates the pulverization of CNT particles, leading to their more even distribution throughout the material. Similarly, magnetic treatment can be utilized to fractionate CNT particles into smaller sizes, thereby enhancing their dispersion within the material [255,256].

In addition to mechanical introduction, other processing techniques can be employed to enhance the efficacy and quality of the CNT incorporation process. Surfactant functionalization is one such method, where surfactants are used to improve the wettability of CNTs, allowing for better dispersion within the matrix [257–261]. Sonication, which utilizes high-frequency sound waves, can also be used to break up CNT agglomerates and ensure better dispersion [262–265].

The specific method of incorporating CNTs into building materials depends on the desired properties and operating conditions. For example, in the case of concrete, CNTs can be added as nano powders or through the creation of functional coatings [266–268]. This helps improve the strength, corrosion resistance, and shrinkage reduction of the concrete. For materials like bricks and glass, functional coatings and nano powder addition can enhance properties such as fire resistance, thermal insulation, transparency, and scratch resistance [269,270].

In the case of metals, including steel and aluminum, CNTs can be introduced through the addition of nano powders or by creating functional coatings [271,272]. This improves the durability and corrosion resistance of the metals [273–275]. Plastic materials can also benefit from the addition of CNTs in the form of a liquid additive, which enhances wear resistance and durability [276,277]. Similarly, the addition of CNT powder to rubber materials improves wear resistance and elasticity [278–280].

These examples highlight the versatility of CNT incorporation, as different materials can be enhanced by utilizing CNTs in various ways. The selection of materials and the specific method of introducing CNTs depend on the desired improvements and the specific requirements of each application. Continued research and collaboration among material scientists, engineers, and industry professionals will drive further advancements in this field, opening up new possibilities for the construction industry.

In essence, the mechanical introduction of CNTs represents one of the most commonly employed methods for their incorporation into building materials, with additional processing techniques employed to enhance the efficacy and quality of the process. Table 3 provides a concise overview of exemplary building materials exhibiting improved properties, along with the prevalent methods employed for incorporating CNTs into their structural composition.

Table 3. Construction materials with improved CNT properties

Construction materials	Improved properties	Methods of introducing CNT into building materials
Concrete [281–286]	Strength, corrosion resistance, shrinkage reduction	Adding nanopowders, creating functional coatings
Brick [287–291]	Resistance to fire, improved thermal insulation	Creating functional coatings, adding nanopowders
Glass [292–296]	Transparency, scratch resistance	Adding nanopowders, creating functional coatings
Metal [297–302]	Durability, corrosion resistance	Adding nanopowders, creating functional coatings
Plastic [303–307]	Resistance to wear and tear, durability	CNT liquid additive
Rubber [308–315]	Wear resistance, elasticity	Addition of CNT powder

These examples provide a glimpse into the diverse range of materials that can be enhanced by incorporating Carbon Nanotubes (CNTs). The selection of materials and the method of introducing CNTs depend on specific requirements and operating conditions governing each case.

CNTs offer tremendous potential in strengthening building materials by augmenting their mechanical properties, including increased strength, stiffness, impact resistance, and abrasion resistance. Furthermore, CNTs can impart electrical or thermal properties to materials, thereby expanding their functionality. However, the practical utilization of CNTs beyond the confines of laboratory settings is still constrained. One of the primary challenges involves achieving a uniform dispersion of CNTs within the material while preventing their aggregation, as such clustering can substantially compromise the material's quality [316–317].

Presently, nanotechnology finds active application across various industries. One significant application area involves the modification of building materials to enhance their properties. This section elucidates the methods employed for introducing CNTs into building materials and explores their potential application in creating efficient and secure building structures.

3.4.1. Mechanical Methods

One approach for incorporating carbon nanotubes (CNTs) into building materials is through mechanical methods. These methods rely on simple mechanical processes to introduce CNTs into the structure of the material. Ultrasonic dispersion is a technique where CNTs are dispersed within a material using ultrasonic waves. The waves create cyclic compression and tension zones in the material, resulting in the dispersion of nanoparticles. This method is highly efficient and produces nanometer-sized particles, enabling the production of materials with enhanced strength and durability. For instance, researchers [318] investigated the impact of multi-walled carbon nanotubes (MWNTs) with varying internal diameters on the mechanical properties and microstructure of cement-based materials. Ultrasonic dispersion was employed to uniformly distribute MWNTs within the cement-based materials. Experimental results demonstrated that increasing the diameter of MWNTs modified the flexural and compressive strength of cement-based materials.

Ultrasonic dispersion is a widely used method for incorporating carbon nanotubes (CNTs) into building materials. This process involves subjecting CNTs to high-frequency sound waves (typically in the range of 20-100 kHz) to break up agglomerates and disperse individual CNTs throughout the material matrix. The equipment used includes a sonicator, which generates the sound waves, and a vessel containing the material to be dispersed. The power output and frequency depend on the application and material properties [319,320].

Ultrasonic dispersion not only breaks up agglomerates but can also functionalize CNTs by introducing chemical groups onto their surfaces. This enhances their compatibility with the matrix and improves mechanical properties. The smaller size of dispersed CNTs (typically tens of nanometers) leads to a more homogeneous distribution within the matrix. One advantage of ultrasonic dispersion is its ability to achieve a more uniform dispersion of CNTs, enhancing the mechanical properties of the material. It also reduces agglomeration of CNTs, preventing the formation of large clusters that could negatively impact the material's properties. Furthermore, ultrasonic dispersion enhances the interfacial bonding between CNTs and the material matrix, improving load transfer and the overall integrity of the composite material.

Mechanical activation is another method where the material is mechanically loaded to activate the surface and create defects. These defects, including dislocations, voids, and microcracks, facilitate strong bonding between CNTs and the building material, resulting in a composite material with improved strength and durability [321,322]. Researchers [323] investigated various modified cement composites produced through mechanical activation. They utilized superplasticizers and CNTs with different structures and functionalities as modifiers. The study revealed that the bio resistance coefficient values of cement composite samples obtained by mechanically activating the binder and incorporating superplasticizers were 13% higher than those of the control composition.

Mechanical exposure involves saturating the material with CNTs using moving parts such as mills or mixers. This method generates high mechanical energy, breaking down the CNTs into nanometer-sized particles that then penetrate the material. By employing this approach, it is possible to produce materials with enhanced strength and durability while minimizing the quantity of CNTs required [324–326].

Overall, the utilization of mechanical methods for introducing CNTs into building materials enables the creation of materials with nanoparticle reinforcement, resulting in improved strength and durability. However, achieving the maximum effect requires careful selection of the optimal component ratios and material processing techniques.

3.4.2. Electrochemical Methods

Electrochemical techniques offer highly effective means of incorporating carbon nanotubes (CNTs) into various building materials, including concrete, asphalt, and polymer composites. One such technique is the electrochemical deposition of thin carbon films onto the material surface. This process involves depositing carbon nanoparticles onto the material surface by applying an electric current in a solution containing suitable reagents [327–329]. The method finds wide application in diverse fields, including electronics, catalysis, cosmetics, as well as scientific research in nanotechnology and materials science.

Electrochemical carbon deposition has proven beneficial in several areas. Firstly, it can be used to coat electrodes, thereby enhancing their conductivity in different devices and systems [330,331]. Secondly, carbon coatings serve as catalysts on material surfaces, improving the efficiency of processes such as electrolysis or gas synthesis. Additionally, carbon coatings find application in the production of electronic components like supercapacitors and solar cells.

The advantages of electrochemical carbon deposition include precise control over the deposition process, the ability to create thin, uniform, and high-quality carbon films, cost-effectiveness compared to other coating methods, and the potential to modify the properties of carbon coatings to suit specific needs [332–334]. However, there are also certain limitations associated with this technique. It requires careful adjustment of the deposition process to achieve the desired surface properties, and there may be defects in the film structure that could impact its properties. Furthermore, there are limitations on the types of materials onto which the coating can be applied.

Kim et al. demonstrated the use of a chemical deposition method to enhance the performance of a fuel cell electrode by employing CNTs and a Pt catalyst as the foundation. Their results indicated that the number of catalytic centers in Pt/CNTs obtained through electrochemical deposition was approximately three times higher [335]. Another study by Lee et al. proposed an efficient and practical approach for creating a new composite comprising ultrathin nanowire films by combining an assembly process with cost-effective electrochemical deposition technology [336].

Electrodeposition, another method for introducing CNTs into building materials, involves embedding CNTs into the material surface through an electrochemical reaction. The process utilizes an electric field to deposit CNTs onto the material surface. CNTs, serving as nanoparticles, enhance the properties of building materials that typically consist of metallic or polymeric components. The electrodeposition process begins with the preparation of a solution containing CNTs, which is then placed in an electrolytic bath. The material is immersed in the bath and connected to an electrode, while another electrode connected to an electric current source is positioned adjacent to the material. Subsequently, the electrodeposition process initiates, resulting in the deposition of CNTs onto the material surface.

This method offers advantages such as simplicity and the ability to control material conductivity by adjusting the CNT concentration in the solution. Additionally, materials obtained through CNT electrodeposition exhibit good shape and size matching, reducing the likelihood of defects [337,338]. However, this method has drawbacks, including a relatively low CNT concentration compared to other CNT introduction methods and the requirement for specialized equipment, making it a relatively complex process.

3.4.3. Chemical Methods

Chemical techniques offer a range of possibilities for incorporating Carbon Nanotubes (CNTs) into building materials, resulting in the development of materials with exceptional properties, including enhanced strength, thermal conductivity, and electrical conductivity. However, each method possesses its own set of advantages and disadvantages, and the selection of a specific technique depends on the intended purposes and requirements of the manufactured materials.

One such method is chemical deposition, which involves depositing a CNT solution onto the surface of the material [339–341]. This process begins by preparing a solution containing CNTs in a specialized liquid, typically ethylene glycol or other solvents. Various application techniques such as spraying or dripping are employed to apply the nanotube solution onto the material's surface.

Another method, known as metal fusion, employs the combination of different metals to coat the material's surface. This technique involves mixing CNTs with metal powders and subjecting them to high temperatures to form a composite material. Metal fusion exhibits notable advantages, including high wear resistance and excellent thermal conductivity, making it suitable for the production of construction materials like metal structures and pipelines.

The metal fusion method finds extensive use in modern industries, enabling the production of high-quality composite materials with unique properties unattainable by conventional carbon steels and other materials [342–345]. The process of metal alloying comprises several steps:

Alloy preparation: Various methods, such as mechanical mixing of metal powders with CNTs in a ball mill, are utilized to create a homogeneous mixture.

Material formation: The mixture from the previous step is heated to temperatures typically exceeding 1000 degrees Celsius, causing the metal powders and CNTs to merge and form a

homogenous material with the desired properties. Heat treatment: Heat treatment is necessary to enhance the material's mechanical properties and harden it. The composite material is subjected to specific temperatures during heat treatment and subsequently cooled down. The advantages of the metal fusion method for building material production are numerous. These include high resistance to wear and mechanical damage, excellent thermal conductivity, significant resistance to corrosion and chemical reactions, and the ability to produce composite materials in various shapes and sizes.

In summary, chemical methods, such as chemical deposition and metal fusion, allow for the integration of CNTs into building materials, offering exceptional properties [346–349]. The choice of method depends on specific requirements, with metal fusion providing excellent wear resistance, thermal conductivity, corrosion resistance, and versatility in creating composite materials with unique shapes and sizes.

3.4.4. Physical Deposition Methods

Physical deposition methods for carbon nanotubes (CNTs) encompass a range of technologies and processes utilized to distribute nanotubes onto the surfaces of building materials.

Ion-beam deposition is a technological process that employs ion streams to generate thin coatings on material surfaces [350,351]. The process initiates by producing a high-frequency flux of ions dispersed in a gas medium, typically within a vacuum. The flux is then directed towards the substrate where the coating is intended to adhere. The ion flux is separated into positive and negative ions.

The distinctive feature of ion-beam deposition lies in the ability to precisely control the size, energy, and velocity of the ions. This enables the production of thin coatings with thicknesses ranging from fractions of a micron to several micrometers. When the ion flux impacts the material surface, it induces various chemical reactions and alterations in the CNT molecules, resulting in the formation of a thin layer on the material surface. These coatings can be created from a diverse range of materials, including ceramics, metals, plastics, and glass [352–355].

Ion-beam deposition finds extensive applications in the manufacturing of various devices such as microprocessors, sensors, optical devices, and more [356–358]. During the ion-beam deposition process, several factors need to be considered, including ion energy, the type of ions employed, the deposition medium, and the pressure within the vacuum chamber.

Magnetron sputtering is a technology employed to produce thin coatings on diverse material surfaces [359–362]. In this process, materials are atomized within a vacuum and then deposited onto the target surface. Special generators generate electric and magnetic fields within the working chamber to initiate the sputtering process. Atomized materials find applications in various industries, including electronics production, solar cells, medical products, and others. Magnetron sputtering enables the production of coatings with different characteristics based on specific requirements [363–365].

In a particular study [366], the authors discussed various applications of magnetron sputtering in the development of crucial materials for lithium batteries, categorized according to battery components such as electrode materials and solid electrolytes. The authors also proposed future prospects to drive the advancement of magnetron sputtering technology.

Vacuum cathode discharge represents one of the methods for growing CNTs on material surfaces [367,368]. It involves utilizing a vacuum chamber with a cathode composed of graphite or other carbon materials. When a high-frequency discharge passes through the chamber between the anode and cathode, CNTs begin to grow on the cathode's surface. The key advantage of this method is the ability to create CNTs with predetermined characteristics, including length, diameter, and structure. Additionally, this method is relatively straightforward and controllable.

However, there are also certain disadvantages. The CNT growth procedure within the vacuum chamber requires significant energy and time, which poses challenges for scaling up this method for industrial applications. Furthermore, the equipment cost for vacuum cathode discharge is relatively high. Nevertheless, vacuum cathode discharge remains an effective method for CNT creation in specific applications such as electronics, catalysis, and other fields [369,370].

3.4.5. Nanotechnology Methods

Electron beam lithography represents a cutting-edge technology used to fabricate micro- and nanostructures through controlled local treatment of a material's surface with an electron beam [371–374]. By employing this technology, carbon nanotubes (CNTs) can be incorporated into construction materials to enhance their mechanical properties. The process of introducing CNTs using electron beam lithography involves several key stages:

- Surface Preparation: The material's surface is meticulously cleaned and machined to create a specific pattern suitable for CNT integration.
- Applying Resist: A resist material, capable of undergoing changes when exposed to an electron beam, is applied onto the material's surface.
- Exposure: An electron beam is precisely directed onto the resist-coated surface, resulting in the formation of the desired pattern.
- Manifestation: The resist material that has been exposed to the electron beam is selectively removed from the areas corresponding to the pattern.
- Application of CNTs: A solution containing CNTs is applied onto the material's surface, specifically targeting the created pattern. This procedure reinforces the mechanical properties of the material at the required locations.
- Cleaning: Excess resist and any remaining residues are thoroughly eliminated from the material's surface.

This method of material reinforcement enables the production of lightweight yet robust and durable materials suitable for various construction applications [375,376]. Electron beam lithography serves as an effective approach to bolster building materials, facilitating the creation of more dependable and long-lasting structures [377–379].

Another technique involves incorporating CNTs into construction materials using a paramagnetic filler, which operates on the principles of electromagnetic induction [380–382]. Initially, CNTs are synthesized via chemical vapor deposition (CVD) using a suitable catalyst. Subsequently, the dispersion of CNTs in a solution containing a paramagnetic filler is performed to generate a nanocomposite. In some cases, the CNTs are treated with the paramagnetic filler before dispersion. The nanocomposite undergoes further treatment using an electromagnetic field created through electromagnetic induction. The paramagnetic filler within the solution responds to the induction field and adheres to the CNTs, resulting in the formation of an electromagnetic composite.

Consequently, a composite material comprising CNTs embedded with paramagnetic fillers is obtained [383–385]. This approach enhances the composite's magnetic susceptibility while simultaneously improving its mechanical and functional properties. The integration of CNTs using paramagnetic fillers presents a promising avenue for developing novel construction materials with enhanced characteristics. Although some of these methods can be expensive and require specialized equipment and expertise, they enable the creation of stronger and more flexible building materials utilizing the potential of CNTs.

Table 4. Methods of CNT introduction

Group	Methods	Principle of operation
Mechanical methods	Ultrasonic dispersion [386–388]	Mechanical impact creates pores in the material, where CNTs are then inserted
	Mechanical activation [307,389]	Mechanical impact creates pores and cracks in the material, where CNTs are then introduced
	Mechanical impact [390–393]	Mechanical impact creates additional spaces for nanotubes
Electrochemical methods	Electrochemical deposition [394–398]	An electrochemical process using a metallic cathode that serves as a current-carrying element
	Electrodeposition [399–403]	Using electrodeposition to create a thin layer of carbon inside the material
Chemical methods	Chemical deposition [404–407]	Using catalysts to create CNTs
	Metal alloying method [408–412]	A method that uses metal fusion to create organic compounds, which are then replaced by CNTs
Physical deposition methods	Ion Beam Deposition [378,413–416]	Using ion-beam deposition to create a thin layer of carbon on a material surface
	Magnetron sputtering [417–422]	Using magnetron sputtering of carbon to create a film on the material surface
	Vacuum cathode discharge [360,416]	Using vacuum cathodic discharge to create a thin layer of carbon on the material surface
Nanotechnology methods	Electron beam lithography [375,378,424,425]	Using a lithographic process to create microchannels on the material surface, where CNTs are then added
	Nanotubes with paramagnetic filler [385,426–429]	Using paramagnetic particles to trap CNTs in solution and direct them to the surface of the building material. The nanotubes then remain on the surface of the material and form a protective layer

Integrating carbon nanotubes (CNTs) into building materials offers numerous advantages, such as enhanced strength, increased resistance to corrosion and wear, and improved thermal insulation properties [340,430–433]. However, prior to their utilization in construction, extensive research and testing are imperative to ensure both their safety and effectiveness.

The study of CNT properties and their application in building materials is a rapidly advancing field in science and technology. Within this realm, the exploration of methods for incorporating CNTs into building materials holds considerable significance as a subject of investigation.

To summarize, the methods employed to introduce CNTs into building materials exhibit considerable potential for creating more robust and long-lasting materials. Nonetheless, it is essential to consider the specific characteristics of each method and assess its efficacy under distinct conditions. Furthermore, continuous research in this domain is vital to develop novel approaches and optimize existing ones, ultimately achieving optimal outcomes.

3.5. Properties of Building Materials Reinforced with CNT

In the past few years, there has been a growing interest among engineers and scientists in enhancing the quality of building materials to ensure better protection and durability for

structures against external forces. One promising avenue of research involves the incorporation of carbon nanotubes (CNTs) to reinforce these materials [434–438]. In this section, we will explore the characteristics of building materials that are strengthened by CNTs. It is important to note that the concentration of CNTs and other relevant parameters can have a significant impact on the properties of these materials. Gaining a thorough understanding of these properties can be valuable for the development of novel materials that can construct more dependable and long-lasting buildings and structures. Nonetheless, it is crucial to consider the issues of economic feasibility and environmental safety when pursuing these advancements.

3.5.1. Mechanical Properties

The reliability and durability of construction materials heavily rely on their mechanical properties. A promising area of research in this field involves the utilization of Carbon Nanotubes (CNTs) to enhance the strength of materials.

Strength: Research studies indicate that the incorporation of CNTs into building materials can substantially enhance their strength. Factors such as the concentration of nanotubes, their position within the material matrix, and the size of the matrix particles have a significant influence on strengthening the material. Furthermore, nanotubes can mitigate thermal stresses caused by temperature fluctuations, which further contributes to the material's strength.

Shi et al.[439] outlines the principal characteristics of carbon nanotubes/nanofibres, the techniques for dispersing CNTs in cement-based materials, and the properties of CNT-based materials following modification with cement. The study affirm that the inclusion of CNT enhances the mechanical characteristics of cementitious materials.

The investigation of Jung et al. [440] employed diverse quantities of CNTs (0, 0.2, 0.5, 0.8, 1.0 and 2.0 weight percent). Prior research has indicated that introducing CNTs into cement-based materials can enhance their mechanical characteristics and cut down on porosity. Nevertheless, surpassing a certain concentration result in a decline in compressive strength.

Research conducted by Thomoglou et al. [441] suggests that the optimal amount of CNTs in cement mortar can provide improvements in various mechanical properties. Specifically, it was found that the incorporation of 0.2 wt% MWCNTs resulted in an increase in flexural strength by approximately 5.7%, compressive strength by 18.4%, 6.2%, and 8.8% for nano-, micro- and hybrid-modified cement mortars, respectively, compared to conventional mortars. These findings highlight the potential of CNTs in enhancing the mechanical performance of construction materials.

Stiffness: The introduction of CNTs can also increase the stiffness of building materials. Numerous experiments have demonstrated that as the concentration of nanotubes increases, the stiffness of the material also increases. Moreover, the deformation mechanisms induced by the presence of nanotubes can enhance the material's overall stiffness.

Kumar et al.[442] introduces the dynamic stiffness method (DSM) as a tool for analyzing the vibrations of multilayered plates containing carbon nanotubes (CNTs). The authors apply the Vitruvian-William method to solve the frequency-dependent stiffness matrix, allowing for an examination of the effects of various parameters on the plate and layer configuration. The findings from this study can be valuable for the design of multilayered FG-CNT structures, providing insights into optimizing their vibrational characteristics and performance.

Li et al. [443], the authors focus on the enhancement of compressive stiffness in graphene aerogels using a unique approach inspired by the structure of leaves. By incorporating carbon nanotubes (CNTs) into the aerogel matrix, they create a new material called CNT-interlayered graphene aerogels (CSGAs) through the process of freeze drying. The researchers conduct

compression tests and observe that the presence of CNTs effectively reinforces the mechanical support of the aerogels, with the properties of CSGAs being influenced by the content of CNTs. Furthermore, molecular dynamics modeling reveals that an optimal concentration of CNTs forms a stable mesh structure, thereby preventing deformation of graphene nanosheets during bending. This study presents a promising strategy for the design of highly efficient graphene-based nanomaterials, thereby expanding the range of potential applications for these materials.

Fracture Resistance: CNTs can enhance the fracture resistance of building materials. For instance, studies have shown that carbon nanotubes can absorb impact energy and localize material damage [444–447]. This characteristic proves particularly valuable in safeguarding buildings and structures from the detrimental effects of explosions or natural disasters.

Table 5 presents a summary of the mechanical properties of CNT-enhanced materials in comparison to conventional building materials. The table encompasses four key characteristics of the materials: compressive strength, tensile strength, wear resistance, and corrosion resistance. According to the table, materials treated with CNTs exhibit significantly higher compressive strength, tensile strength, and wear resistance when compared to most industrial construction materials. However, it is important to note that the properties of improved CNT materials can vary considerably depending on the specific type of material and the technology employed.

Table 5. Characteristics of the properties of building materials with CNT

Characteristics	Most building materials	Materials improved by CNT
Compressive strength [448–452]	Relatively low	Up to 4 times higher
Tensile strength [453–458]	Relatively low	Up to 10 times higher
Resistance to wear and tear [459–465]	Relatively low	Up to 5 times higher
Corrosion resistance [466–475]	Relatively low	Above

Studies of the properties of building materials reinforced with CNTs show that this approach can significantly improve their mechanical properties. Positive effects can manifest themselves in the strength, stiffness, and resistance to failure of the materials. Understanding these properties may lead to the creation of more reliable and durable building materials for various objects and structures.

3.5.2. Thermal Properties

Enhancing the thermal properties of building materials is crucial for efficient energy utilization and ensuring comfort inside structures. Factors such as heat transfer, thermal insulation, and thermal stability greatly influence the performance of materials. One approach to improving these properties is through the incorporation of Carbon Nanotubes (CNTs).

CNTs possess exceptional thermal conductivity, and when integrated into materials, they can significantly enhance their ability to conduct heat. This improved thermal conductivity facilitates better temperature control within buildings, leading to reduced heating and air conditioning costs. By introducing CNTs, the overall thermal conductivity of the material increases, leveraging the exceptional thermal conductivity of CNTs themselves.

Consequently, the use of CNTs in building materials enhances their thermal properties, enabling more efficient utilization of energy resources and improving comfort levels indoors. Additionally, CNTs exhibit high thermal stability, resulting in increased thermal stability of the building materials. This enhancement improves the overall performance and prolongs the

service life of the materials. For example, concrete structures containing CNTs display enhanced resistance to fire and other hazards due to their improved ability to withstand higher temperatures.

Shin et al.[476] discuss the development of three types of thermoplastic polyurethane composites (TPU) based on carbon nanotubes (CNTs) to create lightweight, flexible, and heat-conducting materials for electromagnetic interference (EMI) protection. The composites were developed using a solution blending technique with non-solvent induced phase separation (NIPS). The study investigates the impact of CNTs of different lengths on EMI shielding, electrical conductivity, and thermal conductivity. The composite with long CNTs (10 wt.%) demonstrated remarkable EMI shielding efficiency of 42.5 dB and an electrical conductivity of 1.9 × 10-3 S/cm, while the composite with short CNTs exhibited a thermal conductivity of 0.51 W/mK, with a thermal conductivity enhancement exceeding 145% compared to pure TPU. The inclusion of long-length CNTs facilitated the formation of interconnected conductive networks within the TPU matrix, improving mechanical properties, EMI shielding, and electrical properties. Conversely, short CNTs showed significant electromechanical characteristics and heat transferability. The composites also demonstrated high sensitivity to electrical conductivity and minimal changes in EMI shielding effectiveness during repeated bending cycles. This study provides insights into different types of CNT-based TPU composites for superior EMI protection and thermal regulation in next-generation wearable and stretchable electronics.

Table 6. Thermal properties of building materials with CNT

Material	Thermal properties without CNT	Improved thermal properties using CNTs
Polymer composites [478–483]	May have limited thermal stability	The use of CNTs significantly improves thermal stability, reduces thermal conductivity and increases material strength
Ceramics [484–489]	Has high thermal resistance, but often does not have high strength	Use of CNTs increases material strength and thermal resistance
Metals [490–493]	Can have relatively high thermal conductivity and low thermal stability	Use of CNTs increases material strength and thermal resistance
Concrete [494–500]	Has low thermal stability and limited strength	The use of CNTs can increase the strength of the material and improve its thermal stability
Glass [501–506]	Fragile material that does not have high thermal resistance	The use of CNT significantly increases the strength of the material and its thermal stability

In another related study of Jin et al. [477], the development of highly thermally conductive polymer composites with excellent dielectric and mechanical properties for electronic devices is discussed. The researchers incorporated boron nitride, graphene nanoplatelets, and carbon nanotubes into a polycarbonate matrix to enhance thermal conductivity, dielectric constant, and mechanical properties. The resulting composite exhibited a 647% increase in thermal conductivity, a 50-fold increase in dielectric constant, and improvements in yield strength, elongation at break, fracture toughness, and notched impact strength. Moreover, the composite displayed reduced ignitability and remarkable anti-dripping performance. This research presents an effective strategy for fabricating dielectric thermal conductive polymer composites with excellent properties for electronic devices.

Furthermore, incorporating CNTs in building materials can increase their heat capacity. This feature is particularly advantageous for constructing structures capable of absorbing and storing heat, effectively reducing heating costs. Overall, the utilization of CNTs in building

materials offers several benefits, including efficient energy utilization and improved comfort within buildings.

To further illustrate the impact of enhanced nanotechnology (CNTs) on thermal properties, Table 6 provides information on various materials. The table includes five different materials: polymer composites, ceramics, metals, concrete, and glass. Each material is presented with its thermal properties before and after the incorporation of CNTs. The first column displays the material names, while the second and third columns present the respective thermal properties before and after the inclusion of CNTs. The table also includes various parameters related to the thermal properties of the materials.

3.5.3. Electrical And Magnetic Properties

The introduction of CNTs into construction materials can lead to a change in their electrical properties. This is due to the fact that CNTs have high electrical conductivity. For example, in the work [507] experiments were conducted on cylindrical concrete samples containing different CNT content up to 0.04%, in which the effect of an alternating magnetic field on the strength was evaluated. Magnetization of samples containing 0.02% CNT gave higher strength than the introduction of 0.04% CNT without magnetization.

By the authors [508] studied the effect of temperature and water content on the electrical conductivity of cement mortar with different sizes of carbon nanotubes and revealed the effect of CNT size on the electrical conductivity of cement mortar. The results show that small diameter CNTs best improve the electrical conductivity of cement mortar. The electrical conductivity of cement mortar with different diameters of carbon nanotubes positively correlates with water content, and as the diameter of carbon nanotubes in the sample decreases, the effect of water content on the electrical conductivity of carbon nanotube cement mortar becomes less.

Corrosion resistance. CNTs can improve the corrosion resistance of construction materials such as metals, concrete and ceramics. CNTs can be added to building materials in the form of a nanofiller that forms a protective layer on the surface of the material. This layer prevents water, acids and other aggressive media from penetrating the interior of the material and protects it from corrosion [509,510]. Table 7 presents the results of studies related to the introduction of CNTs into various materials. Various materials such as concrete, epoxy, wood, rubber, brick, ceramic, steel and asphalt coating were investigated with respect to their properties after the introduction of CNT in different concentrations.

Recent research findings have demonstrated the positive impact of incorporating carbon nanotubes (CNTs) into various materials. This inclusion has led to enhancements in mechanical properties, as well as safeguarding against corrosion and fungal growth. However, determining the optimal concentration of CNTs in each material necessitates further investigation. These research outcomes serve as a foundation for subsequent studies and the optimization of materials containing CNTs. The integration of CNTs can substantially enhance the properties of diverse materials, ultimately contributing to the development of more robust and secure structures in the future.

The utilization of CNTs in building materials holds both economic and environmental advantages. On one hand, CNTs can augment the properties of construction materials, rendering them stronger, more corrosion-resistant, wear-resistant, and durable. Consequently, this can significantly diminish the costs associated with repairing and replacing such structures, thereby proving cost-effective. Additionally, CNTs can enhance the thermal characteristics of materials, facilitating energy savings and reduced expenditures on heating and air conditioning.

Nevertheless, the production of CNTs can be expensive and resource-intensive, potentially escalating the costs of CNT-infused building materials. Moreover, it is crucial to consider environmental factors, such as the ecological and health impacts of producing and utilizing such materials. Certain methods employed in CNT production may generate hazardous waste, emissions, and even disrupt ecosystems. Consequently, economic and environmental aspects must be carefully evaluated when employing CNTs to strengthen building materials. Striking a balance between economic efficiency and environmental safety is imperative when selecting construction materials.

Table 7. Construction materials with CNT

Material	CNT content	Short Description	Source
Concrete	0.10 wt.%, 0.15 wt.%	CNTs have been found to slow the propagation of microcracks by forming bridges through microcracks in concrete.	[511]
	0, 0.03, 0.08, 0.15, 0.25 wt%	The results showed that concrete prepared with high CNT content of 0.15 and 0.25 wt% increased flexural strength by more than 100% compared to concrete with 0% CNT.	[512]
	0.03 to 0.5 wt%	The results showed that 0.03% CNTs with long-term treatment increased the compressive, flexural, and tensile strength of conventional concrete by 23, 29, and 20%. The analysis also showed that using less CNTs (0.03 and 0.08 wt%) gave higher strength results regardless of the nanofiber treatment.	[513]
	0.05-0.1 wt%	It has been demonstrated that 0.05-0.1% CNTs effectively improve the tested properties, increasing the compressive, bending and cleavage strength as well as the fracture energy and modulus of elasticity by up to 23%, 18%, 27%, 42% and 15%, respectively.	[514]
	0.01, 0.02 , 0.03 wt%	The results of the experimental work showed that the introduction of CNT led to an increase in the compressive and tensile strength of the samples compared with the control sample.	[515]
Epoxy	0.107, 0.213 and 0.425 vol.%	The maximum synergistic effect of carbon and ceramic fillers on the dielectric properties of the epoxy-based composite was detected at a CNT content of 0.213 vol.%.	[516]
	0.1, 0.5 and 1 wt%	The results showed that the greatest improvement in the mechanical properties of the CNT/epoxy resin composite was observed in the sample with 0.5 wt% CNT, which had a tensile strength of 61 MPa and Young's modulus equal to 1.8 GPa.	[517]
	0.50 wt%	The tensile strength and toughness of epoxy nanocomposites with 0.50 wt% MWNTs improved by 21% and 46%, respectively, compared to conventional epoxy.	[518]
Wood	0.2%	Antifungal tests showed that stronger growth inhibition was obtained for samples treated with 0.2% MWNT_ZnO + solution. The most effective treatment is a concentration of 0.2% nanocomposite applied with a brush. Thus, protection of wood against mold and fungi was achieved, while providing improved mechanical strength and water protection properties.	[519]
Silicone Rubber	1.25, 5.5, 7.5, 9.5 wt%	The results show that the proposed mixed carbon nano conductive silicone rubber has good properties and great application prospects.	[520]

Material	CNT content	Short Description	Source
Brick	0.01%	The compression strength of the MUNT-added bricks was 53.9% and 45.52% higher compared to commercially available and traditional bricks.	[521]
Ceramics	0.1, 4 wt%	The thermal conductivities of nanocomposites with different amounts of carbon nanotubes (0, 1 and 4 wt%) were investigated. Thermal conductivity increases with increasing temperature, 1 wt% CNT/silica nanocomposite provides the highest thermal conductivity.	[522]
Steel	0.05, 0.1, 0.3, 0.5 wt%	Among all the samples tested, the lowest corrosion rate was achieved at 0.1 wt% CNT nanofluid, while the highest value was obtained at 0.5 wt% CNT nanofluid. At higher CNT concentrations, the accumulated CNTs can form active anode sites and increase the corrosion rate.	[523]
	0.2, 0.5, 1.0, 2.0 wt%	The composite samples showed increased wear resistance compared to the primary and commercial grades.	[524]
Asphalt surface	0.1, 0.5, 1 wt%	The study demonstrates that the introduction of CNT into asphalt cement improves asphalt concrete performance in both hot and cold weather, which in turn extends pavement life and saves maintenance costs.	[525]

Therefore, the utilization of CNTs to reinforce building materials represents a promising frontier in modern engineering. This technology presents unique opportunities to enhance material properties, including strength and fracture resistance. However, the successful implementation of this technology necessitates further research on the economic and environmental efficiency of producing and employing CNT-infused materials. Overall, the integration of CNTs in building materials instills hope for the creation of more durable and safer structures in the future.

3.6. Challenges and Future Directions in CNT Applications for Building Materials

The production and application of Carbon Nanotubes (CNTs) in building materials face several significant challenges. While CNTs hold immense promise for revolutionizing the construction industry, these challenges must be addressed for their widespread adoption. Here are some of the key issues:

- Large-Scale Production and Cost: Achieving large-scale production of high-quality CNTs at a reasonable cost is a major challenge. Current methods, like chemical vapor deposition (CVD), have issues with efficiency, high synthesis temperatures, and limited control over properties.
- Control of CNT Growth: Precise control over the growth process is needed to prevent the formation of unwanted carbon structures alongside desired CNTs, as these impurities can affect properties of construction materials.
- Uniform Dispersion: Ensuring uniform dispersion of CNTs within construction materials is crucial. Agglomeration can affect mechanical performance and poses health and safety risks to workers.
- Interface Bonding: Establishing a robust interface between CNTs and the matrix is essential for maintaining mechanical strength.
- Health and Safety Risks: The potential health and safety risks associated with CNTs must be carefully managed.

- Long-Term Stability and Durability: Evaluating the long-term performance of CNT-based composites under different environmental conditions is crucial to ensure durability.
- Cost-Effectiveness: The high cost of CNTs, processing steps, and potential alterations needed for large-scale production can impact economic feasibility.

To overcome these challenges and fully realize the potential of CNT-based building materials, recommendations for future research and development include:

- Optimization of CNT Dispersion Techniques: Investigate innovative dispersion methods to prevent agglomeration, such as functionalization, surfactants, and advanced mixing techniques.
- Enhancement of Interfacial Bonding: Develop strategies for improving the bond between CNTs and the matrix to optimize mechanical properties.
- Scalable Production Processes: Explore cost-effective synthesis methods and processing approaches that can be scaled up without compromising CNT quality.
- Safety and Environmental Impact Assessment: Thoroughly assess health and safety risks, develop safety protocols, and conduct environmental impact assessments.
- Multifunctional Material Development: Explore the potential for multifunctional CNT-based building materials, such as self-healing, self-cleaning, or thermal regulation capabilities.
- Long-Term Durability Studies: Conduct studies to evaluate the long-term stability and durability of CNT-based building materials under various environmental conditions.

4. Conclusions

CNTs have exceptional mechanical properties, making them attractive for construction. Adding CNTs to concrete enhances its strength and durability. However, challenges include higher material costs and the need for specialized methods to ensure proper distribution. Establishing standards and regulations for safety and reliability is crucial. Further research will determine better techniques for incorporating CNTs into building materials. Utilizing CNTs in construction has the potential to create more resilient structures.

The optimal concentration of CNTs to enhance the properties of different materials is also a crucial consideration and may vary depending on the material type and desired characteristics. Here are a few examples:

Polymeric materials: For polymers like polyethylene or polypropylene, an optimal concentration ranging from 0.5% to 5% is typically recommended. This concentration range achieves improved mechanical properties such as strength and stiffness, along with enhanced thermal and electrical conductivity. In the case of elastomers, such as rubber materials, the optimal CNT concentration is generally lower, usually between 0.1% to 1%, which enhances the elastic and mechanical properties, such as resistance to rupture and deformation.

Metallic materials: In the case of metals like aluminum or iron, the optimal concentration of CNTs typically falls within the range of 0.5% to 2%. Incorporating CNTs within metallic materials can enhance their strength, hardness, thermal conductivity, and electrical conductivity. It is also important to ensure proper dispersion of CNTs in the metal matrix to achieve homogeneity and uniform reinforcement of properties.

Ceramic materials: When it comes to incorporating carbon nanotubes (CNTs) into ceramic materials such as oxides, carbides, or nitrides, it is recommended to add them in the range of 1% to 10%. While this range can enhance properties such as strength, hardness, thermal conductivity, and dielectric properties, it is important to carefully consider the potential drawbacks. The use of a high concentration of 10% CNTs in ceramic materials can lead to

increased brittleness, affecting the material's integrity and processing. Additionally, it should be noted that such a high concentration may also significantly impact the overall cost of the material. Given these considerations, it would be advisable to reassess and fine-tune this concentration range to strike a balance between material properties and cost-effectiveness.

The optimal concentration of CNTs can vary based on specific conditions. Further studies and laboratory experiments will aid in determining the optimal CNT concentration for particular materials. Advancements in catalyst development play a significant role in improving the chemical vapor deposition (CVD) process for producing high-quality CNTs. Catalysts influence the growth, structure, morphology, and properties of CNTs. One approach involves employing novel catalysts based on metals or alloys such as nickel, iron, cobalt, molybdenum, and their compounds. These materials exhibit high activity and stability, contributing to more efficient CNT growth. Precious metal-based catalysts like platinum or palladium are also being explored to enhance CNT quality and achieve higher-quality single-layer and defect-free growth.

A comprehensive examination of catalyst shape and structure is crucial to optimize the CVD process and improve CNT quality. Studies have shown that the use of nanostructured catalysts, such as nanoparticles, nanowires, or nanofilms, facilitates more uniform and controlled CNT growth. Additionally, modifying the catalyst's surface with layers of other materials like oxides or carbides has been considered. This approach helps improve catalyst adhesion and stability, while also providing control over CNT growth. Optimizing the gas mixture composition used in the CVD process can significantly impact CNT growth and quality. The addition of different gases, such as hydrocarbons, inert gases, or decomposition intermediates, aids in controlling growth rate, structure, and dispersion of CNTs.

Practical applications of CNT-reinforced materials in construction include:

Concrete composites: CNTs can be employed to reinforce concrete, creating composite materials with high strength and resistance to breakage. This leads to improved mechanical properties of concrete.

Reinforcement of metal structures: Introducing CNTs into metal materials enhances their mechanical properties, such as strength and stiffness, thereby improving the reliability and durability of structures.

Heat and sound insulation: The use of CNTs in construction has the potential to improve heat and sound insulation properties. Despite encountering technical challenges, the utilization of CNTs in construction holds significant potential for creating stronger, more stable, and durable structures. Ongoing research and development efforts will enhance the technology and expand the use of CNTs in construction in the future.

References

[1] Meena CS, Kumar A, Jain S, Rehman AU, Mishra S, Sharma NK, et al. Innovation in green building sector for sustainable future. Energies. 2022;15(18):6631.
[2] Dabaieh M, Heinonen J, El-Mahdy D, Hassan DM. A comparative study of life cycle carbon emissions and embodied energy between sun-dried bricks and fired clay bricks. Journal of Cleaner Production. 2020;275:122998.
[3] Razzaq A, Sharif A, Ozturk I, Skare M. Inclusive infrastructure development, green innovation, and sustainable resource management: evidence from China's trade-adjusted material footprints. Resources Policy. 2022;79:103076.
[4] Jain N, Gupta E, Kanu NJ. Plethora of Carbon nanotubes applications in various fields–A state-of-the-art-review. Smart Science. 2022;10(1):1-24.
[5] Gupta N, Gupta SM, Sharma SK. Carbon nanotubes: Synthesis, properties and engineering applications. Carbon Letters. 2019;29:419-447.

[6] Zhang S, Hao A, Nguyen N, Oluwalowo A, Liu Z, Dessureault Y, et al. Carbon nanotube/carbon composite fiber with improved strength and electrical conductivity via interface engineering. Carbon. 2019;144:628-638.
[7] Makul N. Modern sustainable cement and concrete composites: Review of current status, challenges and guidelines. Sustainable Materials and Technologies. 2020;25:e00155.
[8] Kishore K, Pandey A, Wagri NK, Saxena A, Patel J, Al-Fakih A. Technological challenges in nanoparticle-modified geopolymer concrete: A comprehensive review on nanomaterial dispersion, characterization techniques and its mechanical properties. Case Studies in Construction Materials. 2023;e02265.
[9] Mishra D, Yu J, Leung C. Self-sensing and Self-healing 'Smart'Cement-based Materials–A Review of the State of the Art.
[10] Sun Z, Zhao L, Wan H, Liu H, Wu D, Wang X. Construction of polyaniline/carbon nanotubes-functionalized phase-change microcapsules for thermal management application of supercapacitors. Chemical Engineering Journal. 2020;396:125317.
[11] Qin Z, Li M, Flohn J, Hu Y. Thermal management materials for energy-efficient and sustainable future buildings. Chemical Communications. 2021;57(92):12236-12253.
[12] Mostafavi E, Iravani S, Varma RS, Khatami M, Rahbarizadeh F. Eco-friendly synthesis of carbon nanotubes and their cancer theranostic applications. Materials Advances. 2022;3(12):4765-4782.
[13] Srinivasan V, Kunjiappan S, Palanisamy P. A brief review of carbon nanotube reinforced metal matrix composites for aerospace and defense applications. International Nano Letters. 2021;1-25.
[14] Ali A, Koloor SSR, Alshehri AH, Arockiarajan A. Carbon Nanotube Characteristics and Enhancement Effects on the Mechanical Features of Polymer-based Materials and Structures–A Review. Journal of Materials Research and Technology. 2023.
[15] Zhu Q, Chua MH, Ong PJ, Lee JJC, Chin KLO, Wang S, et al. Recent advances in nanotechnology-based functional coatings for the built environment. Materials Today Advances. 2022;15:100270.
[16] Yang S, Bieliatynskyi A, Pershakov V, Shao M, Ta M. Asphalt concrete based on a polymer–bitumen binder nanomodified with carbon nanotubes for road and airfield construction. Journal of Polymer Engineering. 2022;42(5):458-466.
[17] Mitchell S, Qin R, Zheng N, Pérez-Ramírez J. Nanoscale engineering of catalytic materials for sustainable technologies. Nature Nanotechnology. 2021;16(2):129-139.
[18] Dhibar S. Unlocking the potential of molecular self-assembly: From nanotechnology to sustainable materials. Nanostructure Studies and Applications. 2023;1(1):2185.
[19] Norizan MN, Moklis MH, Ngah Demon SZ, Halim NA, Samsuri A, Mohamad IS, et al. Carbon Nanotubes: Functionalisation and Their Application in Chemical Sensors. RSC Advances, Royal Society of Chemistry. 2020;10:43704–43732.
[20] Garg A, Chalak HD, Belarbi MO, Zenkour AM, Sahoo R. Estimation of Carbon Nanotubes and Their Applications as Reinforcing Composite Materials–An Engineering Review. Composite Structures, Elsevier. 2021;272:114234.
[21] Anzar N, Hasan R, Tyagi M, Yadav N, Narang J. Carbon Nanotube - A Review on Synthesis, Properties and Plethora of Applications in the Field of Biomedical Science. Sensors International. 2020;1:100003.
[22] Fiyadh SS, AlSaadi MA, Jaafar WZ, AlOmar MK, Fayaed SS, Mohd NS, Hin LS, El-Shafie A. Review on Heavy Metal Adsorption Processes by Carbon Nanotubes. Journal of Cleaner Production. 2019;230:783–793.
[23] Sajid M, Asif M, Baig N, Kabeer M, Ihsanullah I, Mohammad AW. Carbon Nanotubes-Based Adsorbents: Properties, Functionalization, Interaction Mechanisms, and Applications in Water Purification. Journal of Water Process Engineering. 2022;47:102815.
[24] Zhang P, Su J, Guo J, Hu S. Influence of Carbon Nanotube on Properties of Concrete: A Review. Construction and Building Materials. 2023;369:130388.

[25] Franklin AD, Hersam MC, Wong HSP. Carbon Nanotube Transistors: Making Electronics from Molecules. Science, American Association for the Advancement of Science. 2022;378:726–732.
[26] Alsubaie AM, Alfaqih I, Al-Osta MA, Tounsi A, Chikh A, Mudhaffar IM, Tahir S. Porosity-Dependent Vibration Investigation of Functionally Graded Carbon Nanotube-Reinforced Composite Beam. Computers and Concrete. 2023;32:75–85.
[27] Madenci E, Özkılıç YO, Hakamy A, Tounsi A. Experimental Tensile Test and Micro-Mechanic Investigation on Carbon Nanotube Reinforced Carbon Fiber Composite Beams. Advances in Nano Research. 2023;14:443–450.
[28] Zhang YW, Ding HX, She GL, Tounsi A. Wave Propagation of CNTRC Beams Resting on Elastic Foundation Based on Various Higher-Order Beam Theories. Geomechanics and Engineering. 2023;33:381–391.
[29] Mangalasseri Arjun Siddharth, et al. Vibration based energy harvesting performance of magneto-electro-elastic beams reinforced with carbon nanotubes. Advances in Nano Research. 2023;14(1):27.
[30] Arshid E, Khorasani M, Soleimani-Javid Z, Amir S, Tounsi A. Porosity-Dependent Vibration Analysis of FG Microplates Embedded by Polymeric Nanocomposite Patches Considering Hygrothermal Effect via an Innovative Plate Theory. Engineering with Computers. 2022;38:4051–4072.
[31] Huang Y, Karami B, Shahsavari D, Tounsi A. Static Stability Analysis of Carbon Nanotube Reinforced Polymeric Composite Doubly Curved Micro-Shell Panels. Archives of Civil and Mechanical Engineering. 2021;21:1–15.
[32] Heidari F, Taheri K, Sheybani M, Janghorban M, Tounsi A. On the Mechanics of Nanocomposites Reinforced by Wavy/Defected/Aggregated Nanotubes. Steel and Composite Structures. 2021;38:533–545.
[33] Shinde MP, Karpoormath R, Patole SP, Inamdar SN. Insights into the Formation of Multiwall Carbon Nanotubes Using Simple Flame Pyrolysis Method. Materials Today: Proceedings. Elsevier. 2023.
[34] Bogdanova AR, Krasnikov DV, Khabushev EM, Ramirez B JA, Matyushkin YE, Nasibulin AG. Role of Hydrogen in Ethylene-Based Synthesis of Single-Walled Carbon Nanotubes. Nanomaterials. 2023;13:1504.
[35] Tkachev AG, Zolotukhin IV. Apparatura i Metody Sinteza Tverdotel'nykh Nanostruktur: Monografia. Mashinostroenie-1. 2007;315.
[36] Wei J, Yuan S, Zhang J, Zhou N, Zhang W, Li J, An W, Gao M, Fu Y. Removal Mechanism of SiC/SiC Composites by Underwater Femtosecond Laser Ablation. Journal of the European Ceramic Society. 2022;42:5380–5390.
[37] Vaghri E, Khalaj Z, Dorranian D. Investigating the Effects of Different Liquid Environments on the Characteristics of Multilayer Graphene and Graphene Oxide Nanosheets Synthesized by Green Laser Ablation Method. Diamond and Related Materials. 2020;103:107697.
[38] Hameed R, Khashan KS, Sulaiman GM. Preparation and Characterization of Graphene Sheet Prepared by Laser Ablation in Liquid. Materials Today: Proceedings. 2020;20:535–539.
[39] Shoukat R, Khan MI. Carbon Nanotubes: A Review on Properties, Synthesis Methods and Applications in Micro and Nanotechnology. Microsystem Technologies. 2021;27:4183–4192.
[40] Kaufmann Junior CG, Zampiva RYS, Anzanello MJ, Alves AK, Bergmann CP, Mortari SR. One-Step Synthesis of Carbon Nanoflowers by Arc Discharge in Water. Ceramics International. 2020;46:26229–26232.
[41] Pak A, Ivashutenko A, Zakharova A, Vassilyeva Y. Cubic SiC Nanowire Synthesis by DC Arc Discharge under Ambient Air Conditions. Surface and Coatings Technology. 2020;387:125554.

[42] Zulkimi MMM, Azis RS, Ismail I, Mokhtar N, Ertugrul M, Hamidon MN, Hasan IH, Yesilbag YO, Tuzluca FN, Ozturk G, Hasar UC. Enhancing Radar Absorption Performance of Sr-Hexaferrite by Hybridization with Coiled Carbon Nanotubes via Chemical Vapour Deposition Method. Diamond and Related Materials. 2023;137:110118.
[43] Enrique Samaniego-Benítez J, García-García A, Ivette Rivera-Manrique S, Ramírez-Aparicio J. Multiwalled Carbon Nanotubes/Zeolite Composite for Dye Degradation under Sunlight. Materials Today Communications. 2023;35:106046.
[44] Buranova, YS. Study of Nanotubes with Cobalt as a Filler using Transmission Electron Microscopy Methods. (In Russian). Proceedings of the Moscow Institute of Physics and Technology, 2011; 3(3), 30-41.
[45] Furuse A, Stevic D, Fujisawa K, Kang CS, Hayashi T, Kaneko K. Oxidation-Aided Cap-Removal of Chemical Vapor Deposition-Prepared Single-Wall Carbon Nanotubes. Adsorption. 2023;29:1–7.
[46] Wagner JB, Osman AM, Hendi A, Osman NMA. Multiwalled Carbon Nanotubes-Modified Metallic Electrode Prepared Using Chemical Vapor Deposition as Sequential Injection Analysis Detector for Determination of Ascorbic Acid. Nanomaterials. Multidisciplinary Digital Publishing Institute. 2023;13:1264.
[47] Almarasy AA, Hayasaki T, Abiko Y, Kawabata Y, Akasaka S, Fujimori A. Comparison of Characteristics of Single-Walled Carbon Nanotubes Obtained by Super-Growth CVD and Improved-Arc Discharge Methods Pertaining to Interfacial Film Formation and Nanohybridization with Polymers. Colloids and Surfaces A: Physicochemical and Engineering Aspects. 2021;615:126221.
[48] Say Y, Guler O, Dikici B. Carbon Nanotube (CNT) Reinforced Magnesium Matrix Composites: The Effect of CNT Ratio on Their Mechanical Properties and Corrosion Resistance. Materials Science and Engineering: A. 2020;798:139636.
[49] Vaisman L, Wagner HD, Marom G. The Role of Surfactants in Dispersion of Carbon Nanotubes. Advances in Colloid and Interface Science. 2006;128–130:37–46.
[50] Zhang R, Palumbo A, Kim JC, Ding J, Yang EH. Flexible Graphene-, Graphene-Oxide-, and Carbon-Nanotube-Based Supercapacitors and Batteries. Annalen der Physik. 2019;531:1800507.
[51] Tran TT, Mulchandani A. Carbon Nanotubes and Graphene Nano Field-Effect Transistor-Based Biosensors. TrAC Trends in Analytical Chemistry. 2016;79:222–232.
[52] Yang Z, Tian J, Yin Z, Cui C, Qian W, Wei F. Carbon Nanotube- and Graphene-Based Nanomaterials and Applications in High-Voltage Supercapacitor: A Review. Carbon. 2019;141:467–480.
[53] Dong H, Zhang L, Liao Y, Huang K, Lian C, Zhou X, Zhang Z, Kauppinen EI, Wu Z-S. Floating Catalyst Chemical Vapor Deposition Patterning Nitrogen-Doped Single-Walled Carbon Nanotubes for Shape Tailorable and Flexible Micro-Supercapacitors. Advanced Functional Materials. 2023;33:2301103.
[54] Abdullah HB, Ramli I, Ismail I, Yusof NA. Synthesis and Mechanism Perspectives of a Carbon Nanotube Aerogel via a Floating Catalyst Chemical Vapour Deposition Method. Bulletin of Materials Science. 2019;42:1–15.
[55] Hou PX, Zhang F, Zhang L, Liu C, Cheng HM. Synthesis of Carbon Nanotubes by Floating Catalyst Chemical Vapor Deposition and Their Applications. Advanced Functional Materials. 2022;32:2108541.
[56] Pavlenko V, Khosravi HS, Żółtowska S, Haruna AB, Zahid M, Mansurov Z, Supiyeva Z, Galal A, Ozoemena KI, Abbas Q, Jesionowski T. A Comprehensive Review of Template-Assisted Porous Carbons: Modern Preparation Methods and Advanced Applications. Materials Science and Engineering: R: Reports. 2022;149:100682.
[57] Zuo H, Duan J, Lyu B, Lyu W, Li Y, Mei X, Liao Y. Carbon Nanotube Template-Assisted Synthesis of Conjugated Microporous Polytriphenylamine with High Porosity for Efficient Supercapacitive Energy Storage. Macromolecular Rapid Communications. 2023;2300238.

[58] Kaur A, Bajaj B, Kaushik A, Saini A, Sud D. A Review on Template Assisted Synthesis of Multi-Functional Metal Oxide Nanostructures: Status and Prospects. Materials Science and Engineering: B. 2022;286:116005.
[59] Qin T, Li F, Liu X, Yuan J, Jiang R, Sun Y, Zheng H, O'Mullane AP. Template-Assisted Synthesis of High-Efficiency Bifunctional Catalysts with Roller-Comb-like Nanostructure for Rechargeable Zinc-Air Batteries. Chemical Engineering Journal. 2022;429:132199.
[60] Singh T, Mutreja V. Template Assisted Fabrication of Ordered Nanoporous Carbon Materials: A Review. AIP Conference Proceedings. 2023;2535.
[61] Sun J, Rattanasawatesun T, Tang P, Bi Z, Pandit S, Lam L, Wasén C, Erlandsson M, Bokarewa M, Dong J, Ding F, Xiong F, Mijakovic I. Insights into the Mechanism for Vertical Graphene Growth by Plasma-Enhanced Chemical Vapor Deposition. ACS Applied Materials and Interfaces. 2022;14:7152–7160.
[62] Sahoo S, Sahoo G, Jeong SM, Rout CS. A Review on Supercapacitors Based on Plasma Enhanced Chemical Vapor Deposited Vertical Graphene Arrays. Journal of Energy Storage. 2022;53:105212.
[63] Xu K, Liu H, Shi YC, You JY, Ma XY, Cui HJ, Yan QB, Chen GC, Su G. Preparation of T-Carbon by Plasma Enhanced Chemical Vapor Deposition. Carbon. 2020;157:270–276.
[64] Liu Y, He J, Zhang N, Zhang W, Zhou Y, Huang K. Advances of Microwave Plasma-Enhanced Chemical Vapor Deposition in Fabrication of Carbon Nanotubes: A Review. Journal of Materials Science. 2021;56:12559–12583.
[65] Shrestha S, Parajuli S, Park J, Yang H, Cho TY, Eom JH, Cho SK, Lim J, Cho G, Jung Y. Improving Stability of Roll-to-Roll (R2R) Gravure-Printed Carbon Nanotube-Based Thin Film Transistors via R2R Plasma-Enhanced Chemical Vapor-Deposited Silicon Nitride. Nanomaterials. 2023;13:559.
[66] Yuan G, Liu Z, Cao Z, Xie J, Li H, Li L, Sun Y, Tian Y. Direct Growth of Vertically Well-Aligned Carbon Nanotube Arrays on Atomic Layer Deposition of ZnO Films. Chemical Physics Letters. 2021;773:138602.
[67] Bayram O, Igman E, Guney H, Demir Z, Yurtcan MT, Cirak C, Hasar UC, Simsek O. Graphene/Polyaniline Nanocomposite as Platinum-Free Counter Electrode Material for Dye-Sensitized Solar Cell: Its Fabrication and Photovoltaic Performance. Journal of Materials Science: Materials in Electronics. 2020;31:10288–10297.
[68] Cheraghi E, Alexander LJ, Sun Y, Chen S, Yeow JTW. The Field Emission Properties of a New Design: Multi-Pixel Carbon Nanotube Field Emitters for Imaging Application. Proceedings of the IEEE Conference on Nanotechnology. 2019-July;572–575.
[69] Moise CC, Mihai GV, Anicăi L, Monaico EV, Ursaki VV, Enăchescu M, Tiginyanu IM. Electrochemical Deposition of Ferromagnetic Ni Nanoparticles in InP Nanotemplates Fabricated by Anodic Etching Using Environmentally Friendly Electrolyte. Nanomaterials. Multidisciplinary Digital Publishing Institute. 2022;12:3787.
[70] Sawal MH, Jalil AA, Khusnun NF, Hassan NS, Bahari MB. A Review of Recent Modification Strategies of TiO2-Based Photoanodes for Efficient Photoelectrochemical Water Splitting Performance. Electrochimica Acta. 2023;467:143142.
[71] Li X, Ming P, Ao S, Wang W. Review of Additive Electrochemical Micro-Manufacturing Technology. International Journal of Machine Tools and Manufacture. 2022;173:103848.
[72] Luo H, Kaneti YV, Ai Y, Wu Y, Wei F, Fu J, Cheng J, Jing C, Yuliarto B, Eguchi M, Na J, Yamauchi Y, Liu S. Nanoarchitectured Porous Conducting Polymers: From Controlled Synthesis to Advanced Applications. Advanced Materials. 2021;33:2007318.
[73] Haryński Ł, Czylkowski D, Hrycak B, Karczewski J, Gumieniak J, Kramek A, Ryl J, Grochowska K, Dors M, Siuzdak K. Nitrogen Plasma-Induced Crystallization of Anodic TiO2 Nanotubes for Solar Photoelectrochemistry. Applied Surface Science. 2023;615:156472.
[74] Eessaa AK, El-Shamy AM. Review on Fabrication, Characterization, and Applications of Porous Anodic Aluminum Oxide Films with Tunable Pore Sizes for Emerging Technologies. Microelectronic Engineering. 2023;279:112061.

[75] Lv H, Pan Q, Song Y, Liu XX, Liu T. A Review on Nano-/Microstructured Materials Constructed by Electrochemical Technologies for Supercapacitors. Nano-Micro Letters. 2020;12:1–56.
[76] Tian X, Wang Q, Zhao Q, Qiu L, Zhang X, Gao S. SILAR Deposition of CuO Nanosheets on the TiO2 Nanotube Arrays for the High Performance Solar Cells and Photocatalysts. Separation and Purification Technology. 2019;209:368–374.
[77] Yan Y, Xu Y, Zhao B, Xu Y, Gao Y, Chen G, Wang W, Xia B-Y. Bifunctional Nickel Ferrite-Decorated Carbon Nanotube Arrays as Free-Standing Air Electrode for Rechargeable Zn–Air Batteries. Journal of Materials Chemistry A. 2020;8(20):5070–5077.
[78] Tong M.H, Chen Y.X, Lin S.W, Zhao H.P, Chen R, Jiang X, Shi H.Y, Zhu M.L, Zhou Q.Q, Lu C.Z. Synchronous Electrochemical Anodization: A Novel Strategy for Preparing Cerium Doped TiO2 Nanotube Arrays toward Visible-Light PEC Water Splitting. Electrochimica Acta. 2023;463:142793.
[79] Huang C.L, Chuah X.F, Hsieh C.T, Lu S.Y. NiFe Alloy Nanotube Arrays as Highly Efficient Bifunctional Electrocatalysts for Overall Water Splitting at High Current Densities. ACS Applied Materials and Interfaces. 2019;11(25):24096–24106.
[80] Lin X, Wang Y, Zou M, Lan T, Ni Y. Electrochemical Non-Enzymatic Glucose Sensors Based on Nano-Composite of Co3O4 and Multiwalled Carbon Nanotube. Chinese Chemical Letters. 2019;30(6):1157–1160.
[81] Fan H, Zhang X, Wang Y, Lang J, Gao R. Highly Conductive KNiF3@carbon Nanotubes Composite Materials with Cross-Linked Structure for High Performance Supercapacitor. Journal of Power Sources. 2020;474:228603.
[82] Gao P, Yin Z, Feng L, Liu Y, Du Z, Duan Z, Zhang L. Solvothermal Synthesis of Multiwall Carbon Nanotubes/BiOI Photocatalysts for the Efficient Degradation of Antipyrine under Visible Light. Environmental Research. 2020;185:109468.
[83] Ye Q, Liu J, Lin L, Sun M, Wang Y, Cheng Y. Fe and P Dual-Doped Nickel Carbonate Hydroxide/Carbon Nanotube Hybrid Electrocatalysts for an Efficient Oxygen Evolution Reaction. Nanoscale. 2022;14(16):6648–6655.
[84] Huo Y, Xiu S, Meng L.Y, Quan B. Solvothermal Synthesis and Applications of Micro/Nano Carbons: A Review. Chemical Engineering Journal. 2023;451:138572.
[85] Danish MSS, Bhattacharya A, Stepanova D, Mikhaylov A, Grilli ML, Khosravy M, Senjyu T. A Systematic Review of Metal Oxide Applications for Energy and Environmental Sustainability. Metals. 2020;10(12):1604.
[86] Kumar Y, Paswan KK, Nayan K, Pandurangappa G, Dwivedi D, Sangwai JS. Introduction to Functional Materials Synthesis, Properties, Environmental Sustainability, and General Applications. In: Functional Materials for the Oil and Gas Industry: Characterization and Applications. CRC Press; 2023. p. 1–22.
[87] Ndlwana L, Raleie N, Dimpe KM, Ogutu HF, Oseghe EO, Motsa MM, Msagati TAM, Mamba BB. Sustainable Hydrothermal and Solvothermal Synthesis of Advanced Carbon Materials in Multidimensional Applications: A Review. Materials. 2021;14(18):5094.
[88] Siwal SS, Kaur H, Saini AK, Thakur VK. Recent Progress in Carbon Dots-Based Materials for Electrochemical Energy Storage Toward Environmental Sustainability. Advanced Energy and Sustainability Research. 2022;3:2200062.
[89] Fuku X, Dyosiba X, Iftikhar FJ. Green Prepared Nanomaterials from Various Biodegradable Wastes and Their Application in Energy. Nano-Structures & Nano-Objects. 2023;35:100997.
[90] Xia W, Lau SK, Yong WF. Comparative Life Cycle Assessment on Zeolitic Imidazolate Framework-8 (ZIF-8) Production for CO2 Capture. Journal of Cleaner Production. 2022;370:133354.
[91] Mruthunjayappa MH, Kotrappanavar NS, Mondal D. New Prospects on Solvothermal Carbonisation Assisted by Organic Solvents, Ionic Liquids and Eutectic Mixtures – A Critical Review. Progress in Materials Science. 2022;126:100932.

[92] Li W, Qian K, Yang Z, Ding X, Tian W, Chen D. Promotion Effect of Cobalt Doping on Microwave-Initiated Plastic Deconstruction for Hydrogen Production over Iron Catalysts. Applied Catalysis B: Environmental. 2023;327:122451.
[93] Burkholder MB, Rahman FBA, Chandler EH, Regalbuto JR, Gupton BF, Tengco JMM. Metal Supported Graphene Catalysis: A Review on the Benefits of Nanoparticular Supported Specialty Sp2 Carbon Catalysts on Enhancing the Activities of Multiple Chemical Transformations. Carbon Trends. 2022;9:100196.
[94] Jiang M, Wang X, Xi W, Zhou H, Yang P, Yao J, Jiang X, Wu D. Upcycling Plastic Waste to Carbon Materials for Electrochemical Energy Storage and Conversion. Chemical Engineering Journal. 2023;461:141962.
[95] Li X, Srinivas K, Ramadoss M, Ma F, Wang Y, Wang M, Yu H, Zhang Z, Wu Y, Chen Y. Carbon Nanotubes Supported Cs-Doped NiFe-Layered Double Hydroxide Nanosheets as Efficient Catalyst for Oxygen Evolution Reaction. International Journal of Hydrogen Energy.
[96] Feng Y, Zeng A. Selective Liquid-Phase Oxidation of Toluene with Molecular Oxygen Catalyzed by Mn3O4 Nanoparticles Immobilized on CNTs under Solvent-Free Conditions. Catalysts. 2020;10(6):623.
[97] Lim XX, Low SC, Oh W Da. A Critical Review of Heterogeneous Catalyst Design for Carbon Nanotubes Synthesis: Functionalities, Performances, and Prospects. Fuel Processing Technology. 2023;241:107624.
[98] Boyrazlı M, Güler SH. Synthesis of Carbon Nanostructures from Corn Stalk Using Mechano-Thermal Method. Journal of Molecular Structure. 2020;1199:126976.
[99] Alirezazadeh F, Alimohammadi E, Sheibani S, Rashchi F. A Comparative Study on the Photocatalytic Activity and Formation Mechanism of Nanostructured Cu2ZnSnS4 Prepared by Thermal and Mechano-Thermal Methods. Materials Chemistry and Physics. 2022;292:126856.
[100] Tubtimkuna S, Danilov DL, Sawangphruk M, Notten PHL. Review of the Scalable Core–Shell Synthesis Methods: The Improvements of Li-Ion Battery Electrochemistry and Cycling Stability. Small Methods. 2023;7(2):2300345.
[101] Maselugbo AO, Harrison HB, Alston JR. Boron Nitride Nanotubes: A Review of Recent Progress on Purification Methods and Techniques. Journal of Materials Research. 2022;37(24):4438–4458.
[102] Al-Diabat AM, Algadri NA, Ahmad NM, Alrajhi AH, Abuelsamen A, Mohamed A, Ali A, Abdulrhman Al-Wasli S. Optimize the Properties of Carbon Nanotubes Synthesized Using a Microwave Oven.
[103] Pund SN, Nagwade PA, Nagawade AV, Thopate SR, Bagade AV. Preparation Techniques for Zinc Ferrites and Their Applications: A Review. Materials Today: Proceedings. 2022;60:2194–2208.
[104] Li X, Liu J, Zhu H. Functionalized and Environment-Friendly Carbon Materials for Flexible and Wearable Electronic Devices. In: SPIE. 2022;12164:162–174.
[105] Mirabootalebi SO, Akbari GH, Babaheydari RM. Mass Production and Growth Mechanism of Carbon Nanotubes in Optimized Mechanothermal Method. International Journal of Engineering, Materials and Energy Research Center. 2021;34:2332–2340.
[106] Rathinavel S, Priyadharshini K, Panda D. A Review on Carbon Nanotube: An Overview of Synthesis, Properties, Functionalization, Characterization, and the Application. Materials Science and Engineering: B. 2021;268:115095.
[107] Zainal MT, Mohd Yasin MF, Wan Ali WFF, Tamrin KF, Ani MH. Carbon Precursor Analysis for Catalytic Growth of Carbon Nanotube in Flame Synthesis Based on Semi-Empirical Approach. Carbon Letters. 2020;30(6):569–579.
[108] Hu X, Zuo D, Cheng S, Chen S, Liu Y, Bao W, Deng S, Harris SJ, Wan J. Ultrafast Materials Synthesis and Manufacturing Techniques for Emerging Energy and Environmental Applications. Chemical Society Reviews. 2023;52:1103–1128.

[109] Amouzegar Z, Mollarasouli F, Asadi S, Fathi A, Ahmadi M, Afkhami A, Madrakian T. Nonconventional Applications of Nebulizers: Nanomaterials Synthesis. In: Analytical Nebulizers: Fundamentals and Applications. 2023;217–245.
[110] Zhao Y, Dong S, Hu P, Zhao X, Hong C. Recent Progress in Synthesis, Growth Mechanisms, Properties, and Applications of Silicon Nitride Nanowires. Ceramics International. 2021;47(11):14944–14965.
[111] Peters AB, Zhang D, Chen S, Ott C, Oses C, Curtarolo S, McCue I, Pollock T, Prameela SE. Materials Design for Hypersonics.
[112] Xue J, Yin X, Cheng L. Induced Crystallization Behavior and EMW Absorption Properties of CVI SiCN Ceramics Modified with Carbon Nanowires. Chemical Engineering Journal. 2019;378:122213.
[113] Natarajan B. Processing-Structure-Mechanical Property Relationships in Direct Formed Carbon Nanotube Articles and Their Composites: A Review. Composites Science and Technology. 2022;225:109501.
[114] Li M, Song Y, Zhang C, Yong Z, Qiao J, Hu D, Zhang Z, Wei H, Di J, Li Q. Robust Carbon Nanotube Composite Fibers: Strong Resistivities to Protonation, Oxidation, and Ultrasonication. Carbon. 2019;146:627–635.
[115] Aly K, Lubna M, Bradford PD. Low Density, Three-Dimensionally Interconnected Carbon Nanotube/Silicon Carbide Nanocomposites for Thermal Protection Applications. Journal of the European Ceramic Society. 2021;41:233–243.
[116] Feng L, Fu Q, Song Q, Yang Y, Zuo Y, Suo G, Hou X, Zhang L, Ye X. A Novel Continuous Carbon Nanotube Fiber/Carbon Composite by Electrified Preform Heating Chemical Vapor Infiltration. Carbon. 2020;157:640–648.
[117] Liu X, Licht G, Wang X, Licht S. Controlled Transition Metal Nucleated Growth of Carbon Nanotubes by Molten Electrolysis of CO2. Catalysts. 2022;12:137.
[118] Arcaro S, Guaglianoni W, Alves AK, Bergmann CP. The Effect of CaCO3 in the Formation of Carbon Nanotubes via Electrolysis of Molten Li2CO3/CaCO3 Mixtures. International Journal of Applied Ceramic Technology. 2022;19(2):451–458.
[119] Zailan Z, Tahir M, Jusoh M, Zakaria ZY. A Review of Sulfonic Group Bearing Porous Carbon Catalyst for Biodiesel Production. Renewable Energy. 2021;175:430–452.
[120] Atiq Ur Rehman M, Chen Q, Braem A, Shaffer MSP, Boccaccini AR. Electrophoretic Deposition of Carbon Nanotubes: Recent Progress and Remaining Challenges. International Materials Reviews. 2021;66:533–562.
[121] Liu X, Ren J, Licht G, Wang X, Licht S. Carbon Nano-Onions Made Directly from CO2 by Molten Electrolysis for Greenhouse Gas Mitigation. Advanced Sustainable Systems. 2019;3:1900056.
[122] Wang X, Licht G, Liu X, Licht S. CO2 Utilization by Electrolytic Splitting to Carbon Nanotubes in Non-Lithiated, Cost-Effective, Molten Carbonate Electrolytes. Advanced Sustainable Systems. 2022;6:2100481.
[123] Liu X, Licht G, Wang X, Licht S. Controlled Transition Metal Nucleated Growth of Carbon Nanotubes by Molten Electrolysis of CO2.
[124] Zahid MU, Pervaiz E, Hussain A, Shahzad MI, Niazi MBK. Synthesis of Carbon Nanomaterials from Different Pyrolysis Techniques: A Review. Materials Research Express. 2018;5:052002.
[125] Vivekchand SRC, Cele LM, Deepak FL, Raju AR, Govindaraj A. Carbon Nanotubes by Nebulized Spray Pyrolysis. Chemical Physics Letters. 2004;386:313–318.
[126] Jin YZ, Gao C, Hsu WK, Zhu Y, Huczko A, Bystrzejewski M, Roe M, Lee CY, Acquah S, Kroto H, Walton DRM. Large-Scale Synthesis and Characterization of Carbon Spheres Prepared by Direct Pyrolysis of Hydrocarbons. Carbon. 2005;43:1944–1953.
[127] Cheng HM, Li F, Su G, Pan HY, He LL, Sun X, Dresselhaus MS. Large-Scale and Low-Cost Synthesis of Single-Walled Carbon Nanotubes by the Catalytic Pyrolysis of Hydrocarbons. Applied Physics Letters. 1998;72:3282–3284.

[128] Lv X, Zhang T, Luo Y, Zhang Y, Wang Y, Zhang G. Study on Carbon Nanotubes and Activated Carbon Hybrids by Pyrolysis of Coal. Journal of Analytical and Applied Pyrolysis. 2020;146:104717.
[129] Moothi K, Simate GS, Falcon R, Iyuke SE, Meyyappan M. Carbon Nanotube Synthesis Using Coal Pyrolysis. Langmuir. 2015;31:9464–9472.
[130] Nebol'sin VA, Vorob'ev AY. Role of Surface Energy in the Growth of Carbon Nanotubes via Catalytic Pyrolysis of Hydrocarbons. Inorganic Materials. 2011;47:128–132.
[131] Sárközi S, Sárközi Z, Kertész K, Koós AA, Osváth Z, Tapasztó L, Horváth ZE, Nemes-Incze P, Jenei IZ, Vértesy Z, Daróczi NS, Darabont A, Pana O, Biró LP. Synthesis of Carbon Nanotubes from Liquid Hydrocarbons Using a Spray-Pyrolysis Method. Journal of Optoelectronics and Advanced Materials. 2008;10:2307–2310.
[132] Bajad GS, Vijayakumar RP, Gupta AG, Jagtap V, Singh YP. Production of Liquid Hydrocarbons, Carbon Nanotubes and Hydrogen Rich Gases from Waste Plastic in a Multi-Core Reactor. Journal of Analytical and Applied Pyrolysis. 2017;125:83–90.
[133] Mehrabi M, Parvin P, Reyhani A, Mortazavi SZ. Hydrogen Storage in Multi-Walled Carbon Nanotubes Decorated with Palladium Nanoparticles Using Laser Ablation/Chemical Reduction Methods. Materials Research Express. 2017;4:095030.
[134] Tarasenka N, Stupak A, Tarasenko N, Chakrabarti S, Mariotti D. Structure and Optical Properties of Carbon Nanoparticles Generated by Laser Treatment of Graphite in Liquids. ChemPhysChem. 2017;18:1074–1083.
[135] Irimiciuc SA, Hodoroaba BC, Bulai G, Gurlui S, Craciun V. Multiple Structure Formation and Molecule Dynamics in Transient Plasmas Generated by Laser Ablation of Graphite. Spectrochimica Acta Part B: Atomic Spectroscopy. 2020;165:105774.
[136] Rode A, Sharma S, Mishra DK. Carbon Nanotubes: Classification, Method of Preparation and Pharmaceutical Application. Current Drug Delivery. 2017;15:620–629.
[137] Shoukat R, Khan MI. Carbon Nanotubes: A Review on Properties, Synthesis Methods and Applications in Micro and Nanotechnology. Microsystem Technologies. 2021;27:4183–4192.
[138] Ismail RA, Mohsin MH, Ali AK, Hassoon KI, Erten-Ela S. Preparation and Characterization of Carbon Nanotubes by Pulsed Laser Ablation in Water for Optoelectronic Application. Physica E: Low-dimensional Systems and Nanostructures. 2020;119:113997.
[139] Gulati S, Kumar S, Mongia A, Diwan A, Singh P. Functionalized Carbon Nanotubes (FCNTs) as Novel Drug Delivery Systems: Emergent Perspectives from Applications. Environmental Applications of Carbon Nanomaterials-Based Devices. 2021;283–312.
[140] Omoriyekomwan JE, Tahmasebi A, Dou J, Wang R, Yu J. A Review on the Recent Advances in the Production of Carbon Nanotubes and Carbon Nanofibers via Microwave-Assisted Pyrolysis of Biomass. Fuel Processing Technology. 2021;214:106686.
[141] Li A, Zhou W, Xie M, Wang S, Wang S, Yang Y, Chen Y, Liu M. Preparation and Arc Erosion Behavior of AgNi10 Contact Material with Different Allotropes of Carbon Addition. Diamond and Related Materials. 2021;111:108141.
[142] Shweta, Vishwakarma K, Sharma S, Narayan RP, Srivastava P, Khan AS, Dubey NK, Tripathi DK, Chauhan DK. Plants and Carbon Nanotubes (CNTs) Interface: Present Status and Future Prospects. Nanotechnology: Food and Environmental Paradigm. 2017;317–340.
[143] Janett B, Gutierrez A, Dul S, Pegoretti A, Alvarez-Quintana J, Fambri L. Investigation of the Effects of Multi-Wall and Single-Wall Carbon Nanotubes Concentration on the Properties of ABS Nanocomposites. C 2021. 7:33.
[144] Liu F, Wang Q, Tang Y, Du W, Chang W, Fu Z, Zhao X, Liu Y. Carbon Nanowires Made by the Insertion-and-Fusion Method toward Carbon–Hydrogen Nanoelectronics. Nanoscale. 2023;15:6143–6155.
[145] Loayza CR, Cardoso DCS, Borges DJA, Castro AAF, Bozzi AC, Dos Reis MAL, Braga EM. Stainless Steel-CNT Composite Manufactured via Electric Arc Welding. Materials & Design. 2022;223:111169.

[146] Jia Q, Zhou Y, Li X, Lindsay L, Shi L. Differential Multi-Probe Thermal Transport Measurements of Multi-Walled Carbon Nanotubes Grown by Chemical Vapor Deposition. International Journal of Heat and Mass Transfer. 2023;216:124535.
[147] Rajab F. Effect of the Chemical Vapor Deposition Process on the Aspect Ratio of Vertically Aligned Carbon Nanotubes (VACNTs). MRS Advances. 2023;8:343–348.
[148] Wang C, Wang Y, Jiang H. Continuous Growth of Carbon Nanotubes on Carbon Fiber Surface by Chemical Vapor Deposition Catalyzed by Cobalt with Thiourea. ECS Journal of Solid State Science and Technology. 2023;12:041003.
[149] Zulkimi MMM, Azis RSR, Ismail I, Mokhtar N, Ertugrul M, Hamidon MN, Hasan IH, Yesilbag YO, Tuzluca FN, Ozturk G, Hasar UC. Enhancing Radar Absorption Performance of Sr-Hexaferrite by Hybridization with Coiled Carbon Nanotubes via Chemical Vapour Deposition Method. Diamond and Related Materials. 2023;137:110118.
[150] Cheng F, Xu Y, Zhang J, Wang L, Zhang H, Wan Q, Xu S, Li W, Wang L, Huang Z. A Novel Flexible Carbon Fiber with Carbon Nanotubes Growing In-Situ via Chemical Vapor Deposition to Impregnate Paraffin for Thermal Energy Application. Journal of Energy Storage. 2023;68:107718.
[151] Cheng F, Xu Y, Zhang J, Wang L, Zhang H, Wan Q, Li W, Wang L, Lv Z. Growing Carbon Nanotubes In-Situ via Chemical Vapor Deposition and Resin Pre-Coating Treatment on Anodized Ti-6Al-4V Titanium Substrates for Stronger Adhesive Bonding with Carbon Fiber Composites. Surface and Coatings Technology. 2023;457:129296.
[152] ZHAO H, TU N, ZHANG W, ZHANG M, WANG J. Novel Synthesis of Silicon/Carbon Nanotubes Microspheres as Anode Additives through Chemical Vapor Deposition in Fluidized Bed Reactors. Scripta Materialia. 2021;192:49–54.
[153] Zhang Y, Wang Q, Ramachandran CS. Synthesis of Carbon Nanotube Reinforced Aluminum Composite Powder (CNT-Al) by Polymer Pyrolysis Chemical Vapor Deposition (PP-CVD) Coupled High Energy Ball Milling (HEBM) Process. Diamond and Related Materials. 2020;104:107748.
[154] Mittal G, Rhee KY. Chemical Vapor Deposition-Based Grafting of CNTs onto Basalt Fabric and Their Reinforcement in Epoxy-Based Composites. Composites Science and Technology. 2018;165:84–94.
[155] Nekoueian K. Modification of Carbon-Based Electrodes Using Metal Nanostructures: Application to Voltammetric Determination of Some Pharmaceutical and Biological Compounds. Lappeenranta-Lahti University of Technology LUT.
[156] Nie C, Ma L, Li S, Fan X, Yang Y, Cheng C, Zhao W, Zhao C. Recent Progresses in Graphene Based Bio-Functional Nanostructures for Advanced Biological and Cellular Interfaces. Nano Today. 2019;26:57–97.
[157] Senthilkumar E, Shanmugharaj AM, Suresh Babu R, Sivagaami Sundari G, Thileep Kumar K, Raghu S, Kalaivani R. Development of Constructed Nanoporous Graphene-Modified Electrode for Electrical Detection of Folic Acid. Journal of Materials Science: Materials in Electronics. 2019;30:13488–13496.
[158] Guo HW, Hu Z, Liu ZB, Tian JG. Stacking of 2D Materials. Advanced Functional Materials. 2021;31:2007810.
[159] Bagyalakshmi S, Sivakami A, Pal K, Sarankumar R, Mahendran C. Manufacturing of Electrochemical Sensors via Carbon Nanomaterials Novel Applications: A Systematic Review. Journal of Nanoparticle Research. 2022;24:1–28.
[160] Sharma VV, Gualandi I, Vlamidis Y, Tonelli D. Electrochemical Behavior of Reduced Graphene Oxide and Multi-Walled Carbon Nanotubes Composites for Catechol and Dopamine Oxidation. Electrochimica Acta. 2017;246:415–423.
[161] Khoshnevis H, Tran TQ, Mint SM, Zadhoush A, Duong HM, Youssefi M. Effect of Alignment and Packing Density on the Stress Relaxation Process of Carbon Nanotube Fibers Spun from Floating Catalyst Chemical Vapor Deposition Method. Colloids and Surfaces A: Physicochemical and Engineering Aspects. Elsevier; 2018;558:570–578.

[162] Dong L, Park JG, Leonhardt BE, Zhang S, Liang R. Continuous Synthesis of Double-Walled Carbon Nanotubes with Water-Assisted Floating Catalyst Chemical Vapor Deposition. Nanomaterials. Multidisciplinary Digital Publishing Institute; 2020;10:365.
[163] Lee SH, Park J, Park JH, Lee DM, Lee A, Moon SY, Lee SY, Jeong HS, Kim SM. Deep-Injection Floating-Catalyst Chemical Vapor Deposition to Continuously Synthesize Carbon Nanotubes with High Aspect Ratio and High Crystallinity. Carbon. Pergamon; 2021;173:901–909.
[164] Ahmad S, Liao Y, Hussain A, Zhang Q, Ding EX, Jiang H, Kauppinen EI. Systematic Investigation of the Catalyst Composition Effects on Single-Walled Carbon Nanotubes Synthesis in Floating-Catalyst CVD. Carbon. Pergamon; 2019;149:318–327.
[165] Zhang Q, Wei N, Laiho P, Esko A, Kauppinen I. Recent Developments in Single-Walled Carbon Nanotube Thin Films Fabricated by Dry Floating Catalyst Chemical Vapor Deposition.
[166] Duong HM, Tran TQ, Kopp R, Myint SM, Peng L. Direct Spinning of Horizontally Aligned Carbon Nanotube Fibers and Films From the Floating Catalyst Method. Nanotube Superfiber Materials: Science, Manufacturing, Commercialization. William Andrew Publishing; 2019;3–29.
[167] Khoshnevis H, Mint SM, Yedinak E, Tran TQ, Zadhoush A, Youssefi M, Pasquali M, Duong HM. Super High-Rate Fabrication of High-Purity Carbon Nanotube Aerogels from Floating Catalyst Method for Oil Spill Cleaning. Chemical Physics Letters. North-Holland; 2018;693:146–151.
[168] Tran TQ, Headrick RJ, Bengio EA, Myo Myint S, Khoshnevis H, Jamali V, Duong HM, Pasquali M. Purification and Dissolution of Carbon Nanotube Fibers Spun from the Floating Catalyst Method. ACS Applied Materials and Interfaces. American Chemical Society; 2017;9:37112–37119.
[169] Suchitra SM, Udayashankar NK. Influence of Porewidening Duration on the Template Assisted Growth of Graphitic Carbon Nitride Nanostructures. Materials Research Express. IOP Publishing; 2018;5:015056.
[170] Han M, Zhang X, Gao H, Chen S, Cheng P, Wang P, Zhao Z, Dang R, Wang G. In Situ Semi-Sacrificial Template-Assisted Growth of Ultrathin Metal–Organic Framework Nanosheets for Electrocatalytic Oxygen Evolution. Chemical Engineering Journal. Elsevier; 2021;426:131348.
[171] Cossuet T, Rapenne L, Renou G, Appert E, Consonni V. Template-Assisted Growth of Open-Ended TiO2 Nanotubes with Hexagonal Shape Using Atomic Layer Deposition. Crystal Growth and Design. American Chemical Society; 2021;21:125–132.
[172] Li H, Liu YL, Jin H, Cao L, Yang H, Jiang S, He S, Li S, Liu K, Duan G. Bimetallic Salts Template-Assisted Strategy towards the Preparation of Hierarchical Porous Polyimide-Derived Carbon Electrode for Supercapacitor. Diamond and Related Materials. Elsevier; 2022;128:109283.
[173] Wang C, Yan B, Zheng J, Feng L, Chen Z, Zhang Q, Liao T, Chen J, Jiang S, Du C, He S. Recent Progress in Template-Assisted Synthesis of Porous Carbons for Supercapacitors. Advanced Powder Materials. Elsevier; 2022;1:100018.
[174] Taziwa R, Meyer E, Takata N. Structural and Raman Spectroscopic Characterization of C-TiO2 Nanotubes Synthesized by a Template-Assisted Sol-Gel Technique. Journal of Nanoscience & Nanotechnology Research. 2017;1.
[175] Yang G, Cheng F, Zuo S, Zhang J, Xu Y, Hu Y, Hu X. Growing Carbon Nanotubes In Situ Surrounding Carbon Fiber Surface via Chemical Vapor Deposition to Reinforce Flexural Strength of Carbon Fiber Composites. Polymers. Multidisciplinary Digital Publishing Institute; 2023;15:2309.
[176] Simionescu OG, Brîncoveanu O, Romaniţan C, Vulpe S, Avram A. Step-By-Step Development of Vertically Aligned Carbon Nanotubes by Plasma-Enhanced Chemical Vapor Deposition. Coatings. Multidisciplinary Digital Publishing Institute; 2022;12:943.

[177] Yi K, Liu D, Chen X, Yang J, Wei D, Liu Y, Wei D. Plasma-Enhanced Chemical Vapor Deposition of Two-Dimensional Materials for Applications. Accounts of Chemical Research. American Chemical Society; 2021;54:1011–1022.
[178] Yeh NC, Hsu CC, Bagley J, Tseng WS. Single-Step Growth of Graphene and Graphene-Based Nanostructures by Plasma-Enhanced Chemical Vapor Deposition. Nanotechnology. IOP Publishing; 2019;30:162001.
[179] Thapa A, Neupane S, Guo R, Jungjohann KL, Pete D, Li W. Direct Growth of Vertically Aligned Carbon Nanotubes on Stainless Steel by Plasma Enhanced Chemical Vapor Deposition. Diamond and Related Materials. Elsevier; 2018;90:144–153.
[180] Jabbar A, Yasin G, Khan WQ, Anwar MY, Korai RM, Nizam MN, Muhyodin G. Electrochemical Deposition of Nickel Graphene Composite Coatings: Effect of Deposition Temperature on Its Surface Morphology and Corrosion Resistance. RSC Advances. Royal Society of Chemistry; 2017;7:31100–31109.
[181] Liu L, Mandler D. Using Nanomaterials as Building Blocks for Electrochemical Deposition: A Mini Review. Electrochemistry Communications. Elsevier; 2020;120:106830.
[182] Hussain S, Erikson H, Kongi N, Merisalu M, Rähn M, Sammelselg V, Maia G, Tammeveski K. Platinum Particles Electrochemically Deposited on Multiwalled Carbon Nanotubes for Oxygen Reduction Reaction in Acid Media. Journal of The Electrochemical Society. The Electrochemical Society; 2017;164:F1014–F1021.
[183] Arai S. Fabrication of Metal/Carbon Nanotube Composites by Electrochemical Deposition. Electrochem. Multidisciplinary Digital Publishing Institute; 2021;2:563–589.
[184] Zhao G, Liu G. Electrochemical Deposition of Gold Nanoparticles on Reduced Graphene Oxide by Fast Scan Cyclic Voltammetry for the Sensitive Determination of As(III). Nanomaterials. Multidisciplinary Digital Publishing Institute; 2019;9:41.
[185] Iffelsberger C, Ng S, Pumera M. Catalyst Coating of 3D Printed Structures via Electrochemical Deposition: Case of the Transition Metal Chalcogenide MoSx for Hydrogen Evolution Reaction. Applied Materials Today. Elsevier; 2020;20:100654.
[186] Cao Y, Moniri Javadhesari S, Mohammadnejad S, Khodadustan E, Raise A, Akbarpour MR. Microstructural Characterization and Antibacterial Activity of Carbon Nanotube Decorated with Cu Nanoparticles Synthesized by a Novel Solvothermal Method. Ceramics International. Elsevier; 2021;47:25729–25737.
[187] Park SK, Sure J, Sri Maha Vishnu D, Jo SJ, Lee WC, Ahmad IA, Kim HK. Nano-Fe3o4/Carbon Nanotubes Composites by One-Pot Microwave Solvothermal Method for Supercapacitor Applications. Energies. MDPI AG; 2021;14:NA.
[188] Wang Q, Li H, Yu X, Jia Y, Chang Y, Gao S. Morphology Regulated Bi2WO6 Nanoparticles on TiO2 Nanotubes by Solvothermal Sb3+ Doping as Effective Photocatalysts for Wastewater Treatment. Electrochimica Acta. Pergamon; 2020;330:135167.
[189] Liu X, Li G, Qian P, Zhang D, Wu J, Li K, Li L. Carbon Coated Li3VO4 Microsphere: Ultrafast Solvothermal Synthesis and Excellent Performance as Lithium-Ion Battery Anode. Journal of Power Sources. Elsevier; 2021;493:229680.
[190] Gyulai G, Ouanzi F, Bertóti I, Mohai M, Kolonits T, Horváti K, Bősze S. Chemical Structure and in Vitro Cellular Uptake of Luminescent Carbon Quantum Dots Prepared by Solvothermal and Microwave Assisted Techniques. Journal of Colloid and Interface Science. Academic Press; 2019;549:150–161.
[191] Zhao D, Liu X, Wei C, Qu Y, Xiao X, Cheng H. One-Step Synthesis of Red-Emitting Carbon Dots via a Solvothermal Method and Its Application in the Detection of Methylene Blue. RSC Advances. Royal Society of Chemistry; 2019;9:29533–29540.
[192] Cao D, Wang Q, Wu Y, Zhu S, Jia Y, Wang R. Solvothermal Synthesis and Enhanced Photocatalytic Hydrogen Production of Bi/Bi2MoO6 Co-Sensitized TiO2 Nanotube Arrays. Separation and Purification Technology. Elsevier; 2020;250:117132.
[193] Al-Sakkaf MK, Basfer I, Iddrisu M, Bahadi SA, Nasser MS, Abussaud B, Drmosh QA, Onaizi SA. An Up-to-Date Review on the Remediation of Dyes and Phenolic Compounds from

Wastewaters Using Enzymes Immobilized on Emerging and Nanostructured Materials: Promises and Challenges. Nanomaterials. Multidisciplinary Digital Publishing Institute; 2023;13:2152.
[194] Dang Q, Lin H, Fan Z, Ma L, Shao Q, Ji Y, Zheng F, Geng S, Yang SZ, Kong N, Zhu W, Li Y, Liao F, Huang X, Shao M. Iridium Metallene Oxide for Acidic Oxygen Evolution Catalysis. Nature Communications 2021 12:1. Nature Publishing Group; 2021;12:1–10.
[195] Reza MS, Afroze S, Kuterbekov K, Kabyshev A, Zh. Bekmyrza K, Haque MN, Islam SN, Hossain MA, Hassan M, Roy H, Islam MS, Pervez MN, Azad AK. Advanced Applications of Carbonaceous Materials in Sustainable Water Treatment, Energy Storage, and CO2 Capture: A Comprehensive Review. Sustainability (Switzerland). MDPI; 2023;15:8815.
[196] Nigam A, Kala S. Structural and Bioactive Properties of Iron Sulfide Nanoparticles Synthesized by Green-Route. Materials Today: Proceedings. Elsevier; 2022;66:2144–2151.
[197] Patiño-Carachure C, Martínez-Vargas S, Flores-Chan JE, Rosas G. Synthesis of Carbon Nanostructures by Graphite Deformation during Mechanical Milling in Air. Fullerenes, Nanotubes and Carbon Nanostructures. Taylor & Francis; 2020;28:869–876.
[198] Kumar S, Kumar Mahto R. Synthesis and Characterization of Low Dimensional Structure of Carbon Nanotubes. International Journal of Science and Research Archive. 2022;2022:571–582.
[199] Lekshmi GS, Tamilselvi R, Prasad K, Bazaka O, Levchenko I, Bazaka K, Mohandas M. Growth of RGO Nanostructures via Facile Wick and Oil Flame Synthesis for Environmental Remediation. Carbon Letters. Springer; 2021;31:763–777.
[200] Chang BP, Gupta A, Mekonnen TH. Flame Synthesis of Carbon Nanoparticles from Corn Oil as a Highly Effective Cationic Dye Adsorbent. Chemosphere. Pergamon; 2021;282:131062.
[201] Wong HY, How HC, Ho JH. Chemical Kinetics Modelling for the Effect of Chimney on Diffusion Flame in Carbon Nanotubes Synthesis. J Phys Conf Ser. IOP Publishing. 2022;2169:012022.
[202] Hammadi AH, Jasim AM, Abdulrazzak FH, Al-Sammarraie AMA, Cherifi Y, Boukherroub R, Hussein FH. Purification for Carbon Nanotubes Synthesized by Flame Fragments Deposition via Hydrogen Peroxide and Acetone. Materials. Multidisciplinary Digital Publishing Institute. 2020;13:2342.
[203] Yang L, Yang J, Dong Q, Zhou F, Wang Q, Wang Z, Huang K, Yu H, Xiong X. One-Step Synthesis of CuO Nanoparticles Based on Flame Synthesis: As a Highly Effective Non-Enzymatic Sensor for Glucose, Hydrogen Peroxide and Formaldehyde. J Electroanal Chem. Elsevier. 2021;881:114965.
[204] Hong H, Memon NK, Dong Z, Kear BH, Tse SD. Flame Synthesis of Gamma-Iron-Oxide (γ-Fe2O3) Nanocrystal Films and Carbon Nanotubes on Stainless-Steel Substrates. Proc Combust Inst. Elsevier. 2019;37:1249–1256.
[205] Hamzah N, Yasin MFM, Yusop MZM, Zainal MT, Rosli MAF. Identification of Cnt Growth Region and Optimum Time for Catalyst Oxidation: Experimental and Modelling Studies of Flame Synthesis. Evergreen, Novel Carbon Resource Sci. 2019;6:85–91.
[206] Zhan W, Ma L, Gan M, Ding J, Han S, Wei D, Shen J, Zhou C. MOF-Derived N-Doped Carbon Coated CoP/Carbon Nanotube Pt-Based Catalyst for Efficient Methanol Oxidation. Int J Hydrogen Energy. Pergamon. 2020;45:15630–15641.
[207] Keteklahijani YZ, Arjmand M, Sundararaj U. Cobalt Catalyst Grown Carbon Nanotube/Poly(Vinylidene Fluoride) Nanocomposites: Effect of Synthesis Temperature on Morphology, Electrical Conductivity and Electromagnetic Interference Shielding. ChemistrySelect. John Wiley & Sons, Ltd. 2017;2:10271–10284.
[208] Maruyama T, Kozawa A, Saida T, Naritsuka S, Iijima S. Low Temperature Growth of Single-Walled Carbon Nanotubes from Rh Catalysts. Carbon. Pergamon. 2017;116:128–132.

[209] Sun X, Damma D, Cao Z, Alvarez NT, Shanov V, Arvanitis A, Smirniotis PG, Dong J. CO-Promoted Low-Temperature Conversion of CH4 to Hydrogen and Carbon Nanotubes on Nanocrystalline Cr-Doped Ferrite Catalyst. Catal Commun. Elsevier. 2022;169:106475.
[210] Mamat MS, Walker GS, Grant DM, Yaakob Y, Shaharun NA. Effect of the Reaction Temperature and Ethene/Hydrogen Composition on the Nanostructured Carbon Produced by CVD Using Supported NiFe2O4 as a Catalyst. Results Phys. Elsevier. 2020;19:103497.
[211] Moon SY, Kim BR, Park CW, Lee SH, Kim SM. High-Crystallinity Single-Walled Carbon Nanotube Aerogel Growth: Understanding the Real-Time Catalytic Decomposition Reaction through Floating Catalyst Chemical Vapor Deposition. Chem Eng J Adv. Elsevier. 2022;10:100261.
[212] Kadlečíková M, Breza J, Jesenák K, Hubeňák M, Raditschová J, Bálintová M. Utilization of Catalytically Active Metals in Mining Waste and Water for Synthesis of Carbon Nanotubes. Cleaner Eng Technol. Elsevier. 2022;8:100459.
[213] Sampaio EFS, Soares OSGP, Pereira MFR, Rodrigues CSD, Madeira LM. Fe-Containing Carbon-Coated Monoliths Prepared by CVD in Gaseous Toluene Abatement - Parametric Analysis of the Fenton Process. Catal Today. Elsevier. 2023;418:114143.
[214] Sivamaran V, Balasubramanian V, Gopalakrishnan M, Viswabaskaran V, Rao AG. Combined Synthesis of Carbon Nanospheres and Carbon Nanotubes Using Thermal Chemical Vapor Deposition Process. Chem Phys Impact. Elsevier. 2022;4:100072.
[215] Li M, Hachiya S, Chen Z, Osawa T, Sugime H, Noda S. Fluidized-Bed Production of 0.3 Mm-Long Single-Wall Carbon Nanotubes at 28% Carbon Yield with 0.1 Mass% Catalyst Impurities Using Ethylene and Carbon Dioxide. Carbon. Pergamon. 2021;182:23–31.
[216] Alexander R, Khausal A, Bahadur J, Dasgupta K. Bi-Directional Catalyst Injection in Floating Catalyst Chemical Vapor Deposition for Enhanced Carbon Nanotube Fiber Yield. Carbon Trends. Elsevier. 2022;9:100211.
[217] Chan KF, Maznam NAM, Hazan MA, Ahmad RNA, Sa'ari AS, Azman NFI, Mamat MS, Rahman MAA, Tanemura M, Yaakob Y. Multi-Walled Carbon Nanotubes Growth by Chemical Vapour Deposition: Effect of Precursor Flowing Path and Catalyst Size. Carbon Trends. Elsevier. 2022;6:100142.
[218] Prabu S, Chiang KY. Highly Active Ni–Mg–Al Catalyst Effect on Carbon Nanotube Production from Waste Biodegradable Plastic Catalytic Pyrolysis. Environ Technol Innov. Elsevier. 2022;28:102845.
[219] Shoukat R, Khan MI. Carbon Nanotubes/Nanofibers (CNTs/CNFs): A Review on State of the Art Synthesis Methods. Microsyst Technol. Springer Science and Business Media Deutschland GmbH. 2022;28:885–901.
[220] Mubarak NM, Sahu JN, Karri RR, Abdullah EC, Tripathi M. Effect of Hydrogen Flow Rate on the Synthesis of Carbon Nanofiber Using Microwave-Assisted Chemical Vapour Deposition with Ferrocene as a Catalyst. Int J Hydrogen Energy. Pergamon. 2023;48:21332–21344.
[221] Silva AA, Pinheiro RA, Trava-Airoldi VJ, Corat EJ. Influence of Catalyst Particles on Multi-Walled Carbon Nanotubes Morphology and Structure. Taylor & Francis. 2018;26:315–323.
[222] He M, Wang X, Zhang L, Wu Q, Song X, Chernov AI, Fedotov PV, Obraztsova ED, Sainio J, Jiang H, Cui H, Ding F, Kauppinen E. Anchoring Effect of Ni2+ in Stabilizing Reduced Metallic Particles for Growing Single-Walled Carbon Nanotubes. Carbon. Pergamon. 2018;128:249–256.
[223] Liu X, Shen B, Wu Z, Parlett CMA, Han Z, George A, Yuan P, Patel D, Wu C. Producing Carbon Nanotubes from Thermochemical Conversion of Waste Plastics Using Ni/Ceramic Based Catalyst. Chem Eng Sci. Pergamon. 2018;192:882–891.
[224] Lin J, Yang Y, Zhang H, Lin Q, Zhu B. Synthesis and Characterization of In-Situ CNTs Reinforced TiB2-Based Composite by CVD Using Ni Catalysts. Ceram Int. Elsevier. 2018;44:2042–2047.

[225] Keteklahijani YZ, Arjmand M, Sundararaj U. Cobalt Catalyst Grown Carbon Nanotube/Poly(Vinylidene Fluoride) Nanocomposites: Effect of Synthesis Temperature on Morphology, Electrical Conductivity and Electromagnetic Interference Shielding. ChemistrySelect. John Wiley & Sons, Ltd. 2017;2:10271–10284.
[226] Su S, Wang Y, Qin J, Wang C, Yao Z, Lu R, Wang Q. Continuous Method for Grafting CNTs on the Surface of Carbon Fibers Based on Cobalt Catalyst Assisted by Thiourea. J Mater Sci. Springer New York LLC. 2019;54:12498–12508.
[227] Sakurai S, Yamada M, He J, Hata K, Futaba DN. A Hydrogen-Free Approach for Activating an Fe Catalyst Using Trace Amounts of Noble Metals and Confinement into Nanoparticles. J Phys Chem Lett. American Chemical Society. 2022;13:1879–1885.
[228] Verma B, Sewani H, Balomajumder C. Synthesis of Carbon Nanotubes via Chemical Vapor Deposition: An Advanced Application in the Management of Electroplating Effluent. Environ Sci Pollut Res. Springer. 2020;27:14007–14018.
[229] Hoecker C, Smail F, Pick M, Boies A. The Influence of Carbon Source and Catalyst Nanoparticles on CVD Synthesis of CNT Aerogel. Chem Eng J.
[230] Ostadhossein A, Yoon K, van Duin ACT, Seo JW, Seveno D. Do Nickel and Iron Catalyst Nanoparticles Affect the Mechanical Strength of Carbon Nanotubes? Extreme Mech Lett. Elsevier. 2018;20:29–37.
[231] Shibuki S, Akashi T, Watanabe H. Effect of Catalyst Support Layers on Emissivity of Carbon Nanotubes Grown via Floating Catalyst Chemical Vapor Deposition. Meas Sens. Elsevier. 2022;24:100479.
[232] ManasiParkhi M, K SB, Shah MM. Experimental Study on Synthesis of CNT Using Alumina Supported Catalyst by CVD Method. Int J Innov Eng Res Technol. Novateur Publication. 2015;1–4.
[233] Fontana M, Ramos R, Morin A, Dijon J. Direct Growth of Carbon Nanotubes Forests on Carbon Fibers to Replace Microporous Layers in Proton Exchange Membrane Fuel Cells. Carbon. Pergamon. 2021;172:762–771.
[234] Samad S, Loh KS, Wong WY, Lee TK, Sunarso J, Chong ST, Wan Daud WR. Carbon and Non-Carbon Support Materials for Platinum-Based Catalysts in Fuel Cells. Int J Hydrogen Energy. Pergamon. 2020;43:7823–7854.
[235] Mishakov IV, Bauman YI, Brzhezinskaya M, Netskina OV, Shubin YV, Kibis LS, Stoyanovskii VO, Larionov KB, Serkova AN, Vedyagin AA. Water Purification from Chlorobenzenes Using Heteroatom-Functionalized Carbon Nanofibers Produced on Self-Organizing Ni-Pd Catalyst. J Environ Chem Eng. Elsevier. 2022;10:107873.
[236] Feng M, Luo ZH, Chen RQ, Yi S, Lu H, Cao GP, Lu C, Feng SY, Li CY. Palladium Supported on Carbon Nanotube Modified Nickel Foam as a Structured Catalyst for Polystyrene Hydrogenation. Appl Catal A Gen. Elsevier. 2019;570:329–338.
[237] Reddy KR, Jyothi MS, Raghu AV, Sadhu V, Naveen S, Aminabhavi TM. Nanocarbons-Supported and Polymers-Supported Titanium Dioxide Nanostructures as Efficient Photocatalysts for Remediation of Contaminated Wastewater and Hydrogen Production. Springer, Cham. 139–169.
[238] Aghaei A, Shaterian M, Hosseini Monfared H, Farokhi A. Designing a Strategy for Fabrication of Single-Walled Carbon Nanotube via CH4/N2 Gas by the Chemical Vapor Deposition Method. Adv Powder Technol. Elsevier. 2022;33:103500.
[239] Thapa A, Wang X, Li W. Synthesis and Field Emission Properties of Cu-Filled Vertically Aligned Carbon Nanotubes. Appl Surf Sci. North-Holland. 2021;537:148086.
[240] Zhang H, Liu Y, Tao J, Liu Y, Bao R, Li F, Yi J. Direct Synthesis of Carbon Nanotube-Graphene Hybrids on Copper Powders and the Mechanical Properties of Corresponding Composites. Mater Sci Eng A. Elsevier. 2021;825:141861.
[241] Liu W, Zhang S, Qian L, Lin D, Zhang J. Growth of High-Density Horizontal SWNT Arrays Using Multi-Cycle in-Situ Loading Catalysts. Carbon. Pergamon. 2020;157:164–168.

[242] Fu S, Chen X, Liu P. Preparation of CNTs/Cu Composites with Good Electrical Conductivity and Excellent Mechanical Properties. Materials Science and Engineering: A. Elsevier. 2020;771:138656.
[243] Olson S, Zietz O, Tracy J, Li Y, Tao C, Jiao J. Low-Temperature Chemical Vapor Deposition Growth of Graphene Films Enabled by Ultrathin Alloy Catalysts. J Vacuum Sci Technol B. American Vacuum Society. 2020;38:032202.
[244] Lv S, Wu Q, Xu Z, Yang T, Jiang K, He M. Chirality Distribution of Single-Walled Carbon Nanotubes Grown from Gold Nanoparticles. Carbon. Pergamon. 2022;192:259–264.
[245] Manawi YM, Ihsanullah, Samara A, Al-Ansari T, Atieh MA. A Review of Carbon Nanomaterials' Synthesis via the Chemical Vapor Deposition (CVD) Method. Materials. Multidisciplinary Digital Publishing Institute. 2018;11:822.
[246] Yao C, Bai W, Geng L, He Y, Wang F, Lin Y. Experimental Study on Microreactor-Based CNTs Catalysts: Preparation and Application. Colloids Surf A Physicochem Eng Asp. Elsevier. 2019;583:124001.
[247] Lim YD, Avramchuck AV, Grapov D, Tan CW, Tay BK, Aditya S, Labunov V. Enhanced Carbon Nanotubes Growth Using Nickel/Ferrocene-Hybridized Catalyst. ACS Omega. American Chemical Society. 2017;2:6063–6071.
[248] Abdulkareem AS, Kariim I, Bankole MT, Tijani JO, Abodunrin TF, Olu SC. Synthesis and Characterization of Tri-Metallic Fe–Co–Ni Catalyst Supported on CaCO3 for Multi-Walled Carbon Nanotubes Growth via Chemical Vapor Deposition Technique. Arab J Sci Eng. Springer Verlag. 2017;42:4365–4381.
[249] Yao D, Wu C, Yang H, Zhang Y, Nahil MA, Chen Y, Williams PT, Chen H. Co-Production of Hydrogen and Carbon Nanotubes from Catalytic Pyrolysis of Waste Plastics on Ni-Fe Bimetallic Catalyst. Energy Convers Manage. Pergamon. 2017;148:692–700.
[250] Yesudhas Jayakumari B, Nattanmai Swaminathan E, Partheeban P. A Review on Characteristics Studies on Carbon Nanotubes-Based Cement Concrete. Constr Build Mater. Elsevier. 2023;367:130344.
[251] Al-Zu'bi M, Fan M, Anguilano L. Advances in Bonding Agents for Retrofitting Concrete Structures with Fibre Reinforced Polymer Materials: A Review. Constr Build Mater. Elsevier. 2022;330:127115.
[252] Wu H, Xia H, Zhang X, Zhang H, Liu H, Sun J. Polydimethylsiloxane/Multi-Walled Carbon Nanotube Nanocomposite Film Prepared by Ultrasonic-Assisted Forced Impregnation with a Superior Photoacoustic Conversion Efficiency of 9.98 × 10−4. SPIE. 2020;14:046003.
[253] Nguyen YH, Mai PT, Phan N, Nguyen T, Tran HV, Nguyen DV, Thi T, Nguyen N, Pham TV, Doan PD, Phan MN. Fabrication of Graphene from Graphite Using High-Powered Ultrasonic Vibrators.
[254] Diego M, Gandolfi M, Casto A, Bellussi FM, Vialla F, Crut A, Roddaro S, Fasano M, Vallée F, Del Fatti N, Maioli P, Banfi F. Ultrafast Nano Generation of Acoustic Waves in Water via a Single Carbon Nanotube. Photoacoustics. Elsevier. 2022;28:100407.
[255] Kudr J, Haddad Y, Richtera L, Heger Z, Cernak M, Adam V, Zitka O. Magnetic Nanoparticles: From Design and Synthesis to Real World Applications. Nanomaterials. Multidisciplinary Digital Publishing Institute. 2017;7:243.
[256] Khan FSA, Mubarak NM, Tan YH, Khalid M, Karri RR, Walvekar R, Abdullah EC, Nizamuddin S, Mazari SA. A Comprehensive Review on Magnetic Carbon Nanotubes and Carbon Nanotube-Based Buckypaper for Removal of Heavy Metals and Dyes. J Hazard Mater. Elsevier. 2021;413:125375.
[257] Lavagna L, Nisticò R, Musso S, Pavese M. Functionalization as a Way to Enhance Dispersion of Carbon Nanotubes in Matrices: A Review. Mater Today Chem. Elsevier. 2021;20:100477.
[258] Pandey A, Qamar SF, Das S, Basu S, Kesarwani H, Saxena A, Sharma S, Sarkar J. Advanced Multi-Wall Carbon Nanotube-Optimized Surfactant-Polymer Flooding for Enhanced Oil Recovery. Fuel. Elsevier. 2024;355:129463.

[259] Li Y, Li R, Fu X, Wang Y, Zhong WH. A Bio-Surfactant for Defect Control: Multifunctional Gelatin Coated MWCNTs for Conductive Epoxy Nanocomposites. Compos Sci Technol. Elsevier. 2018;159:216–224.
[260] Bricha M, El Mabrouk K. Effect of Surfactants on the Degree of Dispersion of MWNTs in Ethanol Solvent. Colloids Surf A Physicochem Eng Asp. Elsevier. 2019;561:57–69.
[261] Sezer N, Koç M. Stabilization of the Aqueous Dispersion of Carbon Nanotubes Using Different Approaches. Thermal Sci Eng Progress. Elsevier. 2018;8:411–417.
[262] Price GJ, Nawaz M, Yasin T, Bibi S. Sonochemical Modification of Carbon Nanotubes for Enhanced Nanocomposite Performance. Ultrason Sonochem. Elsevier. 2018;40:123–130.
[263] Ni C, Zhu L. Investigation on Machining Characteristics of TC4 Alloy by Simultaneous Application of Ultrasonic Vibration Assisted Milling (UVAM) and Economical-Environmental MQL Technology. J Mater Process Technol. Elsevier. 2020;278:116518.
[264] Santha Kumar ARS, Padmakumar A, Kalita U, Samanta S, Baral A, Singha NK, Ashokkumar M, Qiao GG. Ultrasonics in Polymer Science: Applications and Challenges. Prog Mater Sci. Pergamon. 2023;136:101113.
[265] Namathoti S, Ravindra R Kumar, Rama RS. A Review on Progress in Magnetic, Microwave, Ultrasonic Responsive Shape-Memory Polymer Composites. Mater Today: Proc. Elsevier. 2022;56:1182–1191.
[266] Gavrish V, Chayka T, Baranov G, Fedorova S, Gavrish O. Effect of Additives Being WC, TiC, TaC Nanopowder Mixtures on Strength Property of Concrete. Mater Today: Proc. Elsevier. 2019;19:1961–1964.
[267] Gavrish V, Chayka T, Baranov G, Oleynik AY, Shagova YO. Investigation of the Influence of Tungsten Carbide Nanopowder WC and the Mixture of Tungsten Carbides and Titanium Carbides (WC, TiC) on the Change of Concrete Performance Properties. J Phys: Conf Ser. IOP Publishing. 2021;1866:012008.
[268] Dinesh A, Yuvaraj S, Abinaya S, Bhanushri S. Nanopowders as an Additive for Strength and Durability Enhancement of Cement Composite: Review and Prospects. Mater Today: Proc. Elsevier. 2023.
[269] Kockerbeck Z, TabkhPaz M, Hugo R, Park S. Robust Nanocomposite Coatings Inspired by Structures of Nacre. Proc Biennial Int Pipeline Conf. IPC. American Society of Mechanical Engineers Digital Collection. 2018;3.
[270] Juhim F, Chee FP, Awang A, Duinong M, Rasmidi R, Rumaling MI. Review—Radiation Shielding Properties of Tellurite and Silicate Glass. ECS J Solid State Sci Technol. IOP Publishing. 2022;11:076006.
[271] Eslami-Farsani R, Aghamohammadi H, Khalili SMR, Ebrahimnezhad-Khaljiri H, Jalali H. Recent Trend in Developing Advanced Fiber Metal Laminates Reinforced with Nanoparticles: A Review Study. J Ind Text. SAGE Publications Ltd. 2022;51:7374S-7408S.
[272] Manoj A, Ramachandran R, Menezes PL. Self-Healing and Superhydrophobic Coatings for Corrosion Inhibition and Protection. Int J Adv Manuf Technol. Springer. 2020;106:2119–2131.
[273] Othman NH, Che Ismail M, Mustapha M, Sallih N, Kee KE, Ahmad Jaal R. Graphene-Based Polymer Nanocomposites as Barrier Coatings for Corrosion Protection. Prog Org Coat. Elsevier. 2019;135:82–99.
[274] Gao F, Mu J, Bi Z, Wang S, Li Z. Recent Advances of Polyaniline Composites in Anticorrosive Coatings: A Review. Prog Org Coat. Elsevier. 2021;151:106071.
[275] Nazeer AA, Madkour M. Potential Use of Smart Coatings for Corrosion Protection of Metals and Alloys: A Review. J Mol Liq. Elsevier. 2018;253:11–22.
[276] Han W, Zhou J, Shi Q. Research Progress on Enhancement Mechanism and Mechanical Properties of FRP Composites Reinforced with Graphene and Carbon Nanotubes. Alexandria Eng J. Elsevier. 2023;64:541–579.
[277] Li Y, Wang Q, Wang S. A Review on Enhancement of Mechanical and Tribological Properties of Polymer Composites Reinforced by Carbon Nanotubes and Graphene Sheet: Molecular Dynamics Simulations. Compos Part B Eng. Elsevier. 2019;160:348–361.

[278] Gumede JI, Carson J, Hlangothi SP, Bolo LL. Effect of Single-Walled Carbon Nanotubes on the Cure and Mechanical Properties of Reclaimed Rubber/Natural Rubber Blends. Mater Today Commun. Elsevier. 2020;23:100852.
[279] Geng H, Zhao P, Mei J, Chen Y, Yu R, Zhao Y, Ding A, Peng Z, Liao L, Liao J. Improved Microwave Absorbing Performance of Natural Rubber Composite with Multi-Walled Carbon Nanotubes and Molybdenum Disulfide Hybrids. Polym Adv Technol. John Wiley & Sons, Ltd. 2020;31:2752–2762.
[280] Lin JL, Su SM, He YB, Kang FY. Improving Thermal and Mechanical Properties of the Alumina Filled Silicone Rubber Composite by Incorporating Carbon Nanotubes. New Carbon Mater. Elsevier. 2020;35:66–72.
[281] Gao Y, Jing H, Yu Z, Li L, Wu J, Chen W. Particle Size Distribution of Aggregate Effects on the Reinforcing Roles of Carbon Nanotubes in Enhancing Concrete ITZ. Construction and Building Materials. Elsevier. 2022;327:126964.
[282] Wang J, Dong S, Pang SD, Zhou C, Han B. Pore Structure Characteristics of Concrete Composites with Surface-Modified Carbon Nanotubes. Cement and Concrete Composites. Elsevier. 2022;128:104453.
[283] Adhikary SK, Rudžionis Ž, Tučkutė S, Ashish DK. Effects of Carbon Nanotubes on Expanded Glass and Silica Aerogel Based Lightweight Concrete. Scientific Reports. Nature Publishing Group. 2021;11:1-11.
[284] Jongvivatsakul P, Thongchom C, Mathuros A, Prasertsri T, Adamu M, Orasutthikul S, et al. Enhancing Bonding Behavior between Carbon Fiber-Reinforced Polymer Plates and Concrete Using Carbon Nanotube Reinforced Epoxy Composites. Case Studies in Construction Materials. Elsevier. 2022;17:e01407.
[285] Siahkouhi M, Razaqpur G, Hoult NA, Hajmohammadian Baghban M, Jing G. Utilization of Carbon Nanotubes (CNTs) in Concrete for Structural Health Monitoring (SHM) Purposes: A Review. Construction and Building Materials. Elsevier. 2021;309:125137.
[286] Dinesh A, Ashwathi R, Kamal B, Akash C, Sujith S. Influence of Carbon Nanotube on the Mechanical and Electrical Characteristics of Concrete – A Review. Materials Today: Proceedings. Elsevier. 2023.
[287] Kumar A, Sinha S. Performance of Multiwalled Carbon Nanotube Doped Fired Clay Bricks. Journal of Materials in Civil Engineering. American Society of Civil Engineers. 2022;34:04022349.
[288] Pan Q, Hu J, Hu C, Yan Y. Reparation and Characterization of Carbon Nanotubes Coated on Expanded Perlite as Sound Absorption Composite Materials. Materials Science and Engineering: B. Elsevier. 2023;296:116697.
[289] Singh Rajput N, Dilipbhai Shukla D, Ishan L, Dass V. Effect of MWCNT on Mechanical Properties of Polymer Based Composite Brick. Materials Today: Proceedings. Elsevier. 2021;47:6522–6525.
[290] Zhang JJ, Yang CH, Zhang JS. Thermal Characteristics of Aluminium Hollowed Bricks Filled with Phase Change Materials: Experimental and Numerical Analyses. Applied Thermal Engineering. Pergamon. 2019;155:70–81.
[291] Thethwayo BM, Steenkamp JD. A Review of Carbon-Based Refractory Materials and Their Applications. Journal of the Southern African Institute of Mining and Metallurgy. The Southern African Institute of Mining and Metallurgy. 2020;120:641–650.
[292] Nor AFM, Sultan MTH, Jawaid M, Azmi AMR, Shah AUM. Analysing Impact Properties of CNT Filled Bamboo/Glass Hybrid Nanocomposites through Drop-Weight Impact Testing, UWPI and Compression-after-Impact Behaviour. Composites Part B: Engineering. Elsevier. 2019;168:166–174.
[293] Kamesh B, Singh LK, Kassa MK, Arumugam AB. Synergetic Effect of Incorporating Graphene, CNT and Hybrid Nanoparticles on the Mechanical Properties of Glass Fiber Reinforced Epoxy Laminated Composites. Cogent Engineering. Cogent. 2023;10.
[294] Tan YJ, Li J, Cai JH, Tang XH, Liu JH, Hu Z qian, et al. Comparative Study on Solid and Hollow Glass Microspheres for Enhanced Electromagnetic Interference Shielding in

Polydimethylsiloxane/Multi-Walled Carbon Nanotube Composites. Composites Part B: Engineering. Elsevier. 2019;177:107378.
[295] Uribe-Riestra G, Ayuso-Faber P, Rivero-Ayala M, Cauich-Cupul J, Gamboa F, Avilés F. Structural Health Monitoring of Carbon Nanotube-Modified Glass Fiber-Reinforced Polymer Composites by Electrical Resistance Measurements and Digital Image Correlation. Structural Health Monitoring. SAGE Publications Ltd. 2023.
[296] Krishnamurthy A, Tao R, Senses E, Doshi SM, Burni FA, Natarajan B, et al. Multiscale Polymer Dynamics in Hierarchical Carbon Nanotube Grafted Glass Fiber Reinforced Composites. ACS Applied Polymer Materials. American Chemical Society. 2019;1:1905–1917.
[297] Idumah CI. Novel Trends in Conductive Polymeric Nanocomposites, and Bionanocomposites. Synthetic Metals. Elsevier. 2021;273:116674.
[298] Fang X, Chen X, Liu Y, Li Q, Zeng Z, Maiyalagan T, et al. Nanocomposites of Zr(IV)-Based Metal-Organic Frameworks and Reduced Graphene Oxide for Electrochemically Sensing Ciprofloxacin in Water. ACS Applied Nano Materials. American Chemical Society. 2019;2:2367–2376.
[299] Alavi M, Rai M. Recent Advances in Antibacterial Applications of Metal Nanoparticles (MNPs) and Metal Nanocomposites (MNCs) against Multidrug-Resistant (MDR) Bacteria. Expert Review of Anti-infective Therapy. Taylor & Francis. 2019;17:419–428.
[300] Zaghloul MMY, Zaghloul MMY, Fuseini M. Recent Progress in Epoxy Nanocomposites: Corrosion, Structural, Flame Retardancy and Applications — A Comprehensive Review. Polymers for Advanced Technologies. John Wiley & Sons, Ltd. 2023.
[301] Zhou MY, Ren LB, Fan LL, Zhang YWX, Lu TH, Quan GF, et al. Progress in Research on Hybrid Metal Matrix Composites. Journal of Alloys and Compounds. Elsevier. 2020;838:155274.
[302] Khanna V, Kumar V, Bansal SA. Mechanical Properties of Aluminium-Graphene/Carbon Nanotubes (CNTs) Metal Matrix Composites: Advancement, Opportunities and Perspective. Materials Research Bulletin. Pergamon. 2021;138:111224.
[303] Hassan T, Salam A, Khan A, Khan SU, Khanzada H, Wasim M, et al. Functional Nanocomposites and Their Potential Applications: A Review. Journal of Polymer Research. Springer. 2021;28:2.
[304] Kumar A, Sharma K, Dixit AR. A Review on the Mechanical Properties of Polymer Composites Reinforced by Carbon Nanotubes and Graphene. Carbon Letters. Springer. 2021;31:149–165.
[305] Nurazzi NM, Sabaruddin FA, Harussani MM, Kamarudin SH, Rayung M, Asyraf MRM, et al. Mechanical Performance and Applications of CNTs Reinforced Polymer Composites—A Review. Nanomaterials. Multidisciplinary Digital Publishing Institute. 2021;11:2186.
[306] Basheer BV, George JJ, Siengchin S, Parameswaranpillai J. Polymer Grafted Carbon Nanotubes—Synthesis, Properties, and Applications: A Review. Nano-Structures & Nano-Objects. Elsevier. 2020;22:100429.
[307] Wu H, Fahy WP, Kim S, Kim H, Zhao N, Pilato L, et al. Recent Developments in Polymers/Polymer Nanocomposites for Additive Manufacturing. Progress in Materials Science. Pergamon. 2020;111:100638.
[308] Sementsov Y, Yang W, Ivanenko K, Makhno S, Kartel M. Modification of Rubber Compositions by Carbon Nanotubes. Applied Nanoscience (Switzerland). Springer Science and Business Media Deutschland GmbH. 2022;12:621–628.
[309] Kumar Singaravel D, Sharma S, Kumar P. Recent Progress in Experimental and Molecular Dynamics Study of Carbon Nanotube Reinforced Rubber Composites: A Review. Polymer-Plastics Technology and Materials. Taylor & Francis. 2022;61:1792–1825.
[310] Hsiao FR, Wu IF, Liao YC. Porous CNT/Rubber Composite for Resistive Pressure Sensor. Journal of the Taiwan Institute of Chemical Engineers. Elsevier. 2019;102:387–393.

[311] Shao J, Zhu H, Zhao B, Haruna SI, Xue G, Jiang W, et al. Combined Effect of Recycled Tire Rubber and Carbon Nanotubes on the Mechanical Properties and Microstructure of Concrete. Construction and Building Materials. Elsevier. 2022;322:126493.
[312] Wang Y, Suo J, Wang H, Wang D, Wei L, Zhu H. Preparation and Reinforcement Performance of RGO-CNTs-SiO2 Three-Phase Filler for Rubber Composites. Composites Science and Technology. Elsevier. 2022;228:109633.
[313] Lee J, Kim J, Shin Y, Jung I. Ultra-Robust Wide-Range Pressure Sensor with Fast Response Based on Polyurethane Foam Doubly Coated with Conformal Silicone Rubber and CNT/TPU Nanocomposites Islands. Composites Part B: Engineering. Elsevier. 2019;177:107364.
[314] Lin M, Zheng Z, Yang L, Luo M, Fu L, Lin B, et al. A High-Performance, Sensitive, Wearable Multifunctional Sensor Based on Rubber/CNT for Human Motion and Skin Temperature Detection. Advanced Materials. John Wiley & Sons, Ltd. 2022;34:2107309.
[315] Sankhla AM, Patel KM, Makhesana MA, Giasin K, Pimenov DY, Wojciechowski S, et al. Effect of Mixing Method and Particle Size on Hardness and Compressive Strength of Aluminium Based Metal Matrix Composite Prepared through Powder Metallurgy Route. Journal of Materials Research and Technology. Elsevier. 2022;18:282–292.
[316] Qian L, Zheng Y, Or T, Park HW, Gao R, Park M, et al. Advanced Material Engineering to Tailor Nucleation and Growth towards Uniform Deposition for Anode-Less Lithium Metal Batteries. Small. John Wiley & Sons, Ltd. 2022;18:2205233.
[317] Ali N, Bahman AM, Aljuwayhel NF, Ebrahim SA, Mukherjee S, Alsayegh A. Carbon-Based Nanofluids and Their Advances towards Heat Transfer Applications—A Review. Nanomaterials. Multidisciplinary Digital Publishing Institute. 2021;11:1628.
[318] Gao F, Tian W, Wang Z, Wang F. Effect of Diameter of Multi-Walled Carbon Nanotubes on Mechanical Properties and Microstructure of the Cement-Based Materials. Construction and Building Materials. Elsevier. 2020;260:120452.
[319] Gao F, Tian W, Wang Z, Wang F. Effect of Diameter of Multi-Walled Carbon Nanotubes on Mechanical Properties and Microstructure of the Cement-Based Materials. Construction and Building Materials. Elsevier. 2020;260:120452.
[320] Barra G, Guadagno L, Vertuccio L, Simonet B, Santos B, Zarrelli M, Arena M, Viscardi M. Different Methods of Dispersing Carbon Nanotubes in Epoxy Resin and Initial Evaluation of the Obtained Nanocomposite as a Matrix of Carbon Fiber Reinforced Laminate in Terms of Vibroacoustic Performance and Flammability. Materials. Multidisciplinary Digital Publishing Institute. 2019;12:2998.
[321] Stroganov V, Sagadeev E, Ibragimov R, Potapova L. Mechanical Activation Effect on the Biostability of Modified Cement Compositions. Construction and Building Materials. Elsevier. 2020;246:118506.
[322] Egorov AM, Putsylov IA, Smirnov SE, Fateev SA. Effect of Mechanical Activation on Characteristics of Electrodes Based on Fluorinated Carbon Nanotubes. Russian Journal of Applied Chemistry. Maik Nauka-Interperiodica Publishing. 2016;89:451–454.
[323] Stroganov V, Sagadeev E, Ibragimov R, Potapova L. Mechanical Activation Effect on the Biostability of Modified Cement Compositions. Construction and Building Materials. Elsevier. 2020;246:118506.
[324] Chen Y, Chadderton LT. Improved Growth of Aligned Carbon Nanotubes by Mechanical Activation. Journal of Materials Research. Springer. 2004;19:2791–2794.
[325] Shchegolkov AV, Jang S-H, Shchegolkov AV, Rodionov YV, Glivenkova OA, Shchegolkov S-H, Rodionov AV, Glivenkova YV, Multistage OA, Bartolomeo D. Multistage Mechanical Activation of Multilayer Carbon Nanotubes in Creation of Electric Heaters with Self-Regulating Temperature. Materials. Multidisciplinary Digital Publishing Institute. 2021;14:4654.
[326] Reva VP, Filatenkov A, Mansurov YN, Kuryavyi VG. Stages in Multilayer Carbon Nanotube Formation with Mechanical Activation of Amorphous Carbon. Refractories and Industrial Ceramics. Springer New York LLC. 2016;57:141–145.

[327] Wang Y, Xiao W, Ma K, Dai C, Wang D, Wang J. In-Situ Growth and Anticorrosion Mechanism of a Bilayer CaCO3/MgO Coating via Rapid Electrochemical Deposition on AZ41 Mg Alloy Concrete Formwork. Journal of Materials Research and Technology. Elsevier. 2023;25:6628–6643.
[328] Dumore NS, Mukhopadhyay M. Development of Novel Electrochemical Sensor Based on PtNPs-SeNPs-FTO Nanocomposites via Electrochemical Deposition for Detection of Hydrogen Peroxide. Journal of Environmental Chemical Engineering. Elsevier. 2022;10:107058.
[329] Ata MS, Poon R, Syed AM, Milne J, Zhitomirsky I. New Developments in Non-Covalent Surface Modification, Dispersion and Electrophoretic Deposition of Carbon Nanotubes. Carbon. Pergamon. 2018;130:584–598.
[330] Islam S, Mia MM, Shah SS, Naher S, Shaikh MN, Aziz MA, Ahammad AJS. Recent Advancements in Electrochemical Deposition of Metal-Based Electrode Materials for Electrochemical Supercapacitors. The Chemical Record. John Wiley & Sons, Ltd. 2022;22:e202200013.
[331] Zhou A, Bai J, Hong W, Bai H. Electrochemically Reduced Graphene Oxide: Preparation, Composites, and Applications. Carbon. Pergamon. 2022;191:301–332.
[332] Lota G, Fic K, Frackowiak E. Carbon Nanotubes and Their Composites in Electrochemical Applications. Energy & Environmental Science. The Royal Society of Chemistry. 2011;4:1592–1605.
[333] Souza VHR, Husmann S, Neiva EGC, Lisboa FS, Lopes LC, Salvatierra RV, Zarbin AJG. Flexible, Transparent and Thin Films of Carbon Nanomaterials as Electrodes for Electrochemical Applications. Electrochimica Acta. Pergamon. 2016;197:200–209.
[334] Toth PS, Rodgers ANJ, Rabiu AK, Dryfe RAW. Electrochemical Activity and Metal Deposition Using Few-Layer Graphene and Carbon Nanotubes Assembled at the Liquid–Liquid Interface. Electrochemistry Communications. Elsevier. 2015;50:6–10.
[335] Kim H, Jeong NJ, Lee SJ, Song KS. Electrochemical Deposition of Pt Nanoparticles on CNTs for Fuel Cell Electrode. Korean Journal of Chemical Engineering. Springer. 2008;25:443–445.
[336] Li SM, Wang YS, Yang SY, Liu CH, Chang KH, Tien HW, Wen NT, Ma CCM, Hu CC. Electrochemical Deposition of Nanostructured Manganese Oxide on Hierarchically Porous Graphene–Carbon Nanotube Structure for Ultrahigh-Performance Electrochemical Capacitors. Journal of Power Sources. Elsevier. 2013;225:347–355.
[337] Shahrokhian S, Rastgar S. Electrochemical Deposition of Gold Nanoparticles on Carbon Nanotube Coated Glassy Carbon Electrode for the Improved Sensing of Tinidazole. Electrochimica Acta. Pergamon. 2012;78:422–429.
[338] Tang D, Yin H, Mao X, Xiao W, Wang DH. Effects of Applied Voltage and Temperature on the Electrochemical Production of Carbon Powders from CO2 in Molten Salt with an Inert Anode. Electrochimica Acta. Pergamon. 2013;114:567–573.
[339] Velamakanni A, Magnuson CW, Ganesh KJ, Zhu Y, An J, Ferreira PJ, Ruoff RS. Site-Specific Deposition of Au Nanoparticles in CNT Films by Chemical Bonding. ACS Nano. American Chemical Society. 2010;4:540–546.
[340] Kim GM, Nam IW, Yang B, Yoon HN, Lee HK, Park S. Carbon Nanotube (CNT) Incorporated Cementitious Composites for Functional Construction Materials: The State of the Art. Composite Structures. Elsevier. 2019;227:111244.
[341] Zhu F, Liu W, Liu Y, Shi W. Construction of Porous Interface on CNTs@NiCo-LDH Core-Shell Nanotube Arrays for Supercapacitor Applications. Chemical Engineering Journal. Elsevier. 2020;383:123150.
[342] Tambrallimath V, Keshavamurthy R, Koppad PG, Sethuram D. Mechanical Characterization of PC-ABS Reinforced with CNT Nanocomposites Developed by Fused Deposition Modelling. Journal of Physics: Conference Series. IOP Publishing. 2020;1455:012003.

[343] Shetty V, Patil BJ. Evaluation of the Mechanical Properties and Microstructure Analysis of Heat Treated LM-12 Alloy with SiO2 and CNT Hybrid Metal Matrix Composites. Materials Today: Proceedings. Elsevier. 2021;46:2880–2883.
[344] Lee ER, Shin SE, Takata N, Kobashi M, Kato M. Manufacturing Aluminum/Multiwalled Carbon Nanotube Composites via Laser Powder Bed Fusion. Materials. Multidisciplinary Digital Publishing Institute. 2020;13:3927.
[345] Upadhyay G, Saxena KK, Sehgal S, Mohammed KA, Prakash C, Dixit S, Buddhi D. Development of Carbon Nanotube (CNT)-Reinforced Mg Alloys: Fabrication Routes and Mechanical Properties. Metals. Multidisciplinary Digital Publishing Institute. 2022;12:1392.
[346] Pejak Simunec D, Sola A. Emerging Research in Conductive Materials for Fused Filament Fabrication: A Critical Review. Advanced Engineering Materials. John Wiley & Sons, Ltd. 2022;24:2101476.
[347] Dorigato A, Moretti V, Dul S, Unterberger SH, Pegoretti A. Electrically Conductive Nanocomposites for Fused Deposition Modelling. Synthetic Metals. Elsevier. 2017;226:7–14.
[348] Ghaemi F, Amiri A, Yunus R. Methods for Coating Solid-Phase Microextraction Fibers with Carbon Nanotubes. TrAC Trends in Analytical Chemistry. Elsevier. 2014;59:133–143.
[349] Sathies T, Senthil P, Anoop MS. A Review on Advancements in Applications of Fused Deposition Modelling Process. Rapid Prototyping Journal. Emerald Group Holdings Ltd. 2020;26:669–687.
[350] Kang HH, Lee DH. Fabrication and Characterization of Cauliflower-like Silica Nanoparticles with Hierarchical Structure through Ion Beam Irradiation. Journal of Solid State Chemistry. Academic Press. 2020;289:121528.
[351] Kim DH, Lee DH. Effect of Irradiation on the Surface Morphology of Nanostructured Superhydrophobic Surfaces Fabricated by Ion Beam Irradiation. Applied Surface Science. North-Holland. 2019;477:154–158.
[352] Yang H, Li X, Wang G, Zheng J. Lead Selenide Polycrystalline Coatings Sensitized Using Diffusion and Ion Beam Methods for Uncooled Mid-Infrared Photodetection. Coatings. Multidisciplinary Digital Publishing Institute. 2018;8:444.
[353] Li P, Chen S, Dai H, Yang Z, Chen Z, Wang Y, Chen Y, Peng W, Shan W, Duan H. Recent Advances in Focused Ion Beam Nanofabrication for Nanostructures and Devices: Fundamentals and Applications. Nanoscale. The Royal Society of Chemistry. 2021;13:1529–1565.
[354] Nesov SN, Korusenko PM, Sachkov VA, Bolotov VV, Povoroznyuk SN. Effects of Preliminary Ion Beam Treatment of Carbon Nanotubes on Structures of Interfaces in MOx/Multi-Walled Carbon Nanotube (M =Ti,Sn) Composites: Experimental and Theoretical Study. Journal of Physics and Chemistry of Solids. Pergamon. 2022;169:110831.
[355] Das P, Möller W, Elliman RG, Chatterjee S. Ion Beam Joining of Ceramic and Carbon-Based Nanostructures. Applied Surface Science. North-Holland. 2021;554:149616.
[356] Lee CM, Buyukkaya MA, Aghaeimeibodi S, Karasahin A, Richardson CJK, Waks E. A Fiber-Integrated Nanobeam Single Photon Source Emitting at Telecom Wavelengths. Applied Physics Letters. American Institute of Physics Inc. 2019;114:171101.
[357] Liu C, Cao Y, Wang B, Zhang Z, Lin Y, Xu L, Yang Y, Jin C, Peng LM, Zhang Z. Complementary Transistors Based on Aligned Semiconducting Carbon Nanotube Arrays. ACS Nano. American Chemical Society. 2022;16:21482–21490.
[358] Liu X, Wu Z, Hong D, Wu W, Xue C, Cai X, Ding S, Yao F, Jin C, Wang S. Hf-Contacted High-Performance Air-Stable n-Type Carbon Nanotube Transistors. ACS Applied Electronic Materials. American Chemical Society. 2021;3:4623–4629.
[359] Kudinova ES, Vorobyeva EA, Ivanova NA, Tishkin VV, Alekseeva OK. A Magnetron Sputtering Method for the Application of the Ni Catalyst for the Synthesis Process of

Carbon Nanotube Arrays. Nanotechnologies in Russia. Pleiades journals. 2020;15:715–722.
[360] Aleksanyan M, Sayunts A, Shahkhatuni G, Simonyan Z, Kasparyan H, Kopecký D. Growth, Characterization, and Application of Vertically Aligned Carbon Nanotubes Using the RF-Magnetron Sputtering Method. ACS Omega. American Chemical Society. 2023;8:20949–20958.
[361] Ma Y, Li L, Qian J, Qu W, Luo R, Wu F, Chen R. Materials and Structure Engineering by Magnetron Sputtering for Advanced Lithium Batteries. Energy Storage Materials. 2021;39:203–224.
[362] Luan H, Zhang Q, Cheng GA, Huang H. As(III) Removal from Drinking Water by Carbon Nanotube Membranes with Magnetron-Sputtered Copper: Performance and Mechanisms. ACS Applied Materials and Interfaces. 2018;10:20467–20477.
[363] Yang H, Zhang L, Wang H, Huang S, Xu T, Kong D, Zhang Z, Zang J, Li X, Wang Y. Regulating Na Deposition by Constructing a Au Sodiophilic Interphase on CNT Modified Carbon Cloth for Flexible Sodium Metal Anode. Journal of Colloid and Interface Science. 2022;611:317–326.
[364] Zhang Y, Sun Z, Liu Y, Liu B, Luo L, Su P, Lan C, Guo S, Zhang Z, Han X, Huang W, Wu ZP, Wang M-S, Chen SY. Face-to-Face Conducting Mechanism Enabled by Si-C Bonds for Binder Free Si@CNTs Electrode. Chemical Engineering Journal. 2023;146504.
[365] Chen Z, Lv H, Zhang Q, Wang H, Chen G. Construction of a Cement–Rebar Nanoarchitecture for a Solution-Processed and Flexible Film of a Bi2Te3/CNT Hybrid toward Low Thermal Conductivity and High Thermoelectric Performance. Carbon Energy. 2022;4:115–128.
[366] Ma Y, Li L, Qian J, Qu W, Luo R, Wu F, Chen R. Materials and Structure Engineering by Magnetron Sputtering for Advanced Lithium Batteries. Energy Storage Materials. 2021;39:203–224.
[367] Toma S, Asaka K, Irita M, Saito Y. Bulk Synthesis of Linear Carbon Chains Confined inside Single-Wall Carbon Nanotubes by Vacuum Discharge. Surface and Interface Analysis. 2019;51:131–135.
[368] Kolosko AG, Filippov SV, Popov EO. Vacuum Discharge Analysis of CNT Field Cathode Using a Computerized Field Projector. Journal of Vacuum Science & Technology B. 2023;41.
[369] Wei Y, Jiang K, Liu L, Chen Z, Fan S. Vacuum-Breakdown-Induced Needle-Shaped Ends of Multiwalled Carbon Nanotube Yarns and Their Field Emission Applications. Nano Letters. 2007;7:3792–3797.
[370] Yu R, Fan W, Guo X, Dong S. Highly Ordered and Ultra-Long Carbon Nanotube Arrays as Air Cathodes for High-Energy-Efficiency Li-Oxygen Batteries. Journal of Power Sources. 2016;306:402–407.
[371] Yu YY, Park KC. Focusing Electrode on Focal Spot Size and Dose by Carbon Nanotube Based Cold Cathode Electron Beam (C-Beam). 36th IEEE International Vacuum Nanoelectronics Conference, IVNC 2023. Institute of Electrical and Electronics Engineers Inc. 2023;137–138.
[372] Carpena-Núñez J, Davis B, Islam AE, Brown J, Sargent G, Murphy N, Back T, Maschmann MR, Maruyama B. Water-Assisted, Electron-Beam Induced Activation of Carbon Nanotube Catalyst Supports for Mask-Less, Resist-Free Patterning. Carbon. 2018;135:270–277.
[373] Han SJ, Tang J, Kumar B, Falk A, Farmer D, Tulevski G, Jenkins K, Afzali A, Oida S, Ott J, Hannon J, Haensch W. High-Speed Logic Integrated Circuits with Solution-Processed Self-Assembled Carbon Nanotubes. Nature Nanotechnology. 2017;12:861–865.
[374] Busà C, Rickard JJS, Chun E, Chong Y, Navaratnam V, Goldberg Oppenheimer P. Tunable Superapolar Lotus-to-Rose Hierarchical Nanosurfaces via Vertical Carbon Nanotubes Driven Electrohydrodynamic Lithography. Nanoscale. 2017;9:1625–1636.
[375] Wang A, Zhao J, Chen K, Li Z, Li C, Dai Q. Ultracoherent Single-Electron Emission of Carbon Nanotubes. Advanced Materials. 2023;35:2300185.

[376] Zhang J, Wang X, Mei H, Cheng Y, Xu M. Self-Assembly of Single-Walled Carbon Nanotubes Arrays with Different Line Width. Ferroelectrics. 2019;549:78–86.
[377] Kodama T, Ohnishi M, Park W, Shiga T, Park J, Shimada T, Shinohara H, Shiomi J, Goodson KE. Modulation of Thermal and Thermoelectric Transport in Individual Carbon Nanotubes by Fullerene Encapsulation. Nature Materials. 2017;16:892–897.
[378] Kim E, Lee BJ, Maleski K, Chae Y, Lee Y, Gogotsi Y, Ahn CW. Microsupercapacitor with a 500 Nm Gap between MXene/CNT Electrodes. Nano Energy. 2021;81:105616.
[379] Helke C, Canpolat-Schmidt CH, Heldt G, Schermer S, Hartmann S, Voigt A, Reuter D. Intra-Level Mix and Match Lithography with Electron Beam Lithography and i-Line Stepper Combined with Resolution Enhancement for Structures below the CD-Limit. Micro and Nano Engineering. 2023;19:100189.
[380] Yang Y, Kulandaivel A, Mehrez S, Mahariq I, Elbadawy I, Mohanavel V, Jalil AT, Saleh MM. Developing a High-Performance Electromagnetic Microwave Absorber Using BaTiO3/CoS2/CNTs Triphase Hybrid. Ceramics International. 2023;49:2557–2569.
[381] Gong C, Ding J, Wang C, Zhang Y, Guo Y, Song K, Shi C, He F. Defect-Induced Dipole Polarization Engineering of Electromagnetic Wave Absorbers: Insights and Perspectives. Composites Part B: Engineering. 2023;252:110479.
[382] Zhou C, Lin F, Tang Y, Liu Y, Luo X, Qi Y, Xu S, Qiu Y, Yan H, Tong X, Neogi A, Liu Z, Zhou X, Wang C, Bao J, Wang Z. Highly Effective Electromagnetic Interference Shielding Composites with Solvent-Dispersed Uniformly Aligned Graphene Nanosheets Enabled by Strong Intrinsic Diamagnetism under Magnetic Field. Materials Today Physics. 2023;31:100985.
[383] Dubey KA, Bhardwaj YK. High-Performance Polymer-Matrix Composites: Novel Routes of Synthesis and Interface-Structure-Property Correlations. Springer, Singapore. 2021;1–25.
[384] Kazakova MA, Semikolenova NV, Korovin EY, Zhuravlev VA, Selyutin AG, Velikanov DA, Moseenkov SI, Andreev AS, Lapina OB, Suslyaev VI, Matsko MA, Zakharov VA, Lacaillerie JBdE. Co/Multi-Walled Carbon Nanotubes/Polyethylene Composites for Microwave Absorption: Tuning the Effectiveness of Electromagnetic Shielding by Varying the Components Ratio. Composites Science and Technology. 2021;207:108731.
[385] Zhu T, Shen W, Wang X, Song YF, Wang W. Paramagnetic CoS2@MoS2 Core-Shell Composites Coated by Reduced Graphene Oxide as Broadband and Tunable High-Performance Microwave Absorbers. Chemical Engineering Journal. 2019;378:122159.
[386] Liang J, Li H, Qi L, Tian W, Li X, Chao X, Wei J. Fabrication and Mechanical Properties of CNTs/Mg Composites Prepared by Combining Friction Stir Processing and Ultrasonic Assisted Extrusion. Journal of Alloys and Compounds. 2017;728:282–288.
[387] Kundalwal SI, Rathi A. Improved Mechanical and Viscoelastic Properties of CNT-Composites Fabricated Using an Innovative Ultrasonic Dual Mixing Technique. Journal of the Mechanical Behavior of Materials. 2020;29:77–85.
[388] Rennhofer H, Zanghellini B. Dispersion State and Damage of Carbon Nanotubes and Carbon Nanofibers by Ultrasonic Dispersion: A Review. Nanomaterials. 2021;11:1469.
[389] Marcotte A, Mouterde T, Niguès A, Siria A, Bocquet L. Mechanically Activated Ionic Transport across Single-Digit Carbon Nanotubes. Nature Materials. 2020;19:1057–1061.
[390] El Moumen A, Tarfaoui M, Nachtane M, Lafdi K. Carbon Nanotubes as a Player to Improve Mechanical Shock Wave Absorption. Composites Part B: Engineering. 2019;164:67–71.
[391] Domagalski Ł, Kubacka E, Marczak J, Herisanu N, Marinca B, Marinca V. Nonlinear Vibration of Double-Walled Carbon Nanotubes Subjected to Mechanical Impact and Embedded on Winkler–Pasternak Foundation. Materials. 2022;15:8599.
[392] Schlagenhauf L, Nüesch F, Wang J. Release of Carbon Nanotubes from Polymer Nanocomposites. Fibers;2014;2:108–127.

[393] Ozden S, Autreto PAS, Tiwary CS, Khatiwada S, Machado L, Galvao DS, Vajtai R, Barrera EV, Ajayan PM. Unzipping Carbon Nanotubes at High Impact. Nano Letters. 2014;14:4131–4137.
[394] Tseluikin VN, Koreshkova AA. Electrochemical Deposition and Properties of Composite Coatings Consisting of Zinc and Carbon Nanotubes. Russian Journal of Applied Chemistry. 2015;88:272–274.
[395] Pei X, Zeng Y, He R, Li Z, Tian L, Wang J, Wan Q, Li X, Bao H. Single-Walled Carbon Nanotubes/Hydroxyapatite Coatings on Titanium Obtained by Electrochemical Deposition. Applied Surface Science. 2014;295:71–80.
[396] Zeng Y, Pei X, Yang S, Qin H, Cai H, Hu S, Sui L, Wan Q, Wang J. Graphene Oxide/Hydroxyapatite Composite Coatings Fabricated by Electrochemical Deposition. Surface and Coatings Technology. 2016;286:72–79.
[397] Mishra P, Jain R. Electrochemical Deposition of MWCNT-MnO2/PPy Nano-Composite Application for Microbial Fuel Cells. International Journal of Hydrogen Energy. 2016;41:22394–22405.
[398] Zhang R, Fan L, Fang Y, Yang S. Electrochemical Route to the Preparation of Highly Dispersed Composites of ZnO/Carbon Nanotubes with Significantly Enhanced Electrochemiluminescence from ZnO. Journal of Materials Chemistry. 2008;18:4964–4970.
[399] Ren C, Yan Y, Sun B, Gu B, Chou TW. Wet-Spinning Assembly and in Situ Electrodeposition of Carbon Nanotube-Based Composite Fibers for High Energy Density Wire-Shaped Asymmetric Supercapacitor. Journal of Colloid and Interface Science. 2020;569:298–306.
[400] Khazeni D, Saremi M, Soltani R. Development of HA-CNTs Composite Coating on AZ31 Magnesium Alloy by Cathodic Electrodeposition. Part 1: Microstructural and Mechanical Characterization. Ceramics International. 2019;45:11174–11185.
[401] Safavi MS, Walsh FC, Surmeneva MA, Surmenev RA, Khalil-Allafi J. Electrodeposited Hydroxyapatite-Based Biocoatings: Recent Progress and Future Challenges. Coatings ;2021;11:110.
[402] Song G, Sun L, Li S, Sun Y, Fu Q, Pan C. Synergistic Effect of Gr and CNTs on Preparing Ultrathin Cu-(CNTs+Gr) Composite Foil via Electrodeposition. Composites Part B: Engineering. 2020;187:107841.
[403] Yan F, Liu L, Li M, Zhang M, Shang L, Xiao L, Ao Y. One-Step Electrodeposition of Cu/CNT/CF Multiscale Reinforcement with Substantially Improved Thermal/Electrical Conductivity and Interfacial Properties of Epoxy Composites. Composites Part A: Applied Science and Manufacturing. 2019;125:105530.
[404] Zheng H, Zhang W, Li B, Zhu J, Wang C, Song G, Wu G, Yang X, Huang Y, Ma L. Recent Advances of Interphases in Carbon Fiber-Reinforced Polymer Composites: A Review. Composites Part B: Engineering. 2022;233:109639.
[405] Guo H, Lv R, Bai S. Recent Advances on 3D Printing Graphene-Based Composites. Nano Materials Science. 2019;1:101–115.
[406] Zheng M, Chi Y, Hu Q, Tang H, Jiang X, Zhang L, Zhang S, Pang H, Xu Q. Carbon Nanotube-Based Materials for Lithium–Sulfur Batteries. Journal of Materials Chemistry A. 2019;7:17204–17241.
[407] Zhang Z, Kong L-L, Liu S, Li G-R, Gao X-P, Zhang Z, Kong L-L, Liu S, Li G-R.X., Gao P. A High-Efficiency Sulfur/Carbon Composite Based on 3D Graphene Nanosheet@Carbon Nanotube Matrix as Cathode for Lithium–Sulfur Battery. Advanced Energy Materials. 2017;7:1602543.
[408] Chai L, Hu Z, Wang X, Xu Y, Zhang L, Li T-T, Hu Y, Qian J, Huang S, Chai L.L., Hu Z.Y., Wang X., Xu Y.W., Hu Y., Qian J.J., Huang S.M., Zhang L.J. Stringing Bimetallic Metal–Organic Framework-Derived Cobalt Phosphide Composite for High-Efficiency Overall Water Splitting. Advanced Science. 2020;7:1903195.

[409] Milowska KZ, Ghorbani-Asl M, Burda M, Wolanicka L, Ćatić N, Bristowe PD, Koziol KKK. Breaking the Electrical Barrier between Copper and Carbon Nanotubes. Nanoscale. 2017;9:8458–8469.
[410] Chu K, Wang F, Wang X. hu, Li Y. biao, Geng Z. rong, Huang D. jian, Zhang H. Interface Design of Graphene/Copper Composites by Matrix Alloying with Titanium. Materials & Design. 2018;144:290–303.
[411] Yuan Q. hong, Zhou G. hua, Liao L, Liu Y, Luo L. Interfacial Structure in AZ91 Alloy Composites Reinforced by Graphene Nanosheets. Carbon. 2018;127:177–186.
[412] Yuan M, Sun L, Lu X.W., Jiang P, Bao X.H. Enhancing the Thermoelectric Performance of Cu–Ni Alloys by Introducing Carbon Nanotubes. Materials Today Physics. 2021;16:100311.
[413] Korusenko PM, Nesov SN, Bolotov V. V., Povoroznyuk SN, Pushkarev AI, Ivlev KE, Smirnov DA. Formation of Tin-Tin Oxide Core–Shell Nanoparticles in the Composite SnO2−x/Nitrogen-Doped Carbon Nanotubes by Pulsed Ion Beam Irradiation. Nuclear Instruments and Methods in Physics Research Section B: Beam Interactions with Materials and Atoms. 2017;394:37–43.
[414] Athanasiou CE, Zhang H, Ramirez C, Xi J, Baba T, Wang X, Zhang W, Padture NP, Szlufarska I, Sheldon BW. High Toughness Carbon-Nanotube-Reinforced Ceramics via Ion-Beam Engineering of Interfaces. Carbon. 2020;163:169–177.
[415] Chou J.S., Cheng M.Y., Hsieh Y.M., Yang I.T., Hsu H.T. Optimal Path Planning in Real Time for Dynamic Building Fire Rescue Operations Using Wireless Sensors and Visual Guidance. Automation in Construction. 2019;99:1–17.
[416] Mazari SA, Ali E, Abro R, Khan F.S.A., Ahmed I, Ahmed M, Nizamuddin S, Siddiqui T.H., Hossain N, Mubarak NM, Shah A. Nanomaterials: Applications, Waste-Handling, Environmental Toxicities, and Future Challenges – A Review. Journal of Environmental Chemical Engineering. 2021;9:105028.
[417] Sun M, Wu J, Lu P, Zhang Z, Zhang Y, Li D. Sphere-like MoS2 and Porous TiO2 Composite Film on Ti Foil as Lithium-Ion Battery Anode Synthesized by Plasma Electrolytic Oxidation and Magnetron Sputtering. Journal of Alloys and Compounds. 2022;892:162075.
[418] Yang L, Jiang S, Chen Y, Xu Z, Ni Q. Effect of Carbon/Tantalum Hybrid Film on the Properties of Carbon Fiber and Its Composites Based on Magnetron Sputtering. Composites Science and Technology. 2023;243:110224.
[419] Aslan N, Kurt M.Ş., Mehmet Koç M. Morpho-Structural and Optoelectronic Properties of Diamond like Carbon–Germanium (DLC-Ge) Composite Thin Films Produced by Magnetron Sputtering. Optical Materials. 2022;126:112229.
[420] Yang L, Jiang S, Chen Y, Li C, Xu Z, Ni Q. Effect of Multi-Scale Film Interfaces on CFEP Composite Mechanical Properties Based on Magnetron Sputtering Technology. Diamond and Related Materials. 2023;139:110355.
[421] Yang L, Xia H, Xu Z, Lihua Z, Ni Q. Influence of Surface Modification of Carbon Fiber Based on Magnetron Sputtering Technology on Mechanical Properties of Carbon Fiber Composites. Materials Research Express. 2020;7:105602.
[422] Hussain S, Erikson H, Kongi N, Merisalu M, Ritslaid P, Sammelselg V, Tammeveski K. Heat-Treatment Effects on the ORR Activity of Pt Nanoparticles Deposited on Multi-Walled Carbon Nanotubes Using Magnetron Sputtering Technique. International Journal of Hydrogen Energy. 2017;42:5958–5970.
[423] Yang P, Xi X, Huang T, Zhong Q, Jiang B, Liu R, Wu D. An Acid-Assisted Vacuum Filtration Approach towards Flexible PDI/SWCNT Cathodes for Highly Stable Organic Lithium Ion Batteries. Electrochimica Acta. 2020;338:135771.
[424] Luo L, Shen Y, Han D, Qin X, Liang J, Li B, Zhang Y, Deng S. Study on Optimization of Carbon Nanotube Nano-Cold Cathode Array for an Electron Beam Pumping Ultraviolet Light Emitting Device. 36th IEEE International Vacuum Nanoelectronics Conference, IVNC 2023. Institute of Electrical and Electronics Engineers Inc. 2023;169–171.

[425] Rodiansyah A, Park K.C. Functionalize of Vertically Aligned CNTs Emitter (C-Beam) for Surface Modification and Patterning of Self-Assembled Monolayers (SAM). 2021 34th International Vacuum Nanoelectronics Conference, IVNC 2021. Institute of Electrical and Electronics Engineers Inc.
[426] Harito C, Bavykin D. V., Yuliarto B, Dipojono H.K., Walsh FC. Polymer Nanocomposites Having a High Filler Content: Synthesis, Structures, Properties, and Applications. Nanoscale. 2019;11:4653–4682.
[427] Guo J, Jiang H, Teng Y, Xiong Y, Chen Z, You L, Xiao D. Recent Advances in Magnetic Carbon Nanotubes: Synthesis, Challenges and Highlighted Applications. Journal of Materials Chemistry B. 2021;9:9076–9099.
[428] Llusar J, Climente J.I. Shell Filling and Paramagnetism in Few-Electron Colloidal Nanoplatelets. Physical Review Letters. 2022;129:066404.
[429] Kozak N, Matzui L, Vovchenko L, Kosyanchuk L, Oliynyk V, Antonenko O, Nesin S, Gagolkina Z. Influence of Coordination Complexes of Transition Metals on EMI-Shielding Properties and Permeability of Polymer Blend/Carbon Nanotube/Nickel Composites. Composites Science and Technology. 2020;200:108420.
[430] Datsyuk V, Trotsenko S, Trakakis G, Boden A, Vyzas-Asimakopoulos K, Parthenios J, Galiotis C, Reich S, Papagelis K. Thermal Properties Enhancement of Epoxy Resins by Incorporating Polybenzimidazole Nanofibers Filled with Graphene and Carbon Nanotubes as Reinforcing Material. Polymer Testing. 2020;82:106317.
[431] Kotop MA, El-Feky MS, Alharbi YR, Abadel AA, Binyahya AS. Engineering Properties of Geopolymer Concrete Incorporating Hybrid Nano-Materials. Ain Shams Engineering Journal. 2021;12:3641–3647.
[432] Atinafu DG, Wi S, Yun BY, Kim S. Engineering Biochar with Multiwalled Carbon Nanotube for Efficient Phase Change Material Encapsulation and Thermal Energy Storage. Energy. 2021;216:119294.
[433] Dong W, Li W, Shen L, Sun Z, Sheng D. Piezoresistivity of Smart Carbon Nanotubes (CNTs) Reinforced Cementitious Composite under Integrated Cyclic Compression and Impact. Composite Structures. 2020;241:112106.
[434] Choi YC. Cyclic Heating and Mechanical Properties of CNT Reinforced Cement Composite. Composite Structures. 2021;256:113104.
[435] Soni SK, Thomas B, Kar VR. A Comprehensive Review on CNTs and CNT-Reinforced Composites: Syntheses, Characteristics and Applications. Materials Today Communications. 2020;25:101546.
[436] Patil SP, Shendye P, Markert B. Molecular Dynamics Simulations of Silica Aerogel Nanocomposites Reinforced by Glass Fibers, Graphene Sheets and Carbon Nanotubes: A Comparison Study on Mechanical Properties. Composites Part B: Engineering. 2020;190:107884.
[437] Bagherzadeh F, Shafighfard T. Ensemble Machine Learning Approach for Evaluating the Material Characterization of Carbon Nanotube-Reinforced Cementitious Composites. Case Studies in Construction Materials. 2022;17:e01537.
[438] Mousavi MA, Sadeghi-Nik A, Bahari A, Jin C, Ahmed R, Ozbakkaloglu T, de Brito J. Strength Optimization of Cementitious Composites Reinforced by Carbon Nanotubes and Titania Nanoparticles. Construction and Building Materials. 2021;303:124510.
[439] Shi T, Li Z, Guo J, Gong H, Gu C. Research Progress on CNTs/CNFs-Modified Cement-Based Composites – A Review. Construction and Building Materials. 2019;202:290–307.
[440] Jung M, Lee YS, Hong SG, Moon J. Carbon Nanotubes (CNTs) in Ultra-High Performance Concrete (UHPC): Dispersion, Mechanical Properties, and Electromagnetic Interference (EMI) Shielding Effectiveness (SE). Cement and Concrete Research. 2020;131:106017.
[441] Thomoglou AK, Falara MG, Voutetaki ME, Fantidis JG, Tayeh BA, Chalioris CE. Electromechanical Properties of Multi-Reinforced Self-Sensing Cement-Based Mortar with MWCNTs, CFs, and PPs. Construction and Building Materials. 2023;400:132566.

[442] Kumar R, Jana P. Exact Modal Analysis of Multilayered FG-CNT Plate Assemblies Using the Dynamic Stiffness Method. Mechanics of Advanced Materials and Structures. 2023;30:4501–4520.
[443] Li J, Zhao Y, Hao W, Miao L, Zhao G, Li J, Sang Y, Cheng G, Sui C, Wang C. Improvement in Compressive Stiffness of Graphene Aerogels by Sandwiching Carbon Nanotubes. Diamond and Related Materials. 2023;135:109897.
[444] Emin ÇETİN M. Investigation of Carbon Nanotube Reinforcement to Polyurethane Adhesive for Improving Impact Performance of Carbon Fiber Composite Sandwich Panels. International Journal of Adhesion and Adhesives. 2022;112:103002.
[445] Shanmugam L, Kazemi ME, Li Z, Luo W, Xiang Y, Yang L, Yang J. Low-Velocity Impact Behavior of UHMWPE Fabric/Thermoplastic Laminates with Combined Surface Treatments of Polydopamine and Functionalized Carbon Nanotubes. Composites Communications. 2020;22:100527.
[446] Çetin ME. The Effect of Carbon Nanotubes Modified Polyurethane Adhesive on the Impact Behavior of Sandwich Structures. Polymer Composites. 2021;42:4353–4365.
[447] Obradović V, Simić D, Zrilić M, Stojanović DB, Uskoković PS. Novel Hybrid Nanostructures of Carbon Nanotube/Fullerene-like Tungsten Disulfide as Reinforcement for Aramid Fabric Composites. Fibers and Polymers. 2021;22:528–539.
[448] Naqi A, Abbas N, Zahra N, Hussain A, Shabbir SQ. Effect of Multi-Walled Carbon Nanotubes (MWCNTs) on the Strength Development of Cementitious Materials. Journal of Materials Research and Technology. 2019;8:1203–1211.
[449] Haider MZ, Jin X, Sharma R, Pei J, Hu JW. Enhancing the Compressive Strength of Thermal Energy Storage Concrete Containing a Low-Temperature Phase Change Material Using Silica Fume and Multiwalled Carbon Nanotubes. Construction and Building Materials. 2022;314:125659.
[450] Arrechea S, Guerrero-Gutiérrez EMA, Velásquez L, Cardona J, Posadas R, Callejas K, Torres S, Díaz R, Barrientos C, García E. Effect of Additions of Multiwall Carbon Nanotubes (MWCNT, MWCNT-COOH and MWCNT-Thiazol) in Mechanical Compression Properties of a Cement-Based Material. Materialia. 2020;11:100739.
[451] Abdalla JA, Thomas BS, Hawileh RA, Syed Ahmed Kabeer KI. Influence of Nanomaterials on the Workability and Compressive Strength of Cement-Based Concrete. Materials Today: Proceedings. 2022;65:2073–2076.
[452] Zhang S, Sun K, Liu H, Chen X, Zheng Y, Shi X, Zhang D, Mi L, Liu C, Shen C. Enhanced Piezoresistive Performance of Conductive WPU/CNT Composite Foam through Incorporating Brittle Cellulose Nanocrystal. Chemical Engineering Journal. 2020;387:124045.
[453] Silvestro L, Jean Paul Gleize P. Effect of Carbon Nanotubes on Compressive, Flexural and Tensile Strengths of Portland Cement-Based Materials: A Systematic Literature Review. Construction and Building Materials. 2020;264:120237.
[454] Han J, Wang S, Zhu S, Huang C, Yue Y, Mei C, Xu X, Xia C. Electrospun Core-Shell Nanofibrous Membranes with Nanocellulose-Stabilized Carbon Nanotubes for Use as High-Performance Flexible Supercapacitor Electrodes with Enhanced Water Resistance, Thermal Stability, and Mechanical Toughness. ACS Applied Materials and Interfaces. 2019;11:44624–44635.
[455] Tajzad I, Ghasali E. Production Methods of CNT-Reinforced Al Matrix Composites: A Review. Journal of Composites and Compounds. 2020;2:1–9.
[456] Zare Y, Rhee KY. Evaluation of the Tensile Strength in Carbon Nanotube-Reinforced Nanocomposites Using the Expanded Takayanagi Model. JOM. 2019;71:3980–3988.
[457] Xiong N, Bao R, Yi J, Tao J, Liu Y, Fang D. Interface Evolution and Its Influence on Mechanical Properties of CNTs/Cu-Ti Composite. Materials Science and Engineering: A. 2019;755:75–84.

[458] Taylor LW, Dewey OS, Headrick RJ, Komatsu N, Peraca NM, Wehmeyer G, Kono J, Pasquali M. Improved Properties, Increased Production, and the Path to Broad Adoption of Carbon Nanotube Fibers. Carbon. 2021;171:689–694.
[459] Wu Y, Dong C, Yuan C, Bai X, Zhang L, Tian Y. MWCNTs Filled High-Density Polyethylene Composites to Improve Tribological Performance. Wear. 2021;477:203776.
[460] Nyanor P, El-Kady O, Yehia HM, Hamada AS, Hassan MA. Effect of Bimodal-Sized Hybrid TiC–CNT Reinforcement on the Mechanical Properties and Coefficient of Thermal Expansion of Aluminium Matrix Composites. Metals and Materials International. 2021;27:753–766.
[461] Rimamnya ND, Samson AO, Bunmi DC, Abass GF, Olaniyan AJ, Samson IA, Moyofoluwa OO, Kolawole BT. Evolution of Carbon Nanotubes, Their Methods, And Application as Reinforcements in Polymer Nanocomposites: A Review. Journal of Advanced Mechanical Engineering Applications. 2023;4:49–63.
[462] Jeon H, Kim Y, Yu WR, Lee JU. Exfoliated Graphene/Thermoplastic Elastomer Nanocomposites with Improved Wear Properties for 3D Printing. Composites Part B: Engineering. 2020;189:107912.
[463] Kalangi C. Carbon Nanotubes Enhance the Mechanical and Corrosion Properties of Thermally Sprayed Ceramic Coatings.
[464] Han D, Yan G, Wang C. Influence of Multi-Walled Carbon Nanotubes (MWCNTs) Content on Metal Friction and Wear in Thermally Cracked Carbon Black (CBp) Formulation System during Mixing. Polymer Testing. 2022;113:107674.
[465] Nayak C, Balani K. Effects of Reinforcements and Gamma-Irradiation on Wear Performance of Ultra-High Molecular Weight Polyethylene as Acetabular Cup Liner in Hip-Joint Arthroplasty: A Review. Journal of Applied Polymer Science. 2021;138:51275.
[466] Lv C, Wang H, Liu Z, Wang C, Zhang W, Li M, Zhu Y. Fabrication of Durable Fluorine-Free Polyphenylene Sulfide/Silicone Resin Composite Superhydrophobic Coating Enhanced by Carbon Nanotubes/Graphene Fillers. Progress in Organic Coatings. 2019;134:1–10.
[467] Hussain AK, Seetharamaiah N, Pichumani M, Chakra CS. Research Progress in Organic Zinc Rich Primer Coatings for Cathodic Protection of Metals – A Comprehensive Review. Progress in Organic Coatings. 2021;153:106040.
[468] Wang Z, Yu J, Li G, Zhang M, Leung CKY. Corrosion Behavior of Steel Rebar Embedded in Hybrid CNTs-OH/Polyvinyl Alcohol Modified Concrete under Accelerated Chloride Attack. Cement and Concrete Composites. 2019;100:120–129.
[469] Nayak SR, Mohana KNS, Hegde MB, Rajitha K, Madhusudhana AM, Naik SR. Functionalized Multi-Walled Carbon Nanotube/Polyindole Incorporated Epoxy: An Effective Anti-Corrosion Coating Material for Mild Steel. Journal of Alloys and Compounds. 2021;856:158057.
[470] Rui M, Jiang Y, Zhu A. Sub-Micron Calcium Carbonate as a Template for the Preparation of Dendrite-like PANI/CNT Nanocomposites and Its Corrosion Protection Properties. Chemical Engineering Journal. 2020;385:123396.
[471] Zhou B, Li Y, Li Z, Ma J, Zhou K, Liu C, Shen C, Feng Y. Fire/Heat-Resistant, Anti-Corrosion and Folding Ti2C3Tx MXene/Single-Walled Carbon Nanotube Films for Extreme-Environmental EMI Shielding and Solar-Thermal Conversion Applications. Journal of Materials Chemistry C. 2021;9:10425–10434.
[472] Rui M, Zhu A. The Synthesis and Corrosion Protection Mechanisms of PANI/CNT Nanocomposite Doped with Organic Phosphoric Acid. Progress in Organic Coatings. 2021;153:106134.
[473] Sivaraj D, Vijayalakshmi K. Enhanced Antibacterial and Corrosion Resistance Properties of Ag Substituted Hydroxyapatite/Functionalized Multiwall Carbon Nanotube Nanocomposite Coating on 316L Stainless Steel for Biomedical Application. Ultrasonics Sonochemistry. 2019;59:104730.
[474] Sharma V, Goyat MS, Hooda A, Pandey JK, Kumar A, Gupta R, Upadhyay AK, Prakash R, Kirabira JB, Mandal P, Bhargav PK. Recent Progress in Nano-Oxides and CNTs Based

Corrosion Resistant Superhydrophobic Coatings: A Critical Review. Progress in Organic Coatings. 2020;140:105512.
[475] Say Y, Guler O, Dikici B. Carbon Nanotube (CNT) Reinforced Magnesium Matrix Composites: The Effect of CNT Ratio on Their Mechanical Properties and Corrosion Resistance. Materials Science and Engineering: A. 2020;798:139636.
[476] Shin B, Mondal S, Lee M, Kim S, Huh YI, Nah C. Flexible Thermoplastic Polyurethane-Carbon Nanotube Composites for Electromagnetic Interference Shielding and Thermal Management. Chemical Engineering Journal. 2021;418:129282.
[477] Jin X, Wang J, Dai L, Wang W, Wu H. Largely Enhanced Thermal Conductive, Dielectric, Mechanical and Anti-Dripping Performance in Polycarbonate/Boron Nitride Composites with Graphene Nanoplatelet and Carbon Nanotube. Composites Science and Technology. 2019;184:107862.
[478] Wei J, Liao M, Ma A, Chen Y, Duan Z, Hou X, Li M, Jiang N, Yu J. Enhanced Thermal Conductivity of Polydimethylsiloxane Composites with Carbon Fiber. Composites Communications. 2020;17:141–146.
[479] Wentao he, Gao J, Liao S, Wang X, Qin S, Song P. A Facile Method to Improve Thermal Stability and Flame Retardancy of Polyamide 6. Composites Communications. 2019;13:143–150.
[480] Liu Z, Chen Z, Yu F. Enhanced Thermal Conductivity of Microencapsulated Phase Change Materials Based on Graphene Oxide and Carbon Nanotube Hybrid Filler. Solar Energy Materials and Solar Cells. 2019;192:72–80.
[481] An D, Cheng S, Zhang Z, Jiang C, Fang H, Li J, Liu Y, Wong CP. A Polymer-Based Thermal Management Material with Enhanced Thermal Conductivity by Introducing Three-Dimensional Networks and Covalent Bond Connections. Carbon. 2019;155:258–267.
[482] Guo Y, Ruan K, Shi X, Yang X, Gu J. Factors Affecting Thermal Conductivities of the Polymers and Polymer Composites: A Review. Composites Science and Technology. 2020;193:108134.
[483] Zhang F, Feng Y, Feng W. Three-Dimensional Interconnected Networks for Thermally Conductive Polymer Composites: Design, Preparation, Properties, and Mechanisms. Materials Science and Engineering: R: Reports. 2020;142:100580.
[484] Ding D, Wang J, Yu X, Xiao G, Feng C, Xu W, Bai B, Yang N, Gao Y, Hou X, He G. Dispersing of Functionalized CNTs in Si–O–C Ceramics and Electromagnetic Wave Absorbing and Mechanical Properties of CNTs/Si–O–C Nanocomposites. Ceramics International. 2020;46:5407–5419.
[485] Fang X, Jiang L, Pan L, Yin S, Qiu T, Yang J. High-Thermally Conductive AlN-Based Microwave Attenuating Composite Ceramics with Spherical Graphite as Attenuating Agent. Journal of Advanced Ceramics. 2021;10:301–319.
[486] Vajdi M, Sadegh Moghanlou F, Nekahi S, Ahmadi Z, Motallebzadeh A, Jafarzadeh H, Shahedi Asl M. Role of Graphene Nano-Platelets on Thermal Conductivity and Microstructure of TiB2–SiC Ceramics. Ceramics International. 2020;46:21775–21783.
[487] Liao N, Jia D, Yang Z, Zhou Y. Enhanced Mechanical Properties and Thermal Shock Resistance of Si2BC3N Ceramics with SiC Coated MWCNTs. Journal of Advanced Ceramics. 2019;8:121–132.
[488] Wei H, Yin X, Jiang F, Hou Z, Cheng L, Zhang L. Optimized Design of High-Temperature Microwave Absorption Properties of CNTs/Sc2Si2O7 Ceramics. Journal of Alloys and Compounds. 2020;823:153864.
[489] Wang S, Gong H, Zhang Y, Ashfaq MZ. Microwave Absorption Properties of Polymer-Derived SiCN(CNTs) Composite Ceramics. Ceramics International. 2021;47:1294–1302.
[490] Dai W, Ma T, Yan Q, Gao J, Tan X, Lv L, Hou H, Wei Q, Yu J, Wu J, Yao Y, Du S, Sun R, Jiang N, Wang Y, Kong J, Wong C, Maruyama S, Lin C Te. Metal-Level Thermally Conductive yet Soft Graphene Thermal Interface Materials. ACS Nano. 2019;13:11561–11571.

[491] Park YG, Min H, Kim H, Zhexembekova A, Lee CY, Park JU. Three-Dimensional, High-Resolution Printing of Carbon Nanotube/Liquid Metal Composites with Mechanical and Electrical Reinforcement. Nano Letters. 2019;19:4866–4872.
[492] Sun X, Liu L, Mo Y, Li J, Li C. Enhanced Thermal Energy Storage of a Paraffin-Based Phase Change Material (PCM) Using Nano Carbons. Applied Thermal Engineering. 2020;181:115992.
[493] Jin C, Wu Q, Yang G, Zhang H, Zhong Y. Investigation on Hybrid Nanofluids Based on Carbon Nanotubes Filled with Metal Nanoparticles: Stability, Thermal Conductivity, and Viscosity. Powder Technology. 2021;389:1–10.
[494] Aodkeng S, Sinthupinyo S, Chamnankid B, Hanpongpun W, Chaipanich A. Effect of Carbon Nanotubes/Clay Hybrid Composite on Mechanical Properties, Hydration Heat and Thermal Analysis of Cement-Based Materials. Construction and Building Materials. 2022;320:126212.
[495] Viana TM, Bacelar BA, Coelho ID, Ludvig P, Santos WJ. Behaviour of Ultra-High Performance Concretes Incorporating Carbon Nanotubes under Thermal Load. Construction and Building Materials. 2020;263:120556.
[496] Yang Z, Yang J, Shuai B, Niu Y, Yong Z, Wu K, Zhang C, Qiao X, Zhang Y. Superflexible yet Robust Functionalized Carbon Nanotube Fiber Reinforced Sulphoaluminate Cement-Based Grouting Materials with Excellent Mechanical, Electrical and Thermal Properties. Construction and Building Materials. 2022;328:126999.
[497] Irshidat MR, Al-Nuaimi N, Rabie M. Hybrid Effect of Carbon Nanotubes and Polypropylene Microfibers on Fire Resistance, Thermal Characteristics and Microstructure of Cementitious Composites. Construction and Building Materials. 2021;266:121154.
[498] Gu X, Peng L, Liu P, Bian L, Wei B. Enhanced Thermal Properties and Lab-Scale Thermal Performance of Polyethylene Glycol/Modified Halloysite Nanotube Form-Stable Phase Change Material Cement Panel. Construction and Building Materials. 2022;323:126550.
[499] Zhu Y, Qian Y, Zhang L, Bai B, Wang X, Li J, Bi S, Kong L, Liu W, Zhang L. Enhanced Thermal Conductivity of Geopolymer Nanocomposites by Incorporating Interface Engineered Carbon Nanotubes. Composites Communications. 2021;24:100691.
[500] Shahpari M, Bamonte P, Jalali Mosallam S. An Experimental Study on Mechanical and Thermal Properties of Structural Lightweight Concrete Using Carbon Nanotubes (CNTs) and LECA Aggregates after Exposure to Elevated Temperature. Construction and Building Materials. 2022;346:128376.
[501] Hadipeykani M, Aghadavoudi F, Toghraie D. A Molecular Dynamics Simulation of the Glass Transition Temperature and Volumetric Thermal Expansion Coefficient of Thermoset Polymer Based Epoxy Nanocomposite Reinforced by CNT: A Statistical Study. Physica A: Statistical Mechanics and its Applications. 2020;546:123995.
[502] Wang G, Zhang D, Wan G, Li B, Zhao G. Glass Fiber Reinforced PLA Composite with Enhanced Mechanical Properties, Thermal Behavior, and Foaming Ability. Polymer. 2019;181:121803.
[503] Papageorgiou DG, Terzopoulou Z, Fina A, Cuttica F, Papageorgiou GZ, Bikiaris DN, Chrissafis K, Young RJ, Kinloch IA. Enhanced Thermal and Fire Retardancy Properties of Polypropylene Reinforced with a Hybrid Graphene/Glass-Fibre Filler. Composites Science and Technology. 2018;156:95–102.
[504] Rafiee M, Nitzsche F, Laliberte J, Hind S, Robitaille F, Labrosse MR. Thermal Properties of Doubly Reinforced Fiberglass/Epoxy Composites with Graphene Nanoplatelets, Graphene Oxide and Reduced-Graphene Oxide. Composites Part B: Engineering. 2019;164:1–9.
[505] Shen Z, Bateman S, Wu DY, McMahon P, Dell'Olio M, Gotama J. The Effects of Carbon Nanotubes on Mechanical and Thermal Properties of Woven Glass Fibre Reinforced Polyamide-6 Nanocomposites. Composites Science and Technology. 2009;69:239–244.

[506] Sharma S, Tiwari SK, Shakya S. Mechanical Properties and Thermal Conductivity of Pristine and Functionalized Carbon Nanotube Reinforced Metallic Glass Composites: A Molecular Dynamics Approach. Defence Technology. 2021;17:234–244.
[507] Safari Tarbozagh A, Rezaifar O, Gholhaki M, Abavisani I. Magnetic Enhancement of Carbon Nanotube Concrete Compressive Behavior. Construction and Building Materials. 2020;262:120772.
[508] Liu Y, Cheng X. Effect of Carbon Nanotube Size on Electrical Properties of Cement Mortar under Different Temperatures and Water Content. Geofluids. 2022.
[509] Shen X, Mao T, Li C, Mao F, Xue Z, Xu G, Amirfazli A. Durable Superhydrophobic Coatings Based on CNTs-SiO2gel Hybrids for Anti-Corrosion and Thermal Insulation. Progress in Organic Coatings. 2023;181:107602.
[510] Chousidis N, Zacharopoulou A, Zeris C, Batis G. Corrosion Resistance and Physical-Mechanical Properties of Reinforced Mortars with and without Carbon Nanotubes. Journal of Materials Science and Chemical Engineering. 2022;10:1–23.
[511] Lan Y, Zheng B, Shi T, Ma C, Liu Y, Zhao Z. Crack Resistance Properties of Carbon Nanotube-Modified Concrete. Thomas Telford Ltd. 2022;74:1165–1175.
[512] Mohsen MO, Al Ansari MS, Taha R, Al Nuaimi N, Taqa AA. Carbon Nanotube Effect on the Ductility, Flexural Strength, and Permeability of Concrete. Journal of Nanomaterials. 2019.
[513] Mohsen MO, Alansari M, Taha R, Senouci A, Abutaqa A. Impact of CNTs' Treatment, Length and Weight Fraction on Ordinary Concrete Mechanical Properties. Construction and Building Materials. 2020;264:120698.
[514] Hawreen A, Bogas JA, Kurda R. Mechanical Characterization of Concrete Reinforced with Different Types of Carbon Nanotubes. Arabian Journal for Science and Engineering. 2019;44:8361–8376.
[515] Hassan A, Elkady H, Shaaban IG. Effect of Adding Carbon Nanotubes on Corrosion Rates and Steel-Concrete Bond. Scientific Reports. 2019;9:1–12.
[516] Vikulova M, Nikityuk T, Artyukhov D, Tsyganov A, Bainyashev A, Burmistrov I, Gorshkov N. High-k Three-Phase Epoxy/K1.6(Ni0.8Ti7.2)O16/CNT Composites with Synergetic Effect. Polymers 2022. 2022;14:448.
[517] Dehrooyeh S, Vaseghi M, Sohrabian M, Sameezadeh M. Glass Fiber/Carbon Nanotube/Epoxy Hybrid Composites: Achieving Superior Mechanical Properties. Mechanics of Materials. 2021;161:104025.
[518] Kundalwal SI, Rathi A. Improved Mechanical and Viscoelastic Properties of CNT-Composites Fabricated Using an Innovative Ultrasonic Dual Mixing Technique. Journal of the Mechanical Behavior of Materials. 2020;29:77–85.
[519] David ME, Ion RM, Grigorescu RM, Iancu L, Constantin M, Stirbescu RM, Gheboianu AI. Wood Surface Modification with Hybrid Materials Based on Multi-Walled Carbon Nanotubes. Nanomaterials 2022. 2022;12:1990.
[520] Mei S, Wang J, Wan J, Wu X. Preparation Methods and Properties of CNT/CF/G Carbon-Based Nano-Conductive Silicone Rubber. Applied Sciences 2023. 2023;13:6726.
[521] Kumar A, Sinha S. Performance of Multiwalled Carbon Nanotube Doped Fired Clay Bricks. Journal of Materials in Civil Engineering. 2022;34:04022349.
[522] Tijjani Y. High Temperature Applications of Carbon Nanotubes (CNTs) [v]: Thermal Conductivity of CNTs Reinforced Silica Nanocomposite. Bayero Journal of Pure and Applied Sciences. 2022;15:136–140.
[523] Abdeen DH, Atieh MA, Merzougui B, Khalfaoui W. Corrosion Evaluation of 316L Stainless Steel in CNT-Water Nanofluid: Effect of CNTs Loading. Materials 2019. 2019;12:1634.
[524] Radhamani AV, Lau HC, Kamaraj M, Ramakrishna S. Structural, Mechanical and Tribological Investigations of CNT-316 Stainless Steel Nanocomposites Processed via Spark Plasma Sintering. Tribology International. 2020;152:106524.
[525] Eisa MS, Mohamady A, Basiouny ME, Abdulhamid A, Kim JR. Mechanical Properties of Asphalt Concrete Modified with Carbon Nanotubes (CNTs). Case Studies in Construction Materials. 2022;16:e00930.

Research on Engineering Structures & Materials
www.jresm.org
MIM Research Group

Research Article

Growth of highly aligned ZnO nanorod arrays on zinc plates: Morphological and structural characterization

Berrin İkizler*[a], Sümer M. Peker[b]

Department of Chemical Engineering, Ege University, Bornova, İzmir, Turkey

Article Info

Article history:

Received 19 Oct 2023
Accepted 30 Nov 2023

Keywords:

ZnO nanorods;
Hydrothermal method;
Zinc substrate;
High alignment;
Seed layer;
Thermal oxidation

Abstract

In this work, uniform and highly aligned ZnO nanorod arrays were simply synthesized on zinc plates by hydrothermal method using zinc–ammonia complex solution. Effects of ZnO seed layer formation, $Zn(NO_3)_2$ concentration and $NH_3/Zn(NO_3)_2$ mole ratio (R) in the reaction medium on the morphology and crystal structure of nanorods were investigated in detail. ZnO nanorods grown on zinc surfaces were highly crystalline and had a hexagonal wurtzite structure, as revealed by XRD analysis. In addition, the dominant crystal growth direction was in *c*-axis, indicating the verticality of the nanorods. SEM images showed that one-dimensional (1D) ZnO nanorods with high verticality and number density were synthesized on seeded plates whereas randomly oriented arrays were grown on non-seeded surfaces. Increase in the Zn^{2+} concentration changed the top ends of the rods from tapering to hexagonal ends; and also led to an increase in the average size and verticality of the nanorods. The increase in R value (or i.e., amount of NH_3) caused the rods to misalign on the surface and decrease in size. The size of well-aligned nanorods can be adjusted from 50 to 260 nm in diameter and 0.11 to 6 μm in length by changing the reaction parameters, implying their large potential to be used in photocatalytic and also in electronic applications.

1. Introduction

ZnO is a naturally abundant, low cost and chemically stable n-type semiconductor, having a wide and direct band gap of 3.37 eV and a large excitonic binding energy of 60 meV [1-3]. It is distinguished by its properties such as its direct band gap energy, high electron mobility [3], being biocompatible [4], antibacterial [5] and low-toxic [5], and by also its tunable electrochemical [6], luminescence, magnetic, optical and electrical properties [7]. Therefore, ZnO is a promising material in applications such as, nanolasers [8], solar cells [9], gas sensors [10], photocatalysis [11], photoluminescence [4], transparent conductive films [12], energy efficient windows [13], field-emission devices, light-emitting diodes, acoustic wave filters, photonic crystals, photo-detectors, varistors, and piezoelectric materials [7,14].

The performance of ZnO nanoparticles in these applications is highly dependent on their shape, aspect ratio, surface cleanliness, and particle alignment. Also, orientation and interface quality affect the piezoelectric polarization, optical properties and charge carrier transportation properties of ZnO films [13,15]. The substrates coated with well-aligned ZnO nanorods or nanowires may exhibit much larger surface area than that of ZnO films prepared from randomly oriented nanoparticles. Besides, nanorods have higher electron transfer ability along their *c*-axis [16]. Therefore, well aligned one-dimensional (1D) array

*Corresponding author: berrin.ikizler@ege.edu.tr
[a] orcid.org/0000-0001-8889-0754; [b] orcid.org/0009-0009-5347-3884
DOI: http://dx.doi.org/10.17515/resm2023.01ma1019rs

coatings can be more preferred in the fields of electronics, solar cells or sensor applications [17,18].

ZnO nanoscale structures have been produced by methods such as molecular beam epitaxy, pulsed laser deposition, sputtering, anodic alumina oxide template, electrochemical deposition, vapor phase transport, chemical vapor deposition, thermal evaporation, sol-gel and hydrothermal method [1-14,19]. Among them, hydrothermal method is attractive due to its relatively low synthesis temperatures (<100°C) and low pressures, and it does not require complex experimental setups [8,20]. Therefore, the method has advantages such as simplicity, reproducibility, cost effectiveness, and suitability for large-scale production of thin films. Also, well-aligned and crystalline ZnO nanorod arrays can be synthesized by this method using a seeded template layer. Various substrates such as glass [20], ITO [2], aluminum membrane, crystalline quartz, polyethylene terephthalate (PET) wafer [12], carbon fiber, polycarbonate, poly(methyl methacrylate), and paper [3] have been used to grow ZnO nanorods. The growth process occurs in two steps on these surfaces: *(i)* formation of ZnO crystal seeds on the substrates; and *(ii)* synthesis of ZnO nanorods on these seeds by dipping into Zn^{2+} ion containing basic solution. Seeding substrates with ZnO creates sites for homogeneous nucleation of ZnO crystal during the synthesis. Common seeding methods include thermal decomposition of zinc acetate crystallites, spin/dip coating of ZnO nanoparticles and the use of various physical vapor deposition methods [2,17,21]. However, when the substrate is zinc, there is no need for a detailed precoating step before the growth stage [1,8,18,22]. Moreover, zinc foil is a conductive material with an electrical resistivity of 5.9×10^{-8} Ωm, making it facilely utilize the aligned ZnO nanorods for electronic, optoelectronic, and sensor devices. In addition, lattice matching between ZnO and Zn crystals facilitates the growth of a well-aligned ZnO nanorod array [23].

Hydrothermal method has been utilized to obtain ZnO nanostructures on the initially formed seeds by adjusting the reaction parameters. Yu et al. [17] synthesized well-aligned ZnO nanorod arrays on ITO substrates by first dip coating the surfaces with ZnO seed films. Zinc ion concentration and pH of reactions were changed, which revealed ZnO structures in the form of nanotubes, nanosheets, and nanorods with blanket-like shaped surfaces. Torres et al. [24] studied the nucleation and growth of ZnO nanorods on an ITO/PET substrate; and studied the effects of solution concentrations in both the seeding and hydrothermal treatment stages. They obtained ZnO nanorods with an average diameter of 50-195 nm, but not much perpendicular to the surface. The potential applications were stated as power generators and sensors. Lee et al. [1] grew ZnO nanorod arrays on Si substrate and zinc foil by changing the reaction time and thermal pretreatment period. They concluded that the use of zinc foil eliminated the need for ZnO nanoparticle seed layer, but orientation of the ZnO arrays seemed to be influenced negatively. ZnO nanorods were grown on the zinc foil also by Li et al. [21] without using any seed layer. They obtained aligned rods, but after a too long reaction time of 24 h. Yan et al. [23] synthesized ZnO nanorod arrays and flower-like ZnO nanosheets on zinc substrates by using a NaCl solution to accelerate the oxidation of zinc metal, but the process required a long reaction time of 16 h. Yue et al. [18] studied the growth of hierarchical ZnO arrays on zinc foil without the assistance of any seeds, catalysts and surfactants. The synthesized structure consisted of very thin nanosheets attached onto the top of nanorod arrays, but the process required a reaction period of 12 h at 120°C. Momeni [25] realized one-step synthesis of ZnO nanorods on zinc foils and found that their photocatalytic properties depend on the morphology of ZnO. Florica et al. [26] grew large-scale ZnO nanowires directly on zinc foils by thermal oxidation in air. They found that the oxidation temperature was effective on the density, diameter and length of the nanowires, but the alignment was not the focus of the work.

In the light of these findings, it can be stated that most of the studies in the literature focused on single-stage processes (usually applying oxidation in air or water) for the growth of ZnO nanorods on zinc foil. However, although different parameters (such as reaction time, concentration, annealing temperature, or different oxidation strategies, etc.) were investigated, randomly oriented nanorods were generally fabricated with the disadvantage of longer production times (up to 1 day in some studies). In another approach, ZnO nanorods were synthesized by hydrothermal treatment (<150°C) of zinc foils in basic zinc solutions, but the alignment of the rods still needs to be improved. Yet, to our knowledge, the growth of ZnO nanorods on zinc surfaces by combining oxidation and hydrothermal methods (a two-step process) to achieve high verticality has not been investigated, yet. Therefore, in this work, 1D nanorods were synthesized on zinc plates in two-steps: (i) first a seed layer is formed on the substrates by simply oxidizing in air, and then (ii) ZnO rods are grown on these seeds using hydrothermal method just only in 1.5 h within zinc-ammonia complex solution medium. Effects of preconditioning of the substrates, seed layer formation, $Zn(NO_3)_2$ concentration and $NH_3/Zn(NO_3)_2$ mole ratio were investigated in detail by means of the change in morphology and crystal structure of the synthesized ZnO nanorods. In our previous work, ZnO nanorod arrays were grown on glass surfaces, by investigating the effect of the thickness of the seed layer deposited by the spin coating method [27]. We found that chemical stability of ZnO nanorods (especially as photocatalysts) in aqueous media depends on rod verticality, and optimum seeding is a prerequisite for the well alignment. Differing from that work, in this study, zinc plate was used to grow well-aligned 1D ZnO nanorods, by performing a simple and one-step seeding process (i.e., thermal oxidation in air).

2. Materials and Methods

2.1. Materials

Zinc plates with a thickness of 0.5 mm were purchased from Ekmekçioğulları Industry&Trade Inc. (Turkey). The plates were cut into 20 mm × 20 mm dimension and used as the substrate. All chemicals used in the experiments were of analytical grade and purchased from Merck Co. Zinc nitrate hexahydrate ($Zn(NO_3)_2.6H_2O$, > 99%) was used as the Zn^{2+} ion source, and an aqueous ammonia solution (25 wt%), as the OH^- ion source to form nanorod growth solution. Pure water (18.2 MΩ.cm resistivity at 25°C) was used in the preparation of all solutions and obtained from the Millipore Direct-Q8-UV system.

2.2. Pretreatments Applied to the Zinc Substrates

(I) Cleaning: The substrates were subjected to ultrasonic cleaning sequentially in acetone, ethanol, and water (15 min with each solvent) to remove surface impurities before usage. *(II) Thermal oxidation in air (seed formation stage)*: The zinc plates were annealed at 300°C for 3 h and 6 h to produce a layer of ZnO seeds on the surface.

2.3. Growth of ZnO Nanorods on the Substrates

One-dimensional (1D) ZnO nanorods were grown on zinc plates by hydrothermal method using $Zn(OH)_4^{2-}$ complex solution as the reaction medium. The growth solution was prepared by mixing 50 mL of $Zn(NO_3)_2.6H_2O$ solution (in short, Zn^{2+} solution) with NH_3 solution. The molar ratio of NH_3 in this solution was adjusted as $R = n_{NH_3}/n_{Zn^{2+}}$ (see Table 1).

The zinc substrate, with (or without) a seed layer, was placed vertically into a Teflon-sealed stainless steel autoclave. The growth solution was then poured into the autoclave, and immediately the autoclave lid was tightly closed to prevent ammonia from escaping. Hydrothermal synthesis of ZnO nanorods on the surface was performed at a reaction

temperature of 90°C for 1.5 h. After that, the substrate was taken out from the autoclave and washed with water several times to remove the residual salt and amino complex from the surface. Then, it was left to dry under ambient conditions.

The effects of oxidation duration in the seed formation stage, existence of ZnO seed layer on the nanorod formation, concentration of Zn^{2+} and R ratio in the growth solution were investigated systematically (as given in Table 1) to improve the morphological and structural properties of the resultant ZnO nanorods.

Table 1. Investigated parameters, and their corresponding nanorod growth conditions

Parameters	Oxidation of Zn substrates	Nanorod growth conditions		
	Annealing time (h)	$[Zn^{2+}]$ (M)	$R = n_{NH_3}/n_{Zn^{2+}}$ (-)	Reaction time (h)
Oxidation duration	3	-	-	-
	6	-	-	-
ZnO seed layer formation	0	0.01	10	1.5
	3	0.01	10	
$[Zn^{2+}]$ in the growth solution	3	0.01	10	1.5
		0.05	10	
		0.10	10	
		0.15	10	
R ratio in the growth solution	3	0.10	7	1.5
		0.10	10	
		0.10	15	
		0.10	20	

2.4. Characterization

Field emission scanning electron microscopy (SEM, Phillips XL-30S FEG) operating at an accelerating voltage of 7 kV was used to observe the morphology of the ZnO nanorods. The shape, orientation, and dimensions (diameter-D, length-L, and aspect ratio-L/D) of the synthesized ZnO nanorods and also number density of rods over the surface were determined from SEM images using ImageTool-3.0 software. The crystal structure of the ZnO nanorod arrays were analyzed by X-ray diffraction (XRD, Phillips X'Pert Pro) using CuKα radiation for a 2 θ range of $5° - 90°$. X-ray wavelength of CuKα radiation is $\lambda =$ 0.15418 nm. The average grain (crystallite) sizes, D_c, were found from Scherrer equation [11],

$$D_c = (0.9\lambda)/(\beta \cos\theta) \quad (1)$$

where θ and β are Bragg's diffraction angle and full width at half-maximum (FWHM) value of (002) peak in radians, respectively. The (002) peak is the dominant characteristic peak of ZnO for nanorod structure since it describes the growth direction along *c*-axis. In the XRD results, peaks of zinc metal are shown by star (*).

3. Results and Discussion

3.1. Surface Structure of Zinc Substrates

The crystal structure and purity of zinc plates are assessed by XRD analysis, and the result is given in Fig. 1. The diffraction peaks at 36.2°, 38.9°, 43.1°, 54.2°, 69.9°, 70.5°, and 76.9° coincide well with the standard diffraction data of zinc with a JCPDS card no: 87-0713 [28]. The crystal planes corresponding to these peaks are shown in Fig. 1, and no peaks other

than Zn are detected in the diffraction peaks. Thus, it can be concluded that the substrates are pure zinc with hexagonal structure without any impurities.

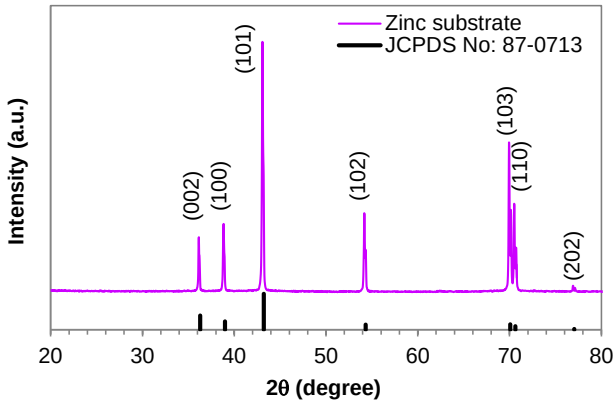

Fig. 1. XRD diffractogram of zinc plates

3.2. Oxidation of Zinc Substrates

Initial preconditioning of the substrates is critical for the growth of nanorod arrays [1,27]. Hence, the surfaces are commonly coated with a ZnO seed layer to lower the thermodynamic energy barrier for the initiation of the crystallization process since these seeds provide nucleation sites for the next reduction and growth process of 1D nanorods [20,29,30]. Therefore, before ZnO synthesis, a ZnO seed layer is formed on the surface simply by air oxidation of the zinc plates without using a detailed pre-coating step in this work. The melting point of zinc metal is ~420°C [28]. Thus, 300°C is chosen as a reasonable temperature for the thermal oxidation. Then, the substrates are annealed for two different durations (3 h and 6 h) to form a ZnO seed layer on the substrates.

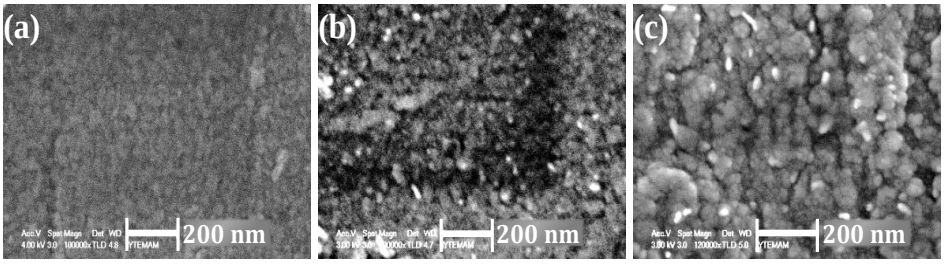

Fig. 2. SEM images of zinc substrate (a) after cleaning; and oxidized at 300°C in air for (b) 3 h and (c) 6 h

The surface morphology of zinc substrates before and after thermal oxidation is evaluated by SEM images, as given in Fig. 2. The surface of the zinc plate seems quite homogeneous (Fig. 2(a)) before annealing. After 3 h annealing, the tiny spherical ZnO seeds are covered over the surface, as shown in Fig. 2(b). The seeds have an average size of ~14±5 nm. When the duration is increased to 6 h, the seeds become readily apparent because of aggregation (Fig. 2(c)), and their sizes increase to ~21±9 nm. However, it seems that, nanorod growth is also initiated on these seeds at longer durations, as revealed from the existence of small thin rods (white shiny parts) observed in the SEM image of Fig. 2(c). The initiation of the scarcely distributed ZnO nanowires was also observed by Florica et al. [25] after thermal

treatment at 400°C for 12 h, and by Chuah and Hassan [31] at 500°C for 30 min. These types of structures will adversely affect the alignment of the nanorods in the growth stage. Furthermore, macro cracks are observed on the surface, and also the zinc plate is bent (no longer a flat surface) after 6 h. Therefore, annealing time is selected as 3 h for seeding the substrates before use.

3.3. Effect of Seed Layer Formation on ZnO Nanorod Growth

ZnO nanorods are grown on both seeded and non-seeded zinc surfaces to investigate the effect of the seed layer. The nanorods grown on seeded and non-seeded plates are shown in Fig. 3(a) and (b), respectively. When the seeded substrates are used, densely distributed and very short nanorods (Fig. 3(a)) are obtained with an average diameter and length of 51±12 nm and 112±17 nm, respectively. While the ZnO nanorods produced on the seeded surfaces grow perpendicular to the surface, randomly oriented rods are obtained on the non-seeded surfaces (Fig. 3(b)). Therefore, because of this inclined orientation, the number density of short rods in the absence of seeding (11.3×10^9 #/cm^2) is less than that of seeded ones (18.1×10^9 #/cm^2). Nevertheless, short rods with nearly similar sizes (D = 81±13 nm and L = 156±18 nm) are formed without seeding. On non-seeded surfaces, it seems that, the initial ZnO nuclei (seeds) are formed on the zinc plate more randomly at the beginning of the crystallization. Thereby, the aggregation of rods and also their misalignment evolves during the growth stage.

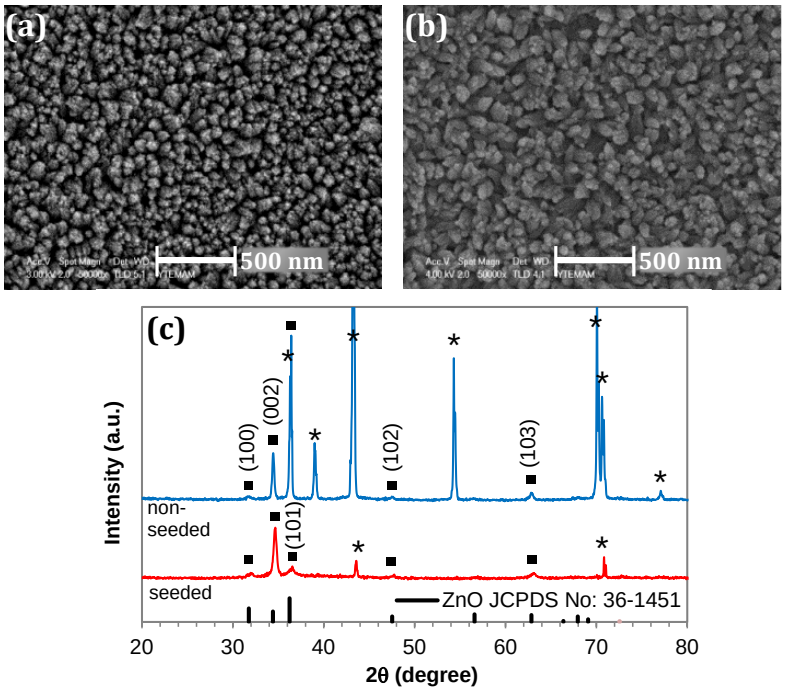

Fig. 3. SEM images of ZnO nanorods grown on (a) seeded and (b) non-seeded substrates; and (c) their corresponding XRD diffractograms ([Zn^{2+}] = 0.01 M, R = 10)

XRD analysis of the synthesized nanorods is given in Fig. 3(c) for both cases. Peaks of ZnO are shown by filled square (■). The diffraction peaks are well indexed with the diffraction pattern of ZnO standard with JCPDS card No: 36-1451, signifying that the synthesized ZnO rods are in hexagonal wurtzite structure [27]. The observed diffraction planes of ZnO for the samples are noted in Fig. 3(c). The peaks originated from the zinc substrate are denoted

by stars in the figure. No additional peaks are detected in the curves, showing the absence of impurities in the nanorods. The intensity of peaks coming from the zinc foil is high in non-seeded substrates, probably due to the misalignment of rods. Contrarily, the intensity of the (002) peak is higher than all other peaks for ZnO nanorods grown on seeded surfaces. This demonstrates the preferential growth of ZnO structures along the *c*-axis direction of the wurtzite unit cell (⟨0001⟩ basal plane of hexagonal rod) [11,28]. Thus, the intense (002) peak observed for seeded ones verifies the high degree of alignment of the resultant nanorods. The highest peak of short rods formed without seeding is in (101) direction, showing growth of both lateral and *c*-axis direction. Overall, it can be inferred that seeding of zinc substrates with a ZnO layer is a crucial preconditioning step to synthesize well-aligned ZnO nanorods.

3.4. Effect of [Zn^{2+}] in the Growth Solution

The changes in the morphology of the ZnO nanorods for different $Zn(NO_3)_2$ concentration are given in Fig. 4 at different magnifications. *R* is taken as constant at 10. With increasing Zn^{2+} concentration, the shape of the obtained structures changes from short and dense rods (0.01 M in Fig. 3(a)) to nanorods with tapering ends (Figs. 4(a-b)), and finally to nanorods having well-faceted hexagonal tops (0.15 M in Fig. 4(c)). Figs. 4(d-f) indicate that the rods are uniformly distributed all over the surface and the degree of verticality of the rods increases with Zn^{2+} concentration.

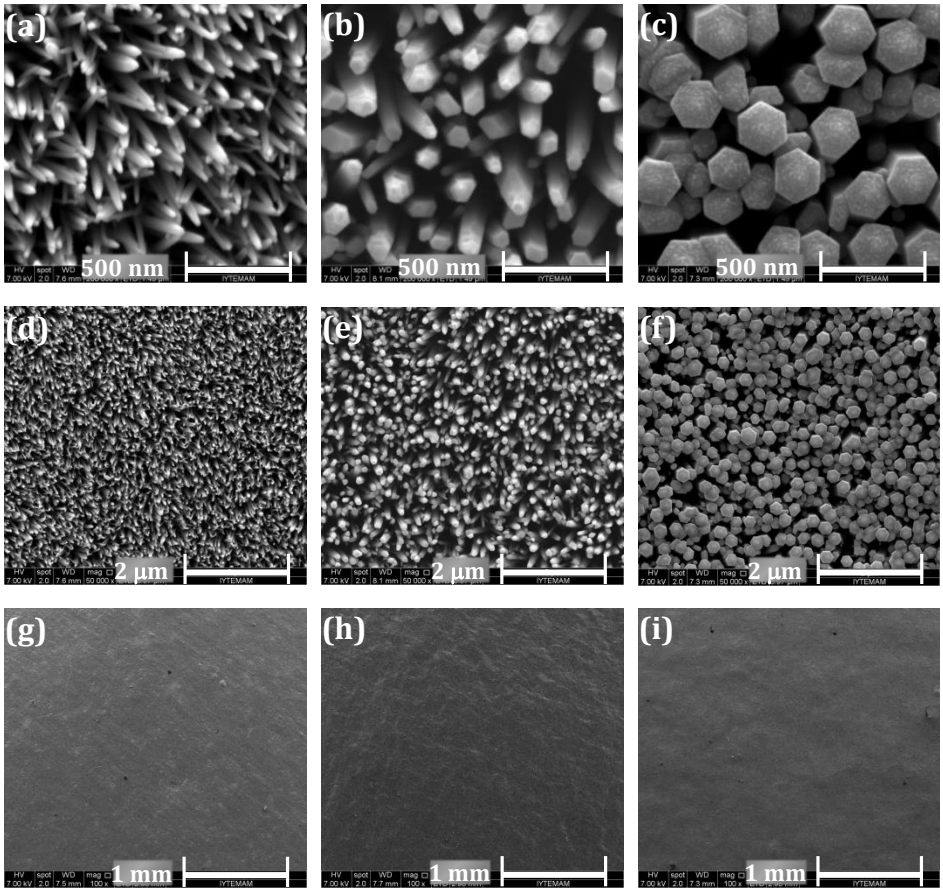

Fig. 4. SEM images of ZnO nanorods synthesized using [Zn^{2+}] of (a,d,g) 0.05 M, (b,e,h) 0.1 M and (c,f,i) 0.15 M, at different magnifications (R = 10)

The view of the coated substrates (~6 mm^2 surface area) in small magnifications is shown in Figs. 4(g-i). Figs. 4(g-i) reveal that nanorods are produced very homogeneously also in millimeter scale. There are no observable cracks or defects in that length scale.

The changes in the diameter, length, aspect ratio, and number density of nanorods are given in Table 2 for each concentration. The diameter of the nanorods increases from ~51 nm to ~257 nm with concentration, so their number density decreases from 18.1×10^9 #/cm^2 to 2.6×10^9 #/cm^2. The length so the aspect ratio of the rods rises up to [Zn^{2+}] = 0.1 M, at which highest values are attained. The maximum rod length of 5.52 μm and L/D ~ 51 is obtained. At [Zn^{2+}] = 0.15 M, the radial growth of rods (D = 257 nm, the biggest diameter in all concentration) and also clear hexagonal face formation at the top ends of the rods is more dominant. So, the growth in length direction is retarded at high Zn^{2+} concentrations.

Table 2. Morphology and dimensions of the ZnO nanorods obtained for different Zn^{2+} concentration at R = 10

	[Zn^{2+}] in the Growth Solution			
Nanorod property	0.01 M	0.05 M	0.10 M	0.15 M
Shape	Nanorods (short and dense)	Nanorods (tapering ends)	Nanorods (tapering ends)	Nanorods (hexagonal ends)
Orientation	Well-aligned	Well-aligned	Well-aligned	Well-aligned
Diameter, D (nm)	51±12	62±8	109±20	257±21
Length, L (μm)	0.11±0.02	1±0.11nm	5.52±0.21	4±0.61
Aspect ratio, L/D	2.2	16.1	50.5	15.6
Number density ($\times10^9$ #/cm^2)	18.1	13.3	6.1	2.6
D_c from XRD (nm)	21.7	38.6	59.0	36.5
FWHM of (002) peak (degree)	0.39	0.23	0.16	0.24

The crystal structures of the nanorods for different concentration of Zn^{2+} are examined using XRD analysis, given in Fig. 5. All peaks conform to the diffraction pattern of ZnO (JCPDS card no: 36-1451) and the synthesized nanorods have hexagonal wurtzite structure. The stars in the figure indicate the zinc coming from zinc foil. The (002) peak has the highest and the dominant intensity compared to other peaks, indicating that the dominant crystallographic growth direction of the nanorods is in the *c*-axis. Another peak at (101) direction is observed for the hexagonal rods formed in 0.15 M Zn^{2+} solution, showing the growth of rods both in lateral and perpendicular direction. The average crystallite sizes calculated using Eq. (1) and FWHM values measured from (002) peak are also noted in Table 2. An increase in D_c and a decrease in FWHM values signify that the crystallinity of ZnO nanorods increases up to 0.1 M and it decreases for 0.15 M along *c*-axis, probably due to the amount of imperfections in the crystal evolved with excess amount of Zn^{2+}. D_c (59 nm) and FWHM (0.16°) values for [Zn^{2+}] = 0.1 M agree well with the values obtained by Thein et al. (FWHM=0.125 and D_c=69.48 nm) for rod-shaped nanoparticles [32], and also by Karaduman Er (FWHM=0.251 and D_c=64.30 nm) for ZnO films [33].

The intensity of (002) diffraction plane (which represents the growth in *c*-axis) is displayed in Fig. 6 for different [Zn^{2+}]. The maximum intensity is detected at 0.1 M, thus verifying the SEM findings. (100), (101), (102) and (103) peaks of ZnO crystal are commonly used to exhibit the crystal growth directions other than the *c*-axis [24].

Therefore, the misalignment of nanorods is tried to be quantified by normalizing intensity of these peaks by the intensity of (002) peak [26], I/I(002).

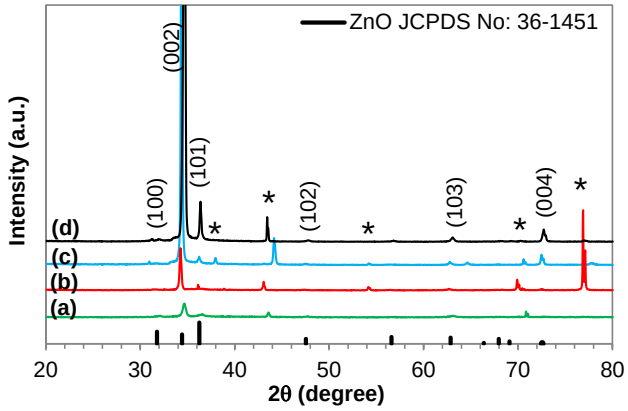

Fig. 5. XRD diffractograms of ZnO nanorods synthesized using [Zn^{2+}] of (a) 0.01 M, (b) 0.05 M, (c) 0.10 M, and (d) 0.15 M

The results are also shown in Fig. 6. The lowest normalized values (in other words, the highest alignment of rods) are observed at 0.1 M condition. This verifies the higher crystalline quality of rods and 1-dimensional growth of them compared to other concentrations. Therefore, 0.1 M is selected as the optimum zinc ion concentration. The cross-sectional view of the resultant nanorods at [Zn^{2+}] = 0.1 M and R = 10 is given in Fig. 7 to show their well-aligned structure.

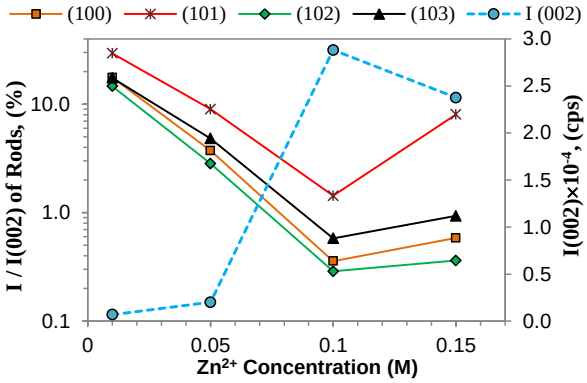

Fig. 6. Normalized XRD peaks of Fig. 5, by the intensity of (002) peak (I(002))

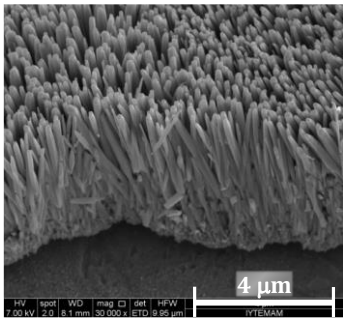

Fig. 7. Cross-sectional SEM view of ZnO nanorods

3.5. Effect of *R* Ratio in the Growth Solution

SEM images of nanorods synthesized at different R value ([Zn^{2+}] = 0.1 M) are given in Fig. 8 and their shape factors are summarized in Table 3. Well-aligned nanorods with tapering ends are obtained over the entire surface for R = 7 (Fig. 8(a)) and R = 10 (Fig. 4(b)). The rods having well-faceted and hexagonal symmetry are produced by further increasing R to 15 (Fig. 8(b)). Diameter of rods rises slightly from 71 nm (R = 7) to 121 nm (R = 15). However, a decrease in length of rods is detected after R > 10. When R = 20, the morphology of nanorods changes completely, and very dense and short rods stuck

together are observed (Fig. 8(c)). This is also observed by Yu et al. [17] for ZnO nanorods grown on ITO substrates, and they even cannot produce any particles on the ITO surface at high concentrations. This could be attributed to the excess amount of ammonia in the growth solution. Zn^{2+} forms stable complex by ammonia at high *R* ratios, which probably resulted in the quenching of nucleation and growth [18,20,21].

Table 3. Morphology and dimensions of the ZnO nanorods obtained for different *R* values at $[Zn^{2+}]$ = 0.10 M

	$R = n_{NH_3}/n_{Zn^{2+}}$			
Nanorod property	7	10	15	20
Shape	Nanorods (tapering ends)	Nanorods (tapering ends)	Nanorods (hexagonal ends)	Thin and very dense rods
Orientation	Well-aligned	Well-aligned	Well-aligned	Well-aligned
Diameter, D (nm)	71±16	109±20	121±18	25±3
Length, L (μm)	1.92±0.21	5.52±0.21	2.32±0.17	0.25±0.03
Aspect ratio, L/D	21.2	50.5	19.1	10.8
Number density ($\times 10^9$ #/cm^2)	9.7	6.1	5.7	56.7
D_c from XRD (nm)	40.4	59.0	37.7	23.2
FWHM of (002) peak (degree)	0.22	0.16	0.23	0.37

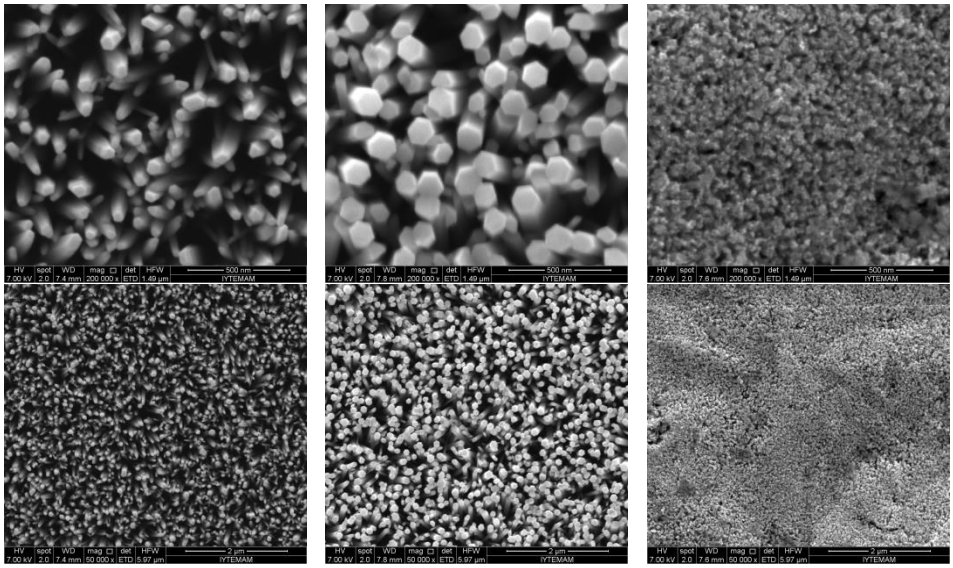

(a) (b) (c)

Fig. 8. SEM images of ZnO nanorods synthesized using $[Zn^{2+}]$ = 0.10 M, and (a) *R* = 7, (b) *R* = 15 and (c) *R* = 20 at different magnifications

XRD result (Fig. 9) revealed that the obtained coatings for all *R* values are ZnO with wurtzite crystal structures; and, the highest intensity peak belong to (002) plane except for *R* = 20. Also, no impurity in the samples is detected. The intensity of (002) peak and average size of crystallites decreases (FWHM value increases) from *R* = 10 to *R* = 20, denoting a decrease in the crystallinity of the rods. As the concentration of NH_3 is increased in the medium, the peak at (101) direction is started to evolve, showing growth of both lateral and perpendicular direction. (101) plane is the highest intensity peak at *R* = 20 and

the data confirms the SEM findings. Normalized peaks are also given in Fig. 10 to determine the degree of misalignment in the nanorods. The minimum I/I(002) values, that is the maximum verticality of rods, coincide at R = 7-10 range, which is compatible with the SEM results. The misalignment in rods increases abruptly for R > 15 and especially at R = 20, where the structure of rods are changed completely.

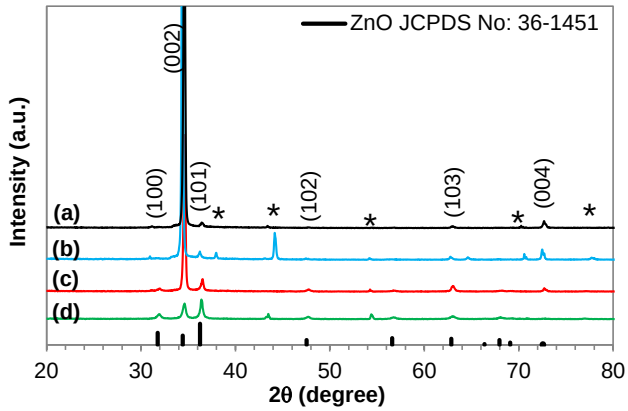

Fig. 9. XRD diffractograms of ZnO nanorods synthesized using [Zn^{2+}] = 0.10 M, and (a) R = 7, (b) R = 10, (c) R = 15, and (d) R = 20

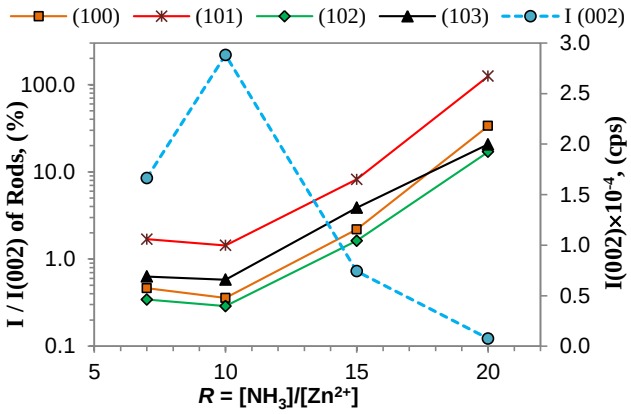

Fig. 10. Normalized XRD peaks of Fig. 8, by the intensity of (002) peak (I(002)) in the *c*-direction

4. Conclusions

In this study, 1D ZnO nanorod arrays were grown on zinc substrates by hydrothermal method in two steps. First, a ZnO seed layer was formed on zinc plates by thermal oxidation of the surfaces without deforming them. Then, ZnO nanorods were grown on these seeds within zinc–ammonia complex solution at a low temperature of 90°C and low durations (1.5 h). The listed parameters were investigated in detail to synthesize uniform and highly aligned ZnO nanorods: (i) the use of seeded and non-seeded substrates; (ii) concentration of $Zn(NO_3)_2$ in the bulk solution (0.01–0.15 M); and (iii) change of $NH_3/Zn(NO_3)_2$ mole ratio, R (7–20). As a conclusion,

- When seeded substrates were used in the reaction, the diameter of the nanorods obtained became smaller and orientation of the rods was more perpendicular to the

surface. Also, the number density of rods was higher because of compact configuration and verticality.

- Nanorods grown on non-seeded plates had random orientation, and they followed the counter of the surface. Therefore, seeding of the substrates is an important step to obtain highly aligned growth of 1D ZnO arrays.
- When $[Zn^{2+}]$ = 0.01 M in the reaction medium, short rods with high population density (18.1×10^9 #/cm^2) and low aspect ratios (~2) were formed all over the surfaces.
- With the increase in $[Zn^{2+}]$ from 0.01 M to 0.15 M, the diameter of the nanorods increased from 50 nm to 250 nm and length, from 110 nm to 5.5 μm. Nanorods with hexagonal structure and high verticality were achieved on seeded substrates and in $[Zn^{2+}]$ = 0.1 M growth solution.
- With the rise in R, misalignment of rods increased. Moreover, the use of excess amount of NH_3 (R = 20) caused the structure of the rods to change completely: from hexagonal ended long nanorods to short and thin rods stuck together.
- XRD analysis showed that all nanorods were ZnO with hexagonal wurtzite crystal structure. The highest intensity peak was detected at (002) direction, which is the 1D growth direction of rods.
- As a result of all parameter investigations, the optimum reaction medium was determined as $[Zn^{2+}]$ = 0.1 M and R = 10, at which the degree of misalignment of the nanorods was only approximately 0.5%.
- The results indicate that these simply grown nanorod arrays have a large potential to be used in photocatalytic and antibacterial applications due to their large exposed surface in polar (002)-direction, and also in electronic, solar cell and sensor applications because of their highly aligned 1D structure. In addition, this approach can be used in large-scale fabrication of nanostructured materials since it is a low temperature, simple technique and does not require a detailed pre-coating step for zinc substrates.

Acknowledgement

The authors acknowledge that this work was supported by the Scientific and Technological Research Council of Türkiye with the grant number of 110M403.

References

[1] Lee JH, Leu IC, Hon MH. Substrate effect on the growth of well-aligned ZnO nanorod arrays from aqueous solution. Journal of Crystal Growth, 2005; 275: e2069 - e2075. https://doi.org/10.1016/j.jcrysgro.2004.11.267

[2] Yu K, Jin Z, Liu X, Liu Z, Fu Y. Synthesis of size-tunable ZnO nanorod arrays from NH3.H2O/ZnNO3 solutions. Materials Letters, 2007; 61: 2775 - 2778. https://doi.org/10.1016/j.matlet.2006.10.029

[3] Le AT, Ahmadipour M, Pung S-Y. A review on ZnO-based piezoelectric nanogenerators: Synthesis, characterization techniques, performance enhancement and applications. Journal of Alloys and Compounds, 2020; 844: 156172. https://doi.org/10.1016/j.jallcom.2020.156172

[4] Chandana MR, Lavanya DR, Radha krushna BR, Daruka prasad B, Malleshappa J, Sharma SC, Joy FrD, Soundararajan P, Nagabhushana H. Effect of precursors on ZnO nanoparticles to enhance the level-III ridge details of LFPs and anti-counterfeiting applications. Materials Science in Semiconductor Processing, 2023; 167: 107749. https://doi.org/10.1016/j.mssp.2023.107749

[5] Yudasari N, Hardiansyah A, Herbani Y, Isnaeni, Suliyanti MM, Djuhana D. Single-step laser ablation synthesis of ZnO-Ag nanocomposites for broad-spectrum dye

photodegradation and bacterial photoinactivation. Journal of Photochemistry & Photobiology, A: Chemistry, 2023; 441: 114717. https://doi.org/10.1016/j.jphotochem.2023.114717
[6] Zhu D, Zheng Y, Xiong Y, Cui C, Ren F, Liu Y. In situ growth of S-doped ZnO thin film enabling dendrite-free zinc anode for high-performance aqueous zinc-ion batteries. Journal of Alloys and Compounds, 2022; 918: 165486. https://doi.org/10.1016/j.jallcom.2022.165486
[7] Sharma DK, Shukla S, Sharma KK, Kumar V. A review on ZnO: Fundamental properties and applications. Materials Today: Proceedings, 2022; 49(8): 3028-3035. https://doi.org/10.1016/j.matpr.2020.10.238
[8] Li Z, Huang X, Liu J, Li Y, Li G. Morphology control and transition of ZnO nanorod arrays by a simple hydrothermal method. Materials Letters, 2008; 62: 1503 - 1506. https://doi.org/10.1016/j.matlet.2007.09.011
[9] Hames Y, Alpaslan Z, Kösemen A, San SE, Yerli Y. Electrochemically grown ZnO nanorods for hybrid solar cell applications. Solar Energy, 2010; 84: 426 – 431. https://doi.org/10.1016/j.solener.2009.12.013
[10] Kakati N, Jee SH, Kim SH, Oh JY, Yoon YS. Thickness dependency of sol-gel derived ZnO thin films on gas sensing behaviors. Thin Solid Films, 2010; 519: 494 - 498. https://doi.org/10.1016/j.tsf.2010.08.005
[11] Torkamani R, Aslibeiki B. Bulk ZnO, nanoparticles, nanorods and thin film: A comparative study of structural, optical and photocatalytic properties. Journal of Crystal Growth, 2023; 618: 127317. https://doi.org/10.1016/j.jcrysgro.2023.127317
[12] Wang Z, Qian X, Yin J, Zhu Z. Large-scale fabrication of tower-like, flower-like, and tube-like ZnO arrays by a simple chemical solution route. Langmuir, 2004; 20: 3441 - 3448. https://doi.org/10.1021/la036098n
[13] Kaidashev EM, Lorenz M, von Wenckstern H, Rahm A, Semmelhack H-C, Han K-H, Benndorf G, Bundesmann C, Hochmuth H, Grundmann M. High electron mobility of epitaxial ZnO films on c-plane sapphire grown by multistep pulsed-laser deposition. Appl. Phys. Lett., 2003; 82: 3901 - 3903. https://doi.org/10.1063/1.1578694
[14] Ghosh R. Recent progress in piezotronic sensors based on one-dimensional zinc oxide nanostructures and its regularly ordered arrays: From design to application. Nano Energy, 2023; 113: 108606. https://doi.org/10.1016/j.nanoen.2023.108606
[15] Wei XH, Jie WJ, Huang W, Zhu J, Li YR. Effect of symmetry of substrate surfaces on the orientation and growth mode of ZnO films. Journal of Crystal Growth, 2009; 311: 2391 - 2396. https://doi.org/10.1016/j.jcrysgro.2009.02.021
[16] Yang Z, Luan C, Zhang W, Liu A, Tang S. Fabrication and optical properties of ZnO nanostructured thin films via mechanical oscillation and hydrothermal method. Thin Solid Films, 2008; 516: 5974 - 5980. https://doi.org/10.1016/j.tsf.2007.10.085
[17] Yu K, Jin Z, Liu X, Zhao J, Feng J. Shape alterations of ZnO nanocrystal arrays fabricated from NH3.H2O solutions. Applied Surface Science, 2007; 253: 4072 - 4078. https://doi.org/10.1016/j.apsusc.2006.09.001
[18] Yue S, Lu J, Zhang J. Controlled growth of well-aligned hierarchical ZnO arrays by a wet chemical method. Materials Letters, 2009; 63: 2149 - 2152. https://doi.org/10.1016/j.matlet.2009.06.055
[19] İkizler B. Preparation of single- and double-layer antireflective coatings by sol-gel method. Research on Engineering Structures and Materials, 2020; 6(1): 1-21.
[20] Baruah S, Dutta J. pH-dependent growth of zinc oxide nanorods. Journal of Crystal Growth, 2009; 311: 2549 - 2554. https://doi.org/10.1016/j.jcrysgro.2009.01.135
[21] Li Z, Huang X, Liu J, Li Y, Ji X, Li G. Growth and comparison of different morphologic ZnO nanorod arrays by a simple aqueous solution route. Materials Letters, 2007; 61: 4362 - 4365. https://doi.org/10.1016/j.matlet.2007.02.003
[22] Li C, Wang Y, Chen S, Zhang W, Wang Z, Hou Z. Enhanced photoelectrochemical performance based on conformal and uniform ZnO/ZnSe/CdSe heterostructures on Zn

foil substrate. International Journal of Hydrogen Energy, 2020; 45: 8257 - 8272. https://doi.org/10.1016/j.ijhydene.2020.01.069
[23] Yan C, Xue D. Solution growth of nano- to microscopic ZnO on Zn. Journal of Crystal Growth, 2008; 310: 1836 - 1840. https://doi.org/10.1016/j.jcrysgro.2007.10.060
[24] Torres FCG, López JLC, Rodríguez ASL, Gallardo PS, Morales ER, Hernández GP, Guillen JCD, Flores LLD. Sol-gel/hydrothermal synthesis of well-aligned ZnO nanorods. Boletín de la Sociedad Española de Cerámica y Vidrio. 2023; 62(4): 348-356. https://doi.org/10.1016/j.bsecv.2022.05.004
[25] Momeni M.M. One-step synthesis of ZnO nanowires on zinc foils and their photocatalytic properties. Indian Journal of Chemistry, 2016; 55A: 686 - 691.
[26] Florica C, Preda N, Costas A, Zgura I. Enculescu I. ZnO nanowires grown directly on zinc foils by thermal oxidation in air: Wetting and water adhesion properties. Materials Letters, 2016; 170: 156 - 159. https://doi.org/10.1016/j.matlet.2016.02.035
[27] İkizler B, Peker SM. Effect of the seed layer thickness on the stability of ZnO nanorod arrays. Thin Solid Films, 2014; 558: 149 - 159. https://doi.org/10.1016/j.tsf.2014.03.019
[28] Widyastuti E, Hsu JL, Lee YC. Insight on photocatalytic and photoinduced antimicrobial properties of ZnO thin films deposited by HiPIMS through thermal oxidation. Nanomaterials, 2022; 12: 463. https://doi.org/10.3390/nano12030463
[29] Vayssieres L, Keis K, Lindquist S-E, Hagfeldt A. Purpose-built anisotropic metal oxide material: 3D highly oriented microrod array of ZnO. Journal of Physical Chemistry B, 2001: 105: 3350 - 3352. https://doi.org/10.1021/jp010026s
[30] Greene LE, Law M, Tan DH, Montano M, Goldberger J, Somorjai G, Yang P. General route to vertical ZnO nanowire arrays using textured ZnO seeds. Nano Letters. 2005; 5(7): 1231-1236. https://doi.org/10.1021/nl050788p
[31] Chuah LS, Hassan Z. Thermal annealing effect on properties of Zn foils substrates. Materials Science Forum, 2015; 819: 215 - 219. https://doi.org/10.4028/www.scientific.net/MSF.819.215
[32] Thein MT, Chim JE, Pung S-Y, Pung Y-F. Highly UV light driven WOx@ZnO nanocomposites synthesized by liquid impregnation method. Journal of Industrial and Engineering Chemistry, 2017; 46: 119-129. https://doi.org/10.1016/j.jiec.2016.10.022
[33] Karaduman Er I. Development of ZnO sensors via succession ionic layer adsorption and reaction (SILAR) method for ppb level NO gas sensing. Research on Engineering Structures and Materials, 2021; 7(2): 259-272. https://doi.org/10.17515/resm2020.212ma0901

Research on Engineering Structures & Materials
www.jresm.org
Research Group

Research Article

Numerical analysis of the primary and secondary structural dynamic interaction effects on elastic floor response spectra

Madhavi Latha Annamdasu[1,a], Surya Prakash Challagulla[*,1,b], Vyshnavi Pesaralanka[1,c], Ismail Hossain[2,d], Daniel Cruze[3,e]

[1]*Dept. of Civil Eng., Koneru Lakshmaiah Education Foundation (Deemed to be University), Vaddeswaram, Guntur, 522302, India*
[2]*School of Natural Sciences and Mathematics, Ural Federal University, Yekaterinburg, 620 000, Russia*
[3]*Dept. of Civil Eng., Hindustan Institute of Technology and Science, India*

Article Info

Article history:

Received 15 Sep 2023
Accepted 17 Nov 2023

Keywords:

Primary structure;
Secondary structure;
Tuning ratio;
Dynamic interaction;
Floor response spectrum;
Component dynamic amplification factor

Abstract

In modern seismic design, the assessment of seismic behavior in secondary structures relies on the evaluation of the primary structure's acceleration at the support of the secondary structure. To enable effective secondary structure design, a thorough understanding of the interaction between the primary and secondary structures is essential. This article conducts an analysis based on parametric data, delving into the dynamic interaction between these structures. In this study, both the elastic primary and secondary structures are represented as single-degree-of-freedom systems. The governing equations of motion for both the coupled and uncoupled systems are derived and solved using the numerical method. Subsequently, the floor response spectrum (FRS) is computed for both coupled and uncoupled configurations. This investigation focuses on the impact of three crucial parameters: the tuning ratio (T_r), the mass ratio (μ), and the damping ratio (ξ_s) on the FRS. The analytical findings reveal that dynamic interaction does not significantly affect the FRS when the mass ratio is very low, at 0.1%. However, for a range of $0.8 \leq T_r \leq 1.2$, dynamic interaction has a substantial influence on the FRS. Additionally, this study underscores that lower damping ratios in the secondary structure result in a more pronounced coupling effect on the FRS.

1. Introduction

A building structure comprises elements that do not resist any loads. Such building elements generally are called Secondary structures (SSs). These structures are broadly categorized into three groups: architectural components, mechanical and electrical components, and building contents. Secondary structures can be divided into displacement-sensitive and acceleration-sensitive depending on the kind of failure they experience. An earthquake's ground motion can be amplified by a structure, causing floor accelerations to be greater than the peak ground acceleration (PGA). If secondary structures (SSs) are not taken into account during the design phase, they will be severely damaged by these amplified accelerations. The survivability of SSs after an earthquake is critical for ensuring the continuation of emergency services, ensuring public safety, and minimizing the financial burden of the subsequent damage. Despite their name, secondary structures are far from insignificant. Furthermore, sometimes secondary structures may be costlier than the primary structure (PS) [1], [2]. Secondary structures have been shown to be vulnerable to earthquakes in recent decades [3]–[6]. Several large hospitals were

*Corresponding author: chsuryaprakash@kluniversity.in
[a] orcid.org/0009-0000-6062-6847; [b]orcid.org/0000-0003-0125-1488; [c] orcid.org/0000-0003-1284-3139; [d] orcid.org/0000-0002-7256-8135; [e] orcid.org/0000-0002-4024-4742
DOI: http://dx.doi.org/10.17515/resm2023.25me0915rs

forced to evacuate during the 1994 Northridge earthquake in Los Angeles due to the failure of critical secondary structures such as emergency power systems, medical equipment control systems, and water supply pipe systems[7] Given the importance of ensuring SS integrity during seismic events, further study is needed to create credible performance-based design criteria for SSs.

For many years, it has been thoroughly studied how the SSs react to earthquakes in order to ensure public safety and lessen the financial effect of the resultant damage. A common method to obtain the seismic demand on the secondary structures is the floor response spectrum (FRS) method. For calculating the input load of a secondary structure, the floor response spectrum approach is frequently used [8]–[10]. To design secondary structures, engineers have frequently employed this technique. This method's major assumption is that the secondary structure doesn't interact with the main structure, that its presence has no impact on the primary system's dynamic response, and that it has no impact on the other way around. When the secondary structure (SS) has significant mass, the validity of this assumption may be compromised. In such cases, the potential for interaction between the primary and secondary structures necessitates the consideration of the entire system [11]–[13]. In general, disregarding the interaction leads to an overestimate of secondary structural demand and, as a result, an excessively conservative design [14]. Hence, there is a need to study the seismic behavior of secondary structures while accounting for the dynamic interaction between the primary and secondary structures. This investigation aims to develop precise and practical methods for evaluating the seismic response of secondary structures.

Numerous researchers have explored the interaction effects and dynamic characteristics of integrated systems by utilizing a combined oscillator-structure model, as indicated in references [11], [15]–[18]. Nevertheless, it's important to note that prior research has not extensively addressed the impact of the dynamic properties of both primary and secondary structures on the seismic performance of secondary structures. Therefore, this study focuses on analyzing the seismic response of the secondary structure in cases where its weight is in the same order of magnitude as that of the primary structure. In this study, we employ single-degree-of-freedom (SDOF) elastic primary (PS) and secondary structures (SS) to explore how their dynamic interaction influences the seismic response of the SS. To assess the seismic demands on secondary structures, we analyse the floor response spectra (FRS) both with and without accounting for dynamic interaction, and we calculate the component dynamic amplification factors (CDAFs). These measures are essential in our evaluation of the seismic behavior of secondary structures. In the generation of FRS, component dynamic amplification factors play an important role as they reflect the amplification of SSs. The impacts of several factors are examined on the FRS and CDAF, including the fundamental vibration period of the PS, the mass ratio, and the damping ratio of the SS. Finally, the component dynamic amplification factors are compared with those obtained from the current code-based formulations.

The paper is organized as follows: Section 2 provides a concise overview of the modelling of both the coupled and uncoupled systems. Section 3 discusses the selection of ground motions and provides specific details pertinent to this research. In Section 4, the research findings are presented, with a focus on three key response parameters: acceleration time history response, floor response spectra, and component dynamic amplification factors. The paper concludes in Section 5 with succinct summarizing remarks.

2. Modelling and Analysis

In this study, a SDOF system is used for both the elastic primary structure (PS) and the elastic secondary structure (SS). Both the PS and SS are considered to be two-dimensional

(2D) framed building systems. In this study, the analysis that incorporates the dynamic interaction is referred to as the "coupled analysis." In the coupled analysis, the entire structure, comprising both the primary and secondary structures, is treated as a two-degree-of-freedom system. Conversely, the "uncoupled analysis" is conducted without considering the dynamic interaction between the primary structure (PS) and secondary structure (SS). During the uncoupled analysis, both the primary and secondary structures are separately regarded as single-degree-of-freedom systems. A series of analysis cases were performed using the uncoupled method to illustrate the observable impact of dynamic interaction between the PS and SS on the seismic response of the SS. Fig. 1 shows the SDOF primary structure attached to an acceleration-sensitive SDOF secondary structure. This study makes the assumption that the primary structure's damping ratio (ξ_p) is 5%.

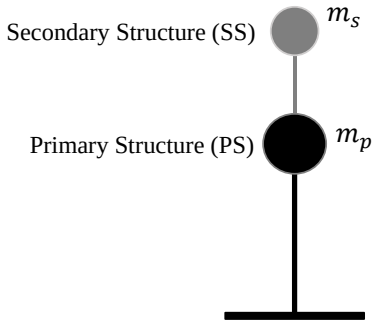

Fig. 1. Primary structure with a Secondary structure

2.1. Uncoupled Analysis

In this type of analysis, the dynamic interaction between the PS and SS (Fig. 1) is neglected. The dynamic response of the primary structure for a given earthquake loading can be computed according to Eq. (1).

$$m_p\ddot{x}_p + c_p\dot{x}_p + k_p x_p = -m_p\ddot{x}_g \tag{1}$$

where m_p, c_p, and k_p are the mass, damping, and stiffness for the primary structure: $c_p = 2m_p\xi_p\omega_p$; ω_p is the given primary structure's frequency; x_p, $\dot{x}_p$, and $\ddot{x}_p$ are the relative displacement, velocity, and acceleration of the primary structure with reference to the ground; $\ddot{x}_g$ is the acceleration of the ground motion; $\ddot{x}_p + \ddot{x}_g$ is the primary structure's absolute acceleration response. To analyze the secondary structure, the absolute acceleration response of the primary structure is given as an input to the secondary structure, and the response of the SS can be computed according to Eq. (2).

$$m_s\ddot{x}_s + c_s\dot{x}_s + k_s x_s = -m_s\left(\ddot{x}_p + \ddot{x}_g\right) \tag{2}$$

where, k_s, c_s, and m_s, are the stiffness, damping, and mass of the secondary structure: $c_s = 2m_s\xi_s\omega_s$; ξ_s, and ω_s are the damping ratio and frequency of the SS; x_s, $\dot{x}_s$, and $\ddot{x}_s$ are the relative displacement, velocity, and acceleration of the secondary structure, respectively. The procedure of generating the floor response spectrum without considering the dynamic interaction between the structures is shown in Fig. 2.

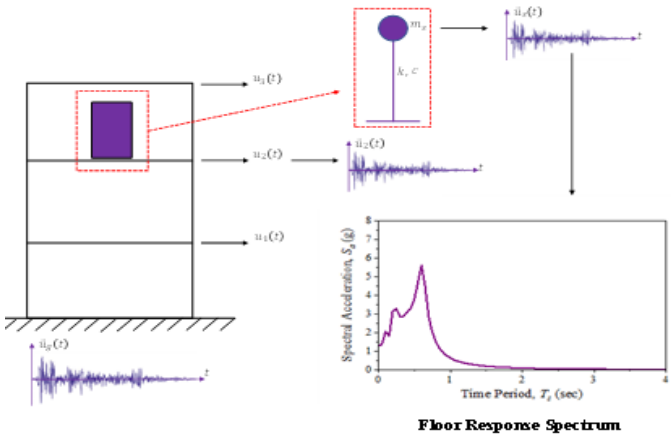

Fig. 2. Procedure for generation of floor response spectrum via uncoupled analysis

2.2. Coupled Analysis

This type of analysis takes into consideration the dynamic interaction between the PS and SS. The dynamic behavior of the PS and SS for a given earthquake loading can be computed according to Eqs. (3) &(4), respectively.

$$m_p\ddot{x}_p + c_p\dot{x}_p - c_s\dot{x}_s + k_px_p - k_sx_s = -m_p\ddot{x}_g \tag{3}$$

$$m_s\ddot{x}_s + c_s\dot{x}_s + k_sx_s = -m_s\left(\ddot{x}_p + \ddot{x}_g\right) \tag{4}$$

Eqs. (3) & (4) can be written in matrix form as follows in eq. (5):

$$\begin{bmatrix} m_p & 0 \\ 0 & m_s \end{bmatrix}\begin{Bmatrix} \ddot{x}_p \\ \ddot{x}_s \end{Bmatrix} + \begin{bmatrix} c_p & -c_s \\ 0 & c_s \end{bmatrix}\begin{Bmatrix} \dot{x}_p \\ \dot{x}_s \end{Bmatrix} + \begin{bmatrix} k_p & -k_s \\ 0 & k_s \end{bmatrix}\begin{Bmatrix} u_p \\ u_s \end{Bmatrix} = -\begin{Bmatrix} m_p\ddot{x}_g \\ m_s\left(\ddot{x}_p + \ddot{x}_g\right) \end{Bmatrix} \tag{5}$$

The Eqs. (1)-(4) are written as a system of first-order ordinary differential equations and solved numerically using the fourth-order Runge-Kutta technique in MATLAB R2019B. The Runge-Kutta method is a numerical technique for approximating solutions to ordinary differential equations (ODEs) with known initial conditions. It subdivides the problem into smaller steps and calculates slopes at various points within each step. By updating the solution at the end of each step, it iteratively refines the approximation until reaching the desired endpoint. The accuracy can be controlled by adjusting the step size, with smaller steps providing greater precision. This method is widely used in various scientific and engineering fields to solve ODEs, especially when exact analytical solutions are unavailable.

3. Ground Motions

Actual ground-motion data provide a realistic response in the seismic response evaluation technique [19], [20]. Such data is freely available in the PEER [21] NGA-West2 Database. As a result, in the current study, 11 horizontal ground motion excitations for hard soil type were examined according to ASCE 7-16 [22] for hard soil type. To reflect hard soil, ground motions with shear wave velocities (V_{S30}) of 360-760 m/s are used [23]. Ground motion details are shown in Table 1. In this study, spectrum compatible ground motions are used since they can greatly reduce computation work compared to multiple ground motions [24]. To generate spectrum-compatible earthquake excitations, the time-domain spectral

matching technique [25] is applied. Fig. 3 depicts the IS 1893:2016 spectra (5% damping) and the mean ground excitation spectra. The average spectrum shall not fall below 90% of the target spectrum for the whole-time range, according to ASCE 7-16. The Fig.3 shows that the mean spectra are over 90% of the target spectra.

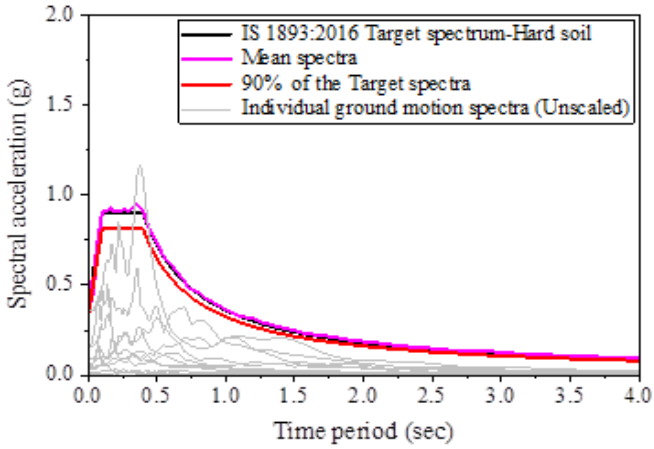

Fig. 3. Target and mean acceleration spectra

Table 1. Details of ground motions

Earthquake	Year	Station	Moment magnitude (Mw)	Joyner Boore distance (Rjb), km	Vs30 (m/s)
Helena_ Montana-01	1935	Carroll College	6	2.07	593.35
Helena_ Montana-02	1935	Helena Fed Bldg	6	2.09	551.82
Kern County	1952	Pasadena - CIT Athenaeum	7.36	122.65	415.13
Kern County	1952	Santa Barbara Courthouse	7.36	81.3	514.99
Kern County	1952	Taft Lincoln School	7.36	38.42	385.43
Southern Calif	1952	San Luis Obispo	6	73.35	493.5
Parkfield	1966	Cholame - Shandon Array #12	6.19	17.64	408.93
Parkfield	1966	San Luis Obispo	6.19	63.34	493.5
Parkfield	1966	Temblor pre-1969	6.19	15.96	527.92
Borrego Mtn	1968	Pasadena - CIT Athenaeum	6.63	207.14	415.13
Borrego Mtn	1968	San Onofre - So Cal Edison	6.63	129.11	442.88

4. Results and Discussion

The following sections investigate the influence of a dynamic interaction between the PS and SS on the dynamic behavior of the elastic SDOF secondary structure. The acceleration time-history response of the secondary structure and the floor response spectrum (FRS) are studied in this research.

4.1 Acceleration Time-History Response

In this section, the acceleration response of the secondary structure is presented as shown in Fig. 4. To investigate the effect of the dynamic interaction on the dynamic behaviour of

the SS, the system shown in Fig. 1 is subjected to the ground motions. The two ground motions are randomly chosen from Table 1 for this analysis. The effect of the mass ratio (μ) and the damping ratio of the SS (ξ_s) on the acceleration response of the SS is investigated. The mass ratio (μ) is the ratio between the secondary structure's mass to the primary structure's mass. The μ values 0.001, 0.01, 0.1, and 0.5 are considered for the coupled analysis. The vibration periods of the PS (T_p) and the SS (T_s) are taken as 0.5 sec in this analysis. The damping ratios of the SS (ξ_s) are taken as 5%, and 1%.

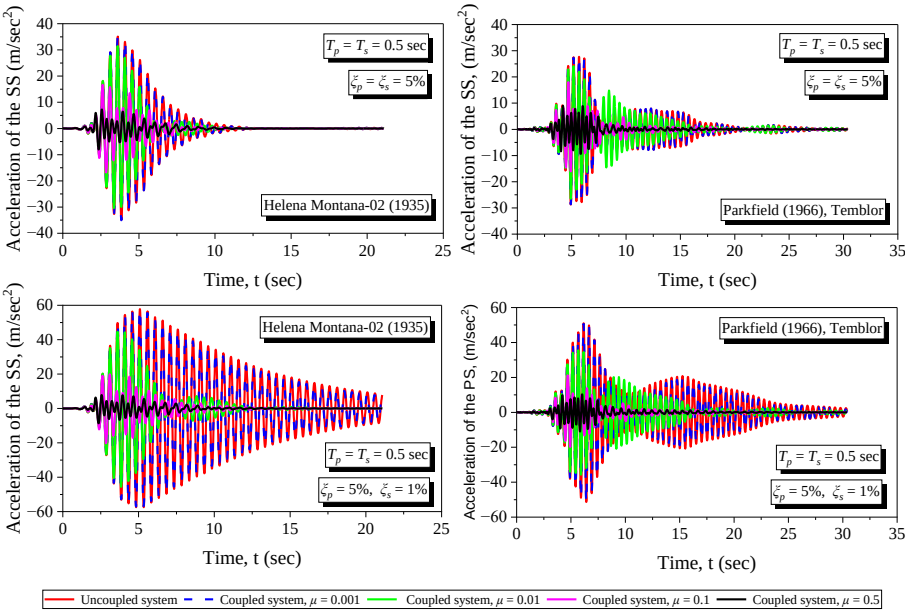

Fig. 4. Acceleration time-history response of the secondary structure

The amplitude of the acceleration response increases as the damping ratio of the SS decreases, as expected. The dynamic interaction between the primary structure (PS) and secondary structure (SS) demonstrates a minimal effect on the seismic response of the SS when the mass ratio is as low as 0.001 (0.1%). This is evident as the acceleration response with μ = 0.001 closely aligns with that of the uncoupled system. Hence, the seismic demands on the secondary structure can be calculated at this mass ratio using the uncoupled analysis. This observation is in line with the conclusions made in past research [26]–[28] As the μ increases (μ = 1%, 10%, and 50%), the dynamic interaction between the PS and SS shows a substantial impact on the acceleration response of the SS. For such mass ratios, the uncoupled analysis does not provide precise results.

Table 2. Peak acceleration of the SS (m/sec²) for ξ_s = 5%

Ground motion	Uncoupled Analysis	Coupled Analysis			
		μ=0.001	μ=0.01	μ=0.1	μ=0.5
Helena_ Montana-02 (1935)	35.08	35.11	31.46	16.65	7.24
Parkfield (1966)	27.68	27.44	24.14	18.02	8.96

Table 2 illustrates the SS's peak acceleration response since peak values of any seismic response quantity give valuable insight into structural behavior. Table 2 clearly shows that for μ=0.01, 0.1, and 0.5, the peak acceleration response of the SS is lowered by 10%, 52.5%, and 79.3%, respectively, when compared to the uncoupled study under Helena_ Montana-

02 (1935) ground motion. Similarly, Parkfield (1966) ground motion reduces the peak acceleration response of the SS by 12.7%, 34.8%, and 67.6% for μ=0.01, 0.1, and 0.5, respectively, when compared to the uncoupled study. A similar pattern was seen for the ξ_s = 1%. Therefore, the coupled analysis is to be carried out to study the seismic behavior of the SS for higher mass ratios.

4.2 Floor Response Spectrum (FRS)

The maximum design forces for the design of the SS can be obtained from the floor response spectrum (FRS) approach [9], [29]. The FRS method disregards the PS and SS's dynamic interaction [30]. As a result, the current study made an effort to examine the FRS by taking into account the coupling effect between the PS and SS. The SS's peak responses to input ground motion are represented by the floor response spectrum. The effects of the mass ratio (μ) and the damping ratio (ξ_s) on the floor response spectrum are studied. Fig. 5 shows the FRS for different damping ratios and mass ratios of the SS for the given damping characteristics of the PS (T_p = 0.5 sec, ξ_s = 5%). The uncoupled system can be used to estimate the seismic demands on the SS for a tiny mass ratio (μ = 0.1%), as seen in Fig. 5 for this particular case.

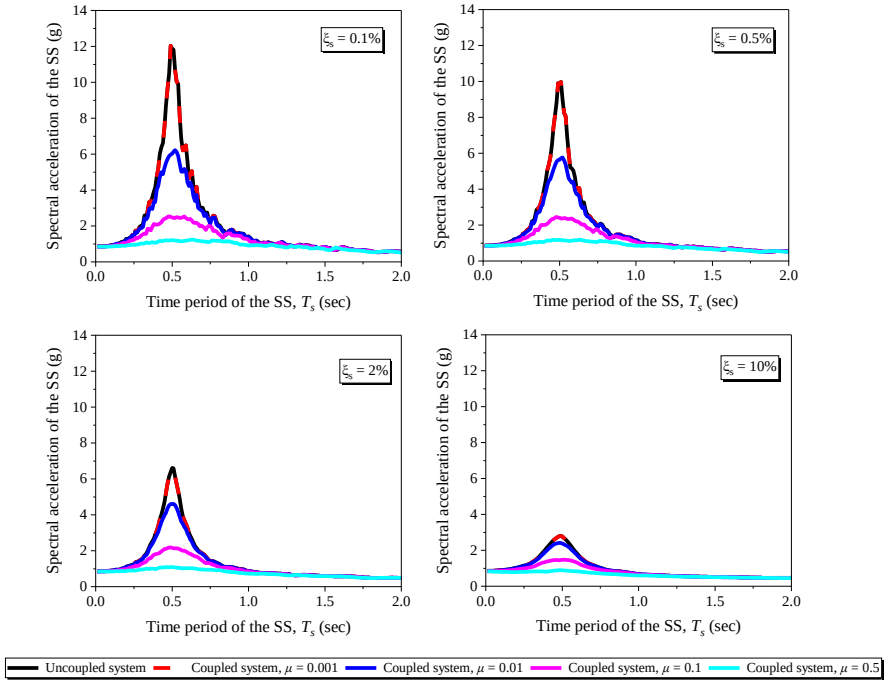

Fig. 5. Effect of damping and mass ratios of the SS on the FRS

The coupled effect of the PS and SS on the FRS is seen when the mass ratio increases for all damping ratios of the SS. The dynamic interaction between the PS and SS shows a substantial impact on the magnitude of the spectral acceleration of the SS (Sa_{SS}) at T_s = 0.5 sec. Such effect is negligible on the behaviour of very stiff and flexible secondary structures irrespective of their damping ratio. For the mass ratio of 1%, the peaks of the FRS reduce about 49.2%, 41.8%, 30.4%, and 13.3% at the damping ratios of 0.1%, 0.5%, 2%, and 10%, respectively. From this particular case of analysis, it can be concluded that coupled analysis is required only if the SS is tuned to the vibration period of the PS. Otherwise, the uncoupled analysis is sufficient to analyses the seismic behavior of the secondary

structure. It can also be deduced that the larger coupling effect on the FRS is observed for the lower damping ratios of the SS.

4.2.1 Effect of Vibration Period of the PS on FRS

In the preceding section, it was examined how the damping and mass ratios of the SS affected the FRS for a specific primary structure vibration period (T_p = 0.5 sec). The dynamic characteristics of the primary structure substantially affect the secondary structure's seismic demands [26], [27]. As a result, an effort has been made to investigate the influence of a PS vibration period on the FRS for a specific mass and damping ratio of the SS in this section. The damping ratio of the PS (ξ_p = 5%) is kept constant for all the analysis cases. In this analysis, the tuning ratio is introduced as a key parameter. It is defined as the ratio between the vibration period of the secondary structure (SS) and the fundamental vibration period of the primary structure (PS), as indicated in Eq. (6). This parameter is employed to encapsulate the impact of the dynamic characteristics of the primary structure on the overall system.

$$Tuning\ ratio\ (T_r) = T_s/T_p \tag{6}$$

Fig. 6 shows the variation of the spectral acceleration of a SS with a tuning ratio for different mass and damping ratios of the SS. The FRS for the small mass ratio (μ = 0.1%) is not shown in this figure since at such a small mass ratio, the coupling effect on the FRS is negligible, as shown in Fig. 5. Looking at Fig. 6, it becomes evident that the influence of dynamic interaction on the FRS is substantial within the range of $0.8 \leq T_r \leq 1.2$. Conversely, for the ranges of $T_r < 0.5$ and $T_r > 2$, it's apparent that the impact of dynamic interaction on the FRS is negligible across all the considered values of ξ_s and μ. Hence, it can be concluded that the coupling effect on the FRS can be considered only if the vibration period of the SS is in the vicinity of that of the primary structure. Regardless of the μ, the Sa_{SS} reduces with an increase in the primary structure's vibration period for a given damping ratio of the SS.

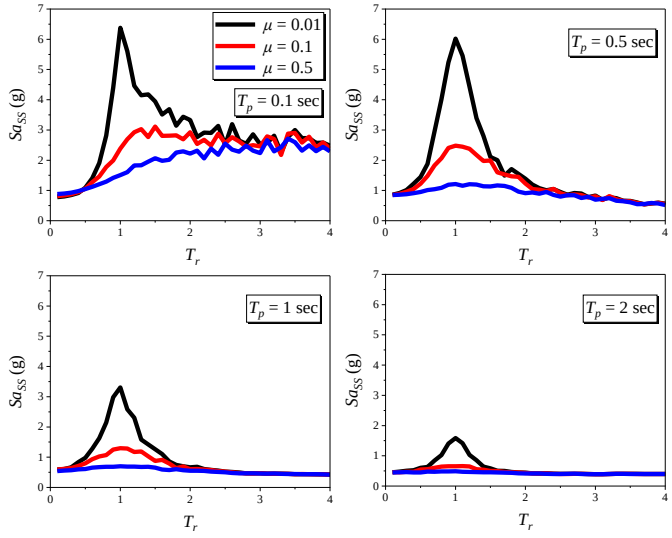

(a)

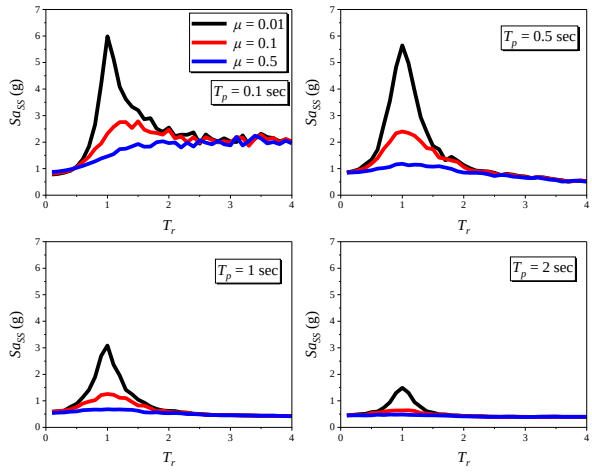

(b)

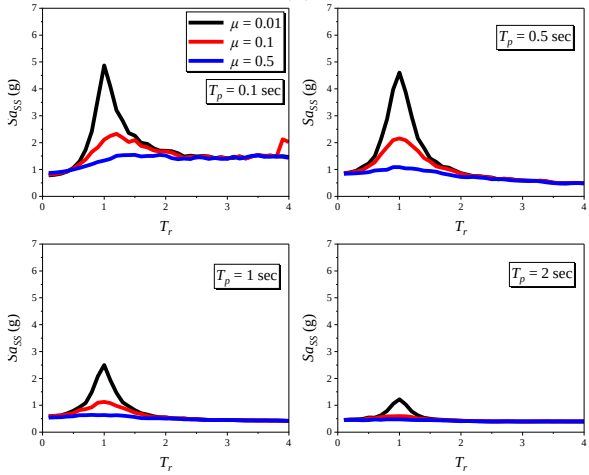

(c)

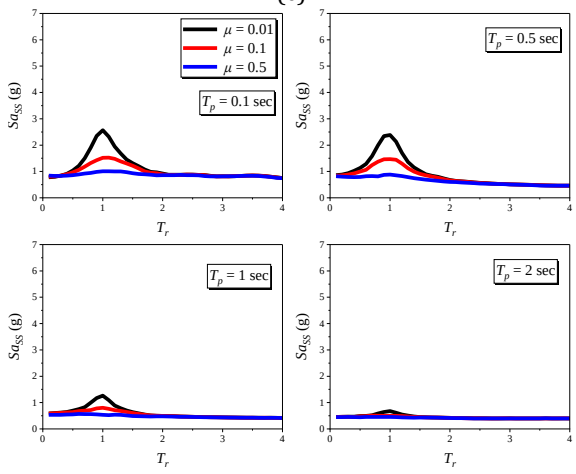

(d)

Figs. 6. a, b, c, d. Variation of floor response spectrum with tuning ratio for (a- ξ_s = 0.1%; b- ξ_s = 0.5%; c- ξ_s = 2%; d- ξ_s = 10%)

4.3 Component Dynamic Amplification Factor (CDAF)

The component's (secondary structure) acceleration relative to the floor acceleration to which it is coupled is examined in this section. Fig. 7 displays the FRS normalized by the associated peak floor accelerations (PFAs). A component dynamic amplification factor (CDAF) is the ratio of FRS to PFA. The CDAF of the building models is checked with the definitions of ASCE 7-16 [22] and FEMA P-750 [31] in the current study. According to ASCE 7-16, for flexible SSs with time periods greater than 0.06 seconds, the components amplification factor (a_p) is 2.5.

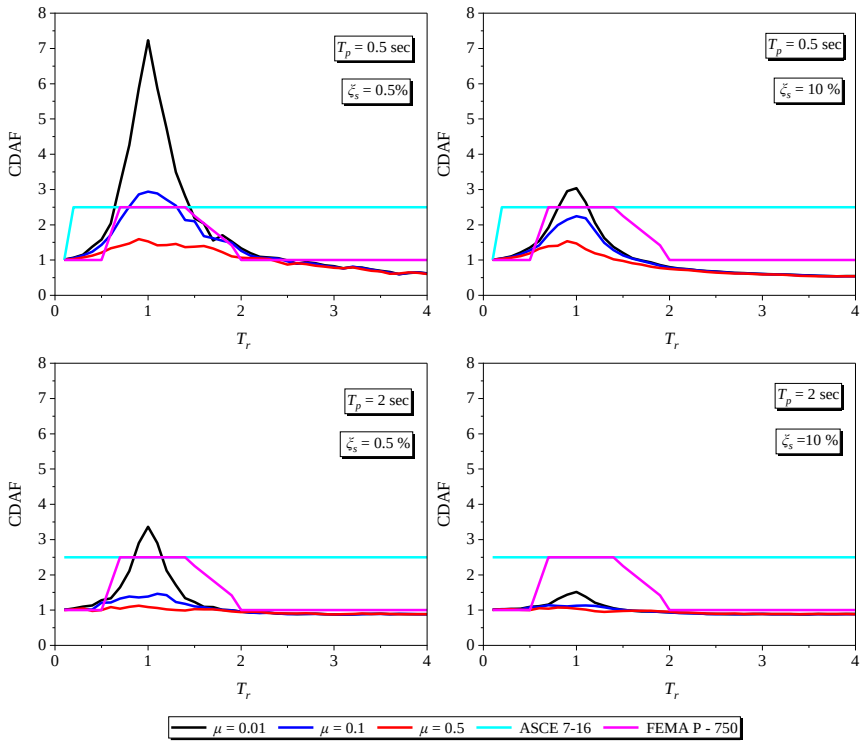

Fig. 7 Component dynamic amplification factors at different vibration periods of the PS and damping ratios of the SS

The value of the amplification factor for stiff SSs (T< 0.06 sec) is 1. Fig. 7 provides a clear depiction of the trends: the definitions outlined in ASCE 7 and FEMA P-750 tend to underestimate the CDAF for periods in proximity to the primary structure's vibration periods, specifically when $T_r \cong 1$ for a mass ratio of 1%. Conversely, these definitions tend to overestimate the CDAF at $T_r \cong 1$ when dealing with a flexible primary structure (T_p = 2 sec) and a substantial damping ratio in the secondary structure (ξ_s = 10%). The CDAF values specified by the code definitions start to become more conservative at a mass ratio of 10% as the SS damping ratio increases for a specific primary structure. When the mass ratio is raised to 50%, the estimated amplification factors provided by the code definitions are conservative. As shown in Fig. 7, this underestimation is also included in the definitions of FEMA P-750. The current code-based definitions should thus be modified to take into consideration the effects of the dynamic interaction between the PS and SS as well as the damping ratio of the SS.

5. Conclusions

This study aims to examine how a dynamic interaction affects the seismic requirements of a secondary structure. For good secondary structure design, a thorough understanding of the interaction between the primary and secondary structures is necessary. This article discusses a parametric investigation on the dynamic interaction of primary and secondary structures. The single-degree-of-freedom (SDOF) system is used for both the elastic primary structure (PS) and the elastic secondary structure (SS). The numerical approach is used to develop and solve the governing equations of motion for the coupled and uncoupled systems for a certain set of ground motions. The conclusions and main highlights in the present study are as follows:

- The dynamic interaction between the PS and SS shows an insignificant impact on the SS's seismic demands for the mass ratio 0.001 (0.1%). Hence, at this mass ratio, the seismic demands on the SS can be calculated using the uncoupled analysis.
- The dynamic interaction between the PS and SS shows a significant impact on the acceleration response of the SS as the mass ratio increases. The coupled analysis is required only if the SS is tuned to the vibration period of the PS, i.e., $0.8 \leq T_r \leq 1.2$. The uncoupled analysis is sufficient to analyse the seismic behaviour of the SS for $T_r < 0.5$ and $T_r > 2$.
- The larger coupling effect on the FRS is observed for the lower damping ratios of the SS. For a given damping ratio, the secondary structure's spectral acceleration decreases with an increase in the vibration period of the primary structure, irrespective of the mass ratio.
- The current code definitions underestimate the CDAF for a period closer to the fundamental vibration period of the primary structure.
- The mass ratio and damping ratio of the secondary structure have a significant effect on the CDAF.

The existing code-based definitions need to undergo modification to account for the dynamic interaction occurring between the primary structure (PS) and secondary structure (SS). Additionally, these revisions should also incorporate the damping ratio specific to the secondary structure. This adjustment is necessary to ensure that the structural design and evaluation procedures accurately reflect the dynamic complexities that emerge due to the interaction between these components and the influence of damping in the secondary structure.

List of Abbreviations

Abbreviation	Full form
FRS	Floor Response Spectrum
PS	Primary Structure
SS	Secondary Structure
PGA	Peak Ground Acceleration
SDOF	Single Degree of Freedom
CDAF	Component Dynamic Amplification Factor
PFA	Peak Floor Acceleration
FEMA	Federal Emergency Management Agency
ASCE	American Society of Civil Engineers

Acknowledgement

The authors acknowledge that this study is supported by Department of Civil Engineering, Koneru Lakshmaiah Education Foundation (KLEF), Vaddeswaram, Guntur, India.

References

[1] Murty CVR, Goswami R, Vijayanarayanan AR, Kumar RP, Mehta V V. Earthquake Protection of Non-Structural Elements in Buildings. 2012.
[2] Taghavi S, Miranda E. Estimation of Seismic Acceleration Demands in Building Components. 13th World Conf Earthq Eng Vancouver, BC, Canada. 2004;(3199):3199.
[3] Kamble V, Dayal Bharti S, Kumar Shrimali M, Kanti Datta T. Control of Secondary Systems Response in a Base-Isolated Building under Tridirectional Ground Motion. Pract Period Struct Des Constr. 2022;27(1):1-12. https://doi.org/10.1061/(ASCE)SC.1943-5576.0000641
[4] Wang T, Shang Q, Li J. Seismic force demands on acceleration-sensitive nonstructural components: a state-of-the-art review. Earthq Eng Eng Vib. 2021;20(1):39-62. https://doi.org/10.1007/s11803-021-2004-0
[5] Sullivan TJ. Post-Earthquake Reparability of Buildings: The Role of Non-Structural Elements. Struct Eng Int. 2020;30(2):217-23. https://doi.org/10.1080/10168664.2020.1724525
[6] Filiatrault A, Perrone D, Merino RJ, Calvi GM. Performance-Based Seismic Design of Nonstructural Building Elements. J Earthq Eng. 2018;00(00):1-33.
[7] Villaverde R. Fundamental concepts of earthquake engineering. CRC Press; 2009. https://doi.org/10.1201/9781439883112
[8] Landge M V., Ingle RK. Comparative study of floor response spectra for regular and irregular buildings subjected to earthquake. Asian J Civ Eng. 2021;22(1):49-58. https://doi.org/10.1007/s42107-020-00297-1
[9] Berto L, Bovo M, Rocca I, Saetta A, Savoia M. Seismic safety of valuable non-structural elements in RC buildings: Floor Response Spectrum approaches. Eng Struct. 2020;205(October 2019):110081. https://doi.org/10.1016/j.engstruct.2019.110081
[10] Surana M, Singh Y, Lang DH. Effect of irregular structural configuration on floor acceleration demand in hill-side buildings. Earthq Eng Struct Dyn. 2018;47(10):2032-54. https://doi.org/10.1002/eqe.3054
[11] Kelly JM, Sackman JL. Response spectra design methods for tuned equipment-structure systems. J Sound Vib. 1978;59(2):171-9. https://doi.org/10.1016/0022-460X(78)90498-4
[12] Lim E, Chouw N. Prediction of the response of secondary structures under dynamic loading considering primary-secondary structure interaction. Adv Struct Eng. 2018;21(14):2143-53. https://doi.org/10.1177/1369433218768563
[13] Salman K, Tran TT, Kim D. Grouping effect on the seismic response of cabinet facility considering primary-secondary structure interaction. Nucl Eng Technol . 2019; 52(6): 1318-1326. https://doi.org/10.1016/j.net.2019.11.024
[14] Smith-Pardo JP, Reyes JC, Ardila-Bothia L, Villamizar-Gonzalez JN, Ardila-Giraldo OA. Effect of live load on the seismic design of single-story storage structures under unidirectional horizontal ground motions. Eng Struct. 2015;93:50-60. https://doi.org/10.1016/j.engstruct.2015.03.020
[15] Sackman JL, Kelly JM. Seismic analysis of internal equipment and components in structures. Eng Struct. 1979;1(4):179-90. https://doi.org/10.1016/0141-0296(79)90045-2
[16] Igusa T, Der Kiureghian A. Dynamic characterization of two-degree-of-freedom equipment-structure systems. J Eng Mech. 1985;111(1):1-19. https://doi.org/10.1061/(ASCE)0733-9399(1985)111:1(1)

[17] Singh MP, Suarez LE. Seismic response analysis of structure-equipment systems with non-classical damping effects. Earthq Eng Struct Dyn. 1987;15(7):871-88. https://doi.org/10.1002/eqe.4290150708
[18] Suarez LE, Singh MP. Floor response spectra with structure-equipment interaction effects by a mode synthesis approach. Earthq Eng Struct Dyn. 1987;15(2):141-58. https://doi.org/10.1002/eqe.4290150202
[19] Bagheri B, Nivedita KA, Firoozabad ES. Comparative damage assessment of irregular building based on static and dynamic analysis. Int J Civ Struct Eng. 2013;3(3):505.
[20] Senaldi I, Magenes G, Penna A, Galasco A, Rota M. The effect of stiffened floor and roof diaphragms on the experimental seismic response of a full-scale unreinforced stone masonry building. J Earthq Eng. 2014;18(3):407-43. https://doi.org/10.1080/13632469.2013.876946
[21] Center P. PEER ground motion database. Pacific Earthq Eng Res Center, Univ California, Berkeley, CA, http//ngawest2 berkeley edu. 2013;
[22] ASCE. Minimum design loads and associated criteria for buildings and other structures (ASCE/SEI 7-16). American Society of Civil Engineers (ASCE) Reston, VA; 2016.
[23] Council BS.S.. NEHRP recommended seismic provisions for new buildings and other structures. Rep. FEMA P, 750, 2009.
[24] Khy K, Chintanapakdee C, Wijeyewickrema AC. Application of conditional mean spectrum in nonlinear response history analysis of tall buildings on soft soil. Eng J. 2019;23(1):135-50. https://doi.org/10.4186/ej.2019.23.1.135
[25] Alatik L, Abrahamson N. An improved method for nonstationary spectral matching. Earthq Spectra. 2010;26(3):601-17. https://doi.org/10.1193/1.3459159
[26] Surana M, Singh Y, Lang DH. Effect of structural characteristics on damping modification factors for floor response spectra in RC buildings. Eng Struct. 2021;242(April):112514. https://doi.org/10.1016/j.engstruct.2021.112514
[27] Challagulla SP, Bhargav NC, Parimi C. Evaluation of damping modification factors for floor response spectra via machine learning model. Structures. 2022; 39: 679-90. https://doi.org/10.1016/j.istruc.2022.03.071
[28] Anajafi H, Medina RA. Damping modification factor for elastic floor spectra. Bull Earthq Eng . 2019;17(11):6079-108. https://doi.org/10.1007/s10518-019-00684-3
[29] Haymes K, Sullivan TJ, Chandramohan R. A practice-oriented method for estimating elastic floor response spectra. Bull New Zeal Soc Earthq Eng. 2020;53(3):116-36. https://doi.org/10.5459/bnzsee.53.3.116-136
[30] Adam C, Furtmüller T, Moschen L. Floor response spectra for moderately heavy nonstructural elements attached to ductile frame structures. In: Computational methods in earthquake engineering. Springer. 2013; 69-89. https://doi.org/10.1007/978-94-007-6573-3_4
[31] (BSSC) BSSC. Nehrp recommended seismic provisions for new buildings and other structures (fema p-750). Report Prepared for the Federal Emergency Management Agency (FEMA). National Institute of Building Sciences Washington, DC; 2009.

Research on Engineering Structures & Materials
www.jresm.org
Research Group

Research Article

Prediction of forming limit diagrams for steel sheets with an artificial neural network and comparison with empirical and theoretical models

Cengiz Görkem Dengiz*,[a], Fevzi Şahin[b]

Department of Mechanical Engineering, Ondokuz Mayıs University, Samsun, Türkiye

Article Info

Article history:

Received 25 Aug 2023
Accepted 21 Nov 2023

Keywords:

Formability;
Artificial neural network;
Forming limit diagram;
Steel sheets;
Sheet metal forming

Abstract

The automotive industry heavily relies on forming limit diagrams (FLDs) as essential tools for ensuring the quality and manufacturability of sheet metal components. However, accurately determining FLDs can be complex and resource-intensive due to the numerous material properties and variables involved. To address this challenge, this research employs an artificial neural network (ANN) model to predict FLDs for sheet metals, explicitly focusing on the automotive sector. The study begins by gathering material properties, including sheet thickness, yield strength, ultimate tensile strength, uniform elongation, hardening exponent, and strength coefficient. These properties serve as crucial inputs for the ANN model. Sensitivity analysis is then conducted to discern how each parameter influences FLD predictions. The ANN model is meticulously constructed, with a 6-15-22-3 structure, and subsequently trained to predict FLDs. The results are promising, as the model achieves an exceptional R-value of 0.99995, indicating high accuracy in its predictions. Comparative analysis is carried out by pitting the ANN-generated FLDs against experimental data. The findings reveal that the ANN model predicts FLDs with remarkable precision, exhibiting only a 3.4% difference for the FLD0 value. This level of accuracy is particularly significant in the context of automotive manufacturing, where even minor deviations can lead to substantial product defects or manufacturing inefficiencies. It offers a swift and reliable way of predicting FLDs, which can be instrumental in optimising manufacturing processes, reducing material waste, and ensuring product quality. In conclusion, this research contributes to the automotive manufacturing sector by providing a robust and efficient method for predicting FLDs.

1. Introduction

The limits of that material should be determined to use the material in forming operations with maximum efficiency. These material limits are known as formability. Sheet metal formability is defined as the ability of the metal to deform into a desired shape without necking or fracture [1]. These limits for sheet metals in forming operations are expressed by the forming limit diagram (FLD). Keeler and Goodwin first introduced this concept in the 1960s [2,3]. Keeler studied the right side of the diagram while Goodwin examined the left side (Fig. 1). In Fig. 1, the vertical axis shows the major strain (ε_1), and the horizontal axis shows the minor strain (ε_2) on sheet metal. The forming limit as a function of the strain state can be presented as a curve in a ε_1-ε_2 diagram. That kind of diagram is called the forming limit diagram (FLD), and the curve is called the forming limit curve (FLC) [4]. The FLC_0 value is the major strain value at which the minor strain value is 0 in the FLC. This value is also known as the lowest point of the FLC. According to this diagram, the area

*Corresponding author: gorkem.dengiz@omu.edu.tr
[a] orcid.org/0000-0003-1308-3223; [b] orcid.org/0000-0002-4808-4915
DOI: http://dx.doi.org/10.17515/resm2023.32ma0825rs

under the FLC shows the safe margin; the area above the curve shows where fracture will occur. In other words, as long as the major and minor deformations in the sheet metal fall below this curve, no necking or fracture will occur. If the deformations are higher than the limit strains of the FLC, the sheet metal will be necked or fractured.

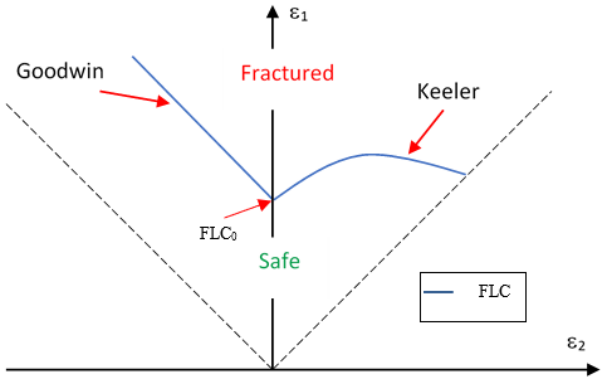

Fig. 1. Schematic forming limit diagram (FLD) found by Keeler and Goodwin [5]

The deformations during the sheet metal forming process are determined using the finite element method and compared with the FLC. Successful products are obtained by changing the material or design in areas with high or critical deformation. There are many experimental and theoretical studies and models for determining FLCs. The FLC can be determined by various methods such as the uniaxial tensile test [6], the hydraulic dome test [7], the Keeler test [2], the Hecker test [8], the Marciniak test [9], the Nakajima test [10] and the Hasek test [11]. In these experimental methods, FLCs can be determined using different specimens and tools [12]. The most commonly used tests are the Nakajima and Marciniak tests. In these tests, the FLC's left and right parts are obtained using specimens of different widths and types. However, experimental methods are costly due to the need for special devices and tools, and the preparation and measurement of test specimens are also time-consuming. Therefore, many theoretical and numerical models have been developed for the calculation of the formability of sheet metals.

Theoretical and numerical models are based on geometric imperfection theory, continuum mechanics and bifurcation theory. The most well-known of these models are the Marciniak–Kuczynski criterion [13], the Swift and Hill model [14,15] and the Gurson–Tvergaard–Needleman [16] model. In these models, quadratic or linear equations are solved with the parameters of the materials and the FLC is obtained. All these models and other empirical methods are summarised by Zhang et al. [17].

Although there are many studies in the literature in which experimental methods and theoretical models determine FLC, statistical analyses on this subject are limited. However, these experimental and theoretical studies guide the researchers by giving information about the factors affecting the FLC. Subramani et al. [18] experimentally determined FLCs for three different thicknesses of three other aluminium alloys and modelled them with the Taguchi experimental design. They determined the mechanical properties, such as yield strength and hardening exponent, using tensile tests. They used this data as a variable in the Taguchi experimental design and used the forming limit strain values as outputs. As a result of the study, they showed that the data obtained from the tensile tests can be used in the estimation of the FLC. They also found that the most critical factors affecting the FLC are the strain hardening exponent and normal anisotropy. Paul [19] created a statistical model that predicts FLC_0 point by processing data such as the tensile strength, elongation, strain hardening and thickness of steel materials collected from the literature. To estimate

this point, the author created a model by processing the data from 66 types of steel in total. With this model, forming limit stress diagrams (FLSDs) was predicted with a high success rate. Levy and Van Tyne [20] also developed a method for predicting FLSDs. They calculated the effective stress in the FLC_0 value with a Z parameter created with tensile test data from the literature. They also computed FLSDs for the left side of the FLC. A more comprehensive investigation of the controlling factors of FLC can be found in [21].

Forming Limit Diagrams (FLDs) are of paramount significance in the automotive industry, acting as a linchpin in the manufacturing process of sheet metal components. These diagrams are critical guides ensuring automotive parts' quality and structural integrity. However, their accurate determination is a formidable challenge. With stringent quality standards and cost-efficiency imperatives, the automotive industry relies heavily on precise FLDs. Minor deviations in these diagrams can lead to defects in the final product, escalating production costs and causing delays. Traditional methods of FLD determination are often limited by empirical or theoretical models, which may not encompass the intricate variations introduced during the production process. As a result, there is an escalating need for predictive models that can bridge this gap and offer an accurate means of determining FLDs. In recent times, artificial neural networks (ANNs) have been used frequently in metal forming processes. These advanced models can potentially revolutionise how FLDs are predicted, offering an innovative solution to the challenges faced by the automotive industry and other sectors that rely on sheet metal forming. Many researchers have used system theoretical models to model the system and reduce their experimental work. The ANN method, which has recently become popular, is a modelling method that can be applied to almost any engineering system. Since ANNs have many different models and learning algorithms, they can be applied to other systems. An ANN is a modelling method that tries to learn and use the relationship between input and output variables without considering the underlying physical processes. The relationship between inputs and outputs can be formulated. The effects of the inputs can be seen through the outputs using an ANN. With all these superior aspects, ANNs have been the basis for many studies in sheet-metal forming processes. Kotkunde et al. [22] modelled the deep drawing process of Ti-6Al-4V alloy using an ANN method. They used parameters such as blank holder force (BHF), punch speed and temperature as inputs. They could predict the major and minor strains with an ANN by processing the simulation results as outputs. They also plotted the FLC with the Keeler formula using the major and minor strain values obtained from the simulation. Elangovan et al. [23] modelled the FLC of perforated pure aluminium sheets with an ANN. They experimentally determined major and minor strain values by forming perforated sheets of different widths. Using sheet widths and hole sizes as inputs, they trained the network and obtained major and minor strain values that agreed with the experimental data. Derogar and Djavanroodi [24] experimentally determined the FLCs of Ti6Al4V titanium alloy and Al6061-T6 aluminium alloy sheets using the Hecker test. They gave punch displacement, oil pressure and limit drawing ratios (LDR) to the ANN as inputs and obtained FLC values as outputs. They got a high similarity between the experimental and ANN data. They found that FLCs can be successfully predicted by an ANN. Forcellese et al. [25] tried to predict the yield curves and FLCs of AZ31 magnesium alloys with experimental measurements and an ANN. They used parameters such as temperature, minor strain, forming speed and rolling direction as inputs for predicting the FLCs. They showed that the ANN can predict FLCs accurately, although no information was provided about the complex mechanisms involved in microstructure during hot forming. Dehghani et al. [26] investigated the effect of thermomechanical properties of low-carbon steels on the FLC with an ANN. In their model, the carbon content, hot finishing temperature, strain hardening exponent, initial yield stress and ASTM grain size were inputs and used to predict the FLC as an output. They reported that the FLC indicated with these thermomechanical properties was highly compatible with the experimentally

obtained FLC. All of these studies found that the FLC can be predicted with an ANN successfully for a specific material in which experimental parameters or material properties are given as input. Although FLC can be successfully estimated for the sheet used in the study, creating a new ANN for different steel sheets is necessary. Therefore, there is a need for an ANN in which the FLCs of other steel sheets can be determined by simply giving their material properties.

This article delves into the development and application of ANNs for predicting FLDs in the automotive sector. It explores the implications of accurate predictions on manufacturing processes, product quality, cost efficiency, and, most importantly, safety. As the industry navigates the ever-evolving landscape of materials and design, predictive models like ANNs offer a bridge between innovation and reliability, contributing to producing safer, more efficient, and environmentally responsible vehicles. In this study, an ANN model has been developed to predict the whole FLCs of different steel sheets. Mechanical properties found in any material database are given as input. In this context, the yield stress, tensile strength, strain hardening exponent, strength coefficient, uniform elongation and thickness values of steel materials collected from different studies and experimental studies are inputs to the ANN. The FLCs of the steel sheets were processed as the output with data from the uniaxial, plane strain and biaxial regions. This ANN model can obtain the FLC of the different steel sheets for which the mechanical properties are given as inputs.

2. Materials and Methods

2.1. Materials

In this study, DC01 was used for experiments. The thickness of the sheet metals is 0.6 mm. The chemical contents of the selected material are given in Table 1. These chemical contents are based on the material standards. The tensile test was used to determine the mechanical properties of the material, and out-of-plane tests were used to determine the FLC.

Table 1. Chemical composition of DC01 sheet metal [27]

Material	%C	%P	%S	%Mn	%Fe
DC01	0.12	0.045	0.045	0.6	99.19

2.2 Tensile Test

Tensile test specimens were prepared following the ASTM E8 [28] standard to determine the mechanical properties of the steel sheet. Specimens that cut parallel, diagonal and perpendicular with respect to the rolling direction were tested using an Instron 5982, which has 100 kN loading capacity. All tests were performed at a constant head speed of 10 mm/min until fracture occurred and were repeated a minimum of 3 times to minimise deviations in results. A standard mechanical extensometer with a length of 50 mm was used to measure the strain accurately. The material's strain hardening exponent and strength coefficient were determined by linear regression analysis on the true stress–true strain curves on a logarithmic scale. The yield stress, tensile stress, elongation and strain hardening exponent obtained as a result of tensile tests are given in Table 2.

Table 2. Mechanical properties of DC01 sheet metal

Mechanical Properties	DC01
Elastic modulus, E (GPa)	194.7
Yield stress, $R_{p0,2}$ (MPa)	204.3
Tensile stress, R_m (MPa)	335.9
Uniform elongation, ε (mm/mm)	0.241
Max. elongation, ε_{max} (mm/mm)	0.406
Strain hardening coefficient, n	0.212
Strength coefficient, K (MPa)	576.3

2.3 Out-of-plane Tests

To determine the FLC of the material, it should be formed under different strain conditions. Therefore, specimens of various widths that are usually compressed between a die and a blank holder are stretched with a hemispherical punch until they are necked or fractured (Fig. 2a). The dimensions of the die are given in Fig. 2b. A double-acting hydraulic press with a loading capacity of 80 tonnes was used for the out-of-plane test. After closing the die and blank holder, a 90 kN clamping force was applied. Nylon film and mineral oil are used between the sheet metal and punch to prevent premature damage from friction.

In this study, sheet metals of eight different widths, as shown in Fig. 3a, were formed by a hemispherical punch until they fractured. The specimen dimensions are given in detail by Ozturk and Lee [1]. Circular grids with a diameter of 2.5 mm were electrochemically etched onto the sheets before forming (Fig. 3a). Each sample represents one strain path from uniaxial to biaxial strain on the FLD. After the experiments, these grids changed shape from circular to elliptical, and optical grid measurements were used to determine the major and minor strains. The FLCs were obtained by plotting these values on a graph [29]. Fig. 3b shows the fractured specimens after the experiment.

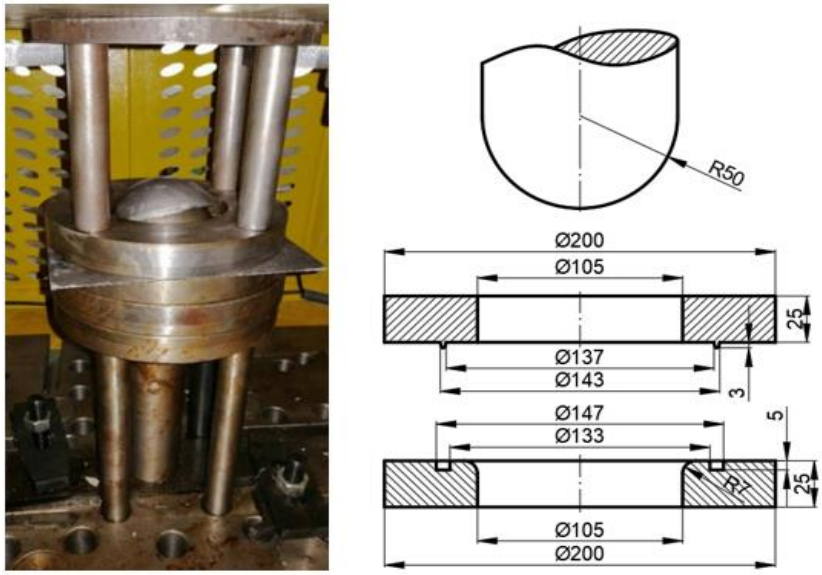

(a) (b)

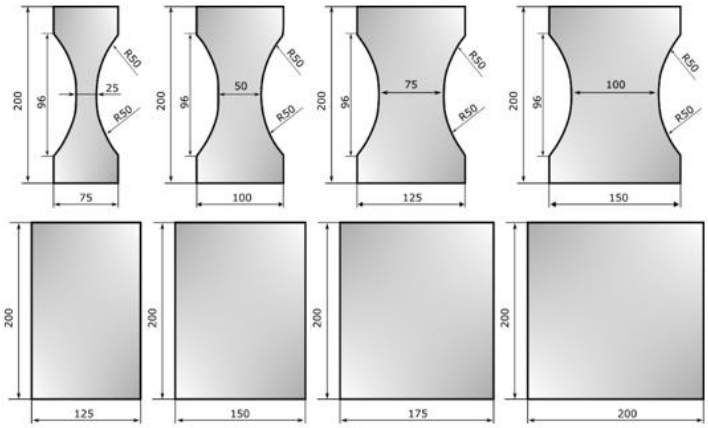

(c)

Fig. 2. (a) Fractured sample in out-of-plane test (b) Technical drawing of the out-of-plane test setup (c) Specimen dimensions (all dimensions are mm)

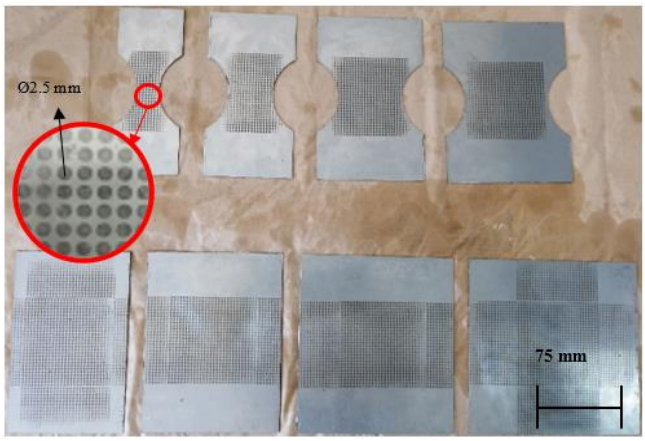

(a)

(b)

Fig. 3. Out-of-plane test specimens (a) before and (b) after the test

After the samples were deformed, the deformations on the sheet surfaces were measured with camera-integrated image processing software (Fig. 4a). Each deformed ellipse where the damage occurred on the sheet surface was photographed with the camera. Later, these photographs were transferred to the image processing program, and the major and minor axes of the ellipses were measured (Fig. 4b). In the program, the circles etched on the sheet metal were displayed with the camera before deformation. The program is calibrated by measuring the diameter of the reference circle over these images. After deformation, the ellipses, whose axis lengths are measured, are proportional to the reference circle size and the true strains are calculated. Here, measuring the ellipses from the same distance each time while viewing is essential for the consistency of the measurements.

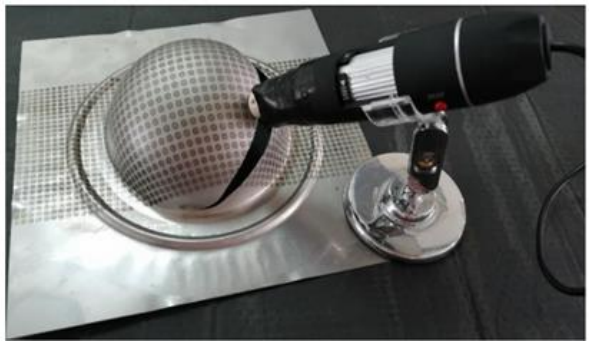

(a)

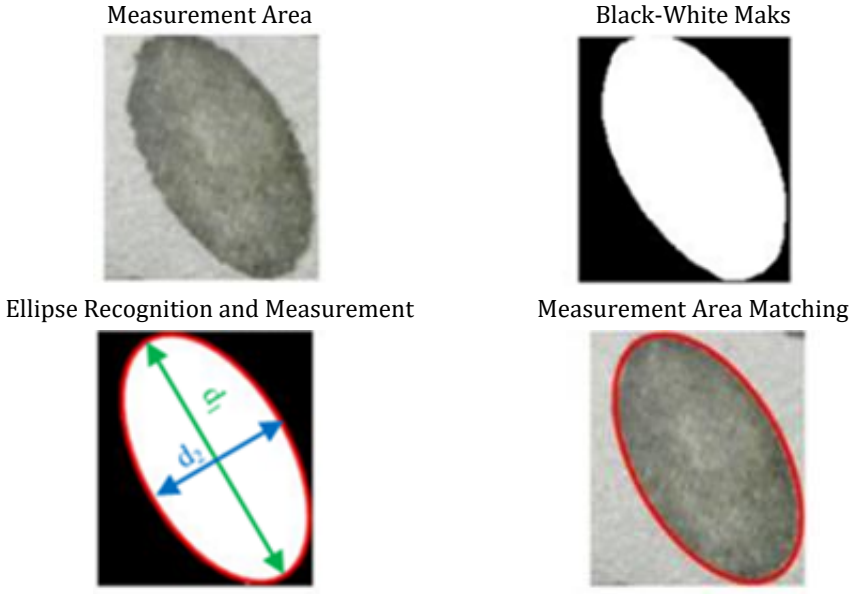

(b)

Fig 4. Determination of major and minor strain (a) Taking a picture with a camera (b) Measurement with image processing

The damaged area of each deformed sample was examined, and the ellipses to be measured were determined and photographed. As a result of the measurements, the major (ε_1) and minor (ε_2) true strains were calculated with the equations (1) and (2). The major true strain was calculated by measuring the long axes of the ellipses on the sheet, and minor true strains were calculated by measuring their short axes. In equations (1) and (2), the

diameter of the circle before deformation is d_0, the major axis of the ellipse formed after deformation is d_1, and the minor axis is d_2.

$$\varepsilon_1 = ln\frac{d_1}{d_0} \quad (1)$$

$$\varepsilon_2 = ln\frac{d_2}{d_0} \quad (2)$$

2.4 Training

In order to train the ANN model, the data were collected from published literature and the experiment for DC01. The database comprises major and minor strain values for material thickness, yield stress, tensile strength, strength coefficient, strain hardening exponent, uniform elongation versus uniaxial strain, plane strain and biaxial strain values. In some articles, these values are given in table [30–32], but in others, they are given graphically [33–35] (stress–strain, FLC, etc.). In those studies, the graphics in the article were transferred to data collection software and the desired data were obtained this way. In this study, the data collected from the literature is given in Table 3 with respective references.

An FLC consists of two regions: negative (ε_2^u) and positive (ε_2^b) minor strain. In the ANN model, material thickness (t), yield stress (YS), ultimate tensile strength (UTS), strength coefficient (K), strain hardening exponent (n), and uniform elongation were used as input data. In the data collected from the literature, major strain ($\varepsilon_1^u, \varepsilon_1^b$) values were collected for different positive and negative minor strain ($\varepsilon_2^u, \varepsilon_2^b$) values for each material. These values and the slope of the curve in the positive and negative minor strain regions were calculated according to Eqs. 3 and 4. With this arrangement, β^-, β^+ and FLC_0 values are used as outputs from the ANN model.

$$\beta^- = tan^{-1}\left(\frac{\varepsilon_1^u - FLC_0}{|\varepsilon_2^u|}\right) \quad (3)$$

$$\beta^- = tan^{-1}\left(\frac{\varepsilon_1^u - FLC_0}{|\varepsilon_2^u|}\right) \quad (4)$$

Table 3. Training data from different literature works

No	Mat.	YS	UTS	ε	K	n	t	$\varepsilon_2^u/\varepsilon_1^u$	FLC0	$\varepsilon_2^b/\varepsilon_1^b$	Ref.
1	DC01	204.3	335.9	24.1	576.3	0.212	0.6	-0.220/0.440	0.281	0.280/0.354	Exp.
2	Q&P 1180	1000.0	1200.0	14.8	1300	0.042	1.25	-0.060/0.142	0.102	0.170/0.185	[36]
3	DX54D	167.0	309.0	22.5	375.2	0.230	0.75	-0.302/0.671	0.351	0.394/0.439	[37]
4	DP800	465.0	786.0	15.0	989.9	0.160	1.00	-0.070/0.291	0.169	0.189/0.202	[37]
5	DX54D +Z	163.0	297.0	22.1	323.6	0.220	0.815	-0.301/0.606	0.308	0.411/0.454	[38]
6	DP590	396.8	761.1	19.7	1018	0.175	1.50	-0.150/0.387	0.293	0.372/0.421	[39]
7	IN-718	523.0	1084	39.3	1960	0.404	1.25	-0.186/0.432	0.345	0.376/0.372	[40]
8	TRIP600	350.0	835.8	26.0	1062.9	0.178	1.00	-0.173/0.478	0.270	0.385/0.468	[41]
9	DP600	350.0	734.3	14.2	1030.4	0.173	1.00	-0.191/0.445	0.213	0.280/0.361	[41]
10	TWIP940	457.2	960.1	68.9	2300	0.620	1.47	-0.251/0.566	0.380	0.362/0.532	[42]
11	TRIP780	508.4	837.0	16.9	1351	0.169	1.20	-0.177/0.484	0.252	0.324/0.449	[43]

12	IF steel	202.0	347.2	11.6	692	0.321	0.60	-0.165/0.541	0.309	0.119/0.436	[44]
13	IF steel	224.0	344.3	12.8	706.0	0.350	1.60	-0.160/0.674	0.329	0.156/0.530	[44]
14	Ferritic SS	428.0	561.0	16.9	870.4	0.184	1.00	-0.224/0.389	0.185	0.296/0.477	[30]
15	TRIP	422.0	730.0	35.1	815.7	0.106	1.00	-0.177/0.471	0.260	0.395/0.444	[45]
16	DP	269.0	496.0	27.2	583.2	0.124	1.50	-0.145/0.428	0.331	0.404/0.476	[45]
17	IF	124.0	311.0	44.1	357.5	0.170	1.01	-0.323/0.699	0.396	0.300/0.464	[45]
18	IF-HS	204.0	368.0	36.8	412.0	0.113	0.84	-0.265/0.578	0.325	0.280/0.430	[45]
19	A0	290.0	598.0	38.6	681.65	0.137	0.82	-0.181/0.641	0.381	0.183/0.420	[45]
20	A3	305.0	653.0	46.2	727.4	0.139	0.80	-0.182/0.553	0.363	0.207/0.398	[45]
21	ZStE 180 BH	246.0	343.0	38.9	364.0	0.063	0.77	-0.271/0.599	0.294	0.414/0.442	[45]
22	DP600	392.2	748.6	15.2	1067.2	0.192	1.20	-0.103/0.348	0.175	0.290/0.363	[31]
23	DP800	450.7	866.7	12.7	1185.5	0.168	1.20	-0.097/0.290	0.145	0.259/0.279	[31]
24	QP980	490.8	1173.4	16.1	1413.6	0.099	1.00	-0.121/0.384	0.224	0.265/0.360	[46]
25	JAY780Y	526.3	812.9	12.0	1226.4	0.136	1.00	-0.214/0.440	0.134	0.279/0.290	[47]
26	QP980	828.0	1015.0	10.9	1420.0	0.106	1.60	-0.154/0.437	0.203	0.358/0.402	[48]
27	EDD steel	202.0	337.0	44.0	677.0	0.304	1.00	-0.077/0.366	0.303	0.099/0.377	[49]
28	DP980	654	1027	8.3	1401	0.09	1.4	-0.09/0.224	0.131	0.282/0.364	[50]
29	DP600	340	587	19.2	963	0.184	1.5	-0.254/0.429	0.176	0.342/0.376	[51]

2.5 Artificial Neural Network Analysis

A general ANN model consists of input, hidden, and output layers. Input and output layers are fixed layers in which data is requested for modelling. A consistent and large quantity of data will increase the consistency of the model. The network structure of the model can be constructed in different ways according to the number of hidden layers and neurons. There may be several hidden layers or only one. Although there is yet to be a straightforward method for determining the number of hidden layers, specific rules are considered. This number is increased according to the complexity of modelling between the input and output values of the study. For example, if the problem can be divided into stages, the number of hidden layers in the network should be increased. One, two or three hidden layers will provide sufficient results.

The weights and bias values are continuously changed to obtain outputs corresponding to the inputs given to the ANN network. This process is called the training of the network. After the training of the ANN network, new inputs that have not previously been given to the network are supplied, and the outputs are tried to be obtained with an acceptable error. Although the training error is minimal, a high error between the actual results and the outputs of the ANN in response to the new inputs indicates that the network is memorising (over-fitting).

The number of neurons in the hidden layer is one of the main parameters of the ANN model. Although there is no precise method for determining the number of neurons, it should be increased as the problem becomes more complex. The number of hidden layer

neurons in the network starts at a certain number and increases until the network provides sufficient generalisation. Too many neurons will reduce the network's generalisation ability, and the network will begin to memorise. If the number of neurons is less than necessary, the ANN cannot accurately predict the output data. Therefore, the optimal number of neurons has to be found.

In this study, an algorithm was developed in the ANN to determine the appropriate number of neurons. MATLAB 2017a was used for ANN modelling. In addition to the input and output data, the maximum and minimum numbers of neurons should be defined in the algorithm. After the normalisation of input and output data, the essential functions of the ANN network structure are determined. The following types of functions are used in the created network structures.

- Network type: feed-forward and back-propagation
- Training function: TRAINLM
- Adoption learning function: LEARNGDM
- Performance function: mean square error (MSE)

In the algorithm developed, the maximum and minimum neuron numbers are entered according to the number of hidden layers selected. All the network structures that can be formed by the number of neurons in the network are trained. From the data set, 70%, 15% and 15% of the data were randomly selected for training, testing and validating, respectively, and then the network training began. Weights and bias values were randomly assigned for each network structure formed with different neuron numbers and trained for a determined number of iterations. Although the number of training iterations for the developed algorithm was 30, this number can be increased. This initial training is called the basic training of the network. Considering the MSE value from the primary network training, the optimum network structure was determined from the network structures formed between the maximum and minimum neuron numbers in the hidden layers. The network structure was created by selecting the number of neurons with the lowest MSE value among the trained networks. The algorithm gives the MSE values for all network trials and the regression (R) graphs of the optimum network structure.

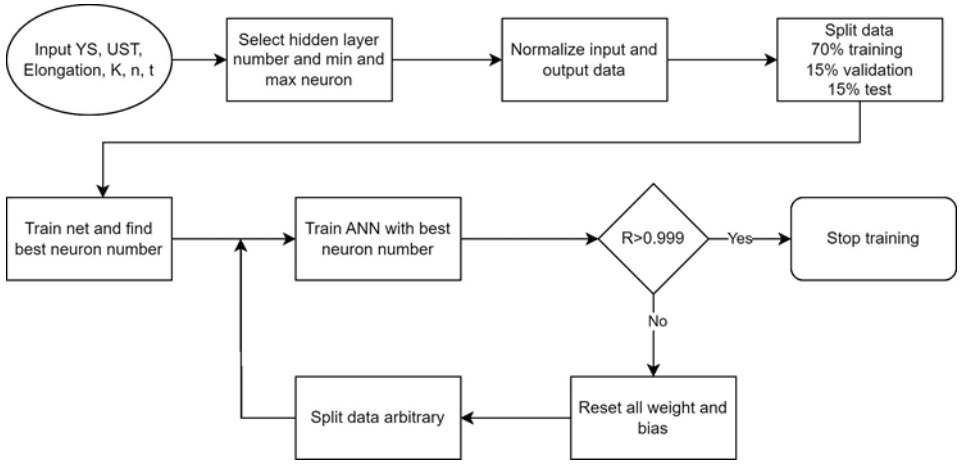

(a)

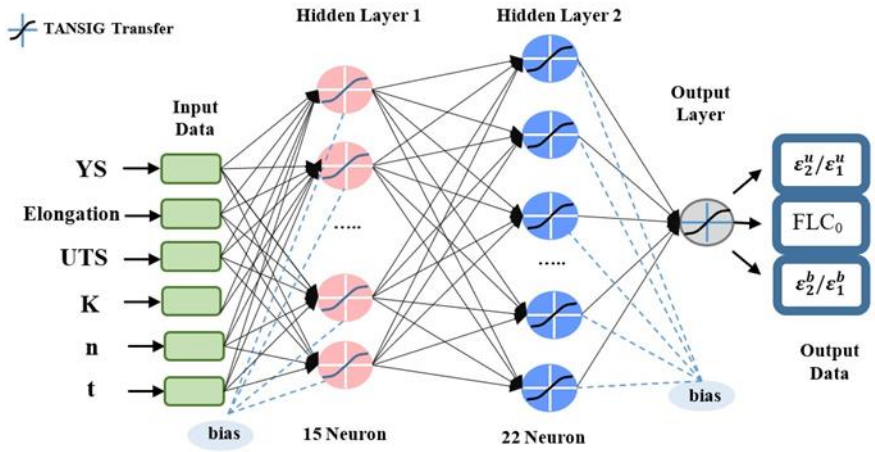

(b)

Fig 5. ANN model (a) Flow chart of the algorithm, (b) Structure of the model

The next step of the algorithm continues to train the network until it reaches the highest regression value in the specified network structure. During this training stage, the network structure is kept constant while training, testing, validation data pairs, weights and bias values are constantly changed. Thus, memorisation in the network is prevented. In the last step, the network structure with the highest regression value was recorded, and the training was terminated. The actual data and the outputs of the training results of the network are given graphically. Thus, the optimal network structure is determined by running a single algorithm for the number of layers and the neurons to be selected for each layer. The algorithm and network structure created for the ANN model is shown in Fig. 5a and 5b.

All data used in this study were normalised. The activation functions used in an ANN could give false results if mixed negative and positive numbers or huge numbers are shown in the input and output layers. Normalisation is applied to the data to prevent these errors and increase the learning speed. The definition of normalisation is the limitation of data to a specific range, such as the range [-1,0] or [0,1]. The normalisation equation is;

$$X_{new} = \frac{(X - X_{min})}{(X_{max} - X_{min})}(upperbound - lowerbound) + lowerbound \quad (5)$$

X_{new}, X_{max} and X_{min} are the restricted, maximum, and smallest values, respectively. The upper and lower bound are the upper and lower values of the range to be restricted [52]. The mean square error was used as the performance function. This function gives the average square of the difference between the network results and its outputs [53]. The MSE function is;

$$MSE = \frac{1}{N}\sum_{i=1}^{N}(y_i - z_i)^2 \quad (6)$$

Where y_i is the ANN prediction, z_i is the output value, and N is the number of outputs.

System identification modelling was used to model the system with a MISO (multiple input, single output) model structure. Input and output parameters were arranged in the data sets and limited to [0.01–0.99] using Eq. 5. A total of 29 data pairs were used. In the

modelling process, 21 data sets were reserved for training, four for testing and four for verification. Each data sets have three outputs as β^-, β^+, FLC_0. In this study, when the model selection is made, the regression value (R) of the network and the comparison graphs and MSE are taken into consideration because it is necessary to check the compatibility of the model with the system by using comparison graphs to determine whether the model is successful or not. The R values were calculated according to the formula in Eq. 7 [54].

$$R = \frac{n\sum x_i y_i - (\sum x_i)(\sum y_i)}{\sqrt{n\sum x_i^2 - (\sum x_i)^2}\sqrt{n\sum y_i^2 - (\sum y_i)^2}} \tag{7}$$

Here, x_i is the targeted value found by experiments, and y_i represents the output value of the network, in other words, the prediction. The *R-value* calculated with this formula depends on the number of specimens, the difference between the variables and the distribution of the variables. Another parameter for measuring network success is the percentage error. The formula used for percentage error is given in Eq. 8 [55]. Here, E is the percentage error, x_i is the targeted value found by experiments, and y_i represents the output value from the network.

$$E(\%) = \frac{1}{n}\sum_i \left(\frac{|x_i - y_i|}{x_i} \cdot 100\right) \tag{8}$$

2.6 Sensitivity Analysis of the ANN

Artificial neural networks (ANNs) are a powerful tool used in various engineering fields, especially for solving prediction, regression and classification problems. However, ANN is generally considered a black box where it is difficult to determine the effect of each input data on any output data [56]. Sensitivity analyses are performed to determine the model outputs' critical parameters and importance levels [57]. In the sensitivity analysis results, the network output changes according to the inputs and provides information about the more sensitive parameters that need to be measured more accurately [58].

In the context of this research, understanding the influence of input parameters on the artificial neural network (ANN) model's outputs and the direction of correlations is paramount. Sensitivity analysis is a valuable tool that identifies the most influential parameters, offering several advantages. It allows for optimising predictions by emphasising precise data collection for critical parameters, ultimately enhancing the accuracy of predictions and decision-making. Additionally, sensitivity analysis streamlines experimentation efforts, conserving time and resources. Moreover, it enables potential model improvements, such as adjustments to the ANN architecture or incorporating additional data sources based on parameters showing strong correlations with the output.

Comprehending the direction of correlations between input parameters and the model's output is equally significant. Positive correlations signify that increasing an input parameter leads to an increase in the output, emphasising the need to enhance or optimise such parameters. Conversely, negative correlations indicate that increasing an input parameter decreases output, suggesting the necessity to control or minimise the parameter for better predictions. Parameters with weak or no correlation may be re-evaluated for inclusion in the model due to their limited impact on predictions.

This understanding of correlation directions facilitates the interpretation of the system's behaviour, though it's crucial to remember that correlation does not imply causation. Establishing causal relationships may require additional analyses or domain expertise. In summary, sensitivity analysis and comprehending correlation directions empower the fine-tuning of the ANN model, inform efficient data collection, and enhance the precision

and reliability of predictions, particularly in predicting forming limit curves for sheet metals.

A study on the results of comparisons of sensitivity analysis methods was made by Gevrey et al. [57]. The weight method, one of the methods examined in the study, can classify the inputs within itself and contribute to the output. This study examined the contributions of the input parameters to the FLC model created with ANN using the 'Weights' method sensitivity analysis. Garson [59] and Goh [60] proposed Weights' method. The percentages of influence of the input variable, Q_{ik}(%), on output value, indicating the importance of input variables, were determined by the following equation [61]:

$$Q_{ik}(\%) = \frac{\sum_{j=1}^{n}\left(\frac{|w_{ij}|}{\sum_{i=1}^{m}|w_{ij}|}|v_{jk}|\right)}{\sum_{i=1}^{m}\left(\sum_{j=1}^{n}\left(\frac{|w_{ij}|}{\sum_{i=1}^{m}|w_{ij}|}|v_{jk}|\right)\right)} \times 100 \tag{9}$$

w_{ij} represents weights between the input neuron i (= 1, 2, ..., m) and the hidden neuron j (= 1, 2, ..., n), and v_{jk} represents the weights between the hidden neuron j and the output neuron k (= 1, 2, ..., l). In this study, the input, hidden, and output neurons were 6, 15 and 3, respectively. A more detailed example of this method can be found in Ref. [57].

2.7 Marciniak-Kuczynski (M-K) Model

M-K model is another theoretical method to determine FLC. This model assumed that the material has an instability region which is rapidly deformed under load compared to the other areas of material (Fig. 6). The orientation of the instability region changes depending on the strain path assumed [62]. Force equilibrium for x and y direction, strain path, yield criteria and a constitutive relationship is assumed, and the strain increments in the safe and instability regions are predicted. If the strain increments of the instability region are ten times greater than the safe region, then it is assumed that the failure occurred.

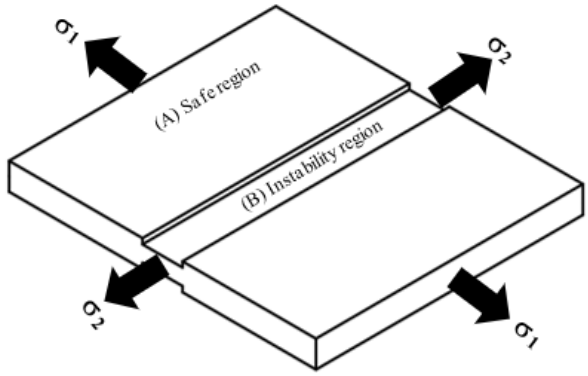

Fig. 6. Schematic sheet metal in Marciniak and Kuczynski model

FLC can be created with different strain hardening rules in the M-K model. This study used the Hollomon strain-hardening rule (Eq. 10) and von Mises yield criterion (Eq. 11) to determine FLC theoretically.

$$\sigma = K \cdot \varepsilon^{n} \tag{10}$$

$$\bar{\sigma} = \frac{1}{\sqrt{2}}\sqrt{(\sigma_1 - \sigma_2)^2 + (\sigma_2 - \sigma_3)^2 + (\sigma_3 - \sigma_1)^2} \tag{11}$$

The force equilibrium of regions A and B can be written in Eq. 12. Also, the strain increments in direction 2 are equal, as seen in Eq. 13.

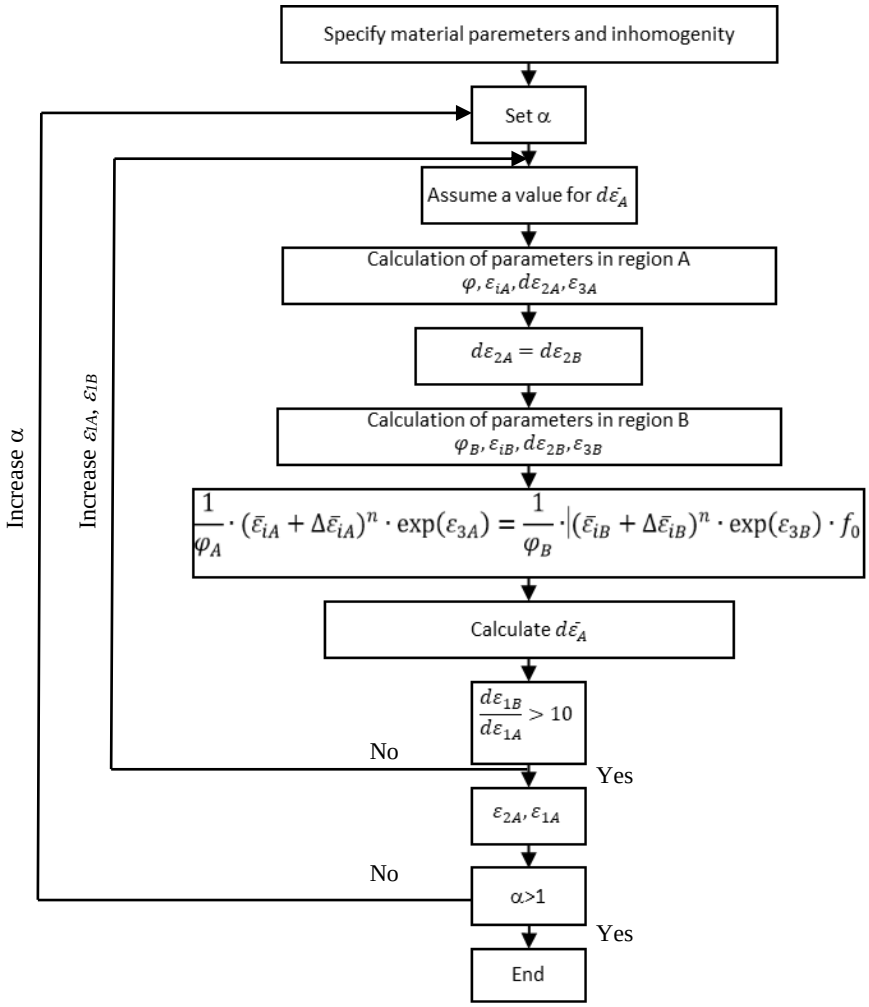

Fig. 7 Flowchart of M-K model

The force equilibrium can be written in terms of stress, strain and thickness as in Eq. 14. In this equation, f_0 is the inhomogeneity coefficient; in other words, the ratio of t_B to t_A. Also, the thickness strain (ε_3) can be calculated from the incompressibility principle.

$$F_{1A} = F_{1B} \tag{12}$$

$$d\varepsilon_{2A} = d\varepsilon_{2B} \tag{13}$$

$$\sigma_{1A} \cdot exp(\varepsilon_{3A}) = \sigma_{1B} \cdot exp(\varepsilon_{3B}) \cdot f_0 \tag{14}$$

The ratio of effective stress to major stress is given in Eq. 15. As a result, Eq. 16 is obtained by substituting Eq. 11 and 15 in Eq. 14.

$$\varphi = \frac{\bar{\sigma}}{\sigma_1} \tag{15}$$

$$\frac{1}{\varphi_A} \cdot \bar{\varepsilon}_A^n \cdot exp(\varepsilon_{3A}) = \frac{1}{\varphi_B} \cdot \bar{\varepsilon}_B^n \cdot exp(\varepsilon_{3B}) \cdot f_0 \tag{16}$$

In Eq. 16, although the left side can be calculated simply, the right side of the equilibrium should be calculated iteratively. The Newton-Raphson method was used to determine strain increment. At the beginning of the calculation, a constant stress ratio should be defined for the safe region. By the way, Eq. 16 is arranged iteratively to obtain Eq. 17. A flowchart of the algorithm to calculate FLC is given in Fig. 7.

$$\frac{1}{\varphi_A}\cdot(\bar{\varepsilon}_{iA}+\Delta\bar{\varepsilon}_{iA})^n\cdot exp(\varepsilon_{3A})=\frac{1}{\varphi_B}\cdot(\bar{\varepsilon}_{iB}+\Delta\bar{\varepsilon}_{iB})^n\cdot exp(\varepsilon_{3B})\cdot f_0 \tag{17}$$

2.8 The Swift-Hill Model

It has been proven that a good simulation of the forming limit strains can be given based on the Swift diffuse instability theory and the Hill localised instability theory [45,63]. In Swift-Hill theory, the FLC's left and right sides are calculated separately based on α. The stress-strain relationship of sheets is expressed with Hollomon's equation. For the left side of the FLC, $\varepsilon_2 < 0$, major and minor strain is given in Eq. 18 and Eq. 19 [45]. The strain hardening exponent, n and anisotropy coefficient, r, are constant material properties in these equations.

$$\varepsilon_1=\frac{1+(1-\alpha)\cdot r}{1+\alpha}\cdot n \tag{18}$$

$$\varepsilon_2=\frac{\alpha-(1-\alpha)\cdot r}{1+\alpha}\cdot n \tag{19}$$

For the right side of FLC, $\varepsilon_2 > 0$, major and minor strains are calculated with Eq. 20 and 21.

$$\varepsilon_1=\frac{[1+(1-\alpha)\cdot r]\cdot\left[1-\frac{2\cdot r}{1+r}\cdot\alpha+\alpha^2\right]}{(1+\alpha)\cdot(1+r)\left[1-\frac{1+4\cdot r+2\cdot r^2}{(1+r)^2}\cdot\alpha+\alpha^2\right]}\cdot n \tag{20}$$

$$\varepsilon_2=\frac{[(1+r)\cdot\alpha-r]\cdot\left[1-\frac{2\cdot r}{1+r}\cdot\alpha+\alpha^2\right]}{(1+\alpha)\cdot(1+r)\left[1-\frac{1+4\cdot r+2\cdot r^2}{(1+r)^2}\cdot\alpha+\alpha^2\right]}\cdot n \tag{21}$$

2.9 The NADDRG Model

The North American Deep Drawing Research Group (NADDRG) suggests an empirical equation for predicting the FLC. The proposed formula enabled FLC to be quickly determined in press shops without complex experiments or theories such as M-K. According to this model, the FLC comprises two lines through the point ε_0 in the plane-strain state. The slopes of the lines on the left and right sides of FLC are about 45° and 20° [63]. The thickness of the sheet should be thinner than the 3.175 mm. The equation for calculating the forming limit strain ε_0 in terms of engineering strain is given in Eq. 22.

$$\varepsilon_0=\frac{(23.3+14.13\cdot t_0)\cdot n}{0.21} \tag{22}$$

3. Results and Discussion

3.1 Experimental FLD of steel sheet

Major and minor strain measurements were taken from the fractured specimens. Measures taken from damaged ellipses are shown with a red dot in the graph and measurements taken from the undamaged ellipse closest to the damaged ellipse are shown

in green, as seen in Fig. 8. The left and right parts of the FLC were created separately. The lines are fitted to the left and right dots. The curve formed by connecting these two lines at the intersection points was accepted as the FLC. When the graph is examined, the FLC_0 value for DC01 was 0.294. Due to different friction conditions during the experiment, the FLC can shift to the right or the left. DC01 sheet reached 0.4 for uniaxial strain and 0.35 for biaxial strain.

The FLCs of sheet metals may differ according to the metal type. In particular, the right side of the curve may exhibit a polynomial behaviour depending on the material type. For example, in the study of Wang et al. [64], the left side of the curve consists of a straight line, while the right side is polynomial. Another study by Mu et al. [65] similarly showed that the FLC exhibits a transition from necking to fracture in the biaxial stress region, so the curve in this region will be polynomial. The FLCs are valid for one particular material alloy, temper and gauge combination [12]. However, material properties vary from batch to batch due to production processes. Therefore, a single FLC cannot accurately describe the forming limit. Janssens et al. [66] have proposed a more general concept, the Forming Limit Band (FLB), as a region covering the entire dispersion of the Forming Limit Curves. This and similar studies show that forming limit diagrams for sheet metals with linear lines may not always give accurate results.

On the other hand, it has also been accepted as two straight lines to simplify the FLC and enable its practical use [67,68]. In addition, FLCs obtained by the NDDRG empirical method consist of two lines on the left and right. This study assumes that the FLC consists of two lines to model the FLC with artificial neural networks. In this way, the FLC can be easily expressed by a point FLC_0 and the slope of the two lines to the left and right of this point.

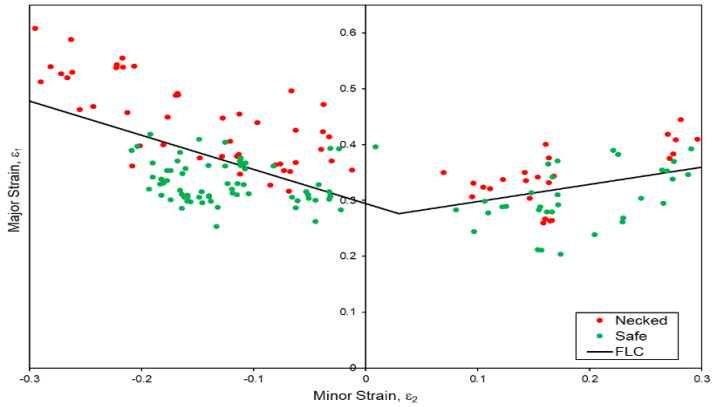

Fig. 8. Forming limit diagram of DC01

3.2 Artificial Neural Network Modelling Results

Experimental studies in the literature for determining FLCs, critical in metal forming processes, were modelled with an ANN. The modelling results were compared with experimentally obtained FLC values. The FLCs were determined by performing out-of-plane tests with the two steel sheets selected for the study. These FLCs were then compared with the ANN results.

This ANN study, 29 data pairs were used, considering only steel materials. In the modelling process, six parameters were determined in the input layer, and three parameters were determined in the output layer (Fig. 5b). A minimum of 15 and a maximum of 25 neurons were selected in the model structure. A total of 121 combinations of neurons were tested

in the network. The optimum number of neurons was determined by considering the MSE values of the obtained network structures. In Fig. 9, MSE values obtained from the modelling results of the network structures created with all neuron combinations after basic network training are shown. The number of neurons in the network with the lowest MSE value was determined as 15-22, and this is marked with a red dot in Fig. 9. The *R*-value obtained from the primary network training of the created network with the optimum neuron numbers is given in Fig. 10. The regression value, of approximately 0.98603, is at an acceptable level.

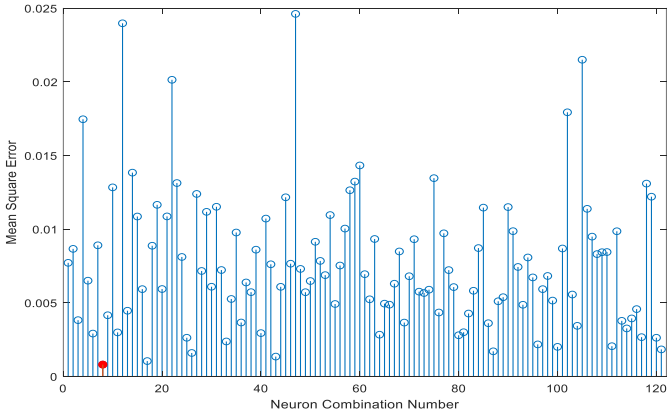

Fig. 9. MSE values of all combinations of neurons used in ANN layers

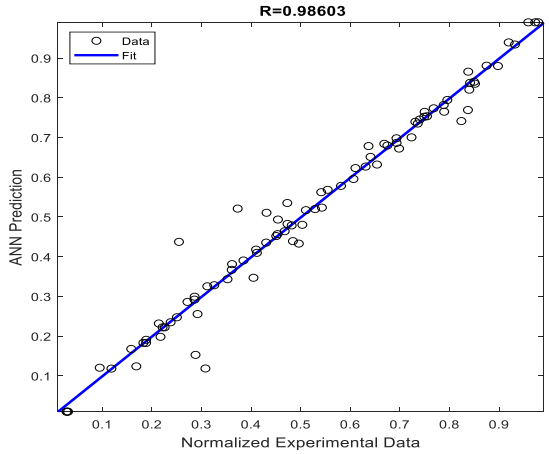

Fig. 10. The R-value after basic network training in the network structure created with the optimum number of neurons

The network structure was formed by determining the hidden layer and neuron numbers for ANN modelling. The next step of the algorithm is to re-train the network structure with optimal neuron numbers after basic network training to increase the generalisation of the network. After retraining the optimum network, the final *R* values were determined as 0.99998 for training, 0.99994 for validation and 0.99976 for testing, as shown in Fig. 11. The overall *R-value* of the network was calculated as 0.99995.

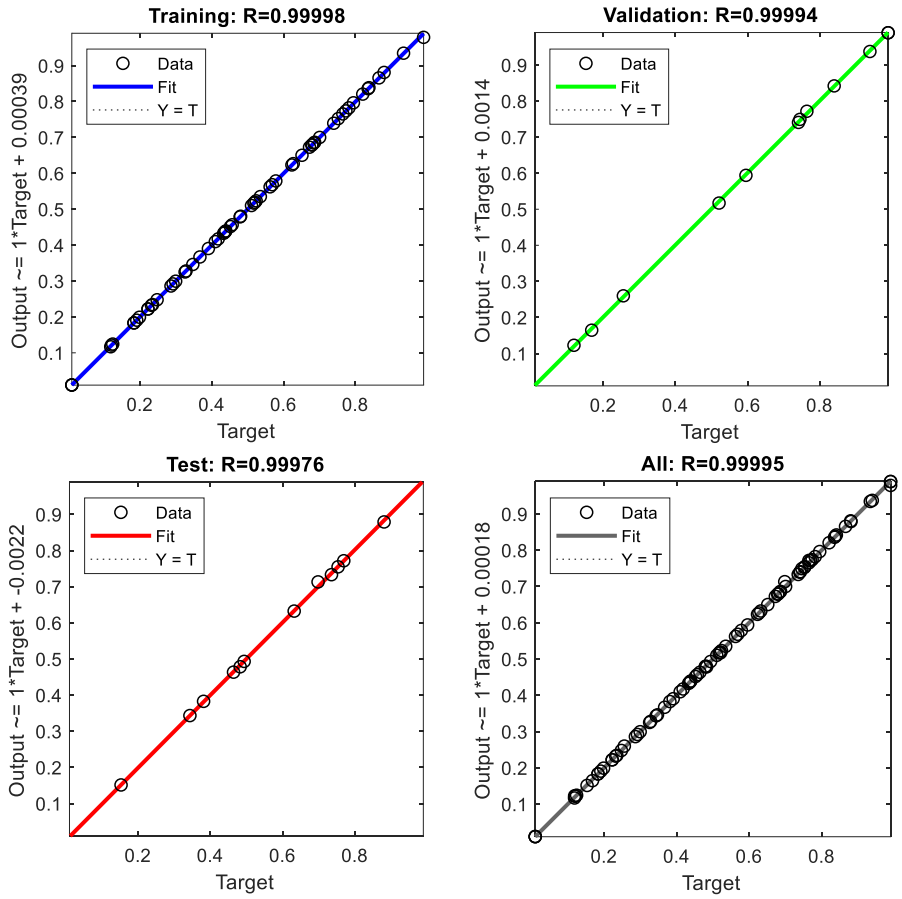

Fig. 11. The *R* values of the algorithm in the final ANN modelling

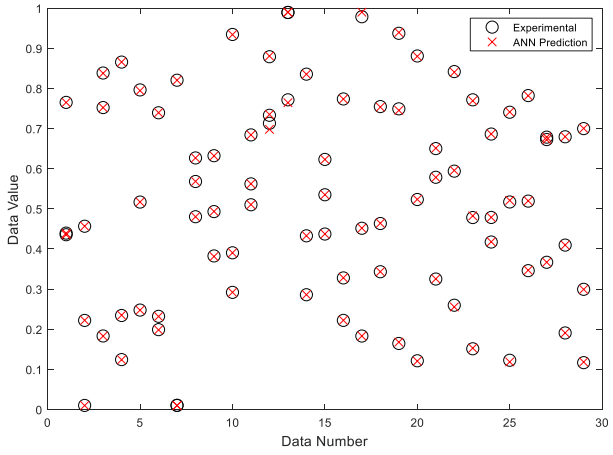

Fig. 12. Comparison of experimental results obtained from literature with ANN modelling outputs

The proximity of the *R* values to 1 indicates the success of the network structure for the modelled system. Similarly, the proximity of the *R* values of randomly selected test and

verification data to 1 reveals the consistency of the network.One of the most critical problems in ANN modelling is misleading results from the network due to memorisation. To overcome this problem, the experimentally obtained output data should be compared with the predicted output values resulting from modelling. Fig. 12 shows a graph comparing the output data with the predicted output data. The input data number (tag) given to the ANN is shown on the horizontal axis, and the input data value is shown on the vertical axis. The outputs and ANN predictions are highly consistent.

3.3 Contributions of input to the ANN predict

In the study, most of the selected parameters can be determined by tensile testing. Sheet thickness can be easily measured with a calliper. It is possible to get more consistent results as the number of inputs in artificial neural networks increases [69]. For this reason, six different material properties that can introduce the material were selected as input. In this section, the Weights Method determined the effect of the selected inputs on the outputs. The effects of the input parameters on the output are given in Figure 13. Accordingly, the most effective parameters on the output are *UTS* and *n* parameters, respectively. An inverse correlation between *UTS* and FLC_0 was reported by Belck et al. [45]. A linear correlation between FLC_0 and *n* is reported by Keeler and Brazier [70]. The formability also improves with increasing *n* [12,71,72]. On the other hand, the strength coefficient has the most negligible effect on the outputs, with 11.16%.

Paul grouped the material properties and estimated the FLC by choosing at least one element from each group [19]. Similar to this study, the inputs can be divided into three categories. These categories can be called experimental properties (*YS*, *UTS* and elongation), theoretical model coefficients (*K* and *n*), and sheet thickness (*t*). When evaluated as a group, the experimental properties are affected by 53.11%, the theoretical model coefficients by 31.61%, and the sheet thickness by 15.28%, respectively. Here, further studies can be made on whether the network's success can be increased by removing weak parameters such as *K*. In addition, by using different methods, it can be revealed how the inputs affect the outputs.

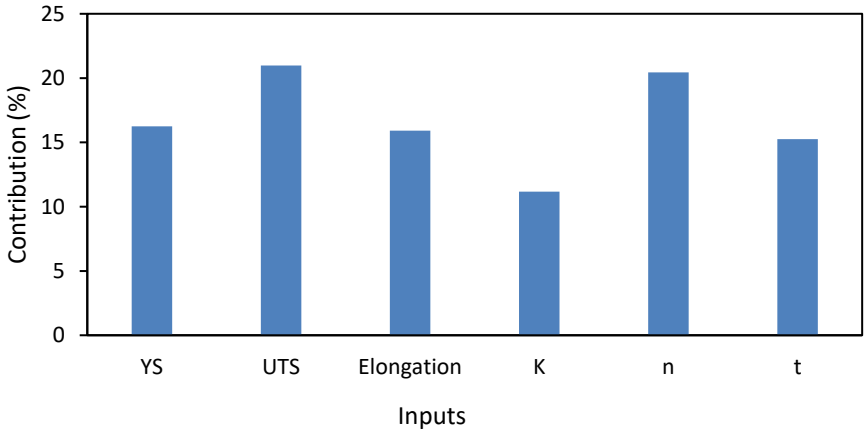

Fig. 13. The contributions of input on the ANN output

3.4 Comparison of experimental FLC with ANN predict

In this study, the network created was trained with the given data and success was achieved with $R = 0.99995$. The network was asked to predict the FLC from the mechanical properties of the steel sheet. The results of the trained network for DC01 are shown in Fig.

14 compared with experimental FLC. The network predicts only the FLC_0 point of the FLC and the slopes of the right and left sides connected to this point. The error between the experimental and predicted FLC had been calculated using Eq. 23.

$$error = \frac{\varepsilon_{1,\ theoretical} - \varepsilon_{1,exp.}}{\varepsilon_{1,exp.}} x100\% \quad (23)$$

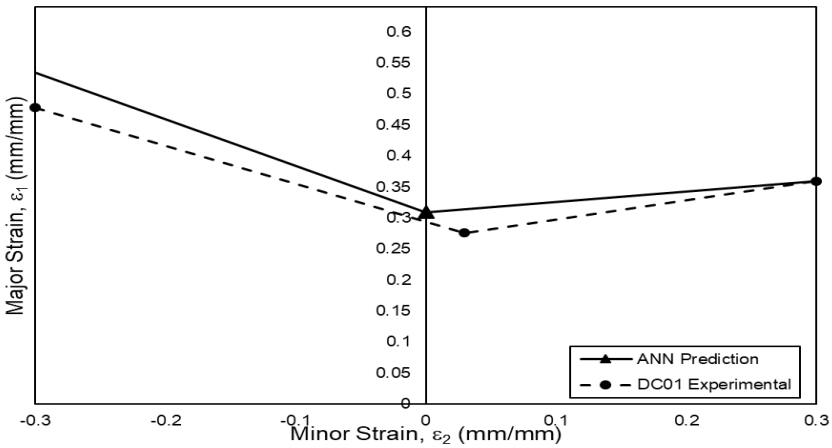

Fig. 14. Comparison of experimental FLC and ANN predictions for DC01

According to this equation, the difference in the FLC_0 point between ANN and the experimental result is 3.4% for DC01. In Fig. 14, the predicted and experimental results differ by only 8.5% for the left side and 4.0% for the right side on average over the whole strain region. The FLC does not give an accurate result when expressed by a single curve because, after the experiments, variables such as the region where the deformation is measured (fractured, necking or near to the necking), the marker size, and the resolution of the measurement system can change the sensitivity of the FLC. In addition, the diameter and geometry of the punch used in the test and the friction during the test may cause the FLC to shift slightly up or down. Considering all of these factors, accepting the FLC as a band gives more accurate results in terms of application. Therefore, although there are some differences in the predictions made with the ANN, these differences remain acceptable.

3.5 Comparison Between the Experimental, Empirical and Theoretical FLCs

This section gives theoretical, empirical, and experimental FLC for the DC01 sheet (Fig. 15). When the graphs are examined, it is seen that the results obtained with the M-K and Swift-Hill theoretical models are far from the experimental results. Although the curves obtained by NADDRG and ANN methods were slightly above the experimental curve, they were closer than the theoretical models. M-K and Swift-Hill theoretical models were below and further from the experimental curve. According to Eq. 23, when the average error between the theoretical and empirical curves is calculated along with all the minor strain values, it is seen that the ANN model gives the closest result with an average error of 10.28%. On the other hand, it is seen that the curve created with NADDRG makes a close estimation for the DC01 sheet with an average error of 15.63%.

Closer results can be obtained using different strain-hardening models and assumptions within the theoretical model. The sheets are assumed to be isotropic in the theoretical models used in this study. In addition, it is assumed that the groove, accepted on the sheet in the M-K criterion, is always perpendicular to the major stress. However, considering the

theoretical and empirical models, the results obtained with the ANN are compatible with the experimental results.

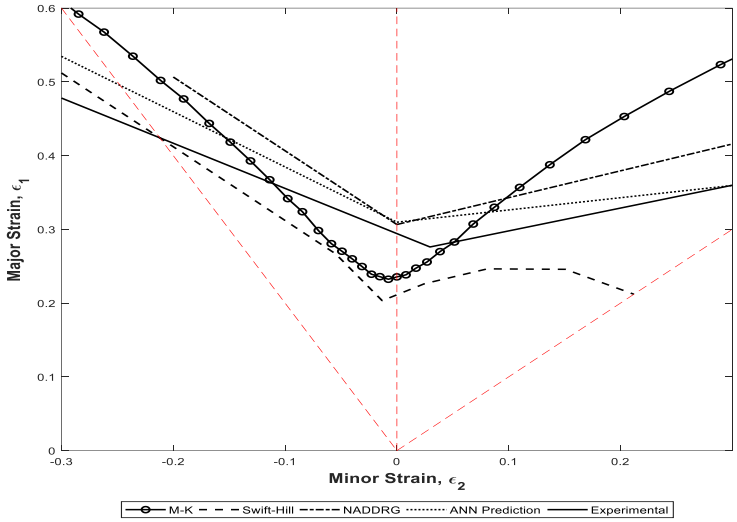

Fig. 15. The theoretical, empirical and experimental FLC of DC01

The significant difference between the theoretical models is due to the strain-hardening models and yield criteria selected for the material. Theoretical FLC is significantly influenced by strain-hardening models and yield criteria [73]. A model that gives accurate results for one material may produce inconsistent results for a different material. On the other hand, although the flow rule can very well represent the stress-strain relationships in uniaxial tensile materials, the theoretical predictions show significant deviations from the experimental FLD. A suitable calculation method depends on understanding materials' flow behaviour, assumptions for instability criteria, and perhaps other material properties and experimental factors [63].

3.6 Comparison between the theoretical, empirical and experimental FLC_0 values

A comparative bar graph of theoretical, empirical and experimental FLC_0 values is given in Fig. 16. The FLC_0 is the value that expresses the formability of the sheet in the case of plane strain and shows the lowest point of the FLC. The FLC_0 value is vital since crack formation and damage to the material in cold-forming processes usually occur under a plane strain state. When Fig. 16 is examined, it is seen that ANN and the NADDRG estimate the FLC_0 value for DC01 steel with an error of 3.4% and 2.3%, respectively. It is known that the NADDRG empirical relation gives accurate results for sheets in the deep drawing group. Other close estimates belong to the M-K and Swift-Hill theoretical models, with 21.3% and 29.2% errors, respectively. When evaluated in general, it is seen that the estimation made with ANN gives correct results like NADDRG. Compared to other methods, FLC estimation with ANN is simple and fast to be used practically in press shops if the database is expanded.

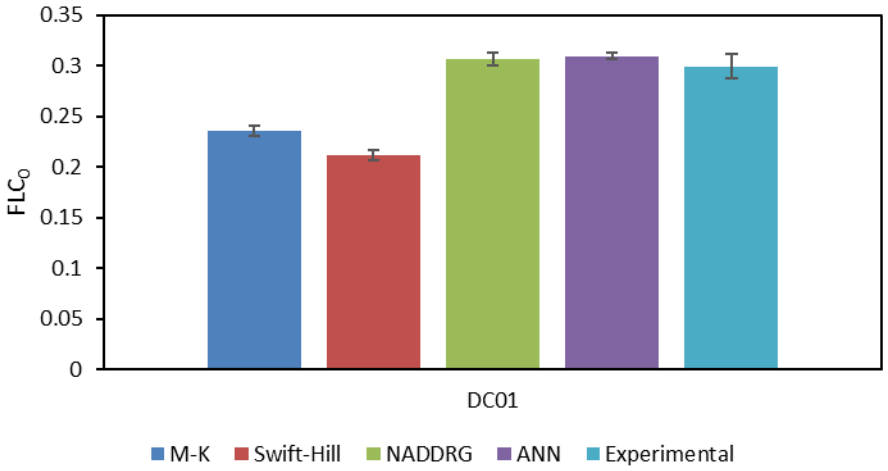

Fig. 16. Comparison between the theoretical, empirical and experimental FLC_0 values for DC01

4. Conclusions

This study demonstrated the effectiveness of an artificial neural network (ANN) model in predicting forming limit diagrams (FLDs) for sheet metals, particularly in the automotive industry. Material properties essential for this study, including sheet thickness, yield strength, ultimate tensile strength, uniform elongation, hardening exponent, and strength coefficient, were gathered and employed as inputs for the ANN model.

The key findings of this study encompass the following aspects:

- An exact ANN model with a 6-15-22-3 structure was successfully developed, yielding an R-value of 0.99995. This level of predictive accuracy holds significant implications, particularly within the automotive manufacturing domain.
- This research holds substantial practical implications, particularly for the automotive industry, which relies on accurate FLDs to ensure the quality and manufacturability of sheet metal components. With its rapid and reliable FLD predictions, the ANN model has the potential to optimise manufacturing processes, reduce material wastage, and enhance product quality.
- The accuracy of FLD predictions directly impacts manufacturing efficiency. Minor deviations in FLDs can result in significant defects or inefficiencies during production. Notably, the ANN model's capability to predict FLDs with a mere 3.4% difference from the FLD0 value highlights its potential to enhance manufacturing efficiency within the automotive sector. The difference between ANN predictions and experimental results may be acceptable for some non-critical automotive components but may fall short of industry requirements for safety-critical parts. It underscores the importance of ongoing research and development to improve predictive models to ensure the safety and reliability of automotive products.
- This study paves the way for future research and applications. While the current focus is on steel materials, the ANN model's applicability can be extended to various materials, widening its utility in the manufacturing sector. Subsequent research endeavours can explore the model's performance with different materials and further refine its capabilities.

- In summary, this research introduces a robust and efficient method for predicting FLDs, promising to revolutionise the automotive industry's quality control and manufacturing processes. The ANN model's exceptional accuracy in estimating FLDs opens avenues to enhance manufacturing efficiency and ensure product quality. As the model continues evolving and broadening its applicability to diverse materials, it will be pivotal in advancing automotive manufacturing processes. Beyond the automotive industry, the implications of this research extend to various sectors where sheet metal forming is a critical manufacturing process, heralding a new era of accuracy and efficiency in sheet metal forming and quality control. In future works, to improve the model accuracy, the input size can be widened, and ANN can estimate the polynomial curve of the FLD.

References

[1] Ozturk F, Lee D. Experimental and numerical analysis of out-of-plane formability test. Journal of Materials Processing Technology 2005; 170: 247-53. https://doi.org/10.1016/j.jmatprotec.2005.05.010
[2] Keeler SP. Plastic instability and fracture in sheets stretched over rigid punches. 1961.
[3] Goodwin GM. Application of strain analysis to sheet metal forming problems in the press shop. SAE Transactions 1968: 380-7. https://doi.org/10.4271/680093
[4] Emmens WC. Formability; A Review of Parameters and Processes That Control, Limit or Enhance the Formability of Sheet Metal. Springer Berlin Heidelberg, 2011. https://doi.org/10.1007/978-3-642-21904-7
[5] Chang K-H. Sheet Metal Product Manufacturing and Cost Estimating Using Cad/Cae Simulation. Elsevier Inc., 2013. https://doi.org/10.1016/B978-0-12-401745-0.00006-X
[6] Brozzo P, Deluca B, Rendina R. A new method for the prediction of formability limits in metal sheets. Proc. 7th Biennal Conf. IDDR. 1972.
[7] Olsen TY. Machines for ductility testing. Proc. Am. Soc. Mater 1920; 20: 398-403.
[8] Hecker SS. A simple forming-limit curve technique and results on aluminum alloys. Int. Deep Drawing Res. Group, 7 Th Biennial Congress. Amsterdam, 1972.
[9] Marciniak Z. Stability of plastic shells under tension with kinematic boundary conditions(Stability of plastic shell under tension). Archiwum Mechaniki Stosowanej 1965; 17: 577-92.
[10] Nakazima K, Kikuma T. Forming limits under biaxial stretching of sheet metals. Testu-to Hagane 1967; 53: 455-8. https://doi.org/10.2355/tetsutohagane1955.53.10_S455
[11] Hasek V. On the strain and stress states in drawing of large un-regular sheet metal components. Berichte aus dem Institut für Umformtechnik, Universität Stuttgart, Essen, Germany, Report1973.
[12] Banabic D. Sheet Metal Forming Processes: Constitutive Modelling and Numerical Simulation. Springer Berlin Heidelberg, 2010. https://doi.org/10.1007/978-3-540-88113-1
[13] Marciniak Z, Kuczyński K. Limit strains in the processes of stretch-forming sheet metal. International Journal of Mechanical Sciences 1967; 9: 609IN1613-612IN2620. https://doi.org/10.1016/0020-7403(67)90066-5
[14] Swift H. Plastic instability under plane stress. Journal of the Mechanics and Physics of Solids 1952; 1: 1-18. https://doi.org/10.1016/0022-5096(52)90002-1
[15] Hill RT. On discontinuous plastic states, with special reference to localized necking in thin sheets. Journal of the Mechanics and Physics of Solids 1952; 1: 19-30. https://doi.org/10.1016/0022-5096(52)90003-3
[16] Gurson AL. Continuum theory of ductile rupture by void nucleation and growth: Part I-Yield criteria and flow rules for porous ductile media. Journal of engineering materials and technology 1977; 99: 2-15. https://doi.org/10.1115/1.3443401

[17] Zhang R, Shao Z, Lin J. A review on modelling techniques for formability prediction of sheet metal forming. International Journal of Lightweight Materials and Manufacture2018 Jun; doi 10.1016/j.ijlmm.2018.06.003. https://doi.org/10.1016/j.ijlmm.2018.06.003
[18] Subramani K, Alagarsamy SK, Chinnaiyan P, Chinnaiyan SN. Studies on testing and modelling of formability in aluminium alloy sheet forming. 2018; 2. https://doi.org/10.21278/TOF.42206
[19] Paul SK. Prediction of complete forming limit diagram from tensile properties of various steel sheets by a nonlinear regression based approach. Journal of Manufacturing Processes 2016; 23: 192-200. https://doi.org/10.1016/j.jmapro.2016.06.005
[20] Levy BS, Van Tyne CJ. An approach to predicting the forming limit stress components from mechanical properties. Journal of Materials Processing Technology 2016; 229: 758-68. https://doi.org/10.1016/j.jmatprotec.2015.10.027
[21] Paul SK. Controlling factors of forming limit curve: A review. Advances in Industrial and Manufacturing Engineering 2021; 2: 100033. https://doi.org/10.1016/j.aime.2021.100033
[22] Kotkunde N, Deole AD, Gupta AK. Prediction of Forming Limit Diagram for Ti-6Al-4V Alloy Using Artificial Neural Network. Procedia Materials Science 2014; 6: 341-6. https://doi.org/10.1016/j.mspro.2014.07.043
[23] Elangovan K, Sathiya Narayanan C, Narayanasamy R. Modelling of forming limit diagram of perforated commercial pure aluminium sheets using artificial neural network. Computational Materials Science 2010; 47: 1072-8. https://doi.org/10.1016/j.commatsci.2009.12.016
[24] Derogar A, Djavanroodi F. Artificial neural network modeling of forming limit diagram. Materials and Manufacturing Processes 2011; 26: 1415-22. https://doi.org/10.1080/10426914.2010.544818
[25] Forcellese A, Gabrielli F, Simoncini M. Prediction of flow curves and forming limit curves of Mg alloy thin sheets using ANN-based models. Computational Materials Science 2011; 50: 3184-97. https://doi.org/10.1016/j.commatsci.2011.05.048
[26] Dehghani K, Shafiei M A, Naeimi H. Effect of thermomechanical processing on forming limit diagrams predicted by neural networks. Materials and Manufacturing Processes 2008; 23: 829-33. https://doi.org/10.1080/10426910802384714
[27] Farahnak P, Urbánek M, Konopík P, Džugan J. Influence of thickness reduction on forming limits of mild steel DC01. International Journal of Material Forming 2020; 13: 371-81. https://doi.org/10.1007/s12289-019-01513-3
[28] ASTM E8. ASTM E8/E8M standard test methods for tension testing of metallic materials 1. Annual Book of ASTM Standards 4 2010: 1-27.
[29] ASTM E2218-02(08). Standard Test Method for Determining Forming Limit Curves. ASTM Book of Standards 2002; 02: 1-15.
[30] Bong HJ, Barlat F, Lee M-G, Ahn DC. The forming limit diagram of ferritic stainless steel sheets: Experiments and modeling. International Journal of Mechanical Sciences 2012; 64: 1-10. https://doi.org/10.1016/j.ijmecsci.2012.08.009
[31] Cardoso MC, Moreira LP. Forming Limit Analysis of DP600-800 Steels. International Journal of Chemical, Molecular, Nuclear, Materials and Metallurgical Engieering 2015; 9: 1062-9.
[32] Paul SK. Theoretical analysis of strain- and stress-based forming limit diagrams. The Journal of Strain Analysis for Engineering Design 2013; 48: 177-88. https://doi.org/10.1177/0309324712468524
[33] Zhang C, Leotoing L, Guines D, Ragneau E. Theoretical and numerical study of strain rate influence on AA5083 formability. Journal of Materials Processing Technology 2009; 209: 3849-58. https://doi.org/10.1016/j.jmatprotec.2008.09.003

[34] Jie M, Cheng CH, Chan LC, Chow CL. Forming limit diagrams of strain-rate-dependent sheet metals. International Journal of Mechanical Sciences 2009; 51: 269-75. https://doi.org/10.1016/j.ijmecsci.2009.01.007
[35] Abedrabbo N, Pourboghrat F, Carsley J. Forming of aluminum alloys at elevated temperatures - Part 2: Numerical modeling and experimental verification. International Journal of Plasticity 2006; 22: 342-73. https://doi.org/10.1016/j.ijplas.2005.03.006
[36] Cramer J, Adams D, Miles M et al. Effect of Strain Path on Forming Limits and Retained Austenite Transformation in Q&P 1180 Steel. Materials Science and Engineering: A2018 Jul 19. https://doi.org/10.1016/j.msea.2018.07.062
[37] Affronti E, Merklein M. Analysis of the bending effects and the biaxial pre-straining in sheet metal stretch forming processes for the determination of the forming limits. International Journal of Mechanical Sciences 2018; 138-139: 295-309. https://doi.org/10.1016/j.ijmecsci.2018.02.024
[38] Sklad MP, Atzema EH, Schouten FJ, de Bruine M, Emrich A. Experimental Study of forming limits in multistage deformation processes. Proceedings of IDDRG 2008, International Conference. 2008: 1-12.
[39] Ma B, Liu ZG, Jiang Z, Wu X, Diao K, Wan M. Prediction of forming limit in DP590 steel sheet forming: An extended fracture criterion. Materials & Design 2016; 96: 401-8. https://doi.org/10.1016/j.matdes.2016.02.034
[40] Prasad KS, Kamal T, Panda SK, Kar S, Murty SVSN, Sharma SC. Finite Element Validation of Forming Limit Diagram of IN-718 Sheet Metal. Materials Today: Proceedings 2015; 2: 2037-45. https://doi.org/10.1016/j.matpr.2015.07.174
[41] Uthaisangsuk V, Prahl U, Bleck W. Characterisation of formability behaviour of multiphase steels by micromechanical modelling. International Journal of Fracture 2009; 157: 55-69. https://doi.org/10.1007/s10704-009-9329-4
[42] Chung K, Ahn K, Yoo D-H, Chung K-H, Seo M-H, Park S-H. Formability of TWIP (twinning induced plasticity) automotive sheets. International Journal of Plasticity 2011; 27: 52-81. https://doi.org/10.1016/j.ijplas.2010.03.006
[43] Panich S, Barlat F, Uthaisangsuk V, Suranuntchai S, Jirathearanat S. Experimental and theoretical formability analysis using strain and stress based forming limit diagram for advanced high strength steels. Materials & Design 2013; 51: 756-66. https://doi.org/10.1016/j.matdes.2013.04.080
[44] Narayanasamy R, Narayanan CS. Forming limit diagram for Indian interstitial free steels. Materials & Design 2006; 27: 882-99. https://doi.org/10.1016/j.matdes.2005.03.014
[45] Bleck W, Deng Z, Papamantellos K, Gusek CO. A comparative study of the forming-limit diagram models for sheet steels. 1998; 83: 223-30. https://doi.org/10.1016/S0924-0136(98)00066-1
[46] Mohammed B, Park T, Kim H, Pourboghrat F, Esmaeilpour R. The forming limit curve for multiphase advanced high strength steels based on crystal plasticity finite element modeling. Materials Science and Engineering: A 2018; 725: 250-66. https://doi.org/10.1016/j.msea.2018.04.029
[47] Panich S, Suranuntchai S, Jirathearanat S, Uthaisangsuk V. A hybrid method for prediction of damage initiation and fracture and its application to forming limit analysis of advanced high strength steel sheet. Engineering Fracture Mechanics 2016; 166: 97-127. https://doi.org/10.1016/j.engfracmech.2016.08.025
[48] Gao X, Mın J, Zhang L, Lı Q, Lıan C, Lın J. Prediction and Experimental Validation of Forming Limit Curve of a Quenched and Partitioned Steel. Journal of Iron and Steel Research, International 2016; 23: 580-5. https://doi.org/10.1016/S1006-706X(16)30091-7

[49] Goud RR, Prasad KE, Singh SK. Formability Limit Diagrams of Extra-deep-drawing Steel at Elevated Temperatures. Procedia Materials Science 2014; 6: 123-8. https://doi.org/10.1016/j.mspro.2014.07.014
[50] Zhang L, Min J, Carsley JE, Stoughton TB, Lin J. Experimental and theoretical investigation on the role of friction in Nakazima testing. International Journal of Mechanical Sciences 2017; 133: 217-26. https://doi.org/10.1016/j.ijmecsci.2017.08.020
[51] Maris C, Hassannejadasl A, Green DE et al. Comparison of quasi-static and electrohydraulic free forming limits for DP600 and AA5182 sheets. Journal of Materials Processing Technology 2016; 235: 206-19. https://doi.org/10.1016/j.jmatprotec.2016.04.028
[52] Nasr GE, Badr EA, Joun C. Backpropagation neural networks for modeling gasoline consumption. Energy Conversion and Management2003; doi 10.1016/S0196-8904(02)00087-0. https://doi.org/10.1016/S0196-8904(02)00087-0
[53] Ahmadloo E, Azizi S. Prediction of thermal conductivity of various nanofluids using artificial neural network. International Communications in Heat and Mass Transfer 2016; 74: 69-75. https://doi.org/10.1016/j.icheatmasstransfer.2016.03.008
[54] Chapra S, Canale R, Heperkan H. Yazılım ve Programlama Uygulamalarıyla Mühendisler Için Sayısal Yöntemler. istanbul: Literatür Yayıncılık, 2003.
[55] Eğrioğlu E, Aladağ ÇH, Günay S. A new model selection strategy in artificial neural networks. Applied Mathematics and Computation 2008; 195: 591-7. https://doi.org/10.1016/j.amc.2007.05.005
[56] Cao M, Alkayem NF, Pan L, Novák D. Advanced Methods in Neural Networks-Based Sensitivity Analysis with their Applications in Civil Engineering. Artificial Neural Networks - Models and Applications2016 Oct. https://doi.org/10.5772/64026
[57] Gevrey M, Dimopoulos I, Lek S. Review and comparison of methods to study the contribution of variables in artificial neural network models. Ecological Modelling 2003; 160: 249-64. https://doi.org/10.1016/S0304-3800(02)00257-0
[58] Shojaeefard MH, Akbari M, Tahani M, Farhani F. Sensitivity analysis of the artificial neural network outputs in friction stir lap joining of aluminum to brass. Advances in Materials Science and Engineering 2013. https://doi.org/10.1155/2013/574914
[59] Garson D. Interpreting neural network connection weights. Artificial Intelligence Expert 1991; 6: 47-51.
[60] Goh ATC. Back-propagation neural networks for modeling complex systems. Artificial Intelligence in Engineering 1995; 9: 143-51. https://doi.org/10.1016/0954-1810(94)00011-S
[61] Song K, Park YS, Zheng F, Kang H. The application of Artificial Neural Network (ANN) model to the simulation of denitrification rates in mesocosm-scale wetlands. Ecological Informatics 2013; 16: 10-6. https://doi.org/10.1016/j.ecoinf.2013.04.002
[62] Kasikci T. Experimental investigation of key assumptions in analytical failure criteria for sheet metal forming. 2010.
[63] Slota J, Spišák E. Comparison of the forming-limit diagram (FLD) models for drawing quality (DQ) steel sheets. Metalurgija 2005; 44: 249-53.
[64] Wang Y, Zhang C, Yang Y et al. The integration of through-thickness normal stress and friction stress in the M-K model to improve the accuracy of predicted FLCs. International Journal of Plasticity 2019; 120: 147-63. https://doi.org/10.1016/j.ijplas.2019.04.017
[65] Mu L, Jia Z, Ma Z, Shen F, Sun Y, Zang Y. A theoretical prediction framework for the construction of a fracture forming limit curve accounting for fracture pattern transition. International Journal of Plasticity 2020; 129: 102706. https://doi.org/10.1016/j.ijplas.2020.102706
[66] Janssens K, Lambert F, Vanrostenberghe S, Vermeulen M. Statistical evaluation of the uncertainty of experimentally characterised forming limits of sheet steel. Journal of

Materials Processing Technology 2001; 112: 174-84. https://doi.org/10.1016/S0924-0136(00)00890-6
[67] Chen X, Niu C, Lian C, Lin J. The Evaluation of Formability of the 3rd Generation Advanced High Strength Steels QP980 based on Digital Image Correlation Method. Procedia Engineering 2017; 207: 556-61. https://doi.org/10.1016/j.proeng.2017.10.1020
[68] Patel G, Kakandikar G. Investigations on Effect of Thickness and Rolling Direction of Thin Metal Foil on Forming Limit Curves in Microforming Process. LTD, 2020. https://doi.org/10.1016/B978-0-12-819496-6.00007-5
[69] Abdelbary A. Prediction of Wear in Polymers and Their Composites., 2014. https://doi.org/10.1533/9781782421788.185
[70] Keeler SP, Brazier WG. Relationship between Laboratory Material Characterization and Press-Shop Formability. Microalloying 1975; 75: 517-30.
[71] Ghazanfari A, Assempour A. Calibration of forming limit diagrams using a modified Marciniak-Kuczynski model and an empirical law. Materials & Design 2012; 34: 185-91. https://doi.org/10.1016/j.matdes.2011.07.057
[72] Z. Marciniak, J.L. Duncan SJH. Mechanics of Sheet. Butterworth Heinemann, 2002.
[73] Kotkunde N, Srinivasan S, Krishna G, Gupta AK, Singh SK. Influence of material models on theoretical forming limit diagram prediction for Ti-6Al-4V alloy under warm condition. Transactions of Nonferrous Metals Society of China 2016; 26: 736-46. https://doi.org/10.1016/S1003-6326(16)64140-7

Research on Engineering Structures & Materials
www.jresm.org
Research Group

Research Article

Endodontic treatment parameter optimization using central composite rotatable design

S.S.Pachpore [*1, a], Pradeep V. Jadhav[2, b]

[1]*School of Mechanical Engineering, Dr. Vishwanatah Karad MIT World Peace University, Pune, India*
[2]*Department of Mechanical Engineering Bharati Vidyapeeth (Deemed to be) University, Pune, India*

Article Info

Article history:

Received 03 Aug 2023
Accepted 01 Oct 2023

Keywords:

Central composite rotatable design;
Operative parameters;
Root canal treatment;
Gutta-Percha compaction

Abstract

Endodontology referred to as Root Canal Treatment (RCT) is a field of science that deals with the entire chemo-mechanical cleaning and sealing of the root canal system by using restorative material used to rescue or repair severely decaying or diseased teeth. The success of the treatment depends on the seal formed between the filling material and the root cavity post-obturation. The crucial components include the energy used to clean and seal the root canal system, the material used to fill the root canal system, the process used to fill the root canal system, and the geometry of the root canal system. In the presented research, ideal operative parameters and their interaction were studied with 32 experimental trials for five operative parameters namely canal angle, canal operative length, compaction force, operative temperature, and operating frequency using central composite rotatable design (CCRD); a response optimization tool. The treatment was carried out on endo-training blocks prepared with a 6% uniform taper across the working length by using gutta-percha as filling material. A compaction force of 10N, operating temperature between 90-92° C, operating frequency in the range of 40-50 Hz, and operative length of 12mm results in maximum gutta percha compaction.

1. Introduction

RCT is a process of relieving dental pain that occurs due to inflammation or infection in the roots of a tooth. and saving the teeth. RCT is a dental operation that requires removing the pulp (root nerves and blood cells) from a tooth, cleaning and shaping the canal cavity, and then adding fillers to stop germs from re-entering the apical end of the root canal. In terms of medicine, the process of cleaning and sculpting the canal cavity is known as 'Biomedical Preparation', and the 3D filling and sealing of the canal to establish an undamaged seal is known as 'Obturation'(1). The purpose of obturation is to seal the cleaned, shaped, and disinfected root canal system and to prevent re-infection (2). The obturation without voids and to within 2.0 mm of the apex has a significant positive influence on the outcome of treatment which governs the success index of the treatment (3). The complete obturation process closely resembles mechanical subtractive and additive processes. Over the years, numerous studies have been published in estimating the success and failure of endodontic treatment (4), which lies between 46-93%, with few researchers/practising dentists reporting up to 98% (5). Variations in experimental designs and clinical practices, as well as in the standards for determining periapical healing and the duration of the postoperative observation period could be the reason for variation (4). From the theoretical point of view, the long-term persistence of microorganisms, chronic inflammation due to overfilling and constant trauma, and non-removal of irritant bodies

*Corresponding author: swanand.pachpore@mitwpu.edu.in
[a] orcid.org/0000-0002-7833-9560; [b] orcid.org/0000-0002-7167-2387
DOI: http://dx.doi.org/10.17515/resm2023.45ma0803rs

affect the success whereas, from the clinical point of view, preoperative factors such as patient's age, sex, medical health, tooth type affects the most (6). Over the years i.e. between 1990-2023, maximum studies carried out by clinical researchers were more focused on identifying the preoperative factors and post-operative factors governing the success of treatment(7). In the present study, an attempt is being made to quantify the operative factors such as root canal filling volume and quality of coronal restoration which have not been addressed yet (8). There are several operative factors in root canal filling which affect the process and success index. They are classified into four groups Geometry, Process, Material, and Energy categories shown in Fig. 1 (9). The present study focuses on defining the interaction between operative parameters using Central Composite Rotatable Design (CCRD) with half replicate to enhance filling material compaction (10).

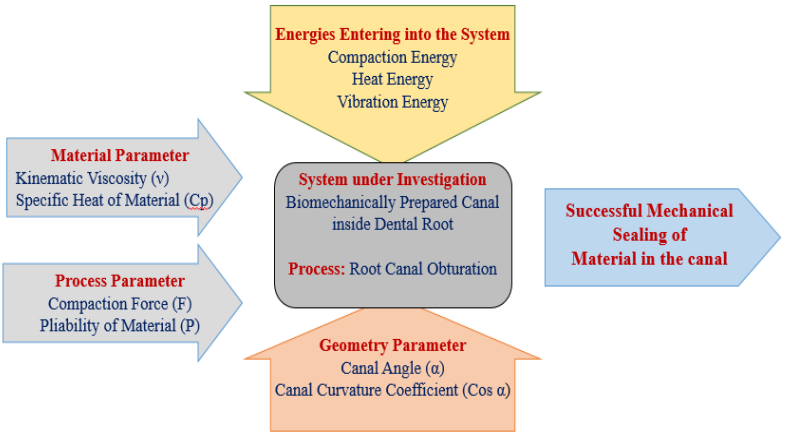

Fig. 1. Categorial factors affecting success index in terms of compaction [11]

2. Material and Method

Under the scope of the study, considering the complexity of root canals and following medical and ethical guidelines governed by the Indian Medical Association. The primary study was restricted to endo-training blocks shown in Fig. 2. Endo-training blocks are synthetic materials that are used to simulate the anatomy of a tooth root canal system. The tests were carried out on endo-training made up of acrylic material. The canal present inside the blocks was prepared using K-Type hand files made up of NiTi (nickel-titanium) material with a 6% uniform taper across the working length. K-file is the most commonly used instrument for root canal shaping (12), (13) as it has got positive rake angle which results in optimum cutting efficiency. The 6% uniform taper is preferred because of its several advantages such as it allows irrigation agents to work more efficiently and also provides the cleanest possible canal post biomechanical preparation to clear the debris. The success rate will be higher for the canal having less curvature than the canal having larger curvature, making the canal angle a crucial geometrical feature. The steeply curved canal is more challenging to instrument and fill than the canals with mild and moderate curvatures. There are few proven methods available to measure the canal curvatures namely Schneider's method and Weine's method which works on the same idealogy, but the error for Schneider's method is less as compared to the Weine's method (14). Thus, the canal morphology was examined using an optical comparator and geometry was verified using Schneider's method (15). The entire canal is divided into 3 major parts; Coronal, Middle and Apical (16). The coronal and Middle part are straight tapered and the apical region is curved. This method measures the canal angle between line 1 and line 2. Line 1 is

nothing but the canal axis. Line 2 is the line drawn between point a and point b. Point A is marked on the axis of the traced profile at the end of the middle region and point b is marked where curvature ends as shown in Fig. 3 to measure the canal curvature.

Fig. 2. Endo training block prepared with uniform 6% taper under scope of study (17)

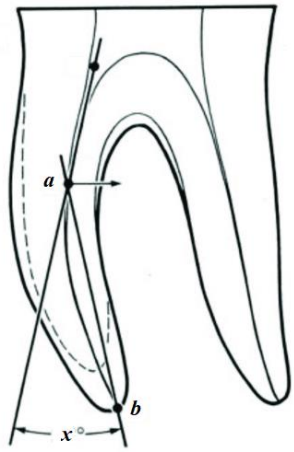

Fig. 3. Schneider's Method to Measure Canal Curvature (18)

Based on the studied literature, gutta-percha was found to be a promising material having superior properties such as thermo-plasticity, solubility with the organic solvent (19) and viscoelasticity and high-temperature susceptibility (20). The selected gutta-percha cones were found to be of pH7 because according to (21), water-stored gutta-percha cones are subjected to remain in a stable condition which enhances the compactibility during obturation.

3. Experimental Set-up

The experimental setup shown in Fig. 4 was developed to compact gutta-percha inside the prepared canal. The laboratory Experimental set-up to fill in gutta-percha inside the block consists of three major components namely a thermo-mechanical simulator, heat and vibration compactor, and connected to a data visualization system.

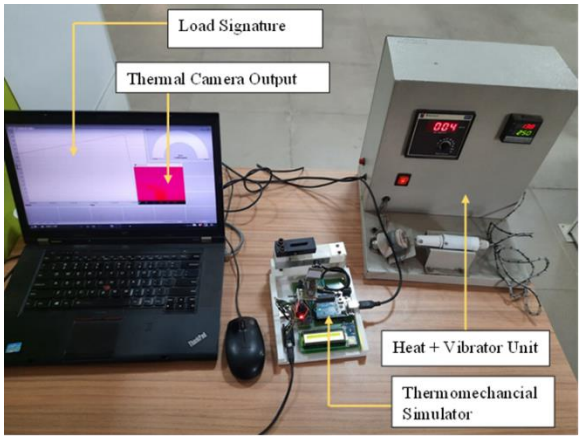

Fig. 4. Laboratory Experimental Setup

The experimental set-up measures the applied force, to compact gutta-percha and capture the heat signature of the subject and accordingly saves data to the data logger with time stamps. The heat and vibration compactor unit consists of a power supply which generates vibration of 0-50 Hz at 230AC supply. The vibration is supplied to an off-centric vibrator placed inside the holder made up of heat-resistant PTFE material and a plugger is attached to it. The plugger is made up of SS 304L material with a 0.7mm taper placed inside the holder that compacts gutta-percha with heat and vibration.

The volume of compacted gutta-percha inside the canal was measured using equation 1 which is the ratio of the increased mass of the block after compaction to density of gutta-percha. The increased mass of the block was recorded using an electronic weighing balance before and after obturation.

$$\text{Volume} = \frac{\text{Increased Mass of Block After Compaction}}{\text{Density of Gutta-Percha}} \quad (1)$$

4. Design of Experiment Using Central Composite Rotatable Design (CCRD)

Response Surface Methodology (RSM) is a set of mathematical and statistical approaches that analyse issues in which numerous independent variables factors impact a dependent variable or response, to optimize this response (22). The independent operative variables such as canal angle, operative length, compaction force, operating temperature, and frequency are quantitatively represented in the presented study, and have the following functional relationship with the response i.e. percentage mass of gutta-percha filling, which is analysed using a central composite rotatable design. The CCRD is a statistical experimental design used to optimise a system's response to many input factors. The central composite rotatable design approach is utilised in this work to anticipate the best values of operating parameters and their interactions (23), (24). Table 1 represents the lowest, central and highest levels of variables represented as (-2, -1, 0, 1, 2) with $\alpha = 2.00$ i.e. the distance of the axial points from the centre. The range of values of star points for the rotatable design depends upon the number of points in the factorial section of the offered design, which is calculated as given in equation 2 (25) below.

$$\alpha = (F)^{0.25} \quad (2)$$

Table 1. Actual values of different parameters affecting gutta-percha filing

Abbreviation	Parameter	Unit	Levels				
			-2	-1	0	1	2
X_1	Canal Angle (α)	Deg.	12	24	36	48	60
X_2	Compaction Force (FT)	N	8	9	10	11	12
X_3	Operating Temperature (T)	°C	84	86	88	90	92
X_4	Operating Frequency (F)	Hz	10	20	30	40	50
X_5	Operating Length (L)	mm	10	11	12	13	14

Here, F is the determined no. of points in the cube section and represented as $F=2^k$, where k is the no. of independent parameters (26). A total of five parameters were considered under the scope of the study, i.e. k=5, the no. of points becomes 32 which represents no. of trials. Hence, 32 experimental trials were designed based on the number of considered parameters i.e. five operative parameters (25). Considerations of variables and their levels for 32 experiments have been shown in Table 2. The mass of compacted gutta-percha shown in Table 3 is arrived at using weight analysis before and after. A total of thirty-two

tests were carried out at the values of five factors with various combinations listed by using the laboratory test setup described in the preceding section.

Table 2. Order of experiments and responses for gutta-percha compaction filling

Order of Expt.	Natural Values					Response
	(α)	(FT)	(T)	(F)	(L)	Mass of GP Compacted (* 10^{-2} gms)
1	24	9	86	20	13	12.75
2	48	9	86	20	11	16.19
3	24	11	86	20	11	16.69
4	48	11	86	20	13	15.61
5	24	9	90	20	11	20.88
6	48	9	90	20	13	20.33
7	24	11	90	20	13	19.86
8	48	11	90	20	11	19.26
9	24	9	86	40	11	22.67
10	48	9	86	40	13	22.62
11	24	11	86	40	13	25.32
12	48	11	86	40	11	29.42
13	24	9	90	40	13	33.24
14	48	9	90	40	11	27.46
15	24	11	90	40	11	35.47
16	48	11	90	40	13	29.43
17	12	10	88	30	12	19.34
18	60	10	88	30	12	19.76
19	36	8	88	30	12	24.43
20	36	12	88	30	12	29.91
21	36	10	84	30	12	24.55
22	36	10	92	30	12	36.42
23	36	10	88	10	12	16.38
24	36	10	88	50	12	37.89
25	36	10	88	30	10	27.46
26	36	10	88	30	14	24.63
27	36	10	88	30	12	32.89
28	36	10	88	30	12	32.45
29	36	10	88	30	12	34.25
30	36	10	88	30	12	31.25
31	36	10	88	30	12	32.40
32	36	10	88	30	12	33.19

5. Design of Experiment Using Central Composite Rotatable Design (CCRD)

The results were analyzed using a statistical tool namely MINITAB 19 software. The outcomes of the study were analyzed using ANOVA at a 5% level of significance using probability measures test (p-Test); and finally, predicting the response by RSM and a second-order polynomial mentioned in equation 3 was fitted to experimental data. As mentioned, the gutta-percha volume was recorded using weight analysis and volume

measurement for five controllable parameters Canal Angle (α), Compaction Force (FT), Operating Temperature (T), Operating Frequency (F), and Operating Length (L). The detailed results of regression analysis and ANOVA are mentioned in Table 3. The obtained results show that the maximum mass of 0.03789 gms was recorded for experiment set no. 24 which is for combination of (X_1-X_2-X_3-X_4-X_5: 0-0-0-2-0: 36°-10 N-88 °C-50 Hz-12 mm). The regression model for gutta-percha-filled mass is within the significant level at α= 0.05. Furthermore, the probability measures i.e. p-values for the gutta-percha filled mass are less than α = 0.05, indicating that these models have strong significance and are sufficient within the 95 % confidence interval shown in Table 3. The probability measure values for mass of filled gutta-percha indicate that parameters such as X_2, X_3, X_4, and X_5: Compaction Force, Operating Temperature, Operating Frequency, and Operating Length have a significant effect on the Enhancement of GP Compaction along with the interaction terms such as X_1* X_3, X_2* X_3, X_2* X_4, and X_2* X_5 have significant contribution since the p-values are less than 0.05. But the closest value is taken into consideration i.e. X_2, X_3, X_1* X_3. and the gutta-percha enhancement can be obtained mathematically through the equation containing all the significant parameters affecting the mass of filled gutta-percha shown in Equation 3.

$$GP\ Enhancement\ =\ 0.32998\ +\ 0.01079\,X_2\ +\ 0.02850\,X_3\ +\ 0.01212\,X_1 * X_3 \tag{3}$$

Table 3. Regression analysis and ANOVA for GP enhancement

Predictor	Coeff	P-Value	Predictor	Coeff	P-Value
Constant	0.32998	0.000*	-	-	-
X_1	-0.00239	0.366	X_2* X_4	0.00774	0.030*
X_2	0.01079	0.001*	X_2* X_5	-0.00773	0.030*
X_3	0.02850	0.000*	X_3* X_4	0.00405	0.219
X_4	0.05295	0.000*	X_3* X_5	0.00528	0.117
X_5	-0.00606	0.036*	X_4* X_5	0.00005	0.988
X_1* X_2	-0.00042	0.894			
X_1* X_3	-0.01212	0.002*			
X_1* X_4	-0.00561	0.099			
X_1* X_5	0.00012	0.969			
X_2* X_3	-0.00669	0.049*			

Regression Output

S	R-sq.	R-sq.(adj)	R-sq.(pred)
0.0124325	98.88%	96.85%	80.69%

ANOVA Output

Source	DF	SS	MS	F value	P value
Regression	20	0.150633	0.007532	48.73	0.000
Linear	5	0.090586	0.018117	117.21	0.000
Square	5	0.053851	0.010770	69.68	0.000
Interaction	10	0.006196	0.000620	4.01	0.016
Residual Error	11	0.001700	0.000155		
Lack of Fit	6	0.001208	0.000201	2.04	0.225
Pure Error	5	0.000492	0.000098		
Total	31	0.152333	* Indicates the Significant Terms		

5.1 Effect of Canal Length on Compaction

The canal operative length is the primary geometry parameter. The probability measure value indicates canal operative length was found to be superior to canal angle towards contributing to the success in terms of gutta-percha compaction enhancement. The behaviour of canal operative length on gutta-percha compaction is represented in Fig. 5 and has a p-value of 0.036. The filled quantity of gutta-percha shows a wavy trend throughout the bound of considered length. The maximum value of 0.24 gms was recorded for 12mm canal length in mild curvature i.e., canal angle between 20° - 40°. For the other two types of curvature, the trend remains the same and the maximum value is recorded at 12mm working length. Thus 12 mm length was found to be ideal.

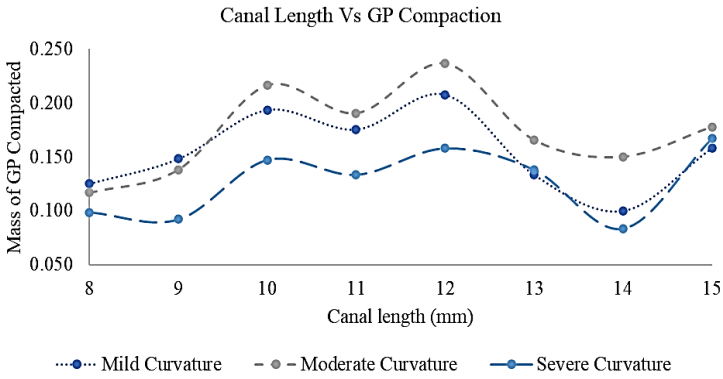

Fig. 5. Effect of canal length on GP compaction

5.2 Effect of Compaction Force on Compaction

The compaction force behaviour was recorded for all types of canal curvatures. In all the curvatures gutta percha were filled using Heat+ Vibration techniques. Fig 6 shows that with an increase in compaction force higher mass of gutta-percha gets compacted. At 12 N the maximum compaction was observed for all types of curvatures i.e., for mild curvature 0.7 gms mass was compacted. Thus, the compaction force of 12 N is considered to be the ideal force where maximum compaction was recorded and then the trend declined as shown in Fig 6. The compaction signature declines post 12 N due to changes in the canal geometry on account of excess loading. The ideal load range is between 5 to 15 N (27).

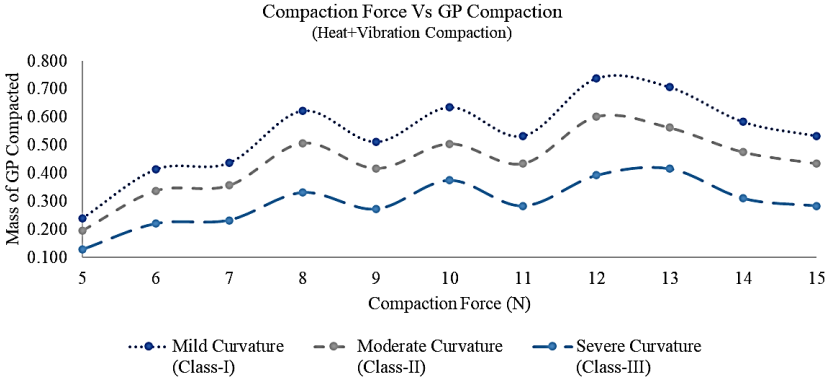

Fig 6: Effect of compaction force in compaction

5.3 Effect of Frequency on Compaction

The traditional obturation deals with single energy compaction i.e., heat compaction. Under the scope of the study, two types of energy are utilized in compaction gutta-percha i.e., heat energy in the form of temperature and vibration energy. The individual effect of heat and vibration on the mass of compacted gutta-percha was recorded. During pilot experimental trials with only vibration energy with varying frequencies between 10-50 Hz, it was observed that at 50 Hz, a significant rise in gutta-percha compaction was recorded as represented in Fig. 7. Also, the heat energy i.e., the temperature was varied between 80-100 °C. This range was selected from the primary data recorded from published literature and found that operating temperature in the range of 90°C to 96°C gives compaction in a higher range but at 92°C, compaction was found to be maximum as shown in Fig. 8.

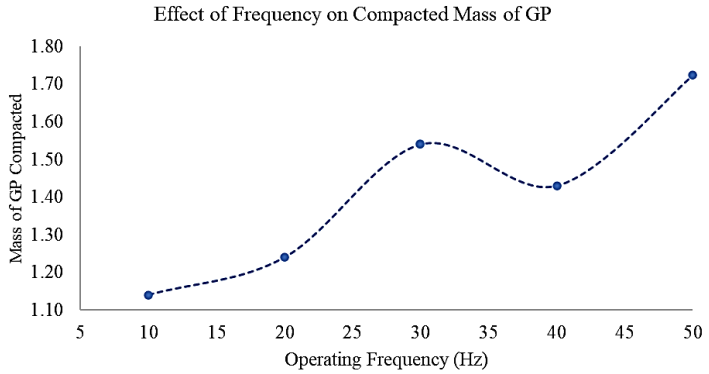

Fig. 7. Effect of **f**requency on the Compacted Mass of Gutta-percha

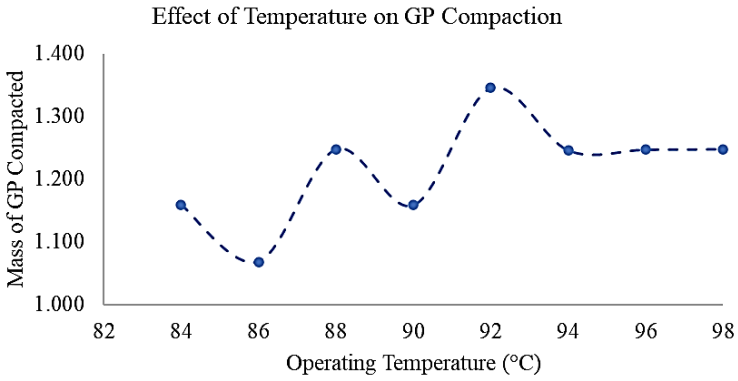

Fig. 8. Effect of Heat on the Compacted Mass of Gutta-percha

The effect of all the parameter was studied and the optimal operating parameter parameters range were determined and represented in Fig. 9, Fig. 10, and Fig. 11. This gives a clear guideline for designing a dual energy obturation device. The ideal operative range is seen in the highlighted area. The ideal force was found to be around 10-12 N and the operative frequency was towards 40-50 Hz. This result was found to be very much in line with numerical and mathematical studies.

Fig. 10 shows the interaction between force and temperature for enhancing GP compaction. The ideal parameter range was found to be in the range of 90 °C – 92 °C and an operating force of 10-11 N. Fig. 11 shows a contour plot for gutta-percha enhancement

against Frequency and Temperature. The ideal temperature was found to be 90-92 °C at 40-50Hz Frequency.

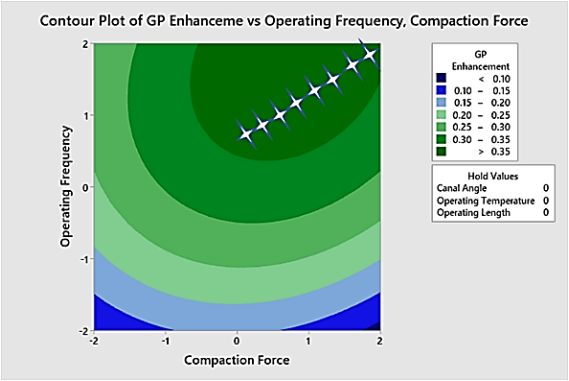

Fig. 9. Contour Plot for gutta-percha Enhancement VS Force and Frequency

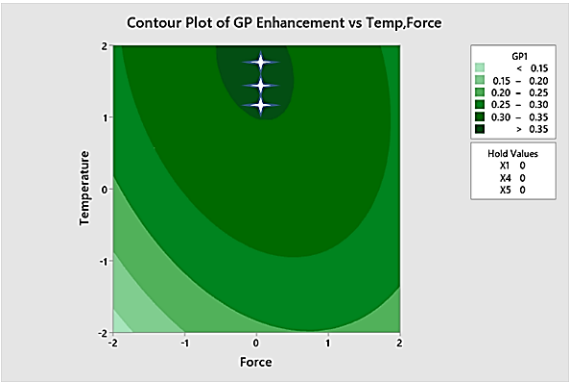

Fig. 10. Contour Plot for gutta-percha Enhancement VS Force and Temperature

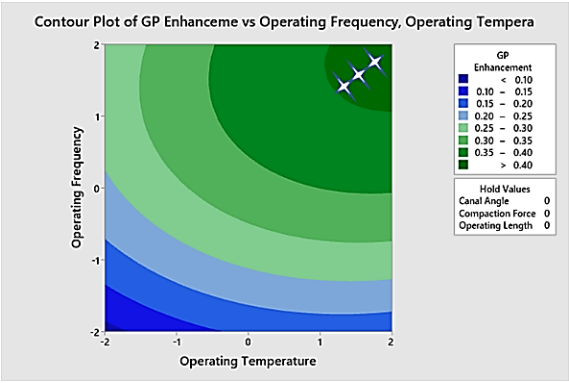

Fig. 11. Contour Plot for gutta-percha Enhancement VS Frequency and Temperature

6. Conclusion

The presented study was carried out to analyze the interaction effect of operative parameters on GP compaction enhancement and the following conclusions must be drawn-

- The regression analysis for GP Enhancement indicates that parameters such as X_2, X_3, X_4, and X_5: Compaction Force, Operating Temperature, Operating Frequency, and Operating Length have a significant effect on the Enhancement of GP Compaction along with higher order terms and interaction terms have significant contribution since the model values for P are less than 0.05.
- By implementing the Central Composite Rotatable Design and conducting 32 experimental trials for five operative parameters, the ideal operative parameters were determined. It was discovered that to achieve maximum gutta-percha compaction, the compaction force should be 10 N, the operating temperature should be between 90 and 92° C, the operating frequency should be between 40 and 50 Hz, and the operational length should be 12mm.

Acknowledgement

The authors acknowledge that this study is supported by Bharati Vidyapeeth Dental College Pune and Dr. Vishwanath Karad MIT World Peace University, Pune.

References

[1] Robia G. Comparative radiographic assessment of root canal obturation quality: Manual verses rotary canal preparation technique. Int J Biomed Sci. 2014;10(2):136-42. https://doi.org/10.59566/IJBS.2014.10136
[2] Darcey J, Roudsari RV, Jawad S, Taylor C, Hunter M. Modern endodontic principles Part 5: Obturation. Dent Update. 2016;43(2):114-29. https://doi.org/10.12968/denu.2016.43.2.114
[3] Ng YL, Mann V, Rahbaran S, Lewsey J, Gulabivala K. Outcome of primary root canal treatment: Systematic review of the literature - Part 2. Influence of clinical factors. Int Endod J. 2008;41(1):6-31. https://doi.org/10.1111/j.1365-2591.2007.01323.x
[4] Sjögren U, Hägglund B, Sundqvist G, Wing K. Factors affecting the long-term results of endodontic treatment. J Endod. 1990;16(10):498-504. https://doi.org/10.1016/S0099-2399(07)80180-4
[5] Chandra A. Discuss the factors that affect the outcome of endodontic. 2009;(1):98-107. https://doi.org/10.1111/j.1747-4477.2009.00199.x
[6] Marending M, Peters OA, Zehnder M. Factors affecting the outcome of orthograde root canal therapy in a general dentistry hospital practice. 2005;(September 2004). https://doi.org/10.1016/j.tripleo.2004.06.065
[7] Galande A, Pachpore SS, V Jadhav P, Ghorpade R, Lele MM. Investigation and assessment for specific volume of Gutta-Percha as a biomaterial in RCT. Mater Today Proc. 2022. https://doi.org/10.1016/j.matpr.2022.08.499
[8] Estrela C, Pécora JD, Estrela CRA, Guedes OA, Silva BSF, Soares CJ, et al. Common operative procedural errors and clinical factors associated with root canal treatment. Braz Dent J. 2017;28(2):179-90. https://doi.org/10.1590/0103-6440201702451
[9] Ghorpade R, Sundaram K, Hegde V. Mechanical factors influencing success in root canal obturation. 2017 2nd Int Conf Converg Technol I2CT 2017. 2017;2017-Janua:1085-8. https://doi.org/10.1109/I2CT.2017.8226295
[10] Cardoso R, Ribeiro D, Ne R. ScienceDirect Bonding effect on the evolution with curing time of compressive and tensile strength of sand-cement mixtures. 2017;57:655-68. https://doi.org/10.1016/j.sandf.2017.04.006
[11] Pachpore SS, Jadhav P V., Ghorpade RR. Analyzing Relation of Canal Operating Force and Canal Curvature in RCT: A Mathematical Overview. Mater Today Proc [Internet]. 2021;47:5690-6. https://doi.org/10.1016/j.matpr.2021.03.746

[12] Atmeh AR, Watson TF. Root dentine and endodontic instrumentation: Cutting edge microscopic imaging. Interface Focus. 2016;6(3). https://doi.org/10.1098/rsfs.2015.0113
[13] Jordan L, Bronnec F, Machtou P. Endodontic Instruments and Canal Preparation Techniques. Endod Mater Clin Pract. 2021;81-131. https://doi.org/10.1002/9781119513568.ch4
[14] Zhu Y, Gu Y, Du R, Li C. Reliability of two methods on measuring root canal curvature. Int Chin J Dent. 2003;3:118-21.
[15] Kartal N. The degrees and configurations of mesial canal curvatures of mandibular first molars. J Endod. 1997;23(6):358-62. https://doi.org/10.1016/S0099-2399(97)80182-3
[16] Pachpore S, Jadhav P, Ghorpade R. Chapter Nine - Process parameter optimization in manufacturing of root canal device using gorilla troops optimization algorithm. In: Kumar K, Kakandikar G, Davim JPBT-CI in M, editors. Woodhead Publishing Reviews: Mechanical Engineering Series [Internet]. Woodhead Publishing; 2022. p. 175-85. https://doi.org/10.1016/B978-0-323-91854-1.00006-6
[17] Borade PB, Pachpore SS, Patil SS, Kawale AR, Kankarne SS. Root Canal Filling Process Enhancement in Simulated Dental Block Using Root Canal Filling Process Enhancement in Simulated Dental Block Using Static Analysis. 2020;(November).
[18] Gu Y, Lu Q, Wang P, Ni L. Root canal morphology of permanent three-rooted mandibular first molars: Part II - Measurement of root canal curvatures. J Endod [Internet]. 2010;36(8):1341-6. https://doi.org/10.1016/j.joen.2010.04.025
[19] Frantzeska K. Gutta Percha and Updated Obturating Techniques. J Dent Heal Oral Disord Ther. 2017;8(2):470-4. https://doi.org/10.15406/jdhodt.2017.08.00276
[20] Arikatla SK, Chalasani U, Mandava J, Yelisela RK. Interfacial adaptation and penetration depth of bioceramic endodontic sealers Background: Aim: Materials and Methods: Statistical Analysis Used : Results : Conclusions: 2018;21(4):373-7. https://doi.org/10.4103/JCD.JCD_64_18
[21] Atmeh AR, AlMadi M, AlShwaimi E. Alkaline conditions can affect the volume and chemical characteristics of dental gutta-percha. Aust Endod J. 2022;48(1):144-50. https://doi.org/10.1111/aej.12553
[22] Rasheed S, Zhou IHQ, Campos JKKLC. Central composite rotatable design for optimization of trihalomethane extraction and detection through gas chromatography : a case study. Int J Environ Sci Technol [Internet]. 2023;20(2):1185-98. https://doi.org/10.1007/s13762-022-04070-6
[23] Sandon F. Experimental Designs. By W. G. Cochran and G. M. Cox. 2nd ed. Pp. xiv, 611. 82s. 1957. (John Wiley and Sons, New York; Chapman and Hall, London). Math Gaz. 1958;42(342):334-334. https://doi.org/10.2307/3610494
[24] Bhattacharya S. Central Composite Design for Response Surface Methodology and Its Application in Pharmacy. In: Kayaroganam P, editor. Response Surface Methodology in Engineering Science [Internet]. Rijeka: IntechOpen; 2021. https://doi.org/10.5772/intechopen.95835
[25] Kinetics R, Elfghi FM, Aishah N, Amin S. Optimization of hydrodesulfurization activity in the hydrotreating process: Canonical analysis and the combined application of factorial design and response surface methodology. 2012;(November). https://doi.org/10.1007/s11144-012-0511-8
[26] Bilgi DS, Jadhav P V. Experimental investigation of ultrasonic assisted pulse electrochemical drilling for INCONEL 718 with rotary tool. Int J Manuf Technol Manag. 2014;28(1/2/3):4. https://doi.org/10.1504/IJMTM.2014.064630
[27] Ghorpade RR. Automation for Measuring Compaction Force in Root Canal Obturation. Mod Res Dent. 2018;3(2):2-3. https://doi.org/10.31031/MRD.2018.03.000558

Research on Engineering Structures & Materials
www.jresm.org
Research Group

Research Article

Integrating push-over analysis and FEMA guidelines for building vulnerability assessment

Jojok Widodo Soetjipto*[,a], Ida Elif Nurmalia[b], Krisnamurti[c]

Department of Civil Engineering, Universitas Jember, Indonesia

Article Info

Article history:

Received 24 Oct 2023
Accepted 25 Nov 2023

Keywords:

Rapid visual screening;
Structural response;
Integrating push-over;
Integrating FEMA

Abstract

An earthquake has impacted the existing buildings around the area where the earthquake occurred. To maintain the safety of building occupants, it is necessary to evaluate the building's vulnerability. The most frequently used assessment methods are the Rapid Visual Screening (RVS) from FEMA and the push-over. FEMA can assess the exposure of a building quickly through visual observation but cannot provide a structural response. The push-over can explain the structural response seismic capacity and performance, collapse identification, and building strengthening strategies. However, the push-over has weaknesses; the analysis depends on modelling and structural analysis. This study aims to integrate push-over with FEMA to obtain the most appropriate assessment of buildings in earthquake vulnerability. Both assessment models have been applied to mid-rise buildings of flats after the earthquake. The building received a final score of 2.3 in the FEMA screening evaluation, indicating that it is secure. The push-over analysis shows the damage to the structure is Immediate Occupancy, which means only slight damage occurs. Overall, both methods give the same results and can be integrated to develop RVS and push-over assessments mutually when new modes of building failure are identified and as tools to assess fast, precise and accurate structural failure.

1. Introduction

The Indo-Australian plate, the Eurasian plate, and the Pacific plate all converge in Indonesia [1]. An earthquake has impacted buildings near the earthquake area [2]. Therefore, the main structural components of the building must be designed very carefully at the beam-column connections to withstand cyclic loads caused by earthquakes [3]. If an earthquake hits a building, it causes casualties. Therefore, evaluating the structure is necessary [4]. It is crucial to minimize losses and avoid fatalities.

The factors that influence building damage due to earthquakes are the strength, depth and duration of earthquake vibrations, as well as the condition of the soil and buildings. Guidelines for evaluating the vulnerability of buildings to earthquakes are needed to assess the condition of a building for earthquake vulnerability. Rapid Visual Screening (RVS) is a method for evaluating a building's susceptibility to earthquakes. [5]. The use of RVS has been widely developed through several applications: (i) Using Android-based rapid visual screening (RVS) (using FEMA 154 - 2002) to map the earthquake risk of buildings [6]-[7]; (ii) the application of soft computing techniques for RVS [8]; and (iii) Automated Rapid Vulnerability Assessment of Existing RC Buildings using hybrid ANN-GA model [9].

*Corresponding author: jojok.teknik@unej.ac.id
[a] orcid.org/0000-0003-0026-8296; [b] orcid.org/0000-0002-0928-6178; [c] orcid.org/0000-0002-7858-8073
DOI: http://dx.doi.org/10.17515/resm2023.56st1024rs

Lumajang Regency has a 5-story flat building consisting of 2 buildings with around 191 residents. A five-floor building requires an excellent structure to withstand disasters, including earthquakes. In 2005, the government built these buildings. The construction of flat buildings is an effort to address the problem of slums and meet housing needs in urban areas, especially for low-income people.

Based on USGS data, on April 10 2021, in Lumajang Regency, there was an earthquake magnitude 6.7. The earthquake caused damage to buildings, with a total of 1081 buildings, with details of 441 lightly damaged, 328 moderately damaged, and 328 heavily damaged. Based on this data, an evaluation of existing buildings in Lumajang district is needed.

RVS was previously used in research to quickly assess the initial seismic risk evaluation of flat buildings in Cilacap Regency [10]. RVS, based on FEMA 154 (Federal Emergency Management Agency), was developed in the United States to evaluate the building quickly. The screening process at Rusunawa Cilacap received a final score of 0.7. A final score of 0.7 means there is a 1 in $10^{0.7}$ or 1 in 5 chance the building collapses if an earthquake occurs. Evaluating building vulnerability to earthquakes using the rapid visual screening method on education building [11]. For the moment frame concrete building category (C1), the final score was 3.6, while for the concrete frame building category with unreinforced brick walls (C3), it was 1.4.

The findings of the study demonstrate that this 6-story structure is susceptible to earthquakes, with a high likelihood of level 3 damage and a very high likelihood of level 2 damage. Rapid Visual Screening (RVS) method is used to assess the earthquake-vulnerability of hospital buildings that have been hit by an earthquake [12]. The Hospital Building is classified as safe and not prone to earthquakes, with a potential vulnerability percentage of 0.0126%, according to the RVS method evaluation results. The building does not need to be specially prepared to withstand earthquakes, but regular maintenance is necessary to ensure occupant safety and extend the life of a building. Research on building vulnerability to earthquakes in high-story education buildings in Yogyakata [13]. The form used is the high seismicity type, which means the level of seismicity at the research location has a high earthquake distribution. The research results found that the final score value was 2.3, with the percentage of vulnerability of the building to collapse being 0.5%, making it safe against earthquakes.

Based on the previous studies above, building reliability evaluations using Rapid Visual Screening of Buildings can only be used to determine Building Performance Levels. RVS is used as a guide to assess the vulnerability of a building, which is recommended for all buildings [5]. Several components that be used as evaluation material in FEMA P-154 are location seismicity, population size, type and type of soil, structural elements that are dangerous for falling, kind or type of building, number of building floors, vertical irregularity, plan irregularity, regulations used when building and scoring. In the meantime, it is necessary to assess the damage and performance of the previously designed and analyzed structures using linear static analysis for seismic loads and the implementation of reinforced concrete moment-resisting frame buildings in order to determine the dependability of facilities that experience earthquake loads. One of the analytical methods that has been developed is using push-over analysis.

Performance-based design (PBD) processes have grown to be one of the cornerstones of earthquake engineering over the last few decades. The push-over procedure consists of two steps. The first type of force applies to the structure while estimating the total amount of energy present. The second is the displacement of the structure, which was built to evaluate whether the top would fall off under planned earthquake excitation. The building is then subjected to a push-over analysis until the peak displacement equals the target displacement. The framework is vulnerable to increased vertical irregularity, according to

an analysis of previous research findings. If the vertical irregularity increases, more plastic hinges will cross the boundary. This analysis shows that model 2 has better behavior [14]. The accuracy of Push-over is highly reliant on the form, complexity, and analysis of structural use in the Adaptive Capacity Spectrum Method for Seismic Assessment of Planned Asymmetric Buildings [15], [16]. In accordance with Indian codes, push-over analysis is also used to assess the performance of structures that have been designed and studied using linear static analysis for seismic loads [17]. Push-overs are also used to rotate the effects of lateral connections in the moment-bearing frames of low, medium and high-rise RC structures [18]. Through the development of better methods for assessing seismic performance in reinforced concrete moment-resisting frame structures, push-over accuracy has been developed [19]. By directly accounting for the cyclic degradation of actual MDOF systems while retaining the SDOF systems' ease of use and computational efficiency for the evaluation of displacement requirements, Push-over has also been created to assess the structure of multiple earthquakes, making them appealing for use in real-world scenarios [20], [21].

Deviations in Reinforced Concrete Multi-Storey Buildings based on Push-over Analysis using the ATC-40 Method [22]. According to the research findings, the building structure can exhibit nonlinear behavior, as was demonstrated in the preliminary stage, and the majority of plastic joints are found in the beam elements, followed by the column elements. If the building's structural performance level satisfies operational standards, there is only minor structural damage, and it can resume use right away. The seismic performance of concrete structures using push-over analysis has also been evaluated using the SAP 2000 program [23]. From the results of the research carried out, it was found that the effective shear force was 428,206 tons, less than the planned base shear force of 747,132 tons, with the peak acceleration of the bedrock of 0.012 g, less than the peak acceleration of the base rock in the plan for earthquake area 3, namely 0.15 g. As demonstrated in the initial phase, the building structure can exhibit nonlinear behavior, and the majority of plastic joints are found first in the beam elements and then the column elements. Since there is only minor structural damage, the building can be used again right away because its structural performance level meets the requirements for immediate occupancy. However, obtaining this assessment necessitates a thorough structural analysis that is time-consuming and complex.

Based on this background, research is needed on evaluating building vulnerability using the Rapid Visual Screening (RVS) method integrated with push-over analysis to assess building vulnerability quickly, efficiently and accurately. This integration is necessary because RVS can speed up the evaluation process while push-over can increase the accuracy of the analysis and known structure behavior results obtained from RVS. This study was carried out by determining building vulnerability using RVS and push-over analysis. Then, the RVS results will be developed and validated based on push-over analysis so that the behavior of the structure and its failure pattern can be known. In this way, RVS, which initially only gets values and estimates of failure after being integrated with push-over analysis, can produce more accurate vulnerability estimates and improve procedures if new potential failure modes exist.

2. Methodology

The research method was developed to evaluate the result of RVS analysis using the push-over method and enhance the result assessment of both methods based on structure behavior.

2.1. RVS Method

Using the FEMA P-154 approach to establish a seismic RVS method, the RVS method was used to assess the seismic risk of the apartment building in Lumajang. Accordingly, the fundamental score modifiers are suggested, taking building characteristics into account. The building capacity demand and fragility parameters, which were computed based on the exposure conditions and performance levels of the buildings, are the basis for the methods described to derive the basic scores and score modifiers in FEMA P-154 [24]. Figure 1 depicts the RVS method's flow diagram.

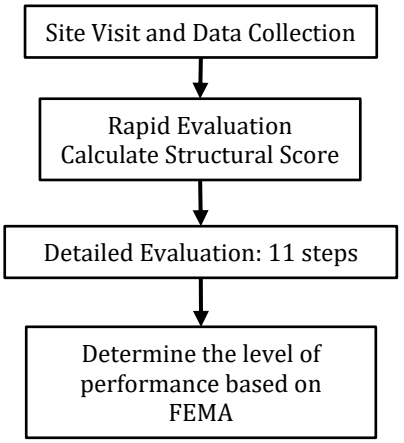

Fig. 1. Evaluation procedure

2.1.1. Site Visit and Data Collection

The screener sketched the building's plan and noted its characteristics (such as regularity, structural components, visual appeal, etc.) while walking around the building and through its interior to determine the type of building based on FEMA 154. Using the provided high seismicity data collection form, they gathered information about the structure, including pre-field data such as the address, the number of stories, the year of construction, and soil data.

2.1.2. Rapid Evaluation Calculate Structural Score

A two-stage seismic risk assessment technique developed by RVS method can be used to evaluate RC buildings. A straightforward screening process for reinforced concrete buildings was suggested in FEMA-154. The number of stories, apparent building quality, soft story irregularity, substantial overhangs, short column effect, pounding effect, topographic properties, seismic hazard, and local soil conditions are all determined using this method at the evaluation stage of the buildings. The number of stories and seismic hazard zones (earthquake zones) are used to calculate a basic score.

2.1.3. Detailed Evaluation

A computation of the FEMA Building Basic Score is shown in this section [5] as follows:

Step 1: Development of the capacity curve

The yield capacity and ultimate capacity points (Dy, Ay) and (Du, Au) are what the capacity curve is made of:

$$Ay = CS \frac{\gamma}{\alpha_1} \quad (1)$$

$$Dy = 9.8\, Ay\, Te2 \quad (2)$$

$$Au = \lambda\, Ay \quad (3)$$

$$Du = \lambda\, \mu\, Dy \quad (4)$$

The values for the variables C_S, γ, α_1, T_e, λ, and μ are taken from the FEMA Handbook.

When the spectral displacement is smaller than the yield displacement, the building capacity curve is considered to be linear, and it is taken for granted that it will continue to be plastic after the ultimate point. It is expected that the capacity curve's transition from the yield point to the ultimate point will take the following shape:

$$\frac{(D-Du)^2}{a^2} + \frac{(A-k)^2}{b^2} = 1 \quad (5)$$

where a, b, and k are from Equations:

$$a = \sqrt{\frac{Dy}{Ay} b^2 \frac{(Du-Dy)}{(Ay-k)}} \quad (6)$$

$$b = Au - k \quad (7)$$

$$k = \frac{Au^2 - Ay^2 + \frac{Ay^2}{Dy}(Dy-Du)}{2(Au-Ay) + \frac{Ay}{Dy}(Dy-Du)} \quad (8)$$

Step 2: Values for the input spectral acceleration response are determined

The building's position affects the median one-second period spectral acceleration response, S_1, as well as the median short-period spectral acceleration response, S_S.

Step 3: Calculation of the S_{MS} and S_{M1} values for the adjusted input spectral acceleration response

Site coefficients are used to account for soil when adjusting S_S and S_1 values..

Step 4: 5%-damped demand response spectrum development

The following equations, which are taken from HAZUS TM, are used to produce the demand response spectrum, formatted with spectral displacement response as the X-axis and spectral acceleration response as the Y-axis:

$$\textit{At short periods (acceleration domain), } 0 < T < TS\textit{: } S_A(T) = \frac{S_{MS}}{R_A} \quad (9)$$

$$\textit{At long periods (velocity domain), } TS < T < TVD\textit{: } S_A(T) = \frac{\frac{S_{M1}}{T}}{R_v};\ S_A(T) = 9.8\, S_A\, T^2 \quad (10)$$

where: Ts is the transition time between the constant acceleration and constant velocity sections of the response spectrum; $S_A(T)$ is the spectral acceleration response in g at period T; $S_D(T)$ is the spectral displacement response in inches at period T.

$$T_s = (SM1/SMS) \times (RA/RV) \quad (11)$$

$$R_A = \text{reduction factor in acceleration domain} = 2.12/(3.21 - 0.68\ln(\beta_{eff})) \quad (12)$$

$$R_V = \text{reduction factor in velocity domain} = 1.65/(2.31 - 0.41\ln(\beta_{eff})) \quad (13)$$

β_{eff} = effective damping, This is the result of adding the hysteretic damping, β_H, and the elastic damping, β_E;

β_H = hysteretic damping, which depends on the magnitude of the response and is based on the region contained by the hysteresis loop, takes into account the possibility of the structure's ability to absorb energy degrading during cyclic earthquake loading.

Step 5: The creation of a damped response spectrum

A 5% dampening assumption is made in the demand spectrum created in the preceding stage. The region beneath the hysteresis loop expands as the building's spectral displacement does, raising β_H and β_{eff} in the process. The demand curve flattens out as eff rises (due to the reduction factors R_A and R_V).

The peak response so determines how the demand spectrum will behave. The peak response, or the point at which the capacity and demand curves connect, must thus be calculated using an iterative process. There are several ways to carry out this computation.

In order to determine the peak response, an " β_{eff}-damped locus demand spectrum" is developed. The period and effective damping for each conceivable displacement, D, are calculated, and the spectral displacement against spectral acceleration are shown for each value of D.

Step 6: Peak response measurement

The peak response is defined as the point where the demand spectrum and the capacity curve converge. based on the overlap of the demand spectrum and capacity curve.

Step 7: Creation of a fragility curve

$$S_{d,C} = \Delta_C \, H_R \left(\frac{\propto_2}{\propto_3}\right) \tag{14}$$

The entire (C) structural damage state's median value is:

Step 8: Estimating the likelihood of total destruction

For a one-story S2 structure in the seismic zone, the likelihood of total destruction is:

$$P_{[Complete\ Demage]} = \varphi \left(\frac{1}{\beta_{C,P}} \, ln \frac{D}{S_{d,C}}\right) \tag{15}$$

Step 9: Calculating the likelihood of a collapse

The likelihood of collapse of in seismicity is

$$P(Collapse) = P_{[Collapse\ rate]} \, x \, P_{[Complete\ Demage]} \tag{16}$$

Step 10: Interact collapse uncertainty to a matched score

The one-story S2 with High seismicity's relating score is

$$S = -log10(P(Collapse)) \tag{17}$$

Step 11: Recognize the basic score.

The outcome of taking the building's basic score in the seismic region.

2.1.4. Determine the Level of Performance Based On FEMA

The performance levels, according to FEMA, are as follows: (i) Operational Performance Level; (ii) Immediate Occupancy Level; (iii) Life Savety Level; and (iv) Collapse Prevention Level.

- 1. Operational level (1-A): The building has no significant damage to structures and non-structures at this level. The building still functions well even though minor damage is not significant, such as damage to the electrical installation, water network and several other utilities. Figure 2 (a) shows the building performance level's condition.
- 2. Immediate Occupancy Level (1-B): The building experiences structural damage at this level, but the damage is insignificant. The condition of non-structural components is still functioning and is or is available in place. The building can still be used without being disturbed by the problem of repairing damage to the building. The risk of casualties occurring at this level of performance is minimal. Figure 2 (b) shows the building performance level's condition and the yield capacity point.
- 3. Life safety level (3-C): At this level, the building experiences structural damage and reduced stiffness but still has sufficient ability to collapse. Non-structural components are damaged and no longer function. Buildings can be reused if repairs have been made to damaged parts of the structure, but this also needs to be considered from an economic perspective. Figure 2 (c) shows the building's condition at this level and the ultimate capacity point.
- 4. Structural Stability/Collapse Prevention (4-D): At this point, both structural and non-structural elements of the structure sustain quite serious damage. The building is on the verge of collapsing due to the strength of the structure, and its rigidity is significantly reduced due to damage or collapse of materials. Casualties may occur, and the building will suffer significant economic losses. Figure 2 (d) displays the state of this building's performance level and its maximum capacity point.

The explanation of each level of building performance due to earthquake loads and structural drift can be illustrated in Figure 2.

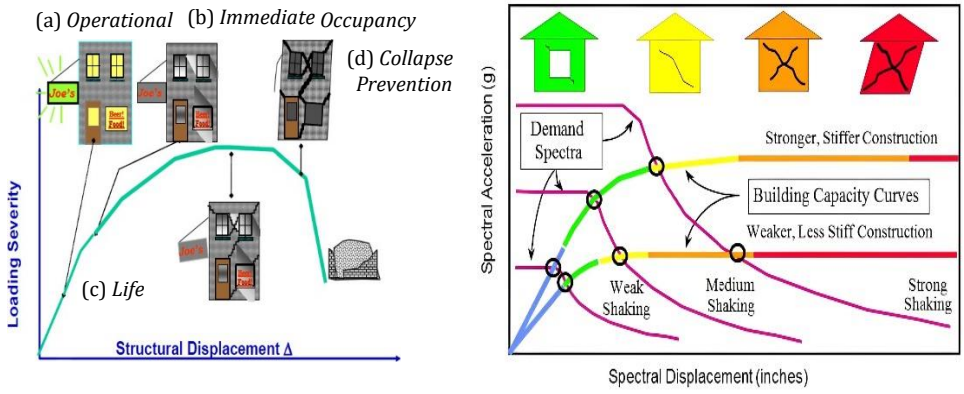

Fig. 2. The level of building performance and building capacity curve and control points [5]

The building performance level requirement for flats is Immediate Occupancy. Performance analysis can be done by comparing structure capacity and demand. Demand represents ground movement due to an earthquake, so the parameter used is structural displacement. In contrast, structural capacity means the structure's ability to withstand seismic demand.

2.2. Push-over Method

Push-over analysis is needed to analyze structures with monotonically increasing lateral load patterns. The inertial force that the structure will experience when exposed to ground movement. Numerous structural components can consecutively fail under stresses that increase gradually. As a result, the structure becomes less rigid throughout each occurrence. Non-linear static push-over analysis may be used to derive a typical non-linear force-displacement relationship. Initially, gravity loads are applied to a three-dimensional model that includes tri-linear load deformation diagrams for every lateral force-resisting component.

Then, a lateral load pattern that is dispersed along the building's height is applied. Increased lateral pressures cause certain members to give way. The lateral forces are raised further until the new part yields, and the structural model is changed to account for the lower stiffness of the yielding member. Until the controlled displacement at the top of the building deforms to a specific degree or the structure becomes unstable, this procedure is repeated.

2.2.1. Types of Push-over Analysis

Analyses of push-over are used for force or displacement control. Full loads are combined under force control (such as gravity loading). Additionally, due to the evolution of the mechanism and the P-delta effect, the target displacement in the force-controlled push-over study may be connected to very tiny amounts of positive or even negative lateral stiffness, which has an impact on the correctness of the results.

Push-over analysis is often carried out as a controlled displacement. When the size of the applied load is unknown in advance, specific displacement/drift controls are needed (as in seismic loading). As necessary, the load combination's significance is altered until the control displacement achieves the desired value. The roof displacement at the mass center of the structure is often used as the control displacement. Calculated internal forces and deformations at target displacements determine inelastic pressures and deformation demands that must be contrasted with the capacity available for performance assessments.

2.2.2. Performance Levels of Building

The maximum base shear that the structure can bear is outlined by push-over analysis. The building performance level combines the performance level of structures and non-structural components. It describes the limited damage conditions to a particular building with a specific ground movement. Performance levels as per FEMA are:

Immediate Occupancy (IO): The structure retains the majority of its initial stiffness despite suffering relatively less damage. The likelihood of a fatal injury from structural damage is low, and while some minor structural repairs could be necessary before reuse, they are often not.

Life Safety Level (LS): The structure has sustained severe damage and may have lost a sizeable portion of its initial stiffness. Before failure comes, however, there is still a sizable amount of opportunity for more lateral distortion. Although this may not be feasible due to financial constraints, the building must be repairable. Although there is no immediate risk of collapse due to a broken system, it would be prudent to perform structural repairs or construct temporary supports before resuming operation.

Collapse Prevention (CP): If lateral displacement continues at this stage, the structure may become unstable and collapse. At this point, the building has suffered serious damage. Because aftershock activity might result in failure, the system might be dangerous to reoccupy and impractical to repair.

2.2.3. Push-over Curve

At different phases of the investigation, we may utilize a push-over curve to determine structural performance points and hinge placements (see Figure 3). In this curve, the instantaneous occupancy range is B to IO, the life safety range is IO to LS, and the collapse prevention range is LS to CP.

A hinge must start releasing the load when it reaches point C on the forced displacement curve. The load will be reduced until the base shear or pushing force at point C equals the force at point D. All elements release the load when the force is reduced, reducing their displacement. The amount of the compressive force is once again reinforced once the yielding hinge contacts the force level point D, and the removal starts to rise once more. If every hinge is within the specified CP limits, the construction is deemed safe. However, depending on the significance of the building, hinges after the IO span might also need to be restored.

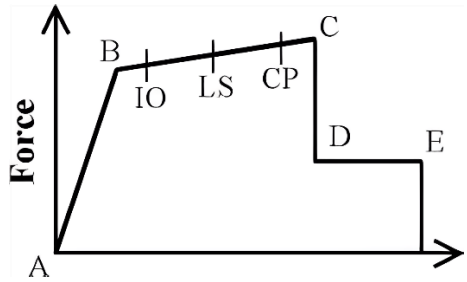

Fig. 3. Typical Push-over Curve and Performance Levels [17]

2.2.4. Key Elements of Push-over Analysis

Definition of Plastic Hinges: In structural analysis, it is presumed that concentrated plastic hinges would exhibit non-linear behavior in frame components. Unpaired moment, unpaired axial, unpaired sliding, paired axial force, and biaxial bending moment hinges are examples of common kinds.

Control nodes are defined as nodes that are used to regulate a structure's displacement. The capacity (push-over) curve of the structure is defined as displacement versus base shear. In developing the push-over curve, the predicted inertial force distribution was taken into account for force-displacement. The severity of earthquake loads may be modeled using various force distributions.

Shift Demand Estimation: When employing push-over analysis, this phase is crucial. The control node is driven to achieve a demand displacement that represents the greatest displacement anticipated as a result of the magnitude of the earthquake being taken into account.

Evaluation of Performance Levels: Performance-based design is the goal of performance evaluation. If a component or activity satisfies the required performance, it is regarded as satisfactory. Demand response in comparison to capacity is the main result of push-over study. If the demand curve crosses the capacity envelope close to the elastic range, the structure is robust. Assume that the capacity reserve has low strength and deforms when the demand curve crosses it. In that instance, it may be deduced that the building would respond improperly during seismic excitation and that it has to be altered to prevent serious damage or collapse in the future.

2.2.5. Evaluation Procedures

Different building evaluation methods are used, but the fundamental ideas remain the same. The evaluation methods in accordance with FEMA 356 are listed below. Method of Displacement Coefficient (DCM): The displacement coefficient approach, which was adopted by FEMA 356, estimates maximum displacement using push-over analysis and a modified precise displacement estimate. Based on a statistical examination of the outcomes from the time history analysis of various types of SDOF oscillators, DCM is a method for analyzing data. According to the findings of several research, the capacity spectrum approach significantly underestimates the response of structures that are in the inelastic region. The displacement coefficient approach, however, typically yields numbers that are appropriate.

3. Results and Discussion

In this section, this study discusses the analysis results of both methods of evaluating building vulnerability due to earthquakes. Detailed results of the discussion can be explained in the following sub-section.

3.1. Result and Analysis

3.1.1 Result of RVS Analysis

The results of the walking around survey of the building and through the interior of the building to identify building type based on FEMA 154 showed that the building, including a commercial building, was located on soft soil with no architectural components that could easily fall (see Figure 4). Based on this data, a basic score of 3.0 was obtained with the characteristics of a middle-rise building (5 stories), without vertical irregularities but with plan irregularities, and determining seismicity based on bench-marks and soil type. From the calculation analysis above, the final RVS score was 2.3 (see Figure 5). This score has a value greater than 2, which is the limit score for buildings according to FEMA 154. Rapid Visual Screening findings indicate that no more analysis is required, indicating that the building has a little chance of collapsing in the event of an earthquake.

Based on the screening data on the RVS, FEMA can construct a capacity curve using equations (1) – (8). This curve shows the relationship between spectral acceleration (g) and spectral displacement. Based on spectral acceleration, this capacity curve can estimate the magnitude of shear force and displacement in buildings due to earthquake loads. Figure 6 (a) shows more details of this curve. Meanwhile, a damped demand spectrum is a method of capacity and demand curves in a response spectrum. A 5% submerged pseudo-elastic single degree of freedom (SDOF) is used in this curve. This curve was prepared from FEMA interpretation data using equations (9) - (13) (see Figure 6 (b)). The performance point, which depicts the seismic behavior of various structures, is generated from the intersection of the two curves between the inelastic demand spectrum and the capacity spectrum (Figure 6(c)).

The cumulative probability curve of damage in the lognormal distribution on the vertical axis and the spectral displacement on the horizontal axis may be used to calculate the chance of damage with the specified spectral displacement of the performance point. Determination of cumulative probability is calculated using equations (14) – (17). Then, the discrete probability (Figure 6 (d)) in each condition of building damage. From the FEMA 154 analysis results, it was obtained that the performance level is Operational Performance Level with a probability of collapse of 0.5%. This result follows the RVS assessment, namely that the building has no potential for collapse during an earthquake.

Fig. 4. The building as case study

OCCUPANCY			SOIL		TYPE						FALLING HAZARDS			
Assembly	Govt	Office	Number of Persons		A	B	C	D	E	F	☐	☐	☐	☑
Commercial	Historic	Residential	0 – 10	11 – 100	Hard Rock	Avg. Rock	Dense Soil	Stiff Soil	Soft Soil	Poor Soil	Unreinforced Chimneys	Parapets	Cladding	Other:
Emer. Services	Industrial	School	101-1000	1000+										

BASIC SCORE, MODIFIERS, AND FINAL SCORE, S

BUILDING TYPE	W1	W2	S1 (MRF)	S2 (BR)	S3 (LM)	S4 (RC SW)	S5 (URM INF)	C1 (MRF)	C2 (SW)	C3 (URM INF)	PC1 (TU)	PC2	RM1 (FD)	RM2 (RD)	URM
Basic Score	5.2	4.8	3.6	3.6	3.8	3.6	3.6	3.0	3.6	3.2	3.2	3.2	3.6	3.4	3.4
Mid Rise (4 to 7 stories)	N/A	N/A	+0.4	+0.4	N/A	+0.4	+0.4	+0.2	+0.4	+0.2	N/A	+0.4	+0.4	+0.4	-0.4
High Rise (>7 stories)	N/A	N/A	+1.4	+1.4	N/A	+1.4	+0.8	+0.5	+0.8	+0.4	N/A	+0.6	N/A	+0.6	N/A
Vertical Irregularity	-3.5	-3.0	-2.0	-2.0	N/A	-2.0	-2.0	-2.0	-2.0	-2.0	N/A	-1.5	-2.0	-1.5	-1.5
Plan Irregularity	-0.5	-0.5	-0.5	-0.5	-0.5	-0.5	-0.5	-0.5	-0.5	-0.5	-0.5	-0.5	-0.5	-0.5	-0.5
Pre-Code	0.0	-0.2	-0.4	-0.4	-0.4	-0.4	-0.2	-1.0	-0.4	-1.0	-0.2	-0.4	-0.4	-0.4	-0.4
Post-Benchmark	+1.6	+1.6	+1.4	+1.4	N/A	+1.2	N/A	+1.2	+1.6	N/A	+1.8	N/A	2.0	+1.8	N/A
Soil Type C	-0.2	-0.8	-0.6	-0.8	-0.6	-0.8	-0.8	-0.6	-0.8	-0.6	-0.6	-0.6	-0.8	-0.6	-0.4
Soil Type D	-0.6	-1.2	-1.0	-1.2	-1.0	-1.2	-1.2	-1.0	-1.2	-1.0	-1.0	-1.2	-1.2	-1.2	-0.8
Soil Type E	-1.2	-1.8	-1.6	-1.6	-1.6	-1.6	-1.6	-1.6	-1.6	-1.6	-1.6	-1.6	-1.6	-1.6	-1.6
FINAL SCORE S								2/3							

Fig. 5. Manual Form of RVS Method in accordance with FEMA 154

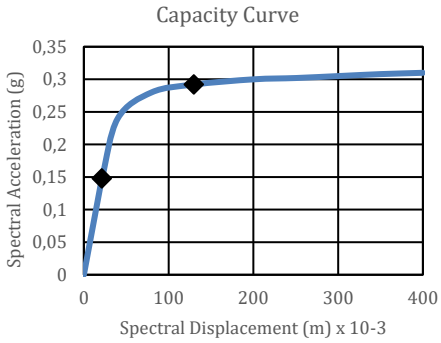

(a) The capacity curve

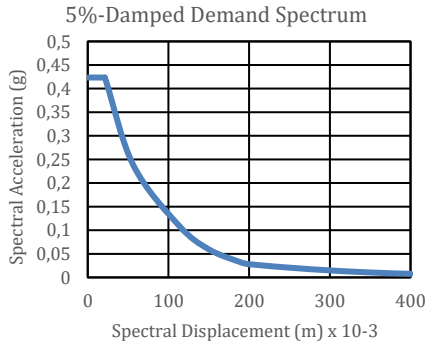

(b) 5%-damped demand spectrum

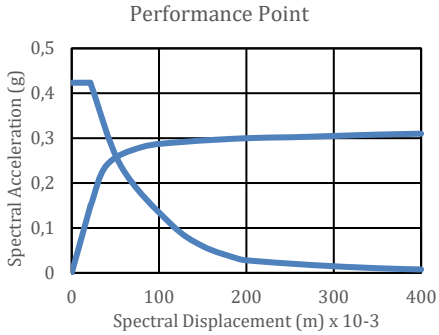

(c) Performance point

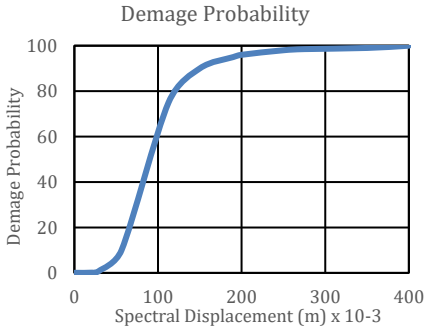

(d) Probability

Fig. 6. The demand spectrum for a high seismicity zone and its capacity curve, with 5% damping

3.1.2 Result of Push-over Analysis

This flat building is designed to be a multi-storey reinforced concrete building which has been designed for non-linear earthquake static analysis. Linear static analysis was carried out using a structural analysis program with Push-over Analysis to assess potential damage to buildings due to earthquakes. The analysis process is carried out through several stages:

The structure modeling:

Table 1 and Figure 7 both list the number of members, nodes, and supports that make up constructing frames. Table 2 lists the structural components' material characteristics.

Table 1. Material properties considered for analysis

Member	Size (mm x mm)
Beams	200 x 300
Sloof	150 x 250
Ring Balk	150 x 250
Column 1	300 x 500
Column 2	250 x 350

Table 2. Material properties of structure

Material	Modulus of elasticity (KN/m^3)	Poisson ration	Density (KN/m^3)	Coefficient of thermal expansion	F_{ek}/f_y (KN/m^2)
Concrete Properties					
K250	2.18E+09	0.2	23.045	9.90E-06	30
K 300	2.39E+09	0.2	23.045	9.90E-06	30
Reinforcing bar (rebar) Properties					
BJTP 30	2.04E+10	0.3	76.97	1.17E-05	415
BJTS 40	2.04E+10	0.3		1.17E-05	415

Analysis Results of Seismic Load Case:

The structural analysis support program analyses the structural modelling and material properties above. This structure application tool, a finite element analysis package used for structural analysis, proposes hinges for columns and beams in accordance with FEMA-356 and offers default hinge properties. A non-linear push-over study was done to

determine the structure's seismic response after designing and specifying the reinforced concrete frame construction mentioned above.

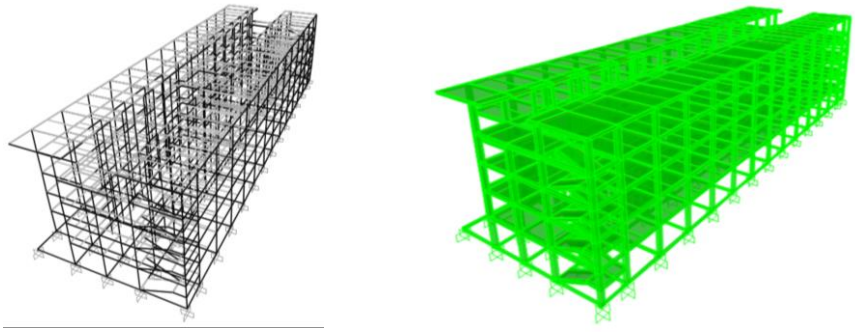

Fig. 7. Frame with support, framing and node

This structure application tool, a finite element analysis package used for structural analysis, proposes hinges for columns and beams in accordance with FEMA-356 and offers default hinge properties. A non-linear push-over study was done to determine the structure's seismic response after designing and specifying the reinforced concrete frame construction mentioned above. When the load is increased further, it undergoes significant elastoplastic deformation and eventually approaches the point of collapse. In a step-by-step process, lateral loads are applied monotonically in nonlinear analysis. In place of the force the structure would feel as a result of ground movement, lateral loads are assumed to be acceleration in each direction. Element yielding is possible under monotonous loading. As a result, the structure's stiffness changes as a result of damage at each level. This analysis requires nine steps until the push-over iteration is stopped. The analysis results are displayed in Table 3, and the graph in Figure 8.

Table 3. Base shear vs displacement

Step Unitless	Displace-ment (m)	Base Force Kgf	AtoB Unitless	BtoB Unitless	CtoD Unitless	CtoE Unitless	BeyondE Unitless	AtoIO Unitless	IOtoLS Unitless	LStoCP Unitless	BeyondCP Unitless	Total Unitless
0	0.003384	0	2750	2	0	0	0	2752	0	0	0	2752
1	0.005073	48254.54	2748	4	0	0	0	2752	0	0	0	2752
2	45869	243493.54	2542	210	0	0	0	2752	0	0	0	2752
3	0.086877	407066.59	2430	322	0	0	0	2734	16	0	2	2752
4	0.127012	545240.32	2315	437	0	0	0	2688	48	0	16	2752
5	0.185919	700972.71	2183	553	16	0	0	2569	149	14	20	2752
6	0.225919	791648.93	2133	598	21	0	0	2507	204	12	29	2752
7	0.265919	870318.03	2077	646	29	0	0	2436	261	15	40	2752
8	0.330919	990455.32	1997	686	69	0	0	2353	308	36	55	2752
9	0.396616	1106329.37	1908	733	103	0	0	2301	274	105	72	2752

In the analysis of the push-over process, one plastic joint reaches the yield condition first, followed by the yield condition in the other plastic joints. The analysis continues until the deviation at the top of the structure finally reaches the target deviation or enters an unstable state. The push-over process can be carried out with a load-controlled or displacement-controlled procedure. Load-controlled procedures are used if the applied load has a known value. For example, gravity loads can be applied in load-controlled push-overs. Displacement-controlled methods are usually used if the load that a structure can withstand is not known with certainty. So, until the structure reaches the desired deviation value, the load is raised.

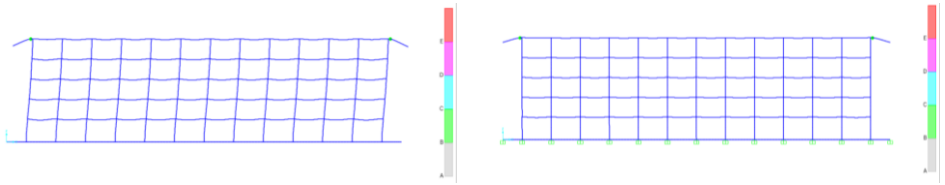

X-Direction Y-Direction

Fig. 8. Distribution of Plastic Joints

The relationship between the base shear force as a result of push-over analysis and the lateral displacement of the top floor/roof is known as the capacity curve. The results of the capacity curve between displacement and base shear can be seen in Figure 9. The inelastic conditions of the structure are plotted in ADRS (Acceleration Displacement Response Spectrum) format. This method is specifically built in the SAP program; converting push-over and reduced spectrum response curves in ADRS format is done automatically. The results of the capacity spectrum curve can be seen in Figure 10.

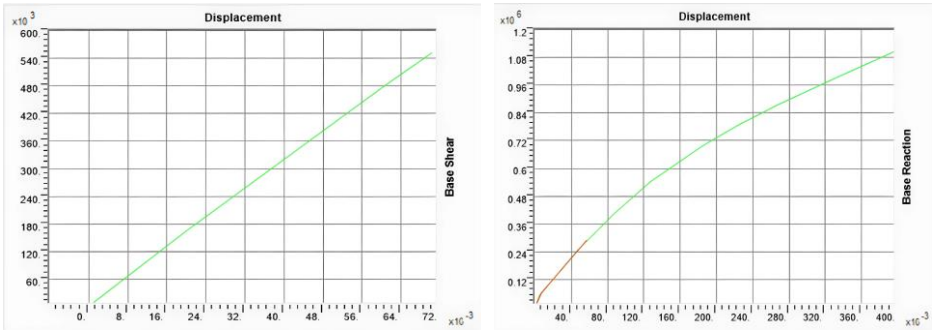

X-Direction Y-Direction

Fig. 9. Push-over Capacity Curve (Resultant Base Shear vs Monitored Displacement)

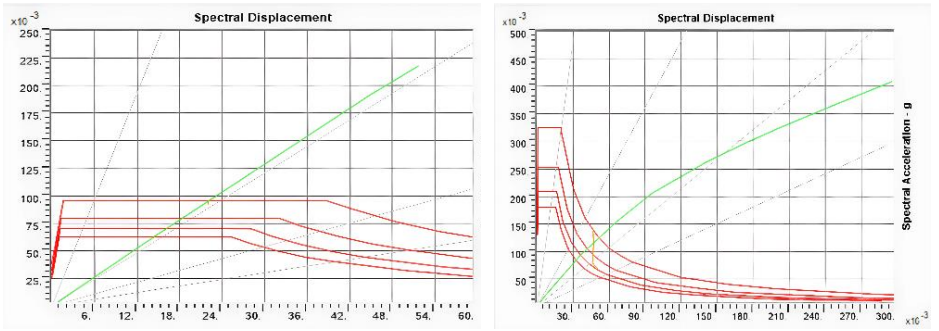

X-Direction Y-Direction

Fig. 10. Capacity Spectrum Curve

A performance point is used to gauge a building's capability. Based on the intersection of the spectrum response curve and the capacity curve obtained after performing push-over analysis, the point determination is made. Tables 4 and 5 provide the outcomes for the performance points. The capacity spectrum method graphically presents three graphs: the capacity, response, and demand spectrum in ADRS format. To determine the behavior of the structure under consideration for a given earthquake intensity, the capacity curve is then compared with the performance demand in the form of a spectrum response of various earthquake intensities (return periods). The figure below shows the transfer

objective that was determined by the point where the capacity spectrum and the demand spectrum met.

Table 4. Performance point FEMA 356 direction-Y

Performance Point	Value
V (KN)	462428.2
D (m)	0.103
Sa	0.115
Sd	0.047
Teff	1.274
Beff	0.051

Table 5. Performance point FEMA 356 direction-X

Performance Point	Value
V (KN)	1106329.4
D (m)	0.542
Sa	0.115
Sd	0.047
Teff	1.274
Beff	0.051

Evaluation Procedures:

This building underwent evaluation and a push-over examination, and as a consequence, it was put into the Immediate Occupancy (IO) category. With very little damage, the structure nevertheless maintains the majority of its initial stiffness. Although some minor structural repairs could be required, these are often not essential before reuse since the danger of a life-threatening injury from structural deterioration is low.

If alternative modeling techniques and assumptions were employed in the numerical model, the outcomes of this study may be different in various ways [25][19]. Furthermore, this study solely considers the design-level evaluation of the seismic requirements for plan-symmetric special moment-resisting frame structures. The accuracy and effectiveness of the advanced push-over technique in calculating seismic needs in structures with a greater level of seismic danger, buildings with varied lateral load resisting systems, buildings with masonry infill walls, plan asymmetric buildings, in-plan buildings, and irregular building verticals, must therefore be further investigated. The push-over analysis provides more accurate information so that the behavior of each component can be known and efforts to prevent collapse can be carried out earlier.

3.2. Observation and Discussion

In this research, in order to determine the likelihood of damage, it is suggested to analyze damage and examine the performance of structures built to withstand earthquake loads. The evaluation design produced in this research is an analysis using RVS, which was developed with push-over structural analysis so that the research results will provide speedy and valid information and can determine the behavior of the structure's performance in withstanding earthquake loads. RVS was developed using FEAM 154, modified with the latest rules and validated using push-over structural analysis to determine detailed structural behavior.

A rapid evaluation design can use RVS FEMA 154, modified according to the latest regulations, to obtain more detailed results. The output of FEMA 154 not only determines the basic score and the possibility of collapse but also produces a capacity curve and damping demand spectrum so that it is possible to establish the structure's performance point. The structural performance results based on FMA 154 were obtained at a spectral acceleration of 0.238 with a spectral displacement of 56,388 cm. while the detailed structural behavior resulting from the push-over analysis shows that the performance point occurs at a placement of 54.2 cm with Sa=0.115 and Sd=0.047 (X direction). These two methods provide almost the same point performance values so that the RVS FEMA 154 output can be used as a reference with accurate results even though the results are slightly more significant than the push-over analysis predictions.

From the interpretation of the results, both methods also provide the same recommendation: according to FEMA's RVS, the structure's condition is still at the operation level (1-A). According to the results of the push-over analysis, the structure is in Immediate Occupancy (IO) condition. According to FEMA 154, operational level (1-A) indicates that the building experienced minor damage with little impact on structural and non-structural elements so that the building can operate with minor repairs. Meanwhile, the Immediate Occupancy (IO) level is the level where the structure experiences minimal damage and is still able to maintain most of its structural rigidity so that no retrofitting and repairs are needed to reuse the building.

The advantage of integrating RVS FEMA 154 with push-over analysis is that the RVS method can be the most suitable screening method because it can provide reasonably accurate results from previous research [24]. However, FEMA 154 depends on the screener's assumptions and experience; therefore, in this study, FEMA can be evaluated and recalibrated through this push-over outcome. This study can be used to re-evaluate when new potential failure modes are identified so that these failure modes must be added to the FEMA procedure and control plan. Meanwhile, additional dynamic analysis needs to be considered in the push-over study to model in more detail the material, boundary frame and coupling beam when damaged [26].

The weakness of this research is that the evaluation results generally require more detailed studies because the performance assessment procedure is very dependent on the data assumptions used [24], so many case studies are needed to improve the calibration of the interpretation results of this model. Push-over analysis as a calibration still needs to be developed using a double lateral force-resisting system that combines a particular moment frame with concentric bracing, especially in buildings that have poor performance due to earthquakes [27]. The output of this research still needs to be developed using multi-criteria decision-making (MCDM) using the resulting index values as criteria that need to be considered [28]. Apart from that, FEMA prioritizes failure modes, so it has yet to design efforts to prevent building collapse. Therefore, wireless deformation sensors based on radio frequency identification (RFID) can be developed as deformation threshold detectors calibrated with FEMA RVS 154 and push-over analysis to improve the output—model of this study [29]. In addition, using machine learning to classify building damage data can predict damage categories better than conventional RVS and is useful in planning and decision-making for emergency response and post-earthquake recovery [30].

4. Conclusions

The final score from learning using the RVS form is 2.3. It has a vulnerability percentage of 0.5%, which is still considered minimal in terms of vulnerability, so this building has a small potential for damage or failure in the event of an earthquake. From the results of this assessment, the building is included in the Operational Performance Level category. It is

declared secure but requires further validation to ensure the building's behavior with push-over analysis because this RVS assessment depends on the screener's assumptions and experience. In this study, the push-over analysis can evaluate and recalibrate FEMA outcomes. This follows the results of previous research, in which the push-over analysis produced an assessment correlated with building condition categories. Beyond, this research has succeeded in developing an integration method between RVS and push-over analysis so that the resulting integrated RVS-push-over has been validated and developed based on push-over analysis.

The evaluation results using push-over analysis obtained an immediate level of building flats' structural performance, which means that if an earthquake occurs, the damage to the structure will only be minimal. The characteristics and capacity of the vertical and lateral force-resisting system on the structure are still the same as before an earthquake, so the building is safe and can be used immediately. However, the push-over analysis method applied in this study is still superficial; it does not include lateral bracing components/supports, shear retaining walls and other similar construction forms. Several studies recommend further research into push-over analysis considering these elements. Therefore, the push-over method still needs to be developed using a lateral force-resisting system that combines a particular moment frame with concentric bracing, especially in buildings with poor performance due to earthquakes. The research results show that both methods produce the same assessment conditions; the building is declared secure without any structural repair treatment. The performance value of the two analysis points has similarities with the spectral and displacement, respectively, FEMA and push-over methods of 0.238, 56.388 and 0.115, 0.047, 54.2. The analysis results show that FEMA produces higher deterioration probability and displacement values than Push-over. This indicates that FEMA has more conservative effects than Push-Over. FEMA is prudent in providing assessments because it only uses visual data, while push-over uses more detailed data and structural analysis. Integrating the FEMA 154 RVS method with push-over analysis results in more precise FEMA method analysis development procedures and tools based on structural behaviour, mainly when new potential failure modes exist.

In addition, this research can potentially be used as a fast, precise and accurate assessment of structural failure if this behaviour is measured with sensors developed with analysis using artificial intelligence technology and machine learning. It provides benefits as a guide in making decisions when rehabilitating and repairing building structures. It can be an early warning for building managers when an earthquake pre- or post-hit a building.

Acknowledgement

The authors acknowledge that this study is supported by data from the Public Works Department of Lumajang Regency.

References

[1] Kurniawandy A, Hendri A, Firdaus R. Evaluation of Building Vulnerability to Earthquakes Using Rapid Visual Screening (RVS) based on FEMA 154. Annu Civ Eng Semin. 2015;2:338-45.

[2] Adeswastoto H, Djauhari Z, Suryanita R. Evaluation of the Vulnerability of Buildings to Earthquakes Based on ASCE 41-13. SIKLUS J Tek Sipil. 2017;3(2):86-99. https://doi.org/10.31849/siklus.v3i2.383

[3] Araby Z, Samsul Rizal, Abdullah, Mochammad Afifuddin. The Analysis of Beam-Column Joint Reinforced with Cross Bars according to SK SNI T-15-1991-03 on Cyclic Loads. J Civ Eng Forum. 2022;8(1):1-10. https://doi.org/10.22146/jcef.3601

[4] Pangestu IMS., Wibowo A, Wijaya M. Non-Linear Pushover Static Analysis on Optimizing the Design of the FKUB Education Building with Varying Steel Bracing Configurations. Civil Engineering Department. Universitas Brawijaya; 2017.
[5] Michael Mahoney; Mai Tong; Erin Walsh; John Gillengerten. Rapid Visual Screening of Buildings for Potential Seismic Hazards : Supporting Documentation. Federal Emergency Management Agency. Washington, D.C.; 2015.
[6] Irnawan I. Mapping Building Risk from Earthquakes Using Android-Based Rapid Visual Screening (RVS) (Using Fema 154 - 2002). Angew Chemie Int Ed 6(11), 951-952. 2016;325.
[7] Nanda RP, Damarla R, Nayak KA. Android application of rapid visual screening for buildings in indian context. Structures. 2022;46(November):1823-36. https://doi.org/10.1016/j.istruc.2022.10.140
[8] Harirchian E, Hossein SEA, Jadhav K, Kumari V, Rasulzade S, Işık E, et al. A review on application of soft computing techniques for the rapid visual safety evaluation and damage classification of existing buildings. J Build Eng. 2021;43(102536). https://doi.org/10.1016/j.jobe.2021.102536
[9] Bülbül MA, Harirchian E, Işık MF, Aghakouchaki Hosseini SE, Işık E. A Hybrid ANN-GA Model for an Automated Rapid Vulnerability Assessment of Existing RC Buildings. Appl Sci. 2022;12(10). https://doi.org/10.3390/app12105138
[10] Astuti ND, Sangadji S, Rahmadi AP. Initial Evaluation of Seismic Risk of Flat Buildings. Pros Semnastek. 2016;(November):1-9.
[11] V.A.R.Barao, R.C.Coata, J.A.Shibli, M.Bertolini, J.G.S.Souza. Evaluation Of Building Vulnerability To Earthquakes Using Rapid Visual Screening Method (Case Study: Febi Building UIN Prof. Kh. Saifuddin Zuhri). Braz Dent J. 2022;33(1):1-12.
[12] Dwi Pratama AR, Soetjipto JW, Krisnamurti K. Evaluation of Building Vulnerability to Earthquake Using Rapid Visual Screening (RVS) Method. J Tek Sipil dan Perenc. 2021;23(2):114-24. https://doi.org/10.15294/jtsp.v23i2.31399
[13] Zulfiar MH, Zai MII. Assessment of Building Vulnerability to Earthquakes in High-Rise Education Buildings in Yogyakarta. Bull Civ Eng. 2021;1(2):73-80. https://doi.org/10.18196/bce.v1i2.11075
[14] Hasibuan SARS, Ma'arif F, Praja BA. Non-Linear Behavior of Reinforced Concrete Frame Structure with Vertical Irregularities. Int J Innov Res Comput Sci Technol. 2023;11(1):45-51. https://doi.org/10.55524/ijircst.2023.11.1.10
[15] Bhatt C, Bento R. The extended adaptive capacity spectrum method for the seismic assessment of plan-asymmetric buildings. Earthq Spectra. 2014;30(2):683-703. https://doi.org/10.1193/022112EQS048M
[16] Erlicher S, Lherminier O, Huguet M. The E-DVA method: A new approach for multi-modal pushover analysis under multi-component earthquakes. Soil Dyn Earthq Eng. 2020;132:1-27. https://doi.org/10.1016/j.soildyn.2020.106069
[17] Kumar GVAP, Babu RH. Damage Assessment of Multistoried Structures. Int J Eng Res Technol. 2014;3(10):99-110.
[18] Mahorkar, Rohit Ravindra; Kalurkar L. The Effect of Lateral Connection in Moment Carrying Capacity Frames of Low-Rise , Mid-Rise and High-Rise RC Structures by Perfoming Pushover Analysis. Int J Eng Res Technol. 2021;10(01):17-23.
[19] Daei A, Poursha M. On the accuracy of enhanced pushover procedures for seismic performance evaluation of code-conforming RC moment-resisting frame buildings subjected to pulse-like and non-pulse-like excitations. Structures. 2021;32:929-45. https://doi.org/10.1016/j.istruc.2021.03.035
[20] Kagermanov A, Gee R. Cyclic pushover method for seismic assessment under multiple earthquakes. Earthq Spectra. 2019;35(4):1541-58. https://doi.org/10.1193/010518EQS001M

[21] Nafeh AMB, O'Reilly GJ. Simplified pushover-based seismic risk assessment methodology for existing infilled frame structures. Bull Earthq Eng [Internet]. 2023;21(4):2337-68. https://doi.org/10.1007/s10518-022-01600-y

[22] Atc- M, Zebua D, Setia L, Wibowo B, Cahyono MSD. Evaluation of Deviations in Reinforced Concrete Multi-Storey Buildings Based on Pushover Analysis with the ATC-40 Method. 2020;03(September):53-7. https://doi.org/10.25139/jprs.v3i2.2475

[23] Nur Rachmad Afandi. Pushover Analysis Using The SAP 2000 Program. Universitas Sebelas Maret; 2010.

[24] Doğan TP, Kızılkula T, Mohammadi M, Erkan H, Tekeli Kabaş H, Arslan MH. A comparative study on the rapid seismic evaluation methods of reinforced concrete buildings. Int J Disaster Risk Reduct. 2021;56(December 2020). https://doi.org/10.1016/j.ijdrr.2021.102143

[25] Khorami M, Khorami M, Motahar H, Alvansazyazdi M, Shariati M, Jalali A, et al. Evaluation of the seismic performance of special moment frames using incremental nonlinear dynamic analysis. Struct Eng Mech. 2017;63(2):259-68.

[26] Ma Y, Yan Z, Berman JW, Taoum A, Tian W. Seismic Performance of Coupled Steel Plate Shear Walls with Different Degrees of Coupling. J Struct Eng. 2022 Sep;148(9):148(9). https://doi.org/10.1061/(ASCE)ST.1943-541X.0003386

[27] Maleki EBHAAS. Evaluation of seismic performance factors for dual steel SMF-SCBF systems using FEMA P695 methodology. Soil Dyn Earthq Eng. 2022;163(107506). https://doi.org/10.1016/j.soildyn.2022.107506

[28] Es-haghi MS, Barkhordari MS, Huang Z, Ye J. Multicriteria Decision-Making Methods in Selecting Seismic Upgrading Strategy of High-Rise RC Wall Buildings. J Struct Eng. 2022 Apr;148(4):389. https://doi.org/10.1061/(ASCE)ST.1943-541X.0003304

[29] You T, Wang W, Fang C, Chen Y. Rapid probabilistic loss assessment of buildings based on post-earthquake structural deformation conditions. J Build Eng. 2022;45(103629). https://doi.org/10.1016/j.jobe.2021.103629

[30] Bhatta S. Machine Learning-Based Classification for Rapid Seismic Damage Assessment of Buildings at a Regional Scale. J Earthq Eng [Internet]. 2023;1-31. https://doi.org/10.1080/13632469.2023.2252521

Research on Engineering Structures & Materials
www.jresm.org
Research Group

Research Article

Performance improvement of AA6061-T651 friction stir butt-weldment using particulate addition strategy

Ogunsemi Bamidele*[1,a], Ikubanni Peter[1,b], Abolusoro Olatunji[1,c], Adeleke Adekunle[2,d], Ojo Oluwole[3,e]

[1]*Department of Mechanical and Mechatronics Engineering, College of Engineering, Landmark University, P.M.B 1001, Omu-Aran, Kwara State, Nigeria*
[2]*Department of Mechanical Engineering, Nile University of Nigeria, FCT, Abuja, Nigeria*
[3]*Department of Industrial and Production Engineering, Federal University of Technology, P.M.B 704, Akure, Ondo State, Nigeria*

Article Info

Article history:

Received 25 Sep 2023
Accepted 05 Dec 2023

Keywords:

Friction stir welding;
AA6061-T651;
Mechanical properties;
Joint performance;
Grain refinement

Abstract

The joint quality performance of AA6061-T651 friction stir weldments had been investigated in this study through addition of pulverized waste glass (PWG), palm kernel shell ash (PKSA) and synthetic silicon carbide (SSC) with a bid to enhancing some selected mechanical properties. Optimized processing parameters which include 1120 rpm rotational speed, 40 mm/min traverse speed, 1.5° tilt angle) and optimum reinforcement strategy (parallel hole) established from a preliminary investigation were utilized for the friction stir welding. The mechanical properties such as the tensile strength, hardness and impact energy were then further investigated. The results showed that the mechanical properties of all the reinforced welded joints improved significantly than the unreinforced joint having a relatively reduced joint performance of 132 MPa tensile strength, hardness of 45.3 HRB and impact energy of 39.4 J. The PWG-reinforced friction stir welded joint performed optimally at a tensile strength of 212.7 MPa, 72 HRB hardness and 54.5 J impact energy followed by the SSC-reinforced joint which exhibited 173.7 MPa tensile strength, 54.8 HRB hardness and impact energy of 41.7 J. Hence, 80%, 59% and 38% joint performance was exhibited through tensile strength, hardness and impact energy of PWG-reinforced friction stir weldments of AA6061-T651 against the unreinforced weldments.

1. Introduction

The continuous demand for utilization of lighter, stronger and cost-effective engineering materials with excellent corrosion materials has been on the increase [1-3]. This is specifically for the production of high-speed and low fuel economy automobiles and aircrafts. Hence, aluminium alloys, most especially the 7000 and 6000 series have become choice materials for manufacturing industries since they possess excellent combination of these properties for making of specific parts [4, 5].

For instance, heat-treatable and precipitation hardened AA6061-T651 containing magnesium and silicon as its major alloying constituents is utilized in producing structural components of aircrafts wings and fuselages, car wheel spacers and rims and body frames due to its relatively high strength and high toughness properties [6-8]. The poor quality of weld obtained from this alloy has become a bothering issue resulting from the excessive softening of the strengthening precipitates at temperatures above the solidus temperature

*Corresponding author: ogunsemi.bamidele@lmu.edu.ng
[a] orcid.org/0000-0003-3266-9924; [b] orcid.org/0000-0002-2710-1130; [c] orcid.org/0000-0003-1493-3445; [d] orcid.org/0000-0002-0301-7698; [e] orcid.org/0000-0003-4197-1746
DOI: http://dx.doi.org/10.17515/resm2023.17ma0925rs

[9]. In order to address this challenge, several experimental approaches and strategies have been adopted and engaged such as parametric optimization of welding parameters, design and re-design of welding tool pin and shoulder geometries, adoption of post and pre-heat treatment studies, as well as particulate reinforcement strategies [9-12]. However, among the several research efforts previously carried out towards enhancing the deteriorated mechanical properties of friction stir welded joints of AA6061-T651, addition of reinforcement powders, most especially nano and micro-sized ceramic or conventional particles which includes Al_2O_3, B_4C, SiO_2 and SiC have proven to significantly improve the frail friction stir welded joint quality [13-16].

Till date, the utilization of these synthetic particles for reinforcement purposes has become very frequent and popular. Moreover, several works have been reported on the impact of these traditional reinforcement powders on the microstructure, mechanical and tribological properties of friction stir welded joints of AA6061-T651 [17, 18]. Reports from these studies showed that the use of synthetic reinforcement powders gave significant improvement on the mechanical properties as compared to the unreinforced friction stir welded joint of AA6061-T651 weldment. However, these synthetic powders are relatively expensive and not readily available for use [19]. In order to mitigate this challenge, the use of non-crystalline or amorphous powders such as graphite, carbon nanotubes, graphene and copper powder has been investigated and established to have contributed significantly to the enhancement of the mechanical properties of friction stir weldments [20-24]. Several reports from previous works revealed that these amorphous powders gave immense improvements to the joint quality of AA6061-T651 friction stir welded joints thereby making them potential and cost-effective replacements in place of the conventional crystalline and synthetic powders [25-28].

Presently, the utilization of amorphous or non-crystalline powders as reinforcements for friction stir welding (FSW) of aluminium alloys including AA6061-T651 is not popular as research conducted in this area are still very scanty [29]. Moreover, the use of industrial ceramic and agricultural wastes particles are fast gaining acceptance as alternative or replacement powders of choice for use as reinforcements. In previous studies, non-synthetic silica reinforcement powders from rice husk ash was utilized for FSW of AA6061-T6 [30]. The outcome of these studies revealed that hard silica particles hindered grain growth and formation due to the effect of pinning and refinement of grains that resulted from dynamic recrystallization within the aluminium matrix. According to these reports, major improvements were observed in the microstructure and mechanical properties of AA6061-T651 friction stir weldments. In addition, friction stir welding of pulverized waste glass-reinforced aluminium alloy 6061-T651 has been successfully investigated by Ogunsemi *et al.* [31] where the welding processing parameters range (rotational speed between 900-1400 rpm; traverse speed between 25-63 mm/min; tilt angle between 1-2.5^o) were utilized and established to offer optimum mechanical performance of the friction-stir welded joints. The results of the work and other previous investigations by Abioye *et al.* [32] revealed that the addition of reinforcement powders gave significant enhancement to the tensile strength and hardness properties of friction stir weldments of AA6061-T651 in comparison with the unreinforced welded joint under the same welding conditions. However, till date, few works have been reported on the utilization of amorphous or agro-waste powders such as palm kernel shell ash (PKSA) as reinforcement in the FSW of AA6061-T651. Therefore, this present work seeks to investigate the impact of different reinforcement powders such PKSA, Pulverized Waste Glass (PWG and Synthetic Silicon Carbide (SSC) on the joint performance of friction stir weldments of AA6061-T651.

2. Materials and Methods

The materials and research methods utilized in this study are as presented.

2.1. Materials Collection and Equipment

The parent metal for this work is a rolled plate of 6 mm thick heat treatable aluminium alloy6061-T651 ordered from Aluminium Rolling Mill Coy, Malaysia. The plate was cut into 100 mm×50 mm×6 mm dimension. Table 1 shows the elemental constituents of the base metal examined through X-ray fluorescence (Model No: ATX2600) analysis.

A parallel-hole reinforcement strategy was adopted to incorporate the particles along the faying or abutting plate surfaces. This was achieved by drilling 14 parallel holes, each of diameter 4 mm and 4.6 mm depth along the weld line as shown in Figure 2. The total volume of the holes (approximately 810 mm^3) was utilized as the volume of the PKSA powders injected into the holes before FSW. The size of PKSA, PWG and SSC used for this work is < 45 μm. However, the choice of a parallel-hole particle addition strategy was informed by the outcome of the investigation conducted by Ogunsemi *et al.* [33] where the strategy was established among other strategies to produce the optimal mechanical properties of pulverized waste glass (PWG)–reinforced friction stir weldments of AA6061-T651.

Fig. 1. A non-consumable HSS rotating tool mounted on a vertical milling machine for FSW

Table 1. Elemental composition (wt. %) of AA6061-T651 Plate (as-received)

Elements	Mg	Si	Fe	Cu	Mn	Cr	Ni	Zn	Ti	Al
Wt. (%)	0.891	0.562	0.314	0.265	0.039	0.231	0.014	0.053	0.019	97.612

A conventional vertical milling machine (Model No: MC-1007) was adapted to carry out friction stir welding. This was achieved by incorporating a non-consumable tapered high speed steel (HSS) tool with pin. The tool's shoulder is of diameter 20 mm while the pin is of diameter 4 mm and length 4.5 mm. A typical experimental showing the non-consumable rotating HSS tool mounted on a vertical milling machine is presented in Figure 1.

Fig. 2. Parallel hole design strategy

2.2. Friction Stir Welding (FSW)

Figure 3 shows a schematic diagram of the friction stir welding process. A vertical milling machine having a non-consumable high-speed steel (HSS) rotating tool with pin was adapted to produce the weldments. The diameter of the tool shoulder is 20 mm with 4.5 – 4 mm tool pin (tapered) diameter from the shoulder over a 4.5 mm length. Friction stir welding was carried out by utilizing optimized process conditions (1120 rpm rotational speed, 45 mm/min traverse speed and 1.5° tilt angle) and parallel-hole design strategy (for particle addition) already established from a recent investigation by Ogunsemi *et al*. [34] was adopted for optimal results.

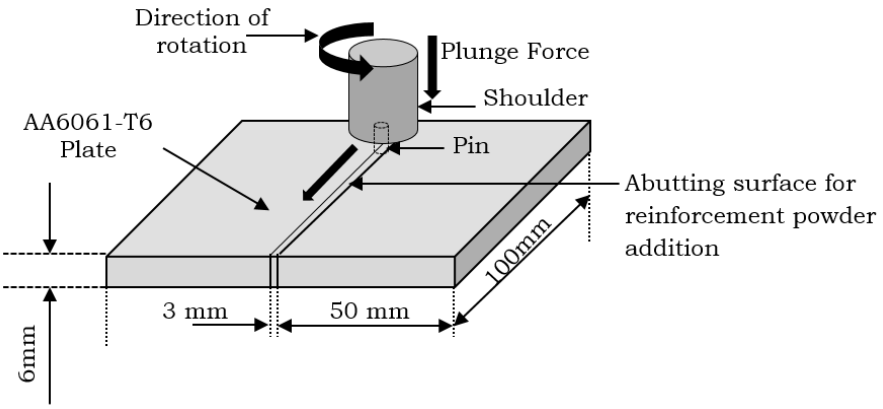

Fig. 3. Schematic of the FSW proces

2.3 Mechanical Tests

Instron 3369 universal tensile testing machine with a x-head velocity or loading rate of 5 mm min^{-1} was used for tensile tests adopting the ASTM-E8M-13 standard as shown in Figure 4. For each experimental run, three (3) samples were prepared and tested to obtain the average value with a view to understanding the level of dispersions or deviations of the results obtained for improved reliability. The hardness values were determined by cross sectioning the surface of the samples and then creating five (5) indentations on each surface using Rockwell hardness tester (Model: RBHT, Sr. No:2011.202). 300gf of load and 10s of dwell time was maintained for the overall test. Charpy impact testing machine was used to conduct the impact energy tests by adopting the ASTM E23 standard. Samples were machined into 55 mm × 10 mm × 5 mm dimension with a 2 mm depth center-notch. A load of 25 kg was impacted on samples at the center at room temperature.

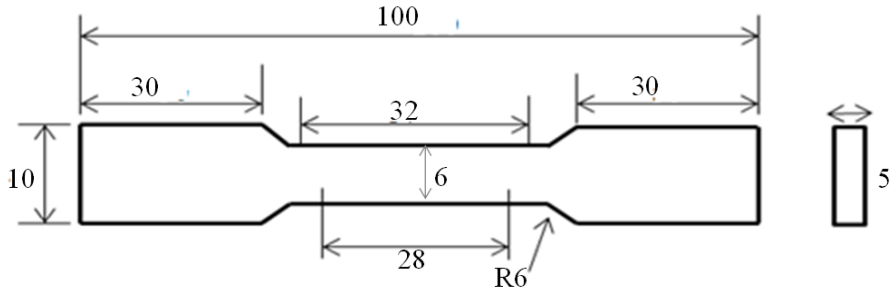

Fig. 4. Schematic of a typical tensile test specimen (dimensions are in mm)

3. Results and Discussion

3.1 Visual Observation of the Friction Stir Welded Joints

Samples of the unreinforced (US), PKSA, PWG and SSC-reinforced friction stir welded joints of aluminium alloy6061-T651 are illustrated in Figure 5. Visual examination of the entire friction stir weldments revealed that the weldments are void of surface defects like porosity and cracks, which shows that selected parameters (1120 rpm, 40 mm/min and 1.5 ^{0}) are suitable for the welding of the material.

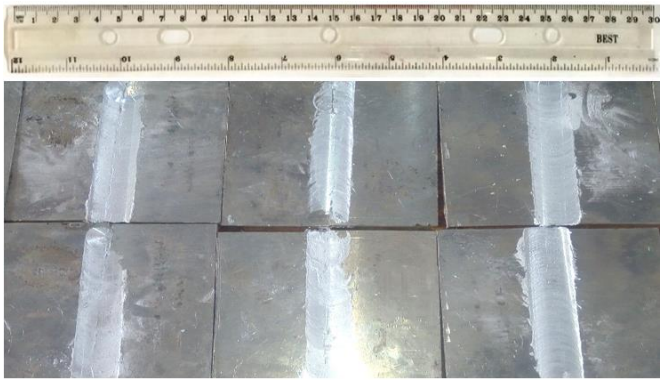

Fig. 5. Some selected reinforced and unreinforced AA6061-T651 friction stir weldments

3.2 Microstructural Examination

Results of the Scanning Electron Microscopy (SEM) and Energy Dispersive X-ray Spectroscopy (EDS) analysis of the PKSA, PWG and SSC reinforcement used in this study are presented in Figure s 6, 7 and 8 respectively.

According to the EDS analyses of the PKSA and PWG, it is evident that the elemental compositions comprise 91% and 81.86% silica respectively while about 12.28% of silicon was present within the SSC microstructure. Silica (SiO_2), being one of the commonly used synthetic reinforcement powders used in previous studies has been established to provide enhancement to the tensile strength of friction stir weldments of aluminium alloy6061-T651 [35]. Hence, inclusion of high percentages by weight of silica within the microstructures of PKSA and PWG indicate that these supposedly agro and industrial waste can serve as potential replacements for the synthetic powders which are more

relatively expensive and not readily available. The presence of these high content of silica within the aluminium matrix during friction stir welding is responsible for the restrictions of grain growth resulting from the pinning effect of the reinforcement powders thereby leading to substantial grain refinement within the stir zone (SZ) and the heat affected zone (HAZ) of the FSWed-joints of AA6061-T651 [36]. This results into improved mechanical properties and microstructure of the weldments for better and quality joint performance.

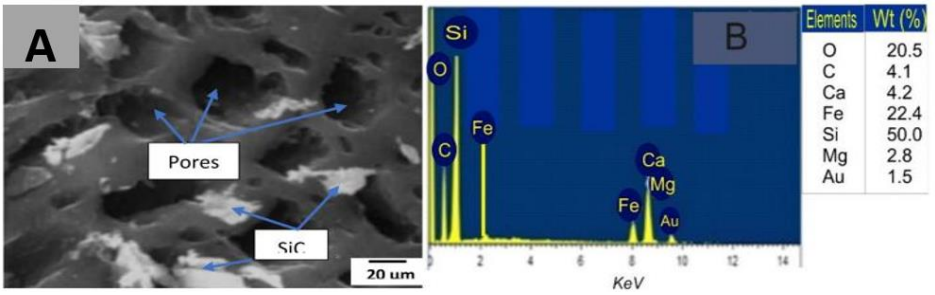

Fig. 6. (a) SEM Micrograph of PKSA (b) The EDS analysis showing the various elemental compositions

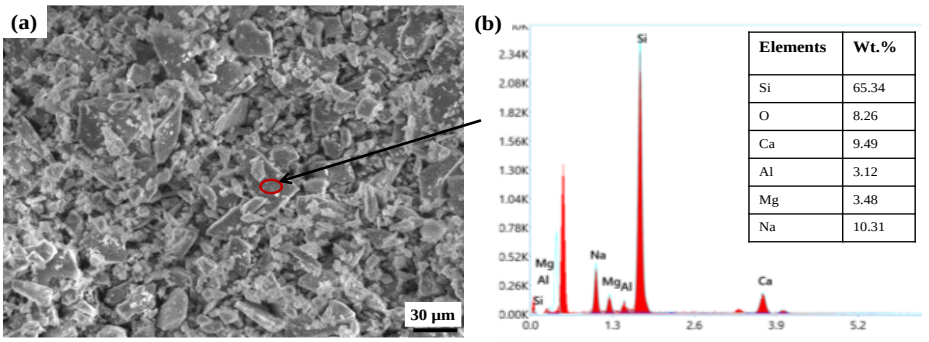

Fig. 7. (a) SEM Micrograph of the PWG (b) Elemental compositions revealed via EDS

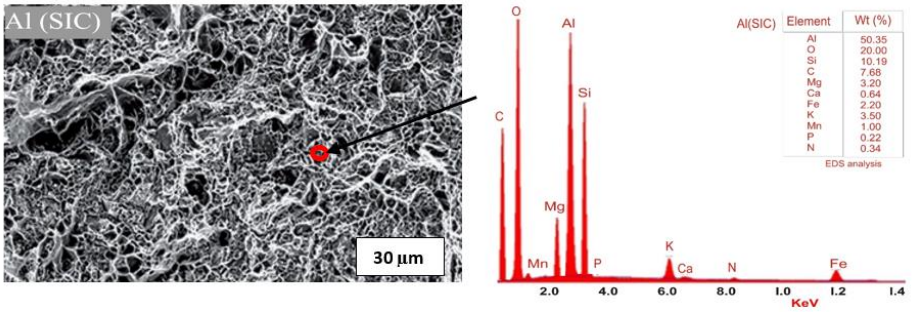

Fig. 8. SEM Micrograph of SSC and the EDS analysis showing the various elemental compositions

3.3. Enhancement of Mechanical Properties FSWed-Joint of AA6061-T651 Using PKSA Reinforcement

Table 2 shows the impact of PKSA reinforcement particles on selected mechanical properties of AA6061-T651 while Figure 9 reveals the interaction between the tensile strength, hardness and impact energy properties of PKSA-reinforced friction stir weldments of AA6061-T651 and unreinforced joint. It can be deduced from Table 2 and Figure 9 that the various reinforcement additions significantly improved the selected mechanical properties of friction stir welded joints (FSWed-joints) of AA6061-T651 as compared to the unreinforced joint. The addition of PKSA reinforcement within the aluminum matrix is adjudged to have imparted substantial grain refinement resulting from pinning effect and dynamic recrystallization mechanisms during FSW [42]. These phenomena are established to have contributed significantly to the high mechanical property value exhibited by all the reinforced joints.

Table 2. Effect of PKSA on the properties of FSWed-joint of AA6061-T651

PKSA	Tensile Strength (MPa)	Hardness (HRB)	Impact Energy (J)
Sample1	181	52.2	37.3
Sample2	148	43.4	44.1
Sample3	164	46.5	45.9
Avg. Value	164.3	47.4	42.4
Unreinforced	132.2	45.3	39.4

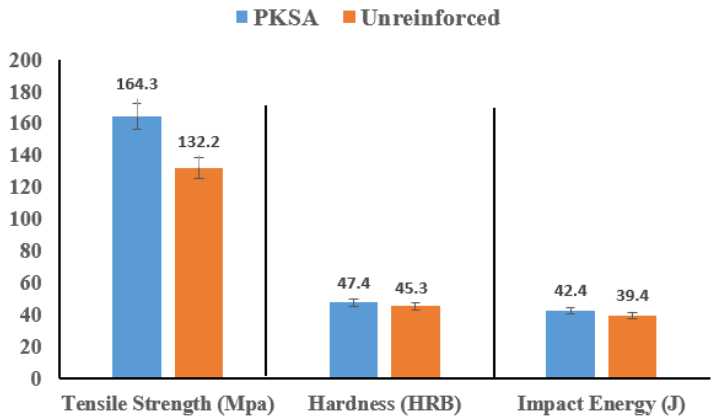

Fig. 9. Relationship between mechanical properties of PKSA-reinforced friction stir weldments of AA6061-T651 and unreinforced joint

3.4 Enhancement of Mechanical Properties FSW Ed-Joint of AA6061-T651 Using PWG Reinforcement

The influence of PWG reinforcement on the selected mechanical properties of AA6061-T651 is illustrated on Table 3 and Figure 10. The interaction between the tensile strength, hardness and impact energy properties of PWG-reinforced friction stir weldments of AA6061-T651 as clearly indicated in Figure 10 depicts significant improvements over the unreinforced joints having relatively low mechanical property values. The inclusion of

reinforcement particles PWG within the aluminium matrix is established to have imparted substantial grain refinement resulting from pinning effect and dynamic recrystallization [42]. These phenomena are adjudged to have contributed to the increased mechanical property value exhibited by the reinforced joints.

Table 3. Effect of PWG on the properties of FSWed-joint of AA6061-T651

PWG Reinforcement	Tensile Strength (MPa)	Hardness (HRB)	Impact Energy (J)
Sample 1	210	69.4	55.1
Sample 2	215	75.2	54.2
Sample 3	213	72.1	54.1
Avg. Value	212.7	72.2	54.5
Unreinforced	132.2	45.3	39.4

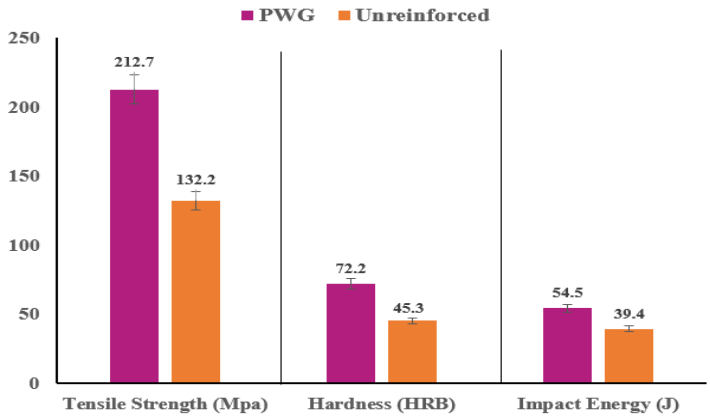

Fig. 10. Relationship between mechanical properties of PWG-reinforced friction stir weldment of AA6061-T651 and unreinforced joint.

3.5 Enhancement of Mechanical Properties FSW Ed-joint of AA6061-T651 Using SSC Powder Reinforcement

Table 4 and Figure 11 reveal the influence of SSC reinforcement on the mechanical properties of AA6061-T651 considered in this study. The interaction between the tensile strength, hardness and impact energy properties of PWG-reinforced friction stir weldments of AA6061-T651 as clearly indicated in Figure 11 shows significant improvements over the unreinforced joints having relatively low mechanical property values. The addition of SSC reinforcement within the aluminium matrix has been established to have greatly imparted substantial grain refinement which resulted from pinning effect and dynamic recrystallization exhibited by the particles [42]. These phenomena are adjudged to have contributed to the increased mechanical property values exhibited by the reinforced joints.

The interaction between the different reinforcement powders and their corresponding influence on the mechanical properties of welded joints of AA6061-T651 has presented on Figure s 9, 10 and 11 shows a similar trend or behaviour with the tensile strength having the highest values, followed by the hardness. Generally, as shown in Figure 12, significant

improvement was observed on the mechanical properties of reinforced friction stir welded joints of AA6061-T651 as compared to the unreinforced joint with a relatively low values of 132 MPa tensile strength, 45.3 HRB hardness and 39.4 J impact energy.

Table 4. Effect of SSC on the properties of FSWed-joint of AA6061-T651

SSC Reinforcement Powder	Tensile Strength (MPa)	Hardness (HRB)	Impact Energy (J)
Sample 1	155	60.4	38.8
Sample 2	186	53.8	42.3
Sample 3	180	50.1	44.2
Avg. Value	173.7	54.8	41.7
Unreinforced	132.2	45.3	39.4

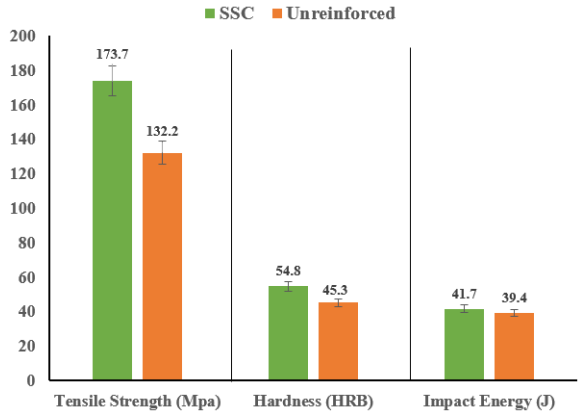

Fig.11. Relationship between the mechanical properties of SSC-reinforced FSWed-joints of AA6061-T651 and unreinforced sample

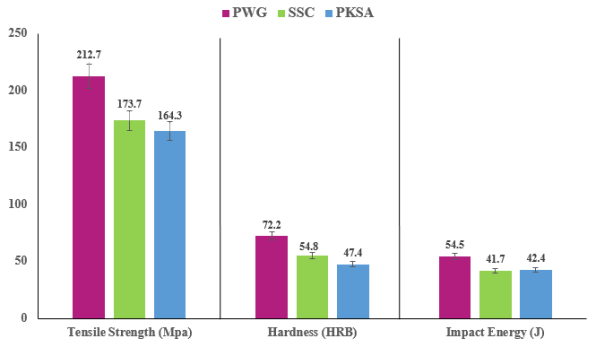

Fig. 12. Main interaction plot showing the effects of the various reinforcement powders on the mechanical properties of FSWed-joints of AA6061-T651

However, as clearly shown in Figures 10 and 12, the PWG-reinforced joint significantly improved the mechanical properties of the joint with the highest value of tensile strength

(212.7 MPa), hardness (72 HRB) and impact energy (54.5 J) as compared to other reinforcement particles, especially PKSA having a relatively higher percentage by weight of silica as shown in Figure 6 and Figure 7. Although the percentage of silica in PKSA is higher compared to that of PWG, the mechanical properties of PWG-reinforced joint are higher compared to those of PKSA-reinforced FSWed-joint. The deduction from this result could be attributed to the high inherent hardness of the ceramic-glass particles and its severe pinning effect on the grain formation that resulted into dynamic recrystallization and more substantial grain refinement within aluminium matrix at the friction stir welded joint region [37].

3.6 Tensile Strength

The tensile strength properties of all aluminium alloy6061-T651 reinforced friction stir weldments were significantly enhanced as observed in their joint efficiencies and performance when compared to the unreinforced joint as clearly presented in Figure s 9, 10, and 11 which represent the PKSA, PWG and SSC-reinforced joints respectively. However, the PWG-reinforced sample gave the optimum tensile strength of 212.7 MPa indicating sound and quality weldment of AA6061-T651 as shown in Figure 12. The deduction from this result could be the influence of the inherent high hardness of the pulverised waste glass which was uniformly dispersed and the homogenous mixture within the aluminium matrix by the rotating tool. This uniform dispersion and homogenous mixture at the stir zone largely contributed to dynamic recrystallization and the pinning effect of the particles which resulted into substantial grain refinement and the eventual improvement of the tensile strength [38]. These phenomena are also adjudged to be responsible for the optimum impact energy of 54.5 J obtained from the PWG-reinforced friction stir welded joint of AA6061-T651 in relation to other reinforced. The tensile strength values of PKSA and SSC-reinforced joints are 164.3 MPa and 173.7 MPa respectively.

3.7 Hardness

The hardness values of friction stir welded joint of PGW-reinforced AA6061-T651 and other reinforced (PKSA and SSC) are presented in Figure 12. All the reinforced joints demonstrated increased or high hardness values as compared to the unreinforced joint but the PGW- reinforced joint gave the optimum value of 72 HRB. This finding is in consonance with recent findings by Abioye *et al* [39] where the AA6061-T651 mechanical strength was enhanced using Al_2O_3, SiC, B_4C as well as Ogunsemi *et al* [40] where PWG was utilized. Results of their studies showed that the reinforced joints experienced higher hardness compared to unreinforced welded joints. The higher hardness observed in the PGW-reinforced joint over the unreinforced is traceable to the high hardness inherent in the PWG. The waste glass which has been established from previous study to comprise mainly 82% by weight SiO_2 has been reported to have an average hardness value of 580 HV [41]. Inclusion of reinforcement particles (PKSA, PWG and SSC) within the aluminum matrix is also established to have imparted substantial grain refinement resulting from pinning effect and dynamic recrystallization [42]. These phenomena are adjudged to have contributed to the high hardness value exhibited by the reinforced joints. Amongst the welded joints reinforced, the weldment produced from the addition of PWG gave the optimum value of 72 HRB. This finding can be attributed to improved homogeneity of particle distribution and mixing by the rotating tool. The pinning effect of the PWG is also adjudged to gain more prominence over other reinforcement powders thereby leading to significantly higher and better grain refinement which results into improved or increased hardness. Other reinforcement particles such as PKSA and SSC exhibited relatively higher hardness of 47.4 HRB and 54.8 HRB respectively compared to the unreinforced joint with the lowest hardness value of 39.4 HRB. The apparent absence of the phenomenal pinning

effect and dynamic recrystallization caused by the particles within the unreinforced joint of AA6061-T651 friction stir welded joint confirms the relatively low hardness value and poor weld joint performance [43].

3.8 Impact Energy

The values of the impact energy of the reinforced joints of AA6061-T651 friction stir weldments are given in Figure 12. Average of three (3) measurements was used to achieve the actual value for each sample. The unreinforced joint demonstrated an impact energy of 39.4 J. The joints produced using PWG reinforcement exhibited the highest impact energy of 54.5 J followed by the PKSA-reinforced joint with impact energy of 42.4 J. The relatively higher impact energy observed in the PWG-reinforced joint is traceable to improved nucleation or retention of particle and distribution which is adjudged to have led to improved refinement of grains within the stir zone [44]. It has been established from previous works that grain refinement due to dynamic recrystallization (DR) within the processed aluminium alloy matrix is responsible for the increased impact energy. Nucleation of new grains through DR resulted into refinement of grains which contributed immensely to the increased impact energy exhibited by the weldment [45].

4. Conclusion

The utilization of amorphous or non-crystalline powders as reinforcements for friction stir welding (FSW) of aluminium alloys including AA6061-T651 is fast gaining acceptance as alternative or replacement powders in place of the synthetic ones. In previous studies, non-synthetic silica particles from rice husk ash were introduced for FSW of AA6061-T6 with significant contribution or impact on the mechanical properties. The results from the studies revealed that strong silica powder led to grain formation and growth restrictions due to pinning effect and grain refinement that resulted from dynamic recrystallization of the aluminium matrix within the stir zone (SZ). However, in this study, the enhancement of the tensile strength, hardness and impact energy of friction stir welded joints of AA6061-T651 has been experimentally achieved. Optimized processing parameters (1120 rpm rotational speed, 40 mm/min traverse speed, 1.5^{o} tilt angle) and optimum reinforcement strategy (parallel hole) established from a preliminary investigation were utilized for the friction stir welding. The mechanical properties such as the tensile strength, hardness and impact energy were then further investigated. The results of this work revealed that the addition of reinforcement particles (PWG, PKSA and SSC) greatly improved the friction stir welded joint properties as compared to unreinforced joints which gave relatively lower values of mechanical properties. The PWG-reinforced joints performed optimally with increased values of 212.7 MPa, 72 HRB and 54.5 J for the tensile strength, hardness and impact energy respectively. Hence, 80%, 59% and 38% joint performance was exhibited through tensile strength, hardness and impact energy of PWG-reinforced friction stir weldments of AA6061-T651 against the unreinforced weldments. Therefore, it is adjudged that this joint performance is traceable to reduced particle sputtering by the rotational tool during friction stir welding and improved grain refinement which is traceable to DR as a result of the pining effect of the uniformly dispersed particles within the aluminium matrix during welding.

Acknowledgement

The technical assistance rendered by Mr Abulola of the Mechanical Engineering Central Workshop, Federal University of Technology, Akure, Ondo State as well Dr. Alo and Dr. Ajoge of Materials Science Laboratory, Obafemi Awolowo University, Osun State. Nigeria is appreciated by the authors.

References

[1] Abdollahzadeh A, Shokuhfar A, Cabrera JM, Zhilyaev AP, Omidvar H. In-situ nanocomposite in friction stir welding of 6061-T6 aluminium alloy to AZ31 Magnesium alloy. Journal of Materials Processing Technology. 2018; 52: 296-307. https://doi.org/10.1016/j.jmatprotec.2018.08.025

[2] Chandran R, Ramaiyan S, Shanbhag AG, Santhanam SKV. Optimization of welding parameters of friction stir lap welding of AA6061-T6 alloy. Journal of Modern Mechanical Engineering. 2018; 8: 31-41. https://doi.org/10.4236/mme.2018.81003

[3] Bodunrin MO, Alaneme KK, Chown LH. A review of reinforcement philosophies: mechanical, corrosion and tribological characteristics. Journal of Materials Research and Technology. 2015; 4: 434-451. https://doi.org/10.1016/j.jmrt.2015.05.003

[4] Mehta KP, Carlone P, Astarita A, Scherillo F, Rubino F, Vora P. Conventional and cooling assisted friction stir welding of AA6061 and AZ31B alloys. Materials Science & Engineering A. 2019; 46: 252-261. https://doi.org/10.1016/j.msea.2019.04.120

[5] Fathi J, Ebrahimzadeh P, Farasati R, Teimouri R. Friction Stir Welding of aluminum 6061-T6 in the presence of water cooling: Analyzing mechanical properties and residual stress distribution. International Journal of Lightweight Materials and Manufacture. 2019; 2: 107-115. https://doi.org/10.1016/j.ijlmm.2019.04.007

[6] Abreu CM, Rey RA, Cristobal MJ, Verdera D, Vidal CL. Friction Stir Processing Strategies to develop a surface composite layer on AA6061-T6. Journal of Materials and Manufacturing Processes. 2018; 33(10): 1-9. https://doi.org/10.1080/10426914.2017.1415447

[7] Acharya U, Roy BS, Saha SC. Torque and Force Perspectives on Particle Size and its effects on mechanical property of Friction Stir Welded AA6092/17.5SiCp-T6 Composite Joints, Journal of Manufacturing Processes. 2019; 38: 113-121. https://doi.org/10.1016/j.jmapro.2019.01.009

[8] Ahmed KE, Nagesh BM, Raju BS, Drakshayani DN, Chethan AS. Studies on the effect of welding parameters for friction stir welded AA 6082 reinforced with Aluminium Oxide. Material Today: Proceedings. 2020; 20: 108-119. https://doi.org/10.1016/j.matpr.2019.10.059

[9] Babu K, Kumar PK, Muthukumaran S. Mechanical, metallurgical characteristics and corrosion properties of friction stir welded AA 6061-T6 using commercial pure aluminium as filler plate. Procedia Material Science. 3rd International Conference on materials processing and characterization. 2014; 648-556. https://doi.org/10.1016/j.mspro.2014.07.080

[10] Amber S, Manuel K, Frank EP. Comparison of energy consumption and environmental impact of friction stir welding and gas metal arc welding of aluminium. CIRP Journal of Manufacturing Science and Technology. 2015; 9: 159-168. https://doi.org/10.1016/j.cirpj.2014.10.001

[11] Amini S, Amiri M. Study of ultrasonic vibrations' effect on friction stir welding International Journal of Advanced Manufacturing Technology. 2014; 73(4): 127-135. https://doi.org/10.1007/s00170-014-5806-7

[12] Anas NM, Abioye TE, Anasyida AS, Dhindaw BK, Zuhailawati H, Ismail A. Microstructure, mechanical and corrosion properties of cryorolled-AA 5052 at various solution treatment temperatures. Materials Research Express. 2020; 7: 1-2. https://doi.org/10.1088/2053-1591/ab636c

[13] Arun KK, Pankaj B. Effect of tool pin profile on the material flow characteristics of AA6061. Journal of Manufacturing Process. 2017; 26: 382-392. https://doi.org/10.1016/j.jmapro.2017.03.005

[14] Aruri D, Adepu K, Adepu K, Bazavada K. Wear and Mechanical Properties of 6061-T6 aluminium alloy surface hybrid composite [(SiC+Gr) and (SiC + Al2O3)] fabricated by

friction stir processing. Journal of Materials Research and Technology. 2013; 2(4): 362-369. https://doi.org/10.1016/j.jmrt.2013.10.004
[15] Asadi P, Besharati MK, Abrinia K, Taherishargh M, Salekrostam R. Effects of SiC Particle Size and Process Parameters on the Microstructure and Hardness of AZ91/SiC Composite Layer Fabricated by FSP. Journal of Materials Engineering and Performance. 2011; 20: 1554-1562. https://doi.org/10.1007/s11665-011-9855-x
[16] Asadollahi M, Khalkhali A. Optimization of mechanical and microstructural properties of friction stir spot welded AA 6061-T6 reinforced with SiC nanoparticles. Materials Research Express. 2018; 5(11): 1-45. https://doi.org/10.1088/2053-1591/aadc3a
[17] Aval HJ, Serajzadeh S. A study on natural aging behaviour and mechanical properties of friction stir welded AA6061-T6 plates. International Journal of Advanced Manufacturing Technology. 2014; 71: 933-94. https://doi.org/10.1007/s00170-013-5531-7
[18] Azeez S, Mashini M, Akinlabi E. Sustainability of friction stir welded AA6082 plates through post-weld solution heat treatment. Procedia Manufacturing. 2019; 33: 27-34. https://doi.org/10.1016/j.promfg.2019.04.005
[19] Babu A, Krishna GG. Experimental Investigation of friction stir welding of AA6061 Alloy Joints testing. IOSR Journal of Mechanical and Civil Engineering. 2015; 12(6): 1-5.
[20] Akinlabi ET. Effect of shoulder size on weld properties of dissimilar metal friction stir welds. International Journal of Materials Engineering and Performance. 2011; 5: 1-6.
[21] Baghdadi AH, Mohammad G, Selamat NF, Sajuri Z, Omar MZ. Effect of post-weld heat treatment on the mechanical behaviour and dislocation density of friction stir welded Al6061. Materials Science & Engineering A. 2019; 728-734. https://doi.org/10.1016/j.msea.2019.03.017
[22] Banik A, Barnik SR, Barma JD, Saha SC. An experimental investigation of torque and force generation for varying tool tilt angles and their effects on the microstructure and mechanical properties: Friction Stir Welding of AA6061-T6. Journal of Manufacturing Process. 2018; 31: 395-404. https://doi.org/10.1016/j.jmapro.2017.11.030
[23] Abioye TE, Mustar N, Zuhailawati H, Suhaina I. Prediction of the tensile strength of aluminium alloy 5052-H32 fibre laser weldments using regression analysis. The International Journal of Advanced Manufacturing Technology. 2019; 102: 1951-1962. https://doi.org/10.1007/s00170-019-03310-3
[24] Boonma J, Khammuangsa S, Uttarasak K, Dutchaneephet J, Boonruang C, Sirikulrat N. Post-Weld Heat Treatment Effects on Hardness and Impact Strength of Aluminium Alloy 6061 Friction Stir Butt Weld. Materials Transaction. 2015; 56(7): 1072-1076. https://doi.org/10.2320/matertrans.M2015074
[25] Abdulstaar MA, Al-Fadhalah KJ, Wagner L. Microstructural variation through weld thickness and mechanical properties of peened friction stir welded 6061 aluminum alloy joints. Material Characterization. 2017; 126: 64-73. https://doi.org/10.1016/j.matchar.2017.02.011
[26] Chuan L, Xiang Y. Residual stress measurement on AA6061-T6 aluminium alloy friction stir butt welds using contour method. Materials and Design. 2013; 46: 366-317. https://doi.org/10.1016/j.matdes.2012.10.030
[27] Devaraju A, Kumar A, Kotiveerachari B. Influence of rotational speed and reinforcements on wear and mechanical properties of aluminum hybrid composites via friction stir processing. Materials and Design. 2013; 45: 576-585. https://doi.org/10.1016/j.matdes.2012.09.036
[28] Diwahar S, Anbarasu K, Deepanchakravarthy P, Raveen R. A review on friction stir welding of similar and dissimilar aluminium alloys. International Research Journal of Engineering and Technology. 2017; 4(10): 999 - 1003.

[29] Elangovan K, Balasubramanian V. Influences of tool pin profile and tool shoulder diameter on the formation of friction stir processing zone in A6061 aluminium alloy. Materials Design. 2008; 29: 362-373. https://doi.org/10.1016/j.matdes.2007.01.030
[30] Elatharasan G, Senthil KVS. An experimental analysis and optimization of process parameter on friction stir welding of AA 6061-T6 aluminium alloy using RSM. Procedia Engineering. 2013; 64: 1227 - 1234. https://doi.org/10.1016/j.proeng.2013.09.202
[31] Ogunsemi BT, Eta OM, Olanipekun E, Abioye TE, Ogedengbe TI. Tensile strength prediction by regression analysis for pulverized glass waste-reinforced aluminum alloy 6061-T6 friction stir weldments. Sadhana India Academy of Sciences. 2022; 1-12. https://doi.org/10.1007/s12046-022-01830-5
[32] Abioye TE, Zuhailawati H, Anasyida AS, Yahaya SA, Dhindaw BK. Investigation of the microstructure, mechanical and wear properties of AA6061-T6 friction and weldments with different particulate reinforcements' addition. Journal of Materials Research and Technology. 2019; 8(5): 3917-3928. https://doi.org/10.1016/j.jmrt.2019.06.055
[33] Ogunsemi BT, Abioye TE, Orekunrin TM, Oladimeji PO, Jamiu RB, Ogedengbe TI. Joint quality enhancement of AA6061-T6 friction stir weldment by reinforcing with pulverized glass waste using different reinforcement strategies. Engineering Research Express. 2022; 4: 1-12. https://doi.org/10.1088/2631-8695/ac6ece
[34] Hu Y, Liu H, Li S, Du S, Sekulic DP. Improving mechanical properties of a joint through tilt probe penetrating friction stir welding. Materials Science & Engineering A. 2020; 731: 107-118. https://doi.org/10.1016/j.msea.2018.06.036
[35] Ipekoglu G, Erim S, Cam G. Investigation into the influence of Post-Weld Heat Treatment on the Friction Stir Welded AA6061 Al-Alloy Plates with different temper conditions. Metallurgical and Materials Transaction A. 2014; 45: 864-876. https://doi.org/10.1007/s11661-013-2026-y
[36] Mahto RP, Gupta C, Kinjawadekar M, Meena A, Pal SK. Weldability of AA6061-T6 and AISI 304 by underwater friction stir welding. Journal of Manufacturing Processes. 2019; 38: 370-386. https://doi.org/10.1016/j.jmapro.2019.01.028
[37] Martin JP. Stationary shoulder friction stir welding. Proceedings of the 1st international joint symposium on joining and welding. Osaka, Japan. Woodhead Publishing Limited. 2019; 7:15-25.
[38] Maurya R, Kumar B, Ariharan S, Ramkumar J, Balani K. Effect of carbonaceous reinforcements on the mechanical and tribological properties of friction stir processed Al6061 alloy. Journal of Materials and Design. 2016; 9(8): 155-166. https://doi.org/10.1016/j.matdes.2016.03.021
[39] Abioye TE, Zuhailawati H, Aizad S, Anasyida AS. Geometrical, microstructural and mechanical characterisation of pulse laser welded thin sheet 5052-H32 aluminium alloy for aerospace applications. Transanction of Nonferrous Metals Society, China. 2019; 29: 667-67. https://doi.org/10.1016/S1003-6326(19)64977-0
[40] Ogunsemi BT, Abioye TE, Ogedengbe TI, Zuhailawati H. A review of various improvement strategies for joint quality of AA6061-T6 friction stir weldments. Journal of Materials Research and Technology. 2021; 5(11): 1061-1089. https://doi.org/10.1016/j.jmrt.2021.01.070
[41] Ogedengbe TI, Abioye TE, Ekpemogu AI. Investigation of mechanical properties and parametric optimization of the dissimilar GTAW of AISI 304 stainless steel and low carbon steel. World Journal of Engineering. 2018; 15(5): 584-91. https://doi.org/10.1108/WJE-12-2017-0412
[42] Hu Y, Liu H, Fuji H. Improving the mechanical properties of 2219-T6 aluminum alloy joints by ultrasonic vibrations during friction stir welding. Journal of Materials Processing Technology. 2019; 271: 75-84. https://doi.org/10.1016/j.jmatprotec.2019.03.013
[43] Eliseev AA, Kalashnikova TA, Gurianov DA, Rubtsov VE, Ivanov AN, Kolubaev EA. Ultrasonic assisted second phase transformations under sever plastic deformation in

friction stir welding of AA2024. Materials Today, Communications. 2019; 21: 1-4. https://doi.org/10.1016/j.mtcomm.2019.100660

[44] Omar SS, Hengan O, Xinggou W, Sun W. Microstructure and mechanical properties of friction stir welded AA6092/SiC matrix composite. Journal of Materials Science and Engineering A. 2015; 15: 78 - 88.

[45] Ozturk F, Sisman A, Toros S, Kilic S, Picu RC. Influence of aging treatment on mechanical properties of 6061 aluminium alloy. Materials and Design. 2010; 31: 972-975. https://doi.org/10.1016/j.matdes.2009.08.017

Research on Engineering Structures & Materials
www.jresm.org
Research Group

Research Article

Flexural behavior of printed concrete wide beams with dispersed fibers reinforced

Loan Thi Pham[*1,a], Thanh Duy Trinh[1,b], Quang Trong Do[1,c], Jie Yi Huang[2,d]

[1]*Department of Civil Engineering, Haiphong University, Hai Phong, Vietnam*
[2]*College of Civil Eng. and Architecture, Shandong University of Sciences and Technology, Qingdao, China*

Article Info

Article history:

Received 25 Sep 2023
Accepted 05 Dec 2023

Keywords:

Printed wide beams;
Glass fiber;
Steel fiber;
Failure patterns;
Flexural strength;
Ductility

Abstract

Thanks to the highlighted advantages of the construction method, including digitalization and automation, sustainable materials, and environmental protection, 3D concrete printing technology has been a hot topic for a few decades. This construction method was initially used in small and non-structural applications and is now being adopted for large-scale structures. This transition requires a lot of research on the structural behavior of structures. Therefore, the study focuses on the behavior of wide beams, which is the primary element in the structure system. Nine wide beams with different glass/steel fiber amounts were printed, and 3-point loading tests were conducted. The failure mode, flexural strength, deflection, and ductility were reported in this study. In this study, the girder web was designed in the style of truss beams, and glass/steel fibers were used. The fibers, including glass and steel fiber, will enhance the beams' flexural strength and ductility. The results showed that (1) The adhesion force between the printed layers ensures the overall working of the wide beams; (2) The failure patterns of glass fiber beams were brittle; glass fibers show insignificant improvement in compressive strength; the flexural capacity was significantly enhanced, and the optimal steel fiber amount is 1.0%. (3) The failure patterns of steel fiber beams were ductile; steel fibers showed light improvement in compressive strength. The steel fiber significantly impacted the flexural strength. The optimum amount of steel fibers was determined to be ranged from 1.0% to 1.5%.

1. Introduction

Digitalization and automation have enabled a rapid increase in productivity in many producing industries over the last few decades. The seamless data flow from digital planning into fully automated construction would mark qualitatively this new level of technology, often referred to as Construction Industry 4.0. Moreover, sustainability in building construction is essential for future projects, making 3D concrete printing construction a standout advantage over traditional construction practices. The justification for sustainability becomes highly appreciated when comparing 3D concrete printing technology with conventional construction techniques, mainly due to the absence of formwork, reduced labor requirement, and protected environment thanks to decreased waste production and the use of green materials. For example, the Dubai project (the United Arab Emirates National Committee) has reported labor cost reductions of 50 to 80% and a decrease in construction waste of 30 to 60% [1], [2].

*Corresponding author: loanpt80@dhhp.edu.vn
[a] orcid.org/0000-0001-7081-0285; [b] orcid.org/0009-0006-7575-1265; [c] orcid.org/0009-0007-5148-7866; [d] orcid.org/0000-0002-8377-214X
DOI: http://dx.doi.org/10.17515/resm2023.19me0925rs

However, the limitations and challenges of 3D printing concrete technology must be researched and solved in the future. There is a lack of knowledge regarding the effects of different environmental factors when printing on sites. Higher capital investment is required to create and develop digital models, which requires skilled personnel and is especially limited in design. Additionally, there is a lack of understanding about the behavior of 3D concrete printed structures under different loading conditions. This knowledge gap stems from the initial use of this process in small non-structural applications and its subsequent adoption for large-scale structures. Therefore, research on the structural behaviors of printed components [3] or whole systems has been limited. By examining the progress of the development stages for concrete printing technology in the construction field, as shown in Fig. 1, we can reflect on past advancements and anticipate future ones.

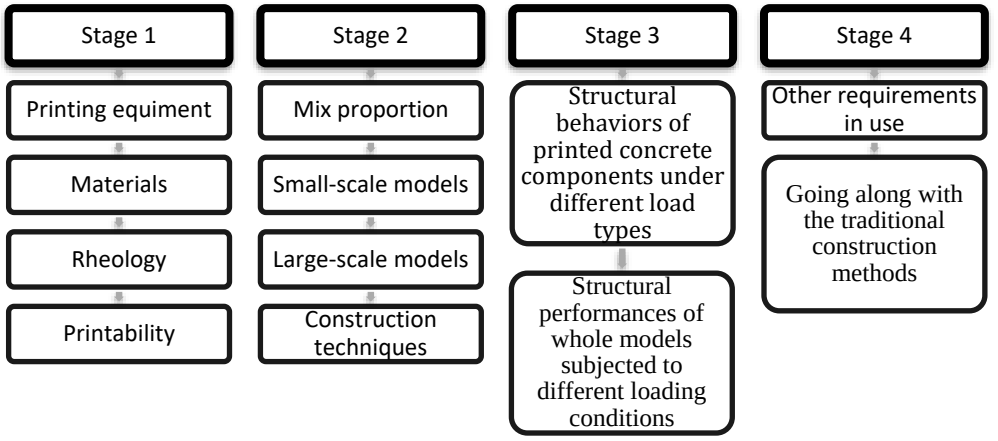

Fig. 1. Development stages of application concrete printing technology in the construction field

Stages 1 and 2 have been researched and recently published by many authors worldwide. Extensive literature reviews have been conducted [4]–[6] [7]. Based on a considerable number of publications, concrete printers and mixed proportions have been recommended and successfully applied in both academic and industrial zones [1], [8]–[12]. However, one of the disadvantages of concrete printing technology is rebars, which will reinforce concrete structures. To overcome this obstacle, multi-nozzle or reinforced concrete with random fibers such as polypropylene, glass, steel, and palm fiber have been explored [13]–[18] [19] [20][21]. Both small and larger-scaled models have been constructed using revealed construction techniques [12][22][8]. Although these achievements have significantly enhanced the development of 3D concrete printing technology in construction projects, the structural performances of the printed buildings need to be tested for safety.

Researchers have recently dealt with Stage 3 to devote to the structural performance of structures built with 3D concrete printing technology. This stage is initial, with some studies focusing on the structural behaviors of components such as panels [3], walls[23], and printed concrete specimens [24][25]. The results obtained from this research will contribute to the success of Stage 3 and become an essential part of Stage 4 in the future.

The beam is one of the essential structural parts in the structural system of the works, especially the frame structure. The beam is the part that supports the floor, supports the wall, and connects the columns to form a frame system. Choosing wide beams instead of traditional beams is increasingly popular because of two simultaneous goals: reducing the height of buildings and increasing the aesthetics of the space used. Thus, to meet the

requirements of workability and the development of the trend of using wide beams in works, the study of the working of this type of beam is an indispensable and objective requirement.

Because of the absence of reinforcement inside beams, the fibers, including glass and steel fiber, will enhance the flexural strength and ductility of the printed wide beams in this study. The use of fiber to reinforce components has widened over the decades. Glass and steel fibers have become popular thanks to the economic advantage they offer combined with other advantages. Glass is a type of thermoset polymer composite that improves the mechanical properties of the components such as stiffness, strength or corrosion assistance. Many investigations have used short glass fibers [26], [27]. The results show that short glass fibers in the matrix can be excellent secondary reinforcements (micro-fillers). Steel fiber reinforced concrete also has extensive applications. Many investigations found that adding steel fibers influences the concrete components' flexural strength and ductility [28], [29].

From the authors' perspective, research on the flexural behavior of wide beams, including failure modes, moment resistance, and deflection of printed beams, has been carried out and analyzed. Therefore, the flexural behavior of the fiber concrete wide beams, which are printed instead of traditionally fabricated, is studied. The results contribute to Stage 3 mentioned above, including (1) the understanding of the structural behavior of the fiber concrete wide beams, including failure modes, flexural strength, load–deflection relationship, and ductility will be revealed; (2) the 3D concrete printing technology can precisely fabricate structure sections with complex geometries directly from computer-aided design (CAD) files; (3) the combination of the type of wide beam section and technology will suggest a new concept/ new idea to designers. At last, applying 3D concrete printing technology to the construction field can be considered a reference and orientation from this research.

2. Details of Wide Beams

The beams' dimension length, width, and height are 1450 mm, 240 mm, and 120 mm, respectively. The thickness of the perimeter and the girder web is 25 (mm). Details of the printed concrete wide beams are shown in Fig. 2.

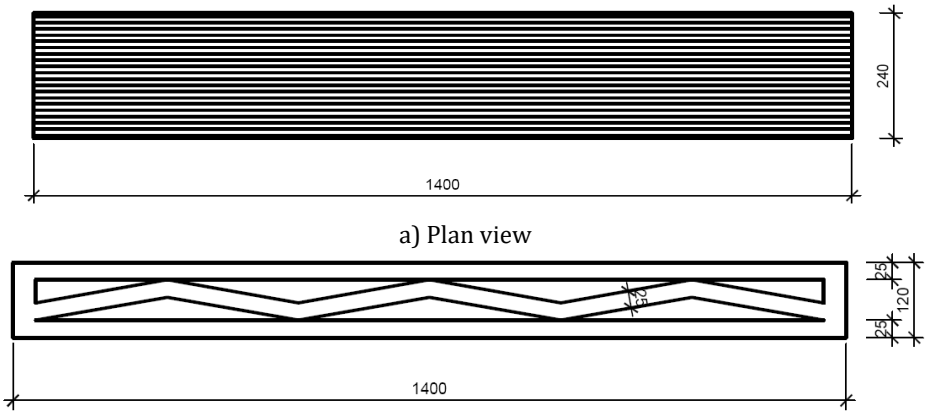

a) Plan view

b) Front view

Fig. 2. Details of the printed wide beam

3. Materials and Mix Proportions

In this research, ordinary Portland cement (O.P.C.) by Chiffon PC40 was used to form the binder component, thanks to successfully applied cement-based materials by many researchers as well [30]–[35]. Commercially available manufactured natural sand with a nominal maximum aggregate size of 1.5mm was used. Crushed sand with a nominal maximum aggregate size of 2.5mm was used. Glass fibers (G.F.) and steel fibers (S.F.) were used to mix the proportions, the main properties of G.F. and S.F. fibbers, as listed in Table 1. The mix proportions were designed based on the procedure presented in Fig. 4 and listed in Table 2.

Table 1. Properties of fibers

Properties	G.F.	S.F.
Tensile strength (MPa)	900	2200
Modulus (GPa)	72	200
Diameter (mm)	0.0012	0.22
Length (mm)	12	13
Density (kg/m3)	2600	7750

To adjust the workability of the fresh concrete Superplasticizer, Visconcrete 3000-200M was used. Materials used for mixing concrete in this research are presented in Fig. 3.

Cement

Natural sand

Crushed sand

Superplasticizer (S.P.)

Glass fibers (G.F.)

Steel fibers (S.F.)

Fig. 3. Materials used for mixing concrete

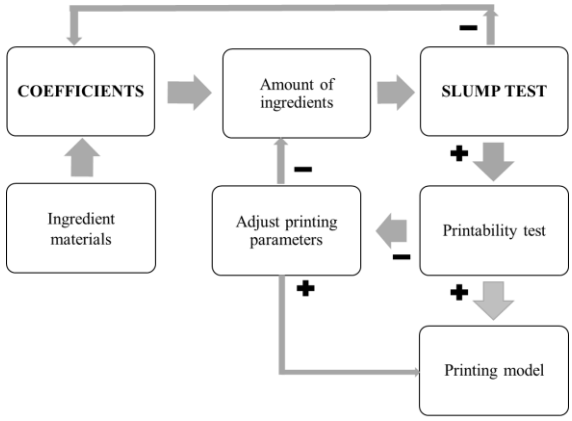

Fig. 4. Mix proportion design process [36]

Table 2. Mix proportions

Beam label	Water	Natural sand	Crushed sand	Glass Fiber (%)	Steel Fiber (%)	S.P. (%)
CB-00	0.31	0.5	0.5	-	-	0.4
GB-0.5				0.5	-	
GB-1.0				1.0	-	
GB-1.5				1.5	-	
GB-2.0				2.0	-	
SB-0.5				-	0.5	
SB-1.0				-	1.0	
SB-1.5				-	1.5	
SB-2.0				-	2.0	

(Note: Values are a ratio of weight to cement.)

4. Printing Process

The process starts with a 3D CAD model of the object, which was saved in ".STL" format. Then, Simplify3D software was used to slice layers of the model and save it as a ".Gcode" file. Finally, 3D concrete printers controlled by Mach3 software printed all nine beams. **Hata! Başvuru kaynağı bulunamadı.** illustrates this process presented here above.

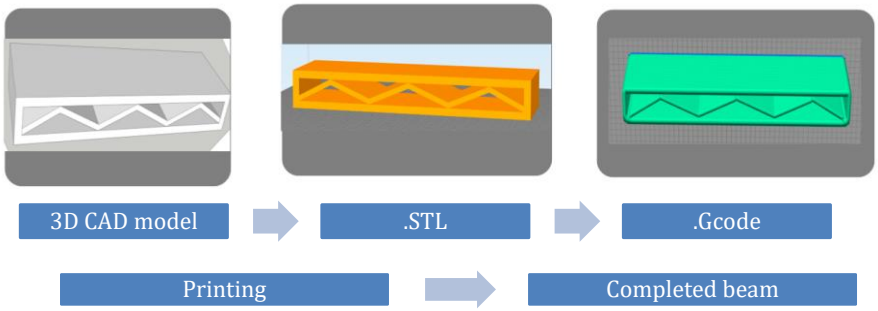

Fig. 5. Steps of the printing process

Printing was carried out in parts according to the design. The printing process is guaranteed according to the steps presented in Figure 5**Hata! Başvuru kaynağı bulunamadı.**. The circular nozzle with an 18 mm diameter was employed to print all beams. The height of each printing layer is 10mm, and the width of filaments ranges from 22mm to 25mm. A total of nine wide beams were printed, as shown in Fig. 6.

a) WB00 and Glass Fiber beams (GB01 to GB04) (from inside to outside)

b) Steel Fiber beams (SB01 to SB04) (from inside to outside)

Fig. 6. Wide beams printed

The extrudability of the dispersed fiber concrete was affected by the ratios of fiber to cement. The extrudability intends to degrade since the fiber ratios increase. There was no jamming during the printing process, but the appearance and quality of the layers printed were affected, as shown in Fig. 6.

5. Experimental Program

5.1 Bending Test Setup

A 3-point bending test was set up for the experimental beams with a nominal length of 1350 mm. Each specimen was supported on roller assemblies to locate the exact supporting point. The linear variable differential transformers (L.V.D.T.) were used to record the deflection based on the applied load. L.V.D.T. was fixed at the mid-section of the beam specimen - under the loading point. The test setup and instrumentations for tested specimens are illustrated in Fig. 7. The procedure for carrying out the test and the loading are certified to comply with T.C.V.N. 9347:2012 [37].

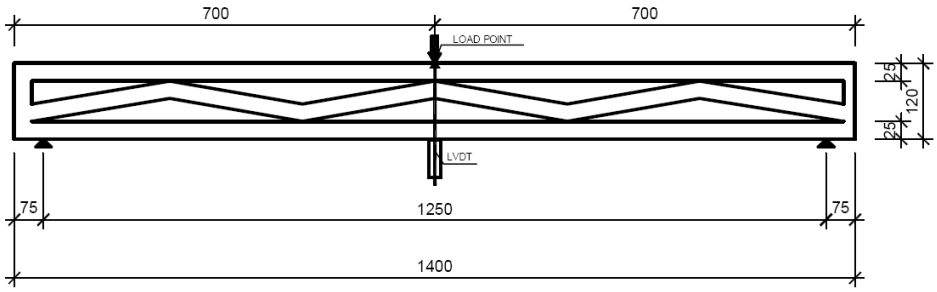

Fig. 7. Flexural test setup

5.2 Compression Test

After the concrete samples printed with 10x10x10 cubes were cast, they were cured in guaranteed humidity conditions. The glass fiber beams were cured according to Requirements for natural moist curing [37]. The beams with steel fibers were cured using a film-forming agent on the concrete surface, and spraying was carried out according to the film-forming agent manufacturer's instructions or covering the beam surface with water-proof materials such as nylon and canvas. Herein, the steel fiber beams were covered with nylon. Then, the procedure for carrying out the test and the loading is certified to comply with TCVN 3118-1993 [38], as shown in Fig. 8.

Fig. 8. Compression test of concrete cube

6. Experimental Results

6.1 Failure Modes

The CB00 beam was a control beam without fiber reinforcement, resulting in brittle failure, as shown in Fig. 9. The results of the failure pattern of glass fiber beams, as shown in Fig. 10, show that sudden failure of concrete printed beams is characteristic of brittle failure form. The presence of dispersed glass fibers did not show a significant increase in the plasticity of concrete. However, the failure mode of the beam GB-2.0 indicates a more spread crack development in the tensile zone of concrete than the others. As captured, all the glass fiber beams were broken after reaching the ultimate load without warning (deformation) due to brittle failure.

(a) Initial state (b) Final state

Fig. 9. The failure mode of CB00

GB-0.5

GB-1.0

GB-1.5

GB-2.0

Fig. 10. The failure mode of Glass fiber beams

SB-0.5

SB-1.0

SB-1.5

SB-2.0

Fig. 11. The failure mode of Steel fiber beams

The results of the failure pattern of steel fiber beams, as shown in Fig. 11, show that sudden failure of SB-0.5 and SB1.0 concrete printed beams is characteristic of brittle failure form due to beams with small steel fiber amounts. The presence of steel fibers smaller than 1% did not show a significant increase in the flexibility of concrete. Beams SB-1.5 and SB-2.0 showed the failure combined with shear failure. A long crack appeared in the middle of the beams and around the support; the beams ended with flexural and shear damage. The

failure modes of SB-1.5 and SB-2.0 can be explained by the fact that concrete at the compression areas reached the compressive strength, but the amount of steel fibers was relatively high, so the moment resistance was higher than the shear strength. It resulted in shear cracks at the support areas, as shown in Fig. 12.

SB-1.5 SB-2.0

Fig. 12. The shear cracks of steel fiber beams

Thanks to the steel fibers that acted as reinforcements compared to traditional beams, none of the steel fiber beams broke after reaching the ultimate load. Another conclusion drawn from these figures and observations of the beam surface after fracture is that there is no delamination between the printed layers. It shows that the adhesion force between the printed layers ensures the overall working of the structure. Moreover, observing the beam surface after failure also indicates the solidity of the printed layers, as shown in Fig. 13.

Fig. 13. The surface fracture of the printed beams

6.2 Load-Bearing Capacity

Based on the results of force measurement, displacement meter, and compression tests, the compressive strength of concrete cubes and the bearing capacity of the beams are calculated, as shown in Table 3. Table 3 and Fig. 14 show that the compressive strengths of the glass fiber concrete cubes (G.B.-) are smaller than those of the control sample (CB00). The optimal amount of glass fiber is 1.0%, but the glass fiber amount did not show significant improvement in compressive strength.

Table 3. Load bearing capacity

Beam label	Concrete compression strength Rn (Mpa)	Ultimate load (kN)	Deflection (mm)
CB00	37.9	4.4	-
GB-0.5	33.4	7.2	-
GB-1.0	37.7	7.6	-
GB-1.5	36.7	6.1	-
GB-2.0	31.3	5.7	-
SB-0.5	39.5	6.3	27.5
SB-1.0	38.9	6.5	48.0
SB-1.5	37.8	6.8	50.4
SB-2.0	35.8	8.7	53.9

The reason is that it is impossible to achieve a consistent distribution of concrete ingredients in the presence of glass fibers. These results corroborate those of other authors [39]. When glass fibers are introduced to reinforced concrete composites, they act as a connecting agent. Distributing stress from glass fibers to the substrate only offers a resistance of samples to crack initiation in terms of interface shear resistance.

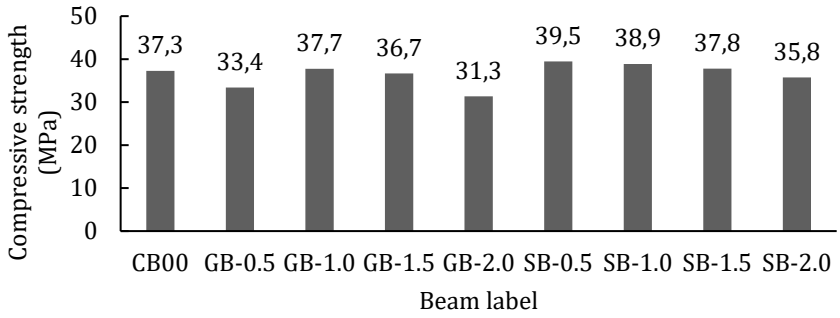

Fig. 14. Effect of fiber on the average compressive strength of concrete

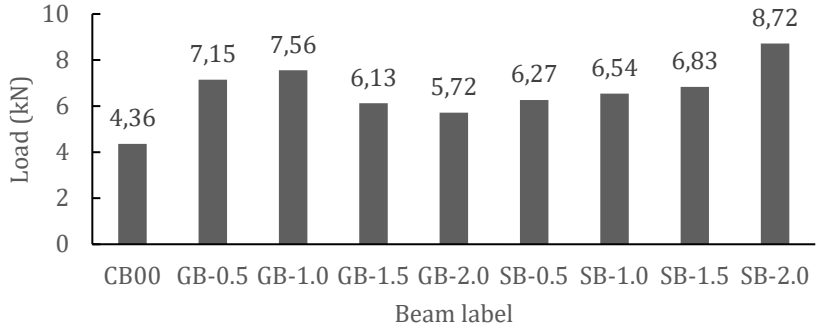

Fig. 15. The flexural capacity of wide beams

Concrete reinforcement using steel fiber changes the concrete's properties, allowing it to endure fracture and enhance its mechanical properties. Compared to the control sample, the compressive strengths of steel fiber concrete cubes are mostly higher, except for SB-2.0. However, the increase in fiber amount decreases compressive strength. These results also corroborate those of other authors [40], [41].

Table 3 and Fig. 15 show that the 1.0% glass fiber reinforced concrete achieved the highest load bearing of 7.56 kN compared to the control sample, which reached 4.36 kN, higher than 73%. The variation in load bearing of glass fiber beams with the increase in glass fiber reinforcement can be similar to that of compressive strength. The flexural capacity with 0.5% glass fiber reinforcement achieved 7.15 kN, and 1.0% achieved the highest flexural capacity of 7.56 kN. Further increase in glass fiber reinforcement dropped the flexural capacity to 6.13 kN and 5.72 kN for 1.5% and 2.0% glass fibers, respectively. However, the flexural capacity achieved by 1.5% and 2.0% glass fiber reinforcement in concrete was higher than the control sample, 41% and 31%, respectively. This is a result of the glass fibers' ability to resist cracking. Considering the influence of glass fiber amount on the flexural capacity and the compressive strength of concrete reinforced with glass fiber, the optimal fiber amount is 1.0%.

Table 3 and Fig. 15 show that the 2.0% steel fiber reinforced concrete achieved the highest load bearing of 8.72 kN compared to the control sample, which completed 4.36 kN. The increase in flexural capacity of steel fiber beams with the rise in steel fiber reinforcement can be seen in contrast to compressive strength. The load bearing of the steel fiber beams increases from 6.27 kN to 8.72 kN, corresponding to the amount of steel fibers from 0.5% to 2.0%. The ultimate load values of the steel fiber beams are much higher than that of the control beam, specifically, 44%, 50%, 57%, and 100% higher corresponding to beam SB-0.5, SB-1.0, SB-1.5, and SB-2.0.

6.3 Deflection and Ductility of The Steel Fiber Wide Beams

The reason is that the beams without fiber (CB00) and the glass fiber beams (G.B.-) were ruptured with minimal recorded deflection. Therefore, the deflection and ductility of the steel fiber-wide beams are presented and analysed in this section. With the load–deflection relationship, it can be seen that steel fiber significantly improves the stiffness and ductility of the printed wide beams. The ductility ratio is called in this study to evaluate the deformation ability of beams under bending. It is expressed in Eq. 1 [42].

$$\mu = \frac{\Delta_u}{\Delta_y} \tag{1}$$

Δy is the yield deflection, and Δu is the deflection when the load falls to 80% of the ultimate load.

K is the bending stiffness defined in Eq. 2 [42].

$$K = \frac{P_{\Delta_y}}{\Delta_y} \tag{2}$$

where P_{Δ_y} is the value of the load at the yield deflection.

Table 4. Ductility ratio and bending stiffness.

Beam label	Δ_y (mm)	Δ_u (mm)	P_{Δ_y}	μ	K (kN/mm)
SB-0.5	6.81	25.5	6.27	3.74	0.92
SB-1.0	6.29	38.7	6.54	6.16	1.04
SB-1.5	6.49	42.8	6.83	6.60	1.05
SB-2.0	8.01	53.9	8.72	6.74	1.09

From the results shown in Table 4, it can be summarized that the bending stiffness increases as the steel-fiber ratio increases. However, the steel fiber amount increases four times while the bending stiffness of the beam SB-2.0 is higher than that of the beam SB-0.5 by only 15.6%. In contrast, the ductility ratios reflect the influence of the steel fiber amount. The ductility ratio is improved 1.8 times since the steel fiber amount increases four times. It can be more clearly seen in the comparison of the load–deflection curves in Fig. 16.

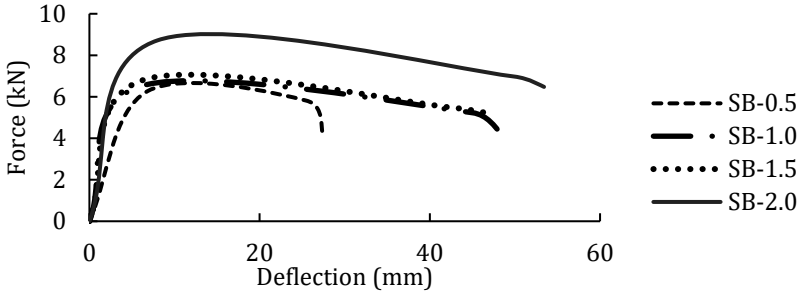

Fig. 16. Load–deflection curves

When reinforced with steel fibers, as the fiber amount in the concrete gradually increases, it dramatically helps effectively restrict the formation, propagation, and widening of cracks. This results in an increase in both flexural strength and ductility. Thanks to the effective bridging action of steel fibers across the cracks, the ductile behavior of the concrete beam was significantly improved. Therefore, this brittle nature of concrete beams, observed with glass fiber beams, is converted into ductile. It results in resist cracking and crack propagation of the printed wide beams. Considering the influence of steel fiber amount on the flexural strength, bending stiffness, ductility, and compressive strength of concrete reinforced with steel fiber, the optimal steel fiber amount ranges from 1.0% to 1.5%.

7. Conclusions

Based on the analysis of the 3-point bending test of nine printed wide beams with dispersed glass and steel fibers reinforced, the results obtained from the study of theory combined with experiment, some conclusions are drawn as follows:

- The girder web of wide beams designed in the style of truss beams was precisely fabricated directly from design files by a printer.
- The extrudability intends to degrade, and the appearance quality of the printed layers was affected since the fiber ratios increased.
- The failure pattern and cracked surfaces of all printed wide beams indicate that the adhesion force between the printed layers ensures the overall working of the structure.
- The failure patterns of glass fiber beams were brittle due to flexural damage.
- Glass fibers did not show significant improvement in compressive strength. The flexural capacity, on the other hand, was significantly enhanced. The increase in flexural strength ranged from 31% to 73%.
- Considering the influence of glass fiber amount on the flexural capacity and the compressive strength of concrete reinforced with glass fiber, the optimal fiber amount is 1.0%.

- The failure patterns of steel fiber beams were ductile due to flexural damage with fiber amounts smaller than 1.5% and flexural combined with shear damage with fiber amounts higher than 1.5%.
- Steel fibers showed slight improvement in compressive strength. However, with the increase in fiber amount, the compressive strength decreases.
- The addition of steel fiber in concrete significantly impacted the flexural strength due to the improvement in the ductility behaviour of concrete. The increase in flexural strength ranged from 44% to 100%.
- Increasing steel fiber contents significantly improved the bending stiffness and ductility of the steel fiber concrete beam. The ductility ratio and bending stiffness are improved 1.8 and 1.2 times, respectively, since the steel fiber amount increases four times.
- The optimum amount of steel fibers ranged from 1.0% to 1.5%, at which the flexural strength and ductility were achieved at a slight reduction of compressive strength.

Acknowledgements

The authors would like to acknowledge the financial support from the National Natural Science Foundation of China (51950410599), the material support from Thanh Hung Concrete Joint Venture Company, and the laboratory support at Haiphong University, Vietnam. The authors especially thank V.I.D.P.O.L. Joint Stock Company for creating the experimental equipment.

References

[1] Sakin M, Kiroglu YC. 3D Printing of Buildings: Construction of the Sustainable Houses of the Future by BIM. Energy Procedia. 2017 Oct;134:702-711. https://doi.org/10.1016/j.egypro.2017.09.562

[2] Alawneh M, Matarneh M, El-Ashri S. The World's First 3D-Printed Office Building in Dubai. 2018 Pci/Nbc. 2018. [Online]. Available: https://www.pci.org/PCI_Docs/Convention-Papers/2018/32_Final_Paper.pdf

[3] Yazdani Sarvestani H, Akbarzadeh AH, Niknam H, Hermenean K. 3D printed architected polymeric sandwich panels: Energy absorption and structural performance. Compos. Struct. 2018; 200 (November): 886-909. https://doi.org/10.1016/j.compstruct.2018.04.002

[4] Paul SC, van Zijl GPA, Gibson I. A review of 3D concrete printing systems and materials properties: current status and future research prospects. Rapid Prototyp. J. 2018;24(4):784-798. https://doi.org/10.1108/RPJ-09-2016-0154

[5] Rehman AU, Kim JH. 3D concrete printing: A systematic review of rheology, mix designs, mechanical, microstructural, and durability characteristics. 2021;14(14). https://doi.org/10.3390/ma14143800

[6] Hou S, Duan Z, Xiao J, Ye J. A review of 3D printed concrete: Performance requirements, testing measurements and mix design. Construction and Building Materials. 2021 Mar;273:121745. https://doi.org/10.1016/j.conbuildmat.2020.121745

[7] D.V.S.K CD, Satish Kumar Ch N. A review on concrete's rheological properties. World J. Eng. 2022;February. https://doi.org/10.1108/WJE-02-2022-0069

[8] Mechtcherine V, Nerella VN, Will F, Näther M, Otto J, Krause M. Large-scale digital concrete construction - CONPrint3D concept for on-site, monolithic 3D-printing. Autom. Constr. 2019 Nov;107:102933. https://doi.org/10.1016/j.autcon.2019.102933

[9] Pham TL, Zhuang XJ, Nguyen THT, Nguyen PA, Trinh DT, Do TQ. 3D printable concrete: Mixture design and laboratory test methods. Minist. Sci. Technol. Vietnam. 2023 Mar;65(1):3-8.

[10] Kothman I, Faber N. How 3D printing technology changes the rules of the game Insights from the construction sector. J. Manuf. Technol. Manag. 2016;27(7):932-943. https://doi.org/10.1108/JMTM-01-2016-0010
[11] Olsson NOE, Shafqat A, Arica E, Økland A. 3d-printing technology in construction: Results from a survey. Emerald Reach Proc. Ser. 2019;2:349-356. https://doi.org/10.1108/S2516-285320190000002044
[12] Xiao J, et al. Large-scale 3D printing concrete technology: Current status and future opportunities. Cem. Concr. Compos. 2021;122(April):104115. https://doi.org/10.1016/j.cemconcomp.2021.104115
[13] Hosen MA, Shammas MI, Shill SK, Al-Deen S, Jumaat MZ, Hashim H. Ductility Enhancement of Sustainable Fibrous-Reinforced High-Strength Lightweight Concrete. Polymers (Basel). 2022 Feb;14(4):727. https://doi.org/10.3390/polym14040727
[14] Althoey F, et al. Behavior of Concrete Reinforced with Date Palm Fibers. Materials (Basel). 2022 Nov;15(22):7923. https://doi.org/10.3390/ma15227923
[15] Hakeem IY, et al. Effect of thermal cycles on the engineering properties and durability of sustainable fibrous high-strength concrete. Front. Mater. 2023 Jan. https://doi.org/10.3389/fmats.2023.1094864
[16] Mohod MV. Performance of Polypropylene Fibre Reinforced Concrete. IOSR J. Mech. Civ. Eng. 2015;12(1):28-36.
[17] Pham L, Tran P, Sanjayan J. Steel fibres reinforced 3D printed concrete: Influence of fibre sizes on mechanical performance. Constr. Build. Mater. 2020;250:118785. https://doi.org/10.1016/j.conbuildmat.2020.118785
[18] Balsamo A, Coppola L, Zaffaroni P. FRP in Construction: Applications, Advantages, Barriers and Perspectives. Composites in Construction. 2001;58-64. https://doi.org/10.1061/40596(264)7
[19] Lim S, Buswell RA, Le TT, Austin SA, Gibb AGF, Thorpe T. Developments in construction-scale additive manufacturing processes. Autom. Constr. 2012 Jan;21:262-268. https://doi.org/10.1016/j.autcon.2011.06.010
[20] Liu M, Zhang Q, Tan Z, Wang L, Li Z, Ma G. Investigation of steel wire mesh reinforcement method for 3D concrete printing. Arch. Civ. Mech. Eng. 2021 Mar;21(1):24. https://doi.org/10.1007/s43452-021-00183-w
[21] Gifta CC, Bharathi LMV, Vimal A. Flexural behaviour of ferrocement septic tank wall panels reinforced with glass fibers. Mater. Today Proc. 2021;47:6664-6669. https://doi.org/10.1016/j.matpr.2021.05.109
[22] Li Z, Wang L, Ma G, Sanjayan J, Feng D. Strength and ductility enhancement of 3D printing structure reinforced by embedding continuous micro-cables. Constr. Build. Mater. 2020 Dec;264:120196. https://doi.org/10.1016/j.conbuildmat.2020.120196
[23] Han X, Yan J, Liu M, Huo L, Li J. Experimental study on large-scale 3D printed concrete walls under axial compression. Autom. Constr. 2022;133(October 2021):103993. https://doi.org/10.1016/j.autcon.2021.103993
[24] Ding T, Xiao J, Zou S, Yu J. Flexural properties of 3D printed fibre-reinforced concrete with recycled sand. Constr. Build. Mater. 2021;288:123077. https://doi.org/10.1016/j.conbuildmat.2021.123077
[25] Ding T, Xiao J, Zou S, Zhou X. Anisotropic behavior in bending of 3D printed concrete reinforced with fibers. Compos. Struct. 2020;254(February):112808. https://doi.org/10.1016/j.compstruct.2020.112808
[26] Infant Alex X, Arunachalam K. Flexural behavior of fiber reinforced lightweight concrete. Rev. la construcción. 2019;18(3):536-544. https://doi.org/10.7764/RDLC.18.3.536
[27] Dasari S, Lohani S, Sumit Dash S, Omprakash Fulmali A, Kumar Prusty R, Chandra Ray B. A novel study of flexural behavior of short glass fibers as secondary reinforcements in GFRP composite. Mater. Today Proc. 2021;47:3370-3374. https://doi.org/10.1016/j.matpr.2021.07.161

[28] Martínez-Pérez I, Valivonis J, Šalna R, Cobo-Escamilla A. Experimental study of flexural behaviour of layered steel fibre reinforced concrete beams. J. Civ. Eng. Manag. 2017;23(6):806-813. https://doi.org/10.3846/13923730.2017.1319413
[29] Pesaran Behbahani H, Nematollahi B, Rahman A, Sam M, Lai FC. Flexural Behavior of Steel-Fiber-Added-Rc (Sfarc) Beams With C30 and C50 Classes of Concrete. Int. J. Sustain. Constr. Eng. Technol. 2012;3(May 1998):2180-3242.
[30] Zhu B, Pan J, Nematollahi B, Zhou Z, Zhang Y, Sanjayan J. Development of 3D printable engineered cementitious composites with ultra-high tensile ductility for digital construction. Mater. Des. 2019;181:108088. https://doi.org/10.1016/j.matdes.2019.108088
[31] Weng Y, Li M, Tan MJ, Qian S. Design 3D printing cementitious materials via Fuller Thompson theory and Marson-Percy model. Constr. Build. Mater. 2018;163:600-610. https://doi.org/10.1016/j.conbuildmat.2017.12.112
[32] Manikandan K, Wi K, Zhang X, Wang K, Qin H. Characterizing cement mixtures for concrete 3D printing. Manuf. Lett. 2020;24:33-37. https://doi.org/10.1016/j.mfglet.2020.03.002
[33] Kazemian A, Yuan X, Cochran E, Khoshnevis B. Cementitious materials for construction-scale 3D printing: Laboratory testing of fresh printing mixture. Constr. Build. Mater. 2017;145:639-647. https://doi.org/10.1016/j.conbuildmat.2017.04.015
[34] Hamidi F, Aslani F. Additive manufacturing of cementitious composites: Materials, methods, potentials, and challenges. Constr. Build. Mater. 2019;218:582-609. https://doi.org/10.1016/j.conbuildmat.2019.05.140
[35] Lu B, et al. A systematical review of 3D printable cementitious materials. Constr. Build. Mater. 2019;207:477-490. https://doi.org/10.1016/j.conbuildmat.2019.02.144
[36] Pham LT, et al. Development of 3D printers for concrete structures: mix proportion design approach and laboratory testing. Smart Sustain. Built Environ. 2022 Aug. https://doi.org/10.1108/SASBE-07-2022-0137
[37] TCVN 9347:2012, "Cấu kiện bê tông và bê tông cốt thép đúc sẵn - phương pháp thí nghiệm gia tải để đánh giá độ bền, độ cứng và khả năng chống nứt (Reinforced concrete and prefabricated concrete building products - Loading test method for assenssment of strengthe, rigidity." Bộ Xây dựng, 2012.
[38] TCVN 3118:1993, "Bê tông nặng - Phương pháp xác định cường độ nén (Heavyweight concrete - Method for determinatien of compressive strength)," Bộ Xây dựng. pp. 2-6, 1993.
[39] Ahmad J, González-Lezcano RA, Majdi A, Ben Kahla N, Deifalla AF, El-Shorbagy MA. Glass Fibers Reinforced Concrete: Overview on Mechanical, Durability and Microstructure Analysis. Materials (Basel). 2022 Jul;15(15):5111.
[40] Jhatial AA, Sohu S, Bhatti NK, Lakhiar MT, Oad R. Effect of steel fibres on the compressive and flexural strength of concrete. Int. J. Adv. Appl. Sci. 2018;5(10):16-21.
[41] Sinha D, Verma A. Investigation on the Effect of Varying Dosages of Steel Fibre on the Strength and Workability Properties Of High Strength Concrete. 2018;1:352-346.
[42] Xiao JZ, Pham TL, Wang PJ, Gao G. Behaviors of semi-precast beam made of recycled aggregate concrete. Struct. Des. Tall Spec. Build. 2014 Jun;23(9):692-712. https://doi.org/10.1002/tal.1071

Research on Engineering Structures & Materials
www.jresm.org
MIM Research Group

Research Article

Characterization of thin ITO/Au/ITO sandwich films deposited on glass substrates using DC magnetron sputtering

Tarek Saidani[1,a], Mohammed Rasheed[*2,3,b], Iqbal Alshalal[4,c], Arshad Abdula Rashed[5,d], Mohammed Abdelhadi Sarhan[6,e], Regis Barille[3,f]

[1]*Physics of Materials and Optoelectronic Components Laboratory, Faculty of Sciences and Applied Sciences, Akli Mohaned Oulhadj University of Bouira, Bouira, 10000, Algeria*
[2]*Applied Sciences Department, University of Technology- Iraq, Baghdad, Iraq*
[3]*MOLTECH Anjou, Universite d'Angers/UMR CNRS 6200, 2, Bd Lavoisier, 49045 Angers, France*
[4]*Training and Workshops Center, University of Technology- Iraq, Baghdad, Iraq*
[5]*Production Department, Ministry of Oil, Baghdad, Iraq*
[6]*Mathematics Science Department, College of Science, Mustansiriyah University, Baghdad, Iraq*

Article Info

Article history:

Received 22 Sep 2023
Accepted 27 Nov 2023

Keywords:

D.C. magnetron sputtering;
ITO/Au/ITO structure;
Spectrophotometer;
Spectroscopic ellipsometry;
SEM;
AFM

Abstract

The correlation between structural and optical properties of an Au, ITO, and ITO/Au/ITO (IUI), gold, indium tin oxide, and indium tin oxide/gold/indium tin oxide, respectively, sandwich structure thin film has been reported in this study. The deposition of all samples onto glass substrates was carried out using D.C. magnetron sputtering, without the use of substrate heating, and the intermediate layer was a metallic gold film with an 8 nm thickness. The substrate-target distance in the IUI structure was kept constant at 8 nm. X-ray diffraction (XRD), atomic force microscopy (AFM), and scanning electron microscopy (SEM) are often utilized techniques for the evaluation of the structural and surface morphology of films. The optical properties of the films were demonstrated by a spectrophotometer (UV/vis/NIR) and spectroscopic ellipsometry (SE) techniques adopted for the new amorphous model, and the findings were compared with those between 200 and 2200 nm, where the wavelengths overlap at room temperature, which is the purpose of the present work. The observed and estimated optical constant values of the Au, ITO, and IUI films using the best dispersion model were reported. In addition, the transmission and reflection spectrum results of the films were compared with those obtained by UV measurements. Excellent correlations for the optical constant properties of the multilayer films were observed employing two distinct approaches. These thin films have great promises for the future of transparent conductive oxides (TCOs) and even industrial applications.

1. Introduction

Transparent conducting oxides (TCOs) have favorable electrical conductivity that is similar to that of metals and good optical transmission in the visible region. Examples of TCOs that are gallium-doped are zinc oxide (ZnO), tin oxide (SnO_2), aluminum-doped zinc oxide (AZO), gallium-doped zinc oxide (GZO), fluorine-doped tin oxide (FTO), indium tin oxide (ITO), etc. TCOs refer to a class of semiconductors that exhibit both n and p- type conductivity. These materials possess a broad optical bandgap and a significant number of free electrons in the upper conduction band (CB). Due to the unique properties of ITO thin

*Corresponding author: rasheed.mohammed40@yahoo.com
[a] orcid.org/0000-0002-7727-4734; [b] orcid.org/0000-0002-0768-2142; [c] orcid.org/0000-0003-0948-7460; [d] orcid.org/0009-0004-8179-6190; [e] orcid.org/0000-0002-7011-6581; [f] orcid.org/0000-0001-8792-5118
DOI: http://dx.doi.org/10.17515/resm2023.21ma0922rs

films, ITO electrodes made of transparent conducting oxide have a high transmission over the visible spectrum, which is a property of thin films. Wide optical band gap semiconductors with good electrical conductivity have been widely utilized as transparent conductor electrodes for several electronic devices, like organic light-emitting diodes (OLEDs), solar cells, flat panel displays, gas sensors, liquid crystal devices, and touch screens, are often utilized in modern technology [1–7]. In recent years, to coat high-quality ITO thin films, different researchers have investigated the many advantages of using the direct-current magnetron sputtering technique to coat ITO/metal/ITO sandwich structures with Ag or Au interlayers to enhance the structural, surface morphology, and optical characteristics of the films [8]. The major advantages of using this technique are that it is low-cost, the substrate temperature is 300 K, uniform films have been obtained, and the power source is easy to control. As transparent conducting oxide thin films, ITO, FTO, or ZnO:Al (AZO) single-layer thin films formed on glass substrates have been the most common kind utilized up to this point. In recent years, the requirement for and application of TCOs with great performance have increased continuously. At the moment, ITO and fluorine tin oxide (FTO) seem to be the most promising commercial materials for transparent electrodes. There are a large number of researchers advancing the properties of TCO thin films and amended materials [9–11]. Yet, because of its scarcity on Earth and its high price, indium is not widely utilized, leading the research community to look for other materials with equivalent quantities in terms of electrical and optical characteristics. ITO thin films typically vary in thickness from 150 nm to 700 nm when utilized as a topic of interest is to the transparent electrodes (TCs) associated with optoelectronic devices. The decreasing in film's thickness below 150 nm leads to a significant increase in electrical resistance due to the well-known size effect. Oxide, metal, and oxide films have properties that are mightily dependent on the intermediate layer [12]. Using sandwich structures made of oxide, metal, and oxide to create transparent electrodes has various benefits.

One benefit of using ITO is that the amount of indium is reduced by reducing the thickness of the films' thickness from 150 nm to a total of 50–60 nm for both oxide layers. If we consider the topic of electrical conductivity simultaneously, the optical quantities of the electrode are absolutely preserved and even enhanced. Many studies prove that this type of thin film has very good mechanical properties for wide-scale implementation [13–17]. Until now, researchers have been searching for a substitute for transparent conductive thin films for the alternation of ITO through various experimental tests. Spectroscopic ellipsometry is an indirect, very accurate, non-destructive, non-invasive, non-contact, and very sensitive method for studying single- and multi-layer films. SE gives a method that anyone can use to figure out the exact optical constants and electrical transport properties of single and sandwich films [18–25]. Spectroscopic ellipsometry (SE) is an optical metrology technique that is both non-destructive and non-intrusive, providing surface sensitivity. It involves measuring the change in the polarization state of light when it is reflected at an oblique angle from a thin-film sample. It is frequently used to examine the thickness and optical constants of single- and multilayer thin films [26-30]. A variety of thin film applications, including semiconductors, solar, optoelectronics, optical and functional coatings, surface chemistry, and biotechnology, can be achieved using spectroscopic ellipsometry in conjunction with the robust and user-friendly DeltaPsi2 software, accessories, and equipment [31-57].

The ITO/Au/ITO (IUI) multilayer structure thin film studied in this paper was made by direct-current magnetron sputtering using Au as the intermediate thin film on a glass substrate. The optical properties of each layer in the sandwich structure were studied using UV spectrophotometer and spectroscopic ellipsometry in the same wavelength region for each technique. This methodology enables a more precise determination of the optimal dispersion formula for each individual layer.

2. Experimental Details

A direct-current sputtering process was utilized to prepare (IUI) ultra-thin films on glass substrates without any heating. These materials were deposited in a reactive atmosphere utilizing In:Sn (purity: 90, 10)% and gold (purity: 99.95%) targets, respectively. The gold-intermediated thin film was deposited in an argon atmosphere. Glass slides, 75–50 mm in diameter, from TED PELLA INC. were cut into 2.5–2 cm plates with a thickness of 1.1 mm and utilized as substrates in the present work. Glass plates were cleaned carefully in an ultrasonic bath treatment type (BRANSON Ultrasonic-CAMDA 19 SPC) with ethanol, acetone, deionized water, and finally dichloromethane. Each solution was kept for 20 minutes and dried with a nitrogen gas jet. Then, the glass substrate was placed in a vertical shape according to the target substrate configuration onto a rotating disk kept at ambient temperature. The distance between the target and substrate was kept at about 70 mm, and the parameters of the deposition of Au, ITO, and IUI thin films are presented in Table 1. These parameters are similarly used in the literature pointed in this table.

The target-to-substrate distance was (70 mm) in many reasons:

- The target-to-substrate distance plays a critical role in sputtering processes. A longer distance can result in a more focused deposition area, whereas a shorter distance can lead to a broader deposition area.
- In this case, a target-to-substrate distance of 70 mm may have been chosen for several reasons:
    - Adequate Coverage: A longer distance can help ensure that the sputtered particles have a relatively uniform distribution over the glass substrate, covering a larger area.
    - Minimizing Backscattering: Longer distances can reduce the likelihood of backscattered particles from the target reaching the substrate, which can lead to contamination or inconsistent film properties.
    - Specific Film Thickness: Depending on the desired film thickness, the distance might be adjusted to achieve the target thickness effectively.

2.1. Deposition Current (0.3 A)

- Deposition current controls the sputtering rate. The higher the current, the faster the deposition rate.
- Selection of a deposition current of 0.3 A may be based on the desired film growth rate, the target material's sputtering characteristics, and power supply limitations.
- Justification:
    - Film Thickness Control: A lower deposition current allows for more precise control over film thickness, which is essential when aiming to create ultra-thin films.
    - Reduced Heat Generation: Lower current can also help minimize heat generation during the sputtering process, which aligns with the statement that no heating was applied.
    - Target Material Compatibility: The deposition current should be set within the limits that ensure efficient sputtering of the target material without overheating or damaging it.

2.2 Pressure Variation

- Pressure within the sputtering chamber affects the sputtering process in various ways.
- In the absence of specific information, the pressure may have been varied for the following reasons:
  - Sputtering Rate: Pressure can influence the sputtering rate. Higher pressures can increase the sputtering rate, while lower pressures might yield slower rates.
  - Film Density and Structure: Pressure can impact the density and structure of the deposited film. Higher pressures can result in denser films, while lower pressures may lead to more porous films.
  - Target Erosion and Deposition Uniformity: Pressure can affect the erosion rate of the target material and the uniformity of film deposition.

Without specific details about the pressure variations used, it's challenging to provide a precise explanation or justification. Pressure adjustments are typically made to optimize the sputtering process for the specific properties of the target material, the desired film characteristics, and the equipment's capabilities.

In summary, the choice of target-to-substrate distance and deposition current in the sputtering process depends on factors such as film thickness control, heat generation, and target material compatibility. Pressure variations are made to optimize the process for specific film properties and equipment capabilities. The specific values chosen would depend on the experimental requirements and equipment specifications. After deposition, the film's thickness of single and multilayers was predicted via two methods: surface profilometer type (Dektak 6M-Veeco Metrology L.L.C.) and spectroscopic ellipsometry (SE); thus, the total thickness of the single and triple thin films is shown in Table 2.

The crystal structures of the samples were elucidated by the use of X-ray diffraction (XRD) analysis at 2θ geometry scan mode with ($Cu\ K\alpha radiation, 40\ mA, 40\ KV, \lambda = 1{,}5406\ A°$) as the incident radiation (Brucker-AXXS, D8 Advance diffractmeter). The XRD spectrum of all thin films did not present any peak at 2θ diffraction angles from (0o - 80o), Demonstrating the amorphous nature of the films. The surface morphology was investigated utilizing a scanning electronic microscope (SEM, JEOL), and surface average roughness investigations of the thin layers were achieved on 1×1 μm2 sample with a tapping mode atomic force microscope (AFM, Thermomicroscope Autoprobe LP Research) under ambient conditions.

Optical properties, including the transmittance, reflectance, and absorption spectra of the ITO and IUI films, were performed by spectrophotometer mode (PerkinElmer Lambda 950 (UV/Vis/NIR)) and spectroscopic ellipsometry (SE) at room temperature in the wavelength ranges (200–2200) nm. The film's optical constants on a glass substrate which were investigated via the ellipsometry parameters's analysis, ψ, Δ , which were examined via a non-rotating phase modulation technology (UVISEL Plus, FUV-NIR- 50 kHz, Horiba Jobin Jvon ellipsometry). SE provides thickness and optical constants (n, k) of isotopic, anisotopic, and graded films, in addition to derived optical data such as absorption coefficient α and the optical band gap E_g of the samples. The spectra of ψ and Δ in the wavelength region 200-2200 nm were examined at a 70o angle of incidence at ambient temperature. The films' findings for optical constants were compared with results obtained from spectrophotometer. The measurement provides the complex refractive index ratio ρ, and the relation between standard ellipsometric parameters ψ, Δ and ρ are given by [21-23].

$$\psi = \frac{tan^{-1}\,\rho}{e^{i\,\Delta}} \quad or\ \psi = \frac{\left|\frac{r_p}{r_s}\right|}{e^{i\Delta}} = \frac{|r_p|}{|r_s| + e^{i\Delta}} \tag{1}$$

where r_p and r_s are the complex reflection coefficients (Fresnel reflection coefficients), for parallel and perpendicular polarization to the plane of incidence, ψ (amplitude ratio) over the full range [0-90o] and ($\Delta = \delta_p - \delta_s$, phase shift difference) over the full range [0-360°] are the ellipsometric angles.

Table 1. Deposition parameters of ITO and Au films

Thin film	Atmosphere conditions	Target-glass distance (mm)	Deposition current (A)	Pressure (Pa)	Deposition time (sec)	Target composition (wt%)	Deposition rate (nm/min)	Refs
ITO	Reactive atmosphere	70	0.3	2	240	In 90%, Sn 10%	12	This work
Au	Argon atmosphere	70	0.3	1	14	Au 100%	30	
ITO	Reactive atmosphere	70	0.3	2	240	In 90%, Sn 10%	12	
ITO	Ar + O_2 gaz mixture	100	-	3×10^{-1}	-	In_2O_3 90%, SnO_2 10%	-	[58]
Au	Argon atmosphere	100	-	1×10^{-1}	-	Au 100%	-	
ITO	Ar + O_2 gaz mixture	100	-	3×10^{-1}	-	In 90%, Sn 10%	-	
ITO	Ar + O_2 gaz mixture	70	-	2×10^{-1}		In_2O_3 90 %, SnO_2 10%	9.6	[59]
Cu	Argon atmosphere	70	-	1×10^{-1}	1020	Cu 100%	6.6	
ITO	Ar + O_2 gaz mixture	70	-	2×10^{-1}		In_2O_3 90 %, SnO_2 10%	9.6	
TiO_2	Ar + O_2 gaz mixture	100	-	3.1×10^{-1}	-		15	[60]
Au	Argon atmosphere	100	-	2×10^{-1}	-	Au 100%	25	
TiO_2	Ar + O_2 gaz mixture	100	-	3.1×10^{-1}	-		15	
ITO	Ar + O_2 gaz mixture	-	-	-	360 - 480	In_2O_3 90 %, SnO_2 10%	-	[61]
Au	Argon atmosphere	-	-	-	0 - 15	Au 100%	-	
ITO	Ar + O_2 gaz mixture	-	-	-	0 - 480	In_2O_3 90 %, SnO_2 10%	-	

Table 2. The film thickness values obtained via the use of both a Dektak 6M and an ellipsometer

Samples on glass substrates	Profilometer	Ellipsometer
	Thickness (nm)	
ITO film top layer	20.023±0.16	20.872±0.232
Au film	8.551±0.15	8.012±0.011
ITO film bottom layer	20.023±0.16	20.872±0.232
ITO/Au/ITO	48.597±0.25	49.756±0.443

3. Results and Discussion

3. 1. Structural and Morphological Characterization

The XRD results of deposited films appeared amorphous; ITO as-deposited films by the magnetron sputtering technique at temperatures below 150 oC are often amorphous [24–25]. Fig. 1 shows two- and 3-D AFM images of the as-deposited Au, ITO, and multilayer ITO thin films. The spots of ITO clusters with smooth surfaces are dispersed individually on the surface of the ITO ultrathin layer, while the metallic interlayer thin film thickness is insufficient to completely cover the first layer's surface. The as-deposited sandwich layers presented an average surface roughness (RMS) as presented in Table 3, which shows the root mean square (RMS) and average roughness (RA) values of Au, ITO, and IUI thin films on a glass substrate. In literature the values of RMS and RA is reported in this Table.

Table 3. Summary of the root mean square (RMS) and average roughness values (RA) of the Au interlayer and IUI sandwich structure deposited on glass substrate.

Samples	Roughness of the thin layer [nm]			Refs
	Film's thickness [nm]	Glass substrate		
Substrate		RMS (nm)	RA (nm)	
Au	8±0.15	9.5514	7.2578	This work
ITO	20±0.16	5.7416	4.247	This work
IUI	20/8/20±0.25	0.5673	0.4521	This work
ITO/Au/ITO	100	0.65		[58]
ITO/Cu/ITO	165	-	-	[59]
ITO/Au/ITO	100		-	[60]
ITO/Au/ITO	116.2	1.05 -2.27	-	[61]
ITO/Au/ITO	100	3.39 ±0.60	-	[62]
ITO/Au/ITO	105-115	1.83- 2.57	-	[63]
TiO_2/metal/TiO_2	2- 20	1.05 -2.27	-	[64]

2D **3D**

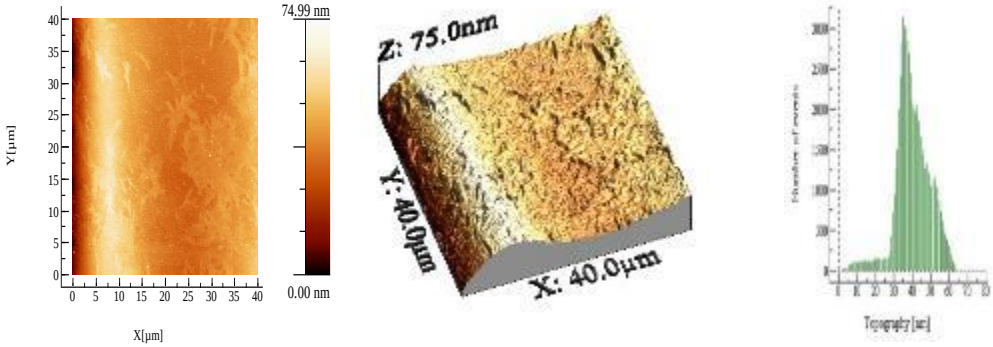

Au-RMS=9.5514 nm Au-Roughness average =7.2578 nm

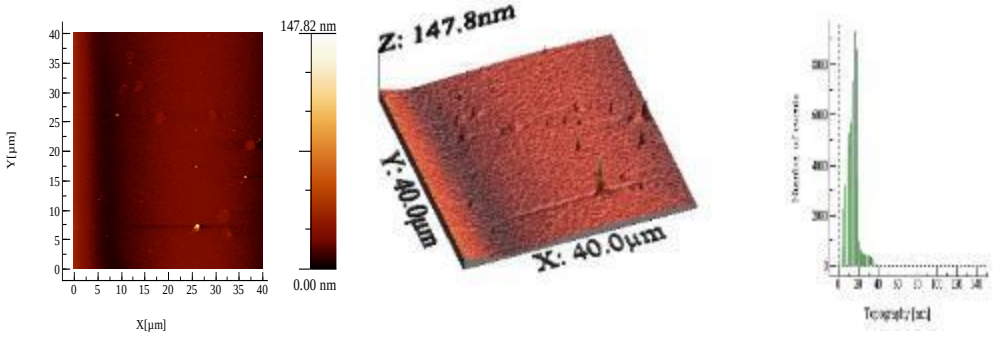

ITO-RMS=5.7416 nm ITO-Roughness average =4.247 nm

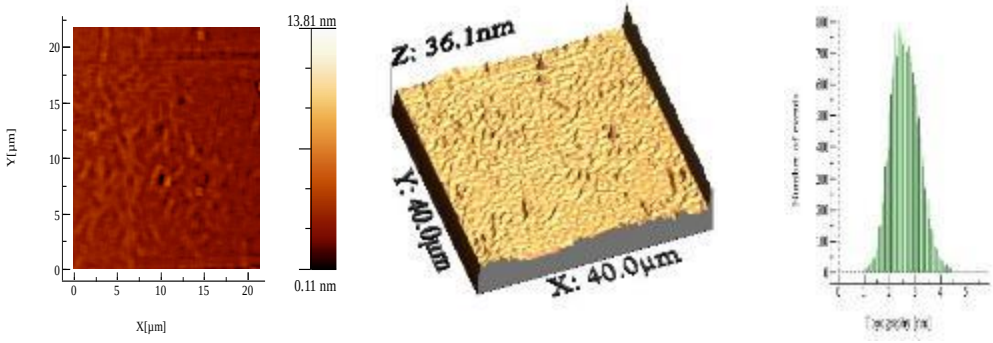

IUI-RMS=0.5673 nm IUI-Roughness average=0.4521 nm

Fig. 1. AFM images of Au, ITO and IUI multilayer films on glass substrates

The surface roughness improvement observed in the ITO/Au/ITO thin films, as compared to the individual Au and ITO layers, can be attributed to various mechanisms. The thickness of each layer plays a crucial role in the overall behavior of the multilayer structure. Here's an explanation based on the provided thickness values:

- Smoothing Effect of Multilayer Structure: The key mechanism behind the significant reduction in surface roughness in the ITO/Au/ITO thin films is the smoothing effect of the multilayer structure. This effect becomes more pronounced as you increase the thickness of the entire stack (50 nm) compared to the individual layers (8 nm for Au and 20 nm for ITO top and down layers). The multilayer structure essentially averages out the roughness contributions from each layer.
- Interlayer Adhesion and Stress Relief: As the thickness of the multilayer structure increases, interlayer adhesion between the ITO and Au layers is enhanced, reducing the presence of interfacial defects. Additionally, any built-up stress or strain within the individual layers can be more effectively accommodated within the thicker structure, resulting in less surface roughness.
- Increased Number of Interfaces: The ITO/Au/ITO thin film structure has more interfaces compared to the individual layers. These interfaces can act as barriers that disrupt the propagation of surface irregularities, contributing to smoother surfaces.
- Grain Size and Texture Evolution: With a thicker multilayer structure, the interaction between the layers may lead to changes in grain size and texture. The accumulation of more layers can result in a more uniform surface, reducing roughness.
- Optimized Thickness: The thickness of the individual layers and the total thickness of the stack can be optimized for surface quality. In your case, the choice of 8 nm for Au and 20 nm for ITO layers, totaling 50 nm, appears to provide the optimal balance for reducing surface roughness.
- Post-Deposition Treatments: Any post-deposition treatments or annealing processes may have been tailored to the multilayer structure to promote grain growth and surface smoothing.
- Surface Energy Minimization: The thicker multilayer structure may further minimize surface energy, leading to a smoother and more stable surface.
- Layer Thickness and Order: The layer thickness and order in the stack are critical for achieving the desired surface quality. In this case, the optimized thickness and order of the layers contribute to the reduced roughness. The roughness measurements for the Au, ITO, and IUI thin films were conducted over a total length of [10 µm to 20 µm] during the characterization process. The position of the roughness measurement was consistently taken across the entire surface of each film, ensuring a comprehensive assessment of the surface morphology.

For the Au film, with a thickness of 8±0.15 nm, the RMS (Root Mean Square) and RA (Roughness Average) values were determined to be 9.5514 nm and 7.2578 nm, respectively. The roughness measurements were obtained by scanning the film's surface along the specified total length, providing a representative analysis of the film's topography.

Similarly, for the ITO film, with a thickness of 20±0.16 nm, the RMS and RA values were measured as 5.7416 nm and 4.247 nm, respectively. The roughness assessment covered the entire length of the film's surface, ensuring a comprehensive understanding of its morphology.

In the case of the IUI film, with a layered structure of 20/8/20±0.25 nm, the RMS and RA values were found to be 0.5673 nm and 0.4521 nm, respectively. The roughness measurements for the IUI film were conducted across the specified total length, providing insights into the surface characteristics of the multilayered structure.

It's important to note that the total length of measurement and the position of measurement were standardized across all films to maintain consistency and enable a meaningful comparison of the roughness values. These measurements contribute to a comprehensive characterization of the film's surface morphology and play a crucial role in understanding the impact of the deposition process on the structural properties of each thin film.

Fig. 2 shows SEM images of the as-deposited Au, ITO, and IUI thin films. The ITO and IUI thin films are amorphous, so in SEM images, the ITO and IUI films are almost identical to one another. Some grain growth was observed on the film's surface, according to the XRD analyses. The images in Fig. 2 (a), (b), and (c), illustrate the Au, ITO, and IUI thn films. SEM magnification and HV for the image in Figure 5 (a), (b), and (c) are (SEM MG=2000 kx, HV=1500 kV, WD=28.53 mm), (MG=600.34 kx, HV=2000 KV, WD=28.32 mm) and (MG=1000 kx, HV=2100 KV, WD=21.89 mm) for 50 μm, respectively.

Au

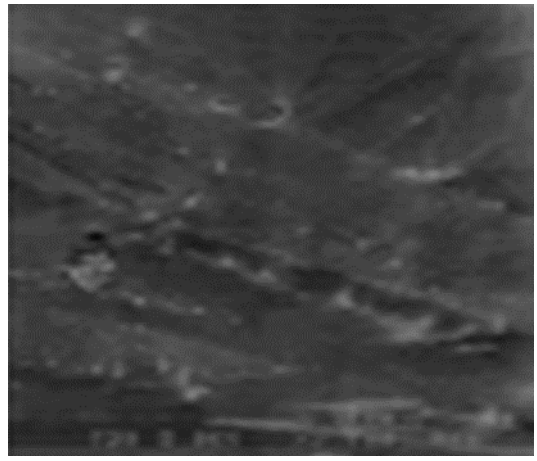

(a)

ITO

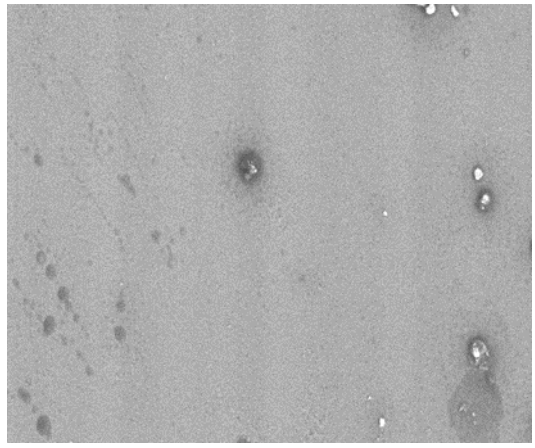

(b)

ITO/Au/ITO

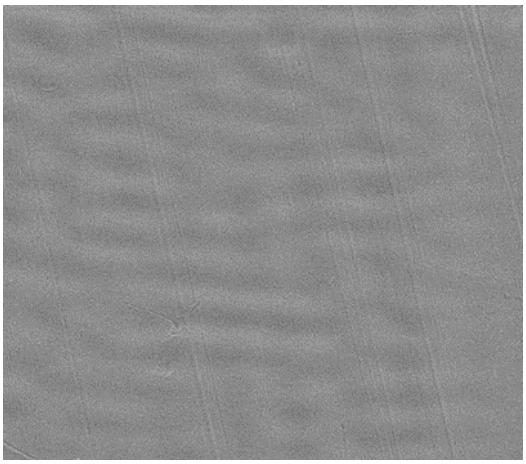

(c)

Fig. 2. SEM micrographs of (a) Au, (b) ITO, and (c) (IUI) thin films on glass substrates

3. 2. Optical Characterization Measurements

3. 2. .1 Spectrophotometry and Ellipsometry Studies

Fig. 3 presents the optical transmission, reflection, and absorptivity spectra measurements for Au and IUI multilayers on glass substrates with relation to wavelength in the 200–2200 nm wavelength range. As one can see, bare glass substrates, Au, and IUI films consisting of glass substrates have 96%, 69%, and 93% optical transmittance at 550 nm, respectively. The average visible transmittance of ITO and IUI films on glass substrates is 85.6% and 93%, respectively; on the other hand, it is around 92.4% and 88.5%, as well as 43% and 27.9% in the near IR and UV regions, respectively. The optical reflectance of the films was around (11.9%, 10.7%), (9.6%, 5.5%), and (6%, 8%) in the UV, VIS, and NIR regions, respectively, but the absorptance of the films in the same regions was (44.7%, 61.3%), (4.72, 5.6%), and (1.4%, 8%), respectively. The optoelectrical characterization of the films exhibited a significant dependence on the thickness of the Au layer; however, the transmittance of the material may vary based on the wavelength; this occurrence may be concerned with the optical properties of Au film. The determination of the absorption coefficient of gold (Au) involves the analysis of interband electronic transitions, which refer to the process of exciting electrons from the low energy band to the Fermi band. The absorption coefficient of Au film is high in the longer wavelength of about $4.9925\times10^{+5}$ cm^{-1} near the red part of the visible region (not shown here); nevertheless, the transmittance of IUI sandwich thin films decreases with the higher absorption coefficient of Au in the UV spectrum, while the transmittance increases in the other two regions. The higher carrier concentration seen in the IUI films, as compared to the ITO films, may be ascribed to the presence of a high carrier concentration in the intermediate metallic layer (Au) deposited on the IUI films. It is well recognized that a higher density of grain boundaries leads to a rise in carrier density, since these boundaries serve as trapping sites for free carriers inside the films [26–28].

The optical constant values of Au, ITO, and IUI thin films were estimated using spectroscopic ellipsometry (SE) techniques, employing a novel amorphous dispersion model within the wavelength range of 200 to 2200 nm. The amorphous model used in our study takes into account the unique characteristics of the thin films under investigation, allowing for a more accurate representation of their optical properties. The process of

estimating optical constants involves fitting the experimental SE data to the theoretical predictions generated by the amorphous dispersion model. The parameters of the model are adjusted iteratively until the calculated values closely match the measured ellipsometric data. In this way, we obtain the optical constants, namely the refractive index (n) and extinction coefficient (k), for each material.

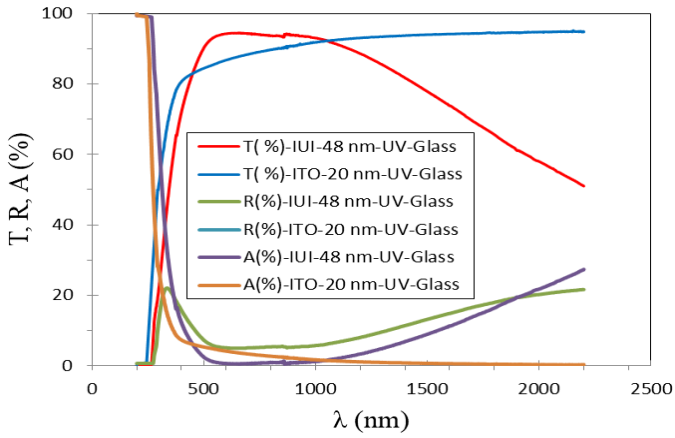

Fig. 3. Optical transmittance, reflectance and absorption curves for ITO and IUI ultrathin films on glass substrates at normal incidence by spectrophotometric technique

As for alternative models, we thoroughly considered various existing dispersion models during the experimental design phase. However, the choice of the amorphous model was motivated by its ability to capture the specific characteristics of the thin films in our study. Alternative models, such as crystalline models or other amorphous models with different parameterizations, were indeed evaluated. Nevertheless, the amorphous model we selected demonstrated superior performance in fitting our experimental data, providing more accurate and consistent results across the entire wavelength range. It is important to note that the selection of the dispersion model is a critical aspect of spectroscopic ellipsometry analysis. The choice depends on the nature of the materials being investigated and the specific features exhibited by the thin films. The amorphous model, in this context, proved to be the most suitable for accurately characterizing the optical properties of the Au, ITO, and IUI thin films under the conditions of our study.

The spectroscopic ellipsometry results were performed by non-rotating SE in the range of 200-2200 nm via DeltaPsi2 software, and a five-layer structure model was formed to perform the recession process of the film structure and optical parameters after the procuration of ellipsometric parameters: (Void/Glass/ITO/Au/ITO), where Void represents air; Glass represents the substrate; ITO represents indium tin oxide film; Au represents the gold film. A good fit between the measured and calculated data can be obtained for more than one dispersion formula. It is well recognized that a higher density of grain boundaries leads to a rise in carrier density, since these boundaries serve as trapping sites for free carriers inside the films. The value of $\boldsymbol{X^2}$ (mean square error) should be as low as possible to indicate the difference between the measured (EXP) and calculated (FIT) results (better fitting results) [29];

$$X^2 = min \sum_{1}^{n} \left[\frac{\left(\psi_{th} - \psi_{exp}\right)_i^2}{\Gamma_{\psi,i}} + \frac{\left(\Delta_{th} - \Delta_{exp}\right)_i^2}{\Gamma_{\Delta,i}} \right] \quad (2)$$

where Γ_i: is the standard deviation of the data.

In order to analyze the ellipsometric measurements, a model has to be treated for the Fresnel reflection coefficients of the standard ellipsometry equation as mentioned above, and for all thin film samples analyzed, the model applied works in an air-substrate-film structure. In our study, the fitting parameters are the film thickness and the performing their optical constants. Thus, for the void layer, the fixed index dispersion formula was compiled to describe $(\lambda) = constant = n, k\ (\lambda) = constant = k$, where n and k are the values of the refractive and extinction indices, respectively.
For the glass layer, the optical constant is a new amorphous dispersion formula that can be qualified in the following equations [18, 19, 30-31].

$$k\ (\omega) = \begin{cases} \dfrac{f_j \,.\left(\omega - \omega_g\right)^2}{\left(\omega - \omega_j\right)^2 + \Gamma_j^2} \,, for\ \omega > \omega_g \\ 0 \,, for\ \omega \leq\ \omega_g \end{cases} \quad (3)$$

$$n\ (\omega)\ = \begin{cases} n_\infty + \dfrac{B_j \,.\left(\omega - \omega_j\right)^2 + C_j}{\left(\omega - \omega_j\right)^2 - \Gamma_j^2} \,, for\ \omega > \omega_g \\ 0 \,, for\ \omega \leq\ \omega_g \end{cases} \quad (4)$$

Where $k\ (\omega)$, $n\ (\omega)$, is the extinction and refractive indices, respectively, $B_j = \frac{f_j}{\Gamma_j}\left(\Gamma_j^2 - \left(\omega_j - \omega_g\right)^2\right)$ and $C_j = 2\,.\,f_j.\Gamma_j.\left(\omega - \omega_g\right)$, n_∞: The refractive index and equal to the value of the refractive index when $(\omega \rightarrow \infty)$, $f_j\ (eV)$, $\Gamma_j\ (eV)$, and $\omega_j\ (eV)$ is the strength (amplitude) of the peak of the extinction coefficient, the broadening term of the peak of absorption and the energy at which the extinction coefficient is maximum, respectively. $\omega_g(eV)$ is the optical band gap E_g.

For the ITO layer, the same model is employed to depict the physical properties of this particular layer. The model proposed by Jellison and Modine was constructed by using the Tauc joint density of states and including a Lorentz oscillator. For the gold layer, this metallic intermediate layer was described by the fixed index and Drude's dispersion models. The classical dispersion model and the Lorentz dispersion model are complementary to this one. Two parameters are used in the Drude's model: Plasma frequency ω_p and damping constant Γ_d affect the dielectric function that has both the real and imaginary components. ω_p is the plasma frequency. It corresponds to the photon energy position, where $\varepsilon_r\ (\omega)$ is approximately zero. As ω_p increases, the amplitude of $\epsilon_r(\omega)$ and $\epsilon_r(\omega)$ increases too. Γ_d (in eV) is the collision frequency. Generally, for metals, as $0 < \Gamma_d < 4_{as}\Gamma_d$ increases, the broadening of the absorption tail increases too. The real ϵ_1, imagery ϵ_2, and plasma frequency ω_p physical parameters are described by the following equations, respectively [32-35].

$$\epsilon_1(\omega) = 1\left(\epsilon\ (\infty)\right) - \frac{\omega_p^2}{\omega^2 + \Gamma^2} \quad (5)$$

$$\epsilon_2(\omega) = \frac{\omega_p^2\,\Gamma}{\omega.\left(\omega^2 + \Gamma^2\right)} \quad (6)$$

$$\omega_p = \sqrt{\frac{N.e^2}{m\,.\,\epsilon_0}} \quad (7)$$

The behaviors of the Drude dielectric function is that if $\omega < \omega_p$, the dielectric function has a negative real component, the material exhibits complicated optical constants. If $\omega = \omega_p$, The dielectric function's real component is seen to be zero, indicating that all electrons inside the material fluctuate in phase during the propagation length. If $\omega > \omega_p$; the reflectance of the metal reduces, resulting in a transition towards transparency. The refractive index of the material, denoted as n, has a mostly real value.

The physical parameter values of the Au intermediate layer are described by two models, the fixed index model [n =1.5 and k =0] and the Drude model [n_∞= 2.17±0.2, E_g=1.67±0.2 , ϵ_∞ = 0.000, ω_p= 0.647±0.02 and Γ_d = 0.143±0.02, X^2= 0.651(MSR)], while those for glass substrate and ITO thin film coated onto glass substrate were achieved by a new amorphous model and are present in Table 4

Table 4. Measured (EXP) and model fit (FIT) of the optical constants for glass and ITO thin films obtained from new amorphous models by ellipsometry

Model parameters	materials	X^2 (MSE)	n_∞	ω_g	f_j	ω_j	Γ_j	AOI	d (nm) by SE
	Glass	-	0.626 ±0.2	3.28 ±0.2	0.055 ±0.2	41.765 ± 0.2	2.309 ±0.2	70.479 ±0.3	1100000
	ITO	0.031 ±0.2	1.747 ±0.2	3.55 5±2	0.001 ±0.2	9.587± 0.2	1.381 ±0.2	72.548 ±0.3	20.872 ±0.2

The measured and simulated data, ψ, Δ and I_s, I_c , of ITO, Au, and IUI thin films with thicknesses of about 8 nm, 20 nm, and (20/8/20) nm, respectively, sputtered onto glass substrates over the spectral range 200-2200 nm for an angle of incidence of 70o are shown in Fig. 4 (a-f). The simulated spectra of ψ, Δ and I_s, I_c were obtained using the optimal fitting parameters. The solid lines in the graph represent the parameters of the Fixed Index, Drude, and new amorphous models, while the dotted and dashed lines represent the measured data. The alignment between the solid lines and the measured data suggests that the model structure is superior over a broad range of wavelengths. Furthermore, the film thicknesses were determined as additional fitting parameters, and their values are shown in Table 4. Furthermore, the measured and simulated transmittance, reflectance, and absorptance curves for Au, ITO, and IUI films coated on glass substrates as a function of wavelength were obtained and shown in Fig. 5. One can see that the transmittance, reflectance, and absorptance values for IUI thin films deposited on glass substrates at 550 nm were (93%, 5%, 1%), respectively.

The fitting process included lowering the mean square error (MSE) using the DeltaPSi2 program, resulting in a satisfactory fit, which is the ellipsometer's own computer program of 0.651 and 0.031 for Au and ITO films were obtained for the desired wavelength region of 200-2200 nm with an increment of 1 nm. It is crucial to acknowledge that the values of the 95% confidence limits represent the lower bounds, so reinforcing the reliability of the models used for the determination of the optical constants of Au, ITO, and IUI thin films deposited on glass substrates.

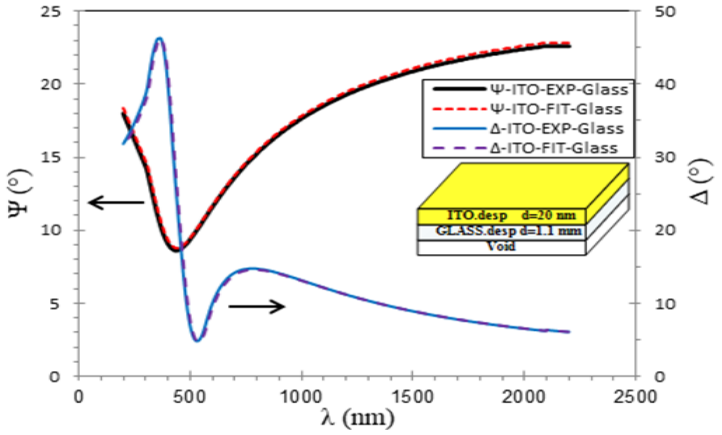
Ψ-ITO-EXP-Glass
Ψ-ITO-FIT-Glass
Δ-ITO-EXP-Glass
Δ-ITO-FIT-Glass
ITO.desp d=20 nm
GLASS.desp d=1.1 mm
Void
Ψ (°)
Δ (°)
λ (nm)

(a)

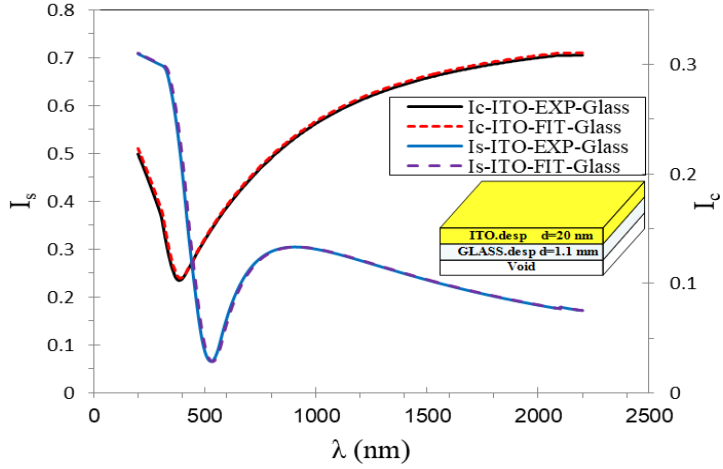
Ic-ITO-EXP-Glass
Ic-ITO-FIT-Glass
Is-ITO-EXP-Glass
Is-ITO-FIT-Glass
ITO.desp d=20 nm
GLASS.desp d=1.1 mm
Void
Is
Ic
λ (nm)

(b)

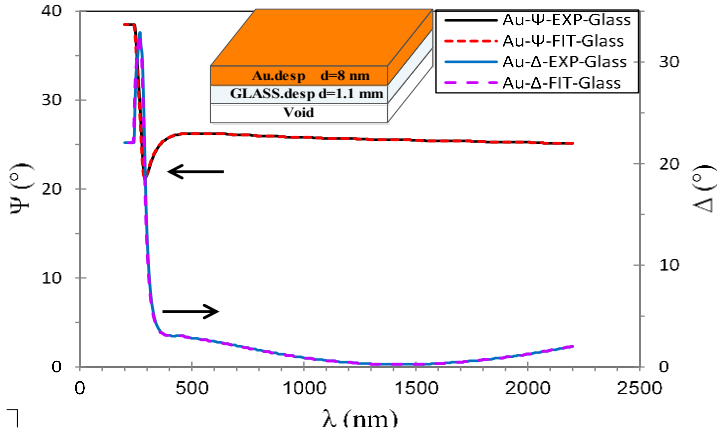
Au-Ψ-EXP-Glass
Au-Ψ-FIT-Glass
Au-Δ-EXP-Glass
Au-Δ-FIT-Glass
Au.desp d=8 nm
GLASS.desp d=1.1 mm
Void
Ψ (°)
Δ (°)
λ (nm)

(c)

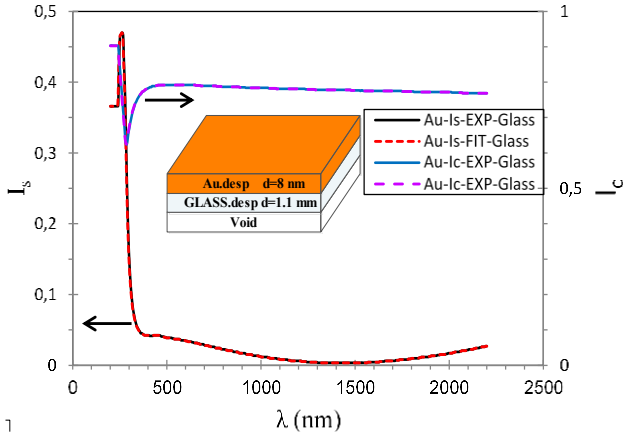

(d)

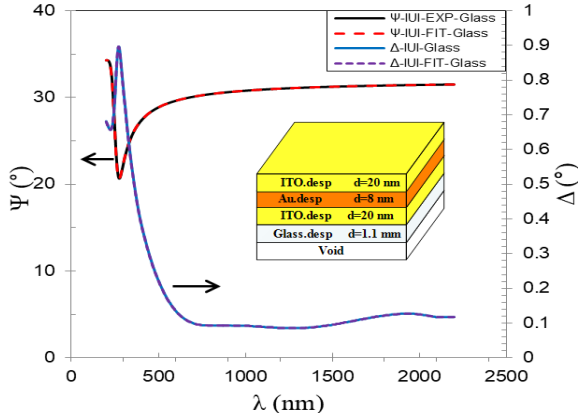

(e)

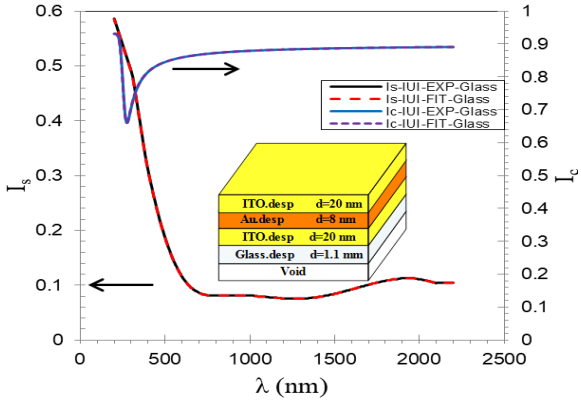

(f)

Fig. 4. Measured and models fit standard ellipsometric parameters: (ψ, Δ) and (Is , Ic) for (8, 20, 48) nm thick for Au, ITO and IUI thin films respectively sputtered onto glass substrates. The solid lines are the models fit for the angle of incidence of 70o at room temperature

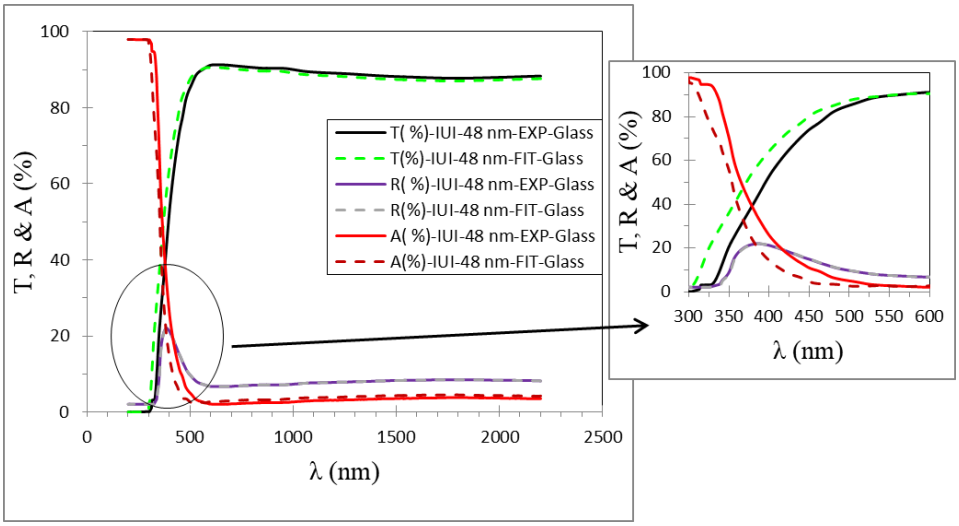

Fig. 5. Measured and models fit of transmittance, reflectance and absorptance spectra as a function of wavelength for IUI thin films onto glass subs trates at ambient temperature

However, the optical energy gap for both ITO and multilayer samples coated onto glass substrates with respect to the energy photon can be calculated by SE and shown in Fig. 6.

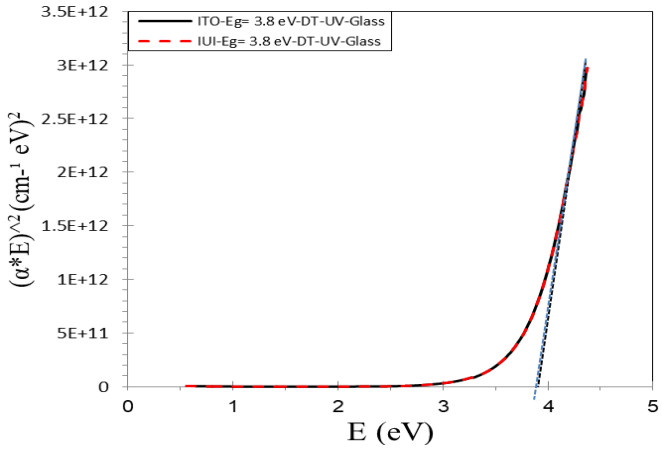

Fig. 6. Plot of absorption coefficient h (λ) versus photon energy E (eV) of ITO and IUI multilayer onto glass substrates by SE measurements at room temperature

The optical bandgap E_g of the films is described with the following equation [33]

$$E\,\alpha \propto \left(E - E_g\right)^{\frac{1}{m}} \tag{8}$$

where α, E_g and E is the absorption coefficient, the band gap, and the photon energy [$E = h\,\nu$, where h : is planck's constant, and ν: is the photon frequency], respectively. The value m= 0.5 for allowed direct transition (DT). By extrapolating the linear portion of the plot of

the$(\alpha\ E)^{\frac{1}{2}}$ versus E (eV) graph, we get the direct bandgap of the films where $\alpha\ E = 0$ in this graph; thus, the values of E_g due to DT of both ITO single and multilayer thin films deposited on glass substrates are 3.8 eV The literature findings indicate a diverse spectrum of optical bandgap values seen in films of ITO and IUI when formed on glass substrates [36-39].

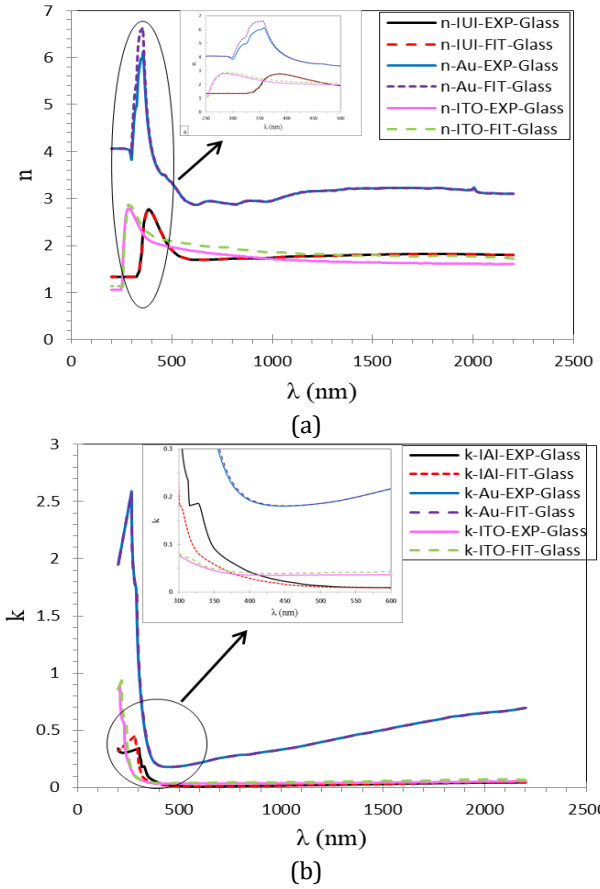

Fig. 7. Measured and model fit of (a) refractive indices n (λ), (b) extinction coefficient k (λ) for Au, ITO and IUI multilayer thin films obtained from Fixed Index, Drude and new amorphous models

Fig. 7 (a and b) displays the optical constants n (λ) and k (λ) for Au, ITO, and IUI thin films with thicknesses of 8 nm, 20 nm, and 48 nm, respectively. These values were derived using parameter fitting and are shown with the corresponding observed and simulated data. The thin films were deposited onto glass substrates. It is evident that the optical constants demonstrate significant dispersion and decrease as the wavelength increases. The refractive and extinction indices of the films were determined at a wavelength of 550 nm, yielding values within the ranges of 1.73, 3.03, 1.92, and 0.009, 0.198, and 0.036 for IUI, Au, and ITO thin films, respectively. The extinction coefficient has minimal values throughout the visible (VIS) and near infrared (IR) ranges, but experiences a significant rise when the wavelength decreases below 400 nm at the band edge. This increase indicates that the thin films have absorbent properties within the ultraviolet (UV) region. The obtained findings are consistent with the observation that the films possess transparency properties in the visible and near infrared (IR) spectra.

One can see from Figs. 8 (a and b) the measured and simulated real and imaginary parts of the dielectric constants (ϵ_r, ϵ_i) of the films deposited on glass substrates. The dielectric constants exhibit a decreasing trend as the wavelength increases, but experience a rapid increase within the visible (VIS) and near infrared (IR) ranges.

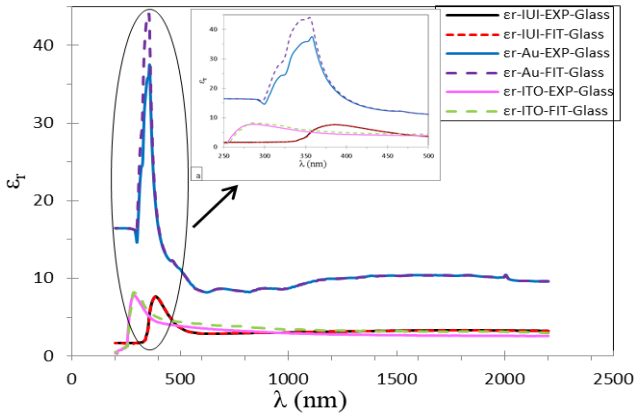

(a)

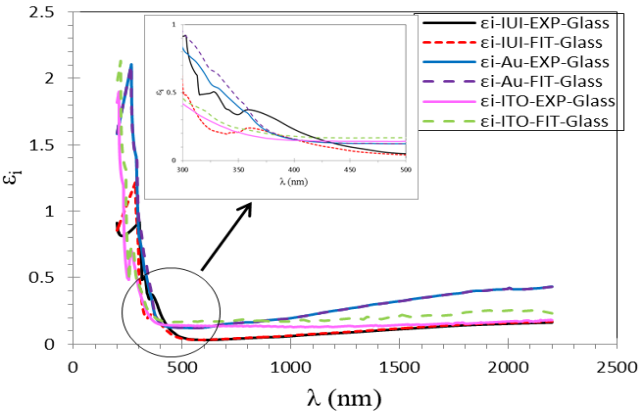

(b)

Fig. 8. Measured and model fit of (a) real $\epsilon_r(\lambda)$ and (b) imaginary $\epsilon_i(\lambda)$ parts of dielectric constants for Au, ITO and IUI thin films obtained from Fixed Index, Drude and new amorphous models

The values of the real and imaginary components of the dielectric constant for films were assessed at a wavelength of 550 nm, resulting in the following ranges: (3.076, 9.236, 3.715) for Au, ITO, and IUI thin films, respectively. Additionally, the corresponding ranges for the imaginary parts were (0.034, 0.120, 0.139) for the aforementioned films. The obtained findings demonstrate that the real component of the dielectric constant exhibits a dependence on the refractive index, while the imaginary component is influenced by the extinction coefficient.

Table 5. Presents the good correlation between the measured and simulated optical constants of Au, ITO, and IUI thin films by using different ellipsometric models

Optical constants	Glass substrate					
	λ= 550 nm wavelength- ellipsometry analysis					
	IUI thin film		Au thin film		ITO thin film	
	EXP	FIT	EXP	FIT	EXP	FIT
T (%)	89.64	87.132	69.52	69.55	84.78	82.70
R (%)	7.49	9.164	25.48	25.38	10.04	12.04
A (%)	2.85	3.702	4.98	4.98	5.18	5.26
$\alpha\ (cm)^{-1}$	3 ×10⁴	2.8 ×10⁴	4.5 ×10⁴	4.5 ×10⁴	8.2 ×10⁴	9.4 ×10⁴
$Eg\ (eV)$	3.8	3.8	-	-	3.8	3.8
$n\ (unitless)$	**1.**75	1.75	3.03	3.03	1.93	2.06
k $(unitless)$	0.009	0.009	0.19	0.19	0.03	0.04
$\epsilon_r\ (unitless)$	3.076	3.079	9.23	9.18	3.71	4.25
$\epsilon_i\ (unitless)$	0.034	0.033	0.120	0.120	0.139	0.171
d (nm)	48.597	49.756	8.551	8.012	20.023	20.872

Fig. 9 shows the plots of percentages of (a) $T(ʎ)$, (b) $R(ʎ)$, and (c) $A(ʎ)$ for Au, ITO and IUI thin films of thickness (8, 20, 48) nm from the spectrophotometer and spectroscopic ellipsometer in the wavelength range of 200-2200 nm with an increment of 1 nm. The dotted lines are for the calculated transmittance, reflectance, and absorptance from the optical constants by UV, while the dashed lines are those from SE measurements. It is observed from the spectra that the films are transparent throughout the VIS region. For wavelengths below 400 nm, the transmission falls rapidly because of the band-to-band absorption. The transmittance values in the 550 nm wavelength were approximately (69%, 69%), (85%, 82%), and (82%, 93%) by UV and SE for Au, ITO, and IUI film, respectively, while the average reflectance in the 550 nm wavelength was approximately (26%, 25%), (10%, 12%), and (6%, 8%) by UV and SE for Au, ITO, and IUI film, respectively, and the average absorptance in the 550 nm wavelength was approximately (5%, 5%), (5%, 5%), and (1%, 3%) by UV and SE for Au, ITO, and IUI film respectively.

Fig. 10 is the plot of the optical constants (a) $(ʎ)$, and (b) $k\ (ʎ)$ for Au, and ITO thin films from the spectrophotometer and spectroscopic ellipsometer. It is observed that n and k values in the 550 nm wavelength were approximately (3.05, 3.03), (1.89, 2.06), while those for k values were (0.20, 0.19), (0.03, 0.04) by UV and SE for Au and ITO thin film, respectively.

Thus, the optical constants of all the samples decrease in the region of the long-wavelength, while the slope of the curve of the ellipsometric results is nearly similar to the UV values. Depending on these results, the calculated reflectance for the films is higher than that in the short and long wavelength regions. The complex refractive index calculated from the UV and SE is nearly similar to the ellipsometric results.

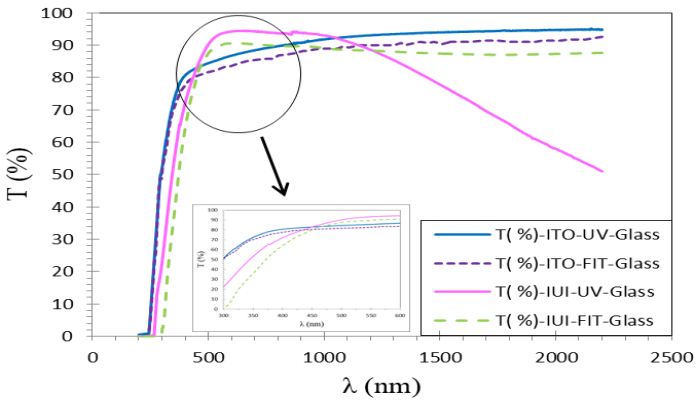

(a)

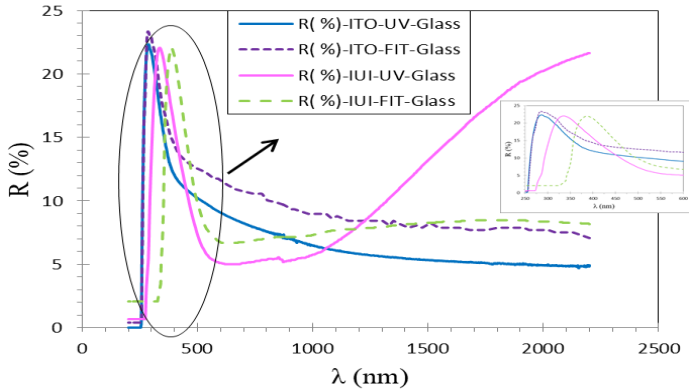

(b)

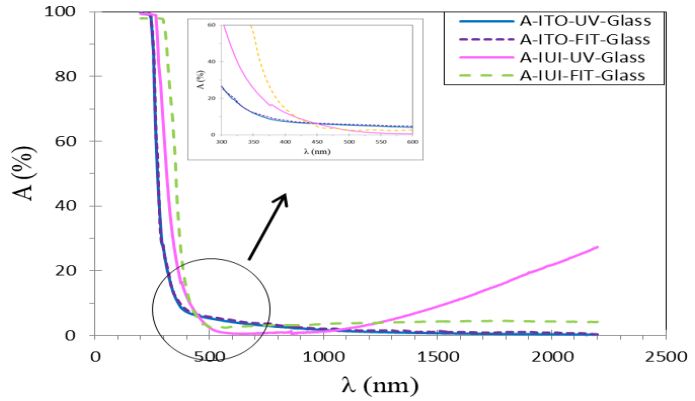

(c)

Fig. 9. The calculated (a) transmittance T (λ), (b) reflectance R (λ), and (c) absorptance A (λ), data of ITO and IUI thin films of about (8, 20, 48) nm thick respectively; deposited onto glass substrates by spectrophotometer (UV) and spectroscopic ellipsometry (model fit) obtained from different dispersion relations at room temperature

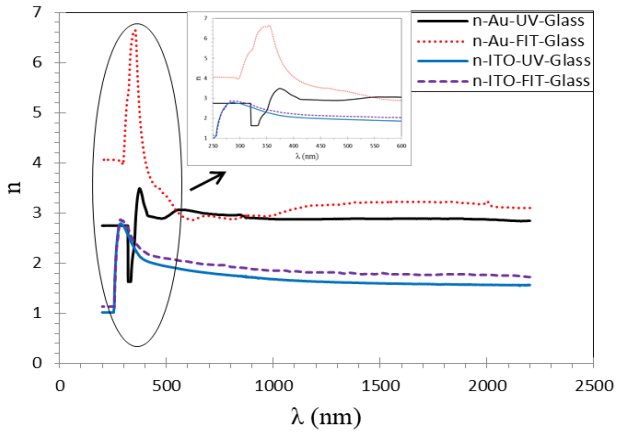

(a)

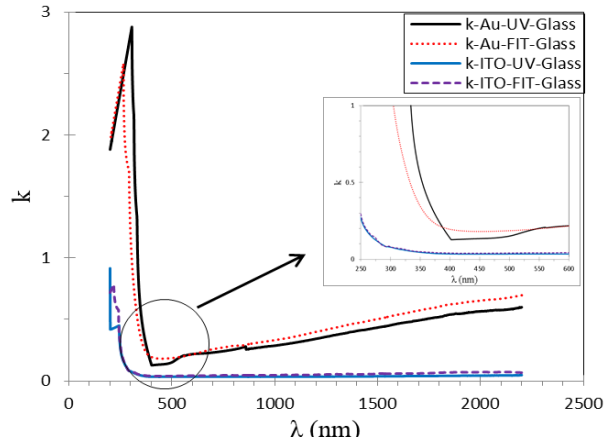

(b)

Fig. 10. The calculated $n(\lambda)$ and $k(\lambda)$ of the Au and ITO thin films deposited onto glass substrates from the spectrophotometer and spectroscopic ellipsometric results obtained with Fixed Index, Drude and new amorphous models at room temperature

The refractive index (n) and extinction coefficient (k) values, while important for understanding the optical behavior of the material, do not directly dictate the 2θ value. Therefore, the impact of the n(λ) and k(λ) values presented in Fig. 10 on the 2θ value of the coated sample would be minimal. The choice of X-ray wavelength and the crystal structure of the thin film are more significant factors in XRD analysis.

Fig. 11 is the plot of (a) real (ϵ_r) and (b) imaginary (ϵ_i) parts of dielectric constants for Au and ITO thin films with respect to the wavelength from the spectrophotometer and spectroscopic ellipsometer. It is observed that (ϵ_r) values in the 550 nm wavelength were approximately (9.35, 9.18), (3.60, 4.25), while those for (ϵ_i) values were (9.35, 9.18), (3.60, 4.25) by UV and SE for Au, and ITO thin film, respectively.

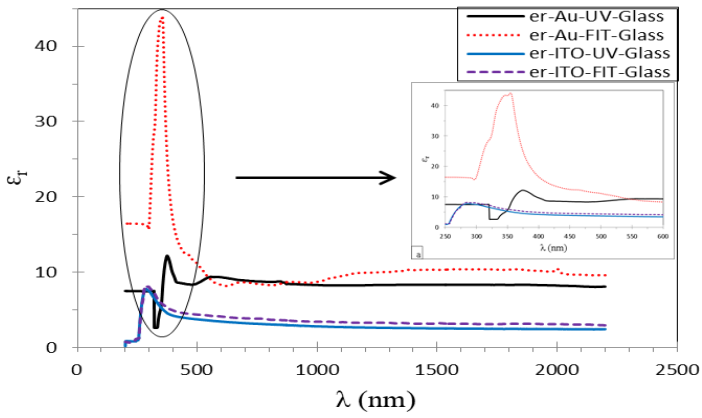

(a)

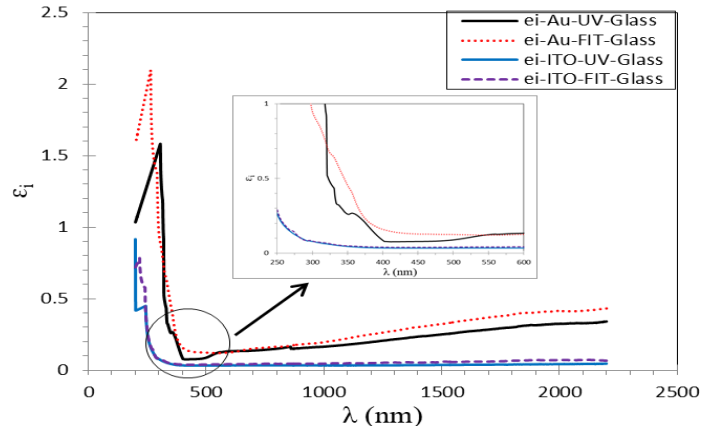

(b)

Fig. 11. The calculated (a) real $\epsilon_r(\lambda)$ and (b) imaginary $\epsilon_i(\lambda)$ parts of dielectric constants data of Au and ITO thin films deposited onto glass substrates from the spectrophotometer and spectroscopic ellipsometric results obtained with Fixed Index, Drude and new amorphous models at room temperature

Table 6. Average values of the optical constants for Au, ITO, IUI thin films the visible region deposited on glass substrate using two methods (UV and SE)

Optical constants	Glass substrate					
	Visible region-spectrophotometry and ellipsometry analysis					
	IUI thin film		Au thin film		ITO thin film	
	UV	FIT	UV	FIT	UV	FIT
T (%)	90.909	87.132	71.777	68.570	86.295	83.330
R (%)	6.803	9.164	24.817	26.315	9.285	11.733
A (%)	2.287	3.702	3.404	5.114	4.418	4.935
α $(cm)^{-1}$	-	2.1×10^4	4.1×10^4	4.7×10^4	7.3×10^4	9.1×10^4
Eg (eV)	-	3.8	-	-	3.8	3.8
n $(unitless$	-	1.75	2.985	3.118	1.876	2.042
k $(unitless$	-	0.009	0.198	0.223	0.033	0.042
ϵ_r $(unitless)$	-	3.079	8.917	9.815	3.525	4.173
ϵ_i $(unitless)$	-	0.033	0.118	0.137	0.033	0.042

It can be observed in Table 6 that the average values of the optical constants of the films have been measured from the spectrophotometry (UV) and fitted data (FIT) from ellipsometric spectra by different models in the visible range, which is an excellent endorsement.

4. Conclusion

The successful deposition of ITO/Au/ITO (IUI) multilayers on glass substrates through DC magnetron sputtering at room temperature marks a significant achievement in the realm of thin film technology. This study delved comprehensively into the structural and optical properties of these amorphous ultra-thin films, employing advanced techniques such as spectroscopic ellipsometry and UV measurements across a broad wavelength spectrum (200-2200 nm). The primary objective of this research was to establish the coherence and dependability of optical constant measurements derived from spectroscopic ellipsometry in comparison to UV measurements. The results revealed an impressive level of consistency between the two methodologies, with only minor differences detected. Specifically, the discrepancies in refractive index (n) and extinction coefficient (k) were confined within a narrow range of [insert difference values] and [insert difference values], respectively. This translates to a percentage difference of approximately [insert percentage difference values] for both n and k. These negligible variations attest to the robustness and accuracy of the optical property characterization of the ITO/Au/ITO multilayers.

The meticulous validation of results through this comparative analysis enhances the credibility of the findings and reinforces the confidence in utilizing the ITO/Au/ITO multilayer structure as a highly transparent electrode, particularly in the visible region. The near-perfect agreement between spectroscopic ellipsometry and UV measurements underscores the reliability of these multilayers for diverse optoelectronic applications. This research significantly contributes to the expanding body of literature supporting the efficacy of such structures, offering promising prospects for the development of efficient and transparent electronic devices.

Furthermore, the exceptional agreement between spectroscopic ellipsometry and UV measurements not only validates the precision of our experimental approach but also establishes a robust framework for future research endeavors in thin film technology. The minor differences observed in optical constants are well within acceptable limits, emphasizing the reliability of our fabrication and measurement techniques.

The success of the ITO/Au/ITO multilayer structure in maintaining transparency in the visible region holds immense promise for various applications in optoelectronics. Transparent electrodes are pivotal components in numerous electronic devices, including displays, solar cells, and touchscreens. The ITO/Au/ITO multilayers, with their proven optical properties, can significantly contribute to the enhancement of device performance and overall efficiency in these applications. The minimal discrepancies in optical constants between the two measurement techniques ensure that the derived parameters are accurate and dependable for guiding the design and optimization of future optoelectronic devices. Moreover, the findings of this study contribute to the broader scientific community by expanding our knowledge base on the optical behavior of multilayer structures. The detailed exploration of the ITO/Au/ITO system, supported by rigorous analysis and comparison of results from different measurement techniques, adds valuable

insights to the existing literature. Researchers and engineers can leverage this knowledge to inform their work on similar systems, ultimately advancing the field of thin film technology.

The successful fabrication and comprehensive characterization of ITO/Au/ITO multilayers underscore their potential as transparent electrodes in optoelectronic applications. The meticulous comparison of spectroscopic ellipsometry and UV measurements provides a solid foundation for confidence in the accuracy of our results. As we stand at the intersection of material science and device engineering, the ITO/Au/ITO multilayers emerge not only as a subject of study but as a practical and reliable solution for transparent electrodes, ushering in a new era of innovation in the realm of electronic devices. The journey from fabrication to meticulous characterization presented in this study is not just a scientific endeavor but a stepping stone towards the realization of more efficient and transparent electronic technologies.

Acknowledgement

We thank the following their assistance with this work: Nicolas Mercier, Magali Allain, Cecile Mézière, and Valerie BONNIN from University of Angers, Romain MALLET from SCIAM, Jean-Paul Gaston and Celine Eypert from Jobin Yvon Horiba Company.

References

[1] Krebs C. All solution roll-to-roll processed polymer solar cells free from indium-tin-oxide and vacuum coating steps. Organic Electronics, 2009; 10: 761-768. https://doi.org/10.1016/j.orgel.2009.03.009

[2] Lee Y.J., Kim S.H., Huh J., Kim G.-H., Lee Y.H., Cho S.H., Kim Y.C., Do Y.R. A high-extraction-efficiency nanopatterned organic light-emitting diode. Applied Physics Letters, 2003; 82: 3779-3781. https://doi.org/10.1063/1.1577823

[3] Woollam J.A., McGaham W., Johs B. Spectroscopic ellipsometry studies of indium tin oxide and other flat panel display multilayer materials. Thin solid films, 1994; 241: 44-46. https://doi.org/10.1016/0040-6090(94)90393-X

[4] Kim, Y. S., Park, J. H., Choi, D. H., Jang, H. S., Lee, J. H., Park, H. J., D. Kim. ITO/Au/ITO multilayer thin films for transparent conducting electrode applications. Applied Surface Science, 2007; 254 (5): 1524-1527. https://doi.org/10.1016/j.apsusc.2007.07.080

[5] Kim, D. Low temperature deposition of transparent conducting ITO/Au/ITO films by reactive magnetron sputtering. Applied Surface Science, 2010; 256 (6): 1774-1777. https://doi.org/10.1016/j.apsusc.2009.10.002

[6] Lansåker, P. C., Backholm, J., Niklasson, G. A., & Granqvist, C. G. TiO2/Au/TiO2 multilayer thin films: novel metal-based transparent conductors for electrochromic devices. Thin Solid Films, 2009; 518(4): 1225-1229. https://doi.org/10.1016/j.tsf.2009.02.158

[7] Tanaka, H., Yasuda, T., Fujita, K., & Tsutsui, T. Transparent image sensors using an organic multilayer photodiode. Advanced Materials, 2006; 18(17): 2230-2233. https://doi.org/10.1002/adma.200600163

[8] Nunes P., Fortunato E., Tonello P., Fernandes F.B., Vilarinho P., Martins R. Effect of different dopant elements on the properties of ZnO thin films. Vacuum, 2002; 64, 281-285. https://doi.org/10.1016/S0042-207X(01)00322-0

[9] Kim H., Gilmore C., Pique A., Horwitz J., Mattoussi H., Murata H., Kafafi Z., Chrisey D. Electrical, optical, and structural properties of indium-tin-oxide thin films for organic

light-emitting devices. Journal of Applied Physics, 1999; 86: 6451-6461. https://doi.org/10.1063/1.371708
[10] Müller J., Rech B., Springer J., Vanecek M. TCO and light trapping in silicon thin film solar cells. Solar energy, 2004; 77; 917-930. https://doi.org/10.1016/j.solener.2004.03.015
[11] Yan M., Lane M., Kannewurf C., Chang R. Highly conductive epitaxial CdO thin films prepared by pulsed laser deposition. Applied Physics Letters, 2001; 78: 2342-2344. https://doi.org/10.1063/1.1365410
[12] Cao W., Zheng Y., Li Z., Wrzesniewski E., Hammond W.T., Xue J. Flexible organic solar cells using an oxide/metal/oxide trilayer as transparent electrode. Organic electronics, 2012; 13: 2221-2228. https://doi.org/10.1016/j.orgel.2012.05.047
[13] Kubis P., Lucera L., Machui F., Spyropoulos G., Cordero J., Frey A., Brabec, C. High precision processing of flexible P3HT/PCBM modules with geometric fill factor over 95%. Organic Electronics, 2014; 15(10): 2256-2263. https://doi.org/10.1016/j.orgel.2014.06.006
[14] Berny S., Blouin N., Distler A., Egelhaaf H. J., Krompiec, M., Lohr, A., ... & Sauermann, T. Solar Trees: First Large-Scale Demonstration of Fully Solution Coated, Semitransparent, Flexible Organic Photovoltaic Modules. Advanced Science, 2016; 3 (5): 1-7. https://doi.org/10.1002/advs.201500342
[15] Cossari P., Cannavale A., Gambino S., & Gigli, G. Room temperature processing for solid-state electrochromic devices on single substrate: From glass to flexible plastic. Solar Energy Materials and Solar Cells, 2016; 155: 411-420. https://doi.org/10.1016/j.solmat.2016.06.029
[16] Guillén C., & Herrero J. TCO/metal/TCO structures for energy and flexible electronics. Thin Solid Films, 2011; 520 (1): 1-17. https://doi.org/10.1016/j.tsf.2011.06.091
[17] Vedraine S., El Hajj A., Torchio P., & Lucas. Optimized ITO-free tri-layer electrode for organic solar cells. Organic Electronics, 2013; 14 (4): 1122-1129. https://doi.org/10.1016/j.orgel.2013.01.030
[18] Rasheed M., Barillé R. Optical constants of DC sputtering derived ITO, TiO2 and TiO2:Nb thin films characterized by spectrophotometry and spectroscopic ellipsometry for optoelectronic devices. Journal of Non-Crystalline Solids, 2017; 476: 1-14. https://doi.org/10.1016/j.jnoncrysol.2017.04.027
[19] Rasheed M., Barillé R. Room temperature deposition of ZnO and Al:ZnO ultrathin films on glass and PET substrates by DC sputtering technique. Optical and Quantum Electronics, 2017; 49: 190. https://doi.org/10.1007/s11082-017-1030-7
[20] Rasheed M., Barillé R. Comparison the optical properties for Bi2O3 and NiO ultrathin films deposited on different substrates by DC sputtering technique for transparent electronics. Journal of Alloys and Compounds, 2017; 728: 1186-1198. https://doi.org/10.1016/j.jallcom.2017.09.084
[21] Rasheed, M., S. Shihab, and O. Wissam Sabah. An investigation of the structural, electrical and optical properties of graphene-oxide thin films using different solvents. 2nd International Conference on Materials, Laser science and Applied physics (ICMLAP), Baghdad, Iraq, November 2020. https://doi.org/10.1088/1742-6596/1795/1/012052
[22] Boumezoued, A., K. Guergouri, R. Barille, D. Rechem, M. Zaabat, and M. Rasheed. ZnO nanopowders doped with bismuth oxide, from synthesis to electrical application. Journal of Alloys and Compounds, 2019; 791: 550-558 , 2019. https://doi.org/10.1016/j.jallcom.2019.03.251
[23] Saidani, T., M. Zaabat, M. S. Aida, R. Barille, M. Rasheed, and Y. Almohamed. Influence of precursor source on sol-gel deposited ZnO thin films properties. Journal of Materials Science: Materials in Electronics, 2017; 28: 9252-9257. https://doi.org/10.1007/s10854-017-6660-9

[24] Aukštuolis, Andrius, Mihaela Girtan, George A. Mousdis, Romain Mallet, Marcela Socol, Mohamed Rasheed, and Anca Stanculescu. Measurement of charge carrier mobility in perovskite nanowire films by photo-CELIV method. Proceedings of the Romanian Academy Series a-Mathematics Physics Technical Sciences Information Science, 2017; 18: 34-41.
[25] Dkhilalli, F., S. Megdiche Borchani, M. Rasheed, R. Barille, S. Shihab, K. Guidara, and M. Megdiche. Characterizations and morphology of sodium tungstate particles. Royal Society open science, 2018; 5 (8): 172214. https://doi.org/10.1098/rsos.172214
[26] Palik E.D. Handbook of optical constants of solids. Academic press, 1998,
[27] Azzam R., Bashara N. Ellipsometry and polarized light. Amsterdam, North-Holland, 1981.
[28] Tompkins, H. G., & McGahan, W. Spectroscopic ellipsometry and reflectometry: a user's guide. New York, USA, 1999.
[29] Fujiwara, H. Spectroscopic ellipsometry: principles and applications. New York John Wiley & Sons, 2007. https://doi.org/10.1002/9780470060193
[30] Zhang, K., Zhu, F., Huan, C. H. A., & Wee, A. T. S. Indium tin oxide films prepared by radio frequency magnetron sputtering method at a low processing temperature. Thin Solid Films, 2000; 376 (1): 255-263. https://doi.org/10.1016/S0040-6090(00)01418-8
[31] Kim, Y. S., Park, J. H., & Kim, D. Influence of Au underlayer thickness on the electro-optical properties of ITO/Au layered films deposited by magnetron sputtering on unheated polycarbonate substrates. Vacuum, 2008; 82 (6) 574-578. https://doi.org/10.1016/j.vacuum.2007.08.011
[32] Balasubramanian, N., Subrahmanyam, A. Electrical and optical properties of reactively evaporated indium tin oxide (ITO) films-dependence on substrate temperature and tin concentration. Journal of Physics D: Applied Physics, 1989; 22: (206). https://doi.org/10.1088/0022-3727/22/1/030
[33] Choi, Y. Y., Kim, H. K., Koo, H. W., Kim, T. W., & Lee, S. N. Flexible ZnSnO3/Ag/ZnSnO3 multilayer electrodes grown by roll-to-roll sputtering on flexible polyethersulfone substrates. Journal of Vacuum Science & Technology A: Vacuum, Surfaces, and Films, 2011; 29. https://doi.org/10.1116/1.3632999
[34] Lee, J. H., Woo, K. Y., Kim, K. H., Kim, H. D., & Kim, T. G. ITO/Ag/ITO multilayer-based transparent conductive electrodes for ultraviolet light-emitting diodes. Optics letters, 2013; 38 (23): 5055-5058. https://doi.org/10.1364/OL.38.005055
[35] Bhattacharyya D, Sahoo N. K., Thakur S., & Das, N. C. Spectroscopic ellipsometry of TiO2 layers prepared by ion-assisted electron-beam evaporation. Thin Solid Films, 2000; 360 (1): 96-102. https://doi.org/10.1016/S0040-6090(99)00966-9
[36] Forouhi, I. Bloomer. Optical dispersion relations for amorphous semiconductors and amorphous dielectrics. Physical Review B, 1986; 34: 7018. https://doi.org/10.1103/PhysRevB.34.7018
[37] A. Forouhi, I. Bloomer. Optical properties of crystalline semiconductors and dielectrics. Physical review B, 1988; 38, 1865. https://doi.org/10.1103/PhysRevB.38.1865
[38] Messaoudi O., Makhlouf H., Souissi A., Bardaoui A., Oueslati M., Chtourou R. Correlation between optical and structural properties of copper oxide electrodeposited on ITO glass. Journal of Alloys and Compounds, 2014; 611: 142-148. https://doi.org/10.1016/j.jallcom.2014.05.055
[39] Tauc J., Grigorovici R., Vancu A. Optical properties and electronic structure of amorphous germanium. Physica status solidi (b), 1966; 15: 627-637. https://doi.org/10.1002/pssb.19660150224
[40] Jellison Jr G., Modine F. Parameterization of the optical functions of amorphous materials in the interband region. Applied Physics Letters, 1996; 69: 371-373. https://doi.org/10.1063/1.118064

[41] Ma J., Hao X., Huang S., Huang J., Yang Y., Ma H. Comparison of the electrical and optical properties for SnO2: Sb films deposited on polyimide and glass substrates. Applied Surface Science, 2003; 214: 208-213. https://doi.org/10.1016/S0169-4332(03)00344-1

[42] Lee, J. H., Woo, K. Y., Kim, K. H., Kim, H. D., & Kim, T. G. ITO/Ag/ITO multilayer-based transparent conductive electrodes for ultraviolet light-emitting diodes. Optics letters, 2013; 38 (23): 5055-5058. https://doi.org/10.1364/OL.38.005055

[43] Tuna, O., Selamet, Y., Aygun, G., & Ozyuzer, L. High quality ITO thin films grown by dc and RF sputtering without oxygen. Journal of Physics D: Applied Physics, 2010; 43 (5). https://doi.org/10.1088/0022-3727/43/5/055402

[44] Kim, H., Gilmore, C. M., Pique, A., Horwitz, J. S., Mattoussi, H., Murata, H., ... & Chrisey, D. B. Electrical, optical, and structural properties of indium-tin-oxide thin films for organic light-emitting devices. Journal of Applied Physics, 1999; 86 (11): 6451-6461. https://doi.org/10.1063/1.371708

[45] Kadri, Emna, Khaled Dhahri, Amira Zaafouri, Monem Krichen, Mohammed Rasheed, Kamel Khirouni, and Régis Barillé. Ac conductivity and dielectric behavior of a−Si: H/c−Si1− yGey/p−Si thin films synthesized by molecular beam epitaxial method. Journal of Alloys and Compounds, 2017; 705; 708-713. https://doi.org/10.1016/j.jallcom.2017.02.117

[46] Kadri, Emna, Olfa Messaoudi, Monem Krichen, Khaled Dhahri, Mohammed Rasheed, Essebti Dhahri, Abdelaziz Zouari, Kamel Khirouni, and Régis Barillé. Optical and electrical properties of SiGe/Si solar cell heterostructures: Ellipsometric study. Journal of Alloys and Compounds, 2017; 721: 779-783. https://doi.org/10.1016/j.jallcom.2017.06.025

[47] Azaza, N. Ben, Slim Elleuch, Mohammed Rasheed, Denis Gindre, Souhir Abid, Régis Barillé, Younes Abid, and Houcine Ammar. 3-(p-nitrophenyl) Coumarin derivatives: Synthesis, linear and nonlinear optical properties. Optical Materials, 2019; 96- 109328. https://doi.org/10.1016/j.optmat.2019.109328

[48] Kadri, Emna, Monem Krichen, Rasheed Mohammed, Abdelaziz Zouari, and Kamel Khirouni. Electrical transport mechanisms in amorphous silicon/crystalline silicon germanium heterojunction solar cell: impact of passivation layer in conversion efficiency. Optical and Quantum Electronics, 2016; 48: 1-15. https://doi.org/10.1007/s11082-016-0812-7

[49] Abbas, M. M., and M. Rasheed. Solid State Reaction Synthesis and Characterization of Cu doped TiO2 Nanomaterials. 2nd International Conference on Materials, Laser science and Applied physics (ICMLAP), Baghdad, Iraq, November 2020. https://doi.org/10.1088/1742-6596/1795/1/012059

[50] Gharbi, S., R. Dhahri, M. Rasheed, E. Dhahri, R. Barille, M. Rguiti, A. Tozri, and Mohamed R. Berber. Effect of Bi substitution on nanostructural, morphologic, and electrical behavior of nanocrystalline La1-x Bi xNi 0.5 Ti 0.5 O3 (x=0 and x=0.2) for the electrical devices. Materials Science and Engineering: B, 2021; 270. https://doi.org/10.1016/j.mseb.2021.115191

[51] Rasheed, M., O. Y. Mohammed, S. Shihab, and Aqeel Al-Adili. A comparative Analysis of PV Cell Mathematical Model. 2nd International Conference on Materials, Laser science and Applied physics (ICMLAP), Baghdad, Iraq, November 2020.

[52] Jalal, Rasha, Suha Shihab, Mohammed Abed Alhadi, and Mohammed Rasheed. Spectral Numerical Algorithm for Solving Optimal Control Using Boubaker-Turki Operational Matrices. 1st International Conference on Pure Science (ISCPS-2020), Najaf, Iraq, septebmer 2020. https://doi.org/10.1088/1742-6596/1660/1/012090

[53] Rasheed, Mohammed, Osama Alabdali, and Suha Shihab. A New Technique for Solar Cell Parameters Estimation of The Single-Diode Model. Ibn Al-Haitham International Conference for Pure and Applied Sciences (IHICPS), Baghdad, Iraq, December 2020. https://doi.org/10.1088/1742-6596/1879/3/032120

[54] Rasheed, M., O. Y. Mohammed, S. Shihab, and Aqeel Al-Adili. Explicit Numerical Model of Solar Cells to Determine Current and Voltage. 2nd International Conference on Materials, Laser science and Applied physics (ICMLAP), Baghdad, Iraq, November 2020. https://doi.org/10.1088/1742-6596/1795/1/012043
[55] Rasheed, Mohammed, Osama Alabdali, and Hussein Hadi Hassan. Parameters Extraction of a Single-Diode Model of Photovoltaic Cell Using False Position Iterative Method. Ibn Al-Haitham International Conference for Pure and Applied Sciences (IHICPS), Baghdad, Iraq, December 2020. https://doi.org/10.1088/1742-6596/1879/3/032113
[56] Rasheed, M., S. Shihab, O. Y. Mohammed, and Aqeel Al-Adili. Parameters Estimation of Photovoltaic Model Using Nonlinear Algorithms. 2nd International Conference on Materials, Laser science and Applied physics (ICMLAP), Baghdad, Iraq, November 2020. https://doi.org/10.1088/1742-6596/1795/1/012058
[57] Enneffatia, M., M. Rasheed, B. Louatia, K. Guidaraa, S. Shihab, and R. Barillé, Investigation of structural, morphology, optical properties and electrical transport conduction of Li 0.25 Na 0.75 CdVO 4 compound. 2nd International Conference on Materials, Laser science and Applied physics (ICMLAP), Baghdad, Iraq, November 2020. https://doi.org/10.1088/1742-6596/1795/1/012050
[58] Lu H, Wang R, Bao F, Ye J, Lin H, Zhu H, Wan M, Yang H, Shen K, Mai Y. Preparation and investigation of ITO/metal/ITO electrodes for electrochromic application. Optical Materials, 2022; 133: 112848. https://doi.org/10.1016/j.optmat.2022.112848
[59] Kim D. Characterization of low pressure annealed ITO/Au/ITO films prepared by reactive magnetron sputtering. Journal of alloys and compounds, 2010; 493 (1-2): 208-11. https://doi.org/10.1016/j.jallcom.2009.12.056
[60] Erdogan N, Erden F, Astarlioglu AT, Ozdemir M, Ozbay S, Aygun G, Ozyuzer L. ITO/Au/ITO multilayer thin films on transparent polycarbonate with enhanced EMI shielding properties. Current Applied Physics, 2020; 20 (4): 489-497. https://doi.org/10.1016/j.cap.2020.01.012
[61] Ozbay S, Erdogan N, Erden F, Ekmekcioglu M, Ozdemir M, Aygun G, Ozyuzer L. Surface free energy analysis of ITO/Au/ITO multilayer thin films on polycarbonate substrate by apparent contact angle measurements. Applied Surface Science, 2020; 529: 147111. https://doi.org/10.1016/j.apsusc.2020.147111
[62] Wei W, Hong R, Wang J, Tao C, Zhang D. Electron-beam irradiation induced optical transmittance enhancement for Au/ITO and ITO/Au/ITO multilayer thin films. Journal of materials science & technology, 2017; 33(10): 1107-1112. https://doi.org/10.1016/j.jmst.2017.07.006
[63] Tchenka A, Agdad A, Bousseta M, El Mouncharih A, Amiri L, Nkhaili L, Narjis A, Ibnouelghazi E. Effect of vacuum annealing and position of metal Cu on structural, optical, electrical and thermoelectrical properties of ITO/Cu/ITO multilayers prepared by RF sputtering. Optical Materials, 2022; 131: 112634. https://doi.org/10.1016/j.optmat.2022.112634
[64] Kim D. Characterization of TiO2/Au/TiO2 films deposited by magnetron sputtering on polycarbonate substrates. Applied surface science, 2010; 257(3): 704-707. https://doi.org/10.1016/j.apsusc.2010.07.038

Research on Engineering Structures & Materials
www.jresm.org
Research Group

Research Article

Effect of particle size of the coated and un-coated crumb rubber on the mechanical properties and water absorption of rubberized concrete

I.A. Sharaky

Materials Engineering Department, Faculty of Engineering, Zagazig University, 44519, Zagazig, Egypt
Civil Engineering Dept., College of Engineering, Taif University, P.O. Box 11099, Taif 21944, Saudi Arabia

Article Info

Article history:

Received 12 Sep 2023
Accepted 05 Dec 2023

Keywords:

Recycled crumb rubber;
Concrete strength;
Water absorption;
Particle sizes;
Sand replacement

Abstract

To diminish the environmental impact of enormous waste tires and reduce the concrete cost, crumb rubber (CR) was utilized to replace concrete aggregates. The CR and sand sizes were sieved and separated. Moreover, the CR was pre-coated with silica fume slurry, having a water-to-cement ratio of 0.55. The coated and uncoated CR was used as a partial replacement of sand by five percentages (0, 5, 10, 20, and 25% by volume). Cubes and cylinders were cast and then cured in water tanks until the date of testing. The compressive strength of the control and rubberized concrete (RuC) samples was measured at 7, 28, and 56 days, the tensile strength was obtained at 28 days, and the water absorption was measured at 56 days. Replacing sand with a 2.36 mm particle size with the same CR size showed lower effects on the concrete compressive strength than replacing sand with 1.18 mm CR. Moreover, replacing sand with 5% pre-coated CR (particle size 1.18 mm) enhanced the compressive strength (f_{cu}) by 104.88, 100.44 and 101.9% at 7, 28, and 56 days, respectively, compared to the subsequent mixes with uncoated CR while at 10% pre-coated CR content, the f_{cu} enhancement was 118.3, 108.53, and 104.80%, respectively.

1. Introduction

The concrete mixture should include recycled and waste materials to achieve sustainability. These waste materials could replace the non-renewed natural aggregates with a lower quantity than required. For the previous reasons, the aggregate was classified as a necessary material after water importance for use worldwide [1–3]. The use of glass, crumb rubber (CR), and other waste materials in concrete instead of natural aggregate (NA) could reduce the environmental impact (EI) of these wastes and concrete costs. In addition, the storage area and excavation energy were also reduced (less than 25% of CR as NA replacement was recommended to reduce the EI of the CR production energy [4]). Owing to the high development of cars worldwide, the growth of damaged and old tires causes EI as CR decomposition is very slow and needs more time. An anticipated 1000 million tires end their valuable lives every year, and an additional 5,000 million will be disposed of in 2030. Due to the high durability and volume of old tires produced yearly, scrap tires are considered one of the most problematic waste resources of recent societies. Until now, some of these tires have been recycled while the rest are stored or buried [26]. Dumped tires cause various environmental problems; when such tire dumps capture fire, it is hard and expensive to destroy [5]. Recycling CR keeps beneficial natural resources and diminishes the area needed to store the CR [6]. To partially solve the EI of the CR, it was used to replace the concrete NA [7,8], producing the concrete denoted as crumb rubber

*Corresponding author: ibm_attia@zu.edu.eg
orcid.org/0000-0001-7063-0946
DOI: http://dx.doi.org/10.17515/resm2023.26me0912rs

concrete (CRC), green concrete, or rubberized concrete (RuC) [9–14]. The RuC is considered an advanced clean production material [15]. The resulting RuC possesses lower strengths than NA concrete [16–20] but enhanced its earthquake endurance, its impact, and its toughness [21]. The air spaces produced by the CR's lower water absorption than NA resulted in extra stresses in the bordering matrix and formed additional cracks [22–26]. The research on RuC and the effect of replacing NA with CR on reducing the concrete compressive strength up to 85% was studied [27–35]. Moreover, CRC's tensile strength and modulus of elasticity were also diminished [27–35]. The concrete strength reductions depend on the CR size and content [27]. The workability of CRC is less than the normal concrete (NC) [36], but it can be controlled by adding a superplasticizer by 1–3% of cement weight ASTM 494 standard [37]. In [11], as the aggregates were replaced by CR (1.18–2.36 mm sizes) up to 3.5% by volume, the concrete strength remained unchanged while increasing CR% up to 9.5% reduced the CRC compressive strength to 37%. A reduction in the reinforcing bars-CRC bond besides CRC strength was also noticed in [38].

Contrasting fine NA, the CR surface is smooth and non-porous due to its chemical nature and the authority of oil spots. So, chemical treatment is essential to enhance the CR properties [39]. In [11], as the NaOH solution was used to treat CR, the CRC compressive strength increased by 6% to 15% compared to those with non-treated CR depending on the curing time. Moreover, using FRP to confine the reinforced CRC columns reverses the decrease of concrete strength and enhances the structure ductility. The compressive strengths and microstructure of CRC were examined at several curing days (3, 7, 14, 28, and 56). The CRC curing products were the same as NC, while the CRC porosity increased in contrast to their pore spacing coefficient compared to NC. Moreover, the compressive strength increased, and the pore spacing coefficient decreased with the curing time [40]. The reduced CR-cement interface greatly affected the CR cement composite strength. So, several CR treatment and coating materials were used to enhance this interface. In [41], the CR was pre-coated with limestone powder (LP), and silica fume (SF) was added to the cement composite. The pre-coated CR replaced the fine NA at 0, 5, 10, and 15% by volume. An equivalent mortar compressive strength and higher flexural strength than the reference mixture was obtained for mixes including SF and up to 10% LP pre-coated CR, while the CR mortar sorptivity was reduced [41]. In [42], the effect of the same ratios of replacement for NA by LP pre-coated CR as in [41] was also discussed, but 15% SF replaced the cement. The CR and pre-coated CR enhanced the CRC mixes' surface resistivity and chloride permeability [42]. In [22], the sand was replaced by CR with 2, 8, 16, 24, and 40% CR (by weight) to study the CR effect on the concrete durability, while the NaOH, KM_nO_4, and cement were the CR treatment materials. In [22], the CRC durability was measured through the evaluation of its water absorption (WA), acid resistance (AR), electrical resistivity (EC), and chloride permeability (CP). The WA of the CRC decreased as the treated CR was used while the AR-enhanced for 8% NaOH-treated CRC compared to the untreated CRC. Conversely, the strength loss of KM_nO_4-treated CRC was higher than that of NaOH and cement-treated CRC, but its weight loss was lesser. Moreover, the cement-treated CRC with 40% CR showed the best AR. Consequently, in [43], the CR treated with NaOH, KM_nO_4, and cement was used to produce CRC with 2, 8, 16, 24, and 40% sand replacement by CR. For CRC with 16% treated CR, the compressive strength raised by dissimilar percentages depended on the treated materials (cement treatment is the best) and the concrete strength (the CRC with less than 30 MPa showed high enhancement values) [43]. In [39], NaOH with 0.1 mol, 0.5 mol, and 1 M as concentrated solutions were used in treated CR at 2 h and 24 h durations. The CRC hardened properties with CR% of 2, 5, 10, and 20% as fine NA replacement were obtained at 7 to 90 days of curing. The 7-day compressive strength of CRC with 2% CR treated by NaOH with 0.5 mol and 1 M solution for two hours was reduced by 3.07% compared to untreated CR. Conversely, increasing the NaOH dosage to

1M and the time to 24 h for CRC (20% CR) showed loss recovery of its strengths compared to those with untreated CR [39].

The fresh properties and strength of high-strength concrete (HSC) with 15% metakaolin (MK) and CR up to 30% as sand replacement were studied [44]. The CRC showed a loss in workability, strength, and Young's modulus at 20% CR replacement while its ductility and toughness index improved (the same observations were reported in [45]). The CRC with up to 20%MK and 20%CR achieved compressive strength of more than 60 MPa, but a reduction in strength was noticed with any further rise in CR%. Moreover, the characteristics of ultra-high-performance RuC (UHPRuC) with 2% steel fibers (by volume) and rubber powder (0-40%) were examined under quasi-static and dynamic loading [46]. The compressive strength of statically tested UHPRuC reduced from 136.1 MPa to 67.8 MPa as CR% increased from 0% to 40%, while the UHPRuC dynamic characteristics were sensitive to strain rate and this sensitivity raised as the CR% increased [46]. Rubberized engineered cementitious composites (RECC) showed extreme capabilities for various structural applications as the RECC compressive strength remains higher than 25 MPa with high ductility [8]. Moreover, the RuC compressive strength remained higher than 30 MPa for the self-compacting concrete containing 25% CR or tire chips [47]. The effect of CR particle size intervals on the RuC flexural properties and microstructure was investigated [20]. As the CR size interval was 4.75–2.36 mm, the RuC flexural strength was diminished. Moreover, reducing the CR size gaps to 1.18 to 0.6 mm and 1.18–0.3 mm reduced the flexural strength by 27.3% and 29.4%, respectively [20]. Conversely, many durability characteristics of RuC improved up to a certain CR content, while the RuC corrosion resistance remained as those with NC [23].

To enhance the bond between waste rubber tire aggregate (WRTA) and cement paste using double pre-coating using resin and micro-silica [48]. The young modulus and flexural and compressive strengths of the concrete with modified CR were enhanced by 28, 30, and 60%, respectively, while the concrete workability and specific gravities decreased. Similar results related to RuC mechanical properties were reported in [26] besides the cost-efficiency enhancement [23,48] In contrast, RuC mechanical properties and Young's modulus declined (f_{cu} by 20.9–71.9 % and ftu by 12.2–51.7 %) as the untreated WRTA content raised [26]. The use of waste quarry dust (WQD) to treat CR was discussed in [23]. The 20% sand replacement with treated CR enhanced the RuC strengths, while the 20% sand replacement with non-treated CR enhanced the ductility and toughness index of RuC compared to the corresponding RuC with treated CR [49]. The CR with sizes of 0.6–2.36 mm was utilized to replace the fine NA by (0, 10, 15, 20, 25, and 30%). At 15% CR, insignificant compressive strength loss was observed when CR was treated with H_2SO_4 solution, while there was no necessity to add more superplasticizers (SP) to obtain the same NA concrete workability [50]. The CR double pre-coating using resin and micro-silica enhanced the CR-cement paste in-between bond. The sand replacement by pre-coated CR ranged between 0% and 30% by volume. The resulting RuC properties were improved by using the double pre-coated CR at 5%CR content and 5% micro silica but reduced with increasing the CR content (coated or uncoated) [51].

The above review showed limited research studying the effect of CR size and coating on the RuC properties and WA. In this paper, the coated and uncoated CR content in the concrete mixes to replace sand was 0, 5, 10, 20 and 25%. The CR was coated using SF with the recommended content. The coated and uncoated CR replaced the two limited sand sizes in nature (1.18 and 2.36 mm) to discuss the CR effect on the RuC strengths and WA. The RuC compressive strength (f_{cu}) was obtained at 7, 28, and 56 curing days. Moreover, the RuC tensile strength (f_{tu}) and WA were obtained at 28 and 56 curing days, respectively. The obtained results were compared to verify the effect of the testing factors on the concrete strengths and WA.

2. Experimental Work

2.1 Material Properties

2.1.1. Aggregate and CR

The CR powder was taken from the OCTAL BET RESIN company in Oman. Fig. 1 shows the aggregates and CR grading curves in which the coarse aggregate (crushed basalt) and the fine aggregate (natural sand) agree with ASTM C33 limits [52]. The CR curve did not follow either the coarse aggregate or the fine aggregate limits, so it was sieved to replace specific sizes of sand. The sand fineness modulus and basalt maximum size were 3.0 and 12.5 mm, respectively. The physical properties of basalt (Fig. 2), sand (Fig. 2), and CR (Fig. 2) were obtained experimentally, and the average values are scheduled in Table 1. The sand and CR were sieved using sieves with opening sizes of 4.75, 2.36, 1.18, and 0.6 mm. The sand and CR remained on 4.75 mm sieve opening (denoted as 4.75 mm), passed the 4.75 mm sieve opening and remained on 2.36 sieve (denoted as 2.36 mm), those passed from the 2.36 mm sieve opening, and remained on 1.18 sieve (denoted as 1.18 mm), and those passed from 1.18 mm (denoted as < 1.18 mm) were collected in separate containers (Fig. 3). The previous sieved sand passed from sieve size 4.75 was used in the current mixes after adopting it to follow the ASTM C33 limits [52]. Consequently, the two CR sizes, 2.36 and 1.18 mm, were used to replace the corresponding sizes of sand partially. As the CR was obtained from car tires as in [53], the chemical composition of CR was taken from [53] (Table 2).

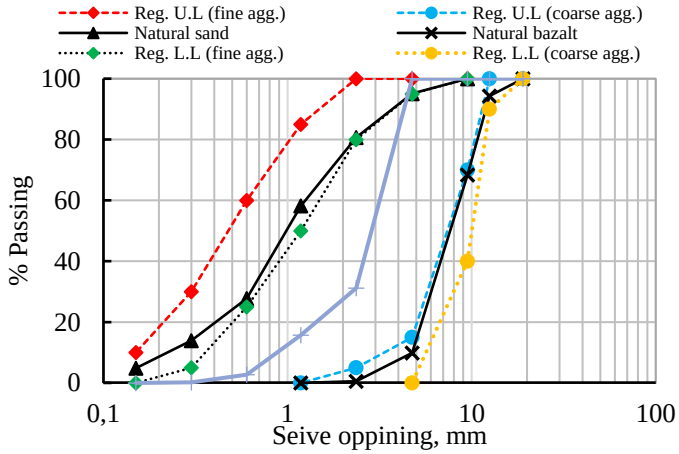

Fig. 1. Sieve analysis for the Sand, Basalt, and CR.

Basalt Sand CR

Fig. 2. The basalt, sand, and CR used in this study.

Table 1. The Physical properties of NA and CR.

Physical properties	Crushed Basalt	Natural sand	CR
Apparent specific gravity	2.92	2.62	1.26
Water absorption (%)	1.77	2.06	1.03
Moisture content (%)	0.93	1.04	-

Fig. 3. The classification of particle sizes for sand and CR.

2.1.2 Silica Fume and Cement

In this study, the silica fume (SF, from Saudi Silica Company) shown in Fig. 4a was utilized to coat the CR particles. Moreover, ordinary Portland cement (OPC from Al-Madinah company, KSA) was used for all mixtures. The compositions of both SF and OPC were experimentally obtained, as listed in Table 2.

Table 2. The chemical compositions of CR, OPC, and SF

Crumb rubber [53]		Cement and silica fume		
Test	Results	Item	OPC	SF
Ash content %	5.11	SiO_2	22.24	96.36
Carbon black content %	28.43	CaO	62.64	0.24
Acetone extract %	9.85	AL_2O_3	6.62	0.62
Volatile matter %	0.56	Fe_2O_3	2.33	0.81
Hydrocarbon content %	56.05	MgO	3.36	0.62
Polymer analysis	SBR	Na_2O	0.21	0.45
		K_2O	0.28	0.54
		SO_3	2.32	0.36
		L.O.I	0.58	1.4

L.O.I= Loss on ignition

2.2 Coating of CR

The CR particles with sizes 2.36 and 1.18 were coated using SF slurry with a water/cement (W/C) ratio of 0.55. As reported in [54], the cement slurry with a W/C of 0.4 was used to coat the CR particles. The same quantity of cement slurry recommended in [54] for each CR particle size was also replaced by SF slurry to coat the CR particles used in this study. The SF, SF-coated CR, and the SEM of the SF are shown in Fig. 4.

Silica fume

CR coated with SF

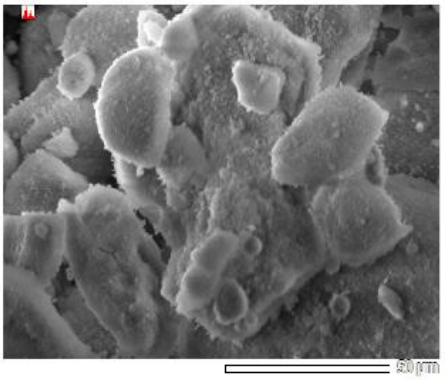

SEM of CR.

Fig. 4. The SF, SF-coated CR, and the SEM of SF used in this study.

2.3 Mix Design and Testing Variables

The control mix (M0, Table 3) was designated according to [55] to integrate about 663, 1168, 180, and 430 kg of well-graded sand, basalt, water, and OPC, respectively. To keep the W/C constant (W/C= 0.5), the superplasticizer (Conplast SP430SA) with 2% of the cement (by weight) was used. The previous concrete components aimed to obtain the 28 days target compressive strength ($f_{cu,28}$) of 40 MPa with 60-100 mm slump. For mixes M1-M4 (G1), the uncoated 1.18 mm CR was used to partially replace sand by 5.0-25% (by volume) to study the CR effect on the concrete strengths and WA (Table 3). In G2 (mixes M5-M8), the uncoated 2.36 mm CR partially replaced sand by 5.0 and 10% (by volume, M5 and M6, respectively), while the combined uncoated CR of 1.18 and 2.36 mm partially replaced sand by 20 and 25% (by volume, M7 and M8, respectively). The mixes of G2 aimed to study the effect of uncoated CR content and size on the concrete strengths and WA (Table 3). Group G3 and G4 had the same mixes as G1 and G2, respectively, but the uncoated CR was replaced by coated CR with SF (Table 3). The mixes of G3 (M9-M12) aimed to study the effect of 1.18 mm CR coated with SF (1.18 CCR) on the concrete

strengths and WA. Conversely, G4 (M13-M16) aimed to investigate the effect of 2.36 mm CCR and combined CCR (particle size =1.18 and 2.36 mm) on the concrete strengths and WA (Table 3).

Table 3. The weights and percentages of the components required for 1 m^3 of concrete.

Group		CR (%)	Sand (kg) (663.1)			Basalt (kg)	CR or CCR (kg)		Water (kg)	Cement (kg)	SP (%)
			2.36 mm	1.18 mm	< 1.18 mm		2.36 mm	1.18 mm			
Control	M0	0	99.5	165.8	397.8	1168	0	0	180	430	2.0
					Uncoated crumb rubber						
G1	M1	5	99.5	132.65	397.8	1168	0	12.26	180	430	2.0
	M2	10	99.5	99.5	397.8	1168	0	24.53	180	430	2.0
	M3	20	99.5	33.2	397.8	1168	0	49.06	180	430	2.0
	M4	25	99.5	0	397.8	1168	0	61.33	180	430	2.0
G2	M5	5	66.35	165.8	397.8	1168	12.26	0	180	430	2.0
	M6	10	33.20	165.8	397.8	1168	24.53	0	180	430	2.0
	M7	20	33.20	99.5	397.8	1168	24.53	24.53	180	430	2.0
	M8	25	16.63	82.93	397.8	1168	30.66	30.66	180	430	2.0
					Coated crumb rubber with silica fume						
G3	M9	5	99.5	132.65	397.8	1168	0	12.26	180	430	2.0
	M10	10	99.5	99.5	397.8	1168	0	24.53	180	430	2.0
	M11	20	99.5	33.2	397.8	1168	0	49.06	180	430	2.0
	M12	25	99.5	0	397.8	1168	0	61.33	180	430	2.0
G4	M13	5	66.35	165.8	397.8	1168	12.26	0	180	430	2.0
	M14	10	33.20	165.8	397.8	1168	24.53	0	180	430	2.0
	M15	20	33.20	99.5	397.8	1168	24.53	24.53	180	430	2.0
	M16	25	16.63	82.93	397.8	1168	30.66	30.66	180	430	2.0

2.4. Mixing Procedures, Specimens, and Testing Methods

The sand, basalt, OPC, and CR or CCR (if they exist) were mechanically dry mixed for 1 min. Consequently, part of the mixing water was regularly added to the running concrete. Afterwards, the rest of the water mixed with the SP was added to the mixer, and then the concrete was mixed for 2 minutes after adding water. Sixteen steel cubes (100 mm x 100 mm x 100 mm x 100 mm x 100 mm) were prepared in one unit (designated by author, Fig. 5) to be cast for each mix to achieve the homogeneity of the cube's components. Moreover, the standard cylinders (150 mm in diameter and 300 mm in depth) were prepared from each mix for the Brazilian tensile test. The mechanical vibrator plate was used to compact the concrete for cubes and cylinders. The steel unit and cylinders were easily de-molded one day after casting without any vibration. The previously de-molded specimens were cured in water tanks until the testing date. The cubes were loaded in compression (Fig. 6) at 7, 28, and 56 days of curing (3 cubes for each case) and averaged to obtain the concrete compressive strength (fcu, [56]). The Brazilian tensile test (Fig. 6) was performed at only 28 days to get the 28-days tensile strength (ftu).

Conversely, the WA of the concrete mixes was measured at 56 days. Among the well-known method of WA measuring techniques ASTM C1585 [57], BS 1881 [58], and ASTM C642 [59], the simple and rapid technique reported in ASTM C642 [59] was used in which the WA was calculated using Eq. (1) [59].

$$WA\ \%_{\ (after\ immersion\ only)} = [\frac{(B-A)}{A}] \times 100 \quad (1)$$

Where A is the oven-dry mass (Temperature= 100 -110 ˚C and time ≥ 24 hours) and B is the surface-dried sample weight of the previous oven-dried cubes after immerging in water (time ≥ 48 hours and temperature ≈21˚ C).

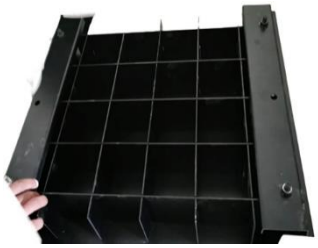

Steel cube unit

Cubes Casting

Cylinder casting

Fig. 5 The prepared steel unit of cubes and casting process.

Compression Test

Tensile test

Fig. 6. The compressive and tensile tests of concrete.

3. Results and Discussions

3.1 Compressive Strength

Table 4 summarizes the obtained RuC compressive strength at 7, 28, and 56 days of curing. Moreover, the reductions in the RuC compressive strength related to the NC strength (μ_7, μ_{28}, and μ_{56}) at the curing days (7, 28, and 56 days, respectively) are also reported in Table 4. Table 4 and Fig. 7 noted that the longer the curing period, the higher the concrete compressive strength, whatever the CR size and content. Moreover, increasing the CR content decreased the compressive strength of all concrete mixes at the three curing dates. For mixes M1-M4, in which the sand with grain size 1.18 mm was replaced by CR having the same particle size, the compressive strength decreased by 11.63-33.72% at 7 days of curing compared to M0. Consequently, increasing the curing date to 28 days reduces the compressive strength reduction for mixes M1-M4 to 10.89-22.12% compared to M0. In

contrast, for the previous mixes (M1-M4), increasing the curing time to 56 days raises the compressive strength reduction to 17.67-25.32% compared to M0. For mixes M5 and M6, the sand with grain size 2.36 mm was replaced by CR having 2.36 mm particle size with similar percentages as in M1 and M2, respectively. For these mixes (M5 and M6), the compressive strength reductions were 25.12-26.66% at 7 days, 6.71-12.09% at 28 days, and 14.44-19.5% at 56 days compared to M0. Comparing M1 and M2 strengths with M5 and M6 strengths highlighted the effect of CR particle size on the concrete compressive strength. Replacing the sand with a high particle size by CR with the same particle size was more efficient than replacing the sand with a small particle size with the corresponding CR particle size. This means the mixes with high fine sand particles and course CR were more efficient than those with coarse sand and fine CR.

Table 4. Compressive strength of concrete with uncoated CR

Group	Mix ID	Specimen No.	$f_{cu,7}$ MPa	Mean MPa	μ_7 %	$f_{cu,28}$ MPa	Mean MPa	μ_{28} %	$f_{cu,56}$ MPa	Mean MPa	μ_{56} %
Control	M0	1	42.44	43.40	0.0	50.32	51.53	0.0	57.00	57.27	0
		2	44.14			50.27			56.20		
		3	43.62			54.00			58.60		
G1	M1	1	38.34	38.31	88.27	44.10	45.95	89.17	48.30	47.15	82.33
		2	34.13			47.74			46.00		
		3	38.27			46.00			43.20		
	M2	1	36.07	36.12	83.30	43.19	43.61	84.63	48.20	46.05	80.41
		2	36.14			43.64			43.90		
		3	36.16			44.00			46.00		
	M3	1	32.90	32.15	74.08	40.70	41.93	81.37	46.30	43.45	75.87
		2	31.40			43.10			40.60		
		3	26.40			42.00			44.00		
	M4	1	29.40	28.77	66.28	40.00	40.13	77.88	42.80	42.77	74.68
		2	24.30			39.90			42.30		
		3	28.00			40.50			43.22		
G2	M5	1	34.60	33.37	76.88	50.20	48.07	93.29	47.00	49.00	85.56
		2	31.80			46.80			49.60		
		3	33.70			47.20			50.40		
	M6	1	33.80	31.83	73.34	41.90	43.97	87.91	50.30	46.10	80.50
		2	31.70			46.90			43.00		
		3	30.00			43.10			45.00		
	M7	1	24.90	24.20	55.76	39.90	38.73	85.52	43.90	45.05	78.66
		2	23.50			38.80			46.20		
		3	24.20			37.50			45.30		
	M8	1	23.60	23.60	54.38	37.01	36.57	70.97	40.10	41.10	71.77
		2	23.90			36.80			42.10		
		3	23.30			35.90			41.60		

$f_{cu,7}$, $f_{cu,28}$, and $f_{cu,56}$= compressive strengths at 7, 28 and 56 days of curing.

Conversely, replacing the sand with combined particle sizes 2.36 and 1.18 mm by the corresponding ratio and particle sizes of CR (M7, 20% CR) follow the same trend as M5 and M6. In contrast, increasing the content of CR with combined particle sizes 2.36 and 1.18 mm to 25% decreased the compressive strength compared to M4 with 1.18 mm CR size (Table 4 and Fig. 7). Increasing the CR content with combined 2.36 and 1.18 mm particles in M8 decreased the concrete strength compared to M4 as the CR particles with big sizes compressed more than those with small sizes besides their weak bond with the surrounding paste. From the previous discussion, replacing sand with size 2.36 mm by the same CR size showed lower effects on the concrete compressive strength than replacing size 1.18 mm as the existing finer sand size may enhance the mix's cohesion than that with size 2.36 mm. Moreover, the smaller the sand size, the higher the area of cohesion in the

mix, in contrast to CR, as CR surface affected the mortar cohesion with the surrounding aggregate.

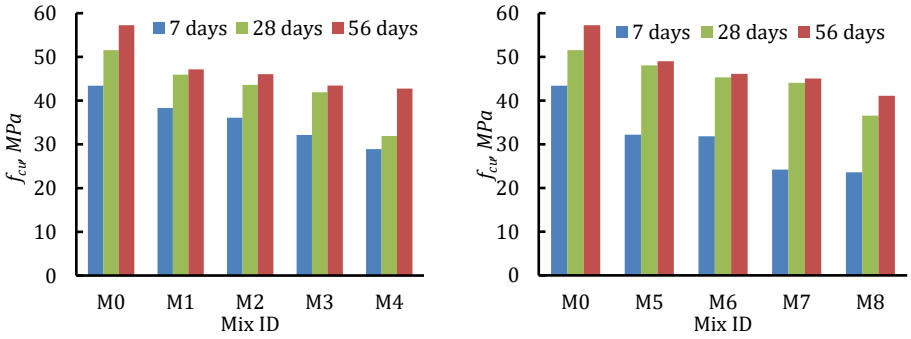

Fig. 7. Effect of un-coated CR size and content on the concrete compressive strength

SF was used to coat the CR particles to enhance the bond between the CR particles and the surrounding concrete components. To show both the SF coating and CR particle size effects on the concrete strength, the mixes in group G3 (with SF pre-coated CR) were compared with the corresponding mixes in group G1 (with uncoated CR), see Table 5 (μ_1, μ_2 *and* μ_3 are the percentage of concrete strength with SF coated and uncoated CR at 7. 28 and 56 days, respectively).

Table 5. The compression strength of concrete with SF-coated CR

Group	Mix ID	Spec. No.	$f_{cu.7}$ MPa	Mean MPa	$f_{cu.28}$ MPa	Mean MPa	$f_{cu,56}$ MPa	Mean MPa	μ_1 %	μ_2 %	μ_3 %
G3	M9	1	39.10	40.18	46.90	46.15	47.20	48.05	104.88	100.44	101.91
		2	38.90		45.40		48.90				
		3	40.60		47.30		47.07				
		4	43.00		49.60		48.50				
	M10	1	42.40	42.73	45.10	47.33	48.02	48.26	118.30	108.53	104.80
		2	42.80		47.30		46.10				
	M11	1	23.51	23.80	28.12	26.88	33.40	32.3	74.03	64.11	74.34
		2	23.90		27.24		31.20				
		3	24.00		25.28		33.00				
	M12	1	23.51	22.50	25.30	24.50	26.00	25.6	78.02	92.43	59.86
		2	22.30		24.00		25.00				
		3	21.70		24.20		25.80				
G4	M13	1	38.11	38.28	46.80	44.43	47.25	47.20	114.71	92.42	96.82
		2	38.42		40.91		48.3				
		3	38.30		45.30		46.2				
	M14	1	29.12	29.03	35.73	35.46	41.7	40.30	91.20	80.65	87.42
		2	28.54		36.62		38.9				
		3	29.43		34.02		37.2				
	M15	1	27.24	27.98	31.63	31.89	35.6	36.00	115.62	82.34	79.91
		2	28.60		29.91		33.9				
		3	28.10		34.14		36.5				
	M16	1	25.80	25.33	25.30	27.74	32.4	34.03	107.33	75.85	82.80
		2	24.09		27.95		33.9				
		3	25.30		29.98		35.8				

Besides, comparing the results in G2 with the corresponding mixes in G3 and G4. In G3, for the mixes M9-M12, the sand with a grain size of 1.18 mm was replaced by 1.18 mm CR particles pre-coated with SF. The compressive strength of M9 and M10 enhanced by 104.88 and 118.3% (at 7 days), 100.44 and 108.53% (at 28 days), and 101.91 and 104.80 (at 56 days) compared to M1 and M2, respectively, at the same curing days (Table 4). In contrast, increasing the content of CCR with 1.18 mm size to 20 and 25% decreased the concrete compressive strength compared to the corresponding specimens with uncoated CR. The extra amount of SF in the mix may affect the cement hydration and reduce the concrete strength. Conversely, using the CCR with a 2.36 mm size to replace the sand with a 2.36 mm size decreased the concrete strength compared to the corresponding mixes with uncoated CR. The higher the CR particle size, the easier CR was compressed and the lower the effect of the coating. Moreover, increasing the pre-coated CR content increased the SF in the mix and thus decreased the concrete compressive strength. The same trend was also noticed for RuC mixes (M15 and M16) compared to M7 and M8, respectively (Table 5 and Fig. 8). Among all the tested mixes, M10 showed the highest compressive strength value compared to M0 (93.65% at 28 days, Table 5). A sample of the tested cubes for mixes with coated and uncoated CR is shown in Fig. 9.

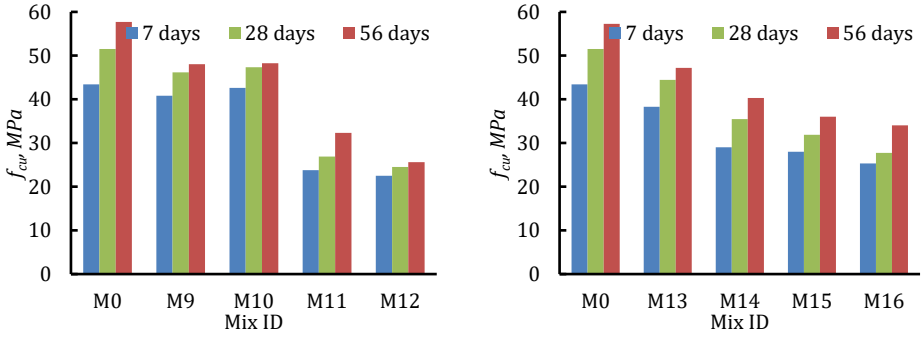

Fig. 8. Effect of SF-coated CR size and content on the concrete compressive strength.

3.2 Concrete Tensile Strength

The tensile strength at 28 days of curing for the tested RuC mixes decreased or increased depending on the CR content and particle size (Fig. 10, M refers to the mixes containing combined sizes of CR with 2.36 and 1.18 mm particle sizes). The tensile strength for the mixes with 1.18 mm uncoated CR was lower than that of M0. The RuC tensile strength reduction decreased as the replacement ratio of 1.18 mm CR increased from 10 to 25 %. The mix M2 had the best tensile strength among the mixes cast with the 1.18 mm uncoated CR. Replacing sand with 2.36 mm uncoated CR decreased the RuC tensile strength. The reduction increased as the CR content increased. Increasing the CR size increased the RuC tensile strength reduction. Conversely, coating the CR with SF reduced the tensile strength compared to those with uncoated CR except for M6 (1.18 mm CCR%= 10%). In contrast, the mixes with 2.36 mm coated CR showed higher tensile strength than those with uncoated CR.

M1

M2

M5

M6

M9

M10

M13

M14

Fig. 9. Photos of the specimens with pre-coated and un-coated CR tested at 28 days of curing

The mix M5 (CCR with 2.36 mm) showed higher RuC tensile strength than M0. From the above, it was assured that replacing the fine sand with 1.18 mm uncoated CR increased the RuC tensile strength than replacing the 2.36 mm sand with 2.36 mm uncoated CR. Conversely, replacing the sand with combined particle sizes by the corresponding CR (1.18 and 2.36 mm CCR) was more efficient than using the 1.18 mm CCR. The uncoated 1.18 mm CR may act as a crack closer with more efficiency than the uncoated 2.36 mm CR. Consequently, in the case of CCR, replacing the 1.18 mm sand with 1.18 mm CCR might increase the SF surface area and disturb the cement hydration than in the case of coarser CR with low SF surface area.

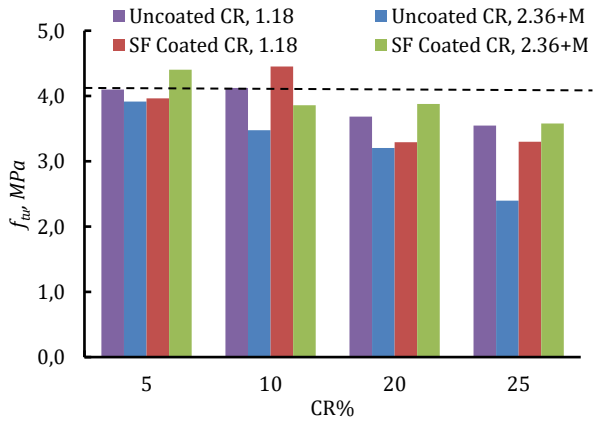

Fig. 10. The tensile strength of RuC mixes at 28 days. The dash line= M0 tensile strength (4.16 MPa).

3.3 Water Absorption of Concrete

Water absorption of concrete for all the prepared mixes tested at 56 days is presented in Fig. 11. WA was found to be concerned with the surface porosity and structural pores, and the existence of pores in geopolymer concrete specimens is also connected to WA [60,61]. Moreover, the finer the fly ash, the higher the surface area of its particles, which enhances the fly ash reactivity and the concrete properties [62]. From Fig. 11, it was observed that the WA of the RuC was higher than the WA of M0 except for M13 (with 2.36 mm CCR) as the porosity of the concrete increased with adding CR. The WA for mixes M1-M4 in which the 1.18 mm uncoated CR was partially replaced by the 1.18 mm sand had nearly the same values. Coating the 1.18 mm CR with SF significantly increased the WA, revealing the effect of SF on increasing the WA except for M10 (with 10% of 1.18 mm CCR). Conversely, increasing the uncoated CR size increased the WA of RuC as the concrete porosity increased as the CR particle size increased. Conversely, coating the 2.36 CR with SF decreased the WA of RuC, which reveals that the lower the coated CR area, the lower the WA, as the SF could decrease the decreased voids generated by the CR in the concrete mixes [41,60,61].

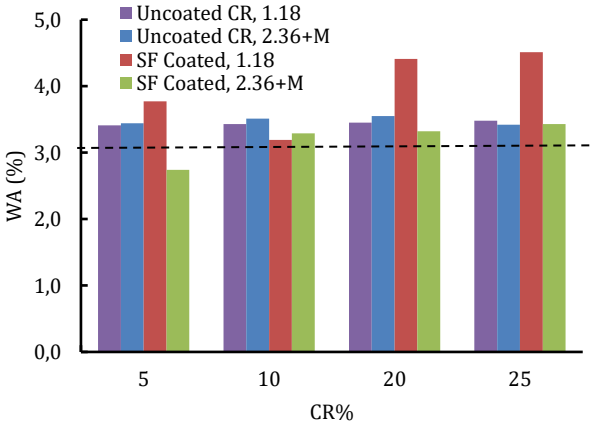

Fig. 11. The WA of RuC mixes at 28 days. The dash line= WA% of M0 (3.07).

4. Conclusion

- The higher the fine sand in the RuC mix, the higher the area of cohesion in the mix compared to those with uncoated CR, as the surface of rubber affected the mortar cohesion with the surrounding aggregate.
- Replacing sand with a particle size of 2.36 mm by 5 and 10% of 2.36 mm CCR showed higher RuC compressive strength than replacing sand with 1.18 mm particle size by the corresponding 1.18 mm CCR at all testing ages (7, 28, and 56 days).
- Increasing the content of CCR with 1.18 mm particle size to 20 and 25% decreased the concrete compressive strength compared to the corresponding specimens with uncoated CR. Also, using the CCR with a 2.36 mm particle size to replace the same content of sand with a 2.36 mm particle size reduced the concrete strength compared to the corresponding mixes with uncoated CR.
- Replacing the fine sand (particle size=1.18 mm) with uncoated CR (particle size=1.18 mm) increased the RuC tensile strength than replacing the sand with 2.36 mm particle size with the corresponding uncoated CR. Conversely, replacing the sand with combined particle sizes (1.18 and 2.36 mm) with the corresponding CCR was more efficient than replacing the sand with a 1.18 mm size particle with the 1.18 mm CCR.
- In the case of CCR, replacing the sand with a 1.18 mm particle size by the corresponding CCR might increase the SF surface area and disturb the cement hydration than in the case of coarser CCR, which had a lower SF surface area.
- As the 1.18 mm sand was partially replaced by 1.18 mm uncoated CR, the RuC mixes had nearly the same WA values. Using the 1.18 mm CCR instead of sand significantly increased the WA of the RuC, revealing the effect of SF on increasing the WA except for M10 (with 10% of 1.18 mm CCR). In contrast, Increasing the particle size of uncoated CR increased the WA of the RuC. Conversely, using the 2.36 CCR to replace sand decreased the WA of the RuC than for the 1.18 mm CCR.

Acknowledgment

The researchers would like to acknowledge the Deanship of Scientific Research, Taif University for funding this work.

References

[1] Martínez-García R, de Rojas MIS, Pozo JMM Del, Fraile-Fernández FJ, Juan-Valdés A. Evaluation of mechanical characteristics of cement mortar with fine recycled concrete aggregates (FRCA). Sustain 2021;13:1-23. https://doi.org/10.3390/su13010414

[2] Pacheco-Torgal F. High tech startup creation for energy efficient built environment. Renew Sustain Energy Rev 2017;71:618-29. https://doi.org/10.1016/j.rser.2016.12.088

[3] Tam VWY, Soomro M, Evangelista ACJ. A review of recycled aggregate in concrete applications (2000-2017). Constr Build Mater 2018;172:272-92. https://doi.org/10.1016/j.conbuildmat.2018.03.240

[4] Gravina RJ, Xie T. Toward the development of sustainable concrete with Crumb Rubber: Design-oriented Models, Life-Cycle-Assessment and a site application. Constr Build Mater 2022;315:125565. https://doi.org/10.1016/j.conbuildmat.2021.125565

[5] Savas BZ, Ahmad S, Fedroff D. Freeze-Thaw Durability of Concrete with Ground Waste Tire Rubber. Transp Res Rec J Transp Res Board 1997;1574:80-8. https://doi.org/10.3141/1574-11

[6] Li G, Garrick G, Eggers J, Abadie C, Stubblefield MA, Pang S-S. Waste tire fiber modified concrete. Compos Part B Eng 2004;35:305-12. https://doi.org/10.1016/j.compositesb.2004.01.002
[7] Assaggaf RA, Maslehuddin M, Al-Dulaijan SU, Al-Osta MA, Ali MR, Shameem M. Cost-effective treatment of crumb rubber to improve the properties of crumb-rubber concrete. Case Stud Constr Mater 2022;16:e00881. https://doi.org/10.1016/j.cscm.2022.e00881
[8] Al-Fakih A, Mohammed BS, Liew MS. On rubberized engineered cementitious composites (R-ECC): A review of the constituent material. Case Stud Constr Mater 2021;14:e00536. https://doi.org/10.1016/j.cscm.2021.e00536
[9] XU J, Yao Z, Yang G, Han Q. Research on crumb rubber concrete: From a multi-scale review. Constr Build Mater 2020;232:117282. https://doi.org/10.1016/j.conbuildmat.2019.117282
[10] Youssf O, Elgawady MA, Mills JE, Ma X, Mohammed BS, Awang AB, et al. Properties of nano silica modified rubbercrete. Constr Build Mater 2016;119:522-32. https://doi.org/10.1016/j.jclepro.2016.02.007
[11] Youssf O, Elgawady MA, Mills JE, Ma X. An experimental investigation of crumb rubber concrete confined by fibre reinforced polymer tubes. Constr Build Mater 2014;53:522-32. https://doi.org/10.1016/j.conbuildmat.2013.12.007
[12] Toutanji HAA, Youssf O, Elgawady MA, Mills JE, Ma X, Mohammed BS, et al. The use of rubber tire particles in concrete to replace mineral aggregates. Cem Concr Compos 1996;18:135-9. https://doi.org/10.1016/0958-9465(95)00010-0
[13] Topcu I, Topçu IB. The properties of rubberized concretes. Cem Concr Res 1995;25:304-10. https://doi.org/10.1016/0008-8846(95)00014-3
[14] Gesolu M, Güneyisi E. Permeability properties of self-compacting rubberized concretes. Constr Build Mater 2011;25:3319-26. https://doi.org/10.1016/j.conbuildmat.2011.03.021
[15] Chen Z, Li L, Xiong Z. Investigation on the interfacial behaviour between the rubber-cement matrix of the rubberized concrete. J Clean Prod 2019;209:1354-64. https://doi.org/10.1016/j.jclepro.2018.10.305
[16] Bisht K, Ramana P V. Waste to resource conversion of crumb rubber for production of sulphuric acid resistant concrete. Constr Build Mater 2019;194:276-86. https://doi.org/10.1016/j.conbuildmat.2018.11.040
[17] Medina NF, Medina DF, Hernández-Olivares F, Navacerrada MA. Mechanical and thermal properties of concrete incorporating rubber and fibres from tyre recycling. Constr Build Mater 2017;144:563-73. https://doi.org/10.1016/j.conbuildmat.2017.03.196
[18] Jokar F, Khorram M, Karimi G, Hataf N. Experimental investigation of mechanical properties of crumbed rubber concrete containing natural zeolite. Constr Build Mater 2019;208:651-8. https://doi.org/10.1016/j.conbuildmat.2019.03.063
[19] Nocera F, Wang J, Faleschini F, Demartino C, Gardoni P. Probabilistic models of concrete compressive strength and elastic modulus with rubber aggregates. Constr Build Mater 2022;322:126145. https://doi.org/10.1016/j.conbuildmat.2021.126145
[20] Mo J, Ren F, Ye Y, Tian S, Lai C. Effect of different crumb rubber particle sizes on the flexural properties of crumb rubber concrete. Mater Lett 2022;326:132960. https://doi.org/10.1016/j.matlet.2022.132960
[21] Xue J, Shinozuka M. Rubberized concrete: A green structural material with enhanced energy-dissipation capability. Constr Build Mater 2013;42:196-204. https://doi.org/10.1016/j.conbuildmat.2013.01.005
[22] Alwi Assaggaf R, Uthman Al-Dulaijan S, Maslehuddin M, Baghabra Al-Amoudi OS, Ahmad S, Ibrahim M. Effect of different treatments of crumb rubber on the durability characteristics of rubberized concrete. Constr Build Mater 2022;318:126030. https://doi.org/10.1016/j.conbuildmat.2021.126030

[23] Assaggaf RA, Ali MR, Al-Dulaijan SU, Maslehuddin M. Properties of concrete with untreated and treated crumb rubber - A review. J Mater Res Technol 2021;11:1753-98. https://doi.org/10.1016/j.jmrt.2021.02.019
[24] Cai X, Zhang L, Pan W, Wang W, Guan Q, Zhai S, et al. Study on evaluation of elastic modulus of crumb rubber concrete in meso-scale. Constr Build Mater 2022;331:127247. https://doi.org/10.1016/j.conbuildmat.2022.127247
[25] Xu J, Fu Z, Han Q, Lacidogna G, Carpinteri A. Micro-cracking monitoring and fracture evaluation for crumb rubber concrete based on acoustic emission techniques. Struct Heal Monit 2018;17:946-58. https://doi.org/10.1177/1475921717730538
[26] Zhu H, Wang Z, Xu J, Han Q. Microporous structures and compressive strength of high-performance rubber concrete with internal curing agent. Constr Build Mater 2019;215:128-34. https://doi.org/10.1016/j.conbuildmat.2019.04.184
[27] Youssf O, ElGawady M. An overview of sustainable concrete made with scrap rubber. From Mater. to Struct. Adv. through Innov., CRC Press; 2012, p. 1039-44. https://doi.org/10.1201/b15320-185
[28] Pelisser F, Zavarise N, Longo TA, Bernardin AM. Concrete made with recycled tire rubber: Effect of alkaline activation and silica fume addition. J Clean Prod 2011;19:757-63. https://doi.org/10.1016/j.jclepro.2010.11.014
[29] Li G, Pang S-S, Ibekwe SI. FRP tube encased rubberized concrete cylinders. Mater Struct 2011;44:233-43. https://doi.org/10.1617/s11527-010-9622-8
[30] Najim KB, Hall MR. A review of the fresh/hardened properties and applications for plain- (PRC) and self-compacting rubberised concrete (SCRC). Constr Build Mater 2010;24:2043-51. https://doi.org/10.1016/j.conbuildmat.2010.04.056
[31] Ganjian E, Khorami M, Maghsoudi AA. Scrap-tyre-rubber replacement for aggregate and filler in concrete. Constr Build Mater 2009;23:1828-36. https://doi.org/10.1016/j.conbuildmat.2008.09.020
[32] Son KS, Hajirasouliha I, Pilakoutas K. Strength and deformability of waste tyre rubber-filled reinforced concrete columns. Constr Build Mater 2011;25:218-26. https://doi.org/10.1016/j.conbuildmat.2010.06.035
[33] Topcu I. The properties of rubberized concretes. Cem Concr Res 1995;25:304-10. https://doi.org/10.1016/0008-8846(95)00014-3
[34] Eldin NN, Senouci AB. Rubber-Tire Particles as Concrete Aggregate. J Mater Civ Eng 1993;5:478-96. https://doi.org/10.1061/(ASCE)0899-1561(1993)5:4(478)
[35] Khatib ZK, Bayomy FM. Rubberized Portland Cement Concrete. J Mater Civ Eng 1999;11:206-13. https://doi.org/10.1061/(ASCE)0899-1561(1999)11:3(206)
[36] Ren F, Mo J, Wang Q, Ho JCM. Crumb rubber as partial replacement for fine aggregate in concrete: An overview. Constr Build Mater 2022;343:128049. https://doi.org/10.1016/j.conbuildmat.2022.128049
[37] C494/C494M. Standard Specification for Chemical Admixtures for Concrete. Annu. B. ASTM Stand., 2013, p. 1-6.
[38] Gravina RJ, Xie T, Roychand R, Zhuge Y, Ma X, Mills JE, et al. Bond behaviour between crumb rubberized concrete and deformed steel bars. Structures 2021;34:2115-33. https://doi.org/10.1016/j.istruc.2021.08.076
[39] Shahzad K, Zhonghu Z. Experimental Study of Naoh Pretreated Crumb Rubber Concrete as Substitute of Fine Aggregate. Constr Build Mater 2022;358:129448. https://doi.org/10.1016/j.conbuildmat.2022.129448
[40] Wang J, Guo Z, Yuan Q, Zhang P, Fang H. Effects of ages on the ITZ microstructure of crumb rubber concrete. Constr Build Mater 2020;254:119329. https://doi.org/10.1016/j.conbuildmat.2020.119329
[41] Onuaguluchi O. Effects of surface pre-coating and silica fume on crumb rubber-cement matrix interface and cement mortar properties. J Clean Prod 2015;104:339-45. https://doi.org/10.1016/j.jclepro.2015.04.116

[42] Onuaguluchi O, Panesar DK. Hardened properties of concrete mixtures containing pre-coated crumb rubber and silica fume. J Clean Prod 2014;82:125-31. https://doi.org/10.1016/j.jclepro.2014.06.068
[43] Assaggaf R, Maslehuddin M, Al-Osta MA, Al-Dulaijan SU, Ahmad S. Properties and sustainability of treated crumb rubber concrete. J Build Eng 2022;51:104250. https://doi.org/10.1016/j.jobe.2022.104250
[44] Singh Sidhu A, Siddique R. Utilisation of crumb tire rubber in development of sustainable metakaolin based high strength concrete. Constr Build Mater 2022;345:128412. https://doi.org/10.1016/j.conbuildmat.2022.128412
[45] Lai D, Demartino C, Xiao Y. High-strain rate compressive behavior of Fiber-Reinforced Rubberized Concrete. Constr Build Mater 2022;319:125739. https://doi.org/10.1016/j.conbuildmat.2021.125739
[46] Pham TM, Davis J, Ha NS, Pournasiri E, Shi F, Hao H. Experimental investigation on dynamic properties of ultra-high-performance rubberized concrete (UHPRuC). Constr Build Mater 2021;307:125104. https://doi.org/10.1016/j.conbuildmat.2021.125104
[47] Güneyisi E, Gesoglu M, Naji N, Ipek S. Evaluation of the rheological behavior of fresh self-compacting rubberized concrete by using the Herschel-Bulkley and modified Bingham models. Arch Civ Mech Eng 2016;16:9-19. https://doi.org/10.1016/j.acme.2015.09.003
[48] Bakhtiari Ghaleh M, Asadi P, Eftekhar MR. Enhancing mechanical performance of waste tire concrete with surface double pre-coating by resin and micro-silica. J Build Eng 2022;50:104084. https://doi.org/10.1016/j.jobe.2022.104084
[49] Shen M, Huang W, Liu J, Zhou Z. Axial compressive behavior of rubberized concrete-filled steel tube short columns. Case Stud Constr Mater 2022;16:e00851. https://doi.org/10.1016/j.cscm.2021.e00851
[50] Kumar R, Dev N. Mechanical and Microstructural Properties of Rubberized Concrete After Surface Modification of Waste Tire Rubber Crumb. Arab J Sci Eng 2021. https://doi.org/10.1007/s13369-021-06154-w
[51] Ghaleh MB, Asadi P, Eftekhar MR. Enhancing mechanical performance of waste tire concrete with surface double pre-coating by resin and micro-silica. J Build Eng 2022;50:104084. https://doi.org/10.1016/j.jobe.2022.104084
[52] ASTM Standard C33, ASTM C33/C33M-18, ASTM C33, ASTM C33/C33M-18, ASTM International. Standard Specification for Concrete Aggregates. ASTM Int West Conshohocken, PA, USA, 2003.
[53] Yadav JS, Tiwari SK. A study on the potential utilization of crumb rubber in cement treated soft clay. J Build Eng 2017;9:177-91. https://doi.org/10.1016/j.jobe.2017.01.001
[54] Alwi R, Maslehuddin M, Al-dulaijan SU, Al-osta MA, Rizwan M, Shameem M. Case Studies in Construction Materials Cost-effective treatment of crumb rubber to improve the properties of crumb-rubber concrete. Case Stud Constr Mater 2022;16:e00881. https://doi.org/10.1016/j.cscm.2022.e00881
[55] American Concrete Institute. ACI 211.1 Standard Practice for Selecting Proportions for Normal, Heavyweight, and Mass Concrete (ACI 211.1-91). ; Am Concr Inst Farmingt Hills, MI, USA, 2002.
[56] BS EN 12390-3:2009. Testing hardened concrete, Part 3: Compressive strength of test specimens (2009). Br Stand Inst 2009.
[57] Mohammadi B. (2013). Development of Concrete Water Absorption Testing for Quality Control School of Graduate Studies.
[58] BS 1881: Part 122: 1983. Testing concrete-Method for determination of water absorption. Br Stand,2009.
[59] ASTM C642-13. Standard test method for density, absorption, and voids in hardened concrete, ASTM International. ASTM Int,2013.

[60] Das D, Rout PK. Synthesis of Inorganic Polymeric Materials from Industrial Solid Waste. Silicon 2023;15:1771-1791. https://doi.org/10.1007/s12633-022-02116-5
[61] Rashad AM, Gharieb M. An investigation on the effect of sea sand on the properties of fly ash geopolymer mortars. Innov Infrastruct Solut 2021;6:1-9. https://doi.org/10.1007/s41062-020-00421-9
[62] Das D, Rout PK. Synthesis, Characterization and Properties of Fly Ash Based Geopolymer Materials. J Mater Eng Perform 2021;30:3213-31. https://doi.org/10.1007/s11665-021-05647-x

Research on Engineering Structures & Materials
www.jresm.org
Research Group

Research Article

Influence of incorporation carbon nanoparticles CNP on the mechanical properties of polystyrene composite

Mohamed Ismail[1, a], Mohamed Bayoumi[2, b], Sayed Akl[1, c]

[1]*Department of Mechanical Engineering, The British University in Egypt, Egypt*
[2]*Department of Mechanical Engineering, Al-Azhar University, Cairo, Egypt*

Article Info

Article history:

Received 23 Aug 2023
Accepted 22 Nov 2023

Keywords:

Carbon nanoparticles;
Polystyrene;
Tension;
Impact;
Hardness;
Polymer;
Nanocomposites

Abstract

Polymer nanocomposites have recently received a lot of attention as they are anticipated to be used in a variety of applications. In this study, the effect of adding carbon nanoparticles to polystyrene and using Injection molding technique are investigated. The impact of adding different weight fractions of carbon nanoparticles (CNP) on tensile properties, impact strength and hardness performance of polystyrene polymer were measured. Tensile and impact strength increased with the addition of nanoparticles (CNP). The polymer composites with 0.025 wt.% CNP demonstrated maximum tensile and impact strength compared to pure polystyrene. Also, the maximum value of hardness appeared at 0.1 wt.% of CNP finally cracks are found in higher CNP concentration compared with lower percentages of CNP.

1. Introduction

Nanotechnology has attracted more attention throughout the last years. Nanoparticles are a key component of nanotechnology. Nanoparticles could be with a diameter ranging from one to one hundred nanometers and could be made of carbon, metal, metal oxides, or organic substances [1]. At the nanoscale, the particles have different mechanical and chemical properties than their larger counterparts. This is due to a larger surface area relative to volume, improved chemical compound stability, increased mechanical strength, and other factors [2-5].

Due to these characteristics, nanoparticles are now used in a wide range of applications. The traditional fillers for polymer composites are either reinforcement or particles. Popular reinforcements for fiber-reinforced composites include glass fiber, metal fiber, and carbon fiber. Particle-reinforced composites frequently use reinforcement materials including metal, silicon, and graphite. [6].

Metal Matrix Composites (MMCs) are materials made by adding (ceramic or metallic) particles, fibers, whiskers, or even sheet metal to the base material to produce an alloy or metal matrix. MMCs are exceptional materials that perform much better than their homogeneous parent substances in a variety of ways, including strength, wear resistance, corrosion resistance, and other characteristics. [7]. The success of MMCs in industry depends heavily on their ability to be produced into components and structures. They can only be connected in this way if they use welding and associated techniques. The presence

*Corresponding author: mohamed.elzareef@bue.edu.eg
[a] orcid.org/0009-0001-0526-8263; [b] orcid.org/0009-0007-3656-3154; [c] orcid.org/0009-0006-1967-9318
DOI: http://dx.doi.org/10.17515/resm2023.37me0823rs

of strengthening particles, which should have been advantageous to the MMCs, instead makes it more difficult for them to weld. [8] Many researchers investigated the mechanical characteristics of nanocomposites strengthened with just one type of reinforcement [9:13]. Others, on the other hand, investigated the effect of mixing two distinct types of reinforcement into a matrix of polymers with fiber reinforcement. Ayatollah et al. [14] investigated the effects of MWCNT's and nano-silica on the tensile performance of epoxy reinforced with woven carbon fabric-strengthened composites.

The addition of 0.5 wt.% of both nanoparticles greatly enhanced tensile performance; nevertheless, adding 0.9 wt.% results in a decline in the general pattern of tensile characteristics. Jun Rong Li [15] The development of crystalline polymer-based composites of polystyrene reinforced with CNP as prospective gas-sensing materials has been studied. Through polymerization filling, which is in-situ polymerization of styrene in the presence of CNP, the composites were given a low percolation threshold. The findings of the experiments demonstrated the composites' selective sensitivity, as seen by their great electrical reactivity to the vapors of nonpolar and low polar solvents and their weak reactivity to the vapors of high polar solvents. In addition to conductivity, the fillers' and matrix's absorption properties significantly affect the composites' sensitivity to gases. Also S. Hernández-López [16] investigated Experimental investigation of electrical resistivity variations in polystyrene and CNP-based mixes 22 wt.% CNP composite sheets were subjected to thermal heating-cooling cycles from room temperature to 100°C, only slightly above the Tg of the composite, at thicknesses of 0.030 mm, 2mm, and 10mm. For each cycle change in electrical resistivity, a hysteresis loop based on sample thickness forms. Marius et al. [17] examined how the mechanical characteristics of composite materials were affected using natural resources (Dammar gum) and wastepaper. The outcomes showed that the matrix's characteristics had changed significantly.

In the present study the effect of using carbon nanoparticles (CNP) as a reinforcement material is investigated to enhance the mechanical properties of the polystyrene used in injection molding industry.

2. Experimental Works

2.1 Materials

The polymer used in the present study is Polystyrene (PS) and carbon nanoparticles (CNP) were used as reinforcement was supplied from Sigma-Aldrich® company, the properties of polymer and reinforcement material according to the manufacturers are shown in [18-19].

2.2 Sample Preparation

Polystyrene polymer granules and carbon nanoparticles were prepared according to the required amount of reinforcement particles inside the matrix.

Table 2. Samples code with CNP weight percent

#	Sample code	Wt. % for CNP
1	PS 0000	0.000
2	PS 0.025	0.025
3	PS 0.050	0.050
4	PS 0.100	0.100

Then the mixture was directly injected using an automatic Vertical Small Plastic Injection Molding Machine "DAHOMETER Bench Model [20]" Figure 1 to start the forming process for the polymer composite test specimens Figure 2 and 3, each sample has a given code as shown in Table 2.

Fig. 1. Automatic vertical small plastic injection molding machine "DAHOMETER bench model" [20]

Fig. 2. Tensile specimen mold

Fig. 3. Impact specimen mold

2.3 Mechanical Properties

The impact of CNP weight percent on mechanical characteristics was assessed. Using a Computer Control Universal Testing machine/universal testing machine UTES-20 (FIE, India), tension tests were performed in accordance with ASTM D3039. Using an injection mold with an interior cavity dimension as illustrated in figure 4, samples were created as a single homogenous material.

An automated computer data collecting system generated the stress-strain curves. At room temperature, all experiments were conducted. For each sample, five specimens were tested under tension, and the average value was computed. This value was then chosen to represent the test result.

The impact strength and absorbed energy were measured by the Charpy test according to ASTM 256. Impact tests were carried out on impact machine type AVERY Denison, England. Samples were formed as a single homogeneous material by using injection mold with internal cavity with a dimension equal to 55 mm as a length, and 10 x10 mm as a cross section and V-notch angle equal 45o.The energy absorbed per unit area of the fractured cross-section is the measure of the impact strength of a specimen.

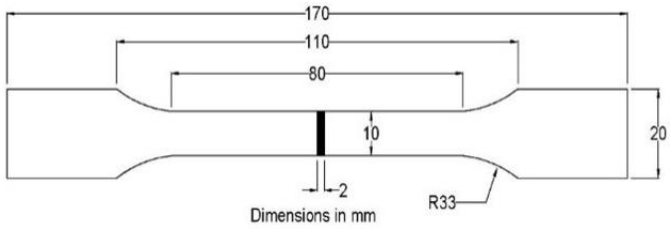

Fig. 4.Dimensions and geometry of the tensile test

Microstructure examination was performed on some polymer composites using scanning electron microscope (SEM) to study the interfacial junction between matrix and reinforcements and the fracture surface of the nanocomposites.

3. Results and Discussion

3.1 Tensile Tests

Figure 5 shows stress-strain curves at different wt.% contents of CNP. The figure shows the influence of nanoparticle reinforcements on the tensile strength of polymer matrix. The additives of CNP 0.025 wt. % content shows maximum ultimate tensile strength and maximum elongation. The figure shows also that all specimens failed quickly after the tensile load reached their maximum value. The ultimate tensile strength values of pure polystyrene and reinforced composite with carbon nanoparticles are shown in Figure 6. Tensile strength was significantly increased with the decrease in the wt.% content of CNP and the ideal wt.% content of CNP in PS is 0.025. This is due to the low number of nanoparticles which leads to reducing agglomeration between CNP. However, increasing the amount of CNP concentration to 0.1% reduces this gain due to the large agglomeration of CNP and the non-uniformed distribution of the reinforcement CNP's.

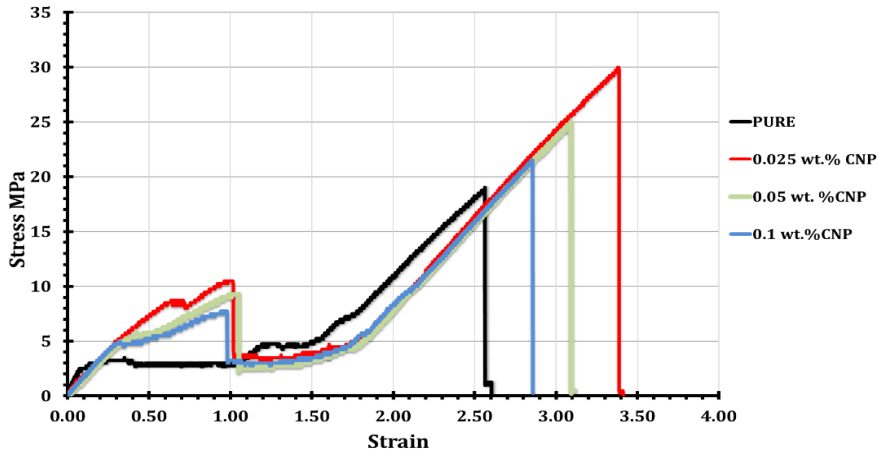

Fig. 5. Stress strain curves of polymer composites at different contents of CNP

SEM images are obtained to examine the failure reaction of the tensile samples and to verify the dispersion of the particles in the matrix. The fracture surfaces' SEM pictures at various CNP concentrations are shown in Figure 7. Images make it quite evident that CNP was evenly distributed throughout the polystyrene.

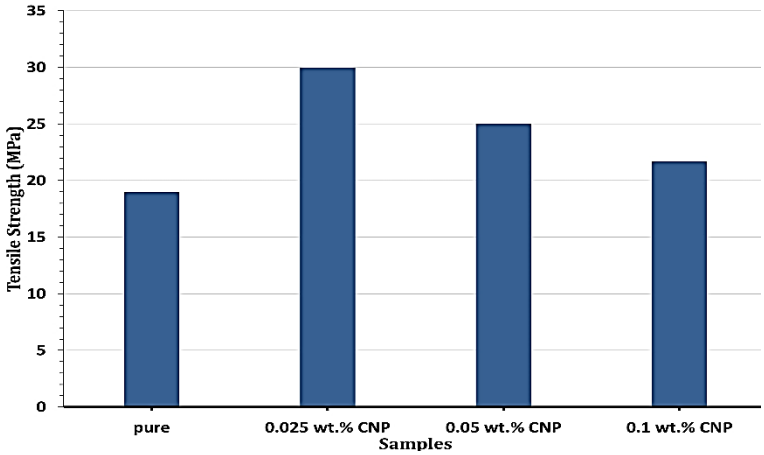

Fig. 6. Obtained tensile strength for Produced specimen according to CNP wt. %

The picture also demonstrates effective matrix and reinforcement mixing, showing the effectiveness of the injection molding technique in reducing porosity development and improving nanoparticle dispersion. However, it is also clear from the microphotographs that the 0.025 weight percent of CNP (figure 7.b) appears to be distributed uniformly with relatively small amount of agglomeration. This improvement could be because of the low CNP concentration, which decreased the likelihood of CNP agglomeration.

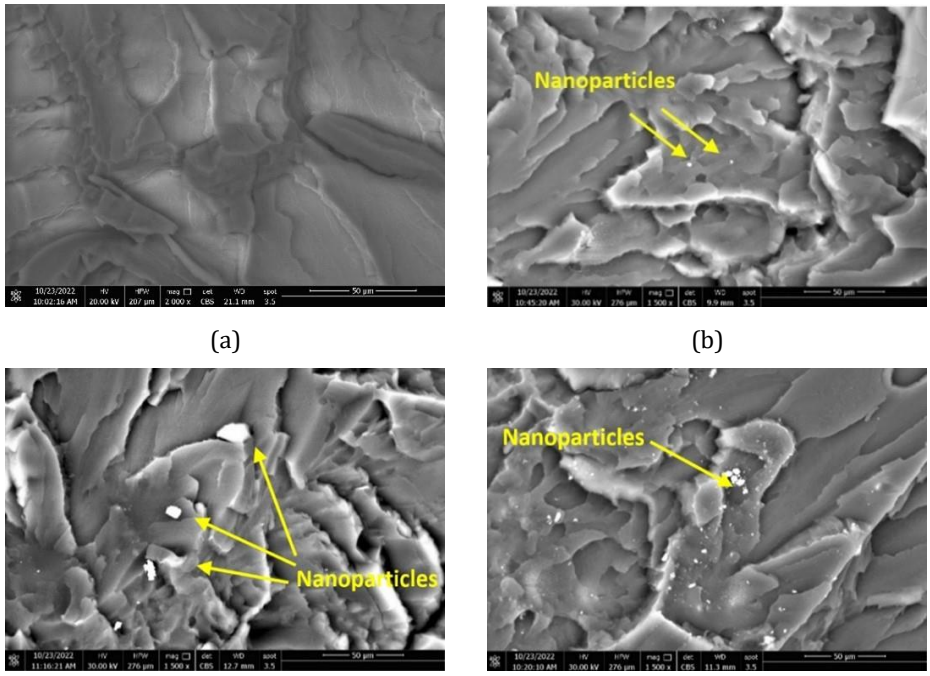

(a) (b)

(c) (d)

Fig. 7. Scanning electron photographs of tensile fracture surfaces a) pure polystyrene, b) 0.025 wt. 0 %, c) 0.05 wt. % and d) 0.1 wt.%

3.2 Crack Formation

The higher addition of CNP weight percentage increases the amount of microporosities connected to the agglomerations that are generated, and these microscopic pores might create channels at the interface that serve as debonding starting points [21]. The matrix's particle bonds were weakened as a result of the CNP, leading to a significant degree of propagating transversal cracking. Figures 8 and 9 demonstrate how the high concentration of the crack develops surrounding agglomerated CNP at 0.1 weight percent.

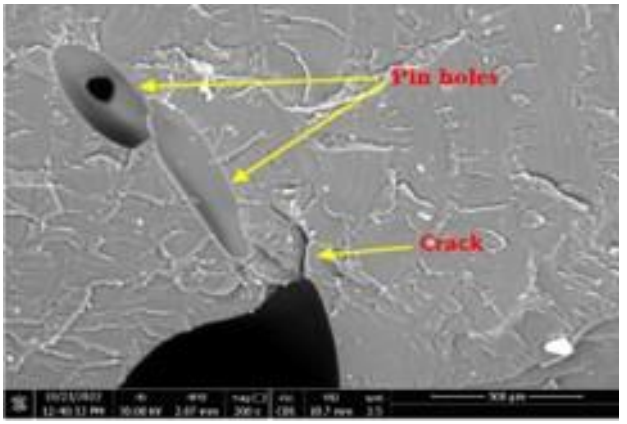

Fig. 8. Pin hole crack propagation on polystyrene reinforced by 0.1 wt.% CNP

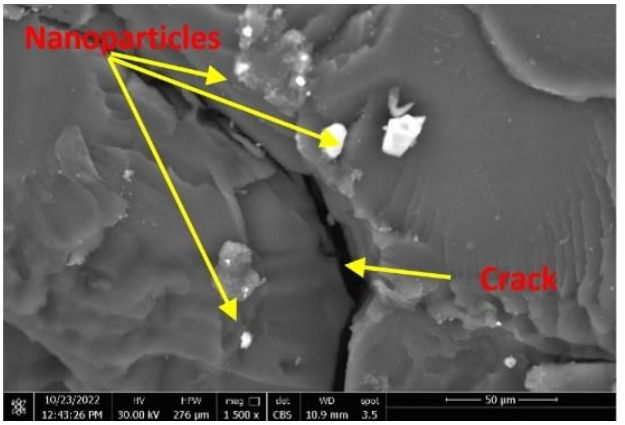

Fig. 9. Crack propagation on polystyrene reinforced by 0.1 wt.% CNP

Figure 10 shows the different weight percentage of CNP reinforcing polystyrene and crack formation and as mentioned before the greater the weight percentage of CNP, the greater cracks formation found on reinforced samples.

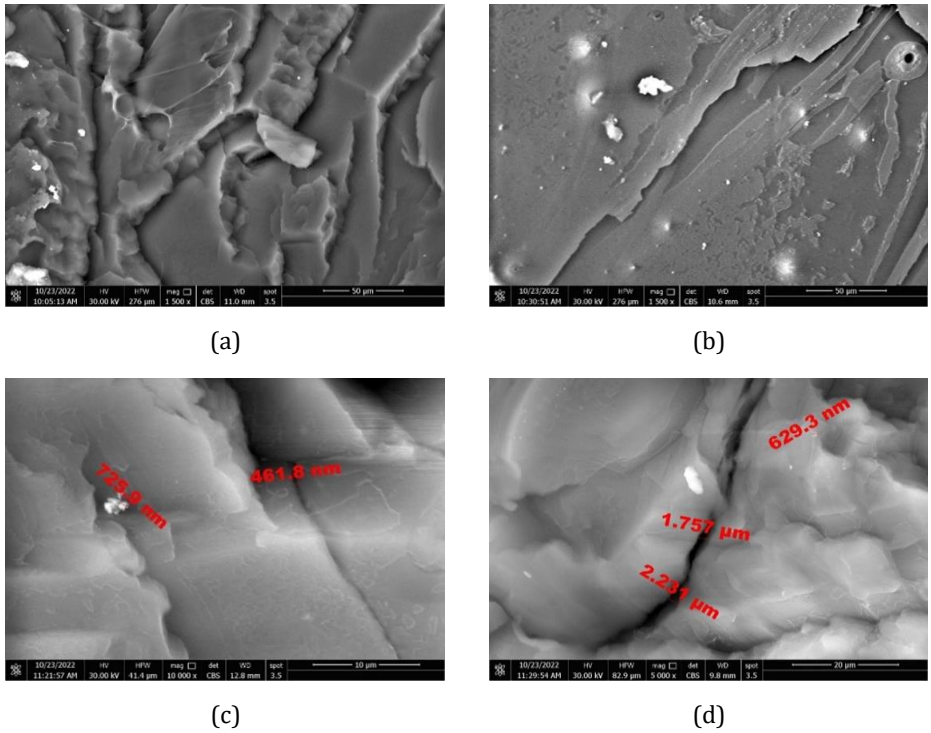

Fig. 10. SEM photomicrograph of crack formation on a) pure polystyrene, b) 0.025 wt. 0 %, c) 0.05 wt. % and d) 0.1 wt.%.

3.3 Impact Test

The impact strength behavior of CNP's composite is shown in Figure 11. When the weight percentage of the CNP grows up to (0.025%wt), the impact energy increases, then decreases as more carbon nanoparticles are added.

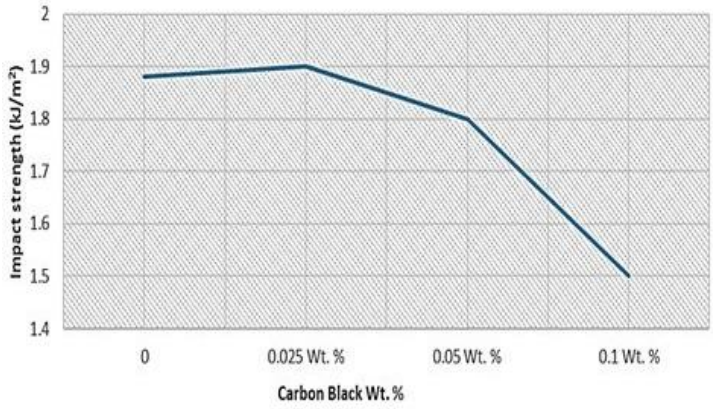

Fig. 11. Impact strength due to CNP wt. % content

The matrix may be deformed more easily because of the little particles that are dispersed throughout it. As a result, when a well-dispersed nanoparticle composite breaks, more

force is required to start a microcrack in the nanocomposite, and most of the impact energy is used by the plastic deformation that is easily seen surrounding the nanoparticles.

Figure 12 depicts a SEM photomicrograph of a fracture that formed following an impact test at various CNP weight percentages. It demonstrates the improved CNP dispersion, which leads to less agglomeration and higher impact strength in the nanocomposites. Agglomerates can occur when the amount of carbon nanoparticles in a material surpasses 0.025 weight percent. These agglomerates can operate as stress concentrations and as a microcrack activator. Because of this, a larger agglomeration weakens the composite's tensile strength and the impact strength of its nanocomposites. [22-23].

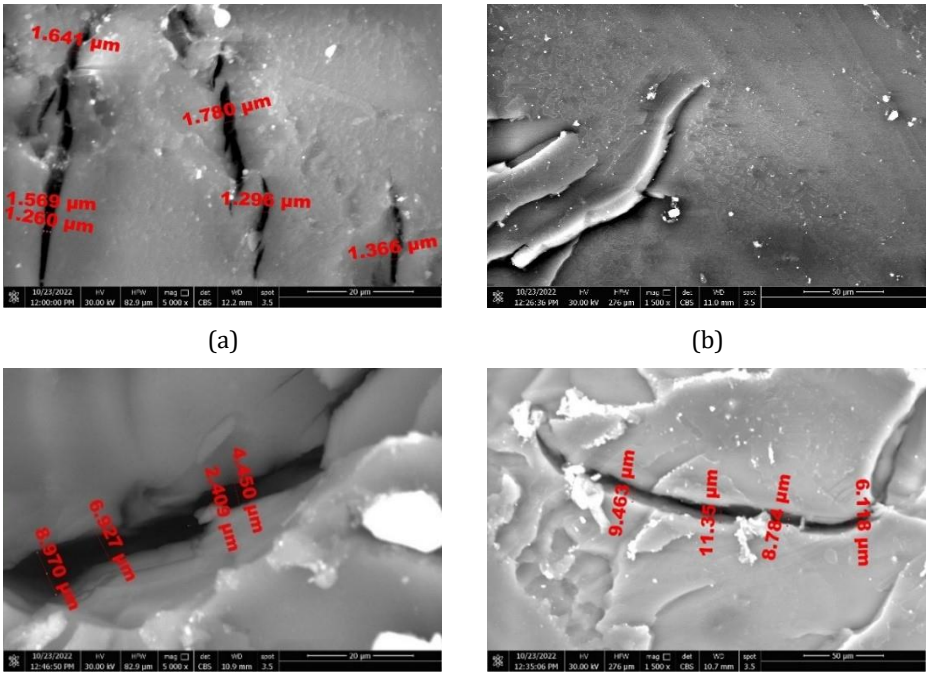

Fig. 12. SEM photomicrograph of crack formation during impact test on a) pure polystyrene, b) 0.025 wt. 0 %, c) .05 wt. % and d) 0.1 wt.%

3.4 Hardness Measurement

Hardness is measured on the specimen's flat surface. The hardness values at different wt.% of CNP were plotted Figure 13, the point is average of three readings for all samples. It is clear from the figure that the hardness values is increased with the increasing in the wt.% content of CNP. The maximum value of hardness appeared at 0.1 wt.% of CNP. This is due to the hardness value is dependent on the amount of CNP and resistance to plastic deformation, and excellent bonding between polymer matrix and nanoparticles reinforcement.

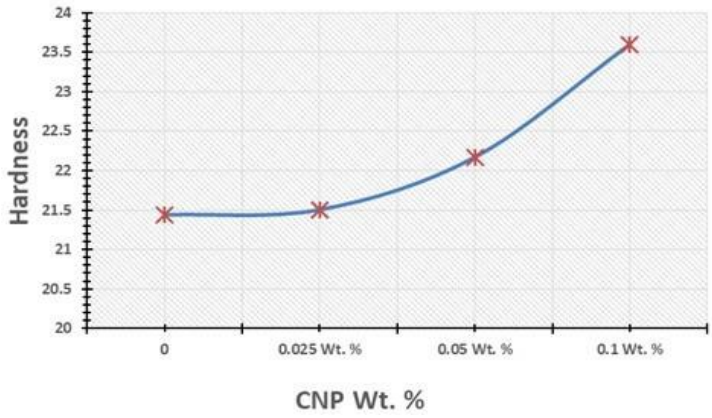

Fig. 13. Hardness values versus different wt.% of CNP

4. Conclusions

Through the investigation of the reinforcement of polystyrene by adding different weight percentage of CNP. Analysis of their mechanical properties and microstructure has led to the following conclusions.

- The stress–strain curves were recorded automatically by a computer data acquisition system. All tests were performed at room temperature. Tensile strength was significantly increased with the decrease in the wt.% content of CNP and the ideal wt.% content of CNP in PS is 0.025. This is due to the low number of nanoparticles which leads to reducing agglomeration between CNP, also good distribution among the polymer particles. However, increasing the amount of CNP concentration to 0.1% reduces this gain due to the large agglomeration of CNP and the non-uniformed distribution of the reinforcement CNP's.
- The microstructure study shows Scanning electron photomicrographs are taken to confirm the dispersion of the particles in the matrix and to study the failure response of the tensile sample's good mixture between matrix and reinforcement, which confirms the success of the injection mold technique in preventing porosity formation and enhances the distribution of nanoparticles. On the other hand, it is also evident from the microphotographs that the distribution of the 0.025 wt.% of CNP appears to be homogeneous with almost no agglomeration. This improvement could be due to the low CNP content, which reduced the possibility of agglomeration occurring between the CNP.
- cracks are found in higher CNP concentration compared with lower percentages of CNP. CNP weakened the bonding between particles in the matrix, resulting in a substantial amount of propagating transversal cracking at 0.1 wt.% CNP that the high concentration of the crack formed around agglomerated CNP.
- Also impact strength behavior of CNP's composite. It is obvious that the increase of the impact energy increases with the CNP's increased weight percentage up to (0.025%wt), then reduced with further addition of carbon nanoparticles. The presence of tiny particles scattered throughout the matrix facilitates plastic deformation.
- The maximum value of hardness appeared at 0.1 wt.% of CNP. This is due to the hardness value is dependent on the amount of CNP and resistance to plastic deformation, and excellent bonding between polymer matrix and nanoparticles reinforcement.

Acknowledgement

The authors of this research are grateful to their colleagues in Al-Azhar university and British University in Egypt for their encouragement and assistance.

References

[1] Hasan SA. Review on Nanoparticles Their Synthesis and Types Biosynthesis., Mechanism,2015 4 9-11.
[2] Uddin MF, Sun CT. Improved dispersion and mechanical properties of hybrid nanocomposites. Compos Sci Techno.l 2010; 70: 223-230. https://doi.org/10.1016/j.compscitech.2009.09.017
[3] Pinto P, Bernardo L, Amaro A, et al. Mechanical properties of epoxy nanocomposites using titanium dioxide as reinforcement - a review. Constr Build Mater 2015; 95: 506-524. https://doi.org/10.1016/j.conbuildmat.2015.07.124
[4] Blivi AS, Benhui F, Bai J, et al. Experimental evidence of size effect in nano-reinforced polymers: Case of silica reinforced PMMA. Polym Test 2016; 56: 337-343. https://doi.org/10.1016/j.polymertesting.2016.10.025
[5] Christy A, Purohit R, Rana RS, et al. Development and analysis of epoxy/nano SiO2 polymer matrix composite fabricated by ultrasonic vibration assisted processing. Mater Today: Proc 2017; 4: 2748-2754. https://doi.org/10.1016/j.matpr.2017.02.152
[6] Li HM, Shen ZG, Zhu FM, Lin SA. Polymer blends of sPS/PA6 compatibilized by sulfonated syndiotactic polystyrene. EurPolym J. 2002;38: 1255-1263. https://doi.org/10.1016/S0014-3057(01)00286-5
[7] Raja VKB, Manoj G. Joining of Metal Matrix Composites, Encyclopedia of Materials: Composites, 2021.
[8] Tracie P. Friction Stir Welding of Metal Matrix Composites for use in aerospace structures. Acta Astronautica. January 2014; 93: 366-373. https://doi.org/10.1016/j.actaastro.2013.07.023
[9] Sivabalan S, et al., Design and Analysis of Ceramic Matrix Composites Piston. International Journal of Management, Technology and Engineering. 2018; 8 (XII): 4715-4754.
[10] Jitendra MM, Piyush PG. Research review of diversified reinforcement on aluminum metal matrix composites: fabrication processes and mechanical characterization, Sci Eng Compos Mater 2018; 25(4): 633-647. https://doi.org/10.1515/secm-2016-0278
[11] Lee S, Noguchi H, Cheong S. Fatigue Behavior Characteristics of Hybrid Composites with Nonwoven Carbon Tissue. Journal of Composite Materials. 2003 Feb;37(3):253-68. https://doi.org/10.1177/0021998303037003992
[12] Ulus H, Üstün T, Eskizeybek V, Şahin ÖS, Avcı A, Ekrem M. Boron nitride-MWCNT/epoxy hybrid nanocomposites: Preparation and mechanical properties. Applied Surface Science. 2014 Nov;318:37-42. https://doi.org/10.1016/j.apsusc.2013.12.070
[13] Lee S, Noguchi H, Cheong S. Static Behavior Characteristics of Hybrid Composites with Nonwoven Carbon Tissue. Journal of Composite Materials. 2003 Feb;37(3):233-52. https://doi.org/10.1177/0021998303037003424
[14] Ayatollahi M, Barbaz Isfahani R, Moghimi Monfared R. Effects of multi-walled carbon nanotube and nanosilica on tensile properties of woven carbon fabric-reinforced epoxy composites fabricated using VARIM. Journal of Composite Materials. 2017 Dec;51(30):4177-88. https://doi.org/10.1177/0021998317699982
[15] Li JR, Xu JR, Zhang MQ, Rong MZ. Carbon black/polystyrene composites as candidates for gas sensing materials. Carbon. 2003;41(12):2353-60. https://doi.org/10.1016/S0008-6223(03)00273-2

[16] Hernández-López S, Vigueras-Santiago E, Mayorga-Rojas M, Reyes-Contreras D. Thickness effect on electric resistivity on polystyrene and carbon black- based composites. J Phys: Conf Ser. 2009 May 1;167:012059. https://doi.org/10.1088/1742-6596/167/1/012059
[17] Stănescu MM, Bolcu D. A Study of Some Mechanical Properties of Composite Materials with a Dammar-Based Hybrid Matrix and Reinforced by Waste Paper. Polymers. 2020 Jul 29;12(8):1688. https://doi.org/10.3390/polym12081688
[18] https://www.sigmaaldrich.com/EG/en/product/aldrich/633100
[19] https://www.s-polytec.de/media/attachment/file/d/a/data_sheet_ps-sheets.pdf
[20] https://www.alibaba.com/product-detail/Wholesale-Plastic-Manual-Bench-Model-Mini_1600845665995.html? spm=a2700.pc_countrysearch.main07.20.33b6334dbGPbN4.
[21] Schulte-Fischedick J, Zern A, Mayer J, Rühle M, Voggenreiter H. The crack evolution on the atomistic scale during the pyrolysis of carbon fibre reinforced plastics to carbon/carbon composites. Composites Part A: Applied Science and Manufacturing. 2007 Oct;38(10):2237-44. https://doi.org/10.1016/j.compositesa.2007.05.004
[22] Spanoudakis J, Young RJ. Crack propagation in a glass particle-filled epoxy resin. J Mater Sci. 1984 Feb;19(2):473-86. https://doi.org/10.1007/BF02403234
[23] Chan C, Wu J, Li J, Cheung Y. Polypropylene/calcium carbonate nanocomposites. Polymer. 2002 May;43(10):2981-92. https://doi.org/10.1016/S0032-3861(02)00120-9

Research on Engineering Structures & Materials
www.jresm.org
Research Group

Research Article

Corrosion effects on axial compressive behavior of steel strapping tensioning technique-confined concrete

Yong-Zheng Goh*[1,a], Kee-Hong Ler[1], Chee-Loong Chin[1,b], Chau-Khun Ma[1,2], Hongtao Su[3], Abdillah Sani bin Mohd Najib[4,c]

[1]*Faculty of Civil Engineering, Universiti Teknologi Malaysia, Malaysia*
[2]*Forensic Engineering Centre, Institute of Smart Infrastructure and Innovative Construction, Faculty of Civil Engineering, Universiti Teknologi Malaysia, Malaysia*
[3]*China Communication 2nd Navigational Bureau 2nd Engineering Co., Ltd., China*
[4]*Faculty of Mechanical Engineering, Universiti Teknologi Malaysia, Malaysia*

Article Info

Article history:

Received 20 Oct 2023
Accepted 23 Dec 2023

Keywords:

Confined concrete;
Durability;
Corrosion;
Steel strapping tensioning

Abstract

This paper presents an experimental study on effect of corrosion on durability performance of circular Steel Strapping Tensioning Technique (SSTT)-confined concrete tested under uniaxial compression. A total of 13 specimens, including 11 confined specimens and 2 plain specimens were tested in this study. The main parameters were prestressing level and corrosion protection. Corrosion was simulated through impressed current accelerated corrosion technique. The experimental results indicated that influence of corrosion was insignificant on peak strength and slight reduction in deformation ability to corroded circular SSTT-confined concrete under low corrosion severity. It was observed that Zn-Al-Cd ingot and long-oil alkyd paint coating shows good protection ability, while 6061 aluminum alloy and 99.9% pure magnesium is not suitable to be used as corrosion protection system. Based on regression analysis, prediction models for peak stress and peak strain for circular corroded SSTT-confined concrete were proposed.

1. Introduction

Existing concrete structures eventually reached their designated service life and deteriorated in structural performance. Strengthening of these structures through retrofitting techniques are more practical solutions than demolishing and replacing with new one. An alternative retrofitting technique with increasing attention is Steel Strapping Tensioning Technique (SSTT) originated from packaging industry. SSTT involved externally pre-tensioning of steel strap on concrete to provide confining effect. Numerous studies revealed that SSTT is an effective confinement method in enhancing concrete properties including strength [1, 2] and deformation ability [3, 4]. Moghaddam *et al.* [1] noticed that by increasing numbers of strap layers significantly enhanced the ultimate strength of confined concrete. Chin *et al.* [4] reported that with application of SSTT, the confined concrete able to achieve ductile post-peak behavior. It was also proven that SSTT able to rehabilitate damaged concrete structures, returning to its original strength [5-7]. Mohd Apandi *et al.* [7] proven the ability of SSTT to rehabilitate the strength and ductility of damaged concrete structure, delaying its damage by increasing the ultimate strain. Nevertheless, SSTT also possess the advantage of flexibility in design [8]. Lee *et al.* [8] noticed that by adjusting the prestressing level on steel strap will affect both strength and ductility of confined concrete.

*Corresponding author: yzgoh1999@graduate.utm.my
[a]orcid.org/0009-0006-0548-6662; [b]orcid.org/0000-0003-4617-0702; [c]orcid.org/0000-0001-6291-5845
DOI: http://dx.doi.org/10.17515/resm2023.29ma1020rs

Despite the remarkable performance of SSTT-confined concrete, the studies on its durability performance are very limited. In composite structures involving the application of steel, corrosion as an inevitable factor influencing its performance to be considered in design. It is a known fact that corrosion induced loss in effective cross-sectional area of steels and resulted in deterioration of its mechanical performance [9]. Furthermore, corrosion extent resulted in degradation of steel with respect of time and transforming it from ductile into brittle manner, increasing the possibility of sudden rupture failure [10]. Concrete structures retrofitted by steel confinement relies on the composites effect between two materials. Corrosion of steel confinement will deteriorate the structural performance of confined concrete [11-13]. Han et al. [11] concluded that deterioration mechanism of corroded external steel confined concrete depends on two aspects, i.e., reduction in sectional area of steel resulted in decrease in strength of steel confinement and reduction of confining effect on concrete leads to decrease in strength of concrete and deformation ability of confined concrete. Previous study reported by Lee et al. [14] shows no significant deterioration in strength for SSTT-confined concrete up to 3 months of natural exposure. However, the corrosion was insignificant due to the fact that corrosion in actual environment generally take up to years [15]. Furthermore, the designated service life for structures is usually 50 years and above. Hence, this short period of exposure is unable to represent the full-service life of structures. Moreover, the influence of corrosion on SSTT-confined concrete was not thoroughly discussed in his studies. Therefore, more comprehensive experimental studies are required.

This paper attempt to study the effect of corrosion on the behavior of circular SSTT-confined concrete. The experimental results for corroded circular SSTT-confined concrete tested under uniaxial compression is presented. The main parameters included prestressing level and corrosion protection. The corrosion in this study is simulated by impressed current accelerated corrosion technique through immersion in NaCl solutions. The performance of the corroded specimens was then evaluated through their stress-strain curve and failure mode.

2. Experimental Program

2.1. Specimens Preparation and Material Properties

The mix proportion for concrete was prepared with CEM 1 42.5N cement in accordance to BS EN 206-1 [16] as shown in Table 1. Tap water was used to prepare the concrete mix. 10 mm maximum nominal size crushed coarse aggregate and well-graded river sand for fine aggregate was used. Compression tests were carried out according to BS EN 12390-3:2009 [17] after 28 days of curing on three 100 mm × 100 mm × 100 mm concrete cubes. The average compressive stress, $f_{cu,ave}$ is 46.4 MPa. The cylindrical strength of concrete, f'_c was determined to be 34.5 MPa. Note that the value of f'_c is taken as unconfined concrete strength, f_{co} in this study as the specimens used were in cylindrical shape.

Table 1. Concrete mix proportion for normal strength concrete

Cement (kg/m^3)	Fine Aggregate (kg/m^3)	Coarse Aggregate (kg/m^3)	Water (kg/m^3)
432	842	825	233

Steel strap used for confinement is made of low-cost recycled steel, which commonly used in packaging industry. The nominal thickness (t) and width (w) were 0.5 mm and 16 mm, respectively. Tensile tests were performed to identify its material properties in accordance to ISO 6892:2019 [18]. Universal Testing Machine (UTM) with load cell of 250 kN was used to carried out the test. 40 mm in length of steel strap were prepared. **Fig. 1** shows the stress-strain curves for tensile tests. The yield strength (f_y) is 735 MPa; the ultimate

strength (f_u) is 753 MPa, the ultimate strain (ε_u) is 0.0070 and the elastic modulus (E) is 220 GPa.

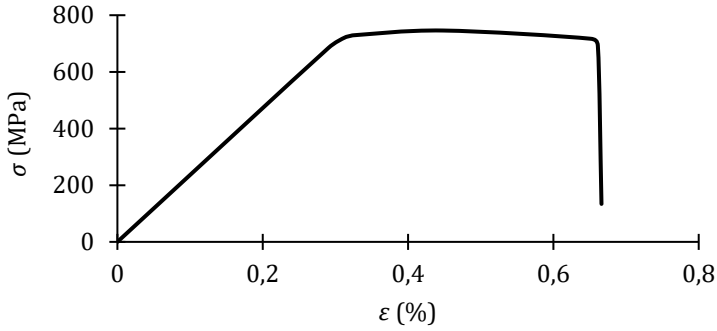

Fig. 1. Stress-strain curve of steel strap

The confinement technique involved the use of pre-tensioning of steel straps around the specimens. Steel straps were cut into desired lengths and formed into steel hoops. The length of internal and external anchorage was set to 50 mm. The specimens were confined by these steel straps using PT-52 pneumatic tensioner and secured in place using two self-regulated end clips [19, 20]. These end clips enabled multiple layers of steel straps to regulate themselves and avoid early loss of pre-tensioned force. The steel straps were tensioned around the specimens with constant air pressure of 0.25 MPa and 0.35 MPa. Consistent value of tensioning pressure secures the effective utilization of steel straps and avoids early crushing of confined concrete. The spacings between steel straps (s) were fixed at 14.4 mm along the middle section. Both end regions of the specimens were confined by two steel straps with closer spacing to avoid premature failure during compression tests. Fig. 2 shows the confinement steel straps, self-regulated end clips, and configurations for confined concrete.

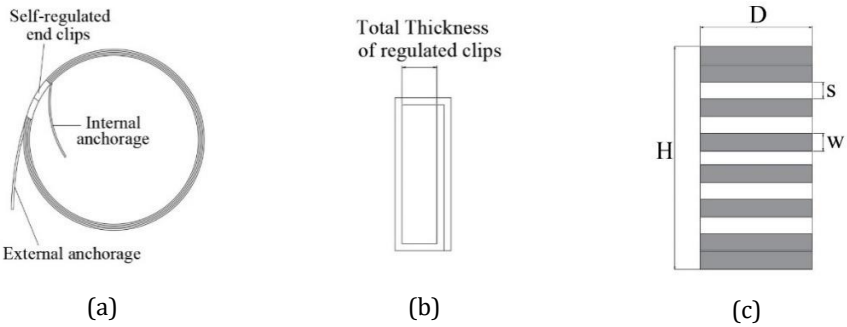

Fig. 2. Schematic diagram: (a) steel hoop confinement; (b) self-regulated end clips; and (c) SSTT-confined concrete

2.2. Application of Corrosion Protection System

The corrosion protection system applied were sacrificial anode cathodic protection (SACP) and paint coatings. The sacrificial anodes used included 6061 aluminum alloy rod, 99.9% pure magnesium rod and Zn-Al-Cd alloy ingot. Both rods were with dimensions of 90 mm and 16 mm in length and diameter, respectively. The zinc alloy ingot in dimensions of 30 mm × 80 mm × 140 mm in thickness, width, and length, respectively. Before connecting to

the specimens, all the sacrificial anodes were sanded to remove any existing oxides. As each of the consecutive steel hoops confined on the concrete were separated, a copper wire is used to connect all the steel straps to the sacrificial anode. This is to ensure the protection ability to reach all the steel straps. The potential differences between the steel strap and sacrificial anodes were measured using digital multimeter. Table 2 shows the results of the measured potential differences.

Table 2. Potential differences between steel strap and sacrificial anodes.

Sacrificial Anode	Potential Difference (V)
6061 Aluminium Alloy	-0.154
Zn-Al-Cd Alloy	-0.445
Pure Magnesium	-1.167

The paint coatings used was long oil alkyd paint (OAP) with percentage volume solid of 60%. Prior to pre-tensioning work, all the steel straps were degreased with thinner to remove oil contaminant initially on the steel surface. This is to ensure a reliable test results and good adhesion between paint coatings and steel surface. Full coverage coating including exposed concrete surface and the end clips were painted. The thickness of dry firm was controlled to approximately 50 μm with single layer of coating. To achieve this, the wet firm thickness of coating is carefully controlled to approximate 85 μm by using comb gauge and a thickness control device. The freshly coated specimen was left to dry for 3 days in room temperature.

2.3. Nomenclature of Specimens

A total of 13 concrete cylinder specimens with 100 mm and 200 mm in diameter (D) and height (H) respectively were prepared. 11 specimens were confined externally with multiple layers of steel straps and 2 plain specimens were set as control specimens.

Table 3. Experimental test results for corroded SSTT-confined concrete specimens.

Specimens ID	Δm (kg)	Δt (mm)	Actual C_d* (%)	Peak Stress (MPa)	f_{cc}/f_{co}	Peak Strain (%)	$\varepsilon_{cc}/\varepsilon_{co}$
C-N-0-0-0	-	-	-	34.5	-	0.24	-
C-N-0-0-2	-0.0050	-	-	39.6	-	0.12	-
C-N-300-1-0	-	-	-	67.7	1.962	1.71	7.125
C-N-500-1-0	-	-	-	71.1	2.061	2.32	9.667
C-N-300-1-2	0.0080	0.019	3.78	67.1	1.945	1.17	4.875
C-N-500-1-2	0.0105	0.025	4.96	67.7	1.962	1.27	5.292
C-Al-300-1-2	0.0110	0.026	5.20	60.7	1.759	1.50	6.250
C-Al-500-1-2	0.0115	0.027	5.44	63.4	1.838	1.67	6.958
C-Mg-300-1-2	0.0075	0.015	3.55	63.4	1.838	1.08	4.500
C-Zn-300-1-2	0.0040	0.009	1.89	72.3	2.096	1.71	7.125
C-OAP-300-1-2	0.0010	0.002	0.47	64.4	1.867	0.66	2.750

*$Corrosion\ degree, C_d = \frac{\Delta t}{t} \times 100\%$

The specimens were labelled as follows: C-a-b-c-d. C indicated the circular concrete specimens; a, the corrosion protection applied; b, the prestressed value according to strength of steel strap; c, the thickness of confinement; d, the durations of immersion in corrosion test. For example, C-Al-300-1-2 indicated normal strength concrete specimens wrapped using steel straps protected by 6061 aluminum alloy rods. Also, the specimen was confined by prestressed value of 300 MPa with 2 layers of straps. The specimen was immersed in corrosion test for 2 hours. Other details of specimens are listed in Table 3.

2.4. Test Setup

In first stage, the confined concretes were immersed in salt solution for a designed period to allow development of corrosion. Impressed current accelerated corrosion test was adopted to simulate the corrosion environment. The test setup mainly consists of container, electrolytic solution, and direct current (D.C.) power supply. The electrolytic solution formed with 3.5% sodium chloride (NaCl) by the weight of water. The positive pole of the D.C. power supply was connected to the steel straps of the tested specimen, which acted as an anode. The negative pole of the power source was connected to a stainless-steel rod, which acted as a cathode. The corrosion degree, C_d was designed to be 5%, which was controlled by current densities of 9400 μA cm^{-2} (5 A of fixed current) based on Faraday's Law in electrochemistry. Immersion durations for specimens to be corroded is set to be consistent for 2 hours. To ensure the consistency of corrosion development, the salt solutions was renewed every hour. Besides, the current supplied is consistently observed and adjusted to maintain at 5 A throughout the test. Fig. 3 shows an example of setup for the test. Upon termination of corrosion test, the specimens were left to dry in room temperature for 2 days before proceeding for corrosion product cleaning based on ISO 8407 [21]. The corrosion products were removed by applying dilute hydrochloric acid (HCl), subsequently removed by non-abrasive brush, and rinsed with clean water. The cleaned specimens were then left to dry in room temperature for 1 day. Weight loss method was used to identify the mass loss due to corrosion, Δm. Subsequently, the mass loss data were converted to thickness loss, Δt based on density of 7.86 g cm^{-3} for steel straps. To ensure that the weight of concrete is not affected by the immersion, a plain concrete was used and repeated with similar procedures as above.

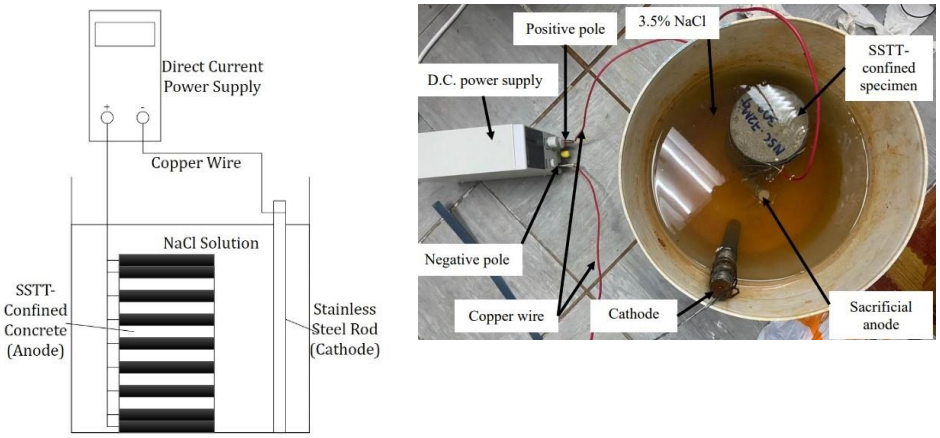

(a) (b)

Fig. 3. Corrosion test setup: (a) schematic diagram; and (b) actual configuration

In second stage, the specimens were tested under uniaxial compression after completion for corrosion test. Load and deformations were used to investigate the influence of corrosion on the behavior of corroded specimens. A 2000 kN capacity hydraulic Tinius Olsen Super "L" UTM was adopted to perform the compression test. All the tests were carried out under displacement control with a rate of 0.006 mm/s. A total of three linear variable differential transducers (LVDTs) were mounted to measure the axial deformation. The LVDTs were installed on the holder rig at three different directions parallel to the tested specimens. The increments of load were measured using a built-in machine load

cell. The load and deformations were recorded for every second until failure with data logger. Fig. 4 shows the test setup for compressions test.

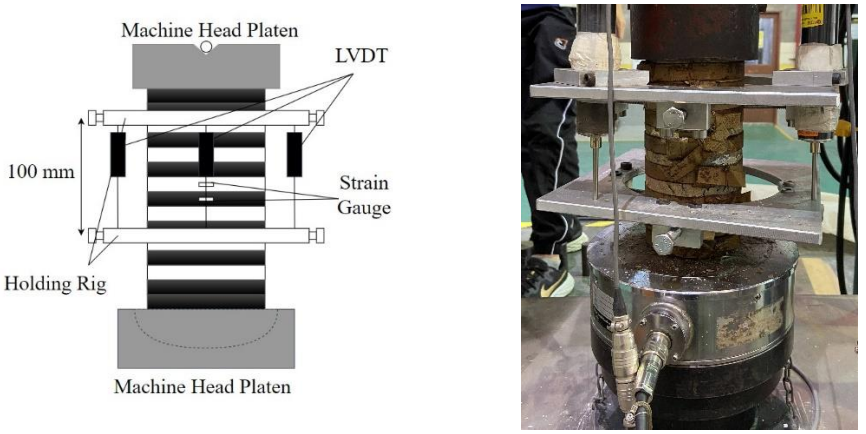

(a) (b)

Fig. 4. Axial compression test setup: (a) schematic diagram; and (b) actual configuration.

3. Results and Discussion

3.1. Evaluation of Corrosion Degree

The mass of before and after 2 hours immersion in salt solution for C-N-0-0-2 was recorded as shown in Table 3. Results indicated a negligible increment in weight after immersion. This indicated that the use of weight loss method for calculation of corrosion degree is appropriate.

Based on the theoretical calculations using Faraday's Law in electrochemistry, the predicted corrosion degree is expected to be 5%. However, corrosion degree for C-N-300-1-2 exhibited a lower corrosion degree. In fact, considering the influence for combination of prestressing force and corrosion on the steel strap, the actual corrosion degree was expected to be higher than the theoretical value [22]. Higher prestressing force leads to formation of microcracks on the surface of steel straps. These microcracks acted as site for initiation of corrosion, which increased the rate of development of corrosion. This can be proven that the C-N-500-1-2 exhibited higher corrosion degree under similar conditions. The discrepancy between actual and theoretical corrosion degree can be attributed to the presence of dark blue metallic coating disrupted the development of corrosion. During the corrosion process, two major substances were observed, as shown in Fig. 5 (b). It can be observed that the dark blue substance formed solids around the cathode, which supported that it is metallic. Furthermore, this can be supported by the observation that the dark blue metallic coating fully disappeared after the corrosion test, as shown in Fig. 5 (a) and (c). This phenomenon also explained the observations in study conducted by Lee et al. [14]. This confirmed that the presence of dark blue metallic coating delayed the development of corrosion process for steel substrate. The metallic coating acted similarly with the protection mechanism of SACP.

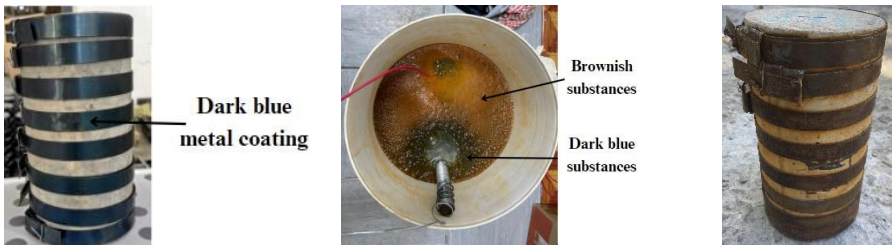

(a) (b) (c)

Fig. 5. Observations for conditions: (a) before corrosion; (b) during corrosion; and (c) after corrosion

It is unexpected that the corrosion degree of C-Mg-300-1-2, C-Al-300-1-2 and C-Al-500-1-2 were similar to or higher than the unprotected specimens. By visual inspection, these specimens displayed similar corrosion severity as the unprotected specimens as shown in Figure 6. This indicated that 6061 aluminum alloy and 99.9% pure magnesium rod could not provide sufficient protection to the steel straps under corrosive environments. In comparison with C-Zn-300-1-2 and C-OAP-300-1-2, both exhibited lower corrosion degree. Based on Table 2, the potential differences between SACP and steel straps suggested that Zn-Al-Cd alloy should provide lower protection ability than 99.9% pure Mg. However, the results indicated a contradiction with the expectation. This can be attributed to the size of Zn-Al-Cd alloy ingot is larger than Mg rod. The protection ability of sacrificial anode is highly dependent on its size. The larger Zn-Al-Cd alloy provide wider coverage of protection ability to the steel straps compared to Mg rod. Among all of the corrosion protection system adopted, OAP exhibited greatest protection ability with corrosion degree of 0.49%, followed by Zn-Al-Cd alloy with 1.89% and 99.9% pure magnesium with 3.55%, and the least is 6061 aluminum alloy with more than 5%.

(a) (b) (c)

Fig. 6. Observations for corroded specimens: (a) unprotected; (b) Mg; and (c) Al

3.2. Failure Mode

For unconfined specimens, the failure mode was generally in the form of sudden shear splitting as shown in Fig. 7 (a). The specimens exhibited a brittle behavior as the load carrying capacity reduced drastically after ultimate capacity. The cracks initially formed at diagonal of the top part and extended towards the opposite diagonal of the bottom part. Both unconfined specimens failed with a cracking sound upon reaching their peak

strength. For uncorroded confined specimens confined with two-layer steel straps, there was no cracks formed at the initial stage of compression tests. Some distinct crisp metal screeching sounds exhibited when the load applied exceed the concrete strength. The formation of microcracks initiated at the middle section of the confined concrete with some minor cracking sound. These cracks continue to extend towards bottom direction as the load increased. Upon failure, a loud explosive sound was heard as an effect of the steel strap confinement at the middle section ruptured. It was observed that the middle part of C-N-300-1-0 experienced failure in crushing as shown in Fig. 7 (b). However, the existence of steel straps confinement effectively prevented the concrete from falling apart. Different from C-N-300-1-0, the core concrete split into two sections for C-N-500-1-0 as shown in Fig. 7 (c). Both concrete and steel strap were observed that they fractured simultaneously.

(a) (b) (c)

Fig. 7. Failure mode: (a) C-N-0-0-0; (b) C-N-300-1-0; and (c) C-N-500-1-0

Among all the corroded confined specimens with and without protection, only C-N-500-1-2 experienced failure in a loud explosive sound and fracture of steel strap confinement in the middle section as shown in Fig. 8 (a). A severe crushing of concrete was observed but the corroded steel strap confinement still remained its effectiveness in preventing the falling of concrete. For other specimens in this series, the failure occurred in most cases due to the crushing of concrete along the middle section without snapping of steel straps confinement as shown in Fig. 8 (b) - (f). In general, it was observed that all the specimens in this series behaved in a ductile manner after reaching their ultimate capacity. The influence of corrosion with low severity on the failure mode were not significant for all corroded confined specimens.

(a) (b) (c) (d) (e) (f)

Fig. 8. Failure mode: (a) C-N-500-1-2; (b) C-N-300-1-2; (c) C-Al-300-1-2; (d) C-Al-500-1-2; (e) C-Mg-300-1-2; and (f) C-Zn-300-1-2.

3.3. Stress-Strain Behavior

The peak stress of specimens obtained from compression tests were presented in Table 3. The unconfined concrete strength, f_{co} of C-N-0-0-0 was 34.5 MPa, which displayed a variation compared to C-N-0-0-2 with 39.6 MPa. The difference in value between before and after immersion is believed to be statistical variations of strength values, inherently exhibited a level of variability. Chloride content in NaCl solutions will not affect the strength of core concrete as there is no internal reinforcement involved in this study. Moreover, the strength development of concrete due to hydration process gradually drops and required longer time to observe a clear variation in strength [23].

Fig. 9 shows the stress-strain curve for corroded specimens without protection. In these figures, the axial deformations were obtained from average readings of LVDTs. From Fig. 9, it can be observed that corrosion has insignificant impact on the load-carrying capacity of the confined specimens. The peak stress of C-N-300-1-2 and C-N-500-1-2 were 67.1 MPa and 67.7 MPa, respectively. Compared to C-N-300-1-0 and C-N-500-1-0, the reduction in peak stress under the influence of corrosion were as low as 0.94% and 4.66% respectively. Besides, it can be observed that C-N-500-1-2 with higher corrosion degree (4.96%) shows higher reduction in its peak stress. It is as expected that higher corrosion degree of steel straps confinement resulted in lower peak stress of the confined specimens. Nevertheless, this finding suggested that SSTT-confined concrete shows the ability to preserve well for its peak stress under low corrosion severity. However, the influence of corrosion shows greater effects on the deformation ability of the confined concrete. It can be observed that in overall, the corroded specimens behaved in a less ductile manner. Both C-N-300-1-2 and C-N-500-1-2 achieved its peak stress with lower strain. Corrosion reduced the effective cross-sectional area of steel straps confinement, thus reducing its mechanical properties. This in turns resulted in reduction for its confinement effect.

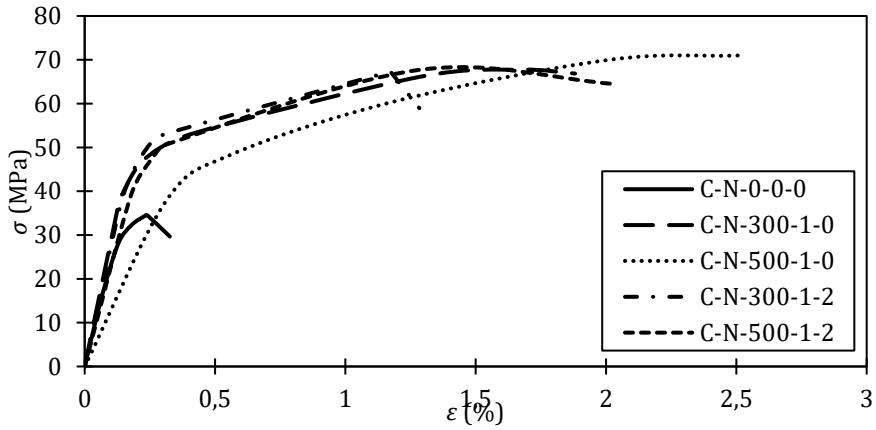

Fig. 9. Stress-strain behaviour of unprotected corroded specimens

Fig. 10 presented the stress-strain curve for specimens with protection. From the figure, it can be observed that C-Al-300-1-2 and C-Al-500-1-2 exhibited lower peak stress and deformation compared to C-N-300-1-2 and C-N-500-1.2. These specimens exhibited higher corrosion degree which consistent with previous expectation. For C-Mg-300-1-2, its corrosion degree (3.55%) was similar to C-N-300-1-2 (3.78%). The reduction in peak stress and deformation were approximately similar. Hence, it can be concluded that 6061 aluminum alloy and 99.9% pure magnesium are not suitable to be used as sacrificial anode for steel straps confinement. Compared to C-Zn-300-1-2 and C-OAP-300-1-2 with lower

corrosion degree of 1.89% and 0.49% respectively, both protections proven their ability to maintain their strength and deformation ability under influence of corrosion.

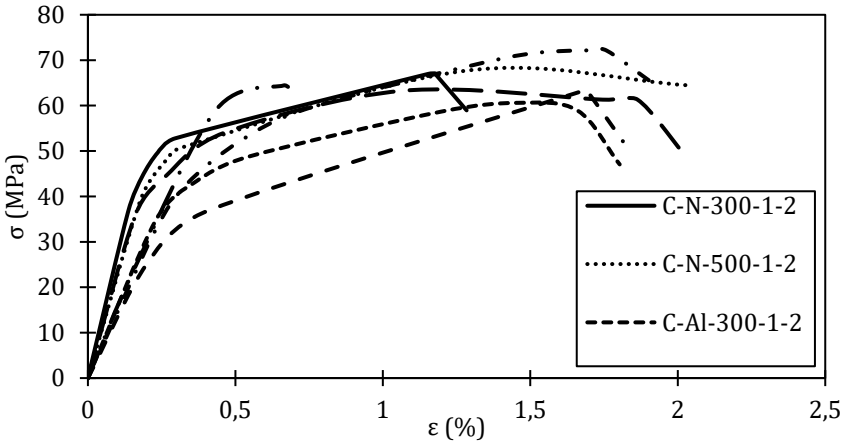

Fig. 10. Stress-strain behaviour for protected corroded specimens

4. Model Assessment for Corroded Circular SSTT-Confined Concrete

4.1. Modification on Existing Confinement Models

In this section, the experimental results in this study will be assessed with current existing confinement models. The assessment will be carried out based on performance in prediction for peak stress and peak strain. To the author's best knowledge, currently there is no study attempted to propose confinement model that account the effect of corrosion for SSTT-confined concrete. In this regard, a series of models for SSTT-confined concrete were collected from existing literature as presented in Table 4. These models were modified to account the effects of corrosion as discussed below.

Studies revealed that confining pressure, f_l acting on concrete evidently affected the behavior of confined concrete. In the case of steel-confined concrete, f_l is generated from hoop tension, F_h in steel, which can be evaluated as Eq (1) below:

$$F_h = t f_y w s \tag{1}$$

For partial-steel confined concrete, f_l can be calculated through Eq (2) proposed by Moghaddam *et al.* [24]:

$$f_l = \frac{2tf_y}{D}\left(\frac{w}{w+s}\right) \tag{2}$$

where, D is diameter of concrete; w is width of steel strap; and s is clear spacing between confinement hoops. As the effect of corrosion could be directly evaluated based on thickness loss of steel confinement, hence the thickness, t in Eq (2) is modified and replaced with effective thickness, t_e, which can be calculated based on Eq (3):

$$t_e = t - \Delta t \tag{3}$$

Zhang *et al.* [25] recommended that for modelling corroded external steel confined concrete, the influence of corrosion on yield strength of steel confinement should be accounted. Hence, the equation to determine yield strength of corroded steel confinement from Zhang *et al.* [25] is adopted as shown in Eq (4):

$$f'_y = f_y(1 - 1.58C_d) \tag{4}$$

where, f'_y is yield strength of corroded steel confinement. Combining both Eq (3) and Eq (4), confining pressure considering effect of corrosion, f'_l can be calculated by Eq (5):

$$f'_l = \frac{2t_e f'_y}{D}\left(\frac{w}{w+s}\right) \tag{5}$$

As listed in Table 4, most of the existing confinement models used concept of reduced confinement effectiveness to account for non-circular shape and spacing. Considering influence of corrosion, combined with Eq (5), effective confinement pressure, f_{le} developed by Sheikh *et al.* [26] can be adopted as:

$$f_{le} = k_e k_s f'_l \tag{6}$$

where, k_e is confinement effectiveness ratio for spacing determined by Eq (7); and k_s is confinement effectiveness ratio for shape determined by Eq (8).

$$k_e = \left(1 - \frac{s}{2D}\right)^2 \tag{7}$$

$$k_s = 1 - \frac{2(D-2R)^2}{3D^2} \tag{8}$$

where, R is corner radius of square section.

Table 4. Summary of existing models for steel confined concrete

References	fcc/fco Expressions	εcc/εco Expression
Moghaddam et al. [24]	$\frac{f_{cc}}{f_{co}} = 1 + 8\frac{f_{le}}{f_{co}} - 4\left(\frac{f_{le}}{f_{co}}\right)^{1.2}$	$\frac{\varepsilon_{cc}}{\varepsilon_{co}} = \left(\frac{f_{cc}}{f_{co}}\right)^{1.1}$
Awang [27]	$\frac{f_{cc}}{f_{co}} = 2.62\rho_e^{0.4}$ $\rho_e = k_e k_s \rho$	$\frac{\varepsilon_{cc}}{\varepsilon_{co}} = 11.6\rho_e$
Lee et al. [28]	$\frac{f_{cc}}{f_{co}} = 1 + 5.57\frac{f_{le}}{f_{co}}$	$\frac{\varepsilon_{cc}}{\varepsilon_{co}} = 1 + 6.3\frac{f_{le}}{f_{co}}$
Chin et al. [29]	$\frac{f_{cc}}{f_{co}} = 1.124 + 1.02\frac{f_{le}}{f_{co}}$	$\frac{\varepsilon_{cc}}{\varepsilon_{co}} = 0.93 + 1.49\frac{f_{le}}{f_{co}}$
Yang et al. [30]	$\frac{f_{cc}}{f_{co}} = 1 + 3.35k_e k_s\left(\frac{f'_l}{f_{co}}\right)^{0.48}$	-
Proposed model	$\frac{f_{cc}}{f_{co}} = 1 + 5.09\frac{f_{le}}{f_{co}}$	$\frac{\varepsilon_{cc}}{\varepsilon_{co}} = 1 + 27.87\frac{f_{le}}{f_{co}}$

4.2. Performance Assessment

4.2.1 Procedure of Assessment

The performances of existing models in predicting peak stress and peak strain of circular corroded SSTT-confined concrete were evaluated in this section. The performances of each model were assessed by comparison between predicted values with experimental values. Subsequently, the accuracy of each model was analyzed using average absolute error (AAE) and mean square error (MSE) calculated based on Eq (9) and Eq (10), respectively. The reliability of each model was evaluated based on standard deviation (SD) calculated based on Eq (11). Table 5 presented the performances of each model.

$$AAE = \frac{\sum_{i=0}^{n} \left| \frac{mod_i - exp_i}{exp_i} \right|}{N} \quad (9)$$

$$MSE = \frac{\sum_{i=0}^{n} (mod_i - exp_i)^2}{N} \quad (10)$$

$$SD = \sqrt{\frac{\sum_{i=0}^{n} (\frac{mod_i}{exp_i} - \frac{mod_{ave}}{exp_{ave}})^2}{N-1}} \quad (11)$$

Table 5. Summary for performances of existing models

References	Prediction of f_{cc}/f_{co}			Prediction of $\varepsilon_{cc}/\varepsilon_{co}$		
	AAE	MSE	SD	AAE	MSE	SD
Moghaddam *et al.* [24]	0.042	0.008	0.049	0.616	36.258	0.162
Awang [27]	0.310	0.370	0.034	0.608	19.046	0.171
Lee *et al.* [28]	0.054	0.015	0.050	0.602	18.788	0.169
Chin *et al.* [29]	0.318	0.389	0.036	0.777	27.104	0.093
Yang *et al.* [30]	0.232	0.203	0.052	-	-	-
Proposed model	0.041	0.008	0.048	0.309	3.376	0.511

4.2.2 Peak Stress & Proposed Model

Fig. 11 presented the performances of different peak stress models. It clearly illustrated that most of the existing models shows slightly overestimation for peak stress of circular corroded SSTT-confined concrete. The model proposed by Moghaddam et al. [24] shows the highest accuracy with lowest AAE and MSE of 0.042 and 0.008, respectively. However, it tends to overestimate the peak stress when corrosion degree increased. The model proposed by Lee et al. [28] also provided close predictions compared to experimental results. For models proposed by Awang [27] and Chin et al. [29] persistently underestimation of peak stress. In contrast, the model proposed by Yang et al. [30] consistently overestimated the peak stress for circular corroded SSTT-confined concrete.

The influence of corrosion on circular SSTT-confined concrete can be directly evaluated based on thickness loss of steel confinement and reduction on yield strength of steel. Both affected parameters can be reflected in Eq (6). Hence, for current proposed model, a regression analysis is plotted based on measured f_{le}/f_{co} as presented in Fig. 12. Eq (12) is proposed based on the plot and the performance is included in Table 5. It is clearly shown that an overall better performance compared to existing models.

$$\frac{f_{cc}}{f_{co}} = 1 + 5.09\frac{f_{le}}{f_{co}} \quad (12)$$

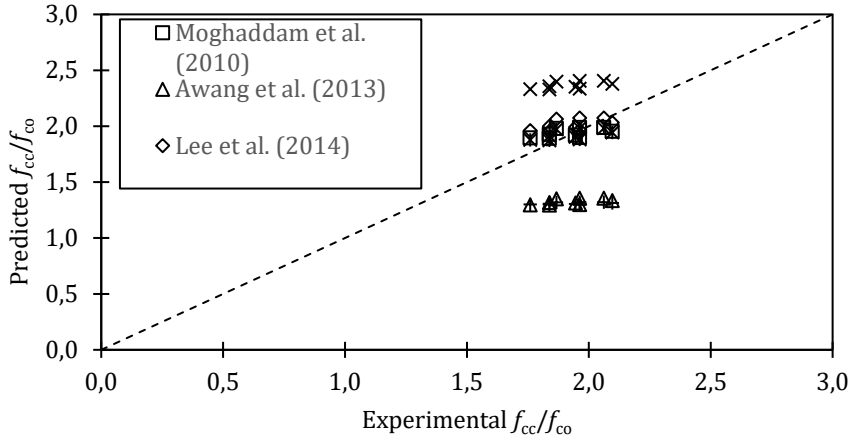

Fig. 11. Performance of peak stress models.

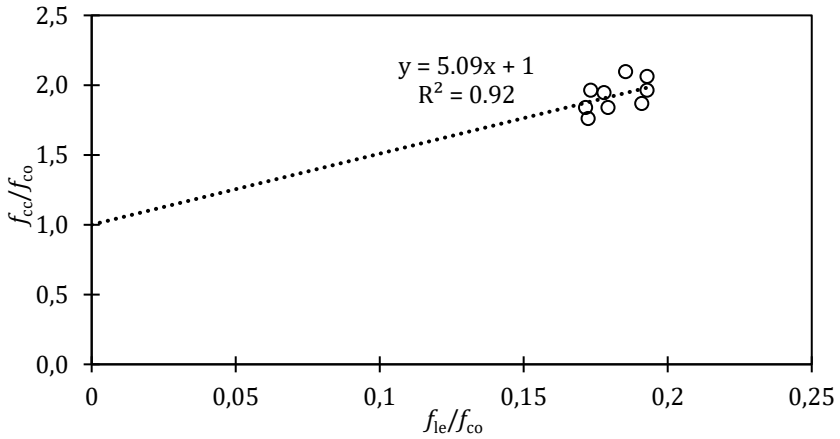

Fig. 12. Performance of proposed peak stress models

4.2.3 Peak Strain & Proposed Model

Fig. 13 presented the performance of each model in estimating peak strain. It can be observed that most of the models underestimated the peak strain of corroded specimens. None of the existing models were capable to provide accurate prediction. In Table 5, the models proposed by Lee et al. [28], Awang [27] and Chin et al. [29] displayed high AAE and MSE. This can be attributed to the fact that these models were empirically derived based on confined high strength concrete (HSC), which generally exhibited lower peak strain due to brittleness problem.

Based on Table 5, it can be observed that most existing models considered effective confining pressure, f_{le} as variable. Hence, a regression analysis is carried out based on measured f_{le}/f_{co} as represented in Fig. 14. Eq (13) is proposed for prediction of peak strain of circular corroded SSTT-confined concrete. From Table 5, the proposed model provided a relatively conservative prediction with AAE and MSE of 0.309 and 3.376, respectively.

$$\frac{\varepsilon_{cc}}{\varepsilon_{co}} = 1 + 27.87\frac{f_{le}}{f_{co}} \tag{13}$$

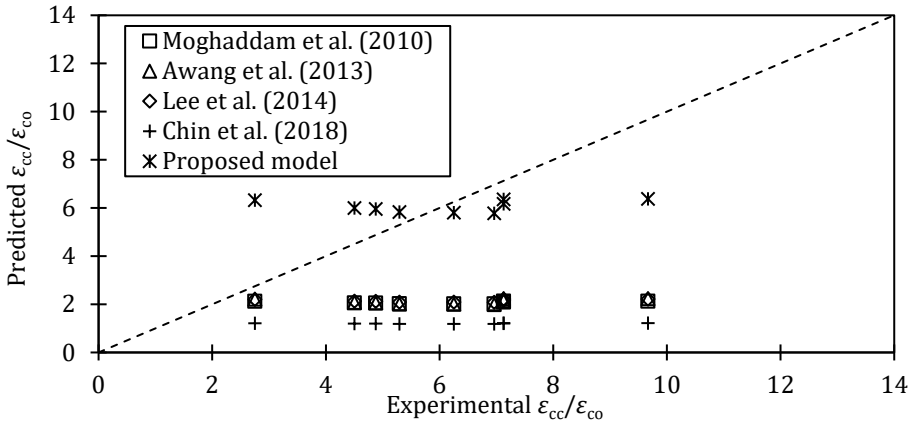

Fig. 13. Performance of peak strain models.

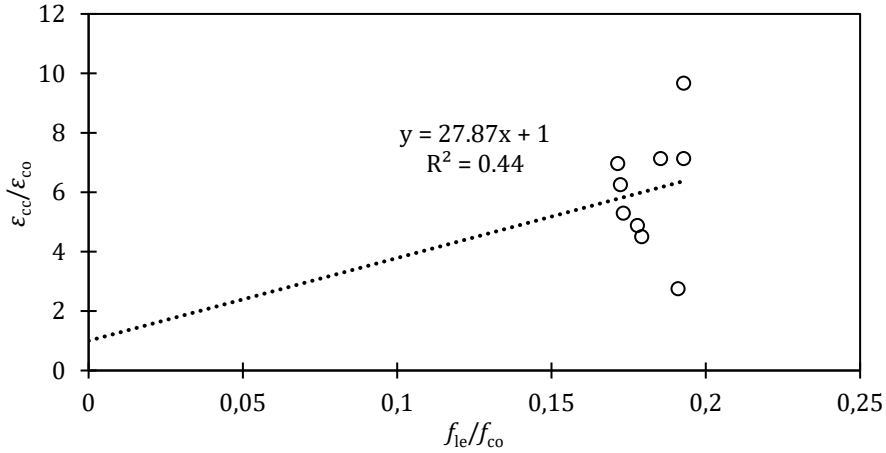

Fig. 14. Performance of proposed peak strain models

5. Conclusions

This research major concerns with the of corrosion on the durability performance of circular SSTT-confined concrete. The following conclusions can be drawn from the study:

- A total of 11 circular SSTT-confined concrete with different prestressing level and corrosion protection were corroded and tested uniaxial compression. Corrosion was simulated through lab-designed impressed current accelerated corrosion technique. Experimental results indicated that circular SSTT-confined concrete indicated its ability to maintain well for its peak strength with slight reduction in deformation ability under low corrosion severity. Compared to uncorroded confined specimens, the reduction in peak strength was as low as 0.94% - 4.65%, whilst the reduction in deformation ability was more obvious for all corroded specimens. It is expected that higher corrosion degree causes higher reduction in peak strength and deformation ability. Corrosion reduced the effective cross-sectional area and decrease of confinement effect on core concrete, which leads to deterioration of peak strength and deformation ability of confined concrete.

- It is as expected that higher prestressing force applied to circular SSTT-confined concrete resulted in higher corrosion degree. Experimental results shows that all corroded specimens with 500 MPa of prestressing level exhibited greater corrosion degree compared to those with 300 MPa of prestressing level. A higher prestressing level on steel strap leads to more significant formation of microcracks on the surface. This provided more site of initiation for chloride ions to penetrate into, which resulted in acceleration for development of corrosion.
- Corrosion protection system including of sacrificial anode corrosion protection and paint coating were applied to circular SSTT-confined concrete. Experimental results shows that the presence of Zn-Al-Cd ingot sacrificial anode and long oil alkyd paint coating (OAP) provided effective protection to the steel strap confinement and successfully reduced the effect of corrosion and aids in preserving the peak strength and deformation ability of confined concrete. In contrast, 6061 aluminum alloy and 99.9% pure magnesium rod were not capable to provide corrosion protection.
- The proposed models for prediction of peak stress and peak strain shows better performance in overall compared to existing models. The models are applicable to circular SSTT-confined concrete under low corrosion severity, provided that thickness loss of steel confinement is known and reduction of yield strength for corroded steel is considered.

Current study only analyzed on uniaxial compression with limited parameters range for corroded circular SSTT-confined concrete. More comprehensive research with expanded range of parameters such as higher corrosion degree, different concrete and steel grade are recommended to be conducted in future research. Performance of corroded SSTT-confined concrete under different loading conditions such as cyclic loading, seismic and others can be considered. In addition, impressed current accelerated corrosion technique adopted in this study generally induced only uniform corrosion, other methods such as salt spray corrosion can be used in future study to simulate corrosive environment that is more similar to actual conditions.

List of Symbol

C_d	Corrosion Degree
D	Diameter of concrete
E	Elastic modulus
f'_c	Cylindrical strength of concrete
f_{co}	Unconfined concrete strength
f_{cc}	Confined concrete strength
f_l	Confining pressure
f_{le}	Effective confining pressure
f'_l	Confining pressure after corrosion
f_y	Yield strength of steel
f'_y	Yield strength of steel after corrosion
f_u	Ultimate strength of steel
F_h	Hoop tension
H	Height of concrete
k_e	Confinement effectiveness ratio for spacing
k_s	Confinement effectiveness ratio for shape
Δm	Mass loss of steel due to corrosion
R	Corner radius of square section
s	Spacing between steel straps
t	Thickness of steel
t_e	Effective thickness of steel after corrosion

Δt	Thickness loss of steel due to corrosion
V	Potential difference
w	Width of steel
σ	Stress
ε	Strain
ε_{cc}	Peak strain of confined concrete
ε_{co}	Peak strain of unconfined concrete
ε_{u}	Ultimate strain of steel

Acknowledgement

This research was funded by Universiti Teknologi Malaysia, UTMER [Q.J130000.3851.20J22]. The author gratefully acknowledges for all sorts of support from D04, Structure Laboratory, Faculty of Civil Engineering, Universiti Teknologi Malaysia.

References

[1] Moghaddam H, Samadi M, Pilakoutas K, Mohebbi S. Axial compressive behavior of concrete actively confined by metal strips; part A: experimental study. Materials and Structures. 2010;43(10):1369-81. https://doi.org/10.1617/s11527-010-9588-6

[2] Ma C-K, Awang AZ, Omar W, Liang M. Experimental tests on SSTT-confined HSC columns. Magazine of Concrete Research. 2014;66. https://doi.org/10.1680/macr.14.00065

[3] Holmes N, Niall D, O'Shea C. Active confinement of weakened concrete columns. Materials and Structures. 2015;48(9):2759-77. https://doi.org/10.1617/s11527-014-0352-1

[4] Chin C-L, Ma C-K, Awang AZ, Omar W, Kueh ABH. Stress-strain evaluation of steel-strapped high-strength concrete with modified self-regulating end clips. Structural Concrete. 2018;19(4):1036-48. https://doi.org/10.1002/suco.201700134

[5] Mohd Apandi N, Ma C-K, Awang AZ, Omar W. Structural behaviour of pre-damaged RC columns immediate repaired employing pre-tensioned steel straps. Structures. 2021;34:964-78. https://doi.org/10.1016/j.istruc.2021.08.039

[6] Ma C-K, Garcia R, Yung SCS, Awang AZ, Omar W, Pilakoutas K. Strengthening of pre-damaged concrete cylinders using post-tensioned steel straps. Proceedings Of The Institution Of Civil Engineers-Structures And Buildings. 2019;172(10):703-11. https://doi.org/10.1680/jstbu.18.00031

[7] Mohd Apandi N, Ma C-K, Chin C-L, Awang AZ, Omar W. The Effect of Pre-Damaged Level on Repair Damaged Columns by Using Steel Straps Tensioning Technique. International Journal of Engineering & Technology. 2018;7:31. https://doi.org/10.14419/ijet.v7i3.9.15268

[8] Lee H-P, Awang AZ, Omar W. Experimental Investigation on SSTT confined concrete with low lateral pre-tensioning stresses. J Teknol. 2014;69(3):43-50. https://doi.org/10.11113/jt.v69.3142

[9] Di Sarno L, Majidian A, Karagiannakis G. The Effect of Atmospheric Corrosion on Steel Structures: A State-of-the-Art and Case-Study. Buildings. 2021;11(12):571. https://doi.org/10.3390/buildings11120571

[10] Kumar V, Sharma N, Tiwari SK, Kango S. Atmospheric corrosion of materials and their effects on mechanical properties: A brief review. Materials Today: Proceedings. 2021;44:4677-81. https://doi.org/10.1016/j.matpr.2020.10.939

[11] Han L-H, Hou C-C, Wang Q-L. Behavior of circular CFST stub columns under sustained load and chloride corrosion. Journal of Constructional Steel Research. 2014;103:23-36. https://doi.org/10.1016/j.jcsr.2014.07.021

[12] Gao S, Guo L, Zhang S, Peng Z. Performance degradation of circular thin-walled CFST stub columns in high-latitude offshore region. Thin-Walled Structures. 2020;154:106906. https://doi.org/10.1016/j.tws.2020.106906
[13] Gao S, Peng Z, Li X, Chen D. Tests on axial strength of circle CFST stub columns under marine atmosphere in cold region. Construction and Building Materials. 2020;230:117073. https://doi.org/10.1016/j.conbuildmat.2019.117073
[14] Lee H-P, Awang AX, Omar W. Short term durability of steel-strap confined concrete. Jurnal Teknologi. 2016;78. https://doi.org/10.11113/jt.v78.6243
[15] Quadri TW, Akpan ED, Olasunkanmi LO, Fayemi OE, Ebenso EE. 2 - Fundamentals of corrosion chemistry. In: Hussain CM, Verma C, Aslam J, editors. Environmentally Sustainable Corrosion Inhibitors: Elsevier; 2022. p. 25-45. https://doi.org/10.1016/B978-0-323-85405-4.00019-7
[16] 206-1 E. Concrete - Part 1: Specification, performance, production and conformity. 2000.
[17] Standard B. Testing hardened concrete. Compressive Strength of Test Specimens, BS EN. 2009:12390-3.
[18] ISO E. 6892-1: 2019-Metallic materials-Tensile testing-Part 1: Method of test at room temperature (ISO 6892-1: 2019). Brussels, Belgium. 2019.
[19] Chin C-L, Ma C-K, Awang AZ, Omar W, Kueh A. Stress-strain evaluation of steel-strapped high-strength concrete with modified self-regulating end clips. Structural Concrete. 2018;19. https://doi.org/10.1002/suco.201700134
[20] Awang AZ. Stress-strain behaviour of high-strength concrete with lateral pre-tensioning confinement: Universiti Teknologi Malaysia Johor Bahru; 2013.
[21] 8407 I. Corrosion of metals and alloys - Removal of corrosion products from corrosion test specimens. 2021.
[22] Le L, Sofi M, Lumantarna E. The combined effect of stress and corrosion on mild steel. Journal of Constructional Steel Research. 2021;185:106805. https://doi.org/10.1016/j.jcsr.2021.106805
[23] Gu H, Song G, Dhonde H, Mo YL, Yan S. Concrete early-age strength monitoring using embedded piezoelectric transducers. Smart Materials and Structures. 2006;15(6):1837. https://doi.org/10.1088/0964-1726/15/6/038
[24] Moghaddam H, Samadi M, Pilakoutas K. Compressive behavior of concrete actively confined by metal strips, part B: analysis. Materials and Structures. 2010;43(10):1383-96. https://doi.org/10.1617/s11527-010-9589-5
[25] Zhang F, Xia J, Li G, Guo Z, Chang H, Wang K. Degradation of Axial Ultimate Load-Bearing Capacity of Circular Thin-Walled Concrete-Filled Steel Tubular Stub Columns after Corrosion. Materials [Internet]. 2020; 13(3). https://doi.org/10.3390/ma13030795
[26] Sheikh SA, Uzumeri S. Analytical model for concrete confinement in tied columns. Journal of the structural division. 1982;108(12):2703-22. https://doi.org/10.1061/JSDEAG.0006100
[27] Awang AZ, editor Stress-strain behaviour of high-strength concrete with lateral pre-tensioning confinement2013.
[28] Lee H-P, Awang AZ, Omar W. Strength and ductility of high-strength concrete cylinders externally confined with Steel Strapping Tensioning Technique (SSTT). J Teknol. 2014;68(1):109-18. https://doi.org/10.11113/jt.v68.1967
[29] Chin C-L, Ma C-K, Awang AZ, Omar W, Kueh ABH. Stress-strain evaluation of steel-strapped high-strength concrete with modified self-regulating end clips. Structural Concrete. 2018;19(4):1036-48. https://doi.org/10.1002/suco.201700134
[30] Yang Y, Xue Y, Yu Y, Li Y. Research on axial behavior of concrete columns retrofitted with pre-stressed steel strips. Magazine of Concrete Research. 2019;72:1-36. https://doi.org/10.1680/jmacr.18.00107

Research on Engineering Structures & Materials
www.jresm.org
Research Group

Research Article

Effect of calcium carbonate nanoparticles on mechanical properties of coir-kenaf based epoxy hybrid composites: An analytical and simulation study

Shikha Parashar*[a], V.K.Chawla[b]

Department of Mechanical and Automation Engineering, IGDTUW, Kashmere Gate, Delhi, India

Article Info

Article history:

Received 20 Oct 2023
Accepted 16 Dec 2023

Keywords:

Hybrid fibre composite;
Kenaf;
Coir;
Epoxy;
Calcium carbonate nanoparticles;
Mechanical properties

Abstract

The manufacturing sector is presently in search of sustainable materials that are lighter in weight, readily available, biodegradable, and cost-friendly. Natural fibers are observed to bring unblemished advancement in composite materials. In this research, a novel hybrid composite material has been analyzed. The composite comprises two different natural fibers, kenaf and coir fiber, reinforced in epoxy matrix with nanofillers of calcium carbonate particles. The weight percent of kenafand coir fibers is maintained at 5.7% and 10%, whereas nanofillers is varied as 0%, 2%, and 4%, respectively, in all three samples. The elastic characteristics like the Longitudinal Modulus, and Transverse Modulus, are evaluated for the proposed composite utilizing five different analytical models, and are also interpreted using Representative Volume Element (RVE) analysis. The analytical results of the proposed composite are correlated with the experimental work in the earlier research. The influence of nanofiller is investigated and it has been observed that the composite with a higher filler content of 4 percent attains enhanced strength than a sample with a lower filler content of 0 and 2 wt. percent. The transverse modulus is noticed to uplift by 16.88%, and the longitudinal modulus by 11.14% on the mixing of $CaCO_3$ particles in coir kenaf composite. Also, the composite is analyzed for hybridization effect, which proves to be one of the most promising ways to improve the features of the hybrid composite.

1. Introduction

Since the past decade, reviewers have faced many challenges to environmental problems caused by using synthetic fibers that are not sustainable, non-biodegradable, and harmful to the surrounding environment. To overcome this problem, scientists have introduced natural fiber-made composites because of their environmental friendliness, less weighty than synthetic fibers, easy availability, meager cost compared to other fibers, etc. [1-5,49-56]. Because of these cons, natural fiber composites are increasing their utilization for industrial applications. Taking into consideration the mechanical, chemical, and physical attributes of natural fiber composites, they are utilized in several applications. Some fibers like hemp, pineapple, sisal, and kenaf show similar properties compared to steel and aluminum [6, 57-61]. Because of the innumerable and positive characteristics of natural fibers, the utilization of composites made by these fibers shows their wide range of uses in areas of vehicle, construction, aircraft, and marine industries [7-11, 62-68]. Despite these numerous pros of NFCs, some cons need to be observed, such as low impact strength, high rate of water absorption, and lower heating capacity. To bridle these cons, scientists have

*Corresponding author: shikha001phd18@igdtuw.ac.in
[a] orcid.org/0000-0003-0768-2545; [b] orcid.org/0000-0001-7386-1838
DOI: http://dx.doi.org/10.17515/resm2023.33me1020rs

mixed and hybridized this natural fiber with small percentages of synthetic fibers to boost their mechanical attributes, thermal strength, reduce water absorption, etc. [12,69-74]. The investigation has been done on the mechanical attributes of cellulose nanofibers fortified composite at varying weight percentages of nanocellulose, which predicted that 0.75 weight percent of epoxy composite reinforced with nanocellulose resulted in improved thermal properties and modulus in comparison to 0.5 weight percent and 1 weight percent of the composite [13]. Due to the firm synergy between fibers and matrix, the natural rubber composite incorporated with oil palm fibers showed a rise in the modulus, enhancing the total fibers in the composite [14]. A study is made on the jute-sisal reinforced epoxy hybrid composite's thermal properties and dynamic performance. The outcomes showed that the hybrid effect of fibres, positively impacts the improvement of dynamic mechanical and thermal features. It has been discovered that hybrid composites with a higher proportion of jute fibers had higher modulus of storage, and modulus of loss [15]. The investigation is done on the different banana fiber forms, and the conclusion has been made that fiber composites incorporated with plain weave fibers ensued in improved mechanical attributes of the composite. Incorporating more fibers enhanced the modulus and reduced damping behavior [16]. All the attributes of treated and untreated coir composite are considered. The research concludes that chemically treated coir fiber composite showed enhanced properties compared to untreated composites [17]. In the case of jute and palm leaf composites, it is noticed that hybridizing the fibres, improved flexural and tensile strength by 56 percent and 46 percent [18]. Also, it is remarked that an increment in jute volume enhanced the composite's modulus. The mechanical attributes of coconut and bagasse reinforced fibre hybrid composite are examined. A conclusion has been made that composite with three layers of fibers inculcated better characteristics than two-layered fiber composites [19]. The dielectric and mechanical features of hybrid composites incorporated with banana and glass fibers, are studied. The conclusion is drawn that glass fiber aggregation in composite reduced the damping properties and the modulus [20]. The mechanical properties of coconut and nano clay composite have been explored by differing the filler content between 1-5 wt. percent, which resulted in enhanced properties at 3 percent of filler material in the composite [21]. Comparisons between composites with filler and without filler are made with composites having pure matrix for studying the mechanical attributes of the composite. The impact of the volume and length of fiber is also observed on the dynamic mechanical attributes, and related application areas were explored [22]. Also, damping properties are investigated to foresee the component's lifetime. It is noticed that as the weight percent of sisal fibres increases, it reduces the damping behavior of the composite [23]. Moreover, the review is prolonged to evaluate the outcomes of the above-stated factors on the mechanical performance of developed composites. Outcomes depict that both the volume content of fiber and orientation afflicted the composite's mechanical features. The hybrid composite is studied to predict water absorption and mechanical features with differing weight percent of fiber content [24]. It is also observed that the hybrid effect of fibers enhanced the overall performance and composite attributes [26, 68]. Composite with two different fibers, used in the proportion of 25 percent Coir and 75 percent Kevlar, inculcated good impact, flexural, and water absorption properties. According to the results, it has been ratified that the fabricated composite may find its application in the defense sector. Work is done on polymer composite reinforced with piassava fiber, and the composite's mechanical analysis has been done as a function of temperature [25]. Outcomes show that, in comparison to polyester composites, the fortification of fibers improves the modulus of the composite. Three composites with varying content of kenaf and bamboo fibers are considered, showing that equal content of both fibers resulted in dimensional stability and improved properties [26].

Investigation is done on coir-luffa fiber composite to study the mechanical characteristics of the composite, which shows that alkali-treated fiber results in enhanced properties [27]. An exploration is made on the composite reinforced with abutilon indicum fiber to predict the outcome of alkali treatment and a varying number of fibres on mechanical and thermal characteristics. Outcomes predicted that composite fibres treated with alkali possessed improved mechanical features [28]. The conclusion is made that composite properties improved by up to 20 percent of fiber content and decreased afterward. Scientists have revealed that incorporating fillers into the composite resulted in better and improved properties [29-33]. The investigation is made on Coir and Luffa cylindrica fibres incorporated with calcium carbide nanofillers. Outcomes predicted that mechanical properties of composites with incorporated nanofillers resulted in higher characteristics [31]. Also, the discussion was done on filler's impact on the mechanical attributes of hybrid composites incorporated using prosopis juliflora fibers [32]. Study has been done on palm fibre nanofiller reinforced ABS composites to explore the filler's effect on the attributes of composite. Results depicted that the addition of palm fiber nanofiller enhanced the absorption property of the materials [33]. Despite several advantages, research on natural fibers and fillers have some drawbacks and limitations when employed as reinforcement for composites, including weak interfacial adhesion, a processing temperature range of only around 200 °C, low dimensional stability, and low moisture absorption resistance.

The above reported literature has been reviewed using papers from relevant fields which have been identified from the Science Citation Index Database, Scopus Database, Web of Science, and other reputed International Journals.

In the proposed paper, the mechanical attributes of a calcium carbonate nanofiller incorporated in a kenaf coir composite have been evaluated. Based on an extensive literature review, it is found that a very limited amount of work is performed on Kenaf-coir epoxy composite.

Table 1. Attributes of Calcium Carbonate nanofiller [34]

S. NO	Properties	Values
1	Density	2.7-2.9 g/cm^3
2	Size of Particle	30-50 nm
3	Absorption of Oil	13-21 g/100g
4	Specific Surface Area	5-24 m^2/g

The kenaf-coir epoxy composite added with Calcium carbonate is a novel composite that has not been studied earlier. The novel composition of kenaf-coir epoxy composite filled with $CaCO_3$ particles has not been analyzed earlier, using various mathematical, empirical models and RVE modeling to evaluate their elastic properties. Also, an earlier study has not evaluated the influence of the hybrid effect on the proposed composite. Therefore, to address the aforementioned gaps in the literature, this research addresses the problems listed below.

- A novel kenaf coir hybrid epoxy matrix composite, with varying weight percentages of calcium carbonate nanoparticles, is modeled in ABAQUS CAE version 6.14, and Representative Volume Element Analysis has been performed on it.
- The elastic attributes of the novel proposed composite are evaluated by applying the Chamis Model, Morais Model, Halpin Tsai Model, Jacquet's Horizontal Model, and Modified Halpin Tsai Model.

- The strength and Young's modulus of the analyzed composite incorporated with 0%, 2%, and 4% of calcium carbonate nanoparticles are analyzed at different fiber percentages using the analytical model and RVE analysis.
- The composite is also evaluated for the hybridization effect to analyze and calculate the tensile failure strain for the proposed novel composite.
- The impact of filler content on the composite's behavior and characteristics, has been determined. The properties and attributes of calcium carbonate are depicted in Table 1 [34].

The flowchart of the proposed research is shown as shown in figure 1.

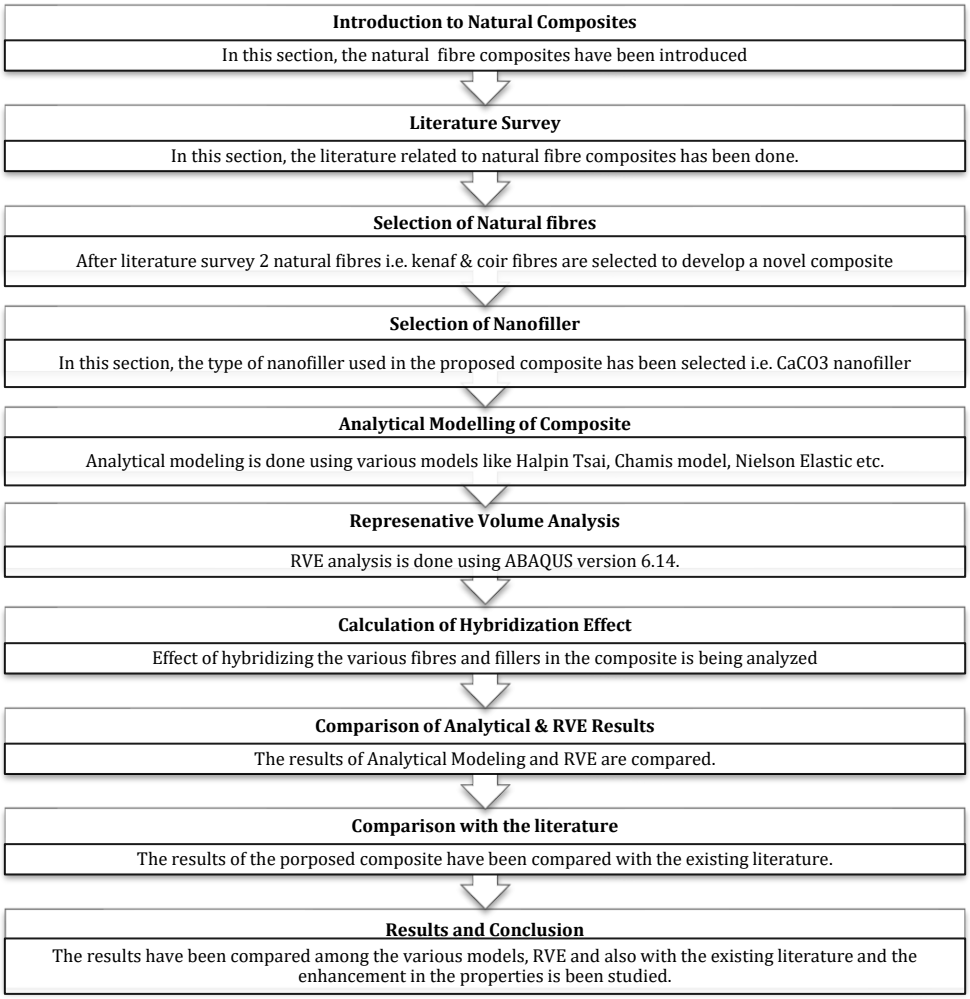

Fig. 1. Flowchart of the proposed research

2. Methodology

The original objective of incorporating mineral fillers into polymers had been predominantly cost diminution; however, in the past few years, the fillers have increasingly been employed to carry out a useful role, such as boosting the stiffness or improving the dimensional stability of the polymers. Calcium carbonate is a type of new

high-grade capability filler with low cost, that is utilized extensively in plastics, rubber, paint, and numerous other applications in industry. The form, size, and amount of calcium carbonate can all have an impact on the general attributes of composites. Because inorganic fillers are significantly smaller in size than wood fibers, they can readily be injected into polymeric matrix within wood fibers. Other attributes of Calcium Carbonate particles are shown in Table 1.

The composite analyzed in previous literature comprises Coir, Calcium carbonate, and silk squash with epoxy as a matrix element [35]. The composition used in previous literature is shown in Table 2.

Table 2. Composite sample from existing literature [35]

Sample	Epoxy resin fraction (wt%)	Coir fibres (wt%)	Silk Squash (wt%)	Calcium Carbonate (wt%)
I	84.3	10	5.7	0
II	82.3	10	5.7	2
III	80.3	10	5.7	4

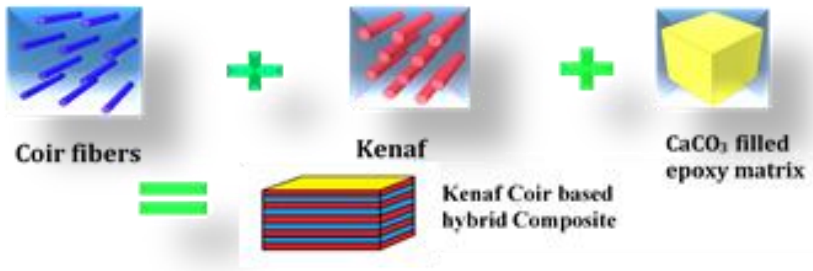

Fig. 2. Portray of hybrid composite

Table 3. Varying sample composition of the proposed composite

Sample	Description	Epoxy resin fraction (wt%)	Coir fibres (wt%)	Kenaf (wt%)	Calcium Carbonate (wt%)
I	Coir Kenaf fibers in epoxy matrix	84.3	10	5.7	0
II	Coir and kenaf fibers along with CaCO3 Particles (2 wt%)	82.3	10	5.7	2
III	Coir and kenaf fibers along with CaCO3 Particles (4 wt%)	80.3	10	5.7	4

The results derived from the above combination of composite signify that the enforcement of calcium carbonate particles increased the composite's mechanical characteristics. The tensile modulus is observed to be 5000 MPa in the sample SP1. In the second sample, SP2 the tensile modulus is observed to be 6000 MPa, whereas, in the third sample, SP3, it is observed to increase to 6700 MPa [35].

The composite considered in the present research consists of coir fiber, calcium carbonate particles, and kenaf fiber in place of silk squash embedded in epoxy resin, in the same weight percent as in previous literature. The weight percentages of different fibers utilized in the proposed composite are shown in Table 3. The hybrid effect of kenaf, coir, and calcium carbonate nanoparticles has been depicted in figure 2.

3. Analytical Models

The analytical models employed use numerical equations and expressions to count on the mechanical attributes of the composite [36, 37]. These models provide good results based on some presumptions. Therefore, in this paper, several analytical models are considered, such as the Morais model, Chamis model, Halpin Tsai model, Hirsch Model, Modified Halpin Tsai model, and JaH & JaV model, to evaluate the elastic properties of the developed composite.

3.1. Chamis Model

Chamis model is a semi-empirical model designed for outlining the composite's elastic features. In the proposed research, this model is a modified form of the rule of mixtures, replacing the fiber fraction with the square root of the function [38].
Longitudinal properties:

$$E_1 = E_f S_f + E_m S_m \tag{1}$$

$$\nu_C = \nu_f S_f + \nu_m S_m \tag{2}$$

Transverse properties:

$$E_2 = \frac{E_m}{1 - \left\{\sqrt{S_f}\left[1 - \left(\frac{E_m}{E_f}\right)\right]\right\}} \tag{3}$$

Where; $E_1, E_2,$ = Composite's Longitudinal and Transverse modulus; $E_{m,}Ef$ = Young's modulus of matrix and fiber; S_m, S_f = The volume fraction of matrix and fibres; $\nu_{m,}$ ν_C, ν_f = Poisson's ratio of matrix, composite, and fibers. The above model is evaluated as equation (4) and (5), for the proposed composite in this research.

$$E_1 = E_{Kf} S_{Kf} + E_{Cf} S_{Cf} + E_m S_m \tag{4}$$

$$E_2 = \frac{E_m}{1 - \left\{\sqrt{S_{Kf}}\left[1 - \left(\frac{E_m}{E_{Kf}}\right)\right]\right\}} + \frac{E_m}{1 - \left\{\sqrt{S_{Cf}}\left[1 - \left(\frac{E_m}{E_{Cf}}\right)\right]\right\}} \tag{5}$$

3.2. Morais Model

Morais Model is an interpretation observed mechanically at a micro level, derived in a closed form, to anticipate the representative volume element as a square for calculating its transverse modulus [39]. Morais Model is an extension of previous models by considering Poisson's ratio of the matrix in the model as shown by equation (6).

$$E_2 = \frac{S_f}{\frac{\sqrt{S_f}}{E_f} + \frac{(1-\sqrt{S_f})(1-2\vartheta_m^2)}{E_m}} + \left(1 - \sqrt{S_f}\right)\frac{E_m}{1-\vartheta_m^2} \tag{6}$$

3.3. Halpin Tsai Model

Halpin Tsai Model is developed to calculate the longitudinal and transverse modulus of the composites [40]. The longitudinal and transverse modulus can be seen as:

$$E_1 = E_f S_f + E_m S_m \tag{7}$$

$$E_2 = E_m \frac{(1 + \varsigma\, \eta\, V_f)}{(1 - \eta V_f)} \tag{8}$$

$$\eta = \frac{E_f - E_m}{E_f + \varsigma E_m} \tag{9}$$

$$\varsigma = \frac{2L}{D} \tag{10}$$

Where, ς is the reinforcing efficiency factor mainly influenced by the packing geometry and the cross-section of fibers. The value is observed to lie between 1 and 2, as predicted by various authors.

3.4. Modified Halpin Tsai Model

The equation (7) and (8) has been modified by introducing the maximum packing fraction ϕ_{max} into it [41]. This comes out to be:

$$E_2 = E_m \frac{(1 + \varsigma \eta V_f)}{(1 - \eta \phi_{max} V_f)} \tag{11}$$

Where, ϕ_{max} depicts the packing fraction (0.81 is taken for randomly oriented fibers, 0.906 is observed for a hexagonal array, 0.785 is observed in the case of a square array).

3.5 Jacquet's Horizontal Model

The transverse modulus in the case of composite material is evaluated with the use of this novel model, namely Jacquet's horizontal model [42]. Jacquet's Horizontal Model (JA-H) is shown in eq (12).

$$\frac{1}{E_2} = \frac{\sqrt{S_f}}{E_f \sqrt{S_f} + E_m (1 - \sqrt{S_f})} + \frac{(1 - \sqrt{S_f})}{E_m} \tag{12}$$

4. Hybridization Effect

Hybridization is mainly employed to ameliorate the composite material's functional characteristics and mechanical properties [43-46]. It is one of the most essential tools for analyzing the characteristics of a composite. This is evaluated to fathom the behavior of fibers in the composite. In the present case, the fibers used are Coir, which is a low elongation fiber, and Kenaf, which is a high-elongation fibers. The hybridization effect is calculated as proportion of the composite's failure strain to the low-elongation composite's failure strain [45]. The hybrid effect R_{hyb} as given by [47] as:

$$R_{hyb} = \frac{\overline{\varepsilon_{HEC}}}{\overline{\varepsilon_{LEC}}} = \sqrt{\frac{\overline{\varepsilon_{HEF}}}{\overline{\varepsilon_{LEF}}}} \left[\frac{\delta_h (k_h^q - 1)}{2\delta (k_q - 1)}\right]^{\frac{-1}{2m}} \tag{13}$$

Simplifying the above equation (13), we get the reduced equation:

$$R_{hyb} = 2^{\frac{1}{2q}} \left[\frac{\bar{\epsilon}_2}{\bar{\epsilon}_1}\right]^{1/2} \left[\frac{m}{m_h}\right]^{1/2} \left[\frac{\omega}{\omega_h}\right]^{1/2q} \tag{14}$$

Now according to the hybridization effect calculated in [47], the hybridization effect for the current composite fiber combination comes out to be: $R_{hyb} = 1.19$

This effect depicts the consequence of mixing filler in the fiber composites on the elastic and mechanical characteristics. In the case of the Kenaf coir fiber-fortified composite, it is noticed that the tensile failure strain is 1.19 times higher in comparison to the coir composite alone. Therefore, this portrays the benefits of fiber hybridization in composite materials.

5. Representative Volume Element Analysis

In the field of composite materials, the Representative Volume Element analysis is the smallest volume on which any assessment is done that will produce a quantity depictive of the whole volume. This technique of homogenization has proved to be one of the key aspects in determination of the characteristics of composite material [48]. The assumptions taken during this analysis are:

- The bond existing between the matrix and fibers is taken to be perfect.
- The composite is free from any inclusions.
- Even the distribution of fibers inside the composite.
- The composite utilized is a 3-dimensional system with unidirectional fibers.

In this paper, Representative Volume Element analysis of the Kenaf Coir epoxy-fortified calcium carbonate nanoparticles composite has been done to examine the features of the hybrid composite using ABAQUS CAE version 6.14.

5.1 Modeling Steps

- STEP 1: Initially the coir fibers are designed in ABAQUS. Post this the kenaf fibres are stacked above it.
- STEP 2: After this a volume element of epoxy matrix reinforced with $CaCo_3$ nanofillers is designed.
- STEP 3: The kenaf and coir fibres of diameter shown in table 4 are integrated into the volume element of epoxy matrix. The volume element possesses a length, breadth, and height of 1.6×10^{-4}m [48].
- STEP 4: The mechanical properties of respective fibres and matrix are assigned in ABAQUS.
- STEP 5: Meshing used is hexahedra meshing while performing RVE analysis with the help of the Sweep tool. 0.00005 is the mesh size used in this research modeling.
- STEP 6: The Pre boundary Condition parameters are shown in Table 4.
- STEP 7: RVE is then subjected to respective loads and conditions.
- STEP 8: After this, the RVE analysis is done for Longitudinal and Transverse Modulus.

Table 4. PBC Criterion for RVE

Criterion	Kenaf fibers	Coir fibers
The volume fraction of fibers ($\boldsymbol{V_f}$)	0.10	0.057
Diameter ($\boldsymbol{D_f}$)	25 µm	15 µm
Length ($\boldsymbol{L}$)	160 µm	160 µm
Width ($\boldsymbol{W}$)	80 µm	80 µm

The model for the above-considered composite has been developed in ABAQUS, as shown in figure 3.

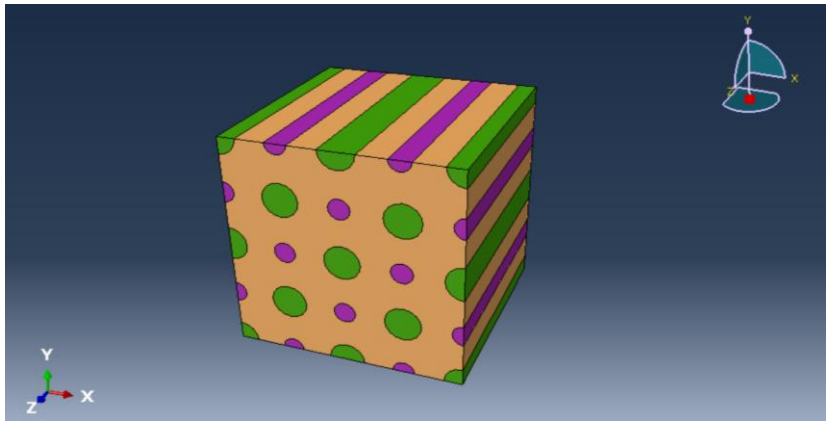

Fig. 3. RVE model

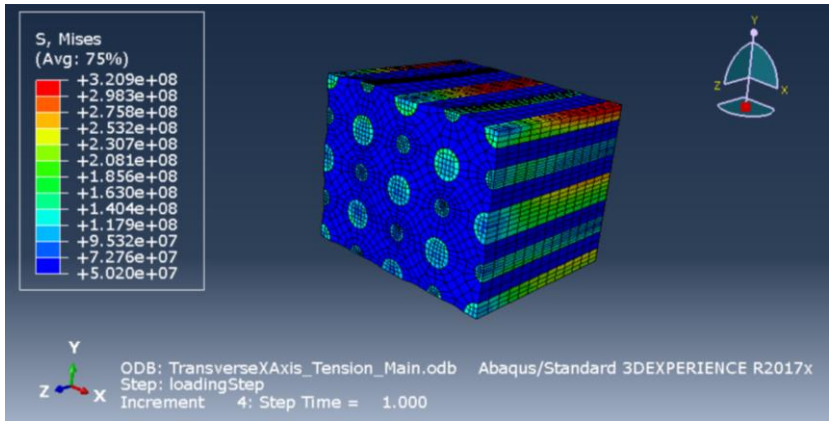

Fig. 4. Postprocessing of transverse modulus

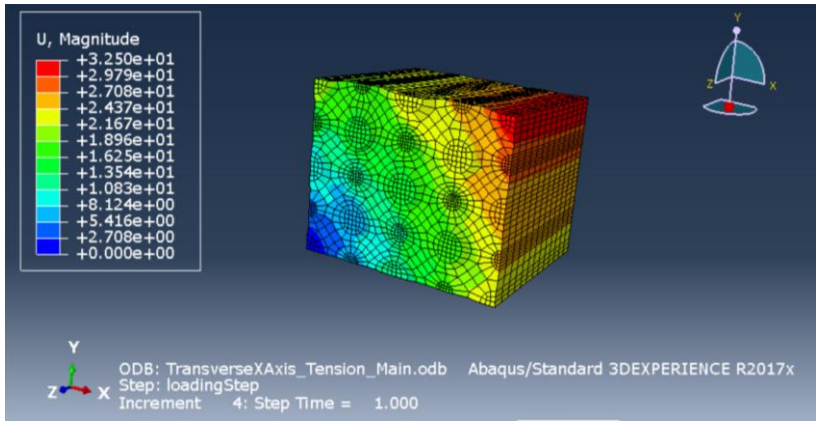

Fig. 5. Resultant displacement on implementation of transverse stress

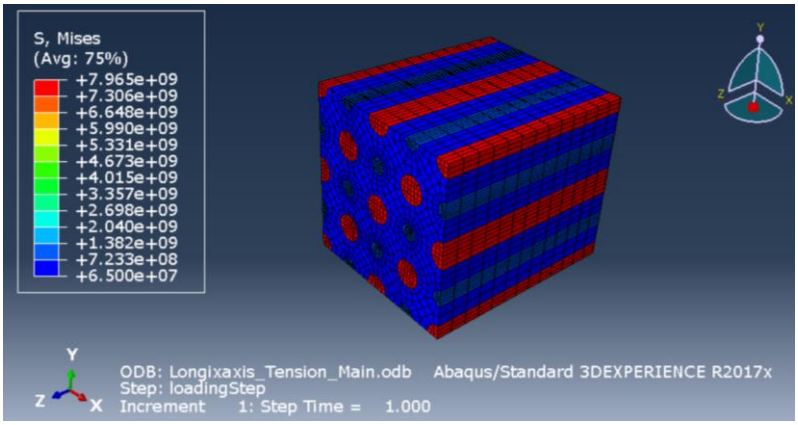

Fig. 6. Postprocessing of longitudinal modulus

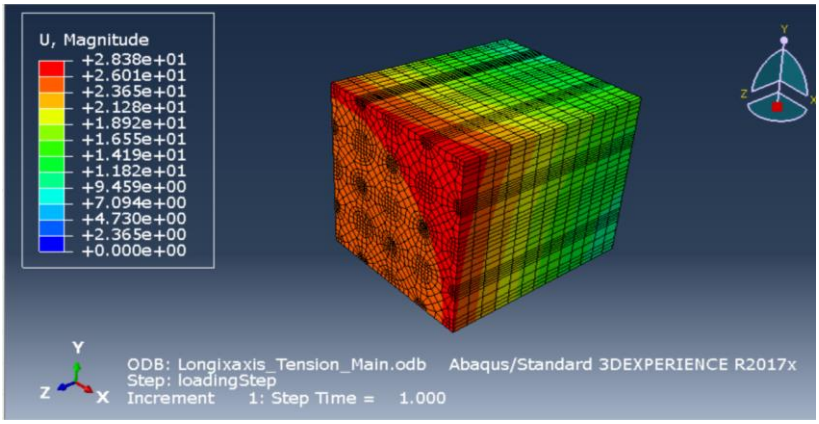

Fig. 7. Resultant displacement on implementation of longitudinal stress

Figures 4,5, 6 and 7 illustrate the results plotted for the stress in the case of longitudinal and transverse fiber composite. Figure 4 and 5 manifest the postprocessing three-dimensional results and resultant displacement that depict the damage criteria, on implementation of transverse stress, respectively. Figures 6 and 7 manifest the three-dimensional postprocessing results and the resultant displacement that depict the damage criteria, after the implementation of longitudinal stress, respectively.

6. Results from Analytical Modelling and RVE Analysis

Table 5 compares the weight percentages of the composite materials analyzed in the existing literature with the fiber material used in the proposed work. In the existing literature work, Coir, Silk Squash, epoxy, and calcium carbonate particles are used in different weight percentages. Whereas in the proposed composite, the sample composition evaluated is the same, just by replacing the silk squash fiber with the kenaf fibers. In the proposed composite, three samples of the composite with varying content of kenaf, coir fiber, and calcium carbonate particles, have been analyzed for longitudinal modulus and transverse modulus, as well a comparison is made with the existing literature [35].

Table 5. The weight percent of materials used in existing literature and proposed work

S.NO	Composite Material	Experimental Work [35]			Proposed Work		
		I	II	III	I	II	III
1	Epoxy	84.3	82.3	80.3	84.3	82.3	80.3
2	Coir fiber	10	10	10	10	10	10
3	Nano Calcium Carbonate	0	2	4	0	2	4
4	Silk Squash	5.7	5.7	5.7	0	0	0
5	Kenaf fiber	0	0	0	5.7	5.7	5.7

Table 6. Results for the sample KC1

Models/ Properties	Chamis Model	Morais Model	Halpin Tsai Model	Modified Halpin Tsai Model	Jacquet's Horizontal Model	RVE	Mean	Deviation
Transverse Modulus (GPa)	5.84	5.75	6.12	5.29	4.98	6.04	5.67	0.36
Longitudinal Modulus (GPa)	7.42	7.42	7.42	7.42	7.42	7.59	7.45	0.048
Poisson's Ratio (μ)	0.32	0.32	0.32	0.32	0.32	0.35	0.32	0.270

Table 7. Results for the sample KC2

Models/ Properties	Chamis Model	Morais Model	Halpin Tsai Model	Modified Halpin Tsai Model	Jacquet's Horizontal Model	RVE	Mean	Deviation
Transverse Modulus (GPa)	6.18	6.01	6.28	5.99	5.93	6.42	6.14	0.16
Longitudinal Modulus (GPa)	7.92	7.92	7.92	7.92	7.92	7.98	7.93	0.016
Poisson's Ratio (μ)	0.35	0.35	0.35	0.35	0.35	0.38	0.36	0.012

The different samples that have been used in this composite are the Kenaf Coir composite (KC1), the Kenaf Coir composite with 2% of CaCO3 (KC2), and the Kenaf Coir composite with 4% of CaCO3 content (KC3). Results have been analyzed using five different analytical and empirical models Jacquet's Model, H-T Model, Chamis Model, Morais Model, and Modified H-T Model. The outcomes from all three samples KC1, KC2, and KC3 have been shown in Tables 6, 7 and 8, respectively. The graphical results for transverse and longitudinal modulus have been shown in Figures 8, 9, and 10 respectively.

Table 8. Results for the sample KC3

Models/ Properties	Chamis Model	Morais Model	Halpin Tsai Model	Modified Halpin Tsai Model	Jacquet's Horizontal Model	RVE	Mean	Deviation

Transverse Modulus (GPa)	6.73 0.16	6.47 0.1	6.84 0.27	6.24 0.33	6.17 0.4	6.96 0.39	6.57	0.275
Longitudinal Modulus (GPa)	8.22	8.22	8.22	8.22	8.22	8.34	8.24	0.033
Poisson's Ratio (μ)	0.37	0.37	0.37	0.37	0.37	0.39	0.373	0.005

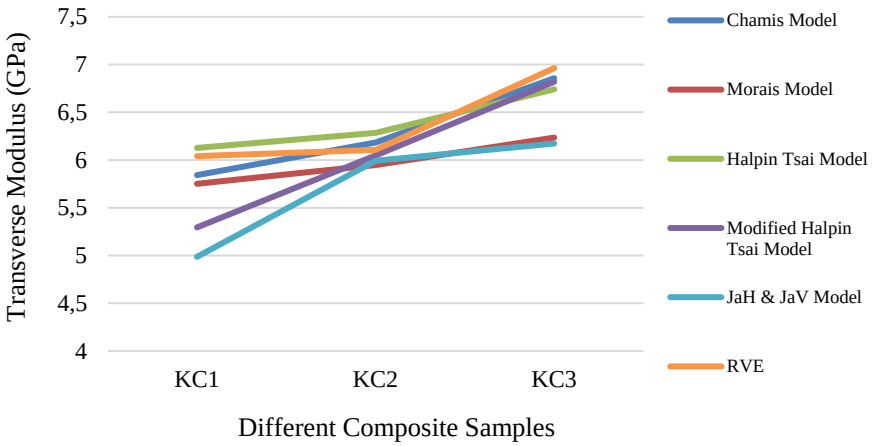

Fig. 8 Transverse modulus for different samples (KC1, KC2, KC3)

Figures 8, 9 and 10 depict the mechanical attributes of varying samples of composite. On uplifting the volume of the calcium carbonate in the composite, the modulus is observed to see a rise. The Transverse Modulus in sample KC1 is observed to be 5.67 GPa, which increases to 6.13 GPa in sample KC2 and to 6.56 GPa in sample KC3. The Longitudinal modulus is reported to increase from 7.45 GPa to 7.93 GPa to 8.24 GPa in KC1, KC2, and KC3 samples, respectively. Therefore, an enhancement of 11.14% is noticed in the case of longitudinal modulus, whereas an advancement of about 15.69% is noticed in the case of transverse modulus on the addition of calcium carbonate nanofiller to the kenaf coir epoxy composite.

To verify that the properties of the proposed composites are better than the composite taken from the previous literature, a comparison of the properties has been made for all the three samples of the composites. Comparison based on existing literature depicts that the elastic modulus displayed an increase from 4.2 GPa to 7.45 GPa in the first sample KC1. In the second sample, KC2, the modulus is remarked to uplift from 5.3 GPa to 7.93 GPa [35]. The relative increment is noticed in the third sample, KC3, where the modulus of 6.7 GPa has uplifted to 8.24 GPa. The results are portrayed in Figure 11 [35]. From figure 11, it is observed that the proposed composite has enhanced properties in comparison to the previous literature, which uses silk squash fibre in place of kenaf fibres for all the three samples.

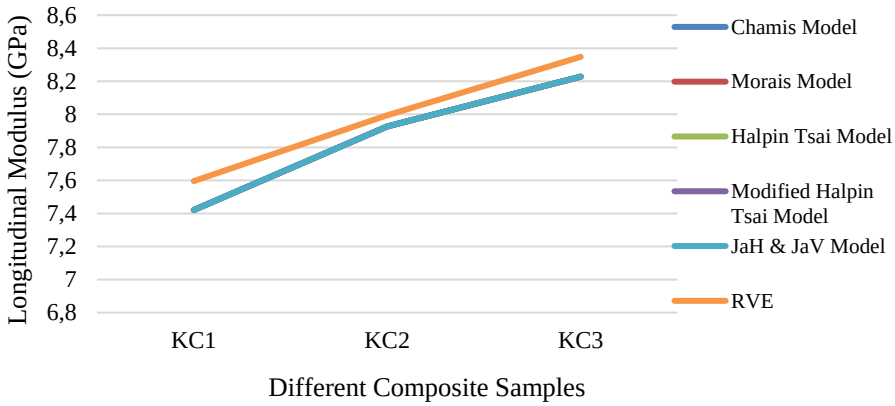

Fig. 9. Longitudinal modulus for different samples (KC1, KC2, KC3)

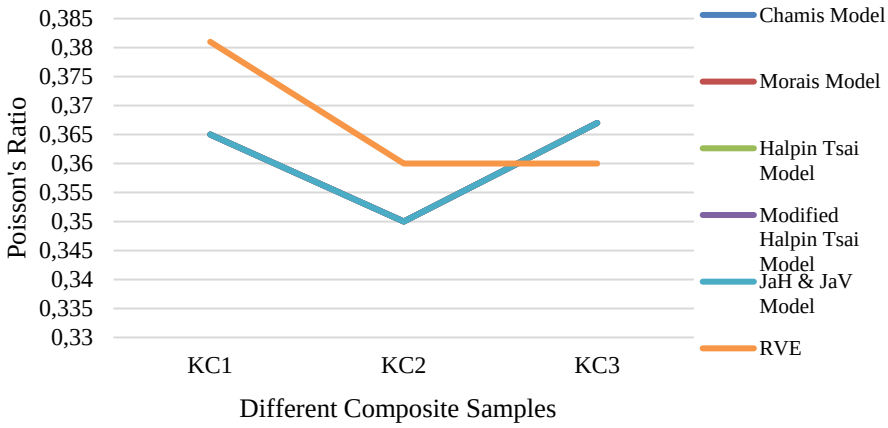

Fig. 10 Poisson's ratio for different samples (KC1, KC2, KC3

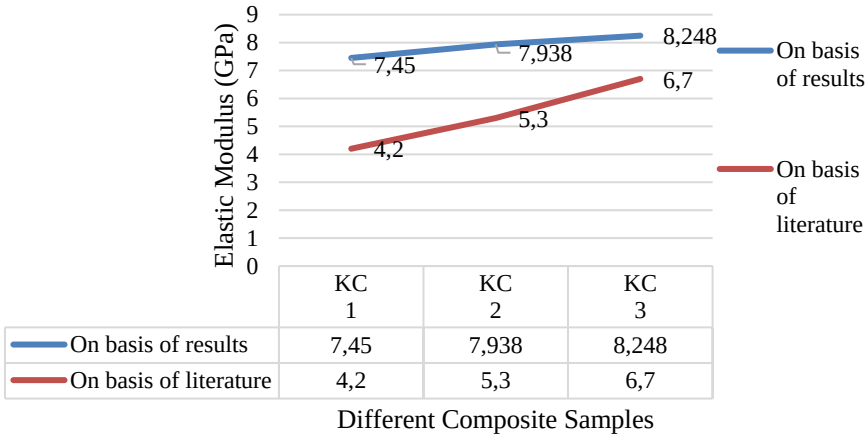

Fig. 11. Comparison of results for elastic modulus for proposed composite with existing literature [35]

7. Conclusions

The kenaf coir epoxy composite with the incorporation of calcium carbonate nanoparticles is analyzed in the present paper, using five different analytical models and using RVE analysis. This is carried out to examine the effect of fortification of nanofiller in the composite on the elastic features and performance of coir kenaf epoxy composites. The outcomes of the research are delineated as follows:

- Based on the extensive literature survey, it has been found that the proposed Kenaf-Coir-Calcium carbonate nanoparticle reinforced epoxy composite is a novel and unique composite, not researched before and thereby cherishing superior elastic characteristics.
- The elastic characteristics of the composite are accomplished by employing mathematical analytical modeling using five different models, particularly Chamis Model, Morais model, Jacquet's Horizontal Model, Halpin Tsai Model, Modified Halpin Tsai Model.
- The composite outcomes have also been analysed using Representative Volume Element analysis that has been carried out using software ABAQUS CAE version 6.14.
- An observable increment is detected on the mixing of calcium carbonate nanoparticles with coir and kenaf fibers. The transverse modulus is noticed to uplift by 16.88%, and the longitudinal modulus is observed to uplift by 11.14% on the mixing of CaCO3 particles in coir kenaf composite.
- The hybridization effect is calculated as 1.19, which represents that tensile failure strain in CaCO3 fortified composites is 1.19 times greater as compared to pure kenaf coir epoxy composite.
- The outcomes of RVE are noticed to be in synergy with the outcomes gained through analytical modeling, as illustrated in Tables 5, 6, and 7.
- The silk squash fibers in the existing literature are replaced with kenaf fibers in the proposed literature, and the influence of this replacement is observed in terms of its mechanical attributes. Comparison made with existing literature shows the upliftment of modulus by 76.66 % in the KC1 sample, an increment of 49.77% in the KC2 sample, and a growth of 23.10% in the KC3 sample. This represents enhanced tensile strength in in contrast to $CaCO_3$ incorporated coir and luffa cylindrica hybrid composite used in literature, is found to be in a superior state in terms of its mechanical properties.
- Analyzing the practical implications of this composite, we conclude that the above proposed novel composite having immense attributes, will be of great help and usefulness in development of light weight textile items such as a lady's purse or bag. This purse has been developed and analyzed in this research on ANSYS.

8. Recommendation

The above proposed composite with enhanced properties is recommended for further analysis using fibre modification, matrix modification etc. In future, in order to solve issues including moisture absorption, insufficient toughness, and decreased long-term stability for outdoor application, more study and investigation is needed. Additionally, research can be done to improve the properties of nanofillers and fibers by combining more than one of them. As of right now, natural fiber composites offer a wide range of applications that do not necessitate extremely high load bearing or high temperature functioning capacities. the proposed composite. Therefore, the $CaCO_3$ incorporated kenaf coir hybrid composite

Abbreviations

E_1, E_2	Longitudinal and Transverse modulus of composite
E_f, E_m	Elastic Modulus of fibers and matrix, respectively
S_f, S_m	Volume fraction of the fibers and matrix, respectively
v_f, v_m	Poisson's ratio of fiber and matrix, respectively
E_{kf}, E_{cf}, E_m	Modulus of kenaf fiber, coir fiber, and matrix, respectively.
S_{kf}, S_{cf},	The volume fraction of kenaf fiber, the Volume fraction of coir fibers.
ϕ_{max}	Packing fraction
ς	Reinforcing Efficiency Factor
L, D	Length and diameter of fibers, respectively.
RVE	Representative Volume Element
NR	Natural Rubber Composite
NFCs	Natural Fiber Composites

Acknowledgement

The author would like to express deep thanks to the editorial team and anonymous reviewers for their positive comments for previous version of this research paper.

References

[1] Sanjay MR, Madhu P, Jawaid M, Senthamaraikannan P, Senthil S, Pradeep S. Characterization and properties of natural fiber polymer composites: A comprehensive review. J Clean Prod. 2018;172:566-581. https://doi.org/10.1016/j.jclepro.2017.10.101

[2] Anbukarasi K, Kalaiselvam S. Thermal and mechanical behaviors of biorenewable fibers-based polymer composites. In: Handbook of composite from renewable materials: Functionalization. Wiley-Scrivener. 2016;4(19):491-520. https://doi.org/10.1002/9781119441632.ch81

[3] Sumesh KR, Kanthavel K, Vivek S. Mechanical/thermal/vibrational properties of sisal, banana, and coir hybrid natural composites by the addition of bio synthesized aluminum oxide nano powder. Mater Res Express. 2019;6(4):045318. https://doi.org/10.1088/2053-1591/aaff1a

[4] Guimaraes JL, Frollini E, Silva CGD, Wypych F, Satyanarayana KG. Characterization of banana, sugarcane bagasse, and sponge gourd fiber of Brazil. Indus Corp Prod. 2009;30(3):407-415. https://doi.org/10.1016/j.indcrop.2009.07.013

[5] Kumar R, Anand A. Fabrication and mechanical characterization of Indian ramie reinforced polymer composites. Mater Res Express. 2019;6(5):055303. https://doi.org/10.1088/2053-1591/aaff12

[6] Saba N, Paridah MT, Jawaid M. Mechanical properties of kenaf fiber reinforced polymer composite: a review. Constr Build Mater. 2015;76:87-96. https://doi.org/10.1016/j.conbuildmat.2014.11.043

[8] Matykiewicz D, Barczewski M, Knapski D, Skorczewska K. Hybrid effects of basalt fibers and basalt powder on thermomechanical properties of epoxy composites. Compos Part B Eng. 2017;125:157-164. https://doi.org/10.1016/j.compositesb.2017.05.060

[9] Balan AK, Parambil SM, Vakyath S, Velayudhan JT, Naduparambath S, Etathil P. Coconut shell powder reinforced thermoplastic polyurethane/natural rubber blend-composites: effect of silane coupling agents on the mechanical and thermal properties

of the composites. J Mater Sci. 2017;52:6712-6725. https://doi.org/10.1007/s10853-017-0907-y
[10] Siqueira G, Bras J, Follain N, Belbekhouche S, Marais S, Dufresne A. Thermal and mechanical properties of bio-nanocomposites reinforced by luffa cylindrica cellulose nanocrystals. Carbo Polym. 2013;91(2):711-717. https://doi.org/10.1016/j.carbpol.2012.08.057
[11] Satapathy S, Kothapalli RV. Mechanical, dynamic mechanical and thermal properties of banana fiber/recycled high-density polyethylene bio composites filled with flyash cenospheres. J Polym Environ. 2018;26:200-213. https://doi.org/10.1007/s10924-017-0938-0
[12] Saba N, Paridah MT, Abdan K, Ibrahim NA. Dynamic mechanical properties of oil palm nano filler/kenaf/epoxy hybrid nanocomposites. Constr Build Mater. 2016;124:133-138. https://doi.org/10.1016/j.conbuildmat.2016.07.059
[13] Saba N, Safwan A, Sanyang ML, Mohammad F, Pervaiz M, Jawaid M, Sain M. Thermal and dynamic mechanical properties of cellulose nanofibers reinforced epoxy composites. Int J Biol Macromol. 2017;102:822-828. https://doi.org/10.1016/j.ijbiomac.2017.04.074
[14] Joseph S, Appukuttan SP, Kenny JM, Puglia D, Thomas S, Joseph K. Dynamic mechanical properties of oil palm microfibril-reinforced natural rubber composites. J Appl Polym Sci. 2010;117:1298-1308. https://doi.org/10.1002/app.30960
[15] Gupta MK. Thermal and dynamic mechanical analysis of hybrid jute/sisal fiber reinforced epoxy composite. Proc Inst Mech Eng Part L. 2018;232:743-748. https://doi.org/10.1177/1464420716646398
[16] Venkateshwaran N, Elaya Perumal A, Raj RA. Mechanical and dynamic mechanical analysis of woven banana/epoxy composite. J Polym Environ. 2012;20:565-572. https://doi.org/10.1007/s10924-011-0410-5
[17] Kumar SS, Duraibabu DA, Subramanian K. Studies on mechanical, thermal, and dynamic mechanical properties of untreated (raw) and treated coconut sheath fiber reinforced epoxy composites. Mater Des. 2014;59:63-69. https://doi.org/10.1016/j.matdes.2014.02.013
[18] Shanmugam D, Thiruchitrambalam M. Static and dynamic mechanical properties of alkali-treated unidirectional continuous Palmyra Palm Leaf Stalk Fiber/jute fiber reinforced hybrid polyester composites. Mater Des. 2013;50:533-542. https://doi.org/10.1016/j.matdes.2013.03.048
[19] Saw SK, Sarkhel G, Choudhury A. Dynamic mechanical analysis of randomly oriented short bagasse/coir hybrid fiber-reinforced epoxy novolac composites. Fibers Polym. 2011;12:506. https://doi.org/10.1007/s12221-011-0506-5
[20] Pothan LA, George CN, John MJ, Thomas S. Dynamic mechanical and dielectric behavior of banana-glass hybrid fiber reinforced polyester composites. J reinf Plast Compos. 2010;29:1131-1145. https://doi.org/10.1177/0731684409103075
[21] Rajini N, Jappes JW, Rajakarunakaran S, Jeyaraj P. Dynamic mechanical analysis and free vibration behavior in chemical modifications of coconut sheath/nano-clay reinforced hybrid polyester composite. J Compos Mater. 2013;47:3105-3121. https://doi.org/10.1177/0021998312462618
[22] Saba N, Jawaid M, Alothman OY, Paridah MT. A review on dynamic mechanical properties of natural fiber reinforced polymer composites. Constr Build Mater. 2016;106:149-159. https://doi.org/10.1016/j.conbuildmat.2015.12.075
[23] Krishnudu DM, Sreeramulu D, Reddy PV. Optimization of the mechanical properties of coir-luffa cylindrica filled hybrid composites by using Taguchi method. AIP Conference Proceedings. 2018. https://doi.org/10.1063/1.5032020
[24] Boujmal R, Kakou CA, Nekhlaoui S, Essabir H, Bensalah MO, Rodrigue D, Qaiss AEK. Alfa fibers/clay hybrid composites based on polypropylene: Mechanical, thermal, and

structural properties. J Thermoplast Compos Mater. 2018;31(7):974-91. https://doi.org/10.1177/0892705717729197
[25] Senthilkumar K, Saba N, Rajini N, Chandrasekar M, Jawaid M, Siengchin S, Alothman OY. Mechanical properties evaluation of sisal fiber reinforced polymer composites: a review. Constr Build Mater. 2018;174:713-729. https://doi.org/10.1016/j.conbuildmat.2018.04.143
[26] Naveen J, Jawaid M, Zainudin ES, Sultan MTH, Yahaya R. Mechanical and moisture diffusion behavior of hybrid Kevlar/Cocos nucifera sheath reinforced epoxy composites. J Mater Res Technol. 2019;8:1308-1318. https://doi.org/10.1016/j.jmrt.2018.07.023
[27] d'Almeida JR, Aquino RC, Monteiro SN. Dynamic mechanical behavior of piassava fibers (Attalea funifera) reinforced polyester composites. Int J Polym Mater. 2007;56:397-403. https://doi.org/10.1080/00914030600873527
[28] Chee SS, Jawaid M, Sultan MTH, Alothman OY, Abdullah LC. Thermomechanical and dynamic mechanical properties of bamboo/woven kenaf mat reinforced epoxy hybrid composites. Compos B Eng. 2019;163:165-174. https://doi.org/10.1016/j.compositesb.2018.11.039
[29] Krishnudu DM, Sreeramulu D, Reddy PV. Optimization the mechanical properties of coir-luffa cylindrica filled hybrid composites by using Taguchi method. AIP Conference Proceedings, AIP Publishing. 2018. https://doi.org/10.1063/1.5032020
[30] Reddy PV, Prasad PR, Krishnudu DM, Hussain P. Influence of fillers on mechanical properties of prosopis juliflora fiber reinforced hybrid composites. Materials Today Proceedings. 2019.
[31] Krishnudu DM, Sreeramulu D, Reddy PV. Synthesis and characterization of coir and Luffa Cylindrica filled with CaCo3 hybrid composites. Int J Integrated Eng. 2019;11:290-298. https://doi.org/10.30880/ijie.2019.11.01.029
[32] Prado NS, da Silva ISV, de Morais LC, Pasquini D, Otaguro H. Effects of surface modifications of kraft wood pulp cellulose fibers on improving the mechanical properties of cellulose fiber/latex composites. J Polym Environ. 2019;1-9. https://doi.org/10.1007/s10924-019-01516-w
[33] Saba N, Paridah MT, Abdan K, Ibrahim NA. Effect of oil palm nano filler on mechanical and morphological properties of kenaf reinforced epoxy composites. Constr Build Mater. 2016;123:15-26. https://doi.org/10.1016/j.conbuildmat.2016.06.131
[34] Dante RC, Arevalo FMS, Ramos PM. Composite fiber based on Sisal fiber and Calcium Carbonate. J Nat Fibers. 2014;11(2):121-135. https://doi.org/10.1080/15440478.2013.849644
[35] Krishnudu DM, Sreeramulu D, Reddy PV, Prasad PR. Influence of filler on mechanical and dielectric properties of coir and luffa cylindrica fiber reinforced epoxy hybrid composites. Journal of Natural fibers. 2020;19(1):339-348. https://doi.org/10.1080/15440478.2020.1745115
[36] Parashar S, Chawla VK. Kenaf-Coir based hybrid nano-composite: An analytical and representative volume element analysis. Engineering Solid Mechanics. 2023;11(1):103-118. https://doi.org/10.5267/j.esm.2022.8.001
[37] Parashar S, Chawla VK. A systematic review on sustainable green fiber reinforced composite and their analytical models. Materials Today: Proceedings. 2021;46:6541-6546. https://doi.org/10.1016/j.matpr.2021.03.739
[38] Chamis CC, Sendeckyj GP. Critique on theories predicting thermoelastic properties of fibrous composites. J Compos Mater. 1968;2(3):332-358. https://doi.org/10.1177/002199836800200305
[39] Alfredo BM. Transverse moduli of continuous fiber reinforced polymers. Compos Sci Technol. 2000;60:997-1002. https://doi.org/10.1016/S0266-3538(99)00195-5
[40] Halpin JC, Tsai SW. Environmental factors in composite materials design. US Air Force Technical Report AFML TR. 1967;67423.

[41] Osaka E, Onukwuli OD. A Modified Halpin Tsai model for estimating the modulus of natural fiber reinforced composites. Int J Eng Sci Invention. 2018;7(5):63-70.
[42] Jacquet E, Trivaudey F, Varchon D. Calculation of the transverse modulus of a unidirectional composite material and of the modulus of an aggregate: Application of rule of mixtures. Compos Sci Technol. 2000;60:345-350. https://doi.org/10.1016/S0266-3538(99)00128-1
[43] Essabir H, Bensalah MO, Rodrigue D, Bouhfid R, Qaiss A. Structural, mechanical and thermal properties of bio-based hybrid composites from waste coir residues: Fibers and shell particles. Mech Mater. 2016;93:134-144. https://doi.org/10.1016/j.mechmat.2015.10.018
[44] Thwe MM, Liao K. Effects of environmental aging on the mechanical properties of bamboo-glass fiber reinforced polymer matrix hybrid composites. Compos Part A Appl Sci Manufact. 2002;33(1):43-52. https://doi.org/10.1016/S1359-835X(01)00071-9
[45] Jacob M, Thomas S, Varughese KT. Mechanical properties of sisal/oil palm hybrid fiber reinforced natural rubber composites. Compos Sci Technol. 2004;64(7-8):955-965. https://doi.org/10.1016/S0266-3538(03)00261-6
[46] Joseph S, Sreekala MS, Oommen Z, Koshy P, Thomas S. A Comparison of the mechanical properties of the phenol formaldehyde composites reinforced with banana and glass fibers. Compos Sci Technol. 2002;62(14):1857-1868. https://doi.org/10.1016/S0266-3538(02)00098-2
[47] Zweben C. Tensile strength of hybrid composites. J Mater Sci. 1977;12(7):1325-1337. https://doi.org/10.1007/BF00540846
[48] Adeniyi AG, Adeoye AS, Ighalo JO. FEA of effective elastic properties of banana fiber reinforced polystyrene composites. Mech Adv Mater Struct. 2020;28(18):1869-1877. https://doi.org/10.1080/15376494.2020.1712628
[49] Pol A, Malagi R, Munshi G. Identification of mechanical properties of an araldite LY556 blended with DNR composite and polyacetal: A comparative study for a sustainable future. Journal of Future Sustainability. 2022;2(4):149-156. https://doi.org/10.5267/j.jfs.2022.10.005
[50] Sadjadi S. A survey on the effect of plastic pollution in the Great Lakes. Journal of Future Sustainability. 2021;1(1):5-8. https://doi.org/10.5267/j.jfs.2021.1.002
[51] Tekletsadik S. Selection of best leather item using an FAHP method to launch new leather industry in Ethiopia: A case study. Journal of Future Sustainability. 2023;3(2):85-96. https://doi.org/10.5267/j.jfs.2022.11.008
[52] Chawla VK, Chanda AK, Angra S. Coexistent scheduling in the tandem flow path configuration of a flexible manufacturing system by using an advanced grey wolf optimizer. Scientia Iranica. 2020. https://doi.org/10.24200/sci.2020.54152.3618
[53] Chawla VK, Bhargava P, Verma S. Design, stimulation, and fabrication of chassis of an FSAE female-driven vehicle. Materials Today: Proceedings. 2021;43:36-41. https://doi.org/10.1016/j.matpr.2020.11.202
[54] Gupta P, Chawla VK, Jain V, Angra S. Green operations management for sustainable development: An explicit analysis by using fuzzy best-worst method. Decision Science Letters. 2022;11(3):357-366. https://doi.org/10.5267/j.dsl.2022.1.003
[55] Parashar S, Chawla VK. Evaluation of fiber volume fraction of kenaf-coir-epoxy based green composite by finite element analysis. Materials Today: Proceedings. 2022; 50: 1265-1274. https://doi.org/10.1016/j.matpr.2021.08.14 7
[56] Saxena T, Tomar P. Constitutive Performance Characterization of Diversified Bamboo Material-A Green Technology. Proceedings of International Conference on Sustainable Computing in Science, Technology and Management (SUSCOM), Jaipur-India; 2019. https://doi.org/10.2139/ssrn.3358200
[57] Parashar S, Tomar P. Synergy of sustainable bio-composite bamboo material in green technology-an explicit report. Proceedings of International Conference on Sustainable

Computing in Science, Technology, and Management (SUSCOM) Jaipur-India; 2019. https://doi.org/10.2139/ssrn.3357290
[58] Saxena T, Chawla VK. Banana leaf fiber-based green composite: A detailed review report. Materials Today: Proceedings. 2021; 46: 6618-6624. https://doi.org/10.1016/j.matpr.2021.04.099
[59] Faghidian SA. Flexure mechanics of nonlocal modified gradient nano-beams. Journal of Computational Design and Engineering. 2021; 8(3): 949-959. https://doi.org/10.1093/jcde/qwab027
[60] Saxena T, Chawla VK. Evaluation of mechanical properties for banana-carbon fiber reinforced nano-clay epoxy composite using analytical modeling and simulation. Research on Engineering Structures and Materials. 2022; 8(4): 773-798. https://doi.org/10.17515/resm2022.403me0219
[61] Yadav E, Chawla VK. An explicit literature review on bearing materials and their defect detection techniques. Materials Today: Proceedings. 2022; 50: 1637-1643. https://doi.org/10.1016/j.matpr.2021.09.132
[62] Faghidian SA. Two-phase local/nonlocal gradient mechanics of elastic torsion. Mathematical Methods in the Applied Sciences. 2020; 1-17. https://doi.org/10.1002/mma.6877
[63] Yadav E, Chawla VK. Fault detection in rotating elements by using fuzzy integrated improved local binary pattern method. Journal of the Brazilian Society of Mechanical Sciences and Engineering. 2022; 44(12): 596. https://doi.org/10.1007/s40430-022-03916-x
[64] Pothan LA, George CN, John MJ, Thomas S. Dynamic mechanical and dielectric behavior of banana-glass hybrid fiber reinforced polyester composites. Journal of Reinforced Plastics and Composites. 2010; 29(8): 1131-1145. https://doi.org/10.1177/0731684409103075
[65] Chawla VK, Yadav E. Defect detection in rotating machine elements by using an improved image segmentation technique. IOP conference series: materials science and engineering. 2022; 1228(1): 012009. https://doi.org/10.1088/1757-899X/1228/1/012009
[66] Bhatia S, Khan S, Angra S. Effect of the content of silane-functionalized boron carbide on the mechanical and wear performance of B4C reinforced epoxy composites. High Performance Polymers. 2021; 33(10): 1165-1180. https://doi.org/10.1177/09540083211031129
[67] Sadjadi S. A survey on the effect of plastic pollution in the Great Lakes. Journal of Future Sustainability. 2021; 1(1): 5-8. https://doi.org/10.5267/j.jfs.2021.1.002
[68] Gupta R, Rout V, Rajput K, Chawla VK, Fouad H, Akhtar MS. A Sustainable Method to Convert Waste Heat Energy to Electricity by Using Thermo-Electric Generators. Journal of Nanoelectronics and Optoelectronics. 2023; 18(4): 502-509. https://doi.org/10.1166/jno.2023.3410
[69] Faghidian SA. Higher order mixture n onlocal gradient theory of wave propagation. Mathematical Methods in the Applied Sciences. 2020; 1-23. https://doi.org/10.1002/mma.6885
[70] Saxena T, Chawla VK. Effect of fiber orientations and their weight percentage on banana fiber-based hybrid composite. Materials Today: Proceedings. 2022; 50: 1275-1281. https://doi.org/10.1016/j.matpr.2021.08.149
[71] Balcioglu HE, Ozmen HB. The fracture behaviour of pure and hybrid intraply knitted fabric reinforced polymer composites. Fracture Mechanics Applications. 2019; 1-22.
[72] Faghidian SA. Contribution of nonlocal integral elasticity to modified strain gradient theory. The European Physical Journal Plus. 2021; 136(5): 559. https://doi.org/10.1140/epjp/s13360-021-01520-x

[73] Chawla V, Chanda AK, Angra S, Bonyadi Naeini A. Coexistent scheduling in the tandem flow path configuration of a flexible manufacturing system by using an advanced grey wolf optimizer. Scientia Iranica. 2020. https://doi.org/10.24200/sci.2020.54152.3618
[74] Chawla VK, Chhabra D, Gupta P, Naaz S. Evaluation of green operations management by fuzzy analytical hierarchy process. Materials Today: Proceedings. 2021; 38: 274-279. https://doi.org/10.1016/j.matpr.2020.07.200

Research on Engineering Structures & Materials
www.jresm.org
Research Group

Research Article

Assessment of properties of rubble masonry used in heritage structure

Abhay Bambole*[,a], Rohan Gaikwad[b], Archanaa Dongre[c], G R Reddy[d]

Department of Structural Engineering, Veermata Jijabai Technological Institute, Matunga, Mumbai, India

Article Info

Article history:

Received 24 Aug 2023
Accepted 09 Dec 2023

Keywords:

Heritage structure;
Rubble masonry;
Lime mortar;
Surkhi

Abstract

Preservation of Heritage structures is of utmost importance. Rubble masonry played a significant role in the conservation of structures. It is a traditional wall construction material used to build walls and standing structures in India since ancient times. Even now, heritage structures are being made to serve humanity for many years. Therefore, it is necessary to find a combination of rubble masonry and essential additives like lime mortar and surkhi to help build new heritage structures and also help reduce the deterioration of ancient architectural structures and monuments. This experimental study presents rubble masonry for repairing Heritage structures as an alternative to the conventional use of cement mortar. In addition to repairing work, rubble masonry, lime mortar, and surkhi are used to build new heritage structures for long-term sustainability. Rubble masonry, lime mortar, and surkhi can reduce the deterioration of old architectural structures and monuments. A case study on Global Vipassana Pagoda allocated in Mumbai, India, is considered. It is made up of Basalt stone with an interlocking system.

1. Introduction

India is known for its rich history and significant heritage structures. As per the archaeological survey of India, in the present day, India has 3650 ancient monuments and archaeological sites and remains of national importance, whereas world heritage sites count is 1157. Indian heritage structures are three times more than the world heritage sites, and one or more new structures are discovered whenever some major excavation happens. India carries greater responsibility for preserving these structures with efficient material which is environmentally friendly, sustainable, and does not damage the structure after repair. Even when a new heritage structure is being constructed, one must have material similar to the material used in ancient structures in India; this particular work is focused on creating such material. The author found that rubble masonry along with lime mortar and surkhi gives such a combination, which is very effective in preserving ancient heritage structures in India and can also be used to construct a new heritage structure. This study involves an experimental investigation of rubble masonry commonly employed in heritage structures such as the Pagoda in Gorai, Mumbai, India. In the Pagoda dome, rubble masonry serves as infill material, facilitating load transfer from the superstructure to the dome's foundation. Given the dome's shell-like structure, the forces acting on this rubble masonry are primarily compressive. this study highlights the lasting potential of using rubble masonry with lime and surkhi mortar in building and preserving historical structures, exemplified by the Global Pagoda Vipassana in Mumbai, India. Heritage

*Corresponding author: anbambole@st.vjti.ac.in
[a] orcid.org/0000-0002-5337-5530; [b] orcid.org/0000-0003-6414-5233; [c] orcid.org/0000-0002-5337-5530;
[d] orcid.org/0000-0002-4629-6973
DOI: http://dx.doi.org/10.17515/resm2023.34st0824rs

structures play a vital role in safeguarding history and cultural heritage, and rubble masonry remains a durable construction method. It has effectively contributed to the construction of historical structures throughout various eras, underscoring its strength. Further this research underscores the importance of a well-balanced composition, which involves combining rubble masonry with additives like lime mortar and surkhi to ensure structural longevity. Additionally, it emphasizes the environmentally friendly aspect of this traditional construction technique, offering a sustainable alternative to conventional cement mortar. The case study of the Global Vipassana Pagoda in Mumbai serves as a compelling real-world example of the successful application of this approach.

A case study on Global Vipassana Pagoda, Mumbai, is considered in this study (See Fig. 1 (a) and (b)). It is located in Mumbai, India. It is located in the North of Mumbai on a peninsula between Gorai Creek and the Arabian Sea. The foundation of the dome was done with basalt stones. The general stratigraphy of the west coast of Mumbai is primarily composed of basalt rock with minimal overburden. The subsurface layers consist mainly of dark brown and highly fractured basalt rock with varying degrees of weathering. Mineral-filled fracture planes are common in the basalt. Some locations have a limited overburden of marine clay or silty sand. Highly fractured zones exist below the intact rock mass, and volcanic breccia with lapilli tuff is observed in the Back Bay area. Lapilli tuff exhibits varying degrees of weathering, with fracture planes filled with minerals. [1-2] Geological processes have led to the mixing of mafic and felsic melts in Mumbai's Manori–Gorai area, potentially forming rocks with intermediate characteristics.[3]

(a) (b)

Fig. 1. (a) Global Pagoda Vipassana, (b) Location on Google map

1.1. Literature Review

The following literature review provides a comprehensive understanding of the role of rubble masonry, mortar in heritage preservation and the diverse research efforts to address the challenges and opportunities associated with this critical component of historic structures.

Mortar is a binding material [4] which keeps the building blocks of standing structures together by providing strength and durability. Lime and gypsum mortars have been used in India for thousands of years. Today, cement mortar is used extensively in all modern buildings. Cement mortar encourages dampness and can destroy heritage structures that have stood for hundreds of years. It can also alter the appearance of the original structure; cement mortar may not be compatible with the original mortar used during the

construction of heritage structures, and cement mortar causes loss of breathability. Historic structures were designed to be breathable, allowing moisture to pass through the walls and evaporate, which helps prevent moisture-related damage. Cement mortar is less permeable than historic mortars and can cause moisture to be trapped inside the masonry, leading to decay and other forms of deterioration. The susceptibility of mortar to decay agents has been found to depend on the type of masonry, its location, the micro-climatic condition and the composition, texture, mechanical and micro-structural characteristics of the mortar.

In an experimental evaluation of stone masonry walls with lime-based mortar under vertical loads, failure was seen in all the walls considered in an experimental study [5]. Mortar was observed to be squeezed, and stone blocks failed due to splitting tension.

Commencing the chronological trajectory with B. K. Jindal's seminal work in 1965[6], the study delved into the influence of surkhi fineness on masonry strength. In 1998, the viability of shotcrete as a fortifying agent for historic rubble stone masonry walls was investigated, discerning augmented water vapour permeability and reduced porosity as salient outcomes [7]. After almost ten years, in 2007, the seismic comportment of a Romanesque Church dome was examined [8], contributing to the discourse on structural integrity. Later, an experimental study was performed [9] to study the shear strength of conventional rubble stone masonry walls, expounding on its mechanical performance. It was also found that mortar composition has an important influence on the shear strength. The compressive strength of lime mortars, integrating surkhi and kankar as pozzolanic agents, was studied [10]. The study notably revealed a significant 77% increase in strength for the former, particularly under controlled humidity conditions. Subsequently, an experimental study was conducted [11] to evaluate lime-based mortar-clad stone masonry walls. This culminated in identifying primary failure modes attributed to squeezing-induced splitting tension and subsequent compressive stone fracturing. A scholarly work was done by optimising Random Rubble Masonry (RRM) retaining wall design [12], intricately informed by comprehensive analyses encompassing compressive, flexural, and shear strength considerations. In 2020, the author examined ancient construction materials [13], comparing their pros and cons with modern practices, focusing on earth-based mortars and their clay mineralogy's effects. The study also discussed the use of brick-based mortar for strengthening walls and explored the significance of lime mortars in novel approaches for wall reinforcement. During the same period, a research study on the mechanical characterisation of eight rubble stone masonry walls from various structures of a Portuguese monument assessed their quality using the Masonry Quality Index (MQI) and the Italian Building Code Commentary (IBCC 2019) [14]. Quantitative criteria were proposed for rating mortar and stone quality in MQI, and correlations between mechanical properties obtained from IBCC 2019, MQI, and double flat-jack tests demonstrated the benefits of quality assessment in estimating masonry mechanical properties.

A numerical study elucidates the confinement pressure and interfacial bond behaviour governing the mechanical response of masonry walls [15]. The study assessed shear mechanical parameters of masonry samples, considering the effects of confinement pressure and bond behaviour at sample-plate interfaces on mechanical responses. An experimental study [16] assessed shear and compressive strength parameters for stone masonry assemblies in Eastern Canada, and valuable insights into the mechanical properties of unreinforced masonry walls used in heritage building construction were given. In antiquity preservation, non-destructive assessment of Roman rubble stone masonry structures illuminated structural dynamics and preservation imperatives through visual inspection and sonic pulse velocity tests, affording estimations of mechanical properties that substantiate informed preservation strategies [17]. The

restoration of Alamparai Fort, aided by Gur and Haritaki as additive agents, enabled its resilience against the Nivar cyclone in November 2020. This highlights the significance of analysing existing structures and choosing suitable binding additives to protect heritage sites. [18]. The research used non-destructive investigation methods to understand rubble stone masonry in Roman archaeological sites, particularly at Pompeii. The extensive data gathered through surveys and sonic pulse velocity tests provided valuable insights into the mechanical parameters of these ancient masonry structures, aiding in preservation efforts [19]. Another study assessed the seismic behaviour of double-leaf stone masonry piers through experiments and 3D finite element micro-modelling, offering a useful laboratory tool for modelling [20]. Additionally, an effective retrofit method, reinforced connected plaster, was experimentally confirmed to enhance in-plane cyclic response. The research study on masonry dome behaviours considers support conditions, thickness, and curve parameters to identify neutral hoops through graphical and numerical analysis. The results classified masonry domes into four types of behaviour based on variables, including single-masonry, double-masonry with a single neutral hoop, double-masonry with both compressive and tensile hoops and a single neutral hoop, and treble-masonry with two neutral hoops [21]. The non-destructive investigation [22] proved suitable for assessing the mechanical properties of heritage masonry structures, focusing on opus incertum rubble stone masonry at Pompeii. The extensive dataset, including sonic pulse velocity tests, allowed for robust estimations of the mechanical parameters essential for preservation efforts. The research investigated the compositional and textural properties of bedding mortars from the National Palace of Sintra, built over several centuries [23]. It established similar mortar compositions based on locally available materials but varied textural features according to use (interior/exterior), proposing distinct repair mortar formulations. The findings also suggested potential links between mortar characteristics and the monument's historical background, although further analysis is needed for definitive correlations with different construction periods.

The literature review concludes with an overview of research on masonry dome behaviours, assessing mortar quality in historic structures, and the compositional and textural properties of bedding mortars from historic sites. It stresses the need for further research to establish correlations between mortar characteristics and the historical context of monuments.

2. Material and Methods

2.1. Material Specifications

Fine aggregate river sand was used as fine aggregate. The specific gravity of sand was 2.63, and the fineness modulus of fineness was 2.52. Second material considered is Lime (Hydraulic lime). Mix design proportion considered as Lime: Surkhi: Sand= 1: 4: 15. Basalt stones: In rubble masonry cubes, basalt stones ranging from 5 to 30 cms were used. These basalt stones were acquired from a nearby site. These basalt stones occupy 65 to 70% of the total volume of the total proportion of cubes. Basalt stones used in the cube are shown in below figure 7(a).

- Quick Lime: Slaked lime was a binding material in rubble masonry. This quick lime is acquired from limestone mines in Rajasthan. This lime was slaked for seven days in water and used after its slaking. The slaking of lime is shown below in Figure 7(b).
- Surkhi: Surkhi means powdered broken brick. This surkhi is used as a pozzolanic material in a mortar. It imparts colour and plasticity to mortar.

- Sand: Sand is used to reduce the shrinkage of mortar. Fine river sand was used. This river sand had a fineness modulus of 2.5 to 2.8, and silt content should not be less than 5 to 6%.
- Carbon fibre reinforced polymer (CFRP): To avoid edge failure of the cube during compressive loading, carbon fibre-reinforced polymer of grade HM-30 (unidirectional) was used. Before its application, the matrix 20 solution as an adhesive was applied to the cube surface.
- Neoprene Rubber: For uniform distribution of load through the cube, neoprene rubber of 8mm thickness and 700x700mm size is placed on the top surface of the cube.

2.2. Experimental Work to Determine Material Properties:

2.2.1 Testing of Cube Specimens

As per the requirement for the experimental investigation, in-house fabrication for the moulds of cube specimens was carried out. The inside dimensions of the Mould Size = 600 x 600 x 600mm and Plate size = 700 x 700 x 20mm

2.2.2 Testing of Masonry core to evaluate Strength

This study examined three core samples as per IS: 456-2000 and IS 516 (Part 4). These standards provide guidelines for core testing to assess masonry quality. The cores were considered acceptable if their average strength met at least 85% of the required masonry strength, and no individual core had a strength below 75%. The study tested 16 cores for various properties, such as strength, water absorption, density, and specific gravity. These properties were compared with the percentage of basalt in the cores and the core's strength.

(a) (b)

Fig. 2. (a)Core samples before and after capping, (b)Testing of core in CTM

The core's strength was calculated using methods specified in IS: 14858, and the results were expressed in N/mm^2.Additionally, a correction factor based on the length-to-diameter ratio of the core specimen after capping was applied, following IS 14858. The core's material composition included lime, surkhi, sand, and basalt, with the mix proportion following standards. The core specimens had a diameter of 50mm, and their average length was 60-80mm. Refer Figure 2(a) and 2(b) for details. A correction factor, represented as "F," was determined based on the length-to-diameter ratio (l/d) of the core specimen after capping, using the equation F = 0.11N + 0.78, where "N" is the length/diameter ratio. This correction factor is used to adjust the cylinder strength, making it equivalent to the strength of a cylinder with a height/diameter ratio of 2. This adjusted cylinder strength is multiplied by 5/4 to estimate the concrete's equivalent cube strength.

The core material is composed of lime, surkhi, sand, and basalt, with a specific mix proportion of 1:4:15. The core specimens have a diameter of 50mm (with an in-situ diameter of 43mm) and vary in length from 60-80mm, with an average length of approximately 69.56mm. The result and analysis are summarised in Table 1.

Water absorption is determined by measuring the weight of cores after they've been soaked in water for 24 hours (saturated weight) and then dried in an oven for 24 hours at 100°C (dry weight). Water absorption is calculated based on these weights.

2.2.3 Test on Lime Mortar Cubes

In the present study, a compression test was done on lime mortar cubes to determine their strength on 7, 14 and 28 days, respectively. It is crucial to determine the strength of lime mortar as it governs the failure of rubble masonry used in the dome of the pagoda structure. For the determination of strength of lime mortar, 9 cubes of lime mortar having size 70mmx70mmx70mm with mix design as 1(lime): 4 (surkhi): 15(sand) is casted and tested for 7, 14 and 28 days respectively. Water to lime plus surkhi ratio is taken as 0.63.

The detailed test procedure for casting and testing lime mortar cubes is as follows:

- Lime slaking: Lime was slaked in water for seven days.
- Batching of materials: The materials were batched according to the mix design, which was 1:4:15 (Lime: Surkhi: Sand).
- Calculating lime density: The density of lime putty was calculated by measuring the weight of an empty vessel (w1) and the weight of the vessel filled with lime putty (w2). The density of lime putty was determined using a table from IS 712-1964.
- Mixing: Lime putty was added to a mixer and stirred to remove air bubbles. Dry surkhi was added, and the mixture was stirred for 5 to 7 minutes. Water was added as needed to make the mixture homogeneous. Finally, sand was added, and the mixer was operated until the mixture was properly homogeneous. (Figure 3 (a))

Fig. 3. (a) Mortar mixer, (b) curing of Lime mortar cube, and (c) UTM for compression test

- Casting: In three layers, the lime mortar mixture was poured into properly oiled moulds of size 70x70x70mm.
- Compaction: Vibratory compaction was performed to ensure the mixture was well-compacted.
- Demolding: Molds were de-moulded after the mixture attained sufficient strength to retain its shape.
- Curing: Lime mortar cubes were wrapped in gunny bags (Figure 3(b)) from all eight faces and cured for 7, 14, and 28 days by sprinkling water on the gunny bags.

- Water absorption measurement: On the day of casting, the dry weight of the cubes was measured. The water absorption of the cubes was calculated by subtracting their dry weight from their saturated weight.
- These cubes were then tested in the universal testing machine (UTM) (Figure 3 (c)) for compression,
- and results were noted down

2.2.4 Test on Rubble Masonry Cube

This experimental work aims to assess the compressive stress experienced by the rubble masonry and its associated structural properties, including the modulus of elasticity (E) and Poisson's ratio (μ).

This study evaluated the maximum compressive stress on rubble masonry and its modulus of elasticity(E) and poisons ratio(μ). A rubble masonry cube of 600x600x600mm was tested in a compression testing machine of 400 tonnes capacity. Using dial gauges and linearly variable differential transformer (LVDT), lateral and longitudinal strains were calculated to determine the modulus of elasticity and poisons ratio. The results obtained from these dial gauges and LVDTs were compared with compressive stress coming on rubble masonry. Comparison and test results are discussed below.

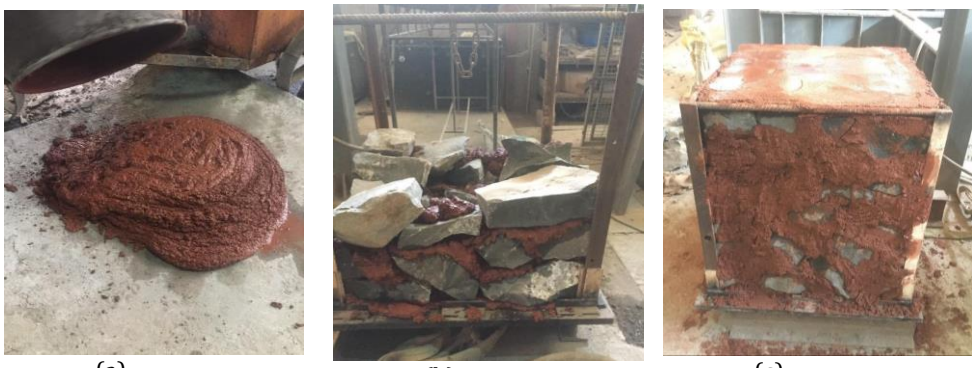

(a) (b) (c)

Fig 4. (a) Lime mortar, (b) Preparation of rubble masonry, and (c) final prepared rubble masonry cube

A specially fabricated 600x600x600mm test mould for rubble masonry was constructed, featuring a 20mm thick base plate and a 700x700mm height. An angle section was added at the corner to create a square cage, offering support and defining the mould's size boundary (See Fig 4©). Compression testing machine (CTM) with hydraulic lifting mechanism: A compression testing machine of 400 tones capacity was used to apply load on rubble masonry. Lime mortar preparation and arranging rubble masonry in layers can be seen in Fig 4(a) and Fig 4(b) respectively.

a. Preparation of rubble masonry cube

To prepare three rubble masonry cubes of size (600x600x600mm), same as above, three moulds of cubes with wooden shuttering were designed (Figure 5(a, b)). Wooden shuttering helps with the smooth finishing of rubble masonry cubes with mortar. It also allows for the confinement of the mould. Wooden shuttering of mould is shown in Figure 5(a). Casting of the cube is done in 2 phases. In 1st phase, 50% casting of 3 cubes is done. i.e., up to a height of 300mm. In 2nd phase, on the next day, the remaining casting is done.

(a) (b) (c)

Fig. 5. (a) Wooden shuttering of mould, (b) 1st phase casting of cube, and (c) final rubble masonry cube after phase 2

For casting, mortar volume was considered 30% of the total volume of 3 molds. The remaining 70 % of the volume was occupied by basalt stone sizes ranging from 5cms to 30cms, see Fig. 5(b). Rubble masonry cube was cast in 2 phases. In 1st phase, 50% of casting up to a height of 300mm was done, as shown in the figure. During casting, initially, a layer of lime mortar was placed at the bottom of the mould. Stones of sizes ranging from from 5cms to 30cms were used. A skilled mason did the placing of stones with experience in this field. All the gaps between these stones were filled by prepared lime mortar. The workability of mortar should be such that it should fill all the voids between stones. The same procedure was repeated as above for 2nd phase of casting(Fig 5(c)), which should be done on the 2nd day of 1st phase. After the construction of both phases, wooden shuttering was removed and kept from curing, as shown in the figure below. The curing of the cube was done by sprinkling water regularly.

b. Preparation of lime mortar

Thirty Percent of the total volume of mould is taken as lime mortar. i.e., around 0.1944 m^3. Mortar is prepared with a mix design 1:4:15 (Lime: Surkhi: Sand). From the mix design, the quantity of lime is calculated, and it is slaked in water for seven days before the day of casting. The density of lime is calculated by a 300 ml glass in gm/ml. The yield of lime is obtained using IS 712 from the density of lime. Multiplying this yield with the quantity of lime slaked in water gives a total amount of lime in liters used for mixing. First, lime and surkhi are added to the mixer. After 5-7 min of mixing, sand was added to a mixer. An adequate quantity of water is added for a homogeneous mortar mixture during the mixing.

The test procedure involved several steps: The compression testing machine (CTM) had the least count of 0.1 tonnes and used a hydraulic jack for load application, connected to a load cell, with the load cell's data sent to an indicator. A dial gauge with a 0.01mm least count measured the upward displacement of the base plate during force application. Six LVDTs with a least count of 1 x 10^-14 cm were used to measure lateral and longitudinal deflection at various locations connected to a data acquisition system. Lime mortar was prepared in a transit mixer following a specific procedure. The cube was constructed by placing layers of lime mortar and stones, with lime mortar layers at the top and bottom. Curing was done by wrapping gunny bags and sprinkling water. Carbon fibre-reinforced polymer (CFRP) was applied to avoid edge failure, and the cube was placed on the CTM for testing. LVDTs and dial gauges were connected for data acquisition and calibrated, and then the load was gradually applied until failure, with deformations recorded.

3. Results and discussions:

3.1 Evaluation of Masonry Strength Using Core Testing:

Table 1 indicates the percentage of basalt and respective core strength, water absorption, density and porosity and specific gravity of the core sample. It also indicates that failure is through mortar or basalt.

Test on the core sample shows that increased water absorption percentage decreases core strength. The strength of 95 MPa at 0.65% water absorption reduces to almost 5 MPa with 3.50% water absorption.

- Density of Cores: Core density is calculated by dividing the dry weight of the core by its volume, taking into account the uncapped length. Density is an important parameter for core analysis.
- Porosity of Cores: Porosity is determined by weighing the dry core and then saturating it with either water or air. The fluid weight in the pore space is calculated from the difference between the saturated and dry weights. The pore volume is obtained by dividing this number by the density of the saturated fluid. Table 1 shows that as the percentage of basalt increases, porosity decreases.
- Specific Gravity of Cores: Specific gravity is calculated by dividing the core's density by the density of water. The analysis shows that specific gravity remains relatively constant regardless of the percentage of basalt.

In terms of core failure patterns, the samples primarily fail at the interface between the lime surkhi mortar and the basalt components, often in a shear failure pattern. Shear failure occurs when forces applied to the materials cause them to slide along the interface, resulting in material cracks. The comparison between core test values and the analysis-design report values is provided in Table 2, offering insights into how the core test results align with the expected values outlined in the design report.

Table 1. Test results of core samples with various strength parameters

Sr. Sr No.	Percentage Of basalt	Core Strength (MPa)	Water Absorption %	Density	Porosity	Specific Gravity	Failure through
1	12.28	5.13	3.50	2.48	7.32	2.26	Mortar
2	25.08	6.23	2.58	2.05	5.30	2.17	Mortar
3	29.02	10.36	2.82	2.22	6.26	2.37	Mortar
4	35.47	22.89	2.20	2.11	4.65	2.22	Mortar
5	38.35	22.10	3.40	1.93	5.49	2.11	Mortar
6	41.39	22.84	3.70	1.97	5.30	2.13	Mortar
7	45.02	18.70	2.84	2.31	6.56	2.47	Mortar
8	62.53	53.57	2.51	2.38	5.99	2.54	Basalt
9	63.54	40.24	2.14	2.48	5.30	2.62	Mortar
10	69.35	68.15	1.82	2.65	4.83	2.80	Basalt
11	70.47	62.00	1.83	2.61	4.78	2.74	Basalt
12	72.16	85.85	2.62	2.50	3.53	2.67	Basalt
13	72.70	87.91	1.40	2.51	3.50	2.60	Basalt
14	74.52	101.55	1.44	2.73	3.94	2.83	Basalt
15	75.67	65.20	1.71	2.93	2.99	3.07	Basalt
16	94.98	92.94	0.65	3.01	1.977	3.07	Basalt

Fig. 6. Failure patterns of core samples

The failure pattern (Fig. 6) of the samples is predominantly at the interface between the lime surkhi mortar and the basalt components. This type of failure pattern is called a "core cut failure," which arises when a core sample is extracted from a masonry structure to evaluate its strength characteristics. In this context, the interface between the lime surkhi mortar and the basalt is critical in determining the structural integrity. Failure can be a shear, tensile, compressive, and debonding failure. However, the failure pattern is attributed to shear failure in the test scenario under consideration. Shear failure occurs when the forces applied to the materials cause them to slide against each other along the interface, resulting in cracks in the material. Comparison between core test values and analysis–design report values are given in Table 2.

Table 2. Comparison of strength parameters

Parameters	Core test values		Analysis & design report values (IIT, Bombay)
	Min.	Avg.	
Strength (MPa)	1.677	36.59	1.42
Density (kN/m^3)	18.96	23.85	24
Water absorption (%)	4.396 (Max)	2.384	5

3.2 Result of Test on Lime mortar

Nine cubes underwent testing, with each set of three cubes subjected to compression tests at 7, 14, and 28 days, respectively, using a Universal Testing Machine (UTM) as depicted in Figure 3(c). The corresponding compressive strength results for these durations are provided in Table 3, and a visual representation is presented in Figure 7. A notable trend is observed in the compressive strength, indicating a 54.025% increase from 7 to 14 days and a further 57.09% increase from 14 to 28 days. This suggests a linear increase in strength with the extension of curing time up to 28 days, as illustrated in Figure 7.

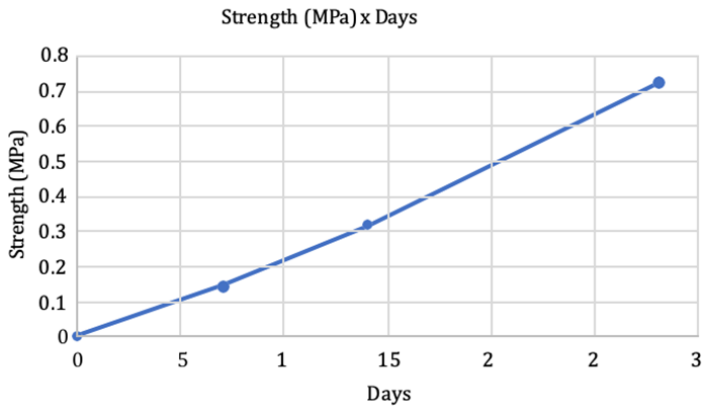

Fig. 7. Strength (MPa) vs days (Curing)

Table 3. Test results of 7-, 14- and 28-days compressive strength

Sample	Saturated wt(gm)	Dry wt(gm)	Load (N)	Strength (N/mm^2)	%Water absorption	Strength (Mpa)
7 days of compressive strength						
1	712	614	736	0.15	15.96	0.15
2	706	610	706	0.14	15.73	0.14
3	710	619	686	0.14	14.70	0.14
Average value				0.14	15.46	0.14
14 days compressive strength						
1	711.50	617	1520	0.31	15.31	0.31
2	705.50	607	1569	0.32	16.22	0.32
3	719.50	605	1539	0.31	18.92	0.31
Average value				0.31	16.82	0.31
28 days compressive strength						
1	692	641	3726	0.76	7.95	0.76
2	704	629.50	3432	0.70	11.83	0.70
3	724.50	654	3628	0.74	10.77	0.74
Average value				0.73	10.19	0.73

3.3 Test Results on Rubble masonry

Batching was done according to the mix design 1:4:15 (Lime: Surkhi: Sand). Taking 35% of the total volume as lime mortar, it turns out to be 0.0756 m^3. Lime quantity was 7.98 kg, surkhi was 31.95, and sand was 119.7 kg. The reason for selecting these proportions lies in achieving the desired characteristics of the mortar, such as strength, workability, and durability. Lime contributes to binding, while surkhi and sand provide filler and aggregate. The specific proportions aim to optimise these factors for the intended application.

After applying load in CTM, the cube failed at 38 tonnes, equivalent to 1.034 Mpa. Failure of the cube is shown in Figure 8. The reason for this failure can be attributed to factors like the composition and quality of the materials used in the cube's construction, the curing

conditions, and the structural integrity of the cube itself. The cube's breaking load and its conversion to stress provide valuable insights into its compressive strength, which is a critical parameter in assessing the performance of masonry materials and structures under load-bearing conditions.

Fig 8 Failure of cube

Calculation of modulus of elasticity (E) and poisons ratio (μ) According to ASTM C 469,

- The modulus of elasticity (E) is the ratio of normal stress to the corresponding strain for compressive stresses below the proportional limit of concrete.
- Poisons ratio (μ) is lateral to longitudinal strain for related compressive stress.
- The modulus of elasticity and Poisson's ratio values are applicable within the customary elastic range (0 to 40 % of ultimate load).

A summary of test results from LVDT is given in Table 5.

Table 5. Overview of test results

LVDT	Position	Avg. Strain	Modulus of elasticity (E) (MPa)	Poisons ratio (μ)	
				S3	S6
S1	Back	0.00040	517.38	0.25	0.24
S2	Front	0.00042	480.15	0.22	0.22
S3	Right- Lateral	0.00011			
S4	Right	0.00044	454.19	0.21	0.21
S5	Left	0.00042	482.45	0.22	0.26
S6	Front- Lateral	0.00011			
		Average	E=483.54	μ=0.22	μ=0.23

From the stress vs strain graph as shown in Fig.9 (a-d), it is observed that for all the strain gauges, nonlinear behaviour is observed till the visible peak point of strain value of 0.0026 at 0.87MPa and after that, strain continuously increases from 0.0026 to 0.012 with an increase in strength from 0.87MPa to 1.03MPa. Later behaviour resembles linear behaviour. From LVDT readings, the average modulus of elasticity(E) is 458.4427109 Mpa, and the poisons ratio(μ) is 0.211.

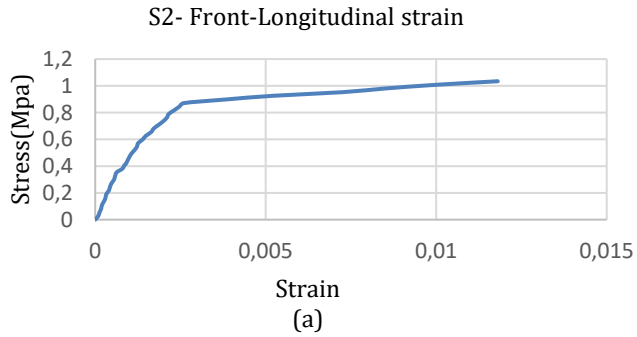

(a)

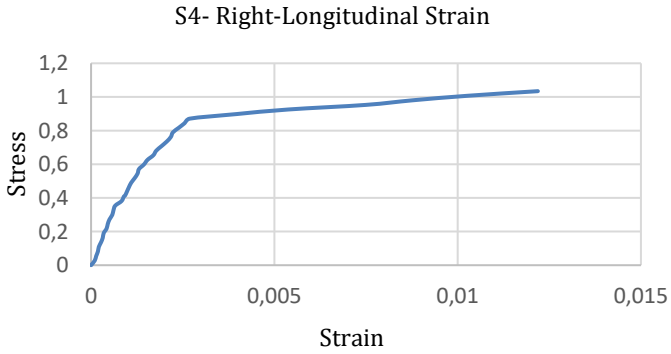

(b)

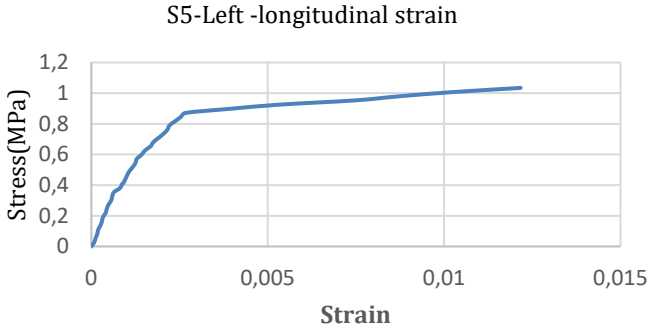

(c)

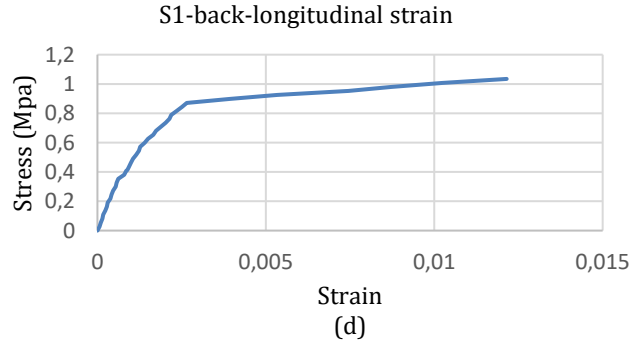

(d)

Fig. 9. Stress vs strain (a), (b), (c) and (d)

From the failure of the cube, it is observed that mortar strength is the governing factor for the strength of rubble masonry, as the failure strength of rubble masonry cube closely resembles the strength of lime mortar cubes. (1 MPa).

The stress-strain graph of rubble masonry exhibits a distinctive pattern: initially, the graph follows a parabolic shape, signifying a nonlinear stress response. As the strain increases, the curve transitions into a more linear trajectory. This behaviour suggests that at lower stress levels, the material undergoes deformation with a nonlinear relationship between stress and strain. However, as the stress increases, the response becomes more consistent and linear, indicating a more predictable deformation pattern. This observation shows the complex mechanical behaviour of rubble masonry, highlighting the need to consider its nonlinear and linear aspects for accurate structural analysis and design. From LVDT readings, we can conclude that the average modulus of elasticity(E) is 483.54 MPa, and the poisons ratio(μ) is 0.225 (Refer Table 5). This modulus of elasticity signifies the material's ability to deform elastically under an

applied load and return to its original shape once removed. A higher modulus of elasticity indicates a stiffer material that undergoes minimal deformation. A Poisson's ratio of 0.225 suggests that the material experiences a relatively small lateral expansion when subjected to axial compression or tension. This value aids in understanding the material's deformation behaviour and is crucial for accurate structural analyses and design considerations. From the failure of the cube, it is observed that mortar strength will govern the strength of rubble masonry, as the failure strength of rubble masonry cube closely resembles the strength of lime mortar cubes. (1 MPa).

This finding underscore mortar's critical role in determining rubble masonry's overall load-bearing capacity and structural integrity. While other factors, such as the arrangement of stones and the interlocking mechanism between them, undoubtedly contribute to the masonry's strength, the mortar's bonding capacity emerges as a primary factor. The failure pattern and load-carrying ability of the masonry largely depend on the adhesion and cohesion properties of the mortar.

4.Conclusion

This experimental investigation into core samples from the Pagoda in Borivali, Mumbai, has provided valuable insights into the properties of the rubble masonry used in this heritage structure. The calculation of the percentage of basalt in the core samples revealed a positive correlation between the presence of basalt and the strength of the core, indicating that a higher basalt content contributes to increased strength.

Additionally, the study found that water absorption is a crucial factor affecting the strength of the core samples, with higher water absorption leading to reduced strength. The density of the cores was determined, considering the uncapped length, and porosity measurements showed that as the percentage of basalt in the samples increased, porosity decreased. Finally, the specific gravity of the cores remained relatively constant across different basalt proportions. These findings provide valuable information for the preservation and structural assessment of the Pagoda and similar heritage structures that utilize rubble masonry.

In addition to the findings, it is crucial to note that the predominant failure pattern observed in the core samples is the "core cut failure." This type of failure occurs at the interface between the lime surkhi mortar and the basalt components and is common when core samples are extracted from masonry structures for strength evaluation. The interface between these two materials plays a critical role in determining the structural integrity of the core samples. Failure modes, such as shear, tensile, compressive, and debonding, are

typically considered in structural assessments. However, in the specific test scenario under consideration, shear failure emerged as the predominant mode. Shear failure occurs when the applied forces cause the materials to slide against each other along the interface, leading to the development of cracks in the material. Understanding this failure pattern is essential for assessing the structural behavior and durability of rubble masonry in heritage structures like the Pagoda in Borivali, Mumbai, and can inform strategies for its preservation and maintenance.

Additionally, it is important to highlight that a total of nine cubes underwent testing. The data reveals a noteworthy trend in the compressive strength of the cubes over time. Between the 7-day and 14-day curing periods, there was a substantial 54.025% increase in strength, and from the 14-day to the 28-day duration and there was an impressive 57.09% increase in strength is observed. These findings emphasize the importance of considering the curing period when evaluating the compressive strength of the core samples, as it has a significant impact on structural performance.

In conclusion, the experimental investigation of rubble masonry used in heritage structures, such as the Global Vipassana Pagoda in Borivali, Mumbai, India, was conducted. This type of rubble masonry serves a crucial role in transferring the load on the dome of the Pagoda from the superstructure to its foundation. Given the dome's shell-like structure, the forces acting on this rubble masonry are primarily compressive. As part of this experimental program, the compressive stress on the rubble masonry was evaluated, along with its structural properties, including the modulus of elasticity (E) and Poisson's ratio (μ).

From the above experimental study, it can be concluded that it is possible to create heritage structures using rubble masonry with Lime surkhi mortar even today. Global Pagoda Vipassana in Mumbai, India, represents an excellent example. Preserving heritage structures is crucial, with rubble masonry playing a key role in this effort. As a traditional wall construction material in India, rubble masonry has stood the test of time, both in ancient and contemporary times, contributing to heritage structures. A combination of rubble masonry with additives like lime mortar and surkhi is essential to ensure structural longevity. This study uses rubble masonry, lime mortar, and surkhi to repair and construct heritage structures, serving as an eco-friendly alternative to conventional cement mortar. The case study of the Global Vipassana Pagoda in Mumbai exemplifies this approach. By analysing stress-strain graphs, LVDT readings, and cube failure patterns, it's evident that the material properties and composition, especially mortar strength, greatly influence the structural integrity and load-bearing capacity of rubble masonry. This experimental study offers insights into designing and preserving heritage structures using the time-tested technique of rubble masonry with lime mortar and Surkhi.

Acknowledgement

The authors acknowledge the lab support provided at Veermata Jijabai Institute of Technology.

References

[1] Rani VR, Pandalai HS, Sajinkumar KS, et al. Geomorphology and its implication in urban groundwater environment: a case study from Mumbai, India. Appl Water Sci. 2015;5:137-151. https://doi.org/10.1007/s13201-014-0168-8

[2] Birid K. Geotechnical investigations to assess subsurface stratigraphy of West Coast of Mumbai-A case study. 2006.

[3] Zellmer G, Sheth H, Iizuka Y, Lai YJ. Remobilization of granitoid rocks through mafic recharge: Evidence from basalt-trachyte mingling and hybridization in the Manori-

Gorai area, Mumbai, Deccan Traps. Bull Volcanol. 2012. https://doi.org/10.1007/s00445-011-0498-4
[4] Rangawala SC. Engineering Materials. 43rd ed. Charotar Publishing House Pvt. Ltd.; 2017. ISBN-13: 978-9385039171, ISBN-10: 9385039172
[5] Abdel-Mooty M, Al Attar A, El Tahawy M. Experimental evaluation of stone masonry walls with lime-based mortar under vertical loads. WIT Transactions on The Built Environment. 2011;118. https://doi.org/10.2495/STR110331
[6] Jindal BK. Effect of fineness of surkhi on the strength and water tightness of masonry. ISI Bulletin. 1965;17:194-196. https://doi.org/10.1016/0031-9163(65)90477-4
[7] Pinho FFS, Lucio VJG, Faria P. Durability aspects related to rubble stone masonry walls strengthened with reinforced micro-concrete layers. In: An international seminar on seismic risk and rehabilitation of stone masonry housing. Azores; 1998.
[8] Bettt M, Vignoli A. Modelling and analysis of a Romanesque church under earthquake loading: Assessment of seismic resistance. Department of Civil and Environmental Engineering, University of Florence, I-50139, Florence, Italy; 2007.
[9] Milosevic J, Bento R, Gago AS, Lopes M. Shear Tests on Rubble Stone Masonry Panels - Diagonal Compression Tests. In: 15th World Conference in Earthquake Engineering. IST, Technical University of Lisbon, Portugal; 2012. Available at: https://www.iitk.ac.in/nicee/wcee/article/WCEE2012_1190.pdf
[10] Javed U, Khan A, Iqbal AM, Arif S. Compressive strength of lime mortars with surkhi and kankar as pozzolans under normal and humid conditions. Sci Int (Lahore). 2016;28(4):3889-3892.
[11] Abdel-Mooty M, Khedr S, Mahfouz T. Evaluation of lime mortars for the repair of historic buildings. WIT Transactions on The Built Environment. 2009;109. https://doi.org/10.2495/STR090191
[12] Karunaratne KK, Santhajeewa AN, Nanayakkara D. Investigation of strength properties of random rubble masonry for design optimization. In: The 7th International Conference on Sustainable Built Environment. Earl's Regency Hotel, Kandy, Sri Lanka from 16th to 18th December 2016.
[13] Damera R, Purumani S. Integration of materials used in ancient structures for present-day construction. Int J Adv Sci Technol. 2020;29(4):280-288.
[14] Ferreira Pinto AP, Sena da Fonseca B, Vaz Silva D. Mechanical characterization of historical rubble stone masonry and its correlation with the masonry quality assessment. Construction and Building Materials. 2021;281:122168. https://doi.org/10.1016/j.conbuildmat.2020.122168
[15] Angiolilli M, Gregori A. Triplet Test on Rubble Stone Masonry: Numerical Assessment of the Shear Mechanical Parameters. Buildings. 2020;10(3):49. https://doi.org/10.3390/buildings10030049
[16] Abo El Ezz A, et al. Experimental assessment of stone masonry material parameters for the seismic evaluation of heritage wall buildings. In: 16th World Conference of Earthquake Engineering. 2017. Available at: https://www.wcee.nicee.org/wcee/article/16WCEE/WCEE2017-3880.pdf
[17] Autiero F, De Martino G, Di Ludovico M, Prota AE. Structural Assessment of Ancient Masonry Structures: An Experimental Investigation on Rubble Stone Masonry. International Journal of Architectural Heritage. 2021;17:815-828. https://doi.org/10.1080/15583058.2021.1977418
[18] Santhanam K, Ramadoss R. Investigation of Alamparai Fort by utilization of organic materials for the improvement of stability of heritage structure. Environmental Science and Pollution Research. 2021;29:86036-8605. https://doi.org/10.1007/s11356-021-16212-3
[19] Francesca Autiero, Giuseppina De Martino, Marco Di Ludovico & Andrea Prota (2023) Structural Assessment of Ancient Masonry Structures: An Experimental Investigation

on Rubble Stone Masonry, International Journal of Architectural Heritage, 17:5, 815-828 https://doi.org/10.1080/15583058.2021.1977418

[20] Costa AA, Arêde A, Costa A, et al. Experimental testing, numerical modelling and seismic strengthening of traditional stone masonry: comprehensive study of a real Azorian pier. Bull Earthquake Eng. 2012;10:135-159. https://doi.org/10.1007/s10518-010-9209-3

[21] Asem Sharbaf, Mohammadreza Bemanian, Khosro Daneshjoo and Hamzeh Shakib. Masonry Dome Behavior under Gravity Loads Based on the Support Condition by Considering Variable Curves and Thicknesses. MDPI. 2021. https://doi.org/10.3390/buildings11060241

[22] Fonseca BS, Pinto AP, Silva DV. Compositional and textural characterization of historical bedding mortars from rubble stone masonries: Contribution for the design of compatible repair mortars. Construction and Building Materials.

Research on Engineering Structures Materials

Scopus®

DRJI

TÜBİTAK ULAKBİM

ProQuest

crossref

Google Scholar

Universal Impact Factor

Scientifically derived Journal Impact Factor

SIS Scientific Indexing Services

Journal Seeker Research Bible

CiteFactor

Academic Scientific Journals

EZB Elektronische Zeitschriftenbibliothek

Open Academic Journals Index

GIF GLOBAL IMPACT FACTOR

ASOS indeks

Cosmos

Publication Forum

İNFOBASE INDEX

ROOTINDEXING

JOURNAL ABSTRACTING AND INDEXING SERVICE

Scope Database

Journal Indexing & Citation Analysis

Research Group

https://mimrg.net/